UNIVERSITÄT OSNABRÜCK

Determination of the spatiotemporal organization of mitochondrial membrane proteins by 2D and 3D single particle tracking and localization microscopy in living cells

Dissertation

Zur Erlangung des akademischen Grades

Doctor rerum naturalium

(Dr. rer. nat.)

Vorgelegt am Fachbereich Biologie/Chemie

der Universität Osnabrück

von

Timo Dellmann
aus
Monheim am Rhein

Osnabrück, 2020

Table of contents

1 Abstract 11

2 Zusammenfassung 13

3 List of Publications 17

3.1 Dynamic Imaging of Mitochondrial Membrane Proteins in Specific Sub-Organelle Membrane Locations 17

3.2 Single Molecule Tracking and Localization of Mitochondrial Protein Complexes in Live Cells 17

3.3 Multi-color Localization Microscopy of Single Membrane Proteins in Organelles of Live Mammalian Cells 17

3.4 The spatiotemporal organization of mitochondrial F_1F_0 ATP synthase in cristae depends on its activity mode 17

4 List of abbreviations 19

5 Introduction 23

5.1 Biological background 23

5.1.1 Mitochondrial structure 23

5.1.2 Subcompartmentalization of mitochondria and distribution of mitochondrial proteins 24

5.1.3 The F_1F_0 ATP synthase 25

5.1.4 The electron transport chain and oxidative phosphorylation 29

5.1.5 Metabolic organization of OXPHOS proteins and bioenergetic pathways 30

5.1.6 The mitochondrial inner membrane organizing system / mitochondrial contact site and cristae organization system 32

5.1.7 Mitochondrial protein import system 34

5.1.8 Central mitochondrial proteins 35

5.2 Studying individual proteins *in situ*: single molecule microscopy and super-resolution microscopy 36

6 Aims 40

6.1 First aim 40

6.2 Second aim 40

6.3 Third aim 40

6.4 Fourth aim 40

7 Strategy 42

8 Methods 44

8.1 Multi-color total internal reflection fluorescence microscope setup 44

8.2 Molecular Biological Methods 46

8.3 Cell Culture and Cultivation of Cells 46

8.3.1 Growth and imaging conditions 47

8.4 Coverslip Coating 47

8.5 Cell Seeding 48

8.6 Transfection 48

8.7 Labeling of fusion proteins 49

8.7.1 Labeling procedure 50

8.8 Specimen Clamping 50

8.9 Dual- or multi-color image splitter alignment 51

8.10 Preparation of samples for astigmatic distortion calibration and 3D point spread function measurement 52

8.11 Imaging mitochondria for tracking and localization microscopy in a TIRF microscope 52

8.12 Single molecule localization and single particle tracking 53

8.12.1 2D Tracking and localization microscopy 53

8.12.2 Alignment of the Cylindrical Lens 55

8.12.3 3D localization, 3D reconstruction and 3D tracking 57

8.12.4 Directionality analysis of diffusive proteins 60

9 Results 62

9.1 Optimized cell density to image mitochondria and single mitochondrial proteins 62

9.2 Mono Color Single Particle Tracking 63

9.2.1 Dynamic Imaging of Mitochondrial Membrane Proteins in Specific Sub-Organelle Membrane Locations 63

9.2.2 F_1F_0 ATP-Synthase tracking during inhibition of ATP synthesis 72

9.2.3 F_1F_0 ATP synthase in starving conditions 77

9.3 Dual-color TALM of mitochondrial membrane proteins 119

9.3.1 Adaptation of labeling concentrations in dual-color experiments 119

9.3.2 Dual-color TALM of Tom20:HaloTag:fSnapTag 120

9.3.3 Dual-color TALM of F_1F_0 ATP synthase subunit-γ and F_1F_0 ATP synthase subunit-e 124

9.3.4 Dual-color TALM of F_1F_0 ATP synthase subunit-γ and MINOS/MICOS subunit-10 134

9.4 Transmission electron microscopy of HeLa cells stably expressing F_1F_0 ATP synthase subunit-γ:HaloTag in different metabolic conditions 140

9.4.1 Transmission electron microscopy of HeLa cells stably expressing F_1F_0 ATP synthase subunit-γ:HaloTag 140

9.4.2 Transmission electron microscopy of of HeLa cells stably expressing the F_1F_0 ATP synthase subunit-γ:HaloTag after 2 hours of starvation 141

9.4.3 Transmission electron microscopy of of HeLa cells stably transfected with F_1F_0 ATP synthase subunit-γ:HaloTag during improved respiration 142

9.5 3D TALM of mitochondrial membrane proteins 147

9.5.1 Calibration of the astigmatic distortion 148

9.5.2 3D axial localization range 148

9.5.3 3D localization precision 149

9.5.4 3D TALM of Tom20 151

9.5.5 3D TALM of F_1F_0 ATP synthase subunit-γ 159

9.5.6 3D TALM of the F_1F_0 ATP synthase subunit-γ in cells during starvation 174

9.5.7 3D TALM of F_1F_0 ATP synthase subunit-γ in improved respiring conditions 176

9.5.8 Trajectory directionality analysis in 3D tracking and localization microscopy of the F_1F_0 ATP synthase subunit-γ in cells in different metabolic conditions 185

9.5.9 3D diffusion of the F_1F_0 ATP synthase subunit-γ in cells during different metabolic conditions 196

9.5.10 Summary of 3D TALM of the F_1F_0 ATP synthase subunit-γ in cells during different metabolic conditions 197

10 Discussion and Conclusion 201

10.1 TALM of mitochondrial proteins 201

10.1.1 TALM allows to determine the spatiotemporal organization of mitochondrial proteins and to detect mitochondrial subcompartments 201

10.1.2 Spatiotemporal protein organization of the F_1F_0 ATP synthase is coupled to its functionality 208

10.1.3 Spatiotemporal protein organization of the F_1F_0 ATP synthase is coupled to the metabolic state of the cell ... 209

10.2 Dual-color TALM of mitochondrial membrane proteins ... 219

10.2.1 Colocalization and co-locomotion events of mitochondrial proteins cannot be revealed by posttranslational and substoichimetric labeling ... 219

10.2.2 Spatiotemporal protein organization of the F_1F_0 ATP synthase is influenced by dimerization inducing subunit-e ... 220

10.2.3 MINOS/MICOS regulates the shape of the IM and influences the spatiotemporal organization of the F_1F_0 ATP synthase ... 222

10.3 3D tracking and localization microscopy compared to 3D super-resolution techniques ... 225

10.3.1 The outer mitochondrial membrane revealed by 3D TALM compared to 3D STORM and TILT3D ... 227

10.3.2 3D TALM of F_1F_0 ATP synthase subunit-γ revealed IM structure in living cells in different metabolic conditions ... 229

11 Outlook ... 243

12 Supplements ... 245

13 Appendix ... 257

13.1 Additional figure ... 257

13.2 Figure legend ... 258

13.3 Table legend ... 264

13.4 Material ... 265

13.4.1 Cells ... 265

13.4.2 Cell Culture ... 265

13.4.3 Chemicals ... 266

13.4.4 Equipment ... 267

13.4.5 Experimental Setups ... 267

13.4.6 Fluorescent Dyes and Beads ... 268

13.4.7 Plasmids ... 268

13.4.8 Software/Algorithms ... 268

13.5 Additional publications ... 270

13.5.1 Single Molecule Tracking and Localization of Mitochondrial Protein Complexes in Live Cells 270

13.5.2 Multi-color Localization Microscopy of Single Membrane Proteins in Organelles of Live Mammalian Cells 289

13.5.3 The spatiotemporal organization of mitochondrial F_1F_0 ATP synthase in cristae depends on its activity mode 302

14 References 325

15 Statutory Declaration 337

16 Acknowledgement 339

1 Abstract

Mitochondria are the power plant of most non-green eukaryotic cells. In order to understand mitochondrial functions and their regulation, knowledge of the spatiotemporal organization of their proteins is important. Mitochondrial membrane proteins can diffuse within membranes. They are involved in diverse functions e.g. protein import, cell respiration, metabolism, metabolite transport, fusion, fission or formation of the mitochondrial architecture. Furthermore, mitochondria compose of different subcompartments with different tasks. Especially, the inner mitochondrial membrane (IM), where the oxidative phosphorylation (OXPHOS) takes places, has a complex architecture with cristae extending into the matrix. The present work revealed the restricted localization of some mitochondrial proteins to specific membrane sections and linked it to their function or bioenergetic circumstances in the living cell.

Single particle tracking (SPT) techniques like tracking and localization microscopy (TALM) allow to localize proteins with a precision below 20 nm. Additionally, tracking single proteins provides information about their mobility, dynamic and their spatiotemporal organization. TALM uses proteins, which were genetically tagged either with the HaloTag® (HaloTag) or the fSnapTag® (fSnapTag). These tags can be orthogonally and posttranslationally stained with specific and self-marking dyes. If the dyes are conjugated to the respective substrate of the tag. Single molecule labeling of mitochondrial proteins was performed substoichiometrically using membrane permeable rhodamine dyes, either tetramethylrhodamine (TMR) or silicon rhodamine (SiR). TALM allowed to localize proteins in different mitochondrial subcompartments. The gained trajectories and trajectory maps of mitochondrial proteins revealed their spatiotemporal organization. In the case of IM proteins like F_1F_0 ATP synthase (Complex V - CV) a restricted diffusion in the CM, which is part of the continuous IM, was determined. The unimpeded diffusion of mitochondrial proteins in the outer mitochondrial membrane (OM) was compared with the mobility of IM proteins. The diffusion of mitochondrial IM proteins was restricted by the IM architecture and their diffusion coefficients were lower. Furthermore, significant differences of different mitochondrial IM proteins were compared, showing different localizations in the IM often coupled to their function, accompanied by different spatiotemporal organization and diffusion coefficients. Furthermore, a distinction was made between diffusion of proteins in the inner boundary membrane (IBM) and proteins that preferentially diffuse in the cristae membrane (CM). Evaluating trajectory maps, the different subcompartments in the IM were revealed by trajectories and the trajectory directionality, allowing the identification of mitochondrial proteins, which mark these subcompartments.

The morphology of mitochondria / mitochondrial networks and their bioenergetic parameters are linked to the metabolic states of the cell. In this work, the connection of the spatiotemporal protein organization of CV and the IM architecture was uncovered on the micro- and nanoscopic level and linked to the metabolic state of the cell. It was determined that the spatiotemporal organization of the CV was altered, when CV was inhibited. In addition, the bioenergetic influence of cells on the spatiotemporal behaviour of CV and the reorganization of the IM architecture was investigated by TALM and compared with results of electron microscopy images. It was shown that starvation of cells led to a loss of cristae and thus to an increased mobility and spatiotemporal reorganization of CV. Taken together, the results presented in this work showed that a correctly functioning and active CV helps to maintain the IM architecture and both, the

spatiotemporal organization of CV and the IM architecture were coupled to the metabolic state.

In order to investigate putative protein-protein interactions by colocalization and co-locomotion studies on single molecule level, dual color SPT is needed. Therefore, posttranslational and substoichimetric labeling as performed in TALM was tested for its potential of protein-protein interaction studies of mitochondrial membrane proteins. Here, a genetically double tagged translocase of the outer membrane subunit-20 (Tom20) (Tom20:HaloTag:fSnapTag) acted as a positive control. It turned out that substoichimetric, posttranslational labeling of mitochondrial proteins was not suitabl for protein-protein interaction studies on mitochondrial proteins, because it was restricted by the low labeling degrees needed for TALM. However, dual-color TALM still allowed to study effects of proteins influencing the IM architecture and to study their influence on the spatiotemporal organisation of CV. The co-transfection of Mic10, as the central protein of the mitochondrial inner membrane organizing system / mitochondrial contact site complex / mitochondrial organizing structure (MINOS / MICOS / MitOS (MINOS/MICOS)), altered the regular and aligned organization of the cristae. This was measured by a changed spatiotemporal organization of the CV, such as the loss of the perpendicular oriented of CV subunit-γ (CV-SUγ) cristae trajectories. In contrast to this, co-transfection of CV subunit-e (CV-SUe), important for dimerization of CV, increased the number of cristae trajectories.

Mitochondria are three-dimensional (3D) cell organelles. Consequntly subcompartments like the IBM and CM are a 3D space in which CV is localized and diffuses. Thus, the diffusion of mitochondrial proteins is underestimated by two-dimensional SPT e.g. lateral confined diffusion can result from mitochondrial proteins diffusing along the z-axis of the microscope. In order to reveal the 3D spatiotemporal organization of CV, the potential of TALM to be extended to a 3D-SPT technique was investigated. Therto a cylindrical lens was installed in the emission path of a total internal reflection fluorescence (TIRF) microscope. This leads to an astigmatically distorted point spread function (PSF) of the fluorescent single molecule signals. This distortion allowed the reconstruction of single molecule localizations of CV to a superresolved image of the IM, in living cells. In addition, 3D-TALM enabled to display the 3D architecture of the IM by 3D trajectories of CV. 3D-TALM was able to detect whether CV diffuses in the IBM or in the CM, and extended the information about its mobility in the CM that it takes place in a disc-like manner. In this way it could be shown that CV is mobile within the cristae in all directions. Finally, 3D-TALM revealed an altered IM architecture caused by the metabolic state of the cell. As performed in two-dimensional TALM, the cells were kept under starving conditions. Here the now tubular IM architecture was revealed by 3D-TALM. The reversed metabolic state under improved respiratory conditions unexpectedly led to a more diverse IM architecture. These ultrastructural changes were also revealed by electron microscopy. Consequently, 3D-TALM enabled the study of IM architecture by tracking CV under different metabolic conditions, allowing an ultrastructural analysis of mitochondria in living cells. In addition, 3D TALM provided the spatiotemporal organization of CV under different metabolic conditions, so that the diffusion coefficients of CV could be related to changes in IM architecture caused by the metabolic condition.

2 Zusammenfassung

Mitochondrien sind das Kraftwerk der meisten nicht-grünen eukaryotischen Zellen. Um die Funktionen der Mitochondrien und ihre Regulation zu verstehen, ist die Kenntnis der raumzeitlichen Organisation ihrer Proteine wichtig. Mitochondriale Membranproteine können innerhalb von Membranen diffundieren. Sie sind an verschiedenen Funktionen beteiligt, wie z.B. Proteinimport, Zellatmung, Stoffwechsel, Metabolitentransport, Fusion, Spaltung oder Gestaltung der mitochondrialen Architektur. Darüber hinaus setzen sich Mitochondrien aus verschiedenen Unterkompartimenten mit unterschiedlichen Aufgaben zusammen. Insbesondere die innere Mitochondrienmembran (IM), in der die oxidative Phosphorylierung (OXPHOS) stattfindet, hat eine komplexe Architektur mit in die Matrix hineinragenden Cristae. Die vorliegende Arbeit zeigt die eingeschränkte Lokalisierung einiger mitochondrialer Proteine auf bestimmte Membranabschnitte und verknüpft diese mit ihrer Funktion oder bioenergetischen Gegebenheiten der lebenden Zelle.

Einzelpartikelverfolgungstechniken (SPT) wie die Verfolgungs- und Lokalisierungsmikroskopie (TALM) ermöglichen die Lokalisierung von Proteinen mit einer Präzision unter 20 nm. Zusätzlich liefert das Tracking einzelner Proteine Informationen über ihre Mobilität, Dynamik und ihre raumzeitliche Organisation. TALM verwendet Proteine die entweder mit dem HaloTag® (HaloTag) oder dem fSnapTag® (fSnapTag) genetisch markiert wurden. Diese Tags können orthogonal und posttranslational mit spezifischen und selbstmarkierenden Farbstoffen gefärbt werden. Wenn die Farbstoffe mit dem jeweiligen Substrat des Tags konjugiert sind. Die Einzelmolekül-Markierung von mitochondrialen Proteinen wurde substöchiometrisch mit membrandurchlässigen Rhodamin-Farbstoffen, entweder Tetramethylrhodamin (TMR) oder Silizium-Rhodamin (SiR), durchgeführt. TALM ermöglichte die Lokalisierung von Proteinen in verschiedenen mitochondrialen Subkompartimenten. Die gewonnenen Laufwege und Laufwegskarten der mitochondrialen Proteine zeigten deren raumzeitliche Organisation. Im Falle von Proteinen in der IM wie der F_1F_0-ATP-Synthase (Komplex V - CV) wurde eine eingeschränkte Diffusion in der CM, die Teil der kontinuierlichen IM ist, festgestellt. Die ungehinderte Diffusion von mitochondrialen Proteinen in der äußeren Mitochondrienmembran (OM) wurde mit der Mobilität von IM-Proteinen verglichen. Die Diffusion der mitochondrialen IM-Proteine war durch die IM-Architektur eingeschränkt und ihre Diffusionskoeffizienten waren niedriger. Darüber hinaus wurden signifikante Unterschiede verschiedener mitochondrialer IM-Proteine festgesellt, sie wiesen eine unterschiedliche Lokalisation in der IM auf, die oft an ihre Funktion gekoppelt waren und von unterschiedlichen raumzeitlichen Organisationen und Diffusionskoeffizienten begleitet wuren. Außerdem wurde zwischen der Diffusion von Proteinen in der inneren Grenzmembran (IBM) und Proteinen, die bevorzugt in die Cristaemembran (CM) diffundieren, unterschieden. Bei der Auswertung von Laufwegskarten wurden die verschiedenen Unterkompartimente in der IM anhand der Laufwege und der Laufwegsorientierung aufgedeckt, was die Identifizierung von mitochondrialen Proteinen ermöglichte, welche die Unterkompartimente markieren. Die Morphologie der Mitochondrien/Mitochondriennetzwerke und ihre bioenergetischen Parameter sind mit den Stoffwechselzuständen der Zelle verbunden. In dieser Arbeit wurde der Zusammenhang zwischen der raumzeitlichen Proteinorganisation des CV und der IM-Architektur, im Zusammenhang mit

Stoffwechselzuständen der Zelle, auf mikro- und nanoskopischer Ebene aufgedeckt. Es wurde festgestellt, dass die raumzeitliche Organisation von CV verändert wurde, wenn die Funktion von CV gehemmt wurde. Darüber hinaus wurde der bioenergetische Einfluss von Zellen auf das raumzeitliche Verhalten von CV und die Reorganisation der IM-Architektur durch TALM untersucht und mit Ergebnissen der Elektronenmikroskopie verglichen. Es konnte gezeigt werden, dass ein Hungerzustand von Zellen zu einem Verlust von Cristae und damit zu einer erhöhten Mobilität und raumzeitlichen Reorganisation des CV führte. Zusammengefasst zeigten die in dieser Arbeit vorgestellten Ergebnisse, dass ein korrekt funktionierender und aktiver CV zur Aufrechterhaltung der IM-Architektur beiträgt und sowohl die raumzeitliche Organisation von CV als auch die IM-Architektur an den Stoffwechselzustand gekoppelt sind.

Um mutmaßliche Protein-Protein-Interaktionen durch Ko-Lokalisierungs- und Ko-Lokationsstudien auf Einzelmolekülebene zu untersuchen, ist zweifarben SPT erforderlich. Daher wurde die posttranslationale und substoichimetrische Markierung, wie sie in TALM durchgeführt wurde, auf ihr Potential für Protein-Protein Interaktionsstudien an mitochondrialen Membranproteinen getestet. Dabei fungierte eine genetisch doppelt markierte Translokase der äußeren Membran-Untereinheit-20 (Tom20) (Tom20:HaloTag:fSnapTag) als Positivkontrolle. Es stellte sich heraus, dass die substoichimetrische, posttranslationale Markierung von mitochondrialen Proteinen für Protein-Protein Interaktionsstudien an mitochondrialen Proteinen nicht geeignet war, da sie durch den für TALM erforderlichen geringen Markierungsgrad eingeschränkt war. Dennoch erlaubte die zweifarben TALM die Untersuchung der Effekte von Proteinen, die die IM-Architektur beeinflussen, und deren Einfluss auf die raumzeitliche Organisation von CV. Die Co-Transfektion von Mic10, als zentrales Protein des mitochondrialen inneren Membran-Organisationssystems / mitochondrialen Kontaktstellenkomplexes / mitochondrialen Organisationsstruktur (MINOS / MICOS / MitOS (MINOS/MICOS)), veränderte die reguläre und ausgerichtete Organisation der Cristae. Dies wurde durch eine veränderte raumzeitliche Organisation des CV gemessen, wie z.B. der Verlust der senkrecht ausgerichteten CV-SUγ Cristae Laufwege. Im Gegensatz dazu erhöhte die Co-Transfektion von CV-Untereinheit-e (CV-SUe), die für die Dimerisierung von CV wichtig ist, die Anzahl der Cristae Laufwege.

Mitochondrien sind dreidimensionale (3D) Zellorganellen. Dementsprechend sind Unterkompartimente wie die IBM und CM ein 3D-Raum, in dem CV lokalisiert ist und diffundiert. Daher wird die Diffusion mitochondrialer Proteine durch zweidimensionale SPT unterschätzt, z.B. kann eine lateral eingeschränkte Diffusion eines Proteins, aus einer Diffusion entlang der z-Achse des Mikroskops resultieren. Um die raumzeitliche Organisation von CV in 3D aufzuzeigen, wurde das Potential von TALM zur Erweiterung auf eine 3D-SPT-Technik untersucht. Dazu wurde eine Zylinderlinse in den Emissionspfad eines TIRF (Total Interne Reflektion Fluoreszenz) Mikroskops eingebaut. Dies führt zu einer astigmatisch verzerrten Punkt-Spreizfunktion (PSF) der fluoreszierenden Einzelmolekülsignale. Diese Verzerrung ermöglichte die Rekonstruktion von Einzelmolekül-Lokalisierungen des CV zu einer hochaufgelösten Bild der IM, in lebenden Zellen. Darüber hinaus ermöglichte 3D-TALM die Darstellung der 3D-Architektur der IM durch 3D-Laufwege des CV. 3D-TALM war in der Lage zu erkennen, ob CV im IBM oder im CM diffundiert, und erweiterte die Information über seine Mobilität in der CM, dass sie scheibenartig stattfindet. Auf diese Weise konnte gezeigt werden, dass CV innerhalb der Cristae in alle Richtungen mobil ist. Schließlich zeigte 3D-TALM dass verschiedene Stoffwechselzustände eine veränderte Architektur der IM verurssachen. Wie im

zweidimensionalen TALM durchgeführt, wurden die Zellen unter Hungerbedingungen gehalten. Hier wurde die nun röhrenförmige IM-Architektur durch 3D-TALM aufgedeckt. Der umgekehrte Stoffwechselzustand unter verbesserten Atmungsbedingungen führte unerwartet zu einer vielfältigeren IM-Architektur. Diese ultrastrukturellen Veränderungen wurden auch durch die Elektronenmikroskopie aufgedeckt. Folglich ermöglichte 3D-TALM die Untersuchung der IM-Architektur durch Verfolgung von CV unter verschiedenen Stoffwechselbedingungen, was zu eine ultrastrukturellen Analyse der Mitochondrien in lebenden Zellen ermöglichte. Darüber hinaus lieferte 3D-TALM die raumzeitliche Organisation von CV unter verschiedenen metabolischen Bedingungen, so dass die Diffusionskoeffizienten von CV mit den durch die metabolische Bedingung verursachten Veränderungen der IM-Architektur in Beziehung gesetzt werden konnten.

3 List of Publications

3.1 Dynamic Imaging of Mitochondrial Membrane Proteins in Specific Sub-Organelle Membrane Locations

Timo Appelhans[1], Karin B. Busch[1,2,*]
[1]Mitochondrial Dynamics Group, School of Biology, University of Osnabrück, D-49076 Osnabrück, Germany;
[2]Institute of Molecular Cell Biology, School of Biology, University of Münster, D-48149 Münster, Germany; *Corresponding author
This article is part of a Special Issue on 'IUPAB Edinburgh Congress' edited by Damien Hall, *Biophys Rev* 9**:** 345–352, 2017, DOI: 10.1007/s12551-017-0287-1 (2017)

3.2 Single Molecule Tracking and Localization of Mitochondrial Protein Complexes in Live Cells

Timo Appelhans[1], Karin B. Busch[2,3]
[1]Mitochondrial Dynamics Group, School of Biology, University of Osnabrück, Osnabrück Germany
[2]Mitochondrial Dynamics Group, School of Biology, University of Osnabrück, Osnabrück Germany
[3]Department of Biology, Institute of Molecular Cell Biology, Westphalian Wilhelms-University Münster, buschkar@uni-muenster.de
Published In: Mokranjac D., Perocchi F. (eds) Mitochondria. Methods in Molecular Biology, vol 1567. Humana Press, New York, NY, https://doi.org/10.1007/978-1-4939-6824-4_17, Print ISBN: 978-1-4939-6822-0, Online ISBN: 978-1-4939-6824-4 (2017)

3.3 Multi-color Localization Microscopy of Single Membrane Proteins in Organelles of Live Mammalian Cells

Timo Appelhans[1], Felix R. M. Beinlich[1], Christian P. Richter[1], Rainer Kurre[2], Karin B. Busch[1,3]
[1]School of Biology, University of Osnabrück,
[2]Center of Cellular Nanoanalytics, Integrated Bioimagin Facility, University of Osnabrück,
[3]Department of Biology, Institute of Molecular Cell Biology, Westphalian Wilhelms-University Münster, buschkar@uni-muenster.de, *Journal of Visualized Experiments (JoVE)***,** (136), e57690, doi:10.3791/57690 (2018)

3.4 The spatiotemporal organization of mitochondrial F_1F_O ATP synthase in cristae depends on its activity mode

Kirill Salewskij[1§], Bettina Rieger[1§], Frances Hager[1], Tasnim Arroum[1], Jimmy Villalta[1], Patrick Duwe[1], Sara Colgiati[2,3], Christian P. Richter[4], Olympia E. Psathaki[4], José A. Enriquez[2], Timo Dellmann[1], Karin B. Busch[1,*]
[1]Westphalian Wilhelms-University Münster, Department of Biology, Institute of Molecular Cell Biology, 48149 Münster, North Rhine-Westphalia (Germany)
[2]Centro Nacional de Investigaciones Cardiovasculares Carlos III, 28029 Madrid, Catania (Spain)
[3]Institute of Nutrition and Food Technology, Biomedical Research Centre, Department of Physiology, University of Granada, Granada, Andalusia (Spain)
[4]University of Osnabrück, School of Biology, University of Osnabrück, 49076 Osnabrück, Lower Saxony (Germany)
[5]Center of Cellular Nanoanalytics, Integrated Bioimaging Facility, University of Osnabrück, 49076 Osnabrück, Lower Saxony (Germany)
§ Authors contributed equally,
Biochimica et Biophysica Acta (BBA) - Bioenergetics 1861: 148091, https://doi.org/10.1016/j.bbabio.2019.148091 (2020)

4 List of abbreviations

Abbreviation	Long form
3D	**3D**
ADP	**adenosine diphosphate**
ATP	**adenosine triphosphate**
CL	**cristae lumen**
CJ	**cristae junction**
CJs	**cristae junctions**
CM	**cristae membrane**
CoQ	**ubiquinone**
CV	**F_1F_0 ATP synthase**
CV-SUe	**F_1F_0 ATP synthase subunit-e**
CV-SUg	**F_1F_0 ATP synthase subunit-g**
CV-SUγ	**F_1F_0 ATP synthase subunit-γ**
DH-PSF	**Double-helix PSF**
ΔpH	**pH value across a membrane or lipid bilayer, in this work across the IM**
$\Delta \Psi m$	**IM membrane potential**
Drp1	**dynamin related protein 1**
ECAR	**extra cellular acidification rate**
EMCCD	**electron multiplying charged coupled device**
ETC	**electron transport chain**
ER	**endoplasmatic reticulum**
FAD	**flavin adenine dinucleotide**
$FADH_2$	**reduced form of FAD**
fPALM	**fluorescent photoactivation localization microscopy**
H^+	**hydrogen proton**
HILO	**highly inclined laminated optical sheet**

Abbreviation	Long form
HTL	**HaloTag ligand**
IBM	**inner boundary membrane**
IEM	**immuno electron microscopy**
IM	**inner mitochondrial membrane**
IMS	**inter membrane space**
LLSM	**lattice light sheet microscopy**
Mff	**mitochondrial fission factor**
MFN1	**mitochondrial fusion factor 1**
MFN2	**mitochondrial fusion factor 2**
MIA	**mitochondrial IMS assembly**
MICOS	**mitochondrial contact site complex**
MINOS	**mitochondrial inner membrane organization system**
MitOS	**mitochondrial organizing structure**
Mic10	**MINOS/MICOS subunit-10**
Mic12	**MINOS/MICOS subunit-12**
Mic13	**MINOS/MICOS subunit-13**
Mic19	**MINOS/MICOS subunit-19**
Mic26	**MINOS/MICOS subunit-26**
Mic27	**MINOS/MICOS subunit-27**
Mic60	**MINOS/MICOS subunit-60**
MPP	**mitochondrial processing peptidase**
mts	**matrix targeting sequence**
NA	**numerical aperture**
NAD	**nicotinamide adenine dinucleotide**
NADH	**reduced form of NAD**
OCR	**oxygen consumption rate**

Abbreviation	Long form
OM	**outer mitochondrial memrbane**
OPA1	**optic atrophy gene 1**
OXA	**oxidase assembly**
OXPHOS	**oxidative phosphorylation**
PALM	**photoactivation localization microscopy**
PAM	**presequence translocase-associated motor**
PARL	**presenilin-associated rhomboid-like**
Parkin	**E3 ubiquitin ligase**
PINK1	**Pten-kinase one**
PMF, Δp	**proton motif force**
POI	**protein of interest**
POIs	**proteins of interest**
pseudo-TIR	**pseudo total internal reflection**
PSF	**point spread function**
PSFs	**point spread functions**
Pten	**phosphatase and tensin homologue**
ROI	**region of interest**
RT	**room temperature**
SAM	**sorting and assembly machinery**
SBR	**signal to background ratio**
SIM	**structured illumination microscopy**
SiR	**silicon rhodamine**
SiR^{HTL}	**SiR conjugated with HTL**
SML	**single molecule localization**
SLM	**spatial light modulator**
SPT	**single particle tracking**

Abbreviation	Long form
sptPALM	**single particle tracking PALM**
star	**benyzlguanine / fSnapTag ligand**
STORM	**stochastic optical reconstrcution microscopy**
TALM	**tracking and localization microscopy**
TEM	**transelectron microscopy**
TILT3D	**tilted light sheet microscopy with 3D PSFs**
Tim	**translocase of the inner mitochondrial membrane**
Tim9	**translocase of the inner mitochondrial membrane subunit-9**
Tim10	**translocase of the inner mitochondrial membrane subunit-10**
Tim23	**translocase of the inner mitochondrial membrane subunit-23**
TIRF	**total internal fluorescence microscopy**
Tom	**translocase of the outer mitochondrial membrane**
Tom20	**translocase of the outer mitochondrial membrane subunit-20**
Tom22	**translocase of the outer mitochondrial membrane subunit-22**
TMR	**tetramethylrhodamine**
TMR^{HTL}	**TMR conjugated with HTL**
TMR^{star}	**TMR conjugated with star**
quasiTIRF	**HILO**
QV2	**QuadView 2**
VDAC	**voltage-dependent anion channel**
W-4PiSMSN	**Whole-cell 4Pi single molecule switching nanoscopy**
z	**axial**

5 Introduction

5.1 Biological background

5.1.1 Mitochondrial structure

Mitochondria are endosymbionts, which derived from α-protobacteria. They possess two membranes which are built up by bilayers of phospholipids. Mitochondria possess different subcompartments (

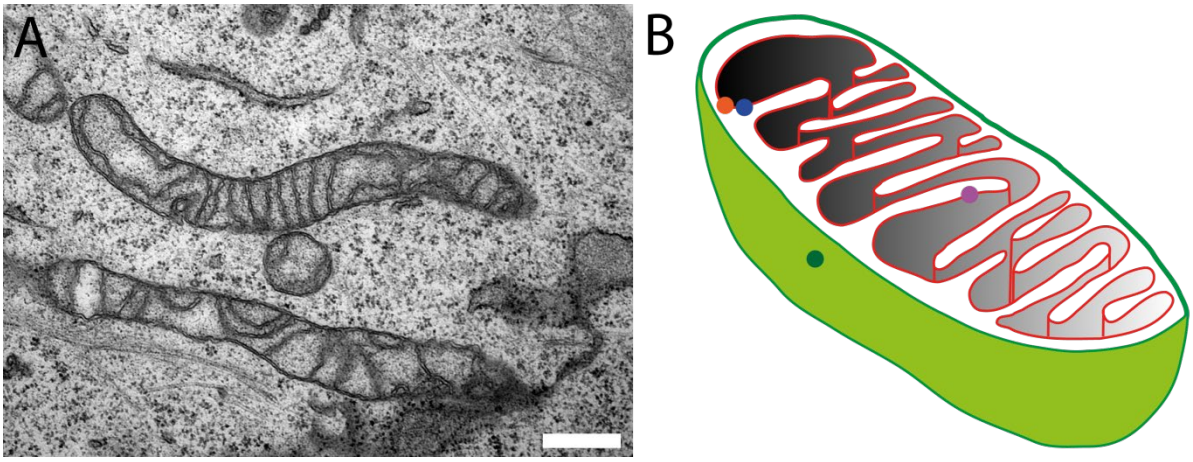

Figure **1**). The OM has a tubular shape, while the IM has multiple invaginations, so called cristae. The space in between these two membranes is called the inter membrane space (IMS). Due to its complex structure the IM can be divided in two different subcompartments. First the IBM, is the part of the IM, which is parallel to the OM. Secondly, the invaginations, so called cristae. Cristae consist of the CM, which envelopes the cristae lumen (CL). The space surrounded by the IM is called the matrix.

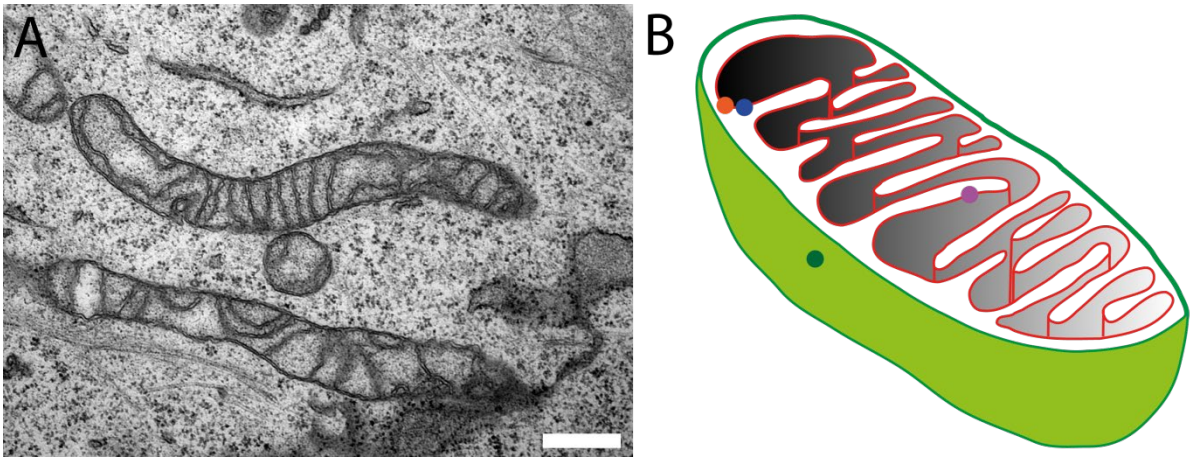

Figure 1 Mitochondria and their structure
A Transmission electron microscopy (TEM) image of mitochondria in a HeLa cell line. Scale bar: 500 nm **B** Scheme of a mitochondrion consisting of the tubular OM (green) and invaginated IM (red). The IMS is between the OM and IM (white). The CM is the part of the IM extending it into the matrix (gray). The matrix is enveloped by the IM. The different dots (green, blue, orange and purple) represent mitochondrial membrane proteins. (TEM image shown with the permission of Katharina Psathaki)

5.1.2 Subcompartmentalization of mit

Mitochondria possess different microcompartments, the OM, the IM, the IMS, the crista, the CM, the IBM and the matrix enveloped by the IM. Especially in the continuous IM with its two microcompartment / subcompartments the IBM and CM, separated by the CJs, a distinct localization of membrane proteins was unknown for a long time. Today, different methods allow to reveal the localization of mitochondrial proteins in subcompartments of mitochondria. A classical approach is to perform IEM, which is a combination of transmission electron microscopy (TEM) and detecting the protein of interest via immunogold labeling. This was performed on mitochondrial proteins (Vogel et al. 2006, Wilkens et al., 2013). In yeast mitochondria, TEM revealed the distribution of a collection of central mitochondrial proteins such as translocase of the outer mitochondrial membrane subunit-20 (Tom20), Core1 - a central subunit of cytochrome-c reductase (cytochrome bc_1 complex, Complex III – CIII), translocase of the inner mitochondrial membrane subunit-23 (Tim23), and Cox2 - a subunit of the cytochrome-c-oxidase (oxygen oxido-reductase, Complex IV – CIV) (Vogel et al. 2006). A similar approach was used in IEM of mitochondrial proteins in mammalian cells (Wilkens et al., 2013) (Figure 2). Taken together nicotinamide adenine dinucleotide (NADH) dehydrogenase (NADH ubiquinone oxidoreductase, Complex I – CI;), Succinat:Ubichinon-Oxido-reduktase (Complex II – CII), CIII, CIV and CV show a dominant localization inside the CM (Figure 2). Another question that arose is, how conserved is the subcompartmentalization of the IM and the distribution of mitochondrial proteins within? Here, IEM of OXPHOS complexes of fused mitochondria together with single particle tracking of mitochondrial proteins in mammalian cells revealed that diffusion and thus spreading of OXPHOS complexes in the IM is restricted but takes place (Appelhans et al. 2012, Wilkens et al., 2013). Thus, subcompartmentalization of mitochondria and following a mosaic model of the IM with a continuous IM were revealed (Wilkens et al., 2013).

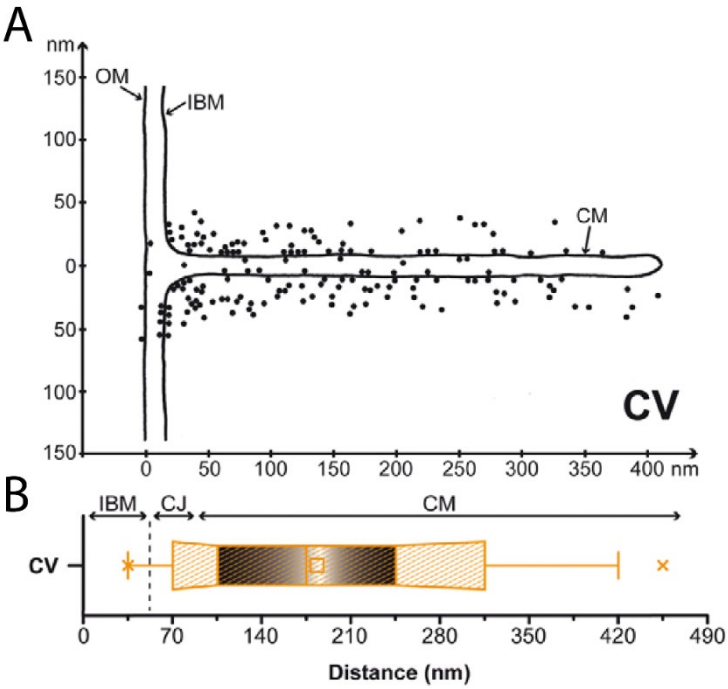

Figure 2 Distributions of OXPHOS complex V in the IM subcompartments of mitochondria in a mammalian cell
A Distribution of CV in a representative cristae membrane model. **B** Box-and-whisker plot of the distribution of CV along the IM. (Figure adapted from Wilkens et al., 2013)

Single molecule localization of individual CV, often apperead orthogonal oriented to the longitudinal axis of mitochondria and allows to measue the distance between cristae, like in TEM (Appelhans et al. 2012) (Figure 3). Furthermore, TALM revealed that CV diffuses in the CM resulting in an orthogonal trajectory

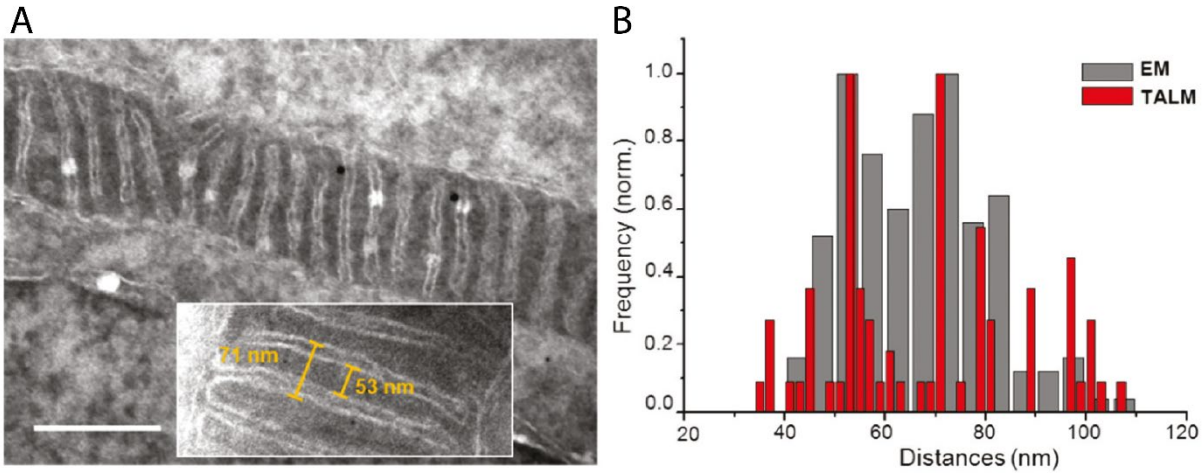

Figure 3 Distances between outward and inward cristae membranes of two adjacent cristae
A IEM image of a typical HeLA mitochondrion with a regular arrangement of cristae. The insert shows the distance between outward and inward membranes two adjacent cristae. Scale bar: 300 nm **B** Measured distances in IEM and TALM. (Figure adapted from Appelhans et al., 2012)

directionality of CV versus the longitudinal mitochondrial axis (Appelhans et al. 2012). IEM revealed that CI, CIII, CIV and CV are predominantly localized in the CM. Interestingly CII which couples citric acid cycle and the eletron transport chain (ETC) is found in both IBM and CM (Wilkens et al., 2013) (Figure A1). As extepted IEM revealed that Tom20 is localized in the OM (Vogel et al. 2006). Interestingly Tim23 was found in the IBM, less in the CM was nearly abundant in the CJ (Vogel et al. 2006). However, it remains to be discovered what leads to the subcompartmentalization of the IM on protein level in living cells. The MINOS/MICOS regulates the formation of the CJs, and is an obvious candidate to hinder the diffusion of protein in and out of the CM. Performing dual-color TALM experiments of the MINOS/MICOS together with CV may answer this question. Additionally, dimers of CV are found at the rim of crista. Therefore, it is of great interest to investigate subunits of CV which induce dimerization of CV, such as CV-SUe.

5.1.3 The F_1F_O ATP synthase

This enzyme is found widely in the biological world. It exits in thylakoid membranes, the IM and the plasma membrane of bacteria. This enzyme catalyses adenosine triphosphate (ATP) synthesis from adenosine diphosphate (ADP) and inorganic phosphate (P_i) by using the electrochemical potential of protons (or sodium ions in some bacteria) across the membrane, i.e. it converts the electrochemical potential into its chemical form (Noji et al., 2011). CV uses the proton motif force, which is produced by CI, CIII and CIV to produce ATP (chapter 5.1.4). CV is a super-complex enzyme with a molecular weight of > 580 kDa and consists of two regions: F_0 and F_1. F_0 is a protein complex of the rotary c-ring and the a-subunit stator (Figure 4). The c-ring itself is an oligomeric ring of 8 to 17 alpha helical c-subunits depending on the species (Kühlbrandt, 2019). The F_0 and F_1 region are connected by the central stalk and the peripheral stalk. The central stalk consists of the subunits δ, ε and γ. The peripheral stalk consists of the subunits A6L, b, d, f, F6 and the oligomycin sensitive conferral protein (OSCP) and is embedded in the IM (Figure 4). In mitochondria the peripheral stalk is attached to F_1 via the OSCP-subunit. F_1 is the non-membranous part of the enzyme. The F_1 catalytic domain consists of the heterotrimeric $\alpha_3\beta_3$-subcomplex and the central stalk (Hekman et al, 1991, Baker at al., 2012) (Figure 4).

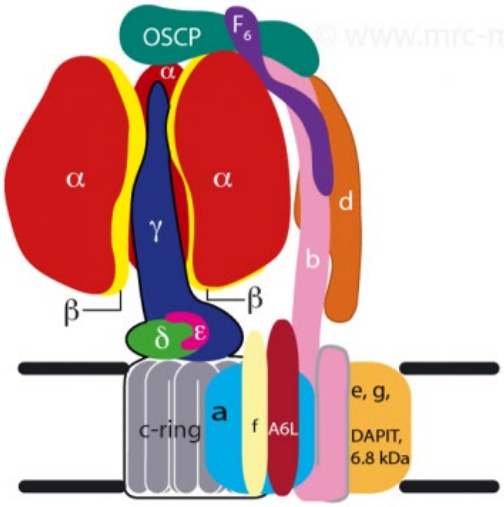

Figure 4 The mitochondrial F_1F_0 ATP synthase
CV consists of the two regions F_0 and F_1.F_0 is embedded in the IM. The F_1 region faces into the matrix. CV uses the H^+ gradient to produce ATP. (Figure adapted from Stock et al, 2000)

Hydrogen protons (H^+) are translocated to the matrix by the F_0 domain (Walker 1998; Watt et al., 2010). When H^+ float through the c-ring, it starts to rotate. This rotation is transmitted via the central stalk to the catalytic domain. During synthesis of one molecule ATP the F_1 region rotates about 120° (Figure 5). ATP

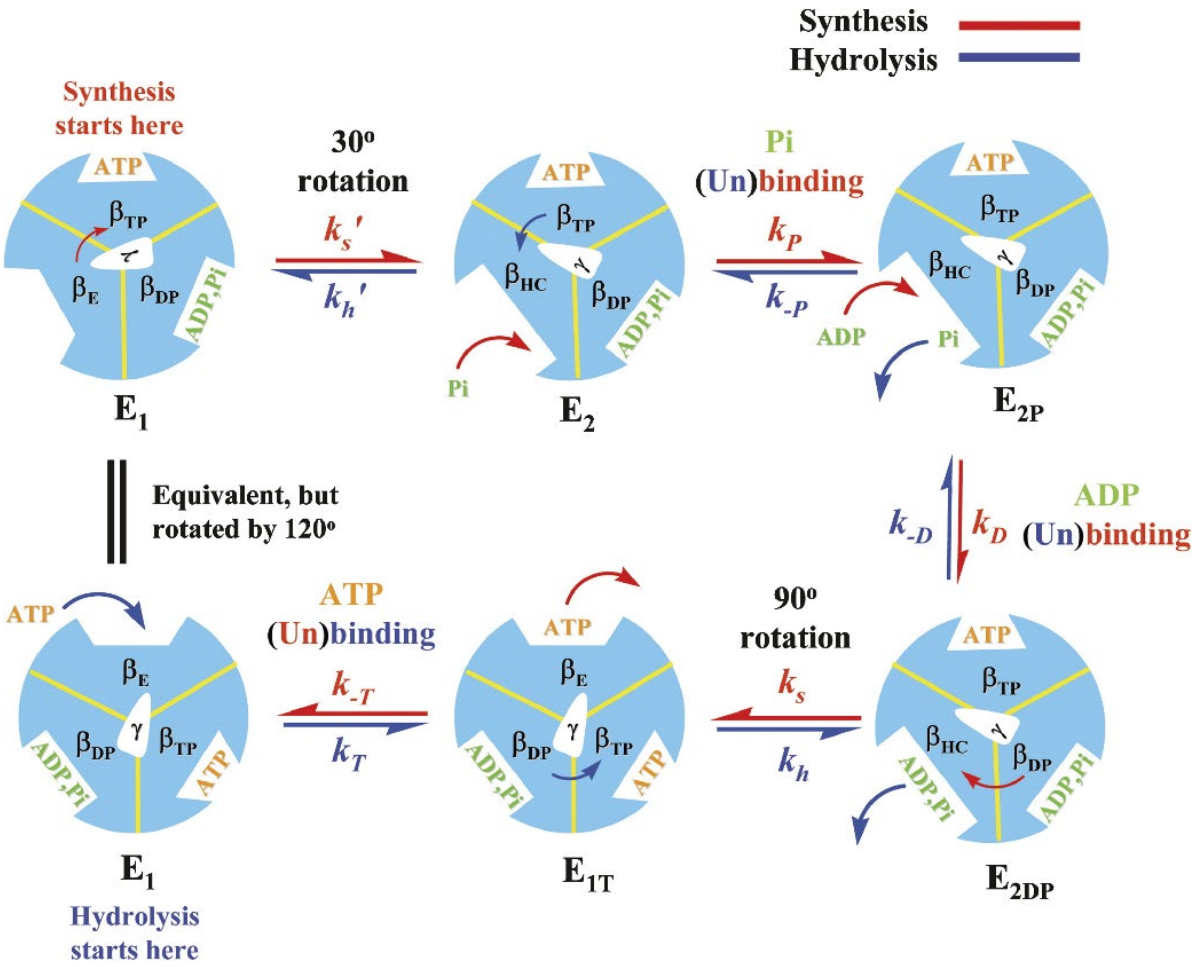

Figure 5 ATP synthesis and hydrolisis
The F1 region rotates 120° and produces ATP. In detail after a rotation of 30° one ß-subunit changes its conformation from the $ß_E$ state to the $ß_{HC}$ state, which allows binding of P_i. Afterwards, ADP is bound. The rotation of additional 90° catalyses the reaction of ADP and Pi to ATP during the $ß_{DP}$ state. Then the ß-subunit returns to the $ß_E$ state and ATP is released. Hydrolysis of ATP and following H^+ pumping by the F_0 region runs in the opposite direction. (Figure adapted from Gao et al., 2005)

synthesis depends on a clockwise rotation of the γ -subunit. The ß-subunit undergoes a conformational change between the open state (empty) ($ß_E$), the half-closed state ($ß_{HC}$), the closed state ($ß_{TP}$) and the ADP bound state ($ß_{DP}$). First, one ß-subunit is in the $ß_E$ state, one ß-subunit is in the $ß_{TP}$ state with bound ATP and the third ß-subunit is in the $ß_{DP}$ state with bound ADP and P_i. A rotation of CV-SUγ by 30° tranfers the ß-subunit, which is in the $ß_E$ state into the $ß_{HC}$ sate allowing P_i to bind. It is suggested that the whole F_1 head rotates along with the central stalk and the c-ring for the first 20 – 30° of a power stroke, which is equivalent to approximately one c subunit, and then returns to the starting position (Kühlbrandt et al., 2019). Then ADP can bind and the following rotation of the γ -subunit by 90° induces the confomartional change of the ß-subunit, which is in the $ß_{HC}$ state into the $ß_{DP}$ state (Figure 5). Manwhile, the ß-subunit which is in the $ß_{DP}$ state is transferred into the $ß_{TP}$ and ATP is produced. Additionally, the ß-subunit, which is in the $ß_{TP}$ state with catalyzed ATP from the first step on undergoes a conformtional change into the $ß_E$ state and ATP can be released. After a total rotation of CV-SUγ of 360° all ß-subunits have passed each state and each ß-subunit produced one molecule ATP (Figure 5). This way, CV synthesizes one molecule of ATP from ADP and one P_i per 3.7 H^+ pumped. Depending on the organism CV produces one molecule of ATP molecules per 3 to 4 H^+. CV also functions in the reverse direction when the electrochemical potential becomes insufficient: it cata-

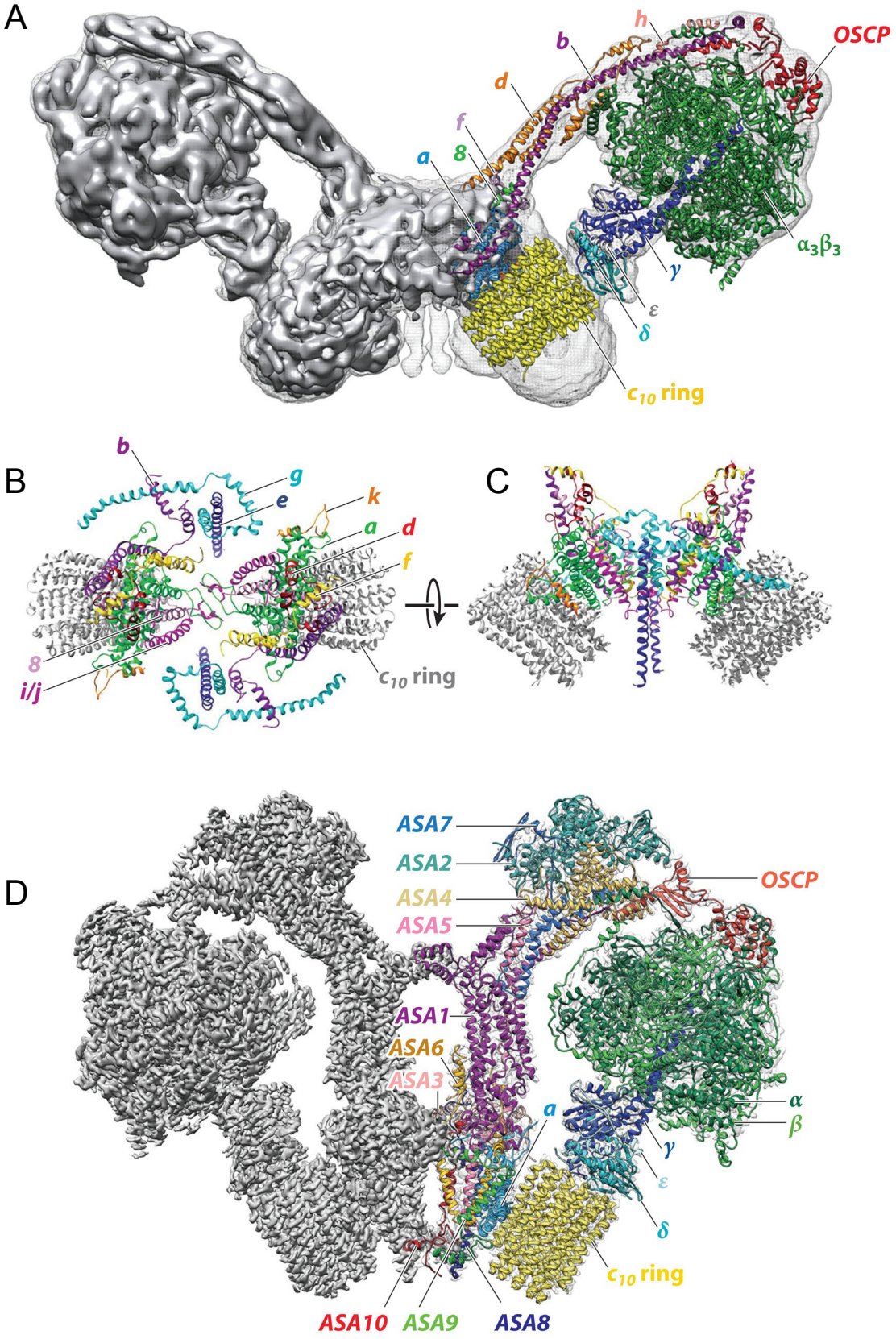

Figure 6 Cryogenic electron microscopy images and models of F_1F_O ATP synthase dimer
A Cryogenic electron microscopy (Cryo-EM) structures of mitochondrial CV dimers including its subunits. The structure was gained from single-particle cryo-EM images of CV from *Yarrowia lipolytica*, resolution is 6.2 Å (gray). **B, C** Model of the FO region of CV in *Saccharomyces cerevisiae*, resolution is 3.6 Å. **D** 2.7 Å model (gray) and atomic model of CV dimer from *Polytomela sp.* All structures have the same scale. (Figure adapted from Kühlbrandt, 2019)

lyses H^+ pumping to form an electrochemical potential by hydrolysis of ATP into ADP and P_i (Noji et al., 2011, Gao et al., 2005) (Figure 5).

CV can be organized as a dimer shown in Figure 6 and in oligomers (Allen et al., 1989; Baker et al., 2012 Davies et al., 2011; Davies et al., 2012, Dudkina et al., 2005; Habersetzer et al., 2013). Dimerization of CV is induced by CV-SUe and the subunit-g of CV (CV-SUg) (Baker et al., 2012). Interestingly these subunits do not interact directly at the dimer interface (Guo et al, 2017, Hahn et al., 2016) but rather form a hydrophobic wedge on either side of the dimer, which induces a local membrane curvature even in monomers (Hahn et al., 2016, Baker et al., 2012, Jiko et al., 2015). The dimer and oligomers are supposed to induce membrane curvature and form the rim of the cristae (Baker et al., 2012, Blum et al., 2018, Davies et al., 2011, Davies et al., 2012, Hahn et al., 2016, Mühleip et al., 2016, Paumard et al., 2002). However, CV was found to be mobile in the CM and IBM (Appelhans et al., 2012). Taken together, CV seems to fulfill a dual role in the IM at the same time. It produces ATP and is involved in shaping the CM. Beside CV the MINOS/MICOS complex is also involved in shaping the cristae membrane (chapter 5.1.6).

5.1.4 The electron transport chain and oxidative phosphorylation

In the IM the five enzymes of the ETC drive the ATP production coupled to O_2-respiration. This process is called oxidative phosphorylation (OXPHOS). Each crista itself is a microcompartment in which the protein complexes of the OXPHOS are enriched (Vogel et al. 2006, Wilkens et al., 2013). First of all, CI uses the electrons of reduced NADH plus one H^+ / NADH + H^+, pumps four H^+ into the CL and transfers the electrons to ubiquinone (CoenzymeQ – CoQ). Secondly, CII connects the tricarboxylic acid cycle with the OXPHOS by oxidizing succinate to fumerate using the coenzyme flavin adenine dinucleotide (FAD / $FADH_2$) and finally also transferring the electron to CoQ. Beside this, CIII uses the electrons of ubiquinol, pumps twice two H^+ into the CL and reduces cytochrome c. Afterwards, CIV uses the electrons delivered by cytochrome c, pumps H^+ into the CL and transfers the electrons to one oxygen molecule, thereby converting one molecular oxygen to two molecules of water. Corresponding to the chemiosmotic hypothesis (Mitchell et al., 1961) the redox-energy, which is gained during OXPHOS is translated into an electrochemical membrane potential of protons called the proton motive force (PMF, Δp). The PMF is derived from the Gibbs free energy:

$$(1)\ \Delta G = zF\Delta p$$

Where z is the charge of the molecule (1 for H^+), F is the Faraday constant The PMF combines a proton gradient concentration and voltage effects. Thus, the Gibbs free energy can also be seen as the sum of the ΔpH and the IM membrane potential ($\Delta\Psi m$). Then this equation can be transformed to:

$$(2)\ \Delta G = -2.303\ RT\ \Delta pH + zF\Delta\Psi_m$$

and by combining both equations to:

$$(3)\ \Delta p = (-2.303\ RT\ \Delta pH)/zF + \Delta\Psi_m$$

Where RT is the room temperature. However, when $\Delta\Psi m$ is only seen as part of the transmembrane potential energy derived by the hydrogen ion gradient ($\Delta\mu H^+$) on the IM (Zorova et al., 2018) the following equation is derived:

$$(4)\ \Delta\mu H^+ = -F\Delta\Psi_m + 2.3\ \Delta pH$$

H^+ pumping by CI, CIII and CIV build up a proton gradient, which generates the $\Delta\Psi m$ and the ΔpH. Both together set up the PMF. The PMF is used by CV to produce ATP (Barrientos et al., 2002, Mitchell et al., 1961, Mitchell et al., 1967). One cycle of the ETC provides the cell with 30 to 32 molecules of ATP. This shows the importance of mitochondria and the OXPHOS in context of providing the cell with energy in form of ATP. However, a strict coupling of the ETC and the maintenance of the $\Delta\Psi m$ and the ΔpH are important for an efficient ATP production via OXPHOS. Furhermore, a heterogenous distribution of protons along the cristae membrane exist (Busch et al, 2013, Pham et al., 2016, Rieger et al., 2014, Wolf et al., 2019). Additionally, the open and closed state of CJs, regulated by the MINOS/MICOS complex or opticatrophy gene1 (Opa1) protein, are important to keep the intramitochondrial heterogeneity of the $\Delta\Psi m$ (Wolf et al., 2019). Moreover, even along the CL side of the CM in single cristae, a lateral pH gradient between CIV and CV exists (Davies et al., 2011, Rieger et al., 2014). However, OXPHOS proteins are embedded in the IM, in which they can potentially diffuse. Therefore, it is of a great importance to investigate the context of the spatiotemporal organization of mitochondrial IM proteins and the IM architecture in different metabolic states of the cell.

5.1.5 Metabolic organization of OXPHOS proteins and bioenergetic pathways

A static localization of OXPHOS proteins is part of the source and sink model (Davies et al., 2011). Here, CI, CIII and CIV build the source, pumping protons into the CL and CV uses the arising PMF as a sink at the rim of the cristae (Davies et al., 2011) (Figure **7**). Nevertheless, it is physically unlikely that CV uses the PMF only at the rim. A functionally active, monomeric CV could also use the PMF while diffusing along the CM and IBM so the entire IM, respectively. A mobile CV would not exclude a proton gradient, but requires a complex imagination of the protein dynamic and the H^+ flow in the CL. However, CV-SUe and CV-SUg are supposed to proceed the tightening of dimers via their GxxxG motifs (Arselin et al., 2003, Hahn et al., 2016). In this model CV-SUg is supposed to crosslink the subunits-b of two individual CV (Soubannier et al., 1999) and thereby contributing to dimers of CV (Soubannier et al., 2002). It has been shown that mobile CV also exists in the CM and IBM (Appelhans et al, 2012, Appelhans and Busch, 2017b). Their trajectories sign cristae by diffusing orthogonal / perpendicular to the longitudinal axis of mitochondria or parallel to the longitudinal axis marking movement in the CM or IBM, respectively (Appelhans et al, 2012). Additionally, OXPHOS proteins have a restricted diffusion, which lowers their exchange between mitochondrial

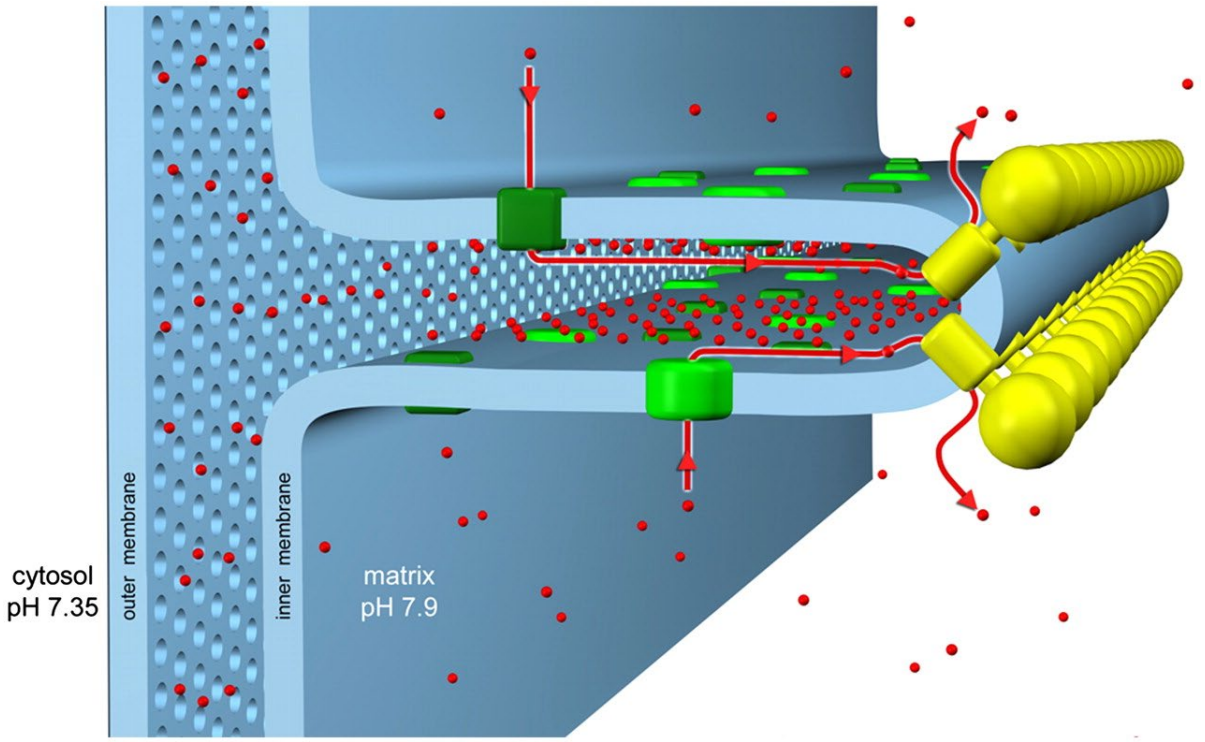

Figure 7 Source and sink model of hydrogen proton flow
In the source and sink model of the H^+ flow CI and CV occupy different rgions in the CM. CV dimer rows / CV oligomers (yellow) are localized at the cristae tip, while proton pumps e.g. CI (green) is predominantly localized in the flat part of the CM. H^+ (red) are pumped into the CL and flow back into the matrix through CV. This model shows a simplified illustration of a proton gradient along the CL and CM. (Figure adapted from Davies et al., 2011)

subcompartments (Wilkens et al., 2013). Nevertheless, in order to maintain the homeostasis of protein distribution and mixture, a healthy $\Delta\Psi m$, PMF and ΔpH are fundamental. However, the efficiency of OXPHOS also depends on protein-protein interaction such as CI, CIII and CIV building a super-complex which is called a respirasome (Acin-Pérez et al., 2008, Althoff et al., 2011, Lapuente-Brun et. al., 2013, Letts et al., 2016, Rieger et al., 2017).

Mitochondrial metabolism gets even more complex when taking the metabolic state of cells into account. Mammalian cells have different ways to gain energy. Additionally, cells can switch their metabolism and prefer one or several metabolic pathways. Beside OXPHOS, the major catabolic pathways are glycolysis, the citric acid cycle and β-oxidation of fatty acids.

In glycolysis, glucose is broken down to two pyruvates, by nine reaction steps, gaining two ATP molecules. Pyruvate is converted to Acetyl-CoA by the Pyruvate-Dehydrogenase with the use of NAD^+ and CoA-SH. The outcome of this reaction is CO_2, $NADH+H^+$ and Acetyl-CoA. This reaction is called the pyruvate decarboxylation. Afterwards Acetyl-CoA is used in the citric acid cycle. It is known that cancer cells produce most of their ATP via glycolisys and secret the majority of pyruvate as lactic acid. This is known as the Warburg-effect or aerobic glycolysis. The secretion of lactic acid leads to an extracellular acidification. Interestingly, cells which grow in medium containing galactose instead of glucose are forced to produce ATP almost exclusively from glutamine-driven oxidative metabolism. These cells show an improved oxygen consumption and less acidification of the medium than cells grown in medium containing glucose (Gohil et al. 2010) (Figure 8). The same is true for cancer cells like HeLa cells (personal communication with Bettina Rieger). Additionally, these cells show a higher oxygen consumption rate (OCR), driven by a metabolic

switch from glycolysis to citric acid cycle and a following upregulation of the ETC. This switch includes a higher activity of the citric acid cycle and a following increased OXPHOS activity (Gohil et al. 2010) (Figure 8B, C). Interestingly, the non-fermentable sugar 2-deoxy-D-glucose (2-DG) acts as a glycolytic inhibitor of the Hexokinase in glycolysis (Pelicano et al., 2006, Yamaguchi et al., 2011). The treatment of cells with 2-DG leads to an increased ATP synthesis via CV accompanied by a spatiotemporal reorganization of CV (Salewskij and Rieger et al., 2019).

During starvation, when nutrients are lacking, the membrane potential decreases. Additionally, the OCR remains nearly constant during short term starvation over 2 hours and increases after 6 hours of starvation. Meanwhile the extracellular acidification rate decreases drastically (personal communication with Bettina Rieger). Furthermore, during short term starvation the ΔpH between IMS and matrix increases and oxidation of fatty acids increases after 20 hours of starvation (Bettina Rieger: personal communication). Together these values show a metabolic switch of the cells from glycolysis to OXPHOS and oxidation of fatty acids. To date little is known about the spatiotemporal organization of CV during starvation. However, single particle tracking of CV during starvation or improved respiration has the potential to uncover if an altered spatiotemporal organization of CV takes place and is part of the metabolic adaptation of mitochondria and cells.

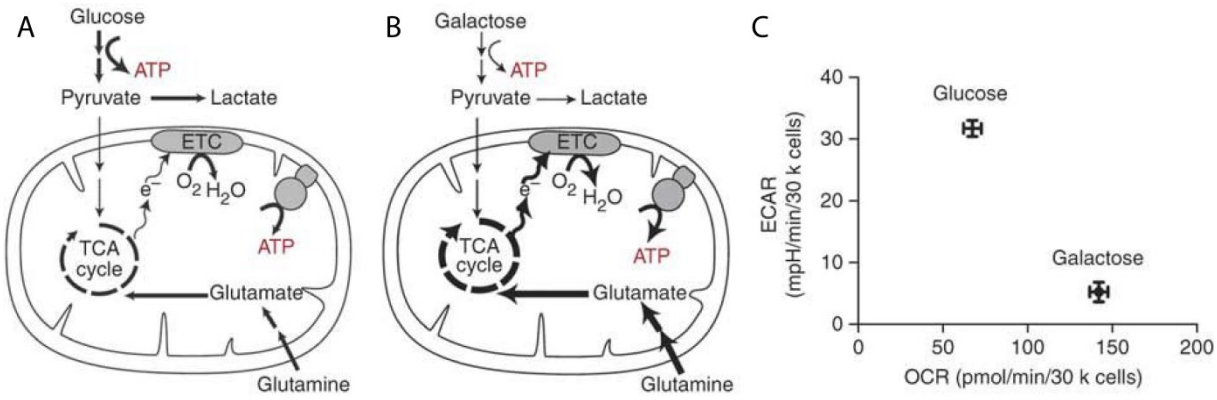

Figure 8 Metabolic switch of cells grown in galactose containing medium
A Cells which grow in medium containing glucose do glycolysis and produce pyruvate. Pyruvate can be transformed to lactic acid. The secretion of lactic acid leads to and increased extracellular acidification rate (ECAR). **B** Cells which grow in medium containing galactose instead of glucose are forced to produce ATP almost exclusively from glutamine-driven oxidative metabolism. This leads to an increased activity of the citric acid cycle and following an increase of the ETC. **C** As a result of this an increased OCR and a decreased ECAR can be measured. (Figure adapted from Gohil et al. 2010)

5.1.6 The mitochondrial inner membrane organizing system / mitochondrial contact site and cristae organization system

The MINOS / MICOS consists off several subunits and is a large, hetero-oligomeric protein complex predominantly located at the CJs (Alkhaja et al., 2012, Harner et al., 2011, Hoppins et al., 2011, van der Laan et al. 2016) (Figure 9). Its assembly, function and regulation are still not fully understood. However, multiple proteins of MICOS are identified. The large subunits of the MINOS/MICOS are Mic10 and Mic60. Both of them are part of two independent MINOS/MICOS subcomplexes: Mic10/Mic12(Mic13)/Mic26 and Mic27 and the subcomplex Mic60/Mic19 (Figure 9). This subcomplex includes multiple Mic10 proteins as

homodimers. The homodimerization of Mic10 is regulated by a Mic26-Mic27 antagonism and stablized by cardiolipin (Ramplet et al., 2017) (Figure 9). Additionally, Mic27 mediates the interaction between Mic10 and the second MINOS/MICOS subcomplex: Mic60/Mic19 (Eydt et al., 2017), which assembles independently of these factors (Friedman et al. 2015).

Mic60 is described as a regulatory protein of MINOS/MICOS and is essential for cristae junction formation (Hessenberger et al. 2017). Mic60 is supposed to form contact sites with several OM proteins like the translocase of outer mitochondrial membrane (Tom) and sorting and assembly machinery (SAM) (Akabane et al, 2016, Alkhaja et al., 2012, Darshi et al., 2011, Ding et al., 2015, Harner et al., 2011, Ott et al., 2012, van der Laan et al. 2016, von der Malsburg et al. 2011, Xie et al., 2007, Michaud et al., 2016,). However, especially Mic10 oligomers are crucial for shaping the cristae and formation of CJs (Barbot et al., 2015, Bohnert et al., 2015, Harner et al., 2011, Jans et al., 2013, von der Malsburg et al. 2011, Rampelt et al., 2018). Additonally, overexpression of Mic10 alters the architecture of the IM independently of other MINOS/MICOS components (Bohnert et al., 2015). Furthermore, Mic10 interacts with the dimeric CV (Rampelt et al., 2017) by the dimer specific CV-SUe and CV-SUg (Eydt et al., 2017, Rabl et al., 2009) (Figure 10). It is important to note that the induced membrane bending of Mic10 oligomers at the CJ and the formation of cristae rim by dimers and oligomers of CV is accompanied by an induction of membrane curvature by cardiolipin-rich domains (Rampelt et al., 2017, Rampelt et al., 2018).

Phospholipids like cardiolipin and phosphatidylethanolamine are localized in the negatively curved leaflet of the IM (Ikon et al., 2017) and are therefore important in bending the IM. As previsously mentioned, cardiolipin and subunit Mic27 have a stabilizing effect on Mic10 oligomerization and thus on cristae formation. In contrast Mic26 counteracts the function of Mic27 and has a destabilizing effect (Rampelt et al., 2018) (Figure 9). However, Mic10 is supposed to interact with Mic60 also called formation of cristae

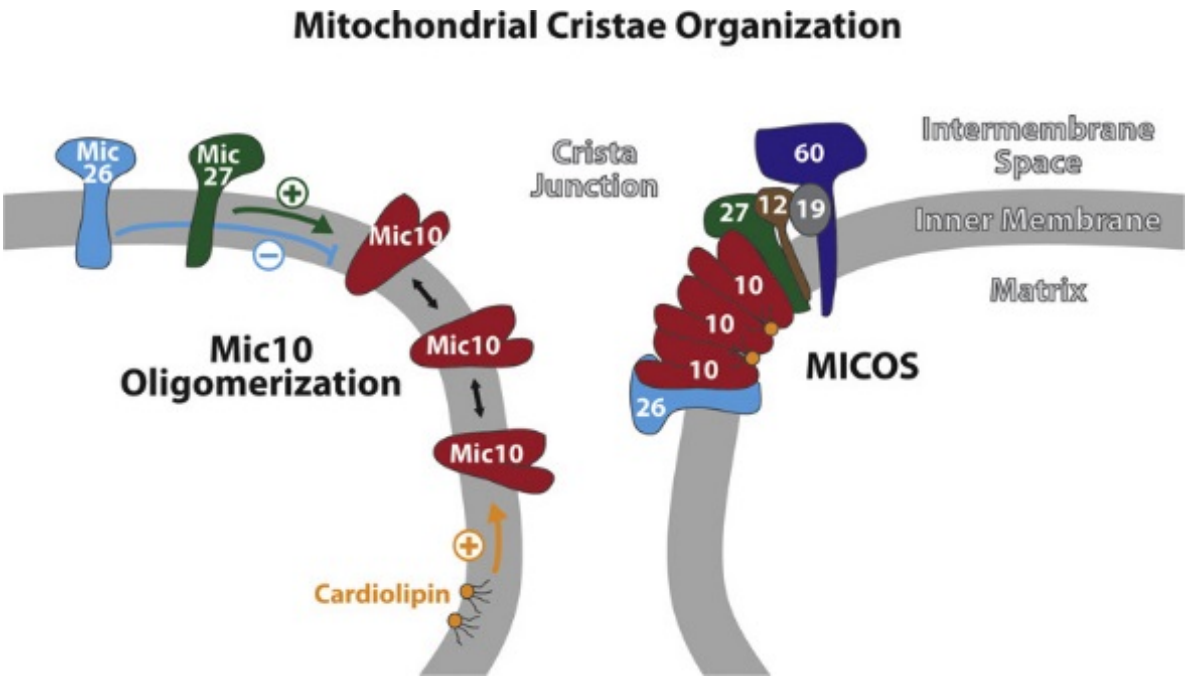

Figure 9 Mic10 oligomerization and MINOS/MICOS formation
Mic10 oligomerization is regulated by Mic26-Mic27 antagonism and cardiolipin. Mic27 and cardiolipin have stabilizing effect on Mic10 oligomers. The formation of MINOS/MICOS is also regulated by Mic12 (Mic13) and Mic19 (Figure adapted from Ramplet et al., 2017)

junction protein 1 (Fcj1) or Mitofilin. Mic60 is supposed to regulate CJs formation (Figure 10) and deletion of either Mic60 or Mic10 leads to loss of CJs and altered cristae morphology (von der Malsburg et al., 2011). So, both proteins Mic10 and Mic60 are important for formation of CJs, cristae formation and shaping of the IM. Additionally, the lack of Mic60 or Mic10 impairs the release of intermembrane space proteins (Malsburg et al., 2011). Furthermore, an evidence for Mic60 acting as an antagonist to CV-SUe and CV-SUg was found and thus imapring oligomers of CV (Rabl et al., 2009). The interplay of Mic60 and CV-SUe and CV-SUg and their influence on dimerization of CV is supposed to regulate the formation of cristae, CJs and the positive and negative shape of the IM and cristae (Figure 10). Taken together the formation of CJs is regulated via the oligomerization of Mic10 in dependence of Mic26 and Mic27, binding of the Mic60/Mic19 subcomplex, formation of the whole MINOS/MICOS complex and stabilized by cardiolipin. In contrast, the rim of cristae and the CJ neck is bended by dimers and oligomers of CV depending on CV-SUe and CV-SUg and also stabilized by cardiolipin in the inner leaflet of the CM at the cristae tip (Friedman et al., 2015, Rabl et al., 2009, von der Malsburg et al., 2011).

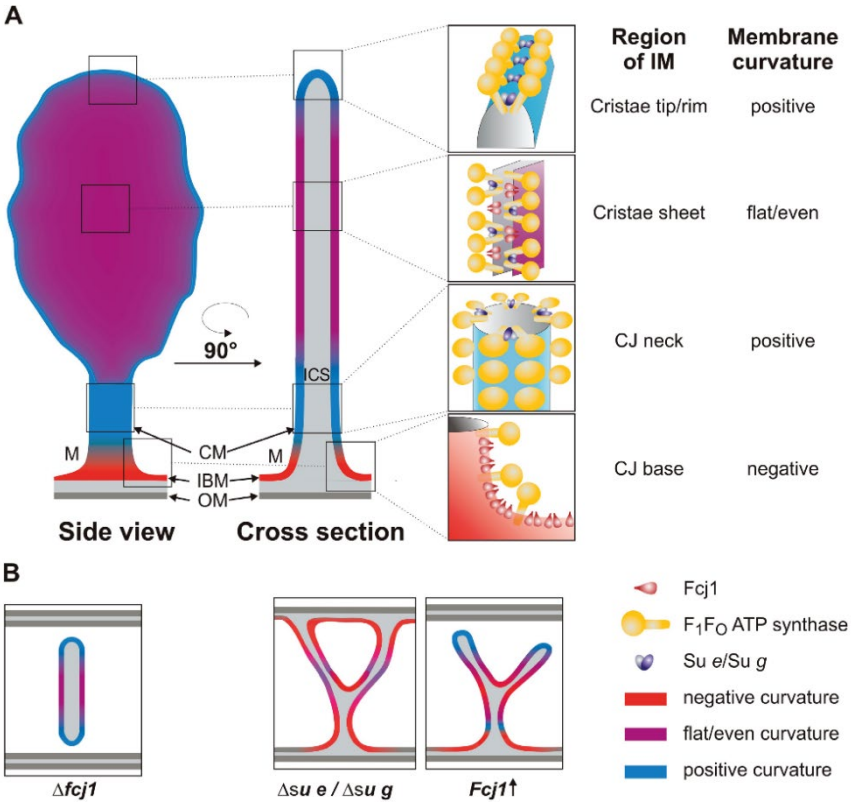

Figure 10 Shape of the inner membrane depends on the interplay of Mic60 and F_1F_O ATP synthase dimers
Beside Mic60 (Fcj1) also Mic10 is important for CJ fomration and IM shaping. **A** Side view and cross section of a cristae. The cristae tip and CJ neck are formed by dimers and oligomers of CV. CV induces a positive membrane curvature. The CJ base is formed by oligomers of Mic60 (Fcj1). Mic60 induces a negative membrane curvature.
B Knockout of Mic60 leads to a loss of CJs. Knockout of CV-Sue or CV-SUg leads to a loss of cristae tips. Overexpression of Mic60 leads to an increased brachning of cristae. (Figure adapted from Rabl et al., 2009)

5.1.7 Mitochondrial protein import system

Approximately 99 % of the mitochondrial proteins are encoded in the nucleus and have to be imported into mitochondria (Kutik et al., 2007, van der Laan et al., 2006). The import of nuclear-encoded mitochondrial proteins is done by the Tom - translocase of inner mitochondrial membrane (Tim) machinery (Tom-Tim machinery) (Pfanner et al., 2004, Kutik et al., 2007) (Figure 11). The Tom-complex binds precursor-proteins at the cytosolic site of mitochondria and translocates them through the OM (Pfanner et al., 2004, Kutik et al. 2007). Proteins with a destination in the matrix are transferred from Tom to Tim23 and then to the

presequence translocase-associated motor (PAM). In the matrix PAM together with the matrix heat shock protein 70, as a central subunit, drive the further protein import into the matrix and mitochondrial processing peptidase (MPP) cleaves the matrix targeting sequence (mts) (Hutu et al., 2008). Small proteins of the IMS are guided from Tom to the mitochondrial IMS assembly (MIA) machinery and are released into the IMS. β-barrel precursors of the OM are transferred from Tom to SAM via Tim subunit-9 (Tim9) and Tim subunit-10 (Tim10) chaperones. SAM integrates and assembles β-barrel precursors into the OM (Pfanner et al., 2004, Kutik et al. 2007). Proteins which should be integrated into the IM are transferred via Tim9-Tim10 chaperones to the Tim22 complex (Figure 11). Proteins encoded in the mitochondrial genome e.g subunits of the OXPHOS proteins are translated by mitochondrial rhibosomes and exported from the matrix, inserted and assembled in the IM via the oxidase assembly (OXA) machinery (Dolezal et al., 2006, Neupert et al., 2007).

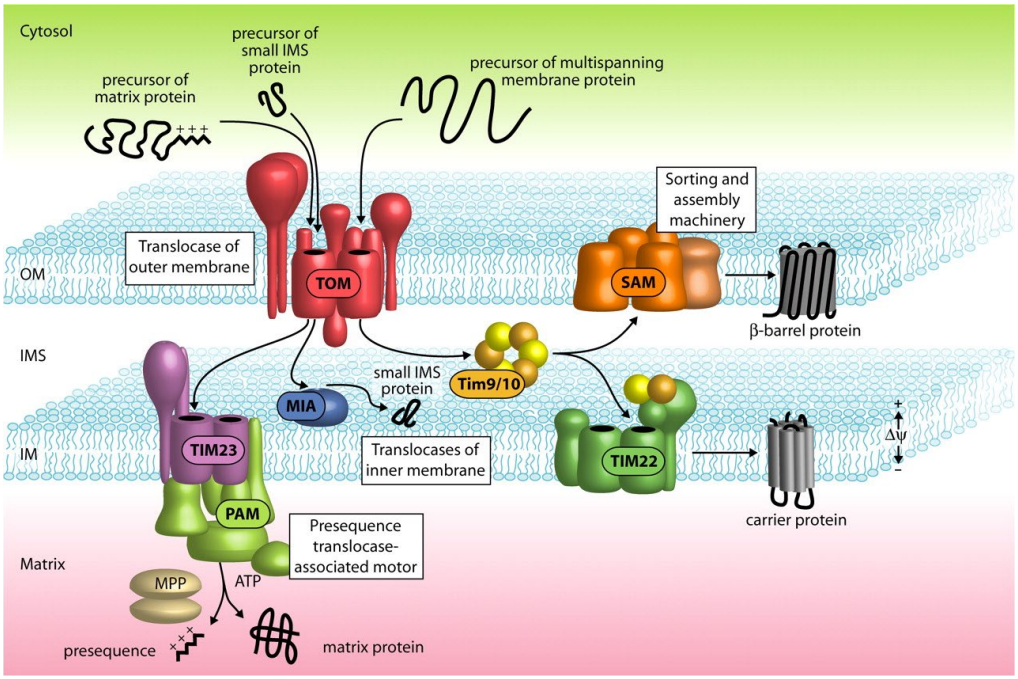

Figure 11 The Tom-Tim machinery of mitochondria and the import pathways for precursor proteins
After import of nuclear-encoded mitochondrial proteins via the Tom-complex presequnece-carrying proteins are transported by the Tim23 complex and the PAM into the matrix. Small proteins with a destination for the IMS are imported by MIA. ß-barrel precursors of the OM are guided via Tim9-Tim10 chaperone from Tom to SAM. Precursor proteins, which need to be inserted into the IM are transferred by Tim9-Tim10 chaperones to Tim22 and integrated into the IM. (Figure adapted from Kutik et al. 2007)

5.1.8 Central mitochondrial proteins

Beside the OXPHOS proeins and proteins needed for protein import other central proteins in mitochondria exist. The voltage-dependent anion channel (VDAC) is assumed to regulate metabolic and energetic flux across the OM. It is supposed to communicate with enzymes from metabolic pathways and thus regulates the transport of ADP, ATP, pyruvate and malate (Blachly-Dyson et al., 2001). In particular, binding of a cytosolic hexokinase is assumed to couple glycolysis and oxidative phosphorylation (Colombini et al., 1996). Furthermore, mitochondria are quality controlled by the *p*hosphatase and *ten*sin homologue Pten-kinase 1

(PINK1) and Parkin1, a cytosolic E3 ubiquitin ligase (McLelland et al., 2014, Narendra et al., 2011, Pickrell et al. 2015). Therefore, PINK1 is fully imported into mitochondria and cleaved by presenilin-associated rhomboid-like (PARL) protease into the short form (Beinlich et al. 2015). Depolarized mitochondria can be ubiquitinilated by Parkin and degraded in mitophagy (Jin et al., 2012, Pickrell et al. 2015, Vincow et al., 2013). This maintains a healthy mitochondrial network of cells.

Furthermore, mitochondria can undergo fusion and fission events. Fusion of the OM is initiated by the proteins mitochondrial fusion factor one and two (MFN1, MFN2) initiate the fusion of the OM (Ishihara et al. 2004). The dynamin related GTPase OPA1 acts as a fusion protein for the IM. For fission, the cytosolic dynamin related protein 1 (Drp1) is recruited to the OM by mitochondrial fission factor (Mff) (Otera et al., 2010). Drp1 forms a ring which initiates fission. Further investigations lead to the model that finally the endoplasmic reticulum proceeds a fission event (Friedman et al., 2011).

5.2 Studying individual proteins *in situ*: single molecule microscopy and super-resolution microscopy

In order to resolve the localization of single proteins, microscopy techniques, which overcome the diffraction limit have to be used. Single molecule microscopy and super-resolution microscopy have revolutionized the ability to study protein organization inside cells. In the past, several microscopy techniques have been established increasing the resolution and breaking the diffraction limit given by Abbe's law:

$$(5)\quad d = \frac{\lambda}{2NA} = \frac{\lambda}{2(n{*}\sin\alpha)}$$

where λ is the emission wavelength of the fluorophore and the combined term of $n{*}\ sin\ \alpha$ is the numerical aperture *NA* of the used objective.

However, the standard error σ in the determination of the PSF center or mean value of the photon distribution ($\mu = x_0, y_0$) can be calculated according to the following equation:

$$(6)\quad \sigma_{\mu i} = \sqrt{\left(\frac{s_i^2}{N}\right) + \left(\frac{a^2/12}{N}\right) + \left(\frac{8\pi s_i^4 b^2}{a^2 N^2}\right)}$$

where N the number of gathered photons of the signal, s_i is the standard deviation or width of the distribution (in dimension i), a is the pixel size of the camera chip and b is the standard deviation of the background. The Rayleigh criterion describes the minimal distance between two single fluorescent signals to be localized as two individual single molecules. Thus single fluorescent signals need to fulfill the Rayleigh criterion d_r to be distinguishable:

$$(7)\quad d_r = \frac{1.22\lambda}{2NA} = \frac{0.61\lambda}{n{*}\sin\alpha}$$

Different microscopy techniques pushed the resolution of microscopy beyond the diffraction limit allowing single molecule imaging and single molecule localization (SML) and opened up the field of super-resolution microscopy. One SML microscopy technique is called fluorescent photoactivation localization microscopy (fPALM) developed in by S. T. Hess (Hess et al., 2006). In the meantime, photoactivation localization microscopy (PALM) was established by E. Betzig in the year 2006 (Betzig et al., 2006). Both methods use UV-light to photoactivate or photoswitch proteins and excite the used fluorophores afterwards with another wavelength. Low laser powers are used to activate only a subset of the fluorophores in order to record separated and single molecule fluorescence. Thus, the amount of excited fluorescent proteins is controlled by the laser power. This allows to localize single fluorescent signals by a fitting their PSF with a two-dimensional Gaussian fit. SML allows to determine the center of the two-dimensional Gaussian fit with a localization precision below 25 nm (Hess et al., 2006, Betzig et al., 2006, Greenfield et al., 2009). A similar approach to fPALM and PALM is stochastic optical reconstruction microscopy (dSTORM). Here, fluorescent dyes with a high blinking propability are used and switched into a dark state, from which they return and can be excited. The described techniques allow to localize thousands of molecules within one second. A different technique to overcome the diffraction limit called stimulated emission depletion (STED) microscopy and was published in 1994 and 1999 by S. W. Hell. This is not a localization technique but rather breaks the diffraction limit optically by depletion of the fluorescent signal. Here a confocal laser scanning microscope (cLSM) is used. The fluorophores get excited by a laser resulting in a diffraction limited signal. Directly after excitation a second laser, which has a donut-shaped profile, depletes the signal in the outer rim of the chromophore in the imaged voxels. Thus, only a small and bright fluorescent signal is detected by the single photon avalanche diode detector. By this the field of view is scanned resulting in a super-resolution image with a full width half maximum value of the PSF of 20 nm to 30 nm. The FWHM can theoretically reduced to an arbitrary width by raising the intensity of the donut-shaped STED laser, according to the following equation

$$(8)\quad \Delta r = \frac{FWHM}{\sqrt{1+I_{max}/I_s}}$$

where Δr is the lateral resolution, I_{max} is the peak intensity of the STED laser, and is the threshold intensity needed in order to achieve saturated emission depletion. Thus a reolution of 2.4 nm has been achieved (Wildanger et al., 2012).

However, fPALM / PALM is the basic for single particle tracking PALM (sptPALM) (Manley et al. 2010). SPT allows also to study protein diffusion in prokaryotes like the treadmilling motion of actin MreB proteins in a *Caulobacter* cell (Kim et al. 2006). Nevertheless, single molecule localization of mitochondrial proteins in living cells could only be carried out successfully by TALM (Appelhans et al., 2012, Appelhans and Busch, 2017a, Appelhans and Busch, 2017b, Salewskij and Rieger et al., 2019).

Tracking mitochondrial proteins deals with the challenge of a complex 3D cell organelle. In order to reveal the complex shape of cell organelles and to reveal the spatiotemporal dynamics of proteins within the cell organelles, a solution to reconstruct the shape of the cell organelle and to localized and tracked the proteins within the cell organelle in all three dimensions (3D). In the past, intended manipulation of the PSF has

become a common way to gain super-resolved images information about the 3D position of single fluorescent molecules (Abrahamsson et al., 2013, Hao et al., 2017, Haij et al., 2014, Huang et al., 2016, Huang et al., 2008, Huang et al., 2016, Juette et al, 2008 Ram et al., 2009, Shao et al. 2011, Shtengel et al., 2009, von Diezmann et al. 2017, Gustavsson et al., 2018).

One method called 3D STORM uses an astigmatic distortion of the PSF by a cylindrical lens placed in the emission pathway of a TIRF microscope. This allows to reconstruct mitochondria in all three dimensions. Unfortunately, this has only been done in fixed cells and due to this it lacks the information of protein dynamics (Huang et al., 2008, Huang et al., 2016, Huang et al., 2018).

Another technique to resolve the 3D-position of proteins and to analyze 3D-trafficking of proteins is double-helix PSF (DH-PSF) microscopy (von Diezmann et al. 2017). DH-PSF can also be combined with light sheet microscopy (TILT3D) (Gustavsson et al., 2018) resulting is an elegant way to track proteins in 3D with the advantage of bright signals and a low background signal. 3D STORM and DH-PSF, as well asTILT3D provide a very suitable method to analyze the 3D position of proteins in all three dimensions. All three allow to reconstruct mitochondrial networks, but so far only DH-PSF and TILT3D allow 3D single particle tracking, revealing the 3D spatiotemporal trafficking of intracellular proteins.

Structured illumination microscopy (SIM) is yet another way to resolve subcellular structures and micro-compartments of cells and cell organelles, like mitochondria and their ultrastructure (Shao et al. 2011, Huang et al., 2008). In contrast lattice light-sheet microscopy (LLSM) can combine the advantages of SIM and astigmatic distortion and allows tracking subcellular structures and also single molecules within these structures in high z-range and an isometric PSF (Chen et al. 2014). However, a LLSM setup is very expensive and difficult to build and operate. Nevertheless, light sheet illumination per se is the best way to increase the signal to background ratio (SBR) by reducing the background coming from out-of-focus fluorophores (Hu et al., 2014, Huisken et al, 2004), and has even been used in thick samples. Unfortunately, most light sheet microscopy or selective plane illumination microscopy (SPIM) techniques use two objectives, one for illumination (excitation objective, EO) and one for detection (detection objective, DO). The greatest advantage is that an EO with a low NA has a high penetration depth independent of the DO. However, in samples with single cells, light sheet microscopy with a broad and short light sheet can also be done with a common TIRF microscope by tilting the illumination angle to produce the so called highly inclined laminated optical sheet (HILO, pseudo-TIR) (Tokunaga et al., 2008) which is easy to apply at a standard TIRF setup. This illumination method needs only one objective for excitation and imaging, which operates below the coverslip and therefore is not dipped into the sample, which decreases the risk for sample contamination, of course this method is only suitable for single cells and not for thick samples. This illumination method has already been used for mitochondrial proteins by TALM. In contrast to fPALM and PALM, in TALM the protein of interest is genetically fused to either the HaloTag or the fSnapTag. Thus, the advantages of membranepermable rhodamine dyes conjudated to substrates for the HaloTag or fSnapTag can be used. Those substrates have a high affinity, specificity and are self-labeling dyes (Appelhans et al., 2012). In TALM the single molecule level is reached by posttranslational and substoichiometric labeling. Unfortunately, this method neither has been tested for dual-color single particle tracking of mitochondrial proteins nor for 3D single particle tracking on mitochondrial proteins.

6 Aims

6.1 First aim

Determination of the spatiotemporal organization of mitochondrial proteins in the OM and IM. Do different mitochondrial proteins in the IM show distinct different localizations along this continuous membrane? Following to this, can the different localization of mitochondrial proteins be used as markers for subcompartments in the IM such as the IBM, CJs or CM? Is the diffusion coefficient of proteins in the IM influenced by the IM architecture?

6.2 Second aim

Does the functionality of CV change its mobility and spatiotemporal organization? Are metabolism and protein organization coupled? Does metabolism influence the mobility and spatiotemporal organization of CV? Are functionality of CV and subcompartmetalization of the IM coupled?

6.3 Third aim

Does dual-color TALM allow to perform colocalization and co-locomotion analysis? Can dual-color TALM be used to investigate effects of proteins on the spatiotemporal organization of the CV? Does Mic10 influence the IM architecture? Does CV-SUe increase the number of CV diffusing in the CM?

6.4 Fourth aim

How can mitochondrial proteins be tracked in all three dimensions? Can subcompartments of mitochondria and the diffusion of mitochondrial proteins within be revealed by 3D SML and SPT microscopy? Does the metabolic state of the cell influence the spatiotemporal organization of CV? Does the metabolic state influence the IM architecture of the IM and can this be revealed by 3D SML or 3D SPT?

7 Strategy

In order to localize and track mitochondrial proteins in living cells and to determine their spatiotemporal organization TALM experiments were performed. Therefore, HeLa cells were used and transfected stably or transiently with the plasmid encoding the protein constructs. The POI was genetically fused to either a HaloTag or an fSnapTag. Fusion proteins of the POI with a HaloTag or an fSnapTag allow orthogonal labeling with a dye conjugated to the substrate of the Tag. Thus, self-labeling with tag-specific dyes was possible. In order to localize and track single fluorescent molecules and thereby single mitochondrial proteins posttranslational, substoichiometric labeling was used. In order to perform TALM experiments a TIRF microscope with the quasiTIRF / HILO illumination was used. Therefore, HeLa cells were grown on glass coverslips. The cells grow adherent on the coverslip surface, which makes them accessible for TIRF microscopy. In order to adapt the HILO illumination to the mitochondrial network imaged, the critical angle of the excitation laser was adjusted and afterwards the illumination angle was tilted to the epi-fluorescent direction until the highest signal to background ratio was obtained. The TIRF microscope was equipped with two lasers with a monochromatic wavelength suitable to the used fluorescent dyes. The fluorescent signals were recorded with an electron multiplying charged coupled device (EMCCD) camera. The used exposure time were either 32 ms or 16 ms. Proteins of interest (POIs) genetically fused to the HaloTag were labeled posttranslational with TMR. Mono-color TALM experiments were done on the OM proteins Tom7, Tom20, Tom40, human fission factor 1 (hFis1), and the IM proteins Mic60, Tim23, CIV and CV. Here, it was also investigated if mitochondrial proteins of the IM showed a distinct different localization in the continuous IM and if those proteins can be used as markers for IBM, CJs or CM. Furthermore, it was investigated if the spatiotemporal organization of CV and the IM architecture depend on the enzymatic activity of CV. Therfore, CV was inhibited with oligomycin and TALM experiments were performed. Additionally, the spatiotemporal organization in different metabolic conditions was determined. Thereto, cells were grown in growth medium containing glucose and starved over 2 h in phosphate buffered saline (PBS).

In dual-color TALM, one POI was genetically fused to the HaloTag and the other one genetically to the fSnapTag. This allowed staining both POIs posttranslational with the combination of SiR and TMR conjugated to either the HaloTag or the fSnapTag ligand. Using optical splitting by a QuadView2 (QV2) in the emission pathway allowed to record the single fluorescent signals of both dyes simultaneously on different areas on the EMCCD camera chip. Dual-color TALM of Tom20, genetically fused to HaloTag and fSnapTag and labeled with SiR and TMR was performed. This double construct acted as a positive control for colocalization and co-locomotion evaluation. Additionally, dual-color experiments were performed in order to investigate the effect of a POI to influence the spatiotemporal organization of CV.

In TALM the recorded signals were localized by a two-dimensional Gaussian fit. SML and SPT was done by the use of the software Slimfast v16c. Trajectory directionalities were analyzed by the MitoOrientedDynamic software. This software allows to mark the mitochondrial longitudinal axis and to analyze the directionality of trajectories in reference to the mitochondrial longitudinal axis. By this the amount of perpendicular oriented versus the longitudinal oriented trajectories of mitochondrial proteins

was determined.

In order to perform 3D TALM a cylindrical lens was installed. The cylindrical lens had a focal distance of 1 m. Thus, an astigmatic distortion of the PSF of single fluorescent signals was induced. The distortion followed the x- and y-axis of the camera axis. The distortion of the PSF in dependence of the distance of the fluorescent signal to the focal plane was calibrated by imaging fluorescent beads in a z-scan. In 3D TALM experiments, single molecules were localized in all three dimensions by Gaussian mixture-model fitting. 3D SPT was performed with the u-track software v2.1.3.

3D TALM experiments of Tom20 and CV-SUγ were performed to investigate the power of 3D TALM to reveal the OM and IM shape, in living cells. Therefore, 3D reconstructions of mitochondria by localized Tom20 or CV-SUγ were created. Aditionally, 3D trajectory maps were also used to reveal the OM and IM architecture as Tom20 and CV-SUγ trajectories reproduced the membrane in which they diffused. Furthermore, it was investigated if diffusion in the IBM and CM can be distinguished in all three dimensions. Next, 3D TALM was performed in cells exposed to different growth conditions. The control was performed in medium containing glucose. Starvation conditions were again induced by exposing the cells to PBS for 2 h. Cells in improved respiratory conditions were grown in medium containing galactose instead of glucose. TALM experiments in improved respiratory conditions were performed with cells grown 3 weeks in galactose medium. 3D TALM of CV-SUγ in living cells, exposed to different metabolic conditions allowed to investigate, if the spatiotemporal organization of CV was coupled to the metabolic state of cells. The results were compared to TEM images of cells kept in the three different metabolic conditions. Here, it was investigated if different metabolic conditions influence the ultrastructure and if so, whether 3D TALM allowed to reveal those changes of the IM architecture by 3D SPT of CV-SUγ, in living cells. Furthermore, the trajectory directionality of 3D trajectories was again analyzed with the MitoOrientedDynamics software and the trajectory directionality of CV-SUγ was quantified.

8 Methods

8.1 Multi-color total internal reflection fluorescence microscope setup

In order to record and track the dynamics of single proteins in living cells a multi-color inverted TIRF microscope was used (microscope body, IX83, Olympus) (Figure 12). Equipped with a motorized xy-stage (Märzhäuser Scan IM 120x80) and a hardware autofocus (IX3-ZDC2, 830 nm version, Olympus) and a fully software controlled piezo-z-stage (NanoScanZ, NZ100, Prior Scientific (range of motion: 100 µm, repeatability: 1nm, accuracy 0.5 % of travel). Excitation of TMR was done with a 561 nm diode-pumped solid-state laser with a maximal power of 500 mW (MPB Communications). For excitation of SiR a 642 nm laser diode with a maximal power of 500 mW (MPB Communications) was used. The setup was equipped with an EMCCD camera from Andor (Andor iXon 987 ultra, 512 x 512 pixel, pixel size 16 µm x 16 µm).

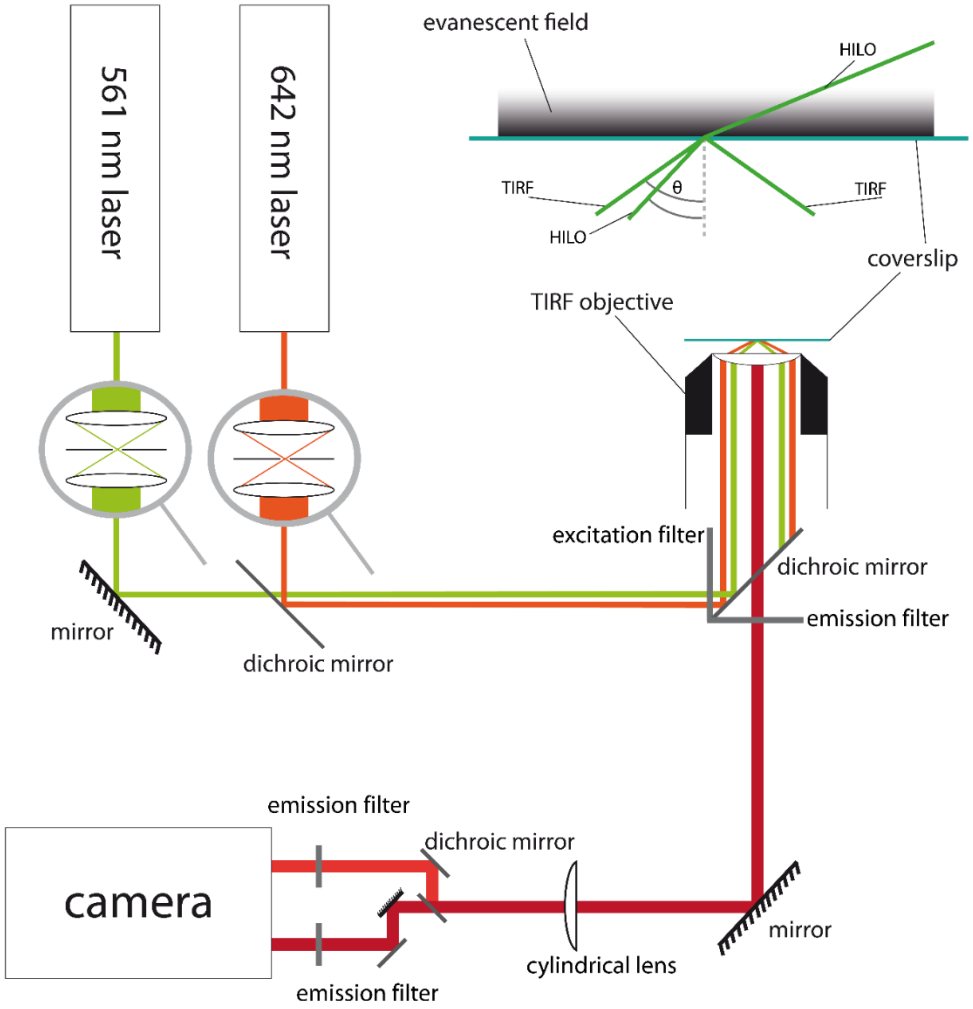

Figure 12 Scheme of a multi-color TIRF microscope setup
The TIRF microscope was equipped with laser of different wavelength to excite the fluorophores at their excitation maximum. The sample was excited through a TIRF objective. The same objective was used to collect the fluorescent signal. The emission was collected filtered and redirected to the camera. In dual-color microscopy the different emissions were separated and redirected to different areas on the camera chip. In 3D TALM the PSF of the single molecule signals was distorted via a cylindrical lens.

In multi-color TALM experiments the laser lines were used simultaneously during recording of the camera, which allowed simultaneous excitation of different fluorophores. The lasers were used simultaneously but shuttered, so that illumination and recording were synchronized and no bleaching occurred while the camera did not record. The lasers were coupled into optical fibers and inserted into the microscope by a TIRF condenser. The TIRF condenser was an Olympus 4-Line TIRF condenser (MITICO TIRF condenser, Olympus) for independent quad-color TIRF microscopy. From there, the lasers passed an excitation filter and were reflected to the objective by a dichroic mirror. The used filter cube included a beamsplitter for 405 nm / 488 nm / 561 nm / 640 nm and 730 nm (zt405/488/561/640/730rpc, Semrock) and a pentabandpass emission filter (440 nm / 521 nm / 607 nm / 694 nm /809 nm (Bright Line HC 440/521/607/694/809). The lasers were focused to the back focal plane of the TIRF objective. For the work presented in this thesis, an oil immersion, apoplanar TIRF objective with a magnification of 150-fold was used (UAPON 150x, NA 1.45, oil immersion, Olympus). The setup fulfilled the Nyquist Shannon sampling theorem and the pixel side length in an image equates to 106.67 nm. In dual-color microscopy the emission spectra were seperated on different areas of the camera by a QV2 (Photometrics) image splitter. For monochromatic experiments the QV2 was used in the ByPass mode. The QV2 including the QV2 image splitter was used to separate the recorded emission spectra of the fluorescence optically, on up to four different regions on the EMCCD camera chip. The image splitter had three dichroic mirrors: a 480 nm longpass (480dcxr), a 565 nm longpass (565dcxr) and a 640nm longpass mirror (640dcxr) and finally a full mirror. Additionally, four emission filter were included in the image splitter. One bandpass filter for light with the wavelength from 426 nm – 450 nm (BrightLine HC 438/24), one bandpass filter transmitting light between 502 nm – 538 nm (BrightLine HC 520/35), a bandpass filter for the wavelength between 582 nm – 619 nm (BrightLineHC 600/37) and one bandpass filter transmitting light between 665 nm – 705 nm (Brightline HC 685/40).

In an inverted TIRF microscope the total internal fluorescence reflection takes place at the bottom of the coverslip. The cells grow as an adherent monolayer on the upper surface of the coverslips. Total internal reflection fluorescence produces an evanescent field in the sample and its intensity decays exponentially along the z-axis according to

$$I(z) = I(0)e^{-z/d} \quad (9)$$

,where d is the distance of the fluorophore in the sample to the coverslip. The evanescent field allows to excite fluorophores in close proximity to the coverslip. The penetration depth d_p of the evanescent field can be calculated by the following equation

$$d_p = \frac{\lambda}{4\pi}(n_2{}^2 sin\theta^2 - n_1{}^2)^{-1/2} \quad (10)$$

The penetration depth of the TIRF depends on the wavelength λ of the used laser, the angle θ of the incident light and the refractive index of the oil below the coverslip n_2 and of the medium surrounding the cells n_1. However, most of the mitochondrial network in a cell is above the evanescent field. In order to illuminate

fluorophores attached to mitochondrial proteins the angle of the incident laser has to be smaller than the critical angle. Then HILO illumination is applied, where background fluorescence of the sample is much lower than in the epi-fluorescence mode.
In mono-color microscopy the whole field of view of the camera could be used. In mono-color 3D TALM the PSF of the single fluorescent molecules was distorted by a cylindrical lens with a focal distance of 1m (f = 1000.0 mm, Ø1", UVFS Mounted Plano-Convex Round Cyl Lens, Thorlabs) installed after the camera port 0.1 m in front of theQV2.

8.2 Molecular Biological Methods

In this thesis HeLa cell lines stable expressing the CV:HaloTag Plasmid (7026, basepairs (bps)) and the Tom20:HaloTag plasmid (6570 bps) were used (Figure S1, Figure S2),). These plasmids encode the gene for the protein of interest (POI) and the gene for the HaloTag on a CMV-D3-psems vector. In dual-color experiments of CV-SUγ:HaloTag in combination with either CV-SUe:fSnapTag or Mic10:fSnapTag, the plasmids encoding for CV-SUe-fSnapTag (6020 bps) (Figure S3) or Mic10-fSnapTag (6018 bps) (Figure S4) were transiently transfected to the cell line stably transfected with the CV-SUγ:HaloTag construct. The restriction enzymes EcoRV and EcoRI were used to exchange the POI in the Tom20:HaloTag plasmid.

8.3 Cell Culture and Cultivation of Cells

The HeLa cell line was derived from cervical cancer cells in the year 1951 (Scherer et al., 1953) from Henrietta Lacks and was used as a model system. HeLa cells have several advantages for establishing microscopy techniques. First of all, they are easy to handle, because they have a high rate of proliferation and are unpretentious in cultivation. Secondly, HeLa cells grow adherent on a glass coverslip and are therefore suitable for TIRF microscopy. Thirdly, HeLa have elongated mitochondria and are easily to transfect. Cells were cultivated in an incubator at 37 °C and 5 % CO_2 in a T-25 flask containing growth medium (Table 1). In order to detach cells from the flask bottom or cell culture dish surface, the medium was removed and the cells were washed with PBS. Afterwards Trypsin / EDTA was added and the cells were incubated at 37 °C and 5% CO_2 for 1-2 minutes. Then medium was added and the cell suspension was homogenized. Cells were passaged when reaching confluence. All cell culture techniques were done under sterile conditions in a laminar airflow cabinet. Each chemical, buffers and cell medium were prewarmed to 37 °C in a water bath before use.

Table 1: Growth and Imaging Media The total volume of the prepared Media was 80 ml.

Glucose growth medium (MEM^{++}(1))	**Imaging medium (limpid) (MEM^{++}(1L))**
8 ml FBS	8 ml FBS
800 µL HEPES	800 µL HEPES
800 µL NEAA	800 µL NEAA
Earle´s MEM (w/ Phenol red, stable L-Gln, 2.2 g/l $NaHCO_3$)	800 µL Alanyl-L-Glutamine
	2.3 mL Sodium Hydrogen Carbonate
	Earle´s MEM (w/o Phenol red, w/o L-Gln, w/o $NaHCO_3$)
Galcatose growth medium (MEM^{++}(2))	**Galactose imaging medium, limpid (MEM^{++}(2L))**
8 ml FBS	8 ml FBS
800 µL HEPES	800 µL HEPES
800 µL NEAA	800 µL NEAA
1.6 mL Alanyl-L-Glutamine	1.6 mL Alanyl-L-Glutamine
144 mg Galactose	144 mg Galactose
2.3 mL Sodium Hydrogen Carbonate	Filled up to 80 mL with A 14430 – DMEM (w/o Glucose, w/o Phenol red, w/o L-Gln, 3.7 g / L $NaHCO_3$)
Fill up to 80 mL with XF Base Medium, Minimal DMEM (0 mM Glucose), Seahorse	

8.3.1 Growth and imaging conditions

Cells were thawed and grown in glucose growth medium (MEM^{++}(1)). Cells in control experiments were grown in MEM^{++}(1) and imaged in MEM^{++}(1L). Cells in starvation conditions were seeded in PBS 2 h before imaging (chapter 8.5). In order to induce improved respiratory conditions cells grown in MEM^{++}(1) were transferred to galactose growth medium (MEM^{++}(2)) containing 0 mM glucose and 10 mM galactose. In order to induce a complete adaptation of the cells to the improved respiratory conditions, the cells were grown over 21 days in MEM^{++}(2). Galactose imaging medium (MEM^{++}(2L)) was used to image cells in improved respiratory conditions. MEM^{++}(2L) also contained 10 mM galactose and no glucose.

8.4 Coverslip Coating

The coverslips used for fluorescent microscopy were coated with Poly-L-Lysine - Polyethylene Glycol - Arginine Glycine Aspartate (PLL-PEG-RGD). PLL-PEG-RGD is a poly-L-Lysine (PLL) derivative attached with a polyethylene glycol 3000 Da and a Cysteine-Glycine-Arginine-Glycine-Aspartate-Serine (CGRGDS) peptide (Figure 13). PLL-PEG prevents unspecific binding of dyes or other fluorescent molecule but does not allow

cells to grow on its surface. Therefore, the CGRGDS peptide is bound to it, enabling the attachment and growth of cells on the coated coverslip**.** This peptide is the binding motif of the integrin receptor presented by e.g. fibronectin. *In situ*, integrins facilitate cell - extracellular matrix adhesion. The coating solution contained 1 mg PLL-PEG-RGD per 1 mL of PBS. The coverslips were plasma cleaned for 15 minutes at 50 W power. Thus, the upper site of the coverslips was plasma cleaned. Then the coverslips were coated with the PLL-PEG-RGD solution. Therfore 6 µL of the PLL-PEG-RGD solution was pipetted on one coverslip and another coverslip was put upside down on the first one. This coverslip sandwich was incubated for 1 h at RT in a dust free environment. Afterwards the coverslips were washed three times with water and dried with nitrogen gas. One side of the coverslips was now coated with PLL-PEG-RGD and used for cell seeding.

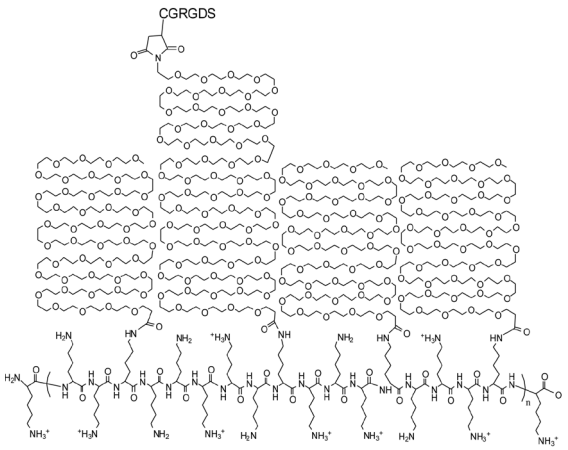

Figure 13 PLL-PEG-RGD layer on a coverslip PLL-PEG-RGD was used to coat the upside of a coverslip to avoid unspecific binding of dyes to the coverslip.

8.5 Cell Seeding

The growth medium in the T-25 flask containing the nearly confluent cell culture was aspirated. Then the cell culture was washed with 4 mL PBS. In order to detach the cells from the bottom surface of the T-25 flask, 1 mL Trypsin / EDTA was added and the T-25 flask was incubated for 1 minute at 37 °C and 5 % CO_2. After the cells were detached, 4 mL growth medium was added and the cell suspension was homogenized. This avoided cell clusters. Cells were only seeded on freshly coated coverslips. Each 3.5 cm cell culture dish contained 2 mL imaging medium and a coated coverslip with the coated side upwards. Next, 200 - 350 µL of the cell suspension was added dropwise. Then the samples were evenly distributed by carefully agitating the dish and incubated for about 16 h at 37 °C and 5 % CO_2 before labeling. Cells grown in glucose medium were seeded in imaging medium containing glucose. Those cells acted as a negative control. Cells used for starvation expermiments were seeded in PBS instead of medium. Therfore cells grown in MEM^{++}(1) were seeded on a PLL-PEG-RGD coated coverslip in a 3.5 cm cell culture dish, as described previously. Instead of 2 mL imaging medium 2mL PBS were used. Cells grown in enhance respiratory conditions were grown in MEM^{++}(2) and seeded in MEM^{++}(2L).

8.6 Transfection

Cells were transfected one day after seeding in a 3.5 cm cell culture dish containing a coated coverslip. Therefore, calcium phosphate transfection was used. The growth medium was replaced before transfection with fresh medium. 10µL of plasmid solution containing 2.5 µg to 5 µg DNA were pipetted into a reaction

cup. Then 20 µL $CaCl_2$ solution (2.5 M) were added and mixed by pipetting up and down carefully. After 30 seconds, 170 µL H_2O was added and the solution was gently pipetted up and down twice. 200 µL HBS Buffer (pH 7 ± 0.04) were pipetted into another reaction cup. Then the 200 µL DNA/$CaCl_2$ solution buffered in H_2O was added dropwise into the HBS Buffer during vortexing the reaction cup containing the HBS Buffer. The buffered DNA solution was added in single drops on a monolayer of cells. Here, an inhomogenous DNA distribution in the sample was avoided. Afterwards the samples were incubated at 37 °C and 5 % CO_2 8 to 12 hours. Then the samples were washed with medium once and fresh growth medium was added. Tansient transfected cells were imaged 36 to 48 hours after transfection. At the day of imaging each sample was washed with 2 mL PBS twice and 2 mL limpid imaging medium once. Cells were kept at 37 °C and 5 % CO_2 in 2 mL fresh imaging medium before labeling.

8.7 Labeling of fusion proteins

Single molecule microscopy of the POI was performed by orthogonal, posttranslational and substoichiometric labeling. Therefore, the POI was genetically fused to a self-labeling tag, either the HaloTag, the fSnapTag or to both (

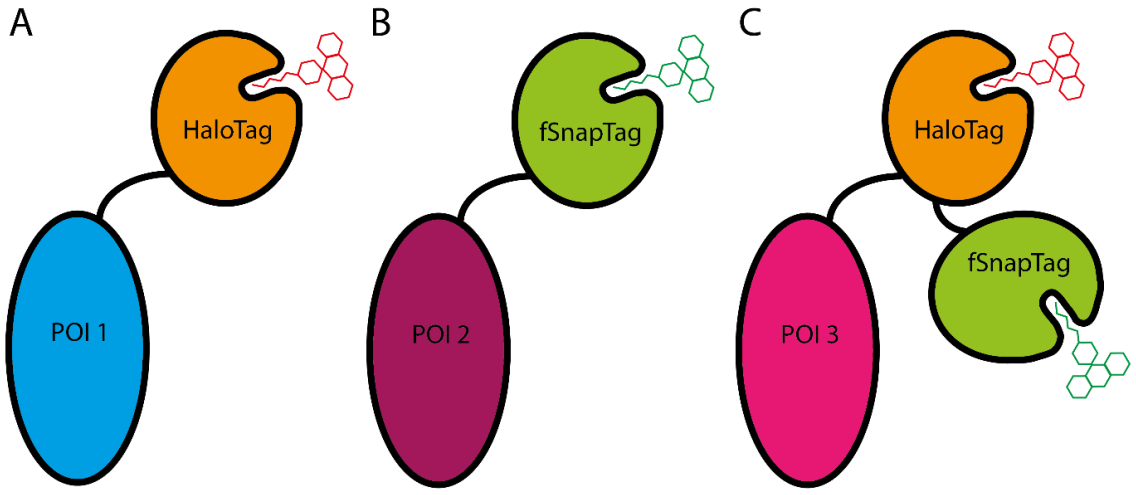

Figure 14). The used dyes were TMR and SiR. In order to stain the HaloTag, a dye conjugated to the HaloTag substrate – the HaloTag ligand (HTL) was used. The HTL binds covalently to the HaloTag. For staining the fSnapTag the substrate, a benzylguanine was conjugated to the dye. The fSnapTag forms covalent thioether bond with the fluorescent dye via the benzylguanine. In this thesis TMR bound to a HaloTag ligand (HTL) is called: TMR^{HTL}, SiR bound to a HTL is called: SiR^{HTL} and TMR bound to an fSnapTag ligand / benzylguanine (star) is called: TMR^{star}. Thus, TMR could be used for both tags, when conjugated the correct substrate. In the case of mono-color experiments the POI was always fused to the HaloTag and stained with TMR^{HTL}. In the case of dual-color experiments one POI was fused to the HaloTag and the other POI to the fSnapTag. In this case labeling was performed with the combination of SiR^{HTL} and TMR^{star}. Due to the different binding kinetics of the two tags (Beinlich et al. 2015), different labeling concentrations of the dyes were used in dual-color microscopy. Labeling with TMR^{star} was done with at least two times higher concentrations

compared to SiR^{HTL}. This will be explained in detail in chapter 9.3.1. However, the goal in posttranslational labeling for mono- and dual-color TALM is a substoichio-mentric labeling. In the case for testing dual-color in order to perform colocalization and co-locomotion the POI (Tom20) was genetically fused to both tags and the combination of SiR^{HTL} and TMR^{star} was used for labeling. In 3D TALM the POI was always fused to the HaloTag and labeled with TMR^{HTL}.

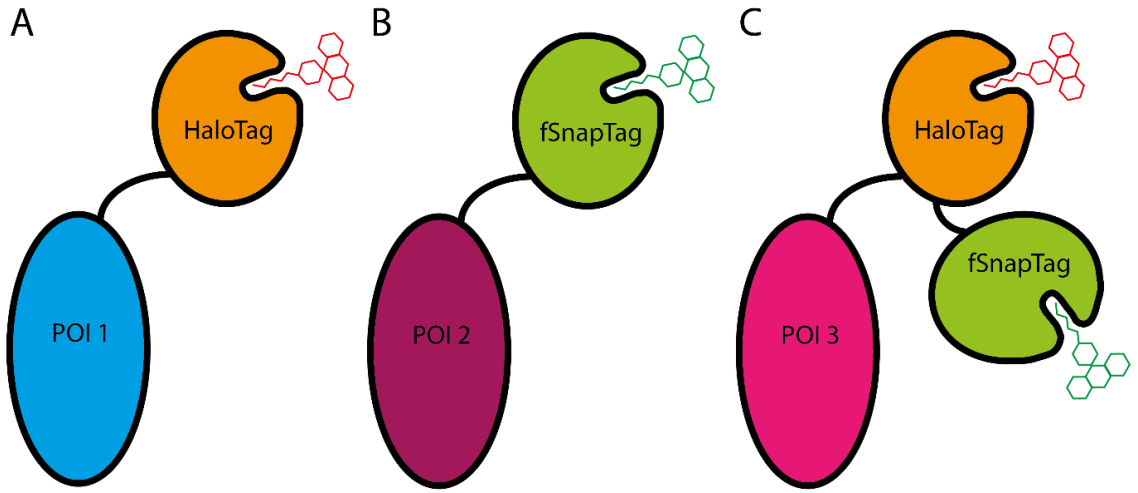

Figure 14 Posttranslational and substoichiometric labeling of fusion proteins
A Scheme of a fusion protein of the POI 1 with a HaloTag. The HaloTag was posttranslational labeled with either TMR^{HTL} or SiR^{HTL}. **B** Scheme of a fusion protein of the POI 2 with an fSnapTag. The fSnapTag was always posttranslational labeled with TMR^{star}. **C** Fusion protein of POI 3 with a HaloTag and an fSnapTag, labeled with both dyes.

8.7.1 Labeling procedure

At first the imaging medium and the PBS were prewarmed to 37° C. For cells grown in glucose medium the imaging medium containing glucose and for cells grown in galactose medium the galactose imaging medium was used. Next the dye solution was prepared. The dye used for staining was diluted in the refering imaging medium. In the case of mono-color TALM experiments 0.8 nM to 1 nM dye concentration was used. Dyes were stored in DMSO. The dye solution contained only 1 ‰ DMSO and was prewarmed to 37° C. The imaging medium in the cell culture dish of the samples was aspirated carefully. Then 1 mL of the labeling solution was added. Next the sample was incubated for 20 minutes at 37 °C and 5 % CO_2. Subsequently the imaging solution was aspirated carefully. Then the sample was washed twice with 2 mL PBS and each time gently agitated. Afterwards the sample was washed with 2 mL imaging medium and 2 mL imaging medium were added before incubating the sample for at least 1h at 37 °C and 5 % CO_2. Before specimen clamping, these 2 mL were again replaced by 2 mL imaging medium.

8.8 Specimen Clamping

Cells on coverslips were imaged via TIRF microscopy in a microscopy chamber (Figure 15). Therfore the coverslip was placed between the polytetrafluoroethylene (PTFE) ring and the rubber ring. The PTFE ring lies on the lower chamber part. The rubber ring was carefully placed onto the coverslip with tweezers. Afterwards the upper part of the chamber was put onto all other parts and thoroughly sealed with caution.

Then 800 µL imaging medium was added carefully to the chamber so that the cells were not affected. Prepared loaded chambers were incubated at 37 °C and 5 % CO_2 for 1 hour but could be stored for up to 4 h before microscopy at 37 °C and 5 % CO_2.

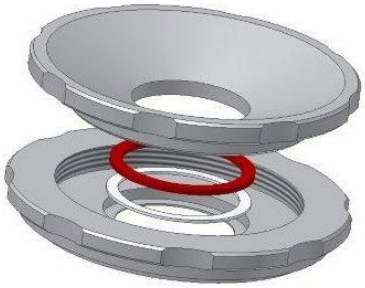

Figure 15 Microscopy chamber for 24 mm diameter coverslips
The coverslips are fixed in the microscopy chamber between the rubber and the Teflon ring. As it is an open system, chemicals can be added during imaging without removing the sample from the microscope.

8.9 Dual- or multi-color image splitter alignment

The fluorescent signals of different wavelengths had to be aligned in order to allow relative correct localization of the different fluorescent signals in the sample. Therefore, tetrasepec beads with a diameter of 110 nm were used. The tetrasepec beads were diluted 1:200 and 10 µL of the solution was pipetted onto an uncoated coverslip. The diameter of tetrasepec beads is below the diffraction limit, which was why they need to be used to align the PSF of the fluorescent signals as precise as possible. Thus the two emission channels can be aligned pixelwise by turning the alignment screws of the DualView to adjust the mirrors of the image splitter and thereby the channels on the camera chip (Appelhans et al., 2018). The fluorescence of each channel was splitted onto the camera chip individually (Figure 16A, B) by the QV2 and the two emission channels were aligned. Due to the clear overlap of the signals in the merged image a perfect alignment of the emission channels of view is shown (Figure 16C). The imaged area here was 256 x 256 pixel in each channel. In order to perform dual-color or multi-color SML and SPT a calibration matrix was created (Appelhans et al., 2018). The calibration matrix corrects for chromatic aberrations.

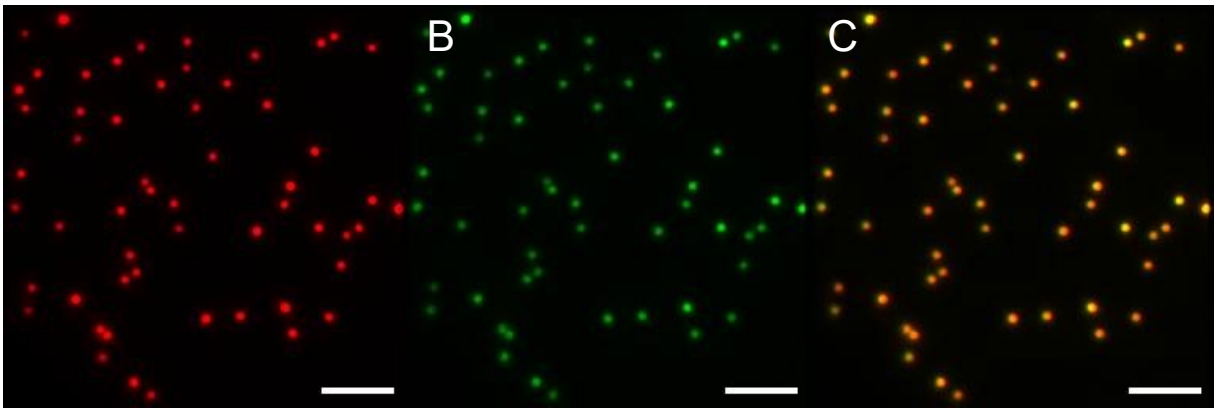

Figure 16 Channel aligment with fluorescent beads
Fluorescent signals are separated by their wavelength (685 ± 40 nm, red signal, A; 600 ± 37 nm, green signal, B). Both channels were aligned (merged image, C). Each image has 256 x 256 pixel with a pixelsize of 106.7 nm. Scale bars: 2 µm

8.10 Preparation of samples for astigmatic distortion calibration and 3D point spread function measurement

Calibration was performed with fluorescent beads of the PS-Speck™ Microscope Point Source Kit with an emission wavelength of 560 nm and a diameter of 110 nm. The beads were diluted 1:200 in H_2O and 10 µL of the solution was added to the middle of an uncoated coverslip. The beads bound unspecificically to the coverslip surface. The samples were dried in a lamiar airflow cabinet in a dust free environment. Dried samples can be stored at 4 °C.

8.11 Imaging mitochondria for tracking and localization microscopy in a TIRF microscope

Most mitochondria are inside in the cell with a distance to the coverslip of more than 200 nm. This makes it difficult to use the evanescent field, which excites only fluorophores approximately <200 nm above the coverslip. Imaging of mitochondria in a TIRF microscope was done by illuminating the sample with the HILO excitation (Tokunaga et al., 2008). Thus, fluorophores above the evanescent field were excited with a quasi-lightsheet. This allowed single particle tracking of mitochondrial proteins (Appelhans et al., 2012). The greatest advantage when using HILO was a low background excitation and thereby a high signal to background ratio (SBR), which is eight-fold greater than in epi-illumination (Tokunaga et al., 2008). In order to use HILO excitation, the angle of the laser needed to be tilted slightly away from the critical angle. Now a thin sheet of laser beam was illuminating the specimen. Additionally, it was important to set the focus perfect to the mitochondria which are illuminated best. Furthermore, all TALM experiments described in this thesis used mitochondria in the cell periphery. Here, mitochondria are elongated and separated in a flat network (**Fehler! Verweisquelle konnte nicht gefunden werden.**). This reduces the chance for false localization and tracking, which may occur when mitochondria overlap and allows imaging single mitochondria in an intact network. The exposure time used in TALM experiments was 16 ms to 32 ms.

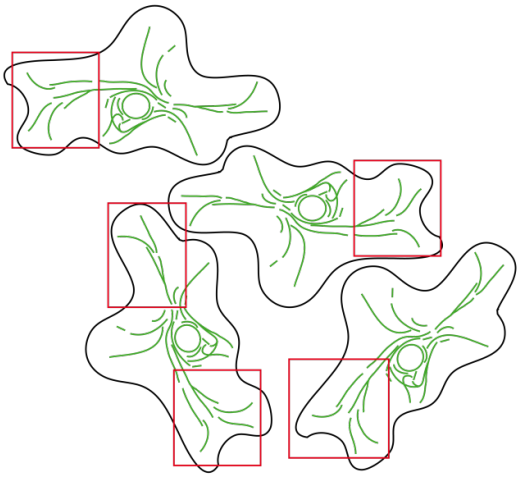

Figure 17 Imaging mitochondria in the cell periphery
In TALM mitochondria in mammalian HeLa cells need to be imaged in the cell periphery. Here separated mitochondria can be seen and imaged without overlapping

8.12 Single molecule localization and single particle tracking

8.12.1 2D Tracking and localization microscopy

The signal size is diffraction limited by Abbe's law. The PSF of the signal can be fitted by a two-dimensional Gaussian fit. This fit allows determination of the center of the signal and thereby to determine the position of the fluorophore (Figure 18A). Using this technique, SML can reach localization precisions below 25 nm (Hess et al., 2006, Betzig et al., 2006, Greenfield et al., 2009). SML of mitochondrial proteins by posttranslational and substoichimetric labeling results in a localization precision below 15 nm (Appelhans et al., 2012). SPT of fluorescent signals depends on the localizations belonging to the same particle at different times. The connection depends on the use of algorithms such as nearest neighbor (Figure 18B). Thus, a chronological series of linked localizations built up a time series of steps, the single particle track, also called trajectory. (Figure 18C). The trajectory of a single molecule includes information about the mobility. The mobility of a single molecule is shown as the diffusion coefficient and determined by the mean square displacement (MSD) over the lag time Δt in seconds (s). Thus, the diffusion coefficient (D), also called the apparent diffusion coefficient (D_{app}) of single molecules like proteins or lipids is specified in $\mu m^2/s$. In order to measure the MSD and to calculate the D of a protein the distance of single steps of a trajectory have to be measured resulting in a MSD plot over the lag time τ (Figure 18D, Figure 19). The MSD can be calculated by the following equation:

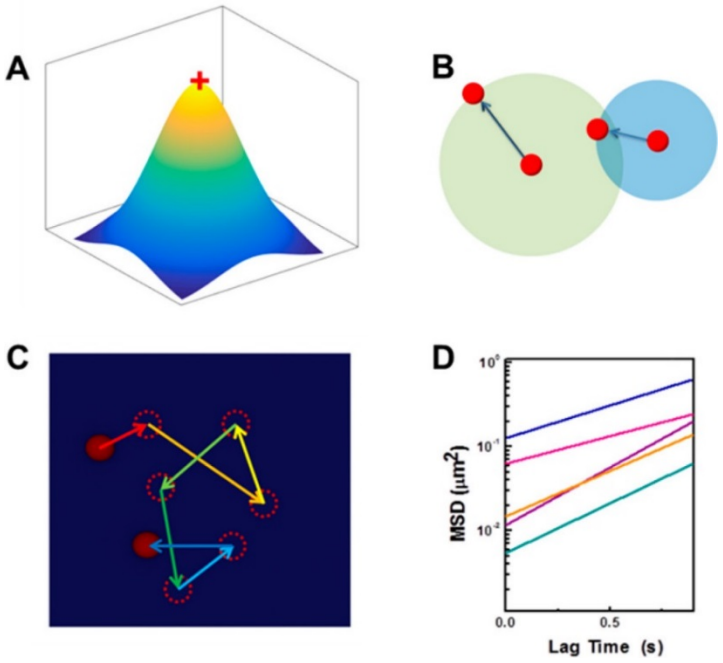

Figure 18 Schematic representation of single molecule localization and single particle tracking
A The localization (red cross) of the PSF center results in SML. **B** The red dots illustrate the localized single molecules. Algorithms, like nearest neighbor allow to connect the localization belonging of the same particle at different time points. **C** Several steps together built a trajectory of the particle. **D** The trajectory provides information about the MSD over time and D_{app} of the particle. (Figure adapted from Shen et al., 2017)

$$MSD = 2nD\Delta\tau \tag{11}$$

where n is the dimension. In order to receive the diffusion constant, the equation can be transformed to:

$$D = \frac{MSD}{2n\Delta\tau} \tag{12}$$

It is also possible is to fit the slope of the MSD plot, which is than $MSD/\Delta\tau$ (Figure 19B). This extracted slope needs to be multiplied by $1/2n$, where n is again the dimension. In the case of two-dimensional tracking n is 2. When diffusing inside a membrane, proteins are per se confined, which is why the fit of the slope is done before the MSD plot gets saturated. Usually, the first 4 to 6 steps allow to extract the slope of a MSD plot. Additionally, the slope should not be fitted through zero thereby the y-axis section also allows to determine the localization precision. However, trajectories of mitochondrial proteins reveal the connectivity between mitochondria and mitochondrial microcompartments in which the tracked protein diffuses (Appelhans et al. 2012). Furthermore, single particle tracking needs high frame rates. Thus, the exposure time of a single frame needs to be reduced. Recording a fluorophore with an exposure time of 16 ms compared to 32 ms results in twice as many localizations without increasing the bleaching of a molecule. Mobile signals produce a dynamic error, which results from particle motion during the exposure time, this error is reduced by lower exposure times. However, reducing the exposure time also results in less photons collected per molecule per frame and this can influence the localization precision.

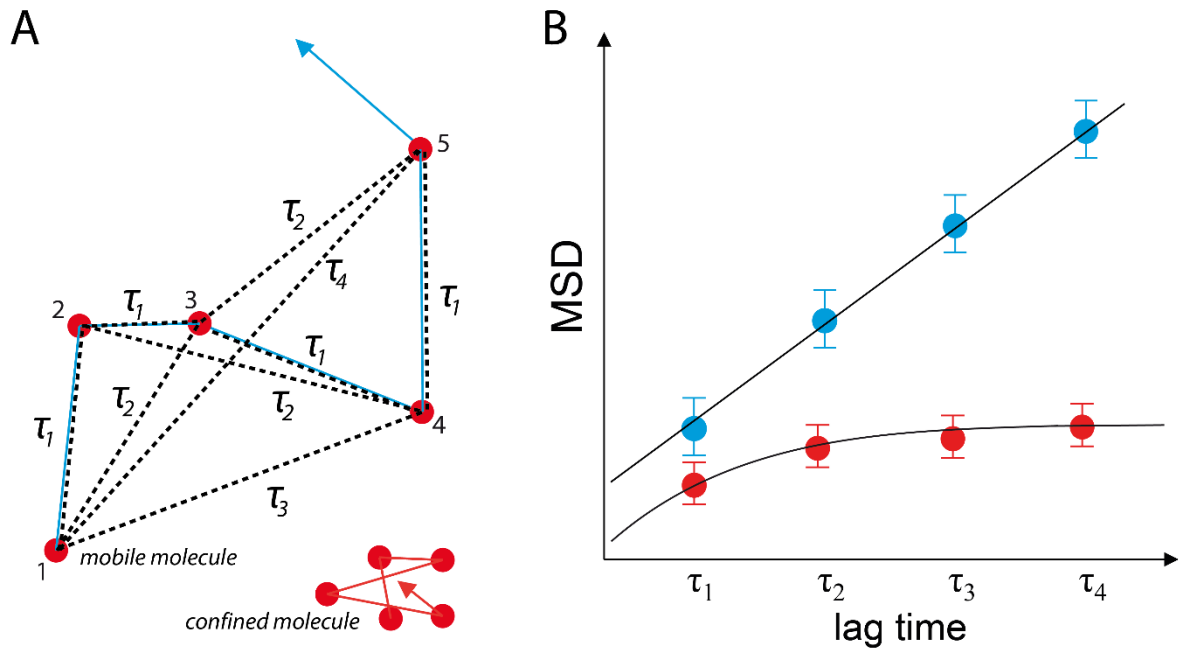

Figure 19 Determination of diffusion constants and diffusion properties
A Trajectories of a mobile molecule and confined molecule localized in five chronological frames. The different distances of the MSD were extracted. **B** MSD over time. The mean square displacements of one or multiple trajectories plotted together allow to extract the diffusion coefficient for single trajectories or all plotted trajectories.

8.12.2 Alignment of the Cylindrical Lens

In order to align the orientation of the cylindrical lens the samples decribed in chapter 8.10 were used (

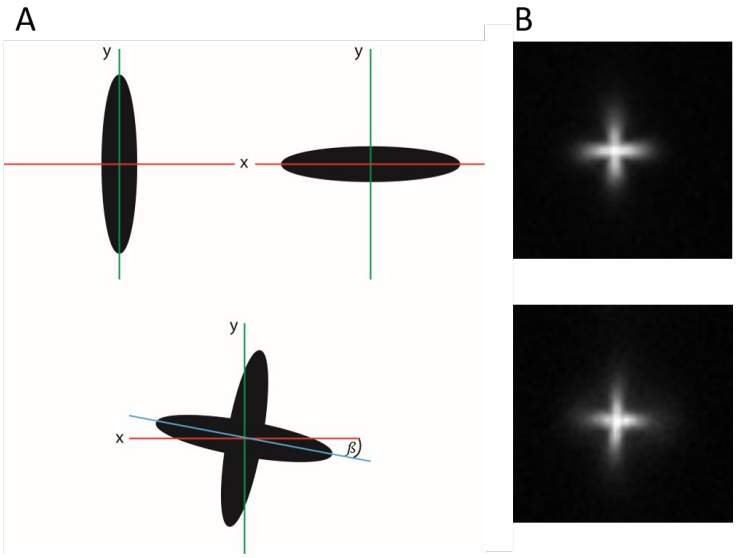

Figure 20 Alignment of the astigmatic distortion to the axis of the camera
A Correct alignment of the cylindrical by the distorted PSF along the x- and y-axis of the camera. The angle β of the PSF to the lateral axis of the camera (green and red line) should be below 0.1°. **B** Summed signals in a z-scan of an astigmatic distorted PSF showing a correct (upper panel) and incorrect (lower panel) adjustment of the cylindrical lens. (Figure adapted from Timo Appelhans, 2014 (Master Thesis))

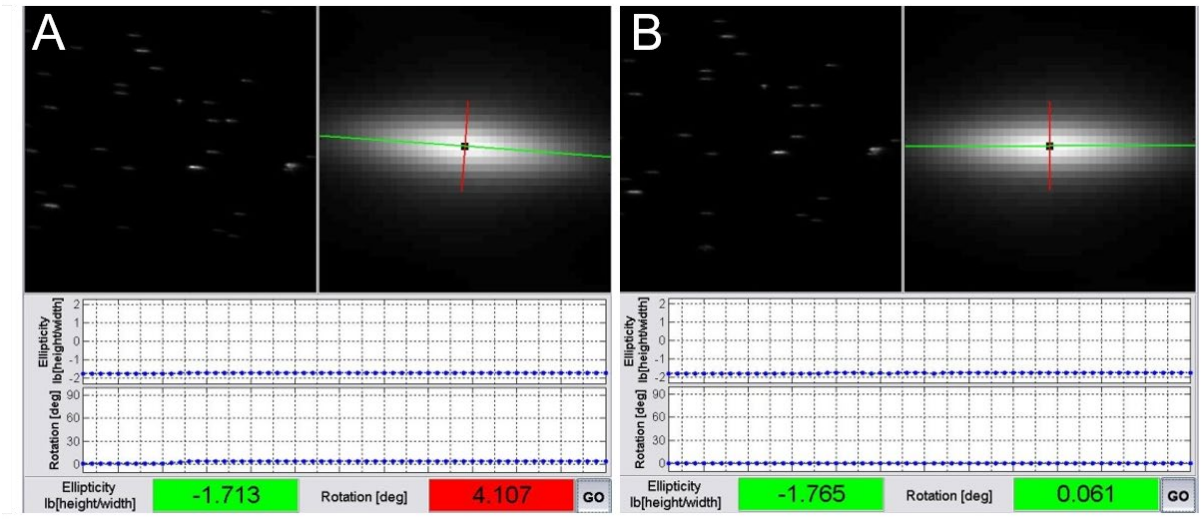

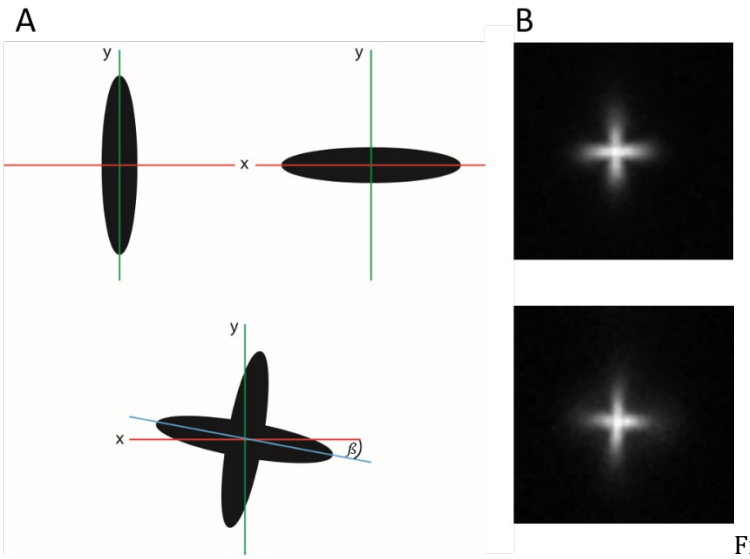

Figure 20). For a correct installation the point spread functions (PSFs) had to follow the x- and y-axis of the camera (

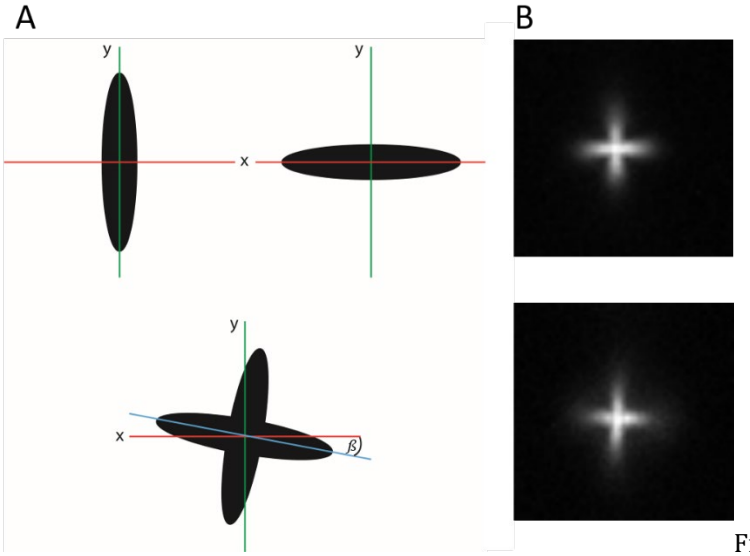

Figure 20B, upper panel). In order to measure the correct installation of the cylindrical lens, the summed PSF of all signals of the calibration sample was used (Figure 21). Therefore, the measurement of the correct installation of the cylindrical lens required a sample without overlapping signals. Additionally, the signals needed to be homogenously distributed in order to allow a qualitative measurement of the summed PSFs. The adjustment of the correct position of the cylindrical lens was done by using a software, called AstigAxisCalibration-Class, a MatLab algorithm which allowed measuring the angle of the distortion direction along the x- and y-axis of the camera (Figure 21). In order to obtain a precise distortion along the lateral axis of the camera an angle $\beta <$ 0.1° was intended (Figure 21B). The software calculates the ellipticity ε of the distortion by division of the height δ_y and width δ_x of the PSF (Equation 13).

Figure 21 Screenshot of the AstigAxisCalibration-Class software
The ellipticity ε of the imaged signals as well as orientation of the cylindrical lens via the the angle β of the x-axis of the PSF to the x-axis of the camera was measured. **A** The cylindrical lens was not installed correct α was ~ 4.11°. **B** The cylindrical lens was precise and correct installed, α ≤ 0.06°. (Sofware developed by C. P. Richter, Biophyisics, University of Osnabrück), (Figure adapted from Timo Appelhans, 2014 (Master Thesis))

$$\varepsilon = \frac{\delta_y}{\delta_x} \tag{13}$$

Additionally, the software allows to determine the angle β of the PSF relative to the lateral axes of the camera. The alignment is an iterative process and requires bright fluorescent beads, which have a smaller diameter than the Rayleigh criterion d_r, in order to minimize the error in fitting the PSF of the summed signals. The signals taken are approximated by an elliptical Gaussian function along the x- and y-axis of the EMCCD chip. Here a high SNR and SBR allow precise determination of the PSF of the signals taken, thereby reducing the error in alignments of the cylindrical lens. Measuring the distortion of the PSF in order to calibrate the z-position of the later imaged fluorescent signals can only be done with fluorescent signals bound on the coverslip surface, because the distortion along the x- and y-axis changes deep inside the sample (Deng et al, 2009) (Figure 22). Thus, the described calibration samples are perfect to measure the correct installation of the cylindrical lens and measuring the astigmatic distortion of the PSF of single fluorescent molecules in order to set up a calibration curve.

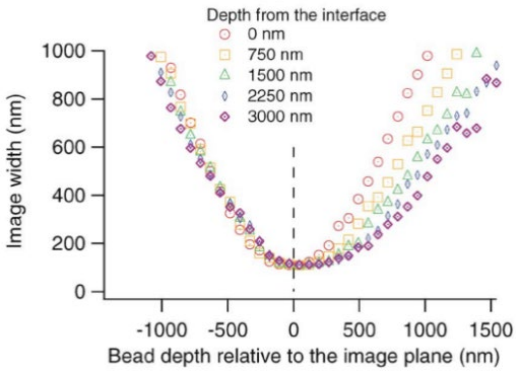

Figure 22 Error in distortion in reference to the depth from the interface
The distortion of the PSF depends on the distance of the fluorescent signal to the coverslip. (Figure adapted from Yi Deng et al., 2009)

8.12.3 3D localization, 3D reconstruction and 3D tracking

3D TALM was performed by using a cylindrical lens in the emission path at the camera port of the microscope (Figure 12, **Fehler! Verweisquelle konnte nicht gefunden werden.**). In this work a cylindrical lens with a focal distance of 1 m was used. The lens was installed in a fixed position, 10 cm before the QV2. Thus, an astigmatic distortion of the fluorescence signals was induced. In single molecule microscopy, a cylindrical lens leads to an astigmatic distortion of the PSF. The direction and intensity of the astigmatic distortion depends on the position of the fluorophore to the focal plane of the microscope (**Fehler! Verweisquelle konnte nicht gefunden werden.**B). The PSF of a fluorophore far away from the focal plane shows a larger distortion than the PSF close to the focal plane. The PSF of a signal in the focal plane is not distorted at all (**Fehler! Verweisquelle konnte nicht gefunden werden.**B). Additionally the PSF of a fluorophore above the focal plane is distorted along the x-axis of the camera and the PSF of a fluorescent molecule below the focal plane is distorted along the y-axis of the camera (**Fehler! Verweisquelle konnte nicht gefunden werden.**B). Turning the lens leads to a turned distortion. The correct alignment of the cylindrical lens was ensured as decribed before (

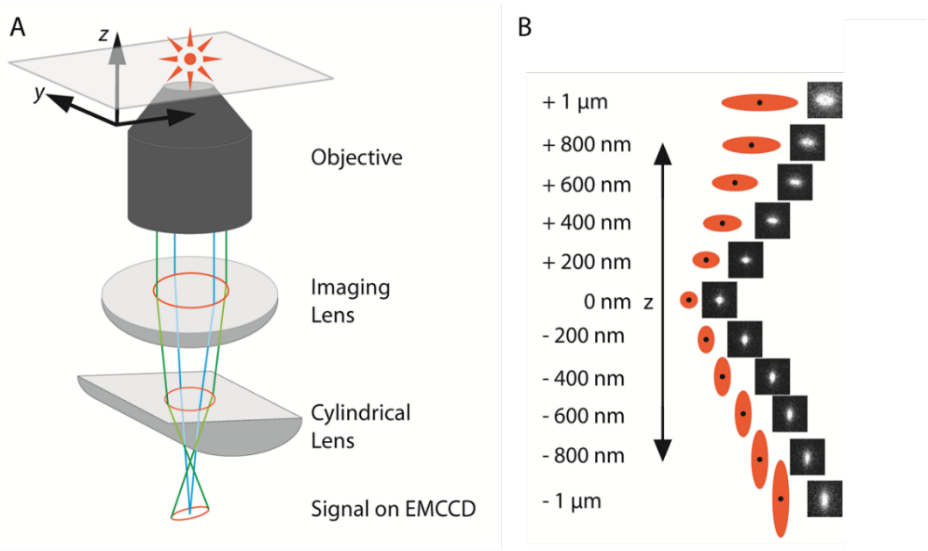

Figure 23 3D TALM setup and astigmatic distortion of the PSF of a single fluorescent signal
A The cylindrical lens was put into the fluorescence emission pathway at the camera port of the microscope body. **B** The intensity and direction of astigmatic distortion depends on the distance to the focal plane of the microscope. (Figure adapted from Timo Appelhans, 2014 (Master Thesis))

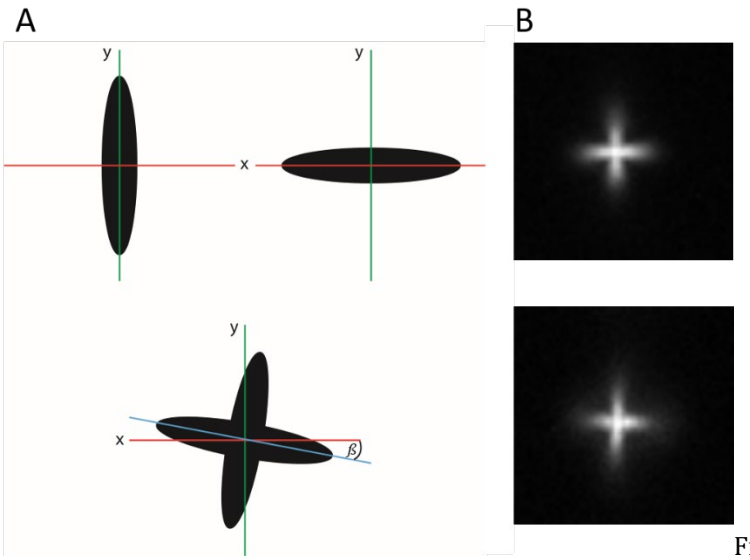

Figure 20). In order to localize proteins in all three dimensions, the PSFs of the fluorescent signals were fitted by Gaussian mixture-model fitting. The software used for 3D localization is called SlimFast, available on request from the division of biophysics, University of Osnabrück, Osnabrück, Germany. 3D reconstruction was done with the ViSP software (El Beheiry and Dahan, 2013). In living cells mitochondria move over time in all dimensions. In order to test if mitochondrial networks can be imaged in all three dimensions in living cells 3D reconstruction of mitochondria was carried out. Additionally, for each dataset a reconstruction allowed to investigate if a movement of mitochondria occurred during imaging. Furthermore, the gained reconstruction enables the possibility to investigate first which part of the network was in focus and secondly allows a quality control of the dataset. Data which showed a movement of mitochondria was excluded from further analysis.

3D tracking was performed with the use of the u-track software (Jaqaman et al., 2008), implemented into MatLab 2016b. The software is open source from the Danuser Laboratory, UT Southwestern Medical Center, Dallas, Texas. U-track allows to localize and track single molecules in all three dimensions by using the

Gaussian mixture-model fitting.

3D single particle tracking allows to extract the MSD over time given by equation (11). In 3D tracking 4 steps were used to fit the *MSD* over $\Delta\tau$ plot. The equation (11) was transformed to equation (12). In the case of 3D tracking, plotting *MSD* over $\Delta\tau$ and fitting the slope m linear allows to transform the equation (12) to:

$$D = \frac{1}{6} m \tag{14}$$

where the slope m is:

$$m = \frac{MSD}{\Delta\tau} \tag{15}$$

Thus, the mean diffusion coefficient of the tracked proteins was calculated by dividing the slope by six. The localization precision σ_i in the ith dimension was directly extracted from the tracking data. In the following equation b_i is the y-axis intercept of the linear fit of the ith dimensional MSD over $\Delta\tau$.

$$\sigma_i = \sqrt{b_i/2 + D\Delta t/3} \tag{16}$$

The gained mean localization precision for each dimension was used in the 3D reconstructions of the localized signals.

8.12.4 Directionality analysis of diffusive proteins

In order to evaluate in which direction trajectories of mitochondrial proteins are oriented the step direction in reference to the longitudinal axis can be analyzed. The MATLAB software MitoOriented-Dynamics allows to mark the longitudinal axis of imaged mitochondria (Figure 24A). This axis functions as a backbone of the trajectories of imaged mitochondria. Next, the trajectories are interpolated in a linearized mitochondrion. Following, the step direction in reference to the backbone axis is calculated. Branching points and ends of mitochondria do mostly not show a clear orientation of cristae or even no cristae at all, independent of the metabolic condition. Thus, branching points and ends of mitochondria have not been taken into account in order to minimize the bias. After marking the longitudinal axis, the step direction is plotted in a pie chart (Figure 24B). This diagram shows the direction of the analyzed steps in degree and the counts of step directions with a 5° binning. Additionally, steps directions were plotted in a heat map with a logarithmic scale along the y-axis showing the magnitude of step directions along the y-axis and the orientation of the step in degree along the x-axis (Figure 24C). The color code illustrates the amount of steps in a certain direction and step magnitude from blue (less counts) to yellow (many counts) Furthermore, the software allows to bin several steps of a trajectories to one step. Therefore, a binning of 4 steps to one step was chosen (Figure 25). By this the continuous movement of proteins can be analyzed without creating a great bias, because a great binning can lead to a false estimation of protein movement. A 4-step-binning is sufficient enough to differentiate between longitudinal and perpendicular trajectory directionalities (Figure 25A). Perpendicular movement with a steps size of about 100 nm would result in a 400 nm step. The diameter of a mitochondrion is about 500 nm to 800 nm. So, a 4-step binning still allowed analyzing the directionality of protein movement in small microcompartments like cristae. Thus, true perpendicular movement in contrast to clear longitudinal movement could be compared. This set the basic statistic to analyze the predominant protein movement in mitochondrial membranes. In the case of the IM it allows to investigate if a protein moves in the CM or in the IBM. If a protein is localized dominantly in the IM and the general trajectory directionality of all proteins tracked is switched from perpendicular to longitudinal movement this could indicate an ultrastructural change of the IM accompanied by a loss of cristae. Due to the before mentioned reasons, the 4-step binning was used in order to analyze the movement

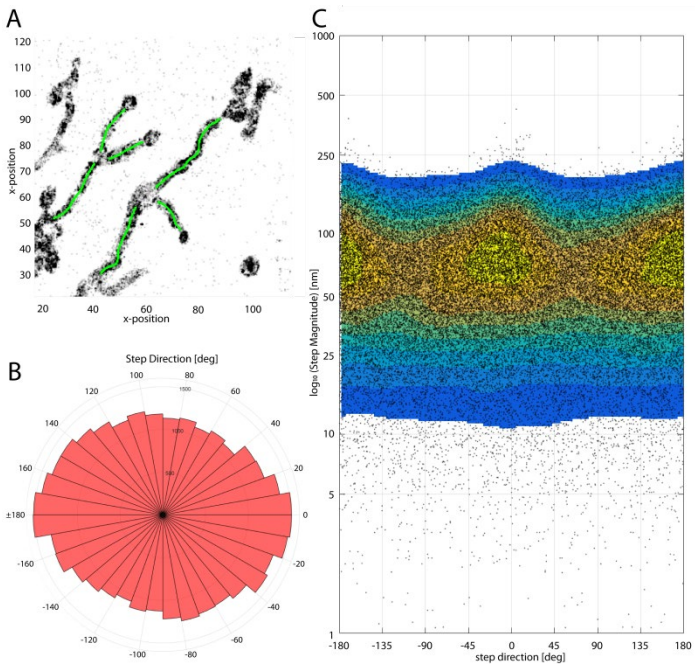

Figure 24 Directionality analysis by MitoOrientedDynamics
A MitoOrientedDynamics allows to mark the longitudinal axis of mitochondria (green lines). Branching points and end of mitochondria have not been taken into account. **B** Pie chart diagram of the given step directionalities. This allows to conclude in which direction the trajectories are oriented. **C** Heat map of the step directions. The jumpsize is plotted logarithmic in nm against the direction in degree.

direction of diffusive proteins. MitoOrientedDynamics was used for 2D and 3D SPT trajectory directionality analysis.

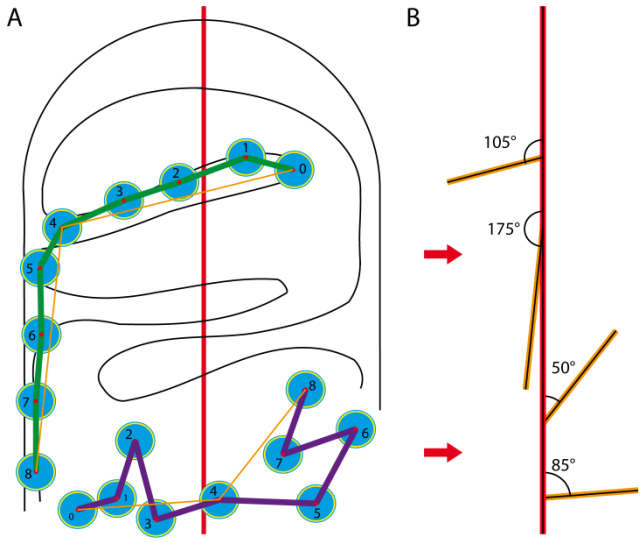

Figure 25 Trajectory orientation by 4-step binning
A Two exemplary trajectories with a trajectory length of 8 steps. The green trajectory shows a movement from the CM into the IBM. The purple trajectory shows a random movement in the OM or IBM. The orange line illustrates the 4-step binning of the steps. The red line shows the longitudinal axis of the mitochondrion. **B** Calculated angles in degree of the binned steps from both trajectories. The angle is measured in context to the longitudinal axis of the mitochondrion (red line).

9 Results

9.1 Optimized cell density to image mitochondria and single mitochondrial proteins

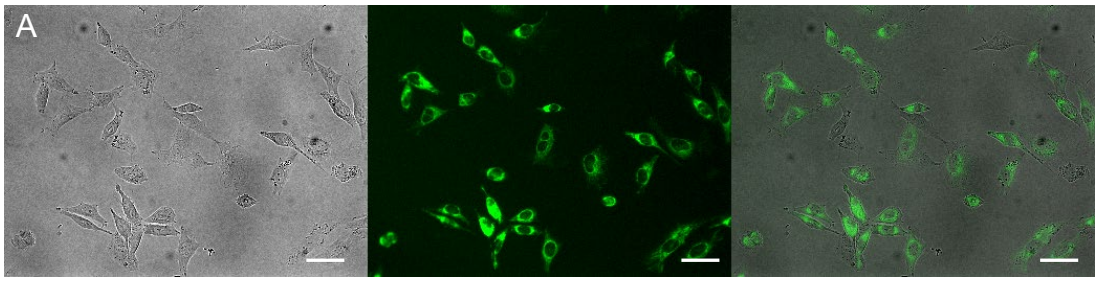

Sample with less cell density and small cells

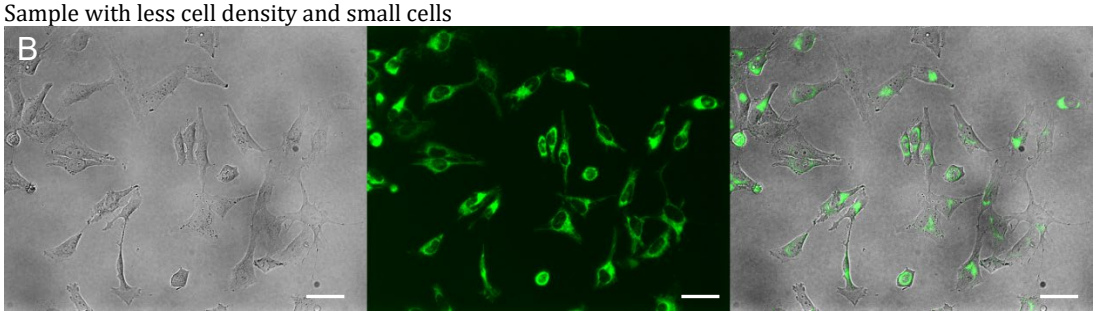

Sample with ideal cell density and cell shape. Cell were individual but cell protrusion were in contact

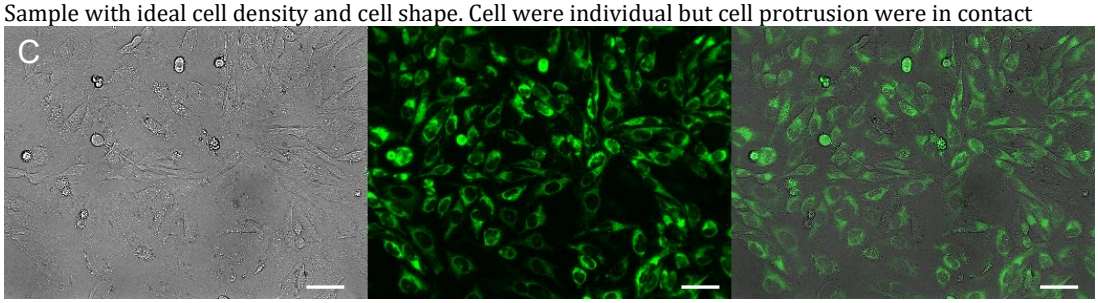

Sample with a too high cell density, mitochondrial networks cannot expand and cells overlap

Figure 26 Critical cell density in samples
HeLa cells stained with 100nM MitoTrackerGreen™. The cell density influenced the shape of the mitochondrial network. Images taken with Axiovert 200 M, Zeiss. Scale bars: 25 µm

In order to exclude false localizations and false tracking events, caused by overlapping of mitochondria or mitochondria which were too close together, mitochondria in the perinuclear regions were not imaged in TALM experiments. Thus, only distinguishable single and separated mitochondria in an intact mitochondrial network in the cell perephery were recorded. Beside this a perfect cell density is fundamental (Figure 26). Imaging HeLa cells in a sample with low cell density leads to small cells with a high chance for overlapping mitochondria (Figure 26A). The ideal cell shape with large cells which were in touch of the neighbor cells at cell protrusions, provided large mitochondrial networks. Here, the mitochondria were part of a network, long and separated (Figure 26B). Samples with a too high cell density had cramped mitochondrial networks or even overlapping cells, thus less separated mitochondria were observed (Figure 26C). Approxiamtelly 90k cells were seeded two days before imaging in a 35 mm cell culture dish containing a coated coverslip. This had proven to result in an ideal cell density for imaging.

9.2 Mono Color Single Particle Tracking

9.2.1 Dynamic Imaging of Mitochondrial Membrane Proteins in Specific Sub-Organelle Membrane Locations

Dynamic imaging of mitochondrial membrane proteins in specific sub-organelle membrane locations

Timo Appelhans[1] & Karin B. Busch[1,2]

Abstract Mitochondria are cellular organelles with multifac- eted tasks and thus composed of different sub-compartments. The inner mitochondrial membrane especially has a complex nano-architecture with cristae protruding into the matrix. Related to their function, the localization of mitochondrial membrane proteins is more or less restricted to specific sub- compartments. In contrast, it can be assumed that membrane proteins *per se* diffuse unimpeded through continuous mem- branes. Fluorescence recovery after photobleaching is a ver- satile technology used in mobility analyses to determine the mobile fraction of proteins, but it cannot provide data on sub- populations or on confined diffusion behavior. Fluorescence correlation spectroscopy is used to analyze single molecule diffusion, but no trajectory maps are obtained. Single particle tracking (SPT) technologies in live cells, such as tracking and localization microscopy (TALM), do provide nanotopic local- ization and mobility maps of mitochondrial proteins in situ. Molecules can be localized with a precision of between 10 and 20 nm, and single trajectories can be recorded and analyzed; this is sufficient to reveal significant differences in the spatio- temporal behavior of diverse mitochondrial proteins. Here, we compare diffusion coefficients obtained by these different technologies and discuss trajectory maps of diverse mitochon- drial membrane proteins obtained by SPT/TALM. We show that membrane proteins in the outer membrane generally dis- play unhindered diffusion, while the mobility of inner mem- brane proteins is restricted by the inner membrane architec- ture, resulting in significantly lower diffusion coefficients. Moreover, tracking analysis could discern proteins in the inner boundary membrane from proteins preferentially diffusing in cristae membranes, two sub-compartments of the inner mito- chondrial membrane. Thus, by evaluating trajectory maps it is possible to assign proteins to different sub-compartments of the same membrane.

Keywords Mitochondrial membrane proteins TOM TIM hFis Mitofilin/Mic60 F_1F_0 ATP synthase Cox Single molecule localization and diffusion Mobility analyses Membrane sub-compartments SPT technologies FRAP FCS

Mitochondria are organelles with a plethora of functions, in- cluding Ca^{2+} signaling, oxidation of fatty acids, respiration, ATP synthesis and recycling of redox-equivalents. To fulfill these tasks, mitochondria are subdivided into several compartments: the outer membrane (OM), the inner membrane (IM) and the matrix space. The IM is further compartmentalized into the inner boundary membrane (IBM) alongside the OM and the cristae membranes (CM) (Mannella et al. 2004) (Fig. 1). Despite the presence of 13 proteins that are mitochondrially encoded and part of the bioenergetic oxi dative phosphorylation (OXPHOS) system, the complete repertoire of mitochondrial proteins (including further subunits of the OXPHOS) has to be imported via the translocase of the outer membrane (TOM) (Straub et al. 2016) and the translocase of the inner membrane (TIM) (Mokranjac and Neupert 2010). Furthermore, the complex IM architecture is under the control of several proteins, including F_1F_0 ATP synthase (Gavin 2004; Paumard et al. 2002) and mitofilin/Mic60 (John 2005; Tarasenko et al. 2017).

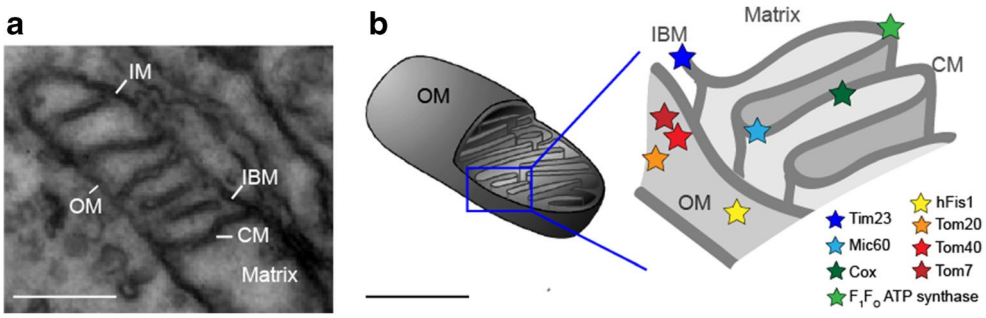

Fig. 1 Ultrastructure of mitochondria and respective localization of important proteins

a Electron microscopy image showing part of a mitochondrion, with the membranes appearing black: OM outer membrane, IM inner membrane [which is partitioned into the inner boundary membrane (IBM) and the cristae membranes (CM)]. The matrix is an aqueous compartment. **b** Scheme showing the localization of the proteins that have been studied in terms of mobility and localization. Tom40 Core subunit of the translocase of the outer membrane (TOM) complex, Tom20 receptor subunit of TOM, Tom7 subunit of TOM (Shiota et al. 2015), hFis human fission factor in the OM (Yu et al. 2005), Mic60 mitofilin, part of the MICOS complex in the IBM (Ding et al. 2015), Tim23 part of the inner membrane translocase (TIM) in the IBM (Demishtein-Zohary and Azem 2017), Cox cytochrome c oxidase, a complex of the oxidative phosphorylation (OXPHOS) system in the CM, F1FOATP synthase, a further OXPHOS complex

To better understand the function and interaction of these proteins, information on their specific sub-mitochondrial localization and spatio-temporal orga- nization is needed (Fig. 1b). Superresolution fluorescence microscopy (including immuno-electron microscopy) has enabled sub-diffraction localization of mitochondrial molecules, resulting in the identification of proteins in different organelle compartments of mitochondria (Appelhans et al. 2012; Beinlich et al. 2015; Jans et al. 2013; Wurm and Jakobs 2006) and revealed that the proteins of the IM are apparently sub-compartmentalized in the IBM and CM part of the IM (Vogel et al. 2006). Information on the temporal dynamics of proteins would help to understand this segregation of proteins in an (in principle) continuous membrane. In the following, three dynamic methods to study mobility and to determine diffusion coefficients of mitochondrial membrane proteins are presented.

The mobility of several inner and outer membrane proteins (Sukhorukov et al. 2010) and of matrix–green fluorescent protein (Partikian et al. 1998) was determined by fluorescence recovery after photobleaching (FRAP), a method in which after spot bleaching the recovery of fluorescence is monitored and analyzed (Reits and Neefjes 2001) (Fig. 2a). The diffusion of a matrix-targeted protein was also determined via fluorescence correlation spectroscopy (FCS) (Koopman et al. 2007), which is not an imaging technology but a spectroscopic method that records changes in fluorescence intensity in the confocal volume over time (Bacia et al. 2006). From autocorrelation curves [G(τ)], the diffusion behavior is analyzed and diffusion coefficients are extracted (Fig. 2b).

Single particle tracking (SPT) combines the spatial and dynamic analysis of proteins by imaging single, labeled proteins at high frame rates until they are bleached. After localization, trajectory maps are generated by, for example, a multi- target tracing algorithm (Sergé et al. 2008) (Fig. 2c). Commonly, fluorescent protein-tags (FP) are used to visualize the proteins of interest (Subach et al. 2010). In a variant of SPT, named tracking and localization microscopy (TALM) (Appelhans and Busch 2017; Appelhans et al. 2012), bright and photostable rhodamine dyes attached to a specific substrate reacting covalently with the HaloTag or SnapTag are used for post-translational labeling (Juillerat et al. 2003; Schröder et al. 2009). The localization and dynamics of several outer and inner membrane proteins have been analyzed using this method. From step length diagrams (Fig. 2c–II), apparent diffusion coefficients are extracted and appointed to subpopulations distinguished by their mobility (e.g. mobile, less mobile and confined mobile

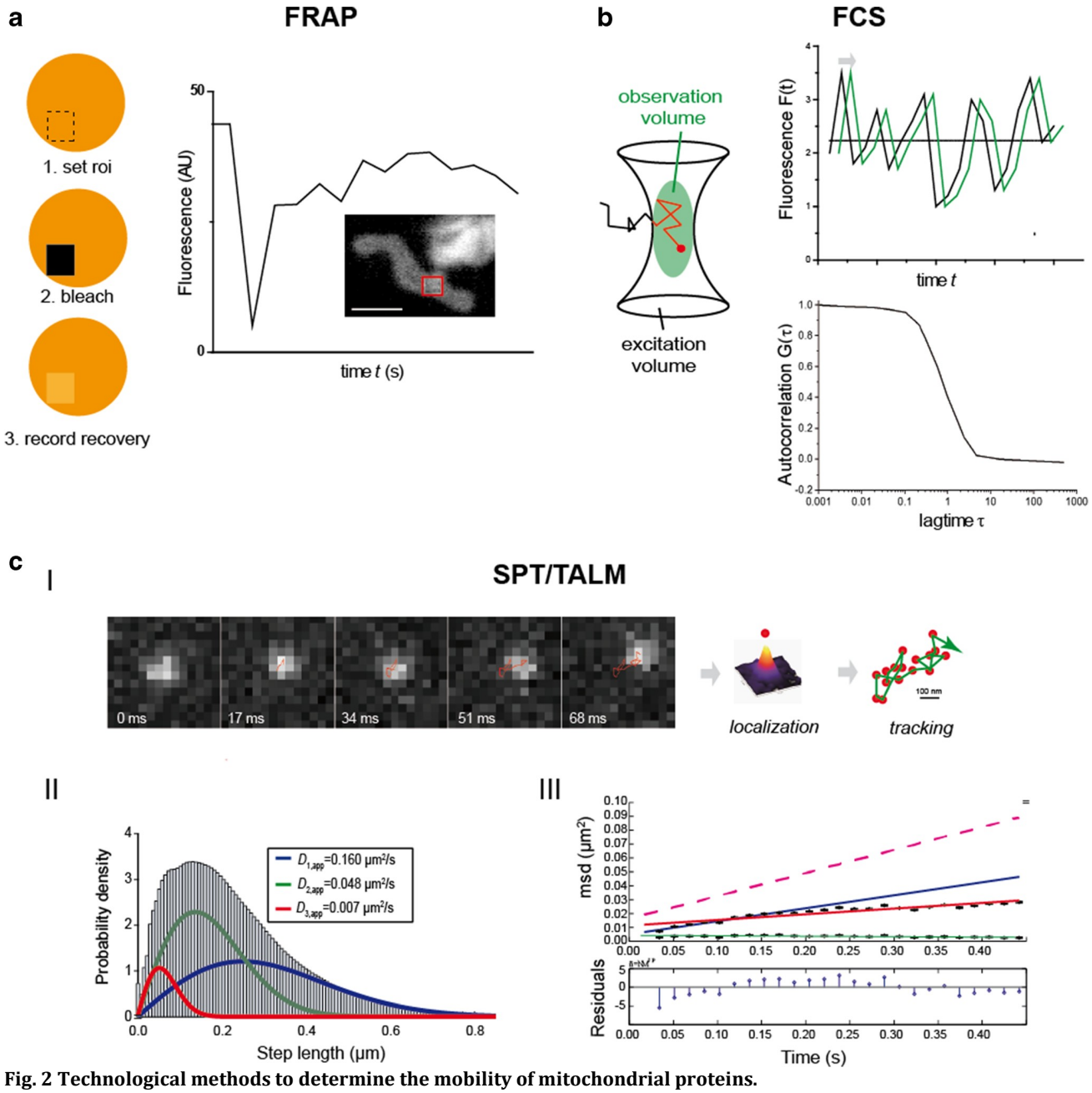

Fig. 2 Technological methods to determine the mobility of mitochondrial proteins.
a Fluorescence recovery after photobleaching (FRAP). Usually, proteins of interest are fused to a fluorescent protein and from a certain region of interest (roi) the pre-bleach fluorescence is recorded. Then, the fluorescence in the roi is bleached down and imme- diately after the recovery of fluorescence is monitored. The recovery curve is fitted and the percentage of mobile and immobile molecules and the diffusion coefficient of the mobile fraction can be determined. Here, a FRAP curve for Tom7, a subunit of the TOM complex, fused to green fluorescent protein is shown. The fluorescence was bleached in the indicated roi (red frame) (Sukhorukov et al. 2010). **b** Fluorescence correlation spectroscopy (FCS) reveals protein diffusion, such as in the mi- tochondrial matrix (Koopman et al. 2007). Fluorescence intensity fluctu- ations from the confocal volume are recorded and an autocorrelation function is generated from which the mean diffusion constant can be calculated. **c-I** Localization and tracking of single molecules in different mitochondrial compartments by tracking and localization microscopy (TALM) (Appelhans et al. 2012), a single particle tracking (SPT) tech- nique. A single molecule is observed for multiple frames until bleached. The fine localization of single molecules is obtained by two-dimensional Gaussian fitting of the diffracted signal in a deflation process, following which a trajectory map is generated using a multi-target tracing algorithm (Sergé et al. 2008). **c-II** Step length diagrams are generated, and from the cumulated distribution function (CDF) diffusion coefficients are extracted by fitting until the least root mean square error is minimized. Usually, several subpopulations characterized by different mobilities (mobile, less mobile and confined mobile) are obtained. **c-III** Mean square displace- ment (msd) plots are analyzed to obtain the confinement for short (2-5 steps, blue line) and long-range diffusion (2–20 steps, red line) (Schütz et al. 1997). The relation between msd and the diffusion coefficient D is: msd = $4D\Delta t\alpha + 4\varepsilon^2$ where ε^2 is the square error (localization precision) and α is the non-linearity coefficient. Scale bar 100 nm (a)

molecules). Mean square displacement plots of >30 ms allow for confinement analysis, following which only the diffusion coefficients of mobile fractions are compared.

Movement of outer mitochondrial membrane proteins

The outer mitochondrial membrane is tubular without extra- invaginations. To date, information on the mobility of four mitochondrial OM proteins is available: hFis, a protein in- volved in mitochondrial fission (Yu et al. 2005) and three different subunits of the TOM complex, i.e. Tom7, Tom20 and Tom40 (Shiota et al. 2015) (Fig. 1b). hFis, Tom7 and Tom20 possess a single transmembrane domain, while Tom40 is a β-barrel protein inserted into the OM. The local- ization and mobility of hFis and Tom7 were determined by FRAP analysis of FP-labeled proteins in mitochondria in situ in cell culture (Sukhorukov et al. 2010), and the obtained mobility was 0.7 $\mu m^2/s$ (hFis) and 0.6 $\mu m^2/s$ (Tom7), respectively (Table 1). The majority of Tom7 molecules showed unhindered diffusion, but approximately 7% were immobile (Sukhorukov et al. 2010). In a different study, the mobility of Tom40, the core subunit of the TOM complex (Rapaport and Neupert 1999), was determined by SPT with a localization precision of 20 nm. Analysis of mean square displacements (*msd*) within 5 ms and cumulative distribution functions (CDF) provided an apparent diffusion coefficient of D_{app} = 0.5 $\mu m^2/s$ for Tom40, which is only marginal slower than the *D* for Tom7 obtained by FRAP. For time windows above 35 ms, the diffusion was clearly confined. Several reasons were discussed for the confine- ment: a complicated geometry, interaction with lipids or an active, anchored complex (Kuzmenko et al. 2011). In complementary studies, hFis and Tom20 mobilities were deter- mined by TALM, a specific SPT method (Appelhans and Busch 2017; Appelhans et al. 2012). Apparent diffusion coef- ficients were $D_{mobile,\ hFis}$ = 0.17 $\mu m^2/s$ for hFis and $D_{mobile,\ Tom20}$ = 0.142 $\mu m^2/s$. The obtained trajectory maps of hFis1 and Tom20 show rather unhindered diffusion for the majority of proteins (Fig. 3a-I, 3a-II) with a random directionality. The calculated localization precision was 10 nm on average, although a subpopulation of 14% of hFis and Tom20 had a diffusion coefficient of D <0.009 $\mu m^2/s$, indicating immobile/confined fractions (as also found for Tom7 in FRAP measurements). Alternatively, this can be an outcome of movement in *z*. Movement in *z* gives small step lengths in two-dimensional (2D) projections and thus results in low diffusion coefficients. A correction taking into account the geometry resulted in an increase in the diffusion coefficients to $D_{app,corr}$ = 0.215 $\mu m^2/s$ for Tom20 and $D_{app,corr}$ = 0.410 $\mu m^2/s$ for hFis (Appelhans et al. 2012). which are still lower than those obtained from FRAP studies (D=0.6 and D= 0.7 $\mu m^2/s$, respectively).

Movement of inner mitochondrial membrane proteins

The mobility of inner mitochondrial membrane proteins Cox and F_1F_0 ATP synthase, both complexes of the oxidative phosphorylation system (CIV and CV of OXPHOS), was de- termined by FRAP (Sukhorukov et al. 2010) and yielded dif- fusion coefficients of D = 0.3 $\mu m^2/s$ (Cox) and D = 0.4 $\mu m^2/s$ (F_1F_0 ATP synthase). In a complementary study, diffusion analysis by TALM resulted in $D_{app,Cox}$ = 0.056 $\mu m^2/s$ and $D_{app,\ F1FO\ ATP\ synthase}$ = 0.070 $\mu m^2/s$ (Table 1). TALM trajec- tory maps also show details about possible confinement and directionality. Contrary to OM proteins (Fig. 3a), the trajectory maps of Cox and F_1F_0 ATP synthase indicate a confine- ment of those specific IM proteins in cristae (Fig. 3b). In contrast, trajectory maps of the IM proteins Tim23 and Mic60 show a different type of confinement: the trajectories are found in a pearl-like arrangement along both sides of the IBM with no preferential directionality (Fig. 3c). The diffusion coefficient for Tim23 was $D_{mobile,Tim23}$ = 0.044 $\mu m^2/s$ (±0.025 $\mu m^2/s$; N = 2 independent assays, >1900 trajectories analyzed); for Mic60 it was $D_{mobile,Mic60}$ = 0.063 $\mu m^2/s$ (±0.010 $\mu m^2/s$; N = 2 independent assays, >2000 trajectories analyzed). Albeit the diffusion coefficients of both proteins were similar to those of Cox and F_1F_0 ATP

Table 1 Diffusion coefficients *D* of mitochondrial proteins in situ in live mammalian cells

Protein[a]	Mitochondrial localization	FRAP, *D* (μm²/s)	SPT/TALM, *D* (μm²/s)	FCS, *D* (μm²/ s)
hFis	OM	0.7 ± 0.1 Sukhorukov and Breiter-Hahn (2009)	0.170 ± 0.05 (90% mobile) Appelhans et al. (this paper)	
Tom7	OM	0.6 ± 0.4 Sukhorukov and Breiter-Hahn (2009)	0.133 ± 0.025 Appelhans et al. (this paper)	
Tom20	OM		0.142 ± 0.014; 0.005 ± 5E-4 Appelhans et al. (2012)	
Tom40	OM		0.5 (% mobile)[b] Kuzmenko et al. (2011)	
F_1F_0 ATP synthase, CV	IM	0.4 ± 0.1 (mobile) 0.0005 ± 0.0001 (immobile) Sukhorukov and Breiter-Hahn (2009)	0.070 ± 0.009 (35% mobile) 0.020 ± 0.004 (47% less mobile); 0.005 (18% immobile); Appelhans et al. (2012)	
Cox, CIV	IM	0.3 ± 0.07; 0.007 ± 0.002 Sukhorukov and Breiter-Hahn (2009)	0.056 ± 0.016 (mobile) 0.016 ± 0.005 (less mobile) 0.003 ± 0.001 (immobile) Appelhans et al. (this paper)	
Mic60	IM		0.068 ± 0.001 (49%) 0.020 ± 0.004 (51%) Appelhans et al. (this paper)	
Tim23	IM		0.057 ± 0.001 (45%) Appelhans et al. (this paper)	
SDH	IM		0.140 ± 0.034 (79%); 0.016 (21%); Wilkens et al. (2012)	
Mt-FP	matrix	22 ± 2 Partikian et al. (1998)		20 – 30 μm²/s Koopman et al. (2007)

FRAP Fluorescence recovery after photobleaching, *FCS* fluorescence correlation spectroscopy, *SPT/TALM* single particle tracking/tracking and localization microscopy, *OM* Outer membrane of mitochondrion, *IM* inner membrane of mitochondrion

[a] *SDH* Succinate dehydrogenase, *Mt-FP* mitochondrial fluorescence-labeled protein. All other proteins are defined in the caption of Fig. 1

[b] In isolated mitochondria from yeast

synthase in the same membrane, their specific localization was clearly distinct as the trajectory maps revealed (Fig. 3c).

The apparent diffusion coefficients for the IM proteins Cox and F_1F_0 ATP synthase determined by TALM were significantly lower than those obtained by FRAP, likely due to a significant quota of molecules being restricted in their diffusion due to geometrical constraints. When *msd* were plotted, for long range diffusion >50 ms, confinement started to dom- inate the mobility in accordance with preferential localization in cristae membranes (Wilkens et al. 2012) (Fig. 3d-II). These confined mobile molecules were probably not recorded by FRAP, since their confinement within 0.01 μm² (Fig. 3c-II) is below the diffraction limit. For Tim23 and Mic60, the con- finement was in a similar range, albeit for a different reason: these molecules are anchored in the membrane in conjunction with supercomplex formation (Harner et al. 2011; van der Laan et al. 2016).

Conclusion

The determination of protein mobility in mitochondrial compart- ments is still a challenge. FCS, which is an established method for the determination of the mobility of soluble proteins, has had no application in the determination of mitochondrial membrane protein mobility, but only for a matrix-targeted soluble FP. The determined diffusion coefficient was similar to that determined by FRAP (Table 1). Indeed, FCS and FRAP are probably the only methods to characterize the mobility of matrix proteins, since diffusion coefficients attributed to soluble FPs are >93 $\mu m^2/s$ (Petrasek and Schwille 2008) and the corresponding step lengths are too large to obtain confident connections be- tween subsequent localizations in SPT. The reduced mobility of FPs with 20–30 $\mu m^2/s$ in the mitochondrial matrix is probably related to diffusion obstacles imposed by cristae membranes dividing the matrix (Sukhorukov and Bereiter-Hahn 2009). For membrane proteins, FRAP studies have provided higher diffu- sion coefficients as SPT analysis, possibly attributable to two factors: (1) FRAP is a diffraction-limited imaging technique and thus is spatially coarse; (2) FRAP measures only highly mobile molecules, since confined molecules or slow mobile molecules are too slow to contribute to a fluorescence recovery. In addition, the bleaching which continues during recording is more of a problem for FRAP than for single molecule imaging (where- by the signal is lost, but has no influence on the analysis). Furthermore, recovery analysis after spot photobleaching of FP in mitochondria is not straightforward to analyze due to geometrical factors, shape changes and the movement of mitochondria themselves (Dikov and Bereiter-Hahn 2013; Mishra and Chan 2016). This also partially impacts SPT analysis and a thorough review of data is necessary. Mitochondrial movement interfering with protein motility can be revealed by superimposing images of mitochondria taken before and after the FRAP analysis or superimposing the first and last 500 frames of SP imaging. The power of single molecule tracking in contrast to FRAP and FCS is that is provides localization *and* trajectory maps and thus en- ables sub-organellar resolution. Based on the pattern of their trajectory maps, Tim23 and Mic60 could be designated to the IBM in line with a functional localization at interaction sites with the TOM complex (Tim23) and the cristae junctions (Mic60) (van der Laan et al. 2016), while Cox (CIV) and F_1F_0 ATP synthase (CV) could be appointed to cristae membranes, which are the site of OXPHOS. On the other hand, in SPT/TALM, the diffusion coefficients are extracted from 2D projected movement, which results in an underestimation of mobility on tubular or spherical structures (Renner et al. 2011). Albeit a variety of methods for obtaining both 3D super-resolution images and 3D tracking information have been devised (von Diezmann et al. 2017), 3D tracking is still a challenging option and to our knowledge has not yet been applied to the analysis of the mobil- ity of mitochondrial proteins. Hitherto, even 2D SPT/TALM has been feasible to elucidate sub-organelle localization from the pattern of the respective trajectory maps. To summarize, FRAP and SPT/TALM are complementary methods revealing different aspects of the spatio-temporal organization of proteins.

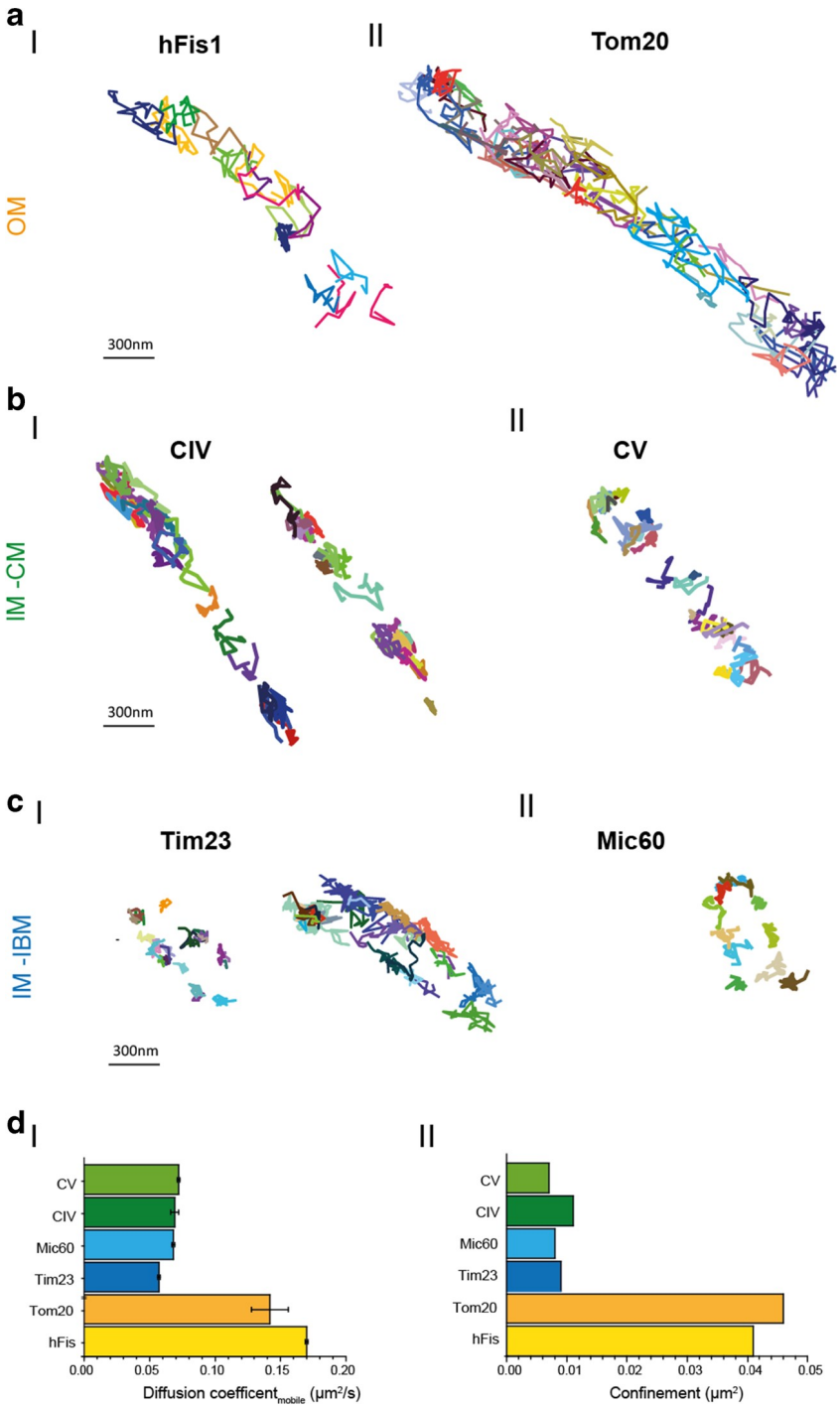

Fig. 3 Motility analysis of mitochondrial membrane proteins by SPT/TALM.
a Trajectory maps of OM proteins hFis (**a-I**) and Tom20 (**a-II**). **b-I** Trajectory maps of Tim32 preferentially found in the IBM. **b-II** Map of Mic60, which is part of the MICOS complex, at cristae junctions (Zerbes et al. 2012). **c-I** Trajectory maps of Cox labeled at its subunit CoxVIIIa in two mitochondria. **c-II** Trajectory map of F_1F_0 ATP synthase labeled at subunit ɣ. For fluorescence labeling of these different protein species, C- terminal HaloTag®-fusion (Los et al. 2008) proteins were generated and posttranslationally labeled by membrane-permeable tetramethylrhodamine functionalized with the HaloTag®-Ligand (TMR^{HTL}). TMR^{HTL} in the specific mitochondrial environment turned out to be a photostable and bright emitter (Appelhans et al. 2012). The labeling was done with substoichiometric concentrations of TMR^{HTL} (0.5–1 nM) to obtain single molecule signals that can be distinguished and localized. The dye was excited with a diode pumped solid-state laser (excitation 561 nm, 200 mW; Cobolt Jive 561 nm, Cobolt), and single molecule signals were recorded with a back-illuminated electron multi- plying charged coupled device EMCCD camera (model iXON 897, pixel size 16 µm²; Andor Technology Ltd., Belfast, UK). The mitochondrial localization of the constructs was tested by co-staining with MitoTracker®DeepRed (not shown). The signal of a single particle was recorded over time until bleaching and analysed by the multi-target tracer algorithm (Sergé et al. 2008), generating a trajectory of the respective molecule. The magnification is the same for all trajectory maps. **d-I** Apparent diffusion coefficients D_{app} for mobile fraction of OM and IM proteins. **d-II** Confinement for OM and IM proteins

Acknowledgments The authors would like to thank Wladislaw Kohl for technical advice and support. We also wish to express our gratitude to Christian Richter for evaluation software. The study was supported by the CRC SFB944 and CiM/Münster.

Author contributions Conception and design: K.B., T.A. Acquisition of data: T.A.; K.B. Analysis and interpretation of data: T.A., K.B. Drafting or revising the article: K.B.

Compliance with ethical standards

Conflict of interest Timo Appelhans declares that he has no conflicts of interest. Karin B. Busch declares that she has no conflicts of interest.

Ethical approval This article does not contain any studies with human participants or animals performed by any of the authors.

References

Appelhans T, Busch K (2017) Single molecule tracking and localization of mitochondrial protein complexes in live cells. Methods Mol Biol 1567:273–291. doi:10.1007/978-1-4939-6824-4_17

Appelhans T, Richter C, Wilkens Vet al (2012) Nanoscale organization of mitochondrial microcompartments revealed by combining tracking and localization microscopy. Nano Lett 12:610–616. doi:10.1021/ nl203343a

Bacia K, Kim SA, Schwille P (2006) Fluorescence cross-correlation spec- troscopy in living cells. Nat Methods 3:83–89. doi:10.1038/ nmeth822

Beinlich F, Drees C, Piehler J, Busch K (2015) Shuttling of PINK1 be- tween mitochondrial microcompartments resolved by triple-color Superresolution microscopy. ACS Chem Biol 10:1970–1976. doi: 10.1021/acschembio.5b00295

Demishtein-Zohary K, Azem A (2017) The TIM23 mitochondrial protein import complex: function and dysfunction. Cell Tissue Res 367:33– 41. doi:10.1007/s00441-016-2486-7

Dikov D, Bereiter-Hahn J (2013) Inner membrane dynamics in mitochon- dria. J Struct Biol 183:455–466. doi:10.1016/j.jsb.2013.06.003

Ding C, Wu Z, Huang L et al (2015) Mitofilin and CHCHD6 physically interact with Sam50 to sustain cristae structure. Sci Rep 5:16064. doi:10.1038/srep16064

Gavin PD (2004) Cross-linking ATP synthase complexes in vivo elimi- nates mitochondrial cristae. J Cell Sci 117(11):2333–2343

Harner M, Neupert W, Deponte M (2011) Lateral release of proteins from the TOM complex into the outer membrane of mitochondria. EMBO J 30:3232–3241. doi:10.1038/emboj.2011.235

Jans DC, Wurm CA, Riedel D et al (2013) STED super-resolution mi- croscopy reveals an array of MINOS clusters along human mito- chondria. Proc Natl Acad Sci USA 110:8936–8941. doi:10.1073/ pnas.1301820110

John GB (2005) The Mitochondrial Inner Membrane Protein Mitofilin Controls Cristae Morphology. Mol Biol Cell 16(3):1543–1554

Juillerat A, Gronemeyer T, Keppler A et al (2003) Directed evolution of O6-Alkylguanine-DNA alkyltransferase for efficient labeling of fu- sion proteins with small molecules in vivo. Chem Biol 10:313–317. doi:10.1016/s1074-5521(03)00068-1

Koopman W, Hink M, Verkaart S et al (2007) Partial complex I inhibition decreases mitochondrial motility and increases matrix protein diffu- sion as revealed by fluorescence correlation spectroscopy. Biochim Biophys Acta 1767:940–947. doi:10.1016/j.bbabio.2007.03.013

Kuzmenko A, Tankov S, English BP et al (2011) Single molecule track- ing fluorescence microscopy in mitochondria reveals highly dynam- ic but confined movement of Tom40. Sci Rep 1:195. doi:10.1038/ srep00195

Los G, Encell L, McDougall M et al (2008) HaloTag: a novel protein labeling technology for cell imaging and protein analysis. ACS Chem Biol 3:373–382. doi:10.1021/cb800025k

Mannella C, Marko M, Penczek P et al (2004) The internal compartmen- tation of rat-liver mitochondria: tomographic study using the high- voltage transmission electron microscope. Microsc Res Tech 27: 278–283.

doi:10.1002/jemt.1070270403
Mishra P, Chan D (2016) Metabolic regulation of mitochondrial dynam- ics. J Cell Biol 212:379–387. doi:10.1083/jcb.201511036
Mokranjac D, Neupert W (2010) The many faces of the mitochondrial TIM23 complex. Biochim Biophys Acta 1797:1045–1054. doi:10. 1016/j.bbabio.2010.01.026
Partikian A, Olveczky B, Swaminathan R et al (1998) Rapid diffusion of green fluorescent protein in the mitochondrial matrix. J Cell Biol 140:821–829. doi:10.1083/jcb.140.4.821
Paumard P, Vaillier J, Coulary B, Schaeffer J, Soubannier V, Mueller DM, Brèthes D, di Rago J-P, Velours J (2002) The ATP synthase is in- volved in generating mitochondrial cristae morphology. EMBO J 21(3):221–230
Petrasek Z, Schwille P (2008) Precise measurement of diffusion coeffi- cients using scanning fluorescence correlation spectroscopy. Biophys J 94:1437–1448. doi:10.1529/biophysj.107.108811
Rapaport D, Neupert W (1999) Biogenesis of Tom40, core component of the tom complex of mitochondria. J Cell Biol 146:321–332. doi:10. 1083/jcb.146.2.321
Reits E, Neefjes J (2001) From fixed to FRAP: measuring protein mobil- ity and activity in living cells. Nat Cell Biol 3:E145–E147. doi:10. 1038/35078615
Renner M, Domanov Y, Sandrin F et al (2011) Lateral diffusion on tubu- lar membranes: quantification of measurements bias. PLoS One 6: e25731. doi:10.1371/journal.pone.0025731
Schröder J, Benink H, Dyba M, Los G (2009) In vivo labeling method using a genetic construct for nanoscale resolution microscopy. Biophys J 96:L1–L3. doi:10.1016/j.bpj.2008.09.032
Schütz GJ, Schindler H, Schmidt T (1997) Single-molecule microscopy on model membranes reveals anomalous diffusion. Biophys J 73(2): 1073–1080
Sergé A, Bertaux N, Rigneault H, Marguet D (2008) Dynamic multiple- target tracing to probe spatiotemporal cartography of cell mem- branes. Nat Methods 5:687–694. doi:10.1038/nmeth.1233
Shiota T, Imai K, Qiu J et al (2015) Molecular architecture of the active mitochondrial protein gate. Science 349:1544–1548. doi:10.1126/ science.aac6428
Straub SP, Stiller SB, Wiedemann N, Pfanner N (2016) Dynamic organi- zation of the mitochondrial protein import machinery. Biol Chem 397:1097–1114. doi:10.1515/hsz-2016-0145
Subach FV, Patterson GH, Renz M et al (2010) Bright monomeric photoactivatable red fluorescent protein for two-color super-resolu- tion sptPALM of live cells. J Am Chem Soc 132:6481–6491. doi:10. 1021/ja100906g
Sukhorukov V, Bereiter-Hahn J (2009) Anomalous diffusion induced by cristae geometry in the inner mitochondrial membrane. PLoS One 4: e4604. doi:10.1371/journal.pone.0004604
Sukhorukov VM, Dikov D, Busch K et al (2010) Determination of pro- tein mobility in mitochondrial membranes of living cells. Biochim Biophys Acta 1798:2022–2032. doi:10.1016/j.bbamem.2010.07. 016
Tarasenko D, Barbot M, Jans DC et al (2017) The MICOS component Mic60 displays a conserved membrane-bending activity that is nec- essary for normal cristae morphology. J Cell Biol 216:889–899. doi: 10.1083/jcb.201609046
van der Laan M, Horvath SE, Pfanner N (2016) Mitochondrial contact site and cristae organizing system. Curr Opin Cell Biol 41:33–42. doi:10.1016/j.ceb.2016.03.013
Vogel F, Bornhövd C, Neupert W, Reichert A (2006) Dynamic subcompartmentalization of the mitochondrial inner mem- brane. J Cell Biol 175 :237 – 247. doi: 10 .1083/jcb. 200605138
von Diezmann A, Shechtman Y, Moerner WE (2017) Three-dimensional localization of single molecules for super-resolution imaging and single-particle tracking. Chem Rev 117:7244–7275. doi:10.1021/ acs.chemrev.6b00629
Wilkens V, Kohl W, Busch K (2012) Restricted diffusion of OXPHOS complexes in dynamic mitochondria delays their exchange between cristae and engenders a transitory mosaic distribution. J Cell Sci 126: 103–116. doi:10.1242/jcs.108852
Wurm C, Jakobs S (2006) Differential protein distributions define two sub-compartments of the mitochondrial inner membrane in yeast. FEBS Lett 580:5628–5634. doi:10.1016/j.febslet.2006.09.012
Yu T, Fox RJ, Burwell LS, Yoon Y (2005) Regulation of mitochondrial fission and apoptosis by the mitochondrial outer membrane protein hFis1. J Cell Sci 118:4141–4151. doi:10.1242/jcs.02537
Zerbes R, Bohnert M, Stroud D et al (2012) Role of MINOS in mito- chondrial membrane architecture: cristae morphology and outer membrane interactions differentially depend on mitofilin domains. J Mol Biol 422:183–191. doi:10.1016/j.jmb.2012.05.004

9.2.2 F_1F_O ATP-Synthase tracking during inhibition of ATP synthesis

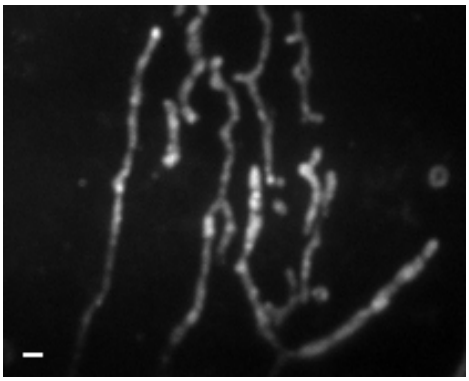

Figure 28 Mitochondrial network 60 min after addition of olygomycin
Diffraction limited image of mitochondria during inhibition of ATP synthesis. Mitochondria stay intact during inhibition of ATP-synthesis. Scale bar: 1 µm

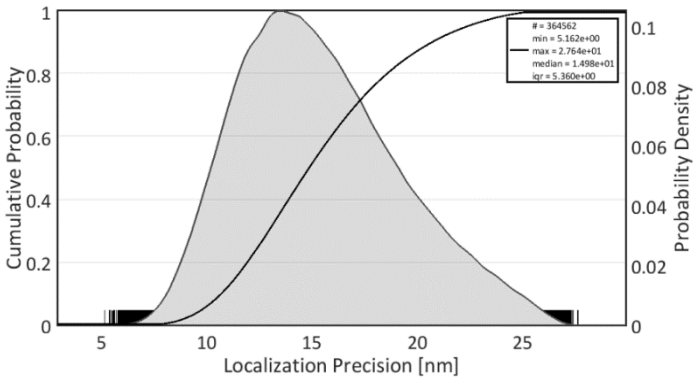

Figure 27 Localization precision of F_1FO ATP synthase subunit-γ during oligomycin treatment
TALM experiments of CV-SUγ proteins during inhibition of ATP synthesis show a mean calculated localization precision of 15.44 ± 2.68 nm

CV is predominantly localized in the CM (Wilkens et al., 2013). TALM experiments revealed that at least monomeric CV also diffuses in the CM (Appelhans et al., 2012, Appelahsn and Busch, 2017b). The typical accumulations of localization identified by TALM, showed that orthogonal localizations of single proteins allow measuring the distance between cristae (Appelhans et al., 2012). The predominant localization and diffusion of CV in the CM, where a high PMF drives the ATP production, evoke the question if the spatiotemporal organization of CV and its functionality are coupled.

In the following section, the ATP synthesis of CV was inhibited by adding 5 µg mL^{-1} of the CV inhibitor oligomycin. It was investigated if inhibition of its function leads to an altered spatiotemporal organization of CV-SUγ, differences in its mobility and an altered trajectory directionality of CV-SUγ. Cells were imaged 10 minutes past adding oligomycin and up to 1.3 hours in imaging medium containing oligomycin. Mitochondrial networks stayed intact during inhibition and imaging (

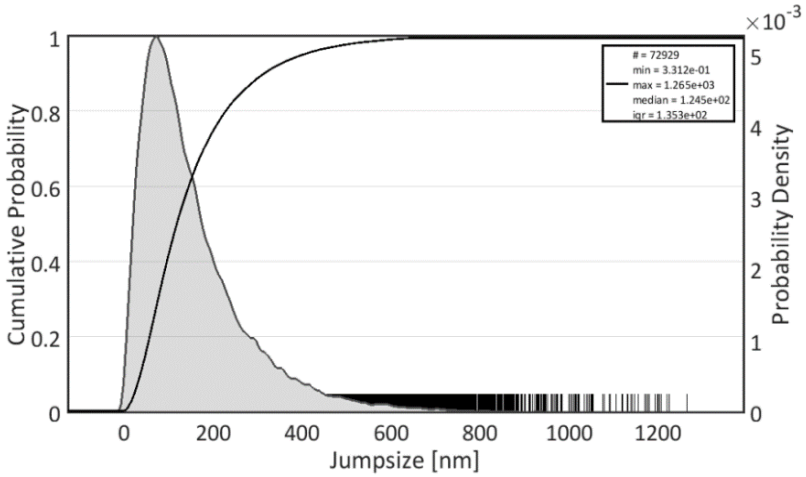

Figure 29 Jumpsize of F_1F_0 ATP synthase subunit-γ during inhibition of ATP synthesis
Inhibition of ATP synthesis by addition of oligomycin resulted in an increased median jumpsize.

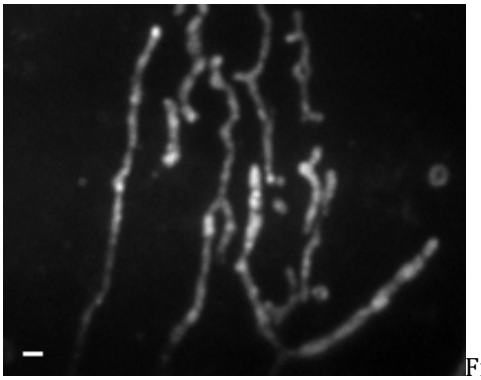

Figure 27). The mean calculated localization precision reached in these experiments was 15.44 ± 2.68 nm (Figure 28). The jumpsize is the step length of a proteins between two frames. The median jumpsize of the tracked proteins was 124.50 nm (Figure 29, Table 2 **Jumpsize of CV-SUγ in control experiments and during inhibition of ATP synthesis**). Thus, the median jumpsize increased by a factor of 1.2843 compared to the control. The minimal and maximal jumpsize remained mostly unchanged (Table 2 **Jumpsize of CV-SUγ in control experiments and during inhibition of ATP synthesis**). The D_{app} of CV-SUγ in the control and during inhibition of the ATP synthesis were fitted by three subpopulations (

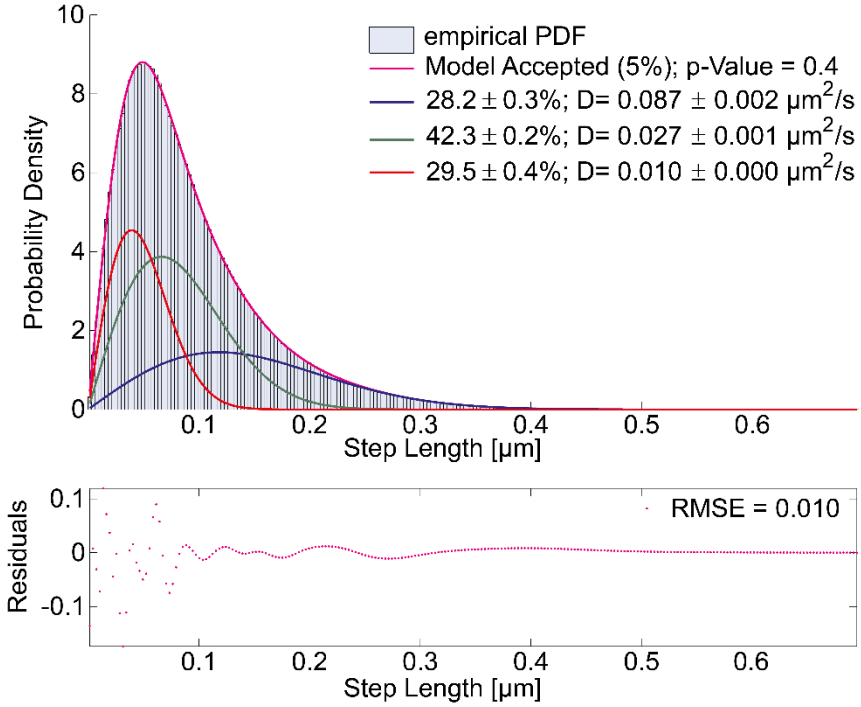

Figure S5,

Table 3). The D_{app} during inhibition of the ATP synthesis remained unchanged. The three fitted populations showed similar percentages. The mobile fraction and the slow mobile fraction were tendentially lower. The confined mobile fraction was reduced by approximately 11 %. Thus, inhibition of ATP-synthesis of CV did not effect the protein mobility significantly and a slight increase in the percentage of the confined mobile fraction occured.

Table 2 Jumpsize of CV-SUγ in control experiments and during inhibition of ATP synthesis

Protein	Number of steps	Median jumpsize	Maximal. jumpsize	Minimal. jumpsize

CV-SUγ control	20124	96.94 nm	1117 nm	0.58 nm
CV-SUγ oligomycin	72929	124.50 nm	1265 nm	0.33 nm

Table 3 Diffusion coefficients of F_1F_O ATP synthase subunit-γ during inhibition of ATP-synthesis

Protein	D_{app} mobile [µm²/s]	relativ amount [%]	D_{app} slow mobile [µm²/s]	relativ amount [%]	D_{app} confined mobile [µm²/s]	relativ amount [%]
CV-SUγ control	0.079 ± 0.009	35 ± 5	0.020 ± 0.006	47 ± 3	0.005 ± 0.002	18 ± 3
CV-SUγ oligomycin	0.087 ± 0.002	28.2 ± 0.3	0.027 ± 0.001	42.3 ± 0.2	0.010 ± 0.000	29.5 ± 0.4

9.2.2.1 Inhibition of F_1F_O ATP synthase activity affects its spatiotemporal organization

The D_{app} of CV-SUγ were not affected by inhibition of the ATP synthesis. However, the relative amount of the fractions was altered slightly (

Table 3). Figure 30 shows a trajectory map of CV-SUγ after 1 hour of ATP synthesis inhibition. The mitochondrial network stayed intact. However, movement of CV-SUγ was obviously altered. The trajectories show a random movement in the IM equal to Tom20 in the OM (Appelhans et al., 2012, Appelhans and Busch, 2017b). Typical perpendicular oriented trajectories of CV-SUγ in reference to the longitudinal mitochondrial axis lack. In order to test, whether the inhibited enzymatic activity of CV was connected to its spatiotemporal organization, the trajectory directionality of CV-SUγ was analyzed (Figure 31, Figure 32). In Figure 31A,B and Figure 32A,B the analysis of two representative mitochondria are shown. The longitudinal axis of the mitochondria had been marked and the trajectory maps were straightend. Perpendicular cristae trajectories vanished nearly completely, instead a random oriented movement of CV-SUγ was observed. In order to quantify this, the trajectory directionality of CV-SUγ was analyzed (Figure 31C, Figure 32C). Trajectory directionality of the shown trajectories in the single mitochondria show a mixture of directionalities in all orientations and no predominant directionality of trajectories could be obtained (Figure 31, Figure 32). The total analysis of trajectory directionality of CV-SUγ in the ATP synthesis inhibited conditions included of 46010 binned steps of CV-SUγ (Figure 33). The result was a randomly oriented directionality with a tendency to a longitudinal movement (Figure 33A). However, the trajectory directionality resulted from a random movement in the IM. It was not clear whether this resulted from random movement in the IBM or an altere IM architecture with random oriented cristae. In the control experiment the trajectory directionality resulted from diffusion along the IBM and movement in cristae (Figure 33B and chapter 9.2.3.1). In

case of ATP synthesis inhibition, no clear cristae trajectories and no movement along the IBM, like a longitudinal trajectory at the outline of a mitochondrion were observed.

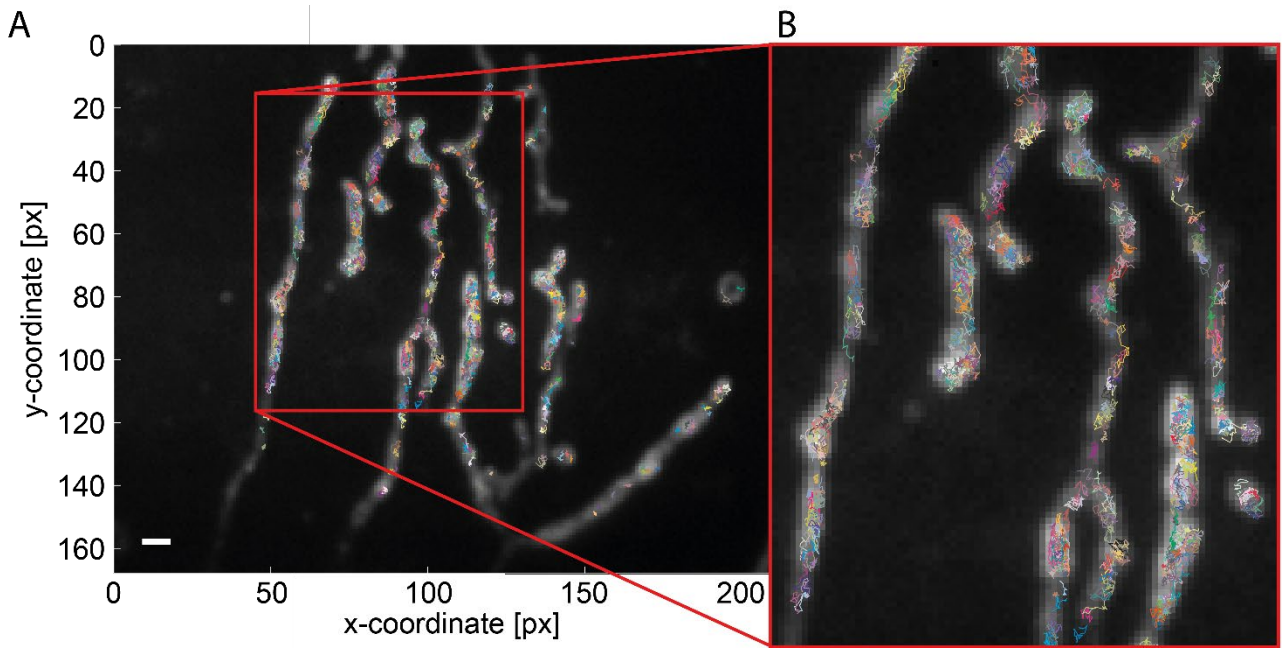

Figure 30 Trajectory map of F_1F_0 ATP synthase subunit-γ during inhibition of ATP-synthesis
A The mitochondrial network was still intact after 1 h of ATP-synthesis inhibition. Shown here is an overlay of the trajectory map of CV-SUγ and diffraction limited image of the same mitochondria in the cell periphery. **B** Enlargements of the trajectory map shown in A. CV-SUγ diffuses in a random like manner during inhibition of the ATP-synthesis. Cristae trajectories vanish completely. Scale bar: 1 µm (A)

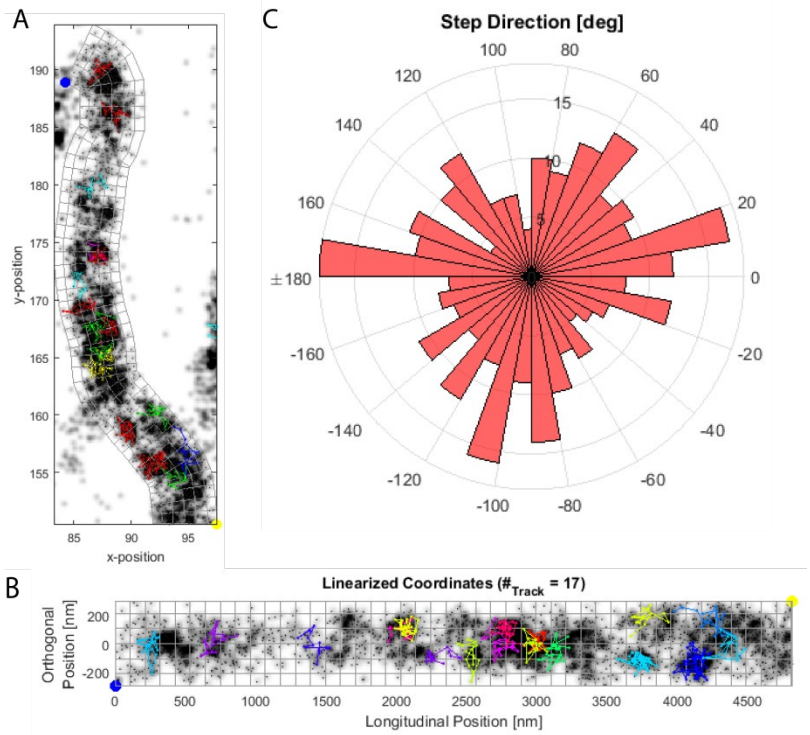

Figure 31 Quantification of trajectory directionality of the F_1F_0 ATP synthase subunit-γ of a representative mitochondrion during inhibition of ATP synthesis
A Localization map of a single mitochondrion and the trajectories of CV-SUγ proteins during inhibition of ATP synthesis. **B** Linearized interpolation of TALM data of the mitochondrion shown in A. Most of the trajectories show a random mobility. **C** Trajectory directionality of all single steps of the 17 trajectories shown in A and B. An orientation in all direction is observed.

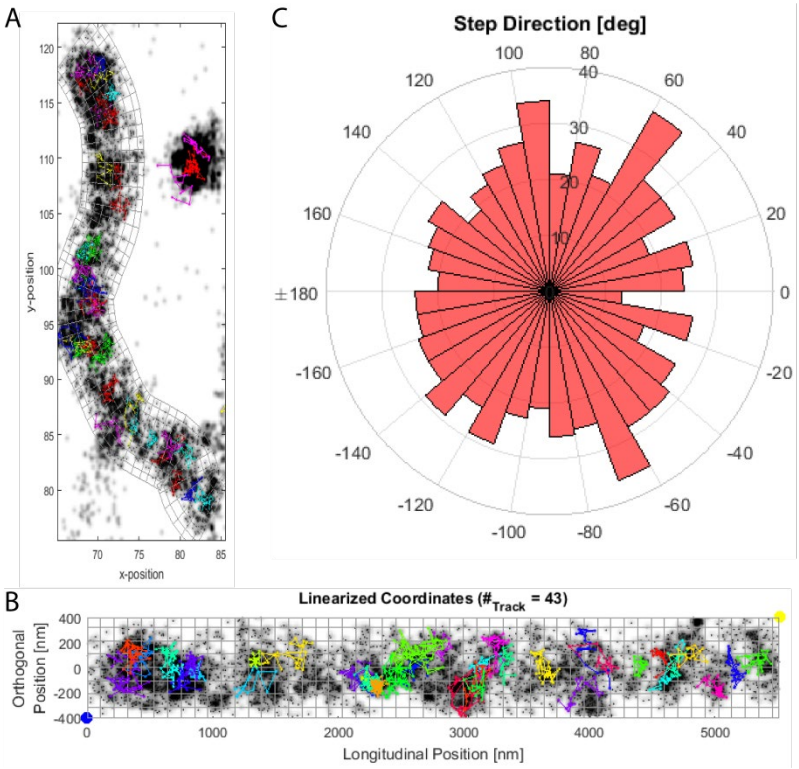

Figure 32 Quantification of trajectory directions of the F_1F_0 ATP synthase subunit-γ of a representative mitochondrion during inhibition of ATP-synthesis
A TALM data of CV-SUγ in a single mitochondrion during inhibition of ATP synthesis. **B** Linearized interpolation of TALM data of the mitochondrion shown in A. The trajectories show a random mobility. **C** Pie chart diagram of trajectory directionalities of 43 trajectories shown in A and B. The trajectories were oriented in all direction.

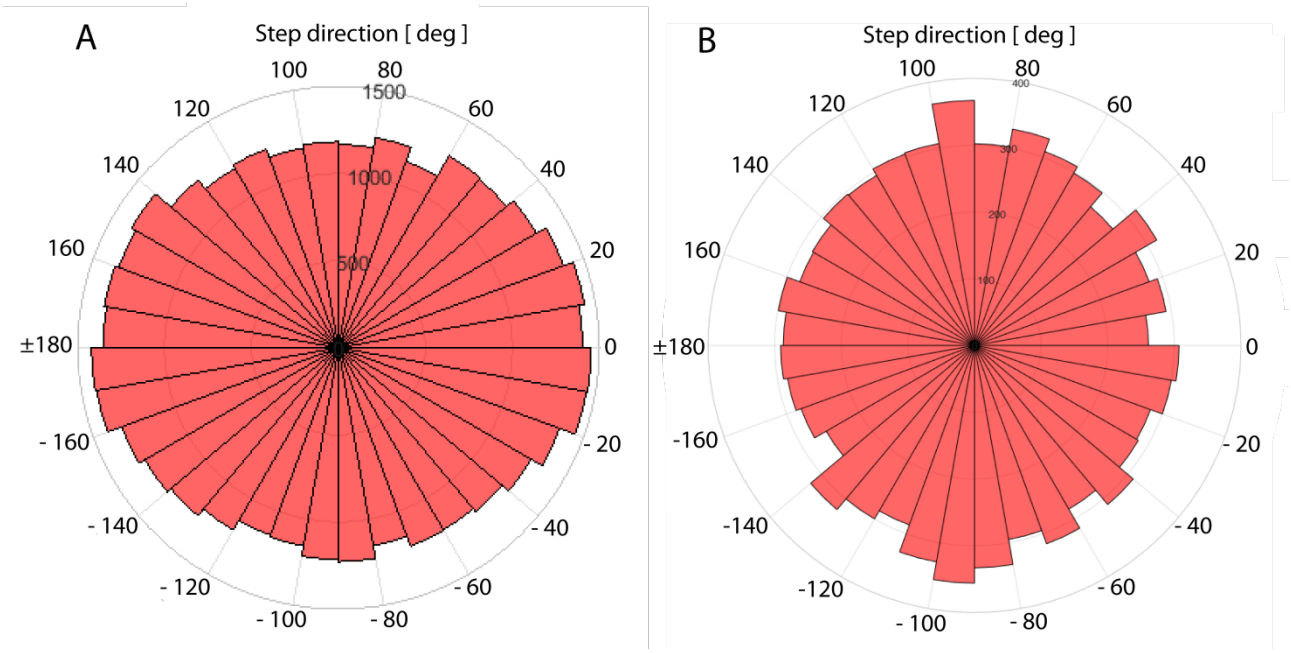

Figure 33 Quantification of step directions of the F_1F_0 ATP synthase subunit-γ of all imaged mitochondria during inhibition of ATP synthesis compared to the control
A Pie chart diagram of CV-SUγ trajectory directionalities in degree during ATP synthesis. 46010 steps were taken into account, showing an orientation with no dominant direction. A tendency to the longitudinal diffusion can be assumed. **B** Pie chart diagram of CV-SUγ trajectory directionality in control experiment. 9558 steps were taken into account. In the control experiment a tendency to perpendicular diffusion was seen.

9.2.3 F_1F_O ATP synthase in starving conditions

Mitochondria are the power plant of cells. Their ability to produce ATP via OXPHOS is coupled to glycolysis, the citric acid cycle and ß-oxidation of fatty acids. In order to produce ATP, a healthy membrane potential is needed. The PMF is needed to drive the ATP synthesis at CV, which is an electrochemical potential of protons across the IM. In mitochondria, the redox-energy is translated into a proton gradient across the IM. Starvation of cells led to a decrease of the $\Delta\Psi m$. Furthermore, during short term starvation over 2 hours the oxygen consumption rate stayed similar, while the extracellular acidification rate increased. Additionally, during starvation the ΔpH increased (Bettina Rieger: personal communication). As previously shown by inhibition of ATP synthesis via oligomycin the spatiotemporal organization and the functionality of CV are coupled. However, still it is unknown if an adaption to a metabolic state of the cell is accompanied by a re-organization of the spatiotemporal organization of CV, in living cells. In order to address this question TALM experiments of CV-SUγ:HaloTag were performed in starving cells and the results were compared to the control. Therfore cells were seeded in starving conditions and starved for 2 h, labeled with TMR^{HTL} and TALM was performed. The exposure time was reduced to 16 ms in order to enhance the sensitivity for single particle tracking analysis. The mean calculated localization precision during starvation was 11.81 ± 2.78 nm, thus similar to control conditions (Figure 34) and literature (Appelhans et al., 2012).

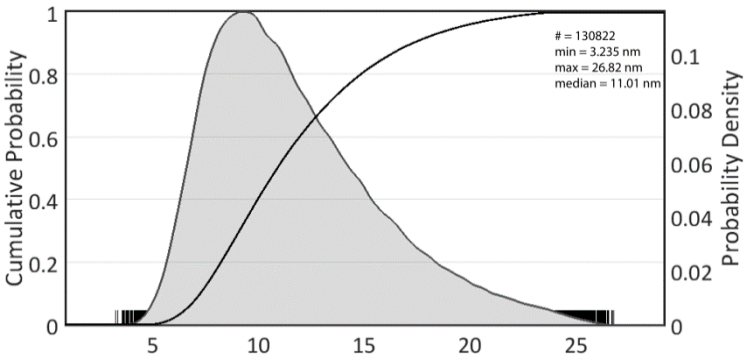

Figure 34 Localization precision of F_1F_O ATP synthase subunit-γ in starving conditions
SML of CVγ proteins in starving conditions resulted in a mean calculated localization precision of 11.81 ± 2.78 nm.

9.2.3.1 Starvation of cells effects the spatiotemporal organization of F_1F_O ATP synthase subunit-γ

The jumpsize of single molecules provides information about the traveled distance of fluorophores between two frames. If CV-SUγ mobility is influenced by starvation the jumpsize should be altered. In Figure 35, 7491 steps of CV-SUγ in starving conditions are plotted and compared to 20124 steps of CV-SUγ in the control. The median jumpsize of CV-SUγ proteins in starving conditions increased by a factor of 1.81 to 175.7 nm (Figure 35**, Fehler! Verweisquelle konnte nicht gefunden werden.**). Additionally, the amount of jumpsizes larger than 200 nm increased (Figure 35). At the same time a clear reduction of steps below 200 nm was obtained. This already shows an increase in the mobility of CV-SUγ during starvation. The maximal jumpsize stayed similar and was 1117 nm in the control and 1211 nm in starving conditions. The minimal jumpsize of CV-SUγ in the control was 0.58 nm and increased by a factor of 3 to 1.79 nm due to starvation. SML of CV-SUγ in the control revealed a heterogeneous distribution of accumulated localizations along mitochondria. This accumulations were interpreted as localizations in the CM, because their orientation showed a perpendicular directionality as expected from literature (Appelhans et al. 2012) (CV-SUγ in the control and under starving conditions directly differentiate, obviuosly in their directionality (**Fehler! Ungültiger Eigenverweis auf Textmarke.**B, D). This indicates either a shift of a longitudinal orientation of cristae or a shift of CV-SUγ into the IBM or even a lost ofcristae. The transition of CV-SUγ

into the IBM can result from avoided diffusion in the CM and a dominant diffusion in the IBM or by a reduction of the CM. In order to analyze the directionality of mobility and to quantify for this, the directionality of trajectories was analyzed with MitoOrientedDynamics. Here, the4-step binning procedure was used. As described, the longitudinal axis of each mitochondria was marked, which was used to interpolate it to a straight mitochondrion and the angle of binned steps to the longitudinal axis was measured. Shown in figure 37 is an example of a straightened mitochondrion in starving conditions and its analysis of the trajectory directionality. In the shown mitochondrion the directionalities of 121 individual trajectories were analyzed (Figure 37A). The majority of them is oriented along the longitudinal axis (Figure 37B, C). The pie chart diagram in figure 37B illustrates the dominant longitudinal movement of CV-SUγ in starvation of the analyzed mitochondrion. Here, the amount of longitudinal directions between -20° to 30° and between -160° to 170° is twice as large as the number perpendicular oriented trajectories. Additionlly, the heatmap in figure 37C shows that steps along the longitudinal axis can reach a larger jumpsize than steps in the perpendicular direction. However, this may be influenced by the 3D morphology of mitochondria. Here, jumpsizes in the perpendicular direction can be scaled down stronger than jumpsizes along the longitudinal direction. The trajectory directionality in starvation was compared to the trajectory directionality in control experiments (Figure 38). In the case of the control, 10784 binned steps were taken into account (Figure 38A, C). The analysis of trajectory directionality during starvation was performed on 59743 binned steps (Figure 38B, D).

Table 4 Jumpsize of CV-SUγ in control experiments and during starvation

Protein	Number of steps	Median jumpsize	Maximal. jumpsize	Minimal. jumpsize
CV-SUγ control	20124	96.94 nm	1117 nm	0.58 nm
CV-SUγ starvation	7491	175.70 nm	1211 nm	1.79 nm

Figure 36A). The directionality of single CV-SUγ trajectories in the control was oriented perpendicular to the longitudinal axis of mitochondria or showed a confined movement (CV-SUγ in the control and under starving conditions directly differentiate, obviuosly in their directionality (**Fehler! Ungültiger Eigenverweis auf Textmarke.**B, D). This indicates either a shift of a longitudinal orientation of cristae or a shift of CV-SUγ into the IBM or even a lost ofcristae. The transition of CV-SUγ into the IBM can result from avoided diffusion in the CM and a dominant diffusion in the IBM or by a reduction of the CM. In order to analyze the directionality of mobility and to quantify for this, the directionality of trajectories was analyzed with MitoOrientedDynamics. Here, the4-step binning procedure was used. As described,

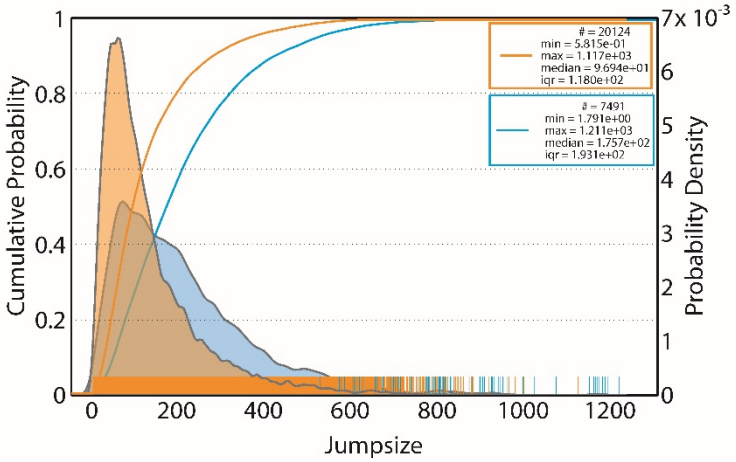

Figure 35 Jumpsize distribution of F_1F_0 ATP synthase subunit-γ in glycolytic and starving conditions
Shown in orange are 20124 steps of CV-SUγ in glycolytic conditions /conrol with a median jumpsize of 97 nm and 98 nm in mean. Shown in blue are 7491 steps of CV-SUγ during starvation with a median jumpsize of 176 nm and 179 nm in mean.

the longitudinal axis of each mitochondria was marked, which was used to interpolate it to a straight mitochondrion and the angle of binned steps to the longitudinal axis was measured. Shown in

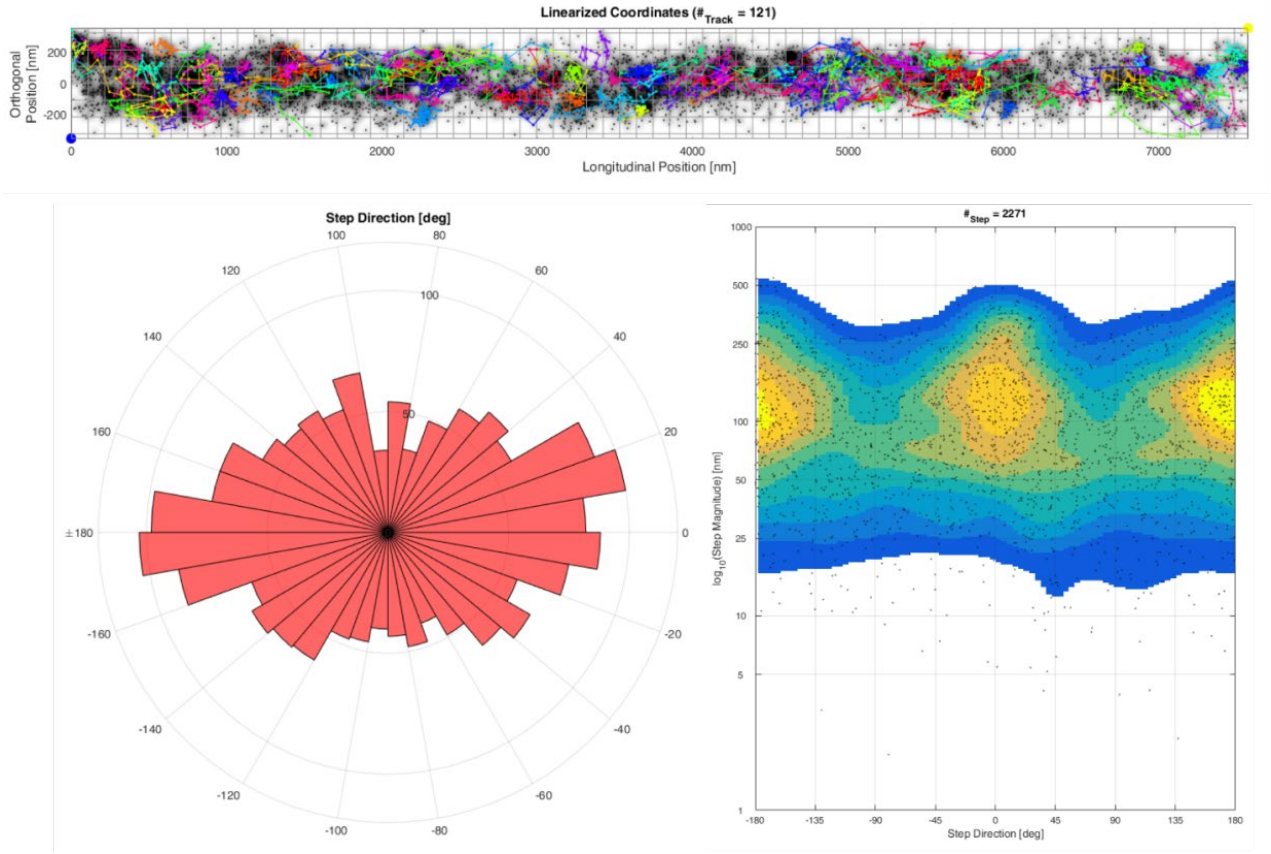

Figure **37** is an example of a straightened mitochondrion in starving conditions and its analysis of the trajectory directionality. In the shown mitochondrion the directionalities of 121 individual trajectories were analyzed (

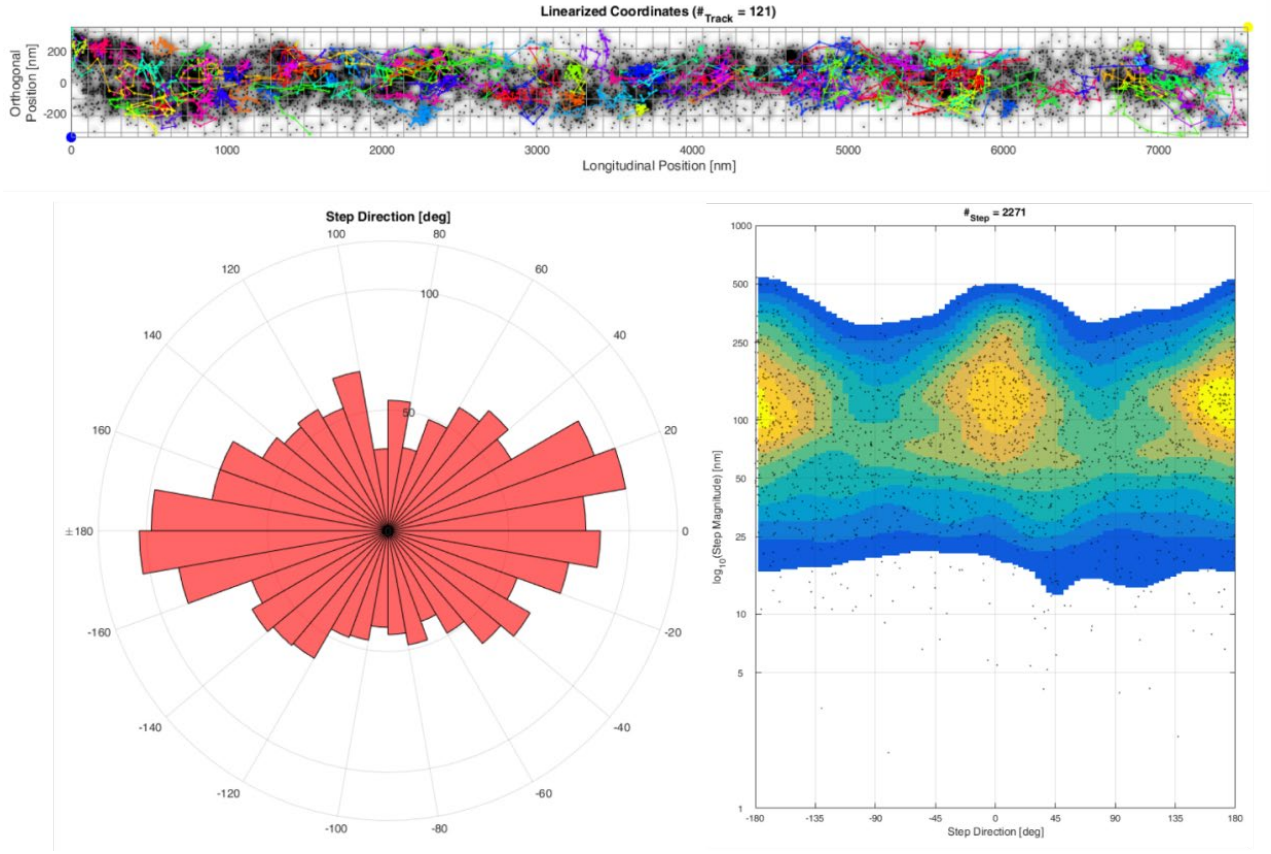

Figure **37**A). The majority of them is oriented along the longitudinal axis (

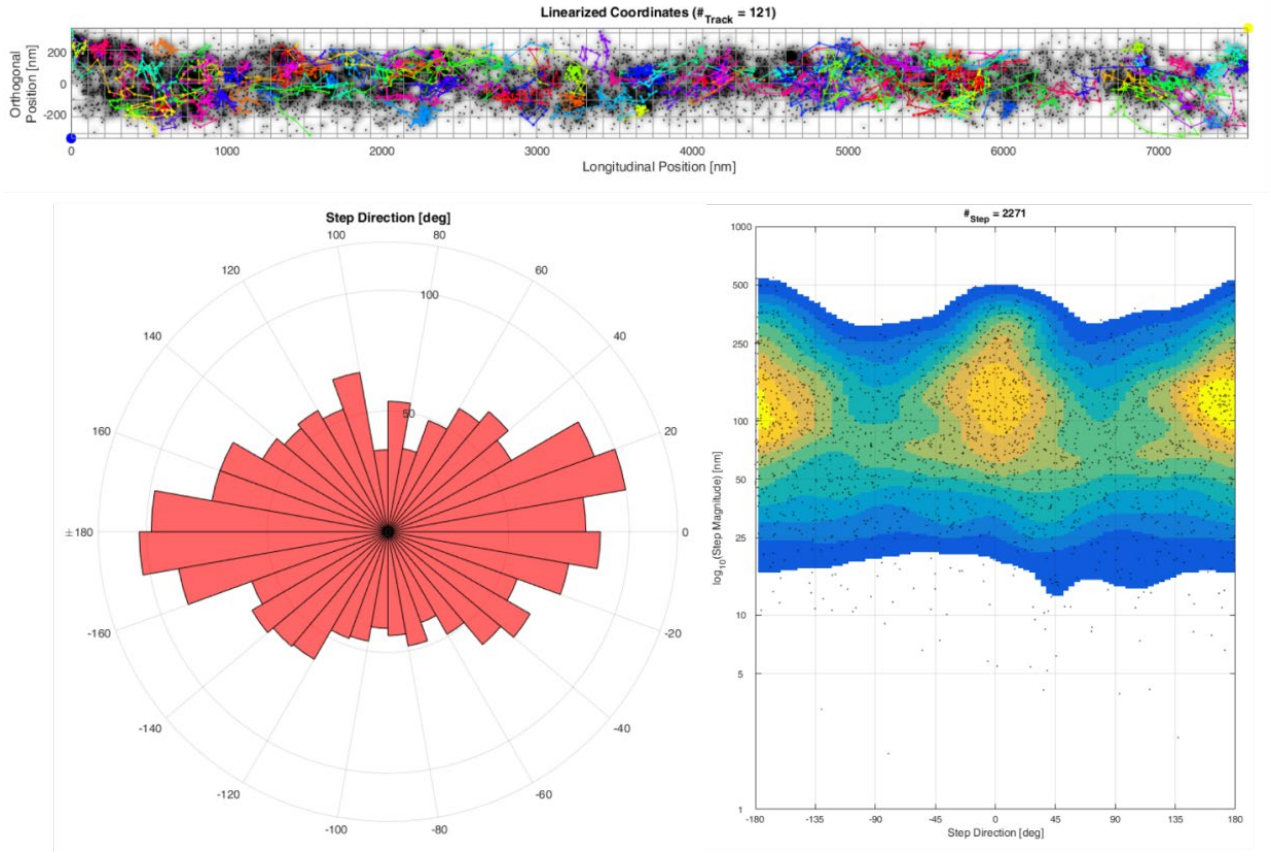

Figure **37**B, C). The pie chart diagram in

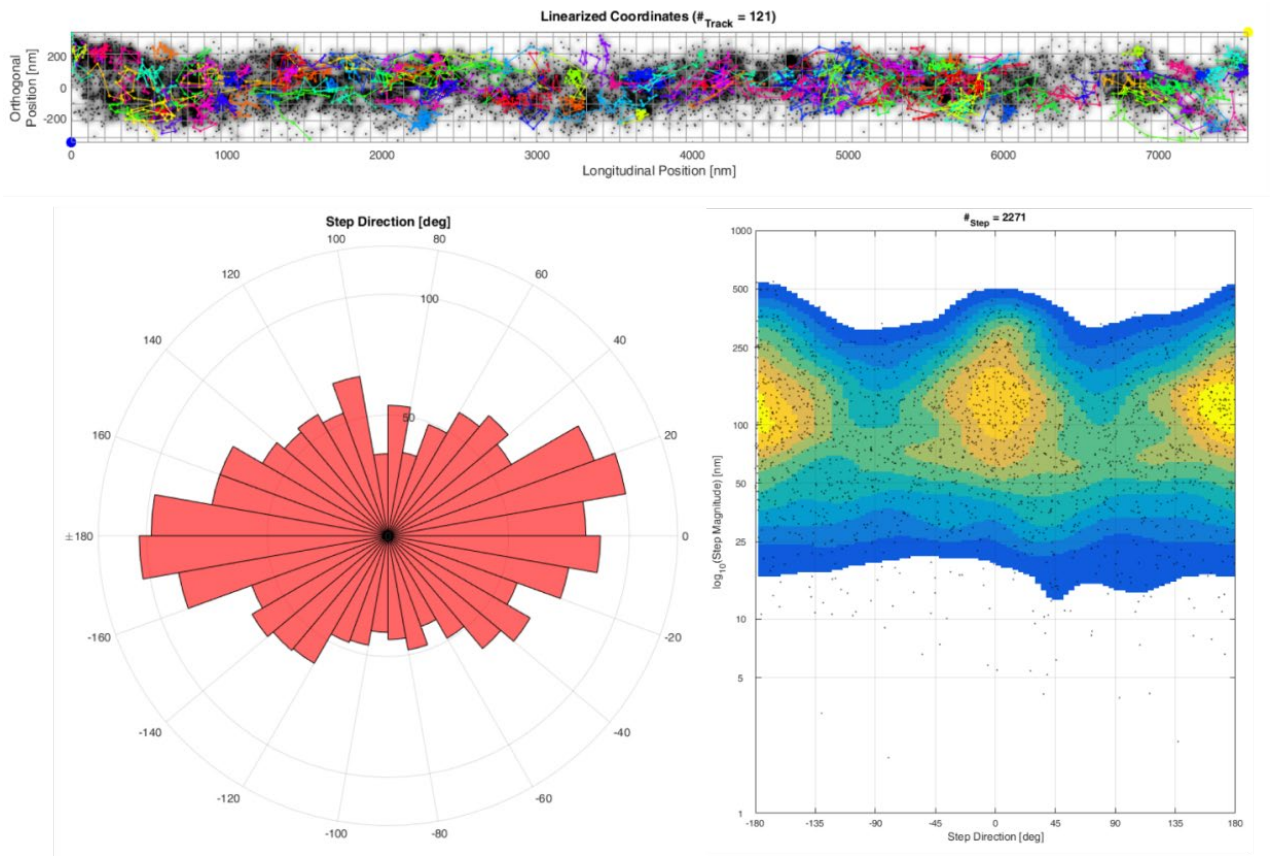

Figure **37**B illustrates the dominant longitudinal movement of CV-SUγ in starvation of the analyzed mitochondrion. Here, the amount of longitudinal directions between -20° to 30° and between -160° to 170° is twice as large as the number perpendicular oriented trajectories. Additionlly, the heatmap in

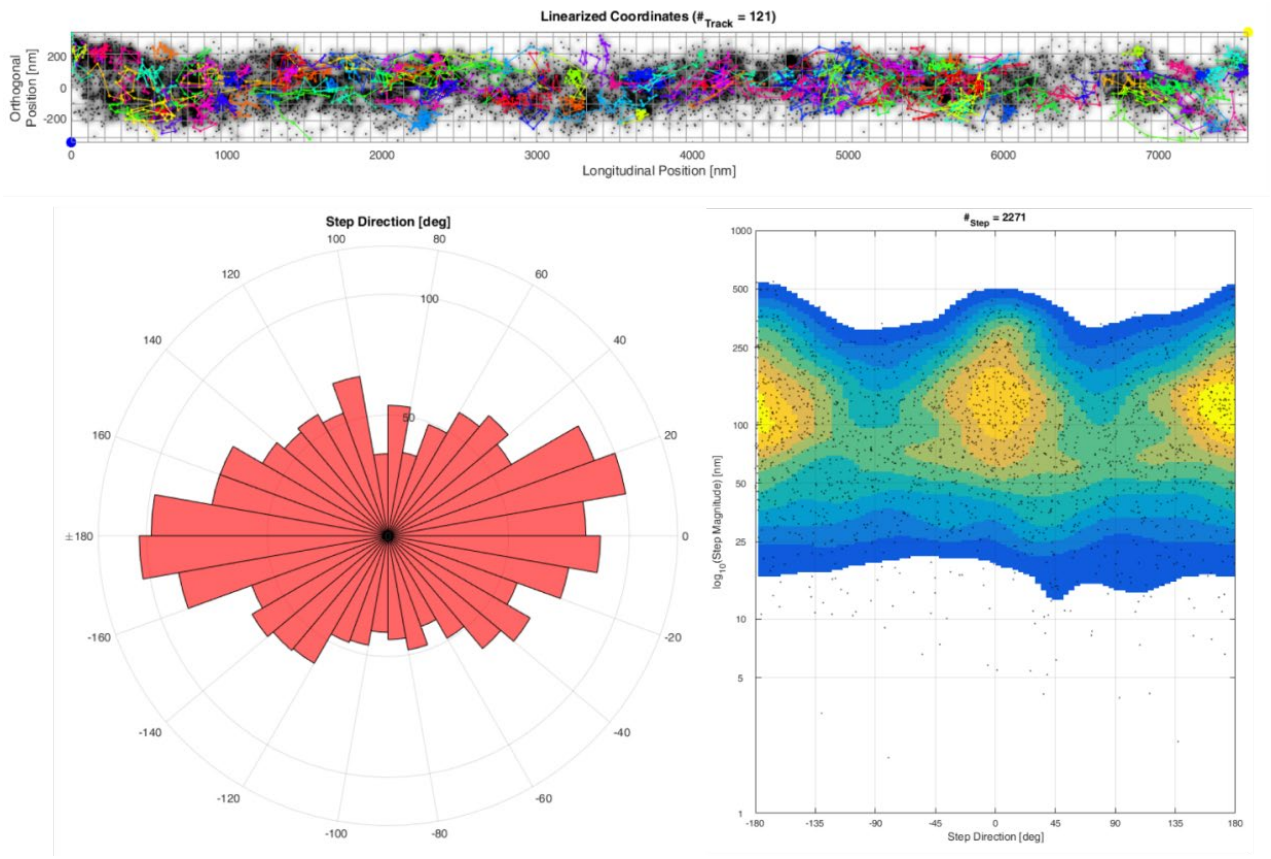

Figure **37**C shows that steps along the longitudinal axis can reach a larger jumpsize than steps in the perpendicular direction. However, this may be influenced by the 3D morphology of mitochondria. Here, jumpsizes in the perpendicular direction can be scaled down stronger than jumpsizes along the longitudinal direction. The trajectory directionality in starvation was compared to the trajectory directionality in control experiments (Figure 38). In the case of the control, 10784 binned steps were taken into account (Figure 38A, C). The analysis of trajectory directionality during starvation was performed on 59743 binned steps (Figure 38B, D).

Table 4 Jumpsize of CV-SUγ in control experiments and during starvation

Protein	Number of steps	Median jumpsize	Maximal. jumpsize	Minimal. jumpsize
CV-SUγ control	20124	96.94 nm	1117 nm	0.58 nm
CV-SUγ starvation	7491	175.70 nm	1211 nm	1.79 nm

Figure 36B, perpendicular and dark blue trajectories). Localizations of CV-SUγ in starving conditions did not show any accumulations and were homogenously distibuted along the IM (CV-SUγ in the control and under starving conditions directly differentiate, obviuosly in their directionality (**Fehler! Ungültiger Eigenverweis auf Textmarke.**B, D). This indicates either a shift of a longitudinal orientation of cristae or a shift of CV-SUγ into the IBM or even a lost ofcristae. The transition of CV-SUγ into the IBM can result from avoided diffusion in the CM and a dominant diffusion in the IBM or by a reduction of the CM. In order to analyze the directionality of mobility and to quantify for this, the directionality of trajectories was analyzed with MitoOrientedDynamics. Here, the4-step binning procedure was used. As described, the longitudinal axis of each mitochondria was marked, which was used

to interpolate it to a straight mitochondrion and the angle of binned steps to the longitudinal axis was measured. Shown in

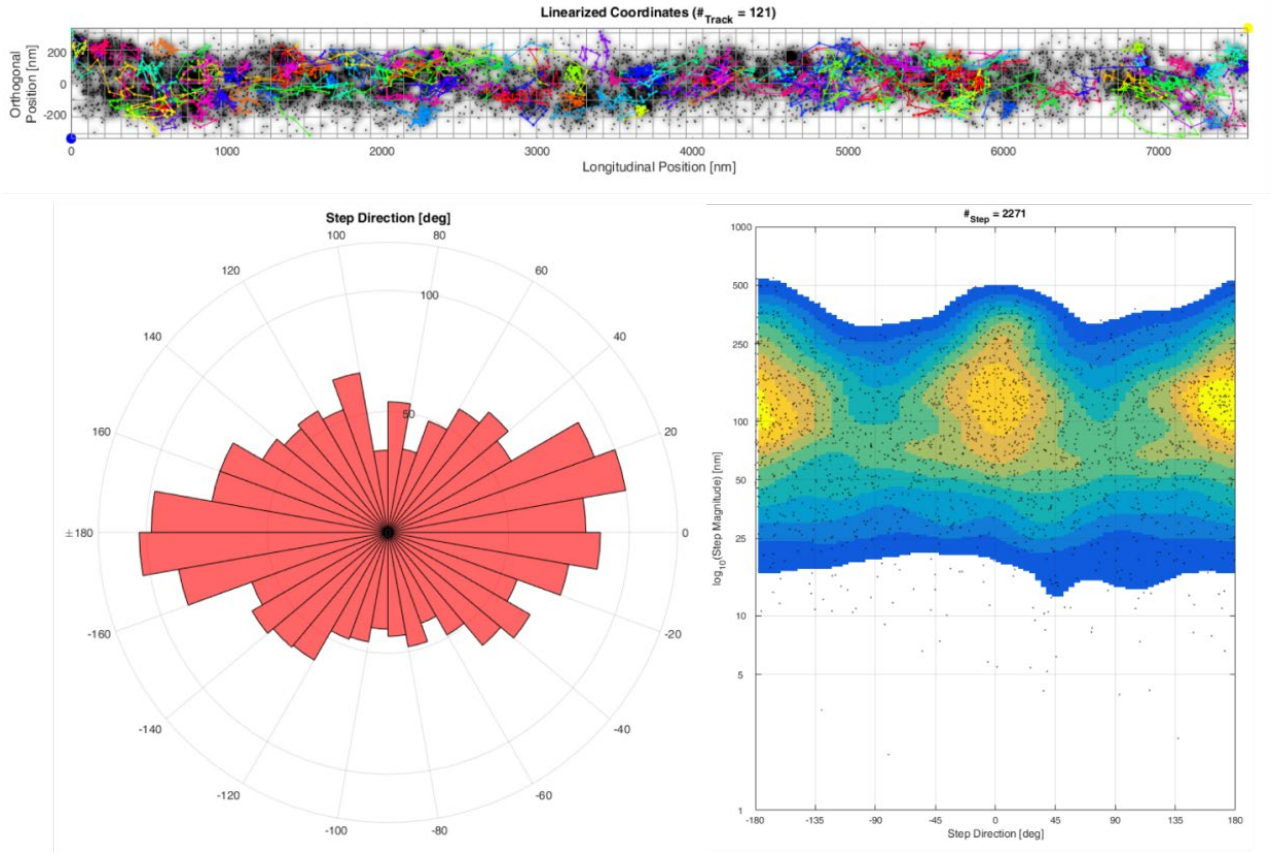

Figure **37** is an example of a straightened mitochondrion in starving conditions and its analysis of the trajectory directionality. In the shown mitochondrion the directionalities of 121 individual trajectories were analyzed (

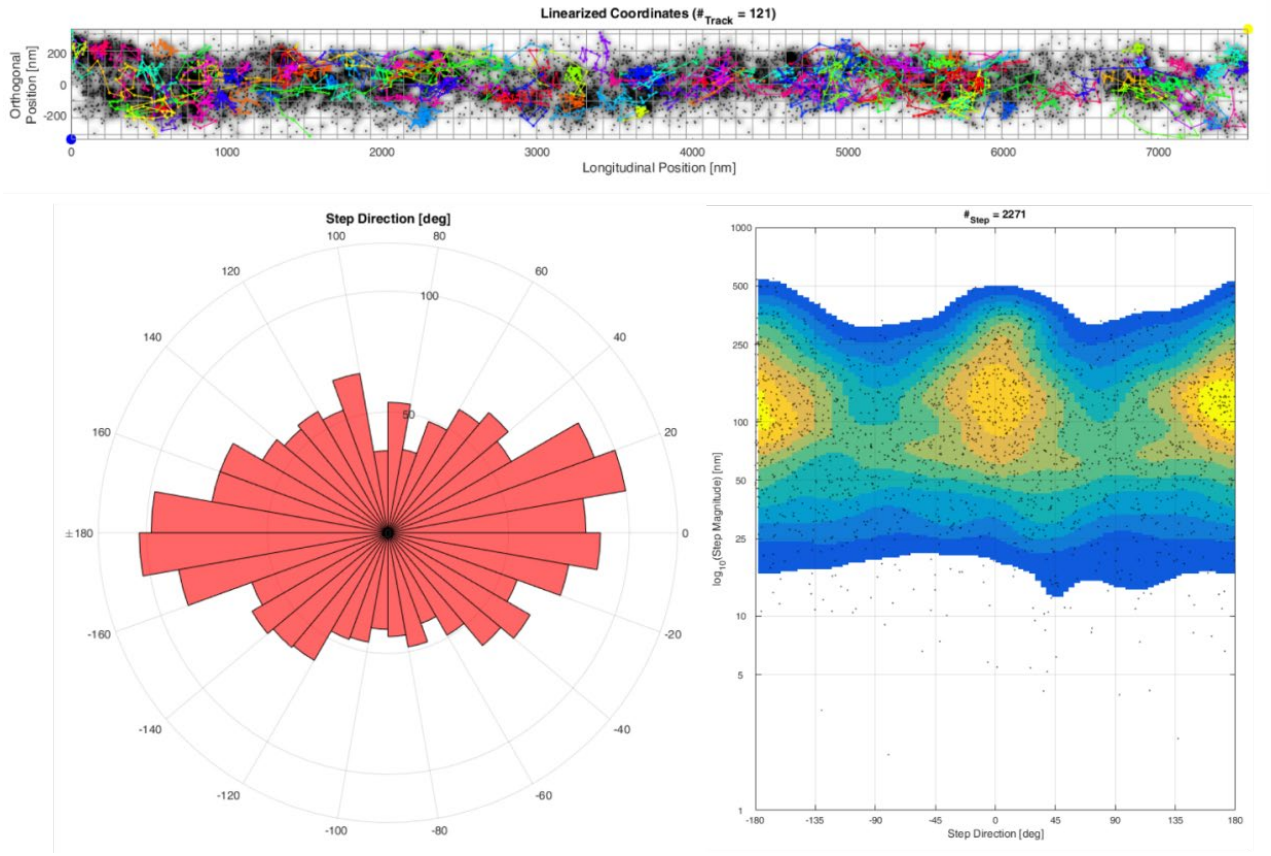

Figure **37**A). The majority of them is oriented along the longitudinal axis (

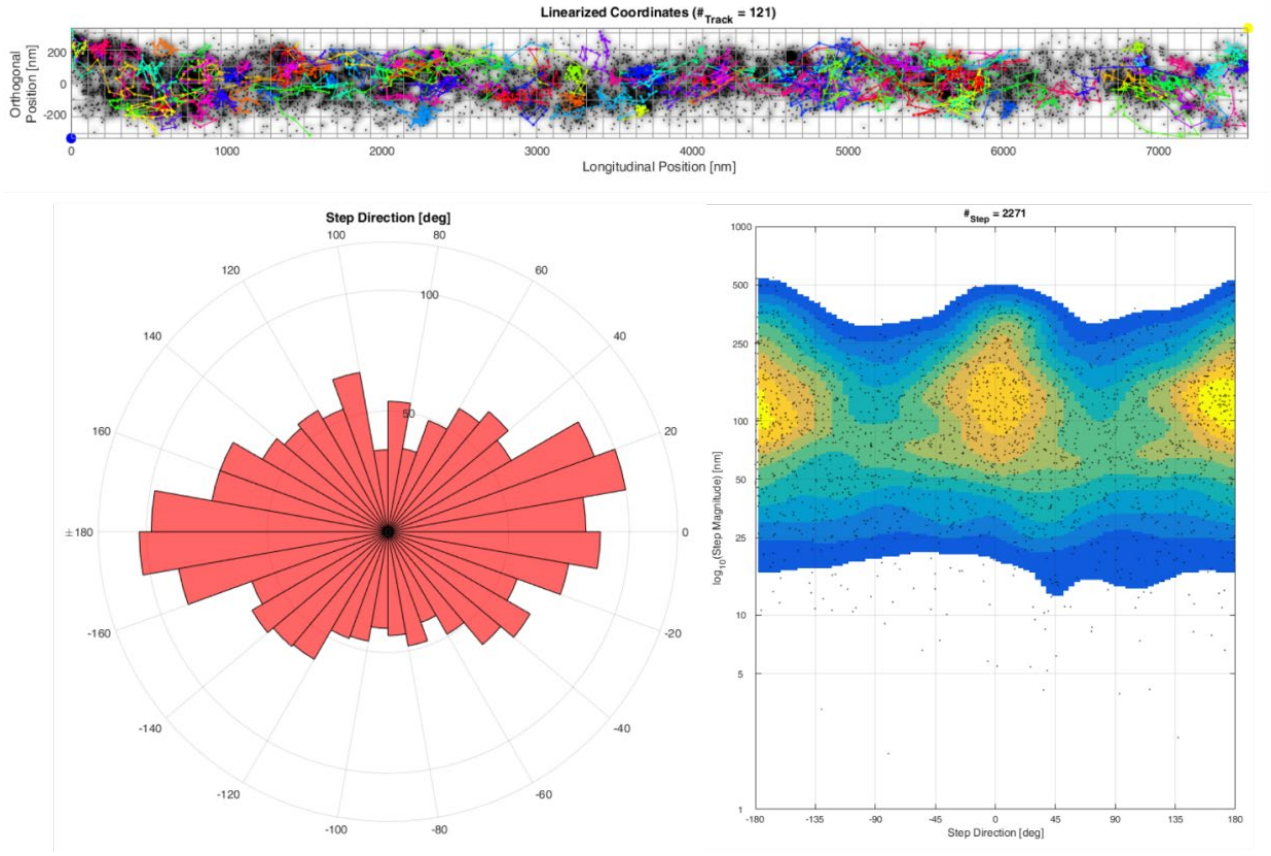

Figure **37**B, C). The pie chart diagram in

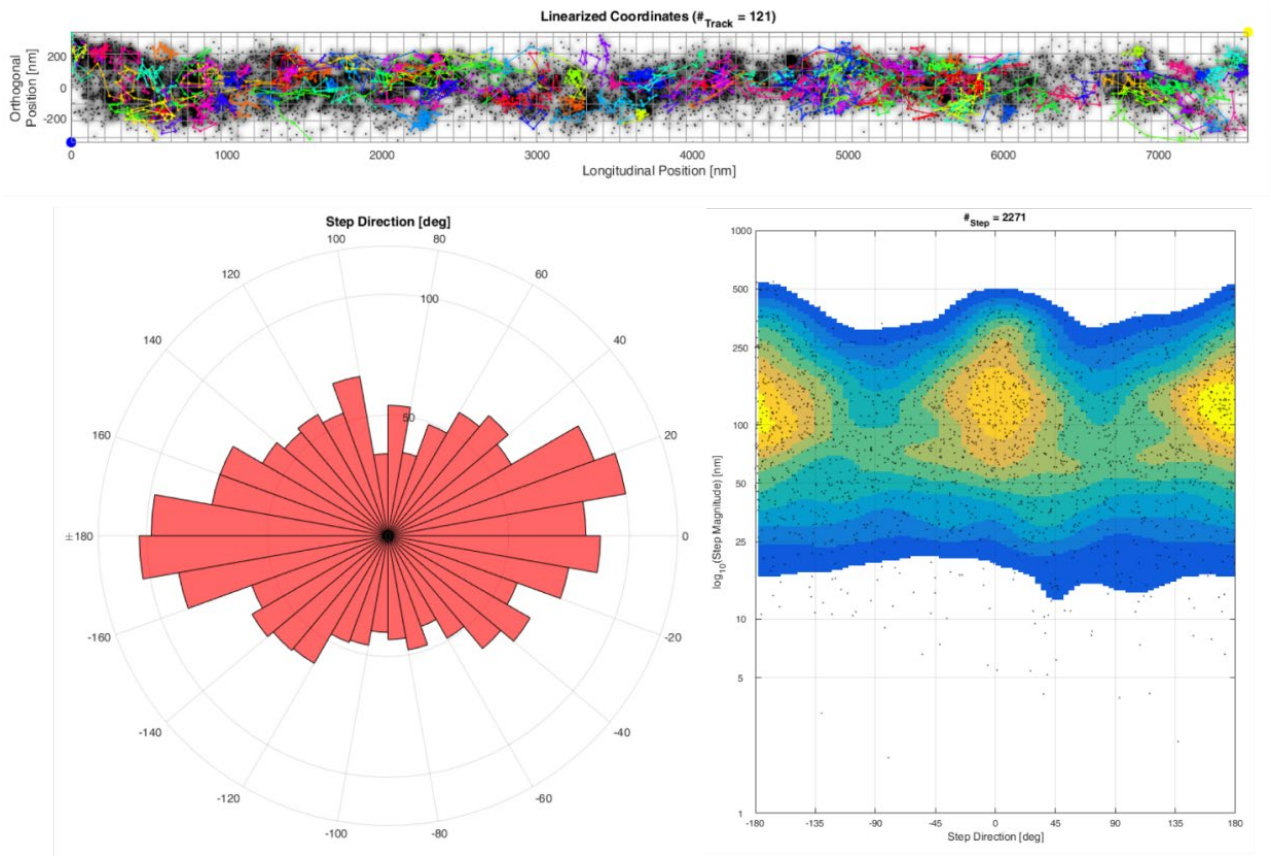

Figure **37**B illustrates the dominant longitudinal movement of CV-SUγ in starvation of the analyzed mitochondrion. Here, the amount of longitudinal directions between -20° to 30° and between -160° to 170° is twice as large as the number perpendicular oriented trajectories. Additionlly, the heatmap in

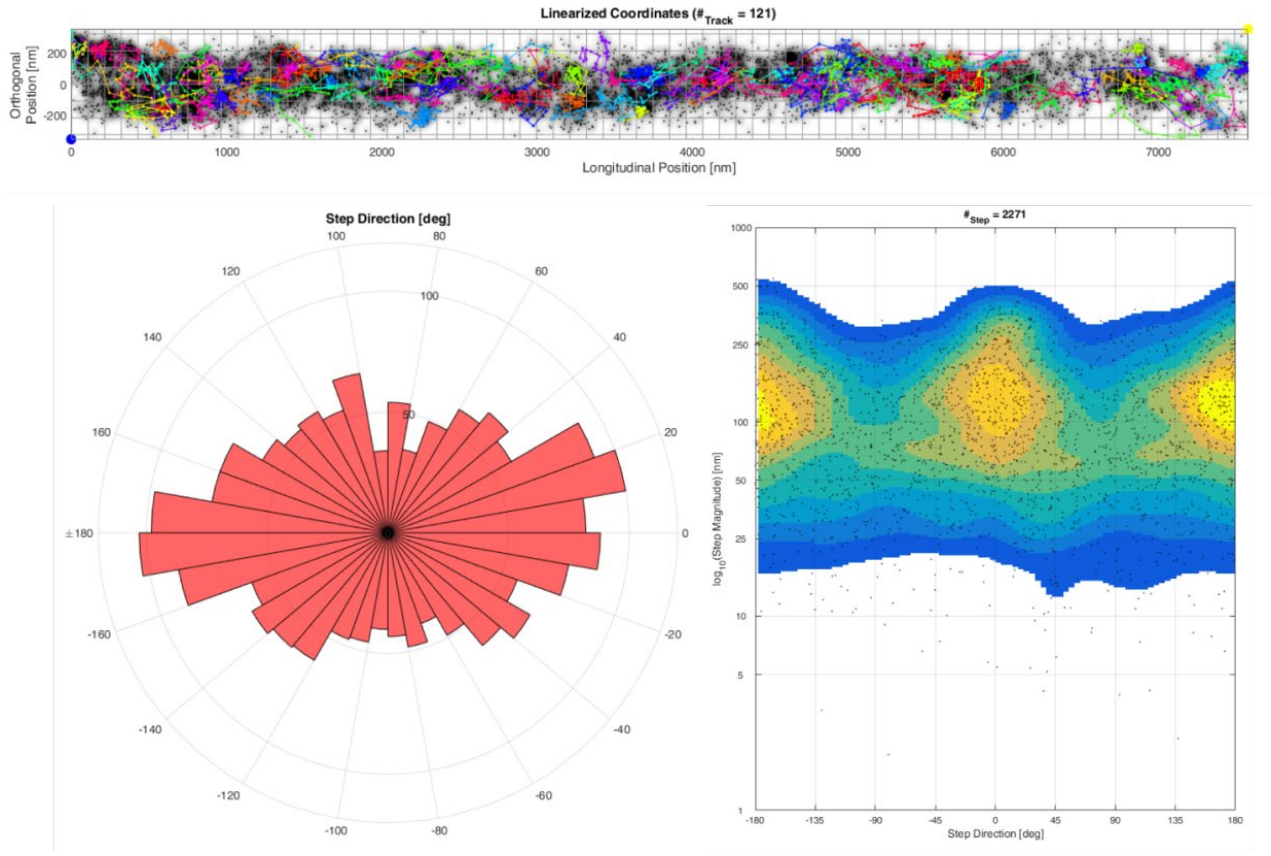

Figure **37**C shows that steps along the longitudinal axis can reach a larger jumpsize than steps in the perpendicular direction. However, this may be influenced by the 3D morphology of mitochondria. Here, jumpsizes in the perpendicular direction can be scaled down stronger than jumpsizes along the longitudinal direction. The trajectory directionality in starvation was compared to the trajectory directionality in control experiments (Figure 38). In the case of the control, 10784 binned steps were taken into account (Figure 38A, C). The analysis of trajectory directionality during starvation was performed on 59743 binned steps (Figure 38B, D).

Table 4 Jumpsize of CV-SUγ in control experiments and during starvation

Protein	Number of steps	Median jumpsize	Maximal. jumpsize	Minimal. jumpsize
CV-SUγ control	20124	96.94 nm	1117 nm	0.58 nm
CV-SUγ starvation	7491	175.70 nm	1211 nm	1.79 nm

Figure 36C), indicating a spatiotemporal re-organization of CV during starvation resulting from localizations in the IBM or even a re-organization of the mitochondrial ultrastructure with a lost of cristae. The trajectories of CV-SUγ in the control and under starving conditions directly differentiate, obviuosly in their directionality (**Fehler! Ungültiger Eigenverweis auf Textmarke.**B, D). This indicates either a shift of a longitudinal orientation of cristae or a shift of CV-SUγ into the IBM or even a lost ofcristae. The transition of CV-SUγ into the IBM can result from avoided diffusion in the CM and a dominant diffusion in the IBM or by a reduction of the CM. In order to analyze the directionality of mobility and to quantify for this, the directionality of trajectories was analyzed with MitoOrientedDynamics. Here, the4-step binning procedure was used. As described, the longitudinal axis of each

mitochondria was marked, which was used to interpolate it to a straight mitochondrion and the angle of binned steps to the longitudinal axis was measured. Shown in

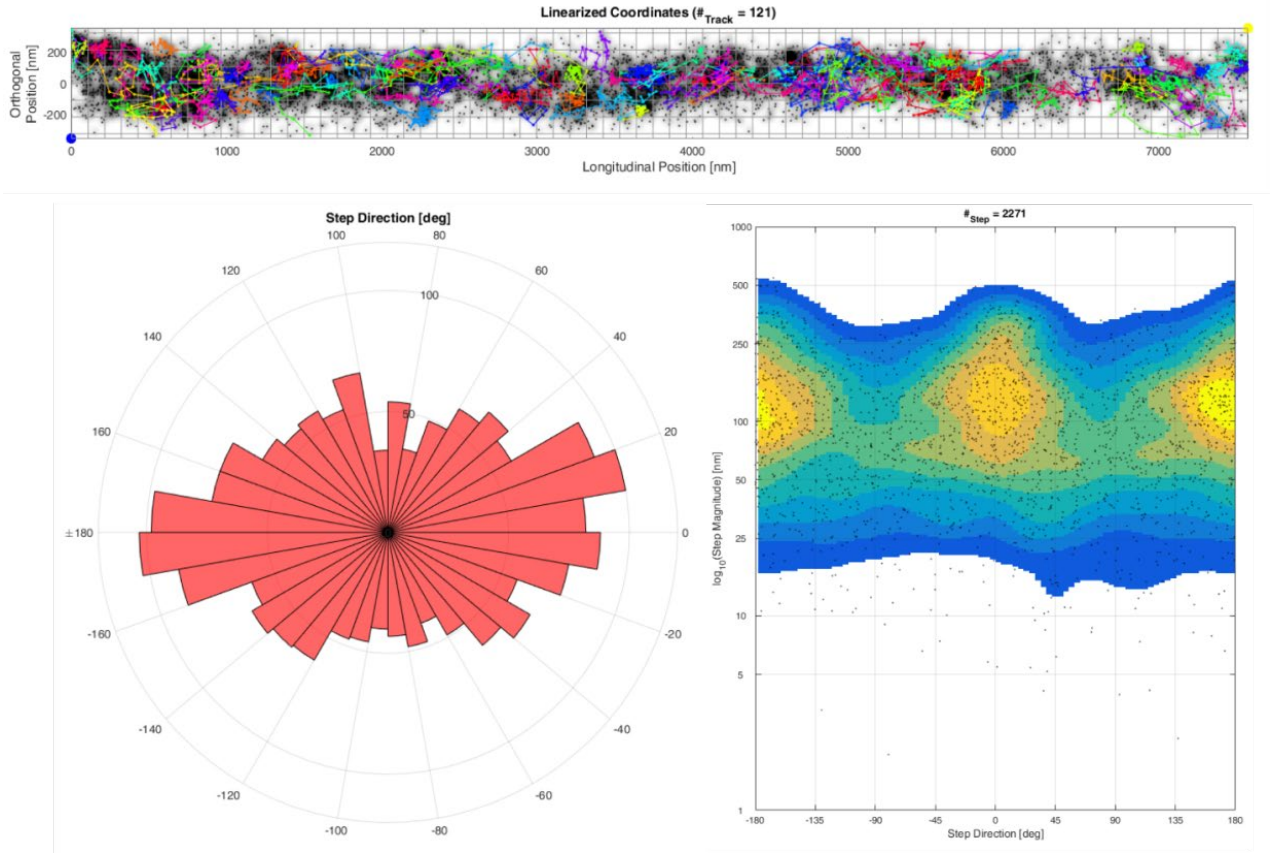

Figure **37** is an example of a straightened mitochondrion in starving conditions and its analysis of the trajectory directionality. In the shown mitochondrion the directionalities of 121 individual trajectories were analyzed (

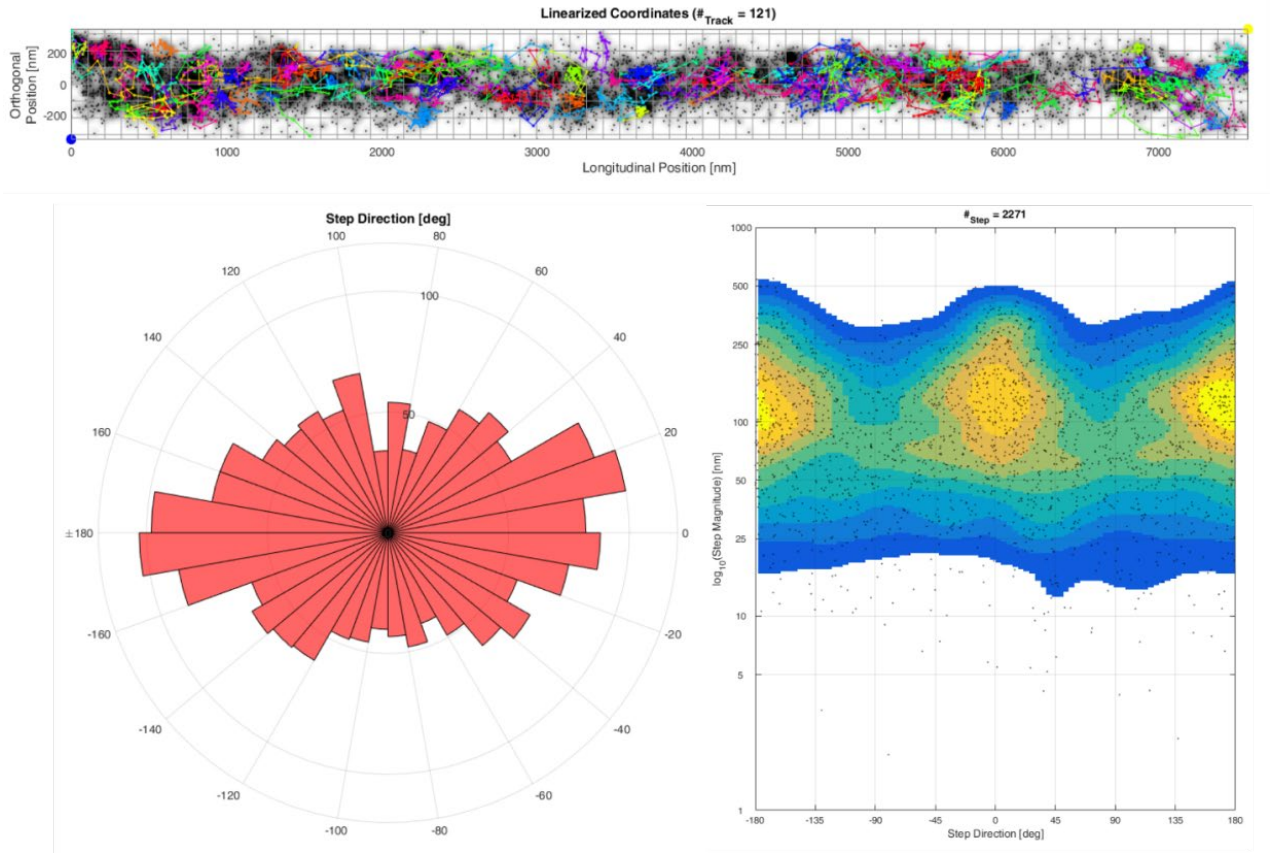

Figure **37**A). The majority of them is oriented along the longitudinal axis (

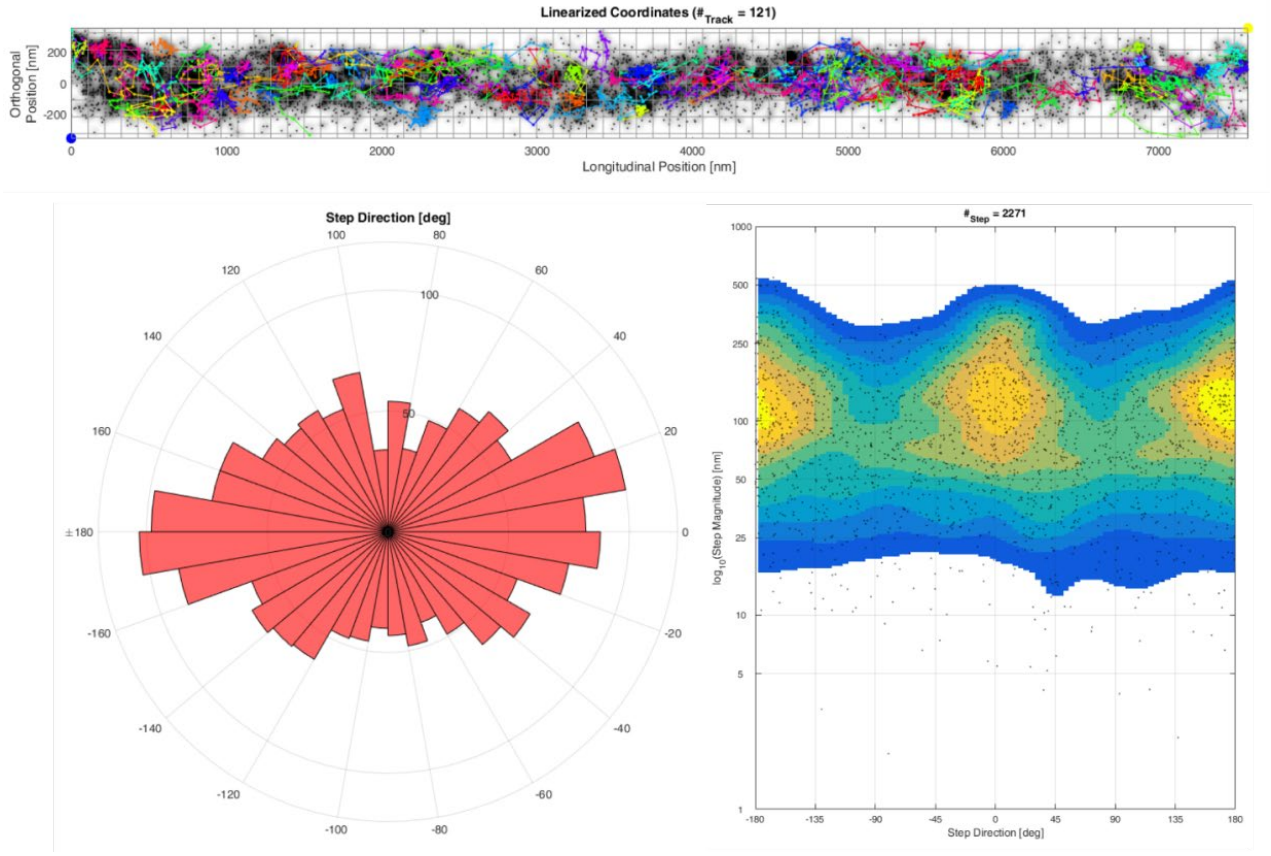

Figure **37**B, C). The pie chart diagram in

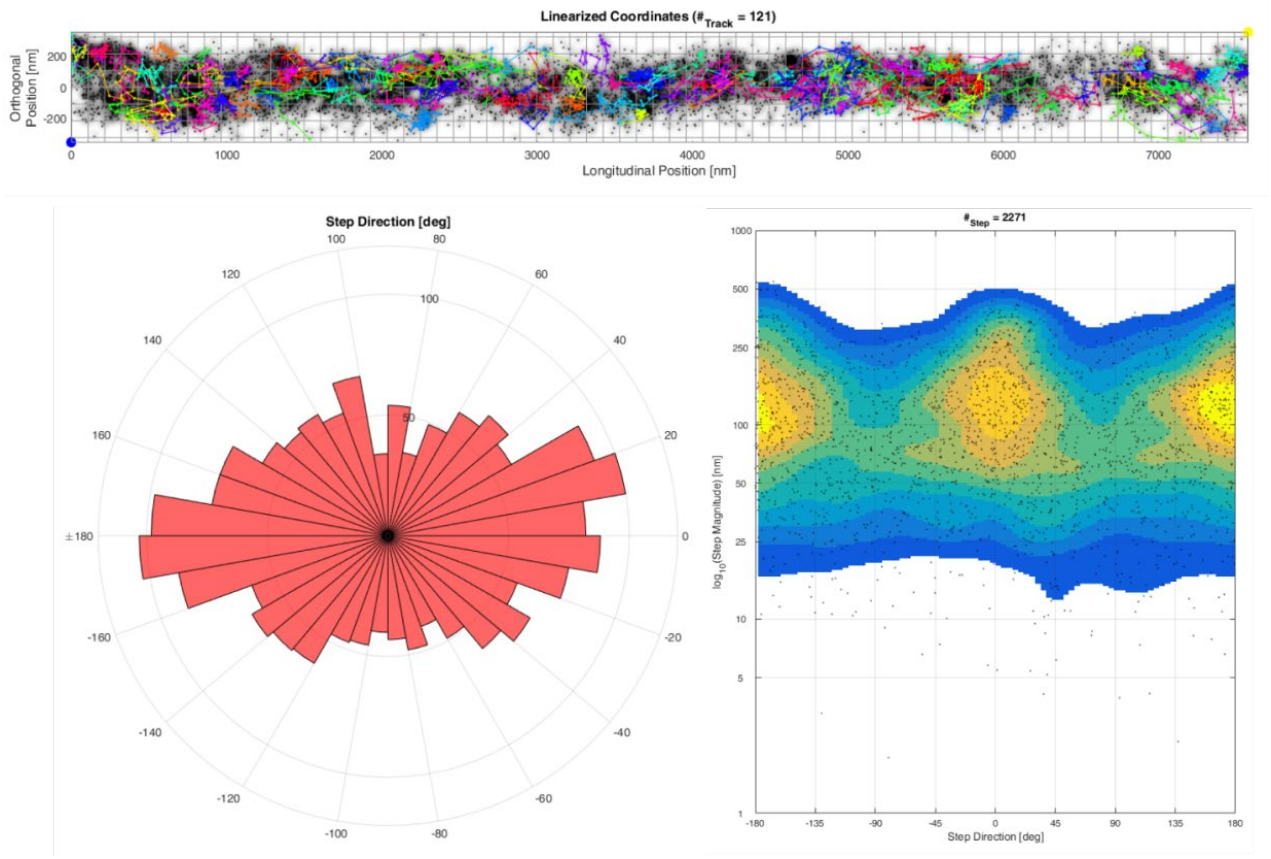

Figure **37**B illustrates the dominant longitudinal movement of CV-SUγ in starvation of the analyzed mitochondrion. Here, the amount of longitudinal directions between -20° to 30° and between -160° to 170° is twice as large as the number perpendicular oriented trajectories. Additionlly, the heatmap in

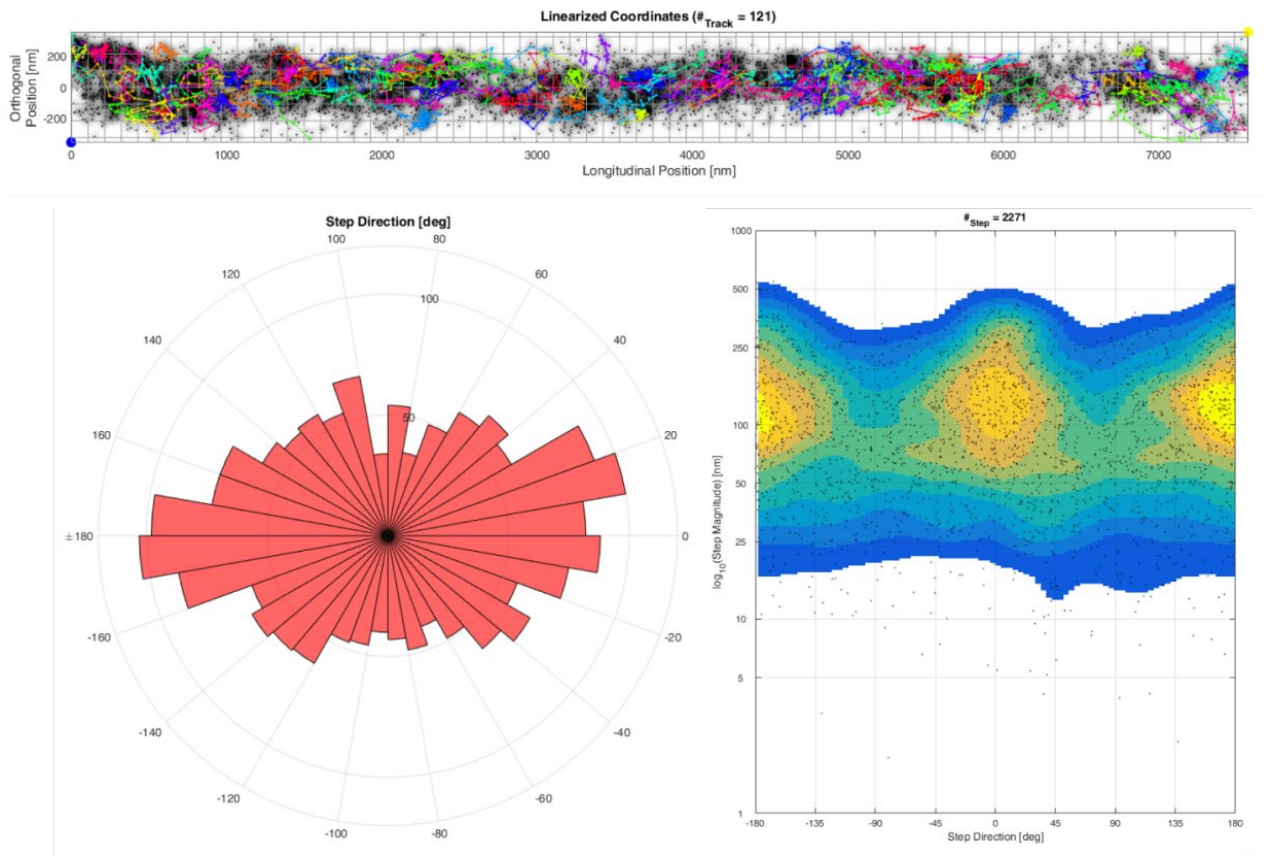

Figure **37**C shows that steps along the longitudinal axis can reach a larger jumpsize than steps in the perpendicular direction. However, this may be influenced by the 3D morphology of mitochondria. Here, jumpsizes in the perpendicular direction can be scaled down stronger than jumpsizes along the longitudinal direction. The trajectory directionality in starvation was compared to the trajectory directionality in control experiments (Figure 38). In the case of the control, 10784 binned steps were taken into account (Figure 38A, C). The analysis of trajectory directionality during starvation was performed on 59743 binned steps (Figure 38B, D).

Table 4 Jumpsize of CV-SUγ in control experiments and during starvation

Protein	Number of steps	Median jumpsize	Maximal. jumpsize	Minimal. jumpsize
CV-SUγ control	20124	96.94 nm	1117 nm	0.58 nm
CV-SUγ starvation	7491	175.70 nm	1211 nm	1.79 nm

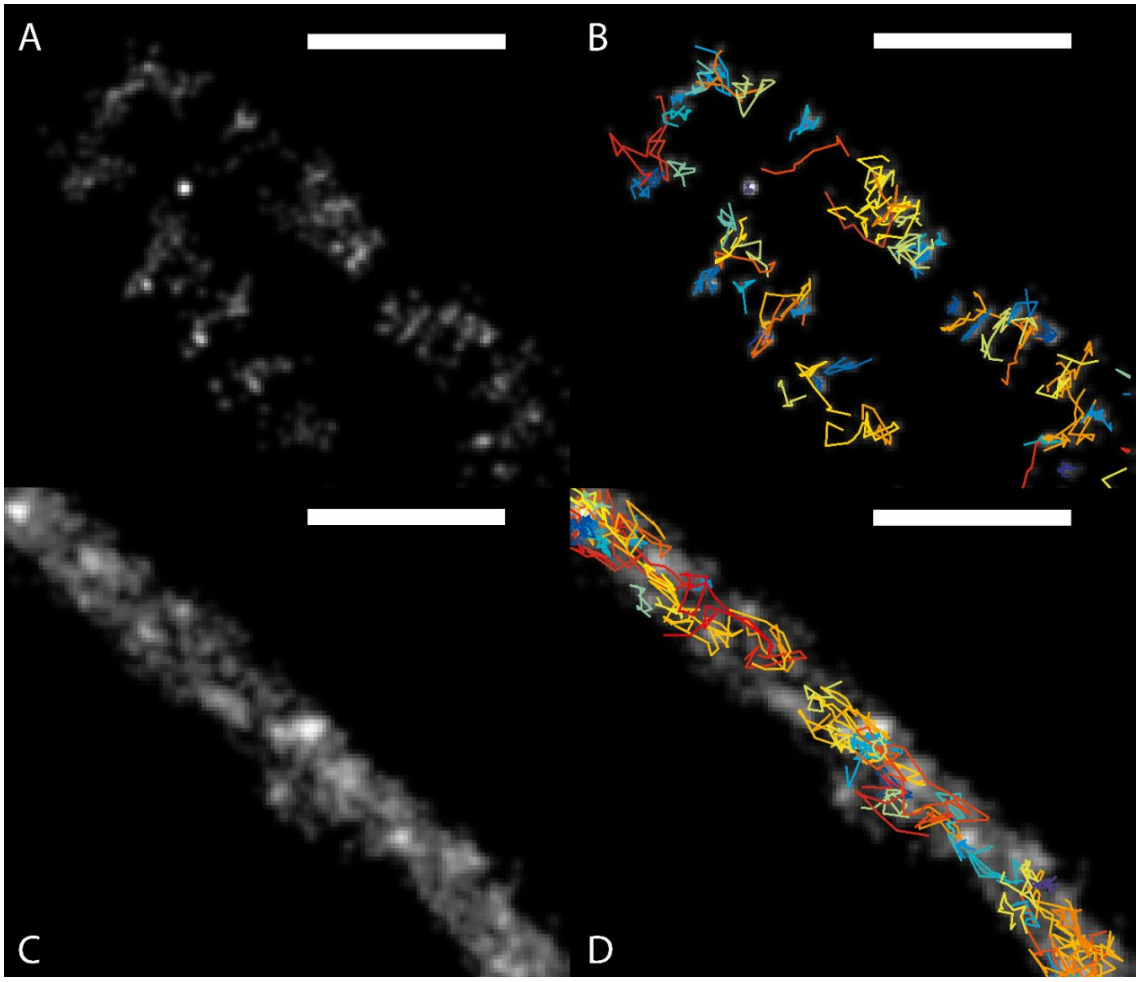

Figure 36 Single trajectories of F_1F_0 ATP synthase subunit-γ in control and starving conditions
A Super-resolution images of CV-SUγ proteins in glycolytic conditions reveals a predominant organization in disc-like accumulations, which are oriented perpendicular relative to the longitudinal axis of the imaged mitochondria. **B** Trajectories of the CV-SUγ proteins in the control experiment show a predominant perpendicular directionality relative to the longitudinal axis of the imaged mitochondria. **C** CV-SUγ proteins in starving conditions are localized homogenously along the IM. **D** Trajectories of the CV-SUγ proteins in starving conditions along the IM mostly following the longitudinal axis of the imaged mitochondria. Still confined mobility can be observed.

In the control the pie chart diagram of CV-SUγ trajectory directionality showed a slightly elliptical directionality with maxima in the perpendicular direction resulting from cristae trajectories along the CM. But also, nearly the same number of longitudinal directionalities resulting from diffusion in the IBM (Figure 38A). Additionally, trajectories of CV-SUγ undergo a confined mobility. Confined mobility of proteins can produce trajectories with steps oriented in all direction. These randomly oriented directions lead to trajectoriy directionalities in all orientations. However, confined mobility was observed in both conditions. In rare cases, CV-SUγ showed a unconfined random diffusion in the control condition, which results in directions in all orientations (Figure 38A). The heatmap of CV-SUγ in the control shows minor step directions around 0° and ±180° and a slight accumulation of trajectory directions between -135° to -45° and 45° to 135°, so in general to the perpendicular direction (Figure 38C). Additionally, the jumpsize is similar in all directions.

The analysis of the trajectory directionality of CV-SUγ during starvation generally showed a longitudinal direction as expected from the trajectory map shown in CV-SUγ in the control and under starving conditions directly differentiate, obviuosly in their directionality (**Fehler! Ungültiger Eigenverweis auf Textmarke.**B, D). This indicates either a shift of a longitudinal orientation of cristae or a shift of CV-SUγ into the IBM or even a lost ofcristae.

The transition of CV-SUγ into the IBM can result from avoided diffusion in the CM and a dominant diffusion in the IBM or by a reduction of the CM. In order to analyze the directionality of mobility and to quantify for this, the directionality of trajectories was analyzed with MitoOrientedDynamics. Here, the4-step binning procedure was used. As described, the longitudinal axis of each mitochondria was marked, which was used to interpolate it to a straight mitochondrion and the angle of binned steps to the longitudinal axis was measured. Shown in

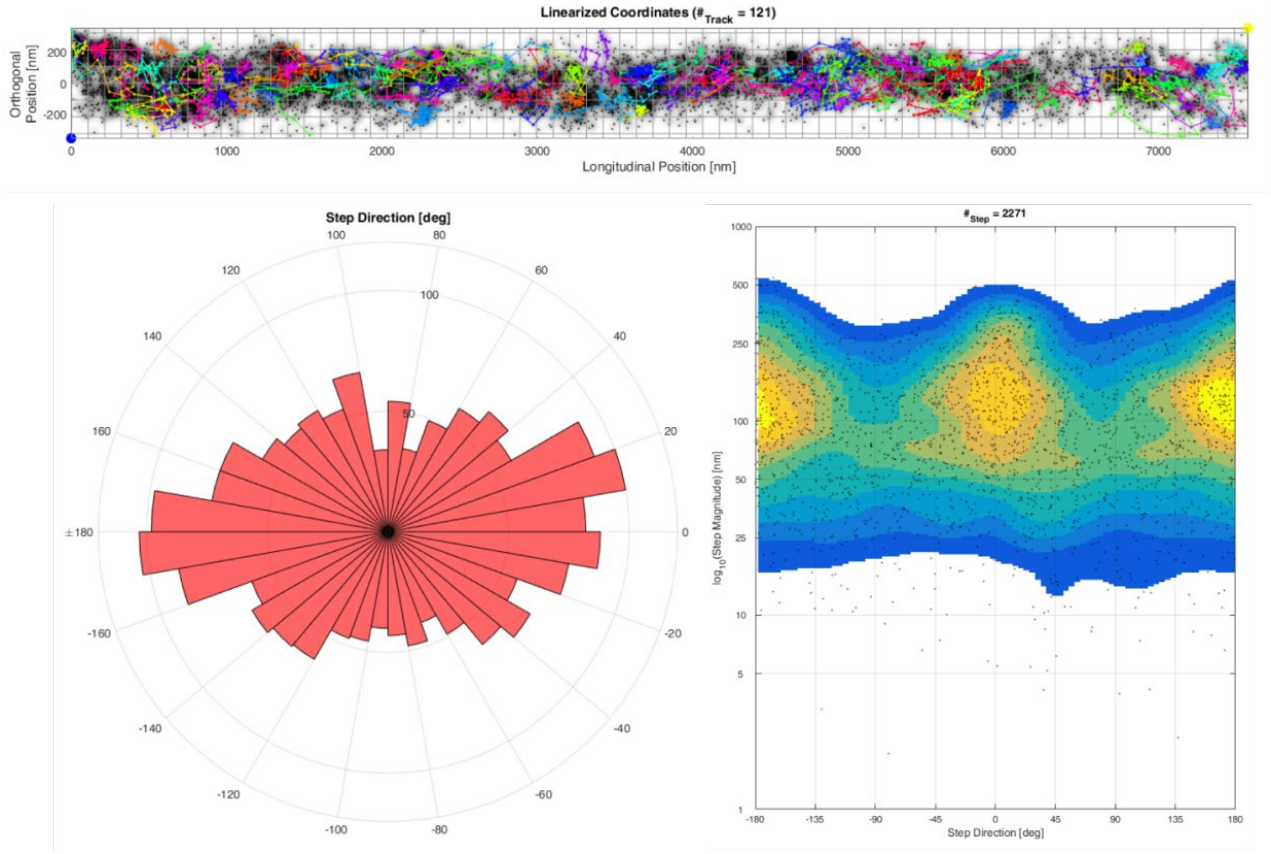

Figure **37** is an example of a straightened mitochondrion in starving conditions and its analysis of the trajectory directionality. In the shown mitochondrion the directionalities of 121 individual trajectories were analyzed (

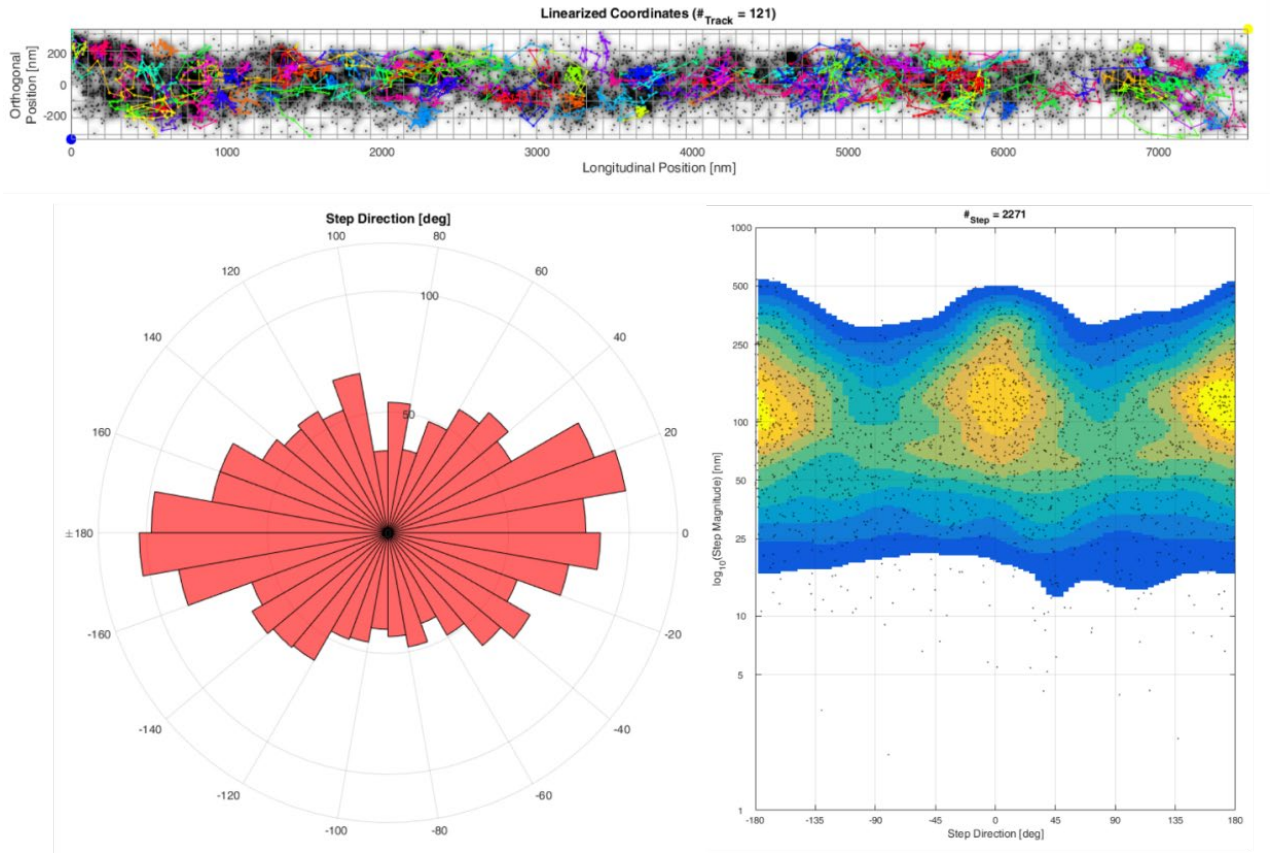

Figure **37**A). The majority of them is oriented along the longitudinal axis (

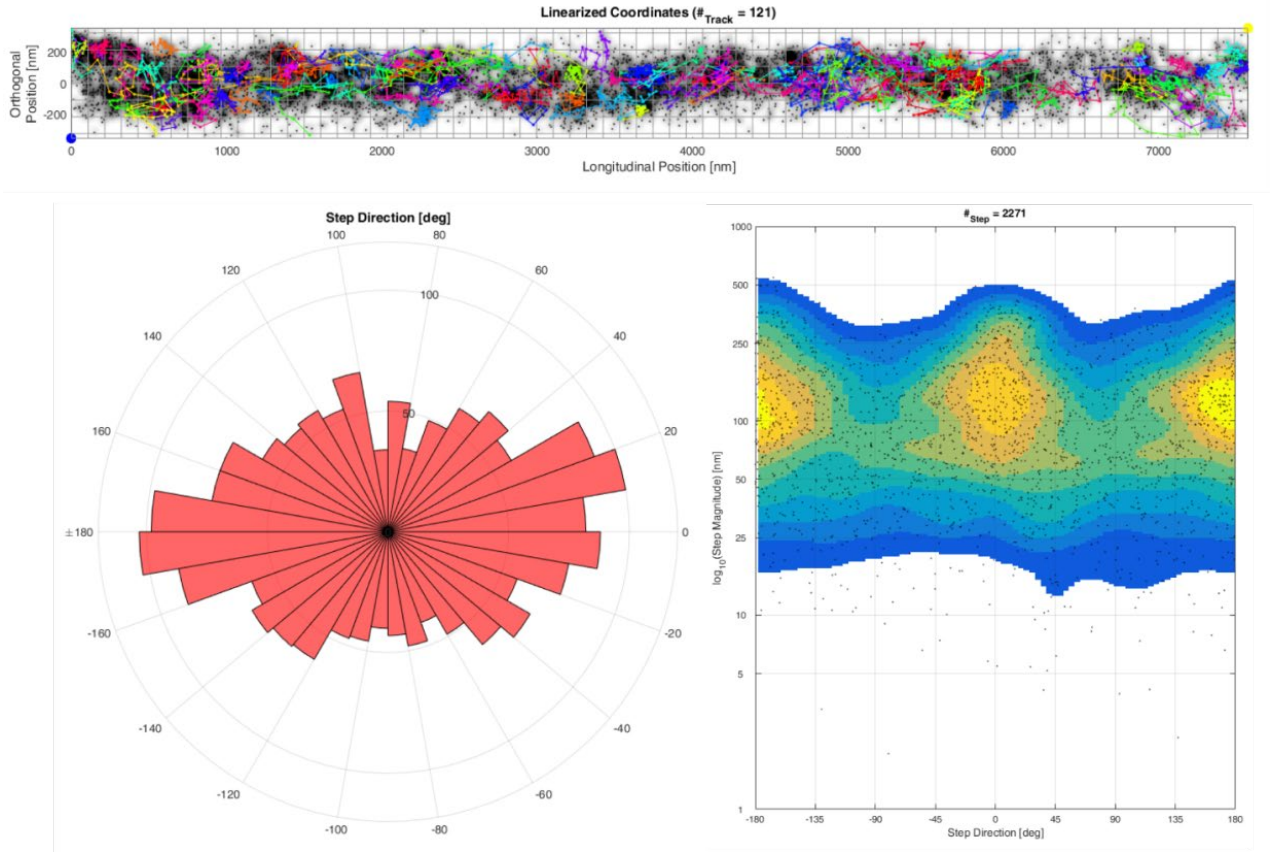

Figure **37**B, C). The pie chart diagram in

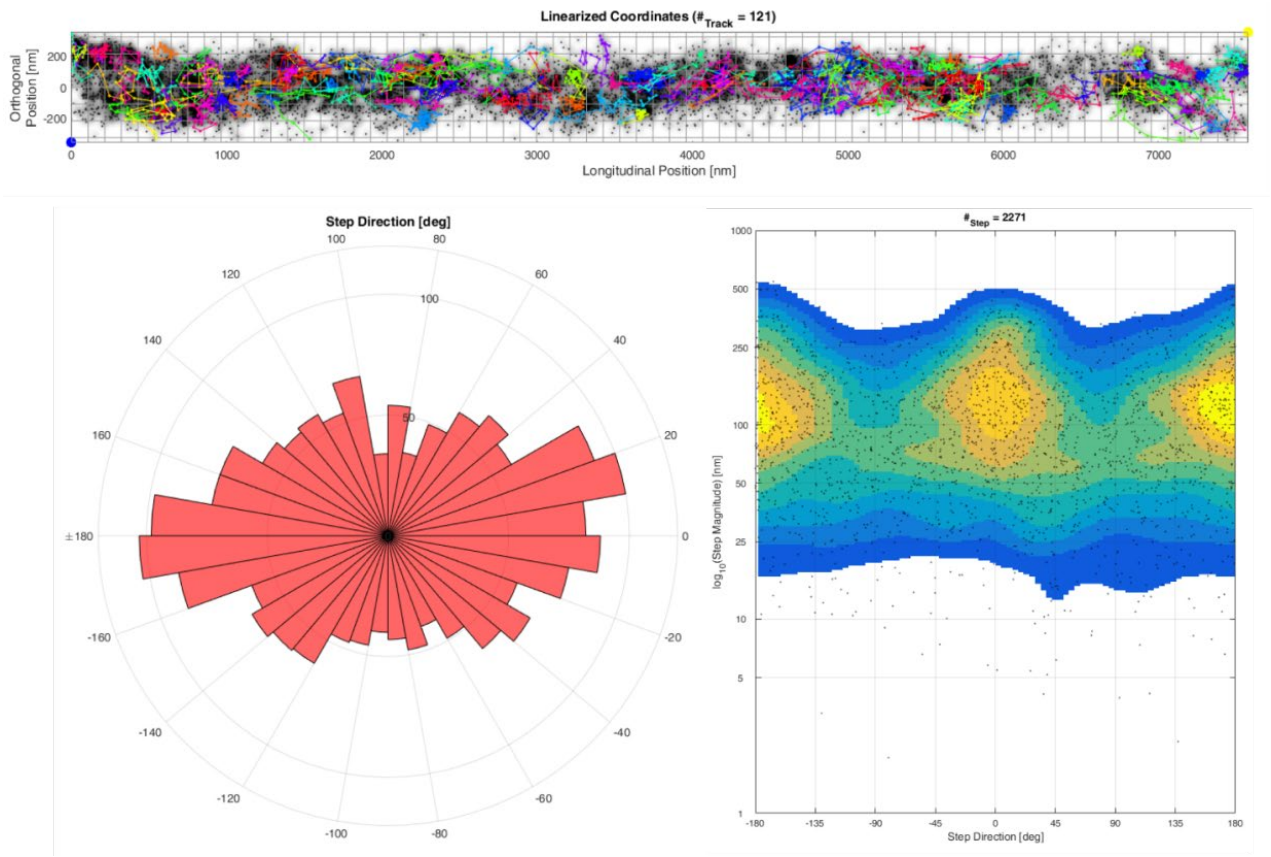

Figure **37**B illustrates the dominant longitudinal movement of CV-SUγ in starvation of the analyzed mitochondrion. Here, the amount of longitudinal directions between -20° to 30° and between -160° to 170° is twice as large as the number perpendicular oriented trajectories. Additionlly, the heatmap in

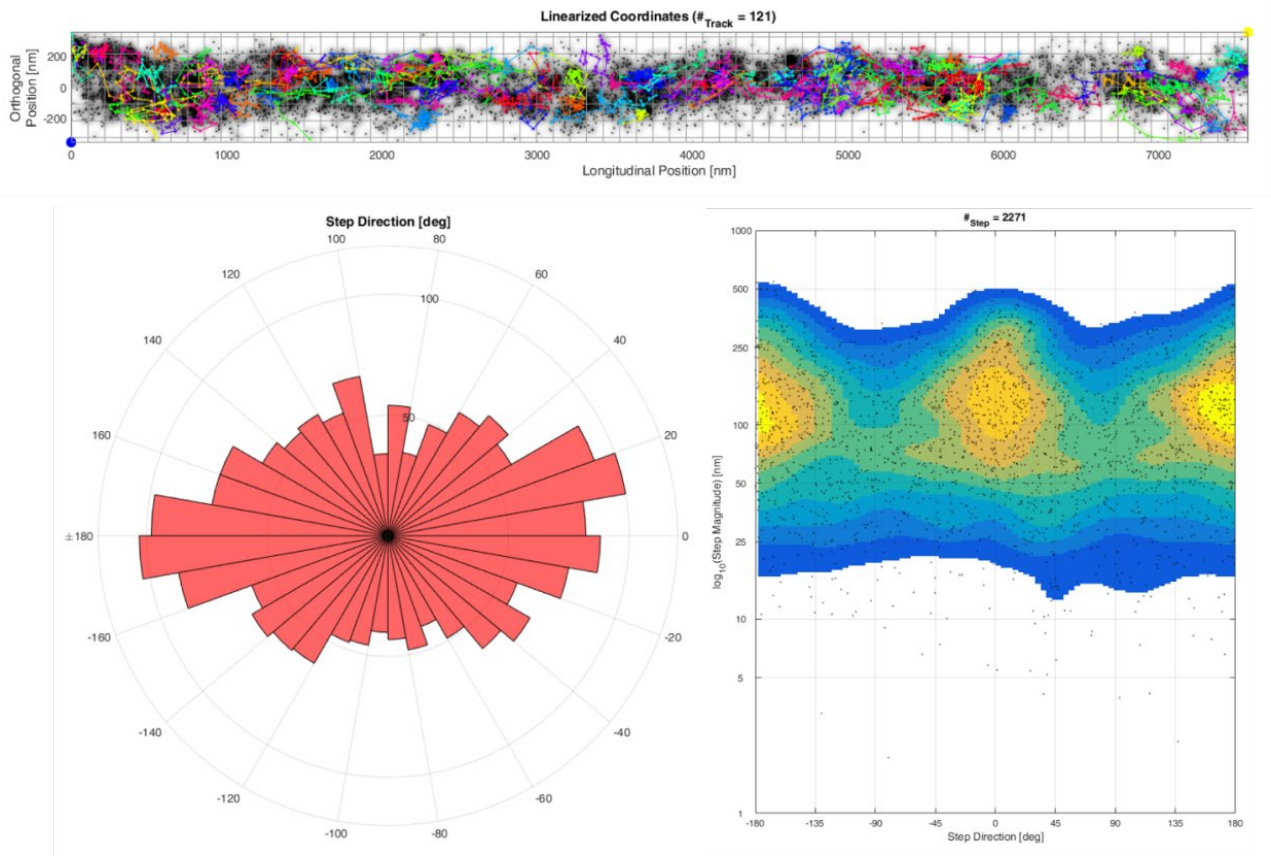

Figure **37**C shows that steps along the longitudinal axis can reach a larger jumpsize than steps in the perpendicular direction. However, this may be influenced by the 3D morphology of mitochondria. Here, jumpsizes in the perpendicular direction can be scaled down stronger than jumpsizes along the longitudinal direction. The trajectory directionality in starvation was compared to the trajectory directionality in control experiments (Figure 38). In the case of the control, 10784 binned steps were taken into account (Figure 38A, C). The analysis of trajectory directionality during starvation was performed on 59743 binned steps (Figure 38B, D).

Table 4 Jumpsize of CV-SUγ in control experiments and during starvation

Protein	Number of steps	Median jumpsize	Maximal. jumpsize	Minimal. jumpsize
CV-SUγ control	20124	96.94 nm	1117 nm	0.58 nm
CV-SUγ starvation	7491	175.70 nm	1211 nm	1.79 nm

Figure 36D and

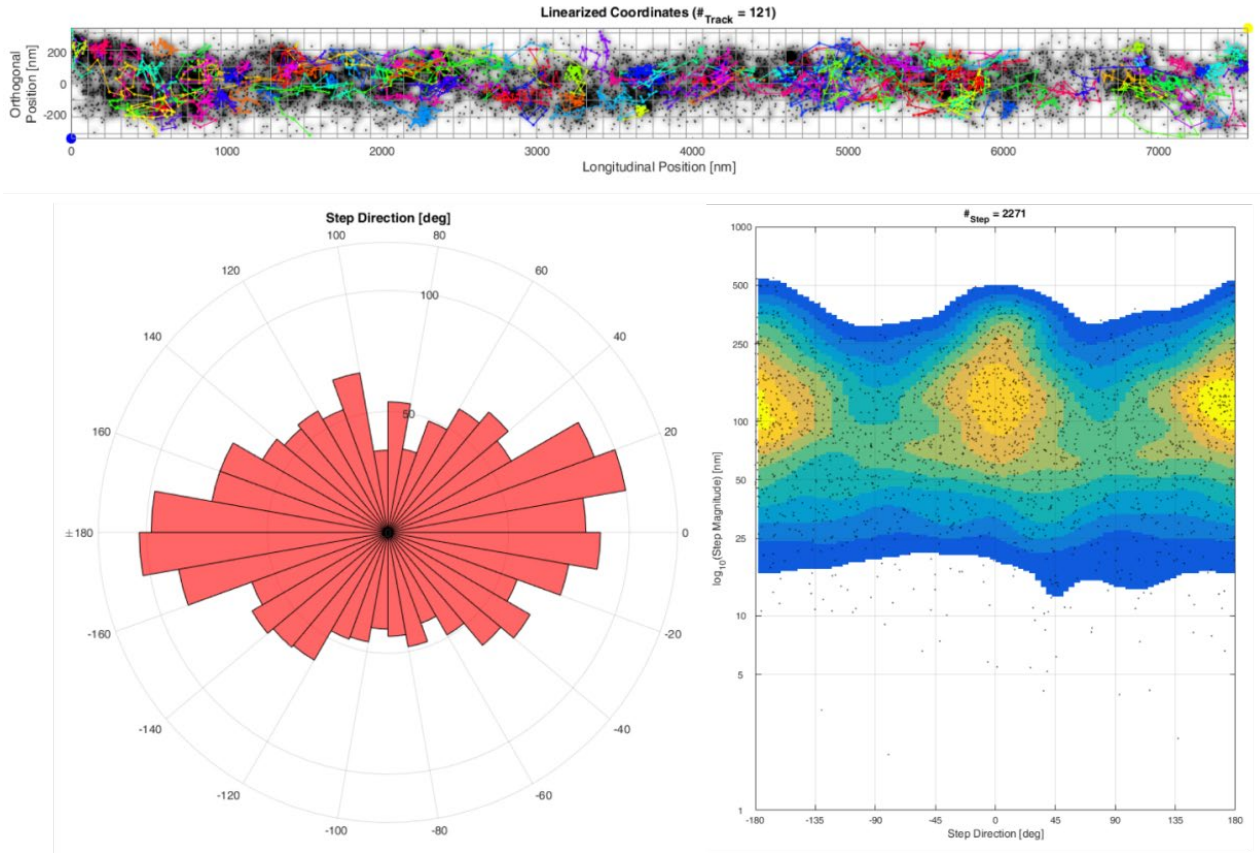

Figure 37A. In

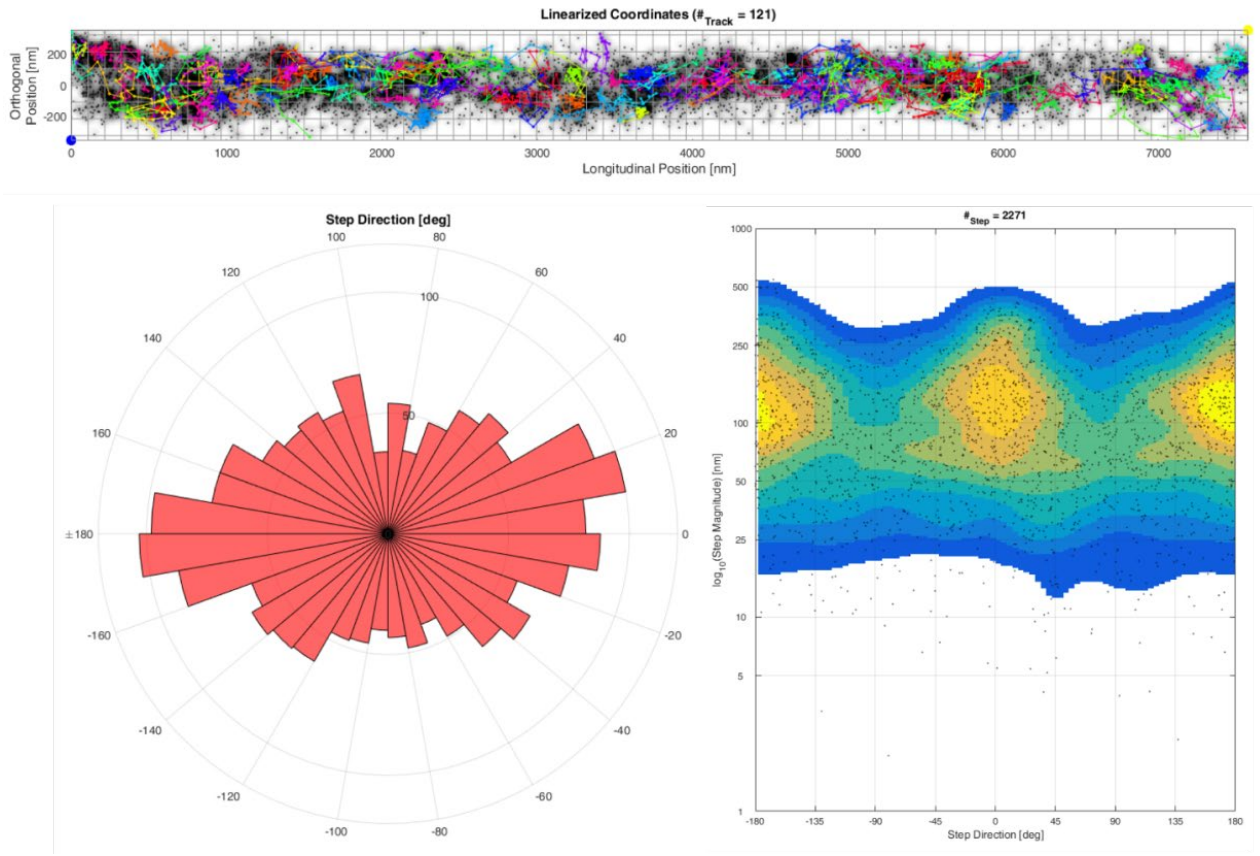

Figure **37** the trajectory directionality analysis of a single mitochondrion during starvtion is shown. Here, a clear longitudinal directionality of CV-SUγ trajectories can be seen (

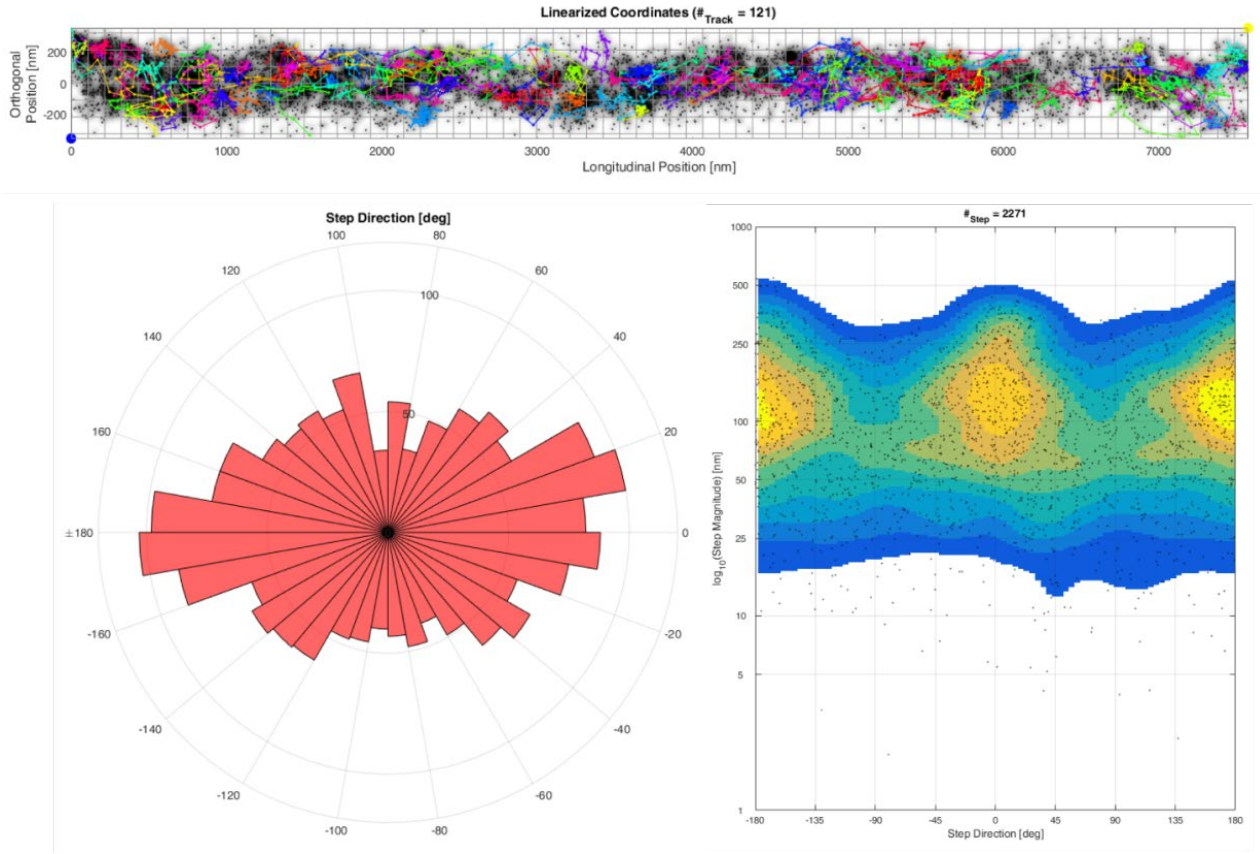

Figure **37**B). Furthermore, the heatmap in

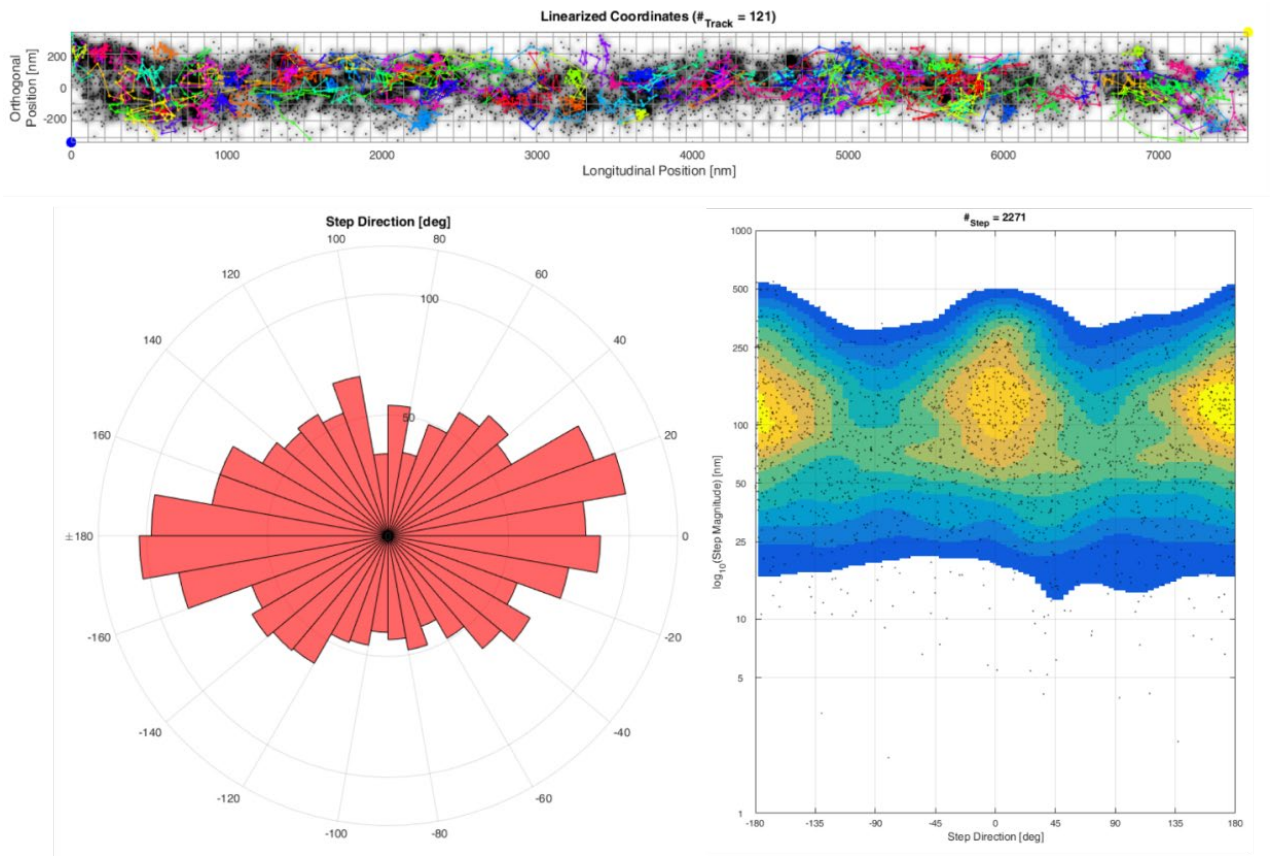

Figure **37**C shows larger jumpsizes along the longitudinal direction, which was never the case for CV-SUγ trajectories in the control. The total analysis of CV-SUγ trajectory directionality in starving conditions supported this single analysis (Figure 38). The number of directions in the longitudinal direction - between -160° to 160° and -30° to 30° - is twice as many as the number of binned step directions in the perpendicular direction - between 70° to 110° and -110° to -70° (Figure 38B). In the heatmap of CV-SUγ during starvation, the longitudinal jumpsize again was larger than the perpendicular jumpsize (Figure 38D). In the longitudinal direction maximal jumpsizes of up to 500 nm were measured. The maximal perpendicular jumspizes of ~250 nm during starvation remained similar to the control (Figure 38C, D). The minimal step size remained mostly unchanged and equal in both conditions between 10 nm and 25 nm. However, the heatmp colorcode illustrates that longitudinal steps in starvation often were above 100 nm (Figure 38D), while in the control the avaerge step size of longitudinal directions was around 75 nm.

Taken together these results clearly show a switch in the spatiotemporal protein organization of CV-SUγ due to starvation. The number of longitudinal trajectory directionality was increased during in starvation. The cristae trajectories vanished and CV-SUγ diffused in the IBM during starvation. Whether these spatiotemporal dynamics resulted from a loss of cristae or from an exclusion of CV-SUγ from cristae and a following dominant localization in the IBM could not be explained. It would be also conceivable that longitudinal diffusion results from a change in the cristae orientation, to cristae with a parallel orientation to the longitudinal axis of mitochondria. However, here only 3D tracking of CV, super-resolution microscopy of the IM or TEM / TEM tomography of mitohcondria in

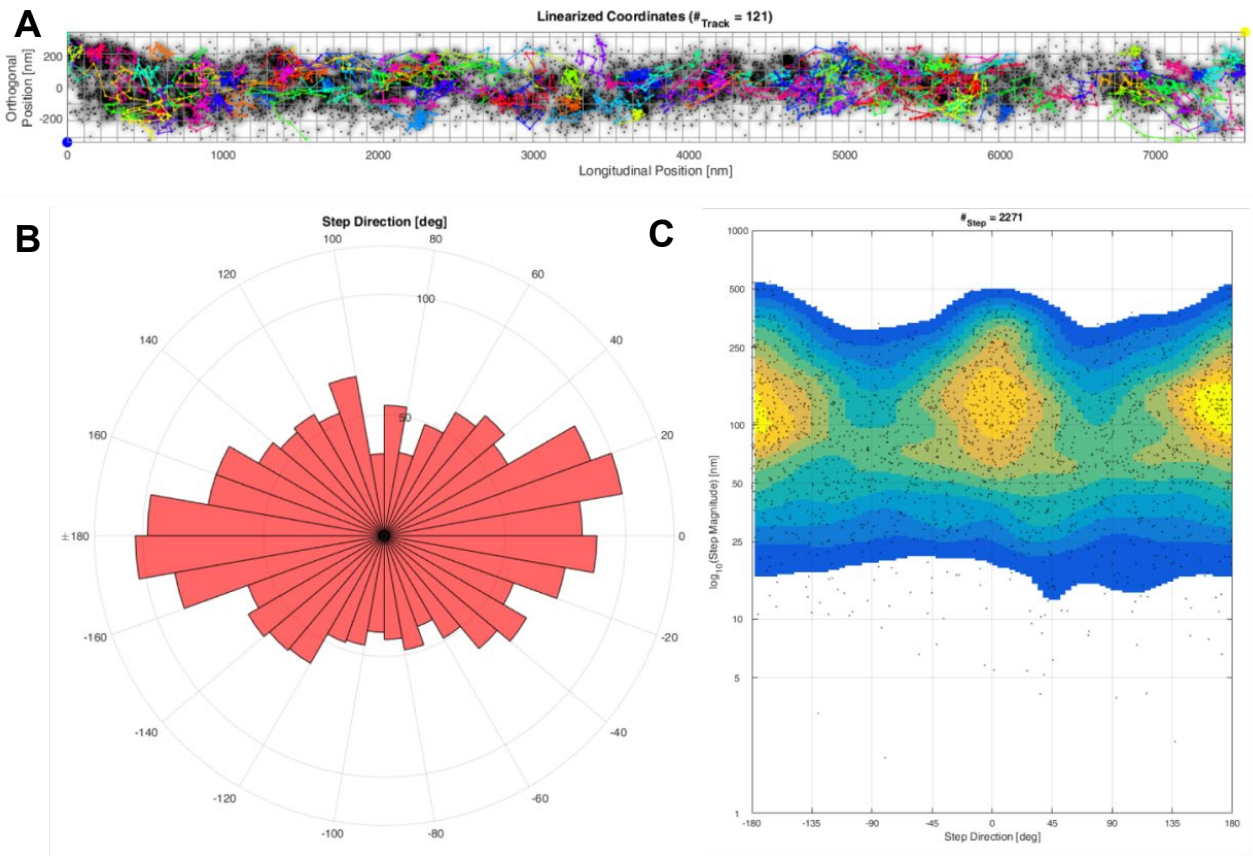

Figure 37 Directionality analysis of the F_1F_0 ATP synthase subunit-γ of a single mitochondrion in starvation Step direction analysis of one mitochondrion during starvation. **A** The 121 trajectories of CV-SUγ proteins transformed to a linear trajectory map of a 7.5 µm long mitochondrion. Beside trajectories following the longitudinal axis, confined mobile proteins can also be observed. **B** Step direction pie chart of the trajectories shown in A, a predominant longitudinal movement was obtained. The majority of trajectories is oriented between + 160° to -160° and 45° to -20°. **C** Step magnitude plot of the analyzed trajectories. A strong longitudinal directionality of the trajectories is shown.

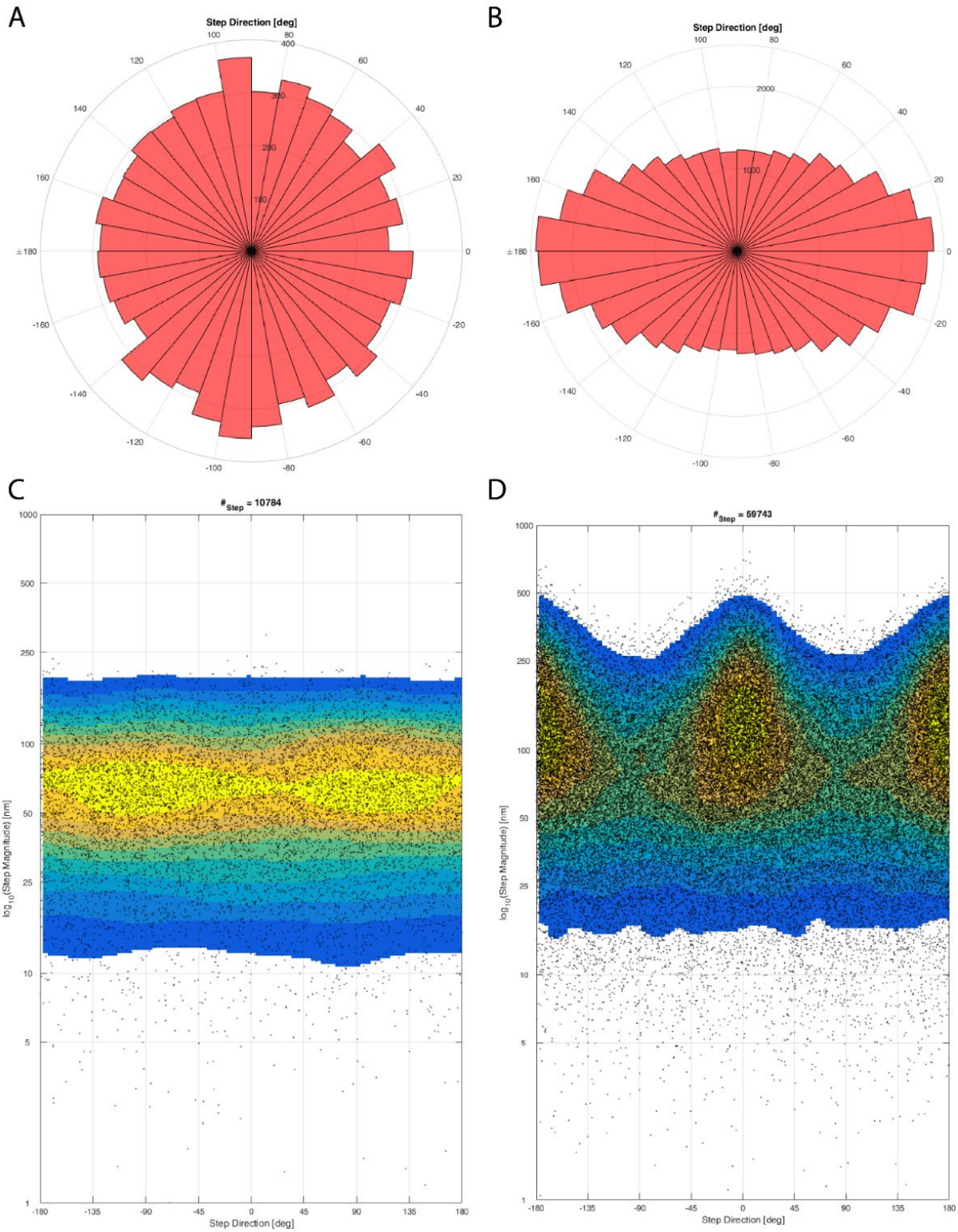

Figure 38 Quantification of trajectory directionalities of the F_1F_O ATP synthase subunit-γ of all tracked proteins in the control- and starving conditions

A Trajectory directionality in degree in a pie chart diagramof CV-SUγ in the control. An orientation of the trajectories in all directions was measured. A tendency to orthogonal diffusion was observed. **B** Trajectory directionality in degree in a pie chart diagram of CV-SUγ in starvation. This diagram shows a predominant longitudinal trajectory directionality. **C** The step magnitude plot shows that the majority of steps of CV-SUγ had a size between 50 nm and 100 nm with accumulations between -45° and -135° and 45° to 135°. **D** The dominant longitudinal directionality of trajectories of CV-SUγ during starvation gets clear in the step magnitude plot in which only a small number of steps is oriented perpendicular to the longitudinal axis of the analyzed mitochondria. The majority of the steps are between -45° and 45° and -135° and 135°. Additionally, the steps size in these directions reached 500 nm and was also in average higher than in C.

starvation can bring clarity to this aspect. This will be investigated in chapter 9.4.2 and chapter 9.5.6.

Tracking of proteins also allows quantification of their Dapp. It allows to analyze the mobility of molecules. Furthermore, an analysis of Dapp allows separating the population into three subpopulations, a mobile fraction, a slow mobile fraction and a confined mobile fraction (Figure 39). In CV-SUγ in the control and under starving conditions directly differentiate, obviuosly in their directionality (**Fehler! Ungültiger Eigenverweis auf Textmarke.**B, D). This indicates either a shift of a longitudinal orientation of cristae or a shift of CV-SUγ into the IBM or even a lost ofcristae. The transition of CV-SUγ into the IBM can result from avoided diffusion in the CM and a dominant diffusion in the IBM or by a reduction of the CM. In order to analyze the directionality of mobility and to quantify for this, the directionality of trajectories was analyzed with MitoOrientedDynamics. Here, the4-step binning procedure was used. As described, the longitudinal axis of each mitochondria was marked, which was used to interpolate it to a straight mitochondrion and the angle of binned steps to the longitudinal axis was measured. Shown in

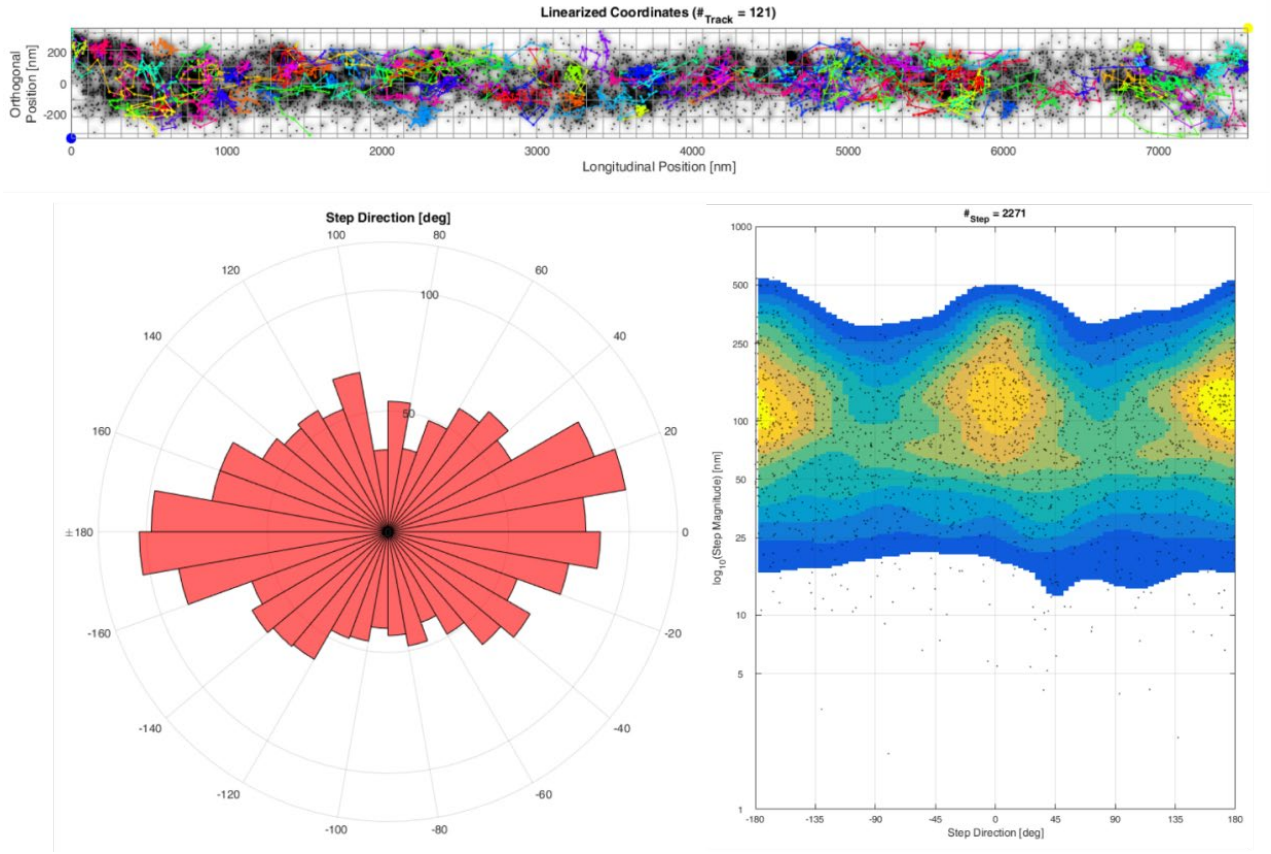

Figure **37** is an example of a straightened mitochondrion in starving conditions and its analysis of the trajectory directionality. In the shown mitochondrion the directionalities of 121 individual trajectories were analyzed (

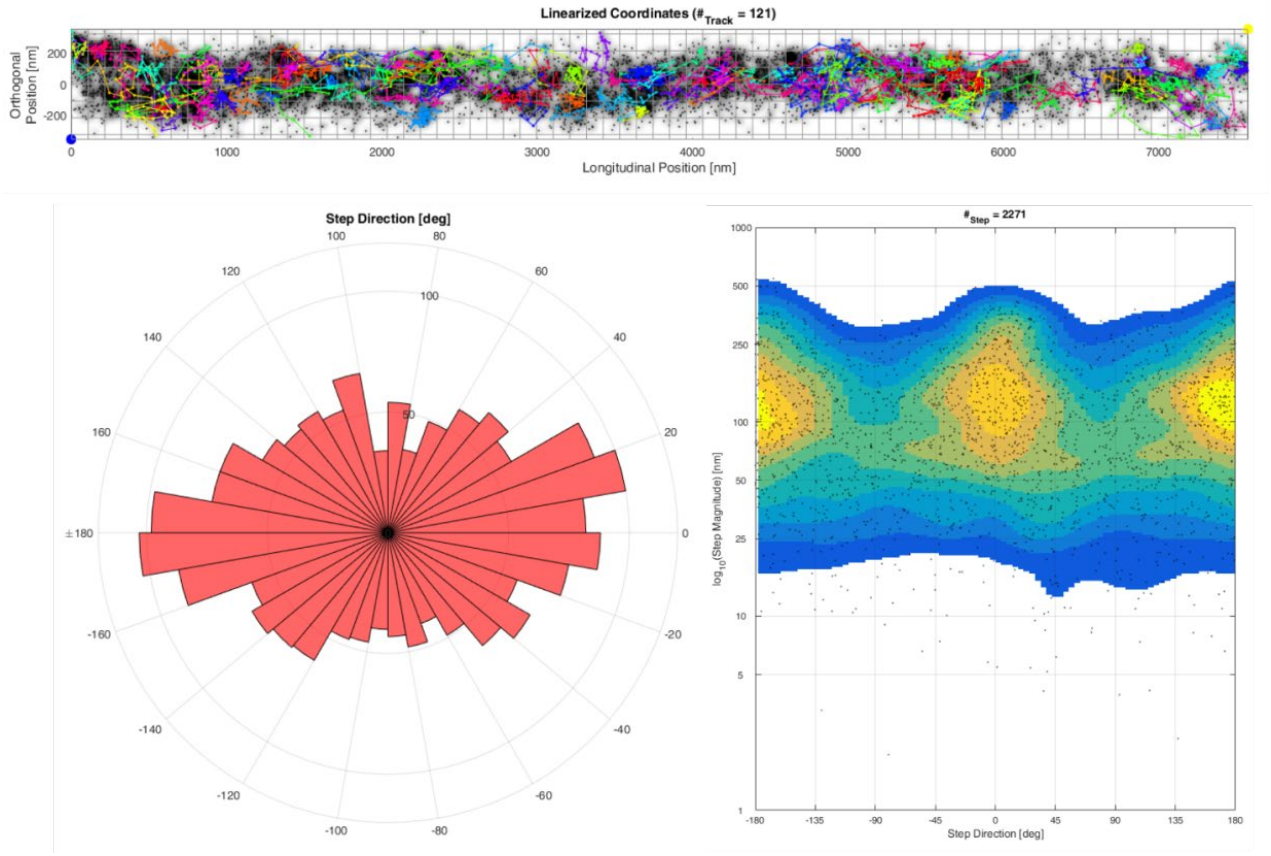

Figure **37**A). The majority of them is oriented along the longitudinal axis (

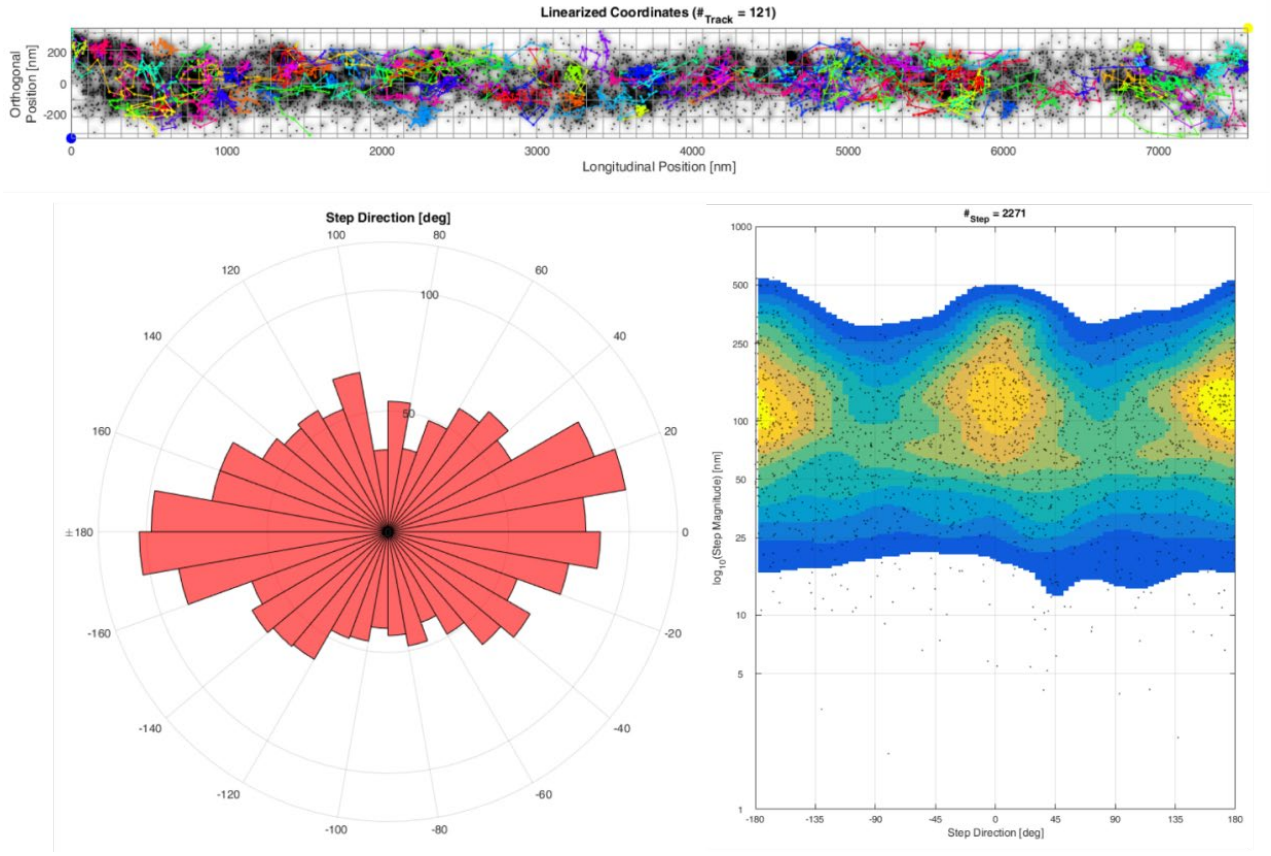

Figure **37**B, C). The pie chart diagram in

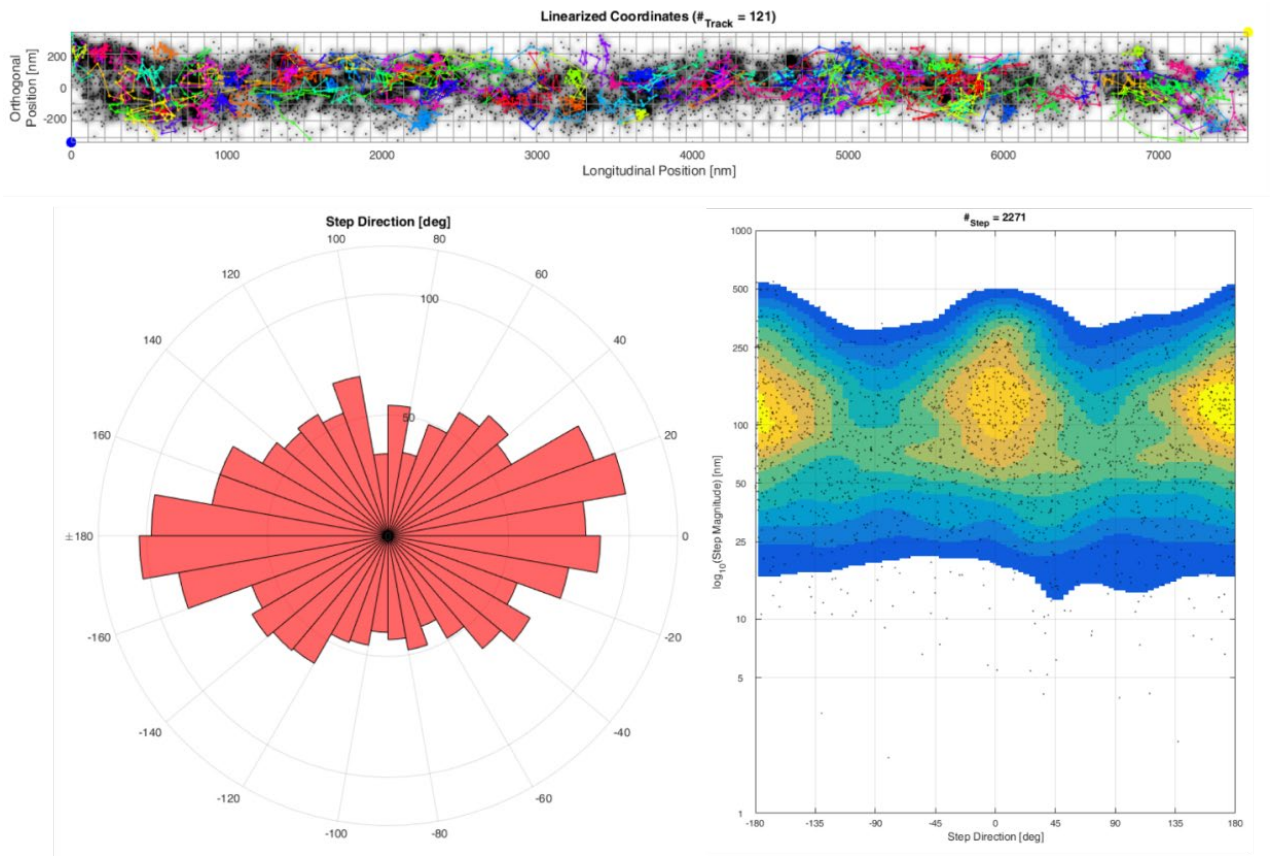

Figure **37**B illustrates the dominant longitudinal movement of CV-SUγ in starvation of the analyzed mitochondrion. Here, the amount of longitudinal directions between -20° to 30° and between -160° to 170° is twice as large as the number perpendicular oriented trajectories. Additionlly, the heatmap in

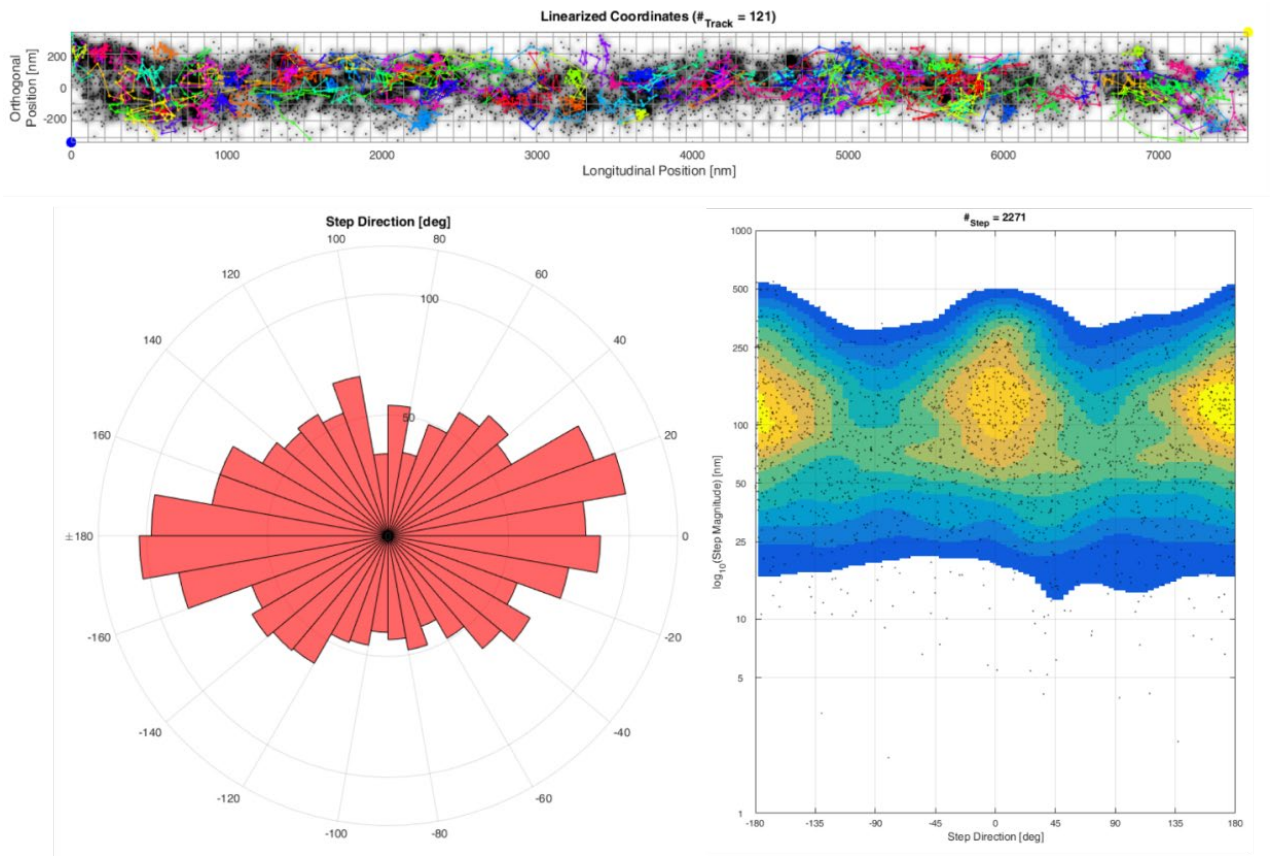

Figure **37**C shows that steps along the longitudinal axis can reach a larger jumpsize than steps in the perpendicular direction. However, this may be influenced by the 3D morphology of mitochondria. Here, jumpsizes in the perpendicular direction can be scaled down stronger than jumpsizes along the longitudinal direction. The trajectory directionality in starvation was compared to the trajectory directionality in control experiments (Figure 38). In the case of the control, 10784 binned steps were taken into account (Figure 38A, C). The analysis of trajectory directionality during starvation was performed on 59743 binned steps (Figure 38B, D).

Table 4 Jumpsize of CV-SUγ in control experiments and during starvation

Protein	Number of steps	Median jumpsize	Maximal. jumpsize	Minimal. jumpsize
CV-SUγ control	20124	96.94 nm	1117 nm	0.58 nm
CV-SUγ starvation	7491	175.70 nm	1211 nm	1.79 nm

Figure 36B a color code already shows that slow mobile (CV-SUγ in the control and under starving conditions directly differentiate, obviuosly in their directionality (**Fehler! Ungültiger Eigenverweis auf Textmarke.**B, D). This indicates either a shift of a longitudinal orientation of cristae or a shift of CV-SUγ into the IBM or even a lost ofcristae. The transition of CV-SUγ into the IBM can result from avoided diffusion in the CM and a dominant diffusion in the IBM or by a reduction of the CM. In order to analyze the directionality of mobility and to quantify for this, the directionality of trajectories was analyzed with MitoOrientedDynamics. Here, the4-step binning procedure was used. As described, the longitudinal axis of each mitochondria was marked, which was used to interpolate it to a straight mitochondrion and the angle of binned steps to the longitudinal axis was measured. Shown in

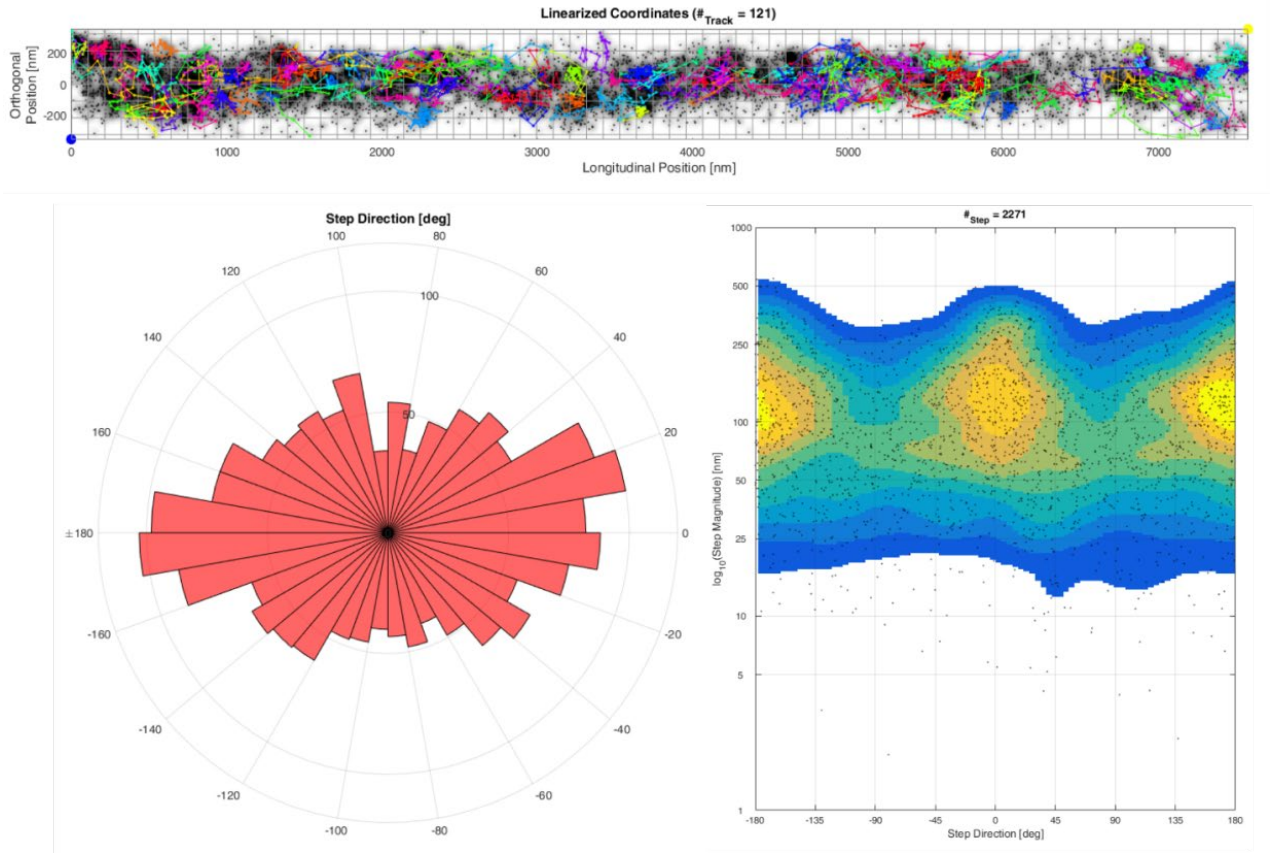

Figure **37** is an example of a straightened mitochondrion in starving conditions and its analysis of the trajectory directionality. In the shown mitochondrion the directionalities of 121 individual trajectories were analyzed (

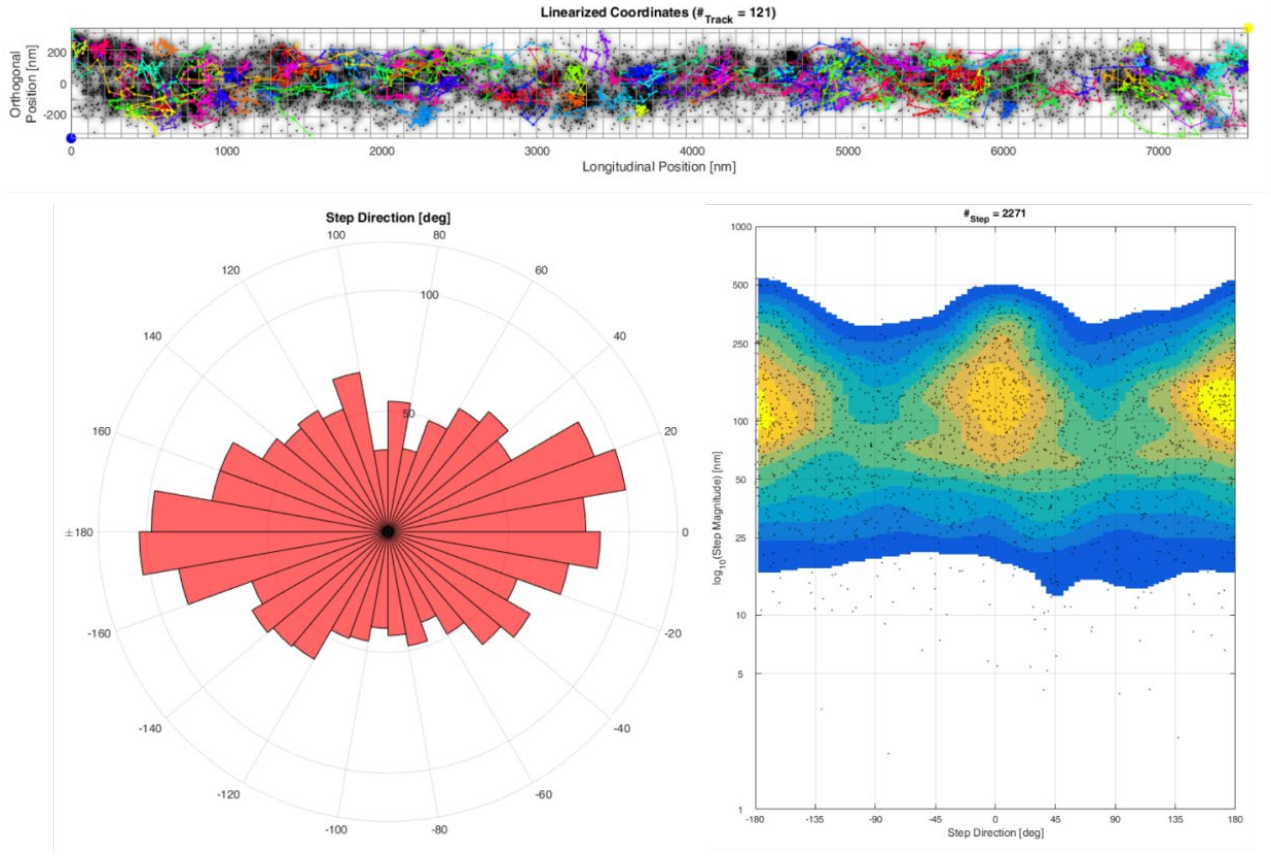

Figure **37**A). The majority of them is oriented along the longitudinal axis (

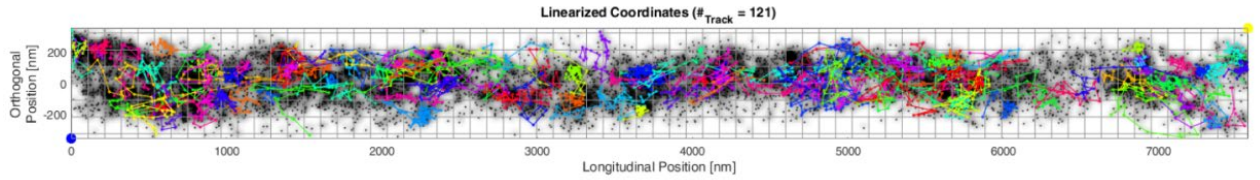

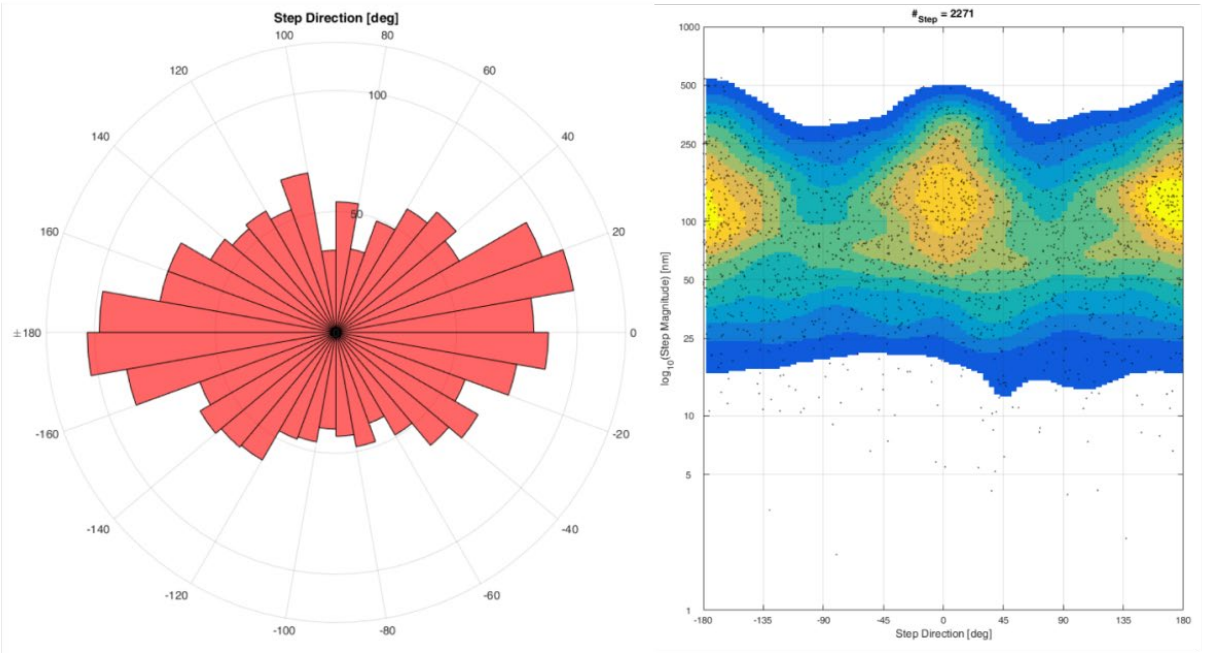

Figure **37**B, C). The pie chart diagram in

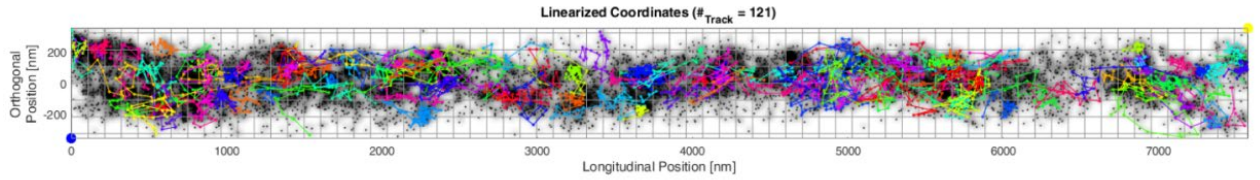

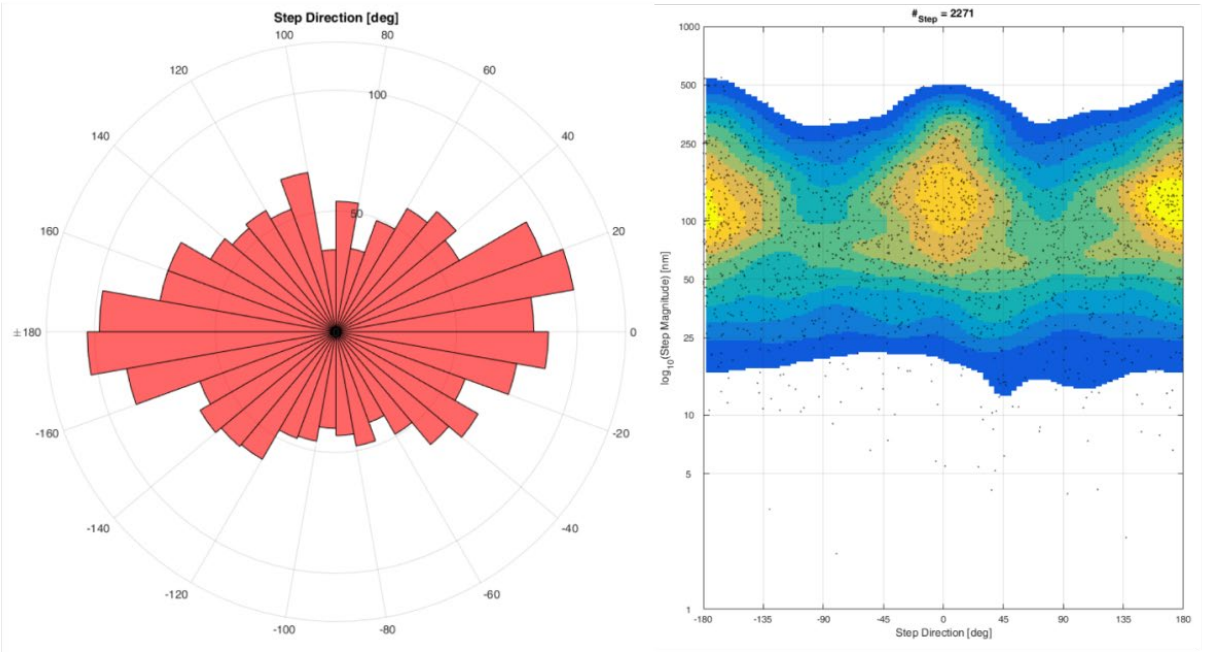

Figure **37**B illustrates the dominant longitudinal movement of CV-SUγ in starvation of the analyzed mitochondrion. Here, the amount of longitudinal directions between -20° to 30° and between -160° to 170° is twice as large as the number perpendicular oriented trajectories. Additionlly, the heatmap in

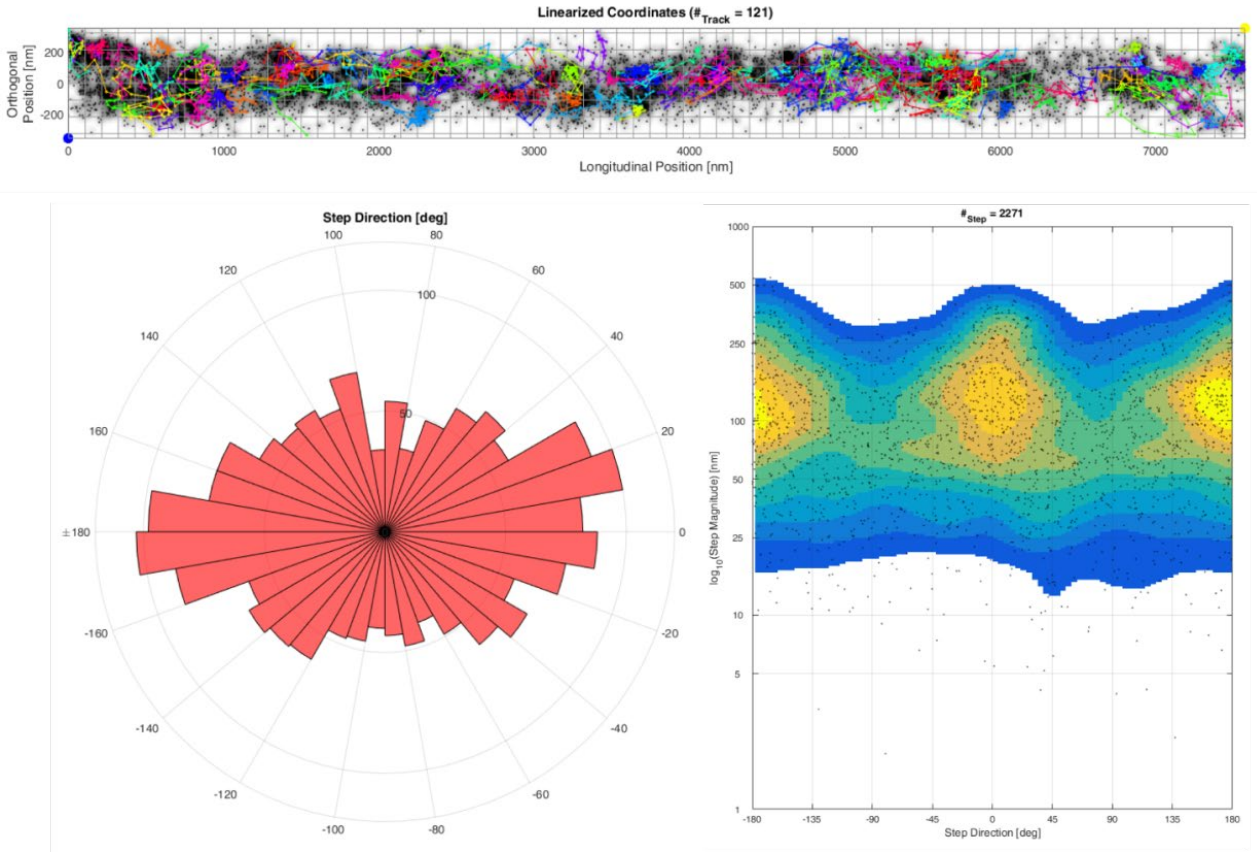

Figure **37**C shows that steps along the longitudinal axis can reach a larger jumpsize than steps in the perpendicular direction. However, this may be influenced by the 3D morphology of mitochondria. Here, jumpsizes in the perpendicular direction can be scaled down stronger than jumpsizes along the longitudinal direction. The trajectory directionality in starvation was compared to the trajectory directionality in control experiments (Figure 38). In the case of the control, 10784 binned steps were taken into account (Figure 38A, C). The analysis of trajectory directionality during starvation was performed on 59743 binned steps (Figure 38B, D).

Table 4 Jumpsize of CV-SUγ in control experiments and during starvation

Protein	Number of steps	Median jumpsize	Maximal. jumpsize	Minimal. jumpsize
CV-SUγ control	20124	96.94 nm	1117 nm	0.58 nm
CV-SUγ starvation	7491	175.70 nm	1211 nm	1.79 nm

Figure 36B, orange trajectories) and confined mobility (CV-SUγ in the control and under starving conditions directly differentiate, obviuosly in their directionality (**Fehler! Ungültiger Eigenverweis auf Textmarke.**B, D). This indicates either a shift of a longitudinal orientation of cristae or a shift of CV-SUγ into the IBM or even a lost ofcristae. The transition of CV-SUγ into the IBM can result from avoided diffusion in the CM and a dominant diffusion in the IBM or by a reduction of the CM. In order to analyze the directionality of mobility and to quantify for this, the

directionality of trajectories was analyzed with MitoOrientedDynamics. Here, the4-step binning procedure was used. As described, the longitudinal axis of each mitochondria was marked, which was used to interpolate it to a straight mitochondrion and the angle of binned steps to the longitudinal axis was measured. Shown in

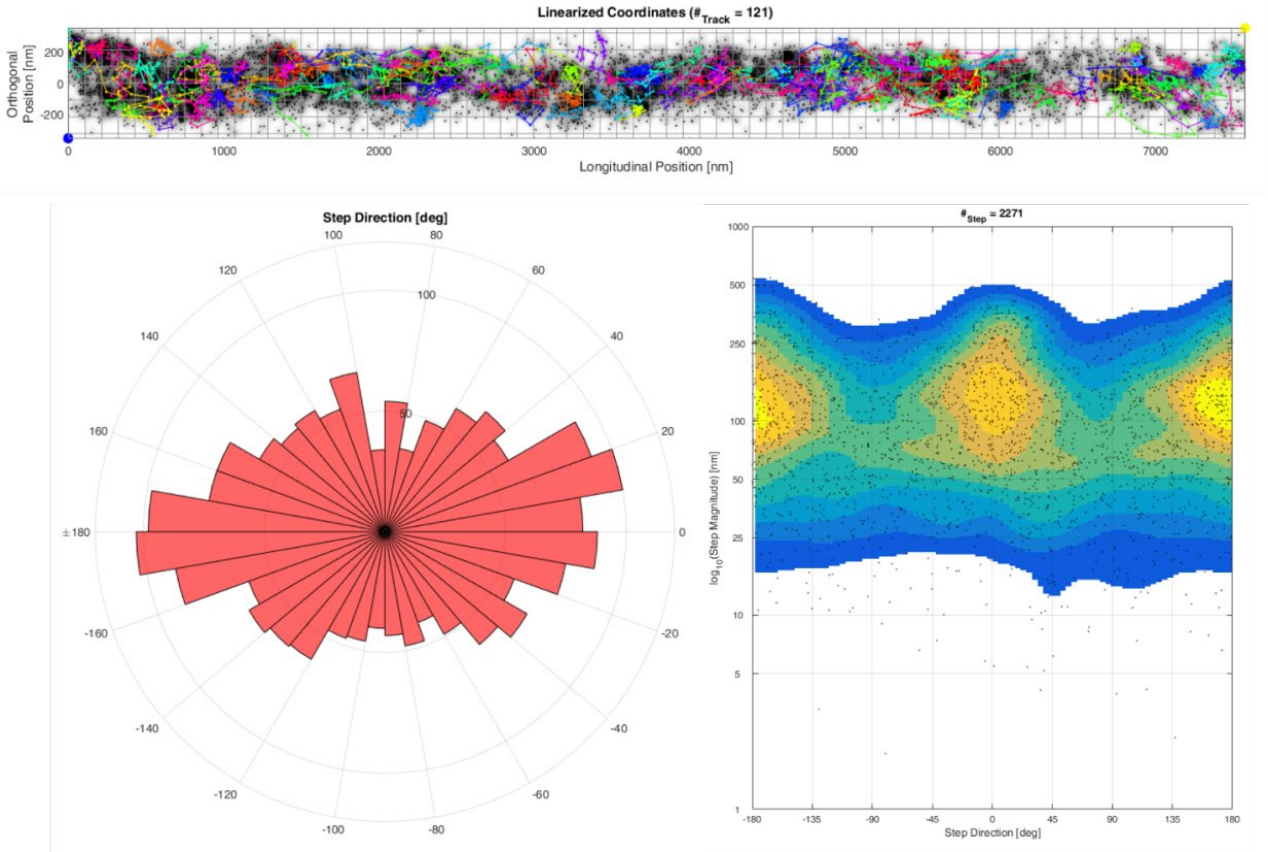

Figure **37** is an example of a straightened mitochondrion in starving conditions and its analysis of the trajectory directionality. In the shown mitochondrion the directionalities of 121 individual trajectories were analyzed (

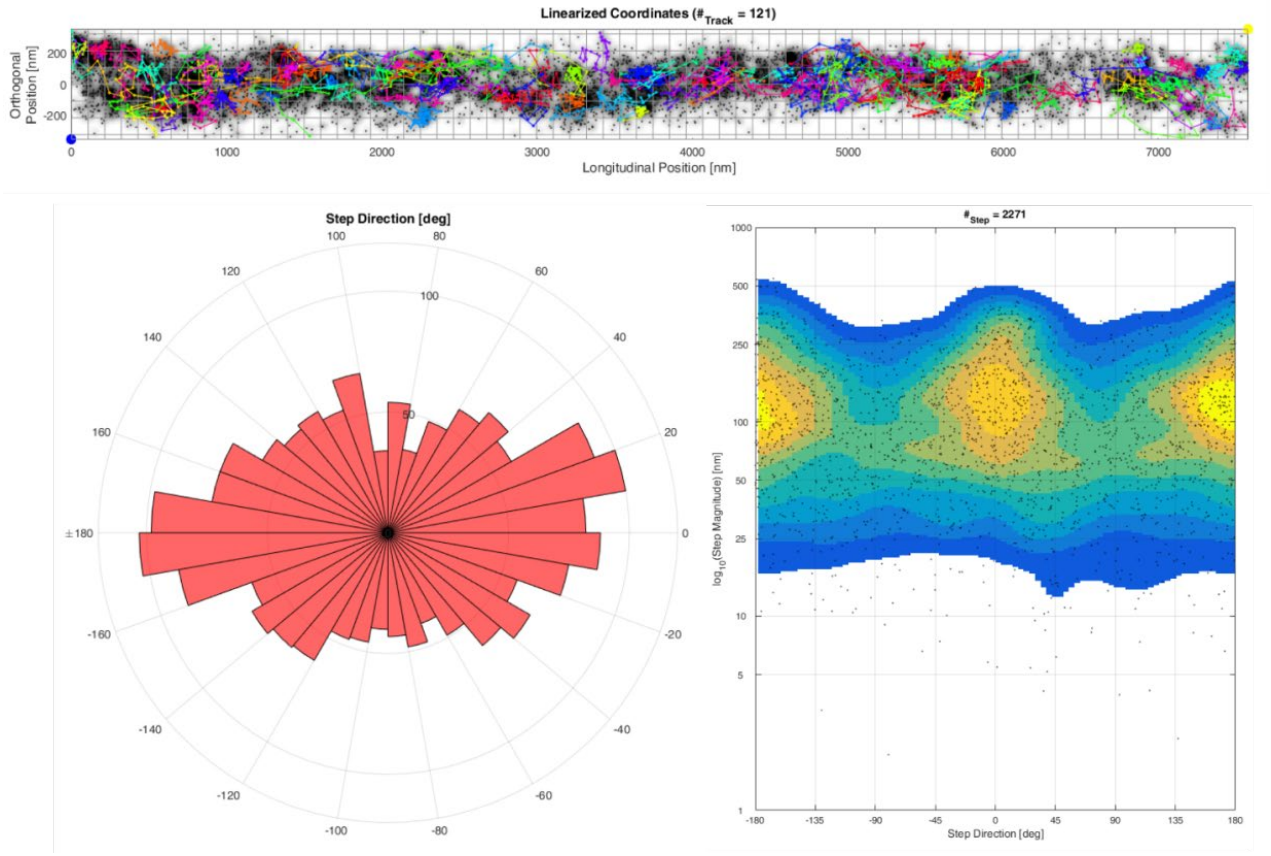

Figure **37**A). The majority of them is oriented along the longitudinal axis (

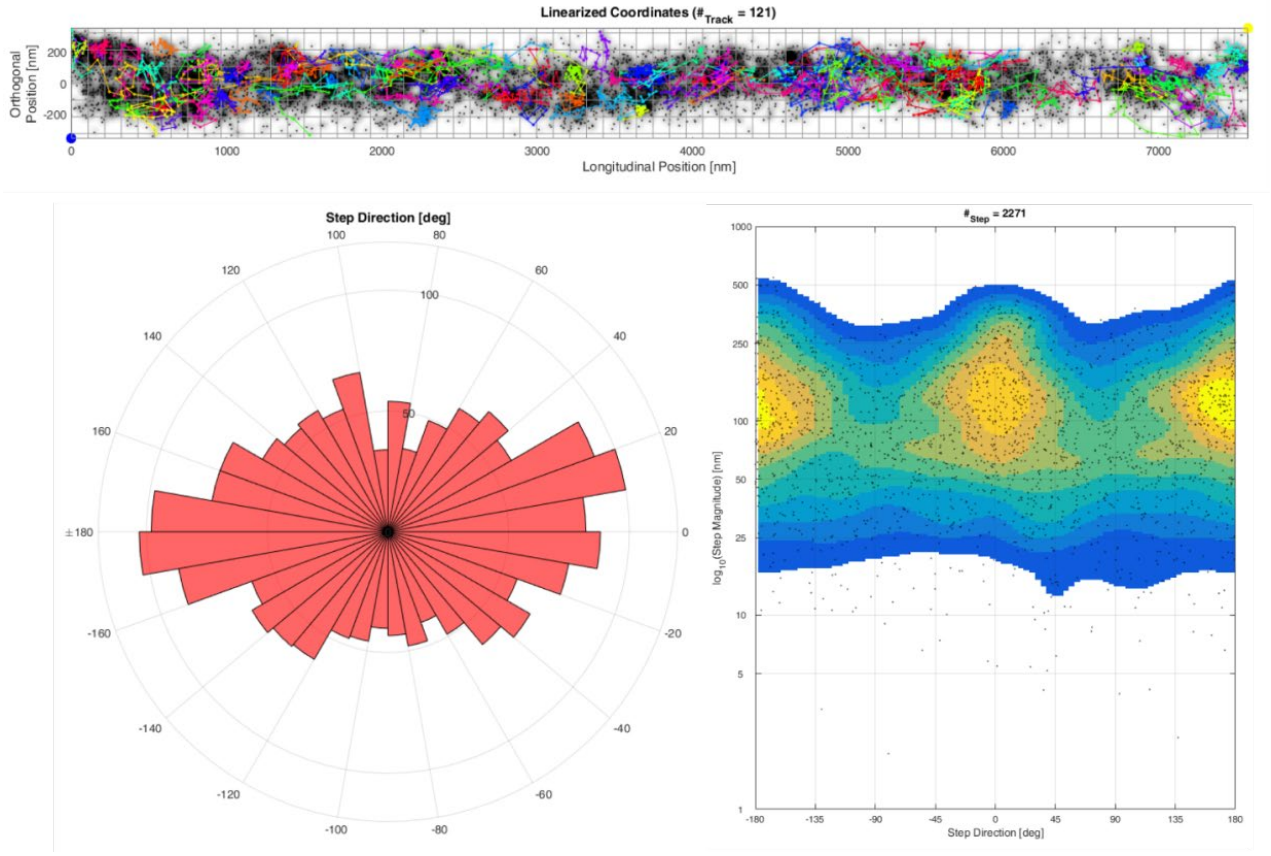

Figure **37**B, C). The pie chart diagram in

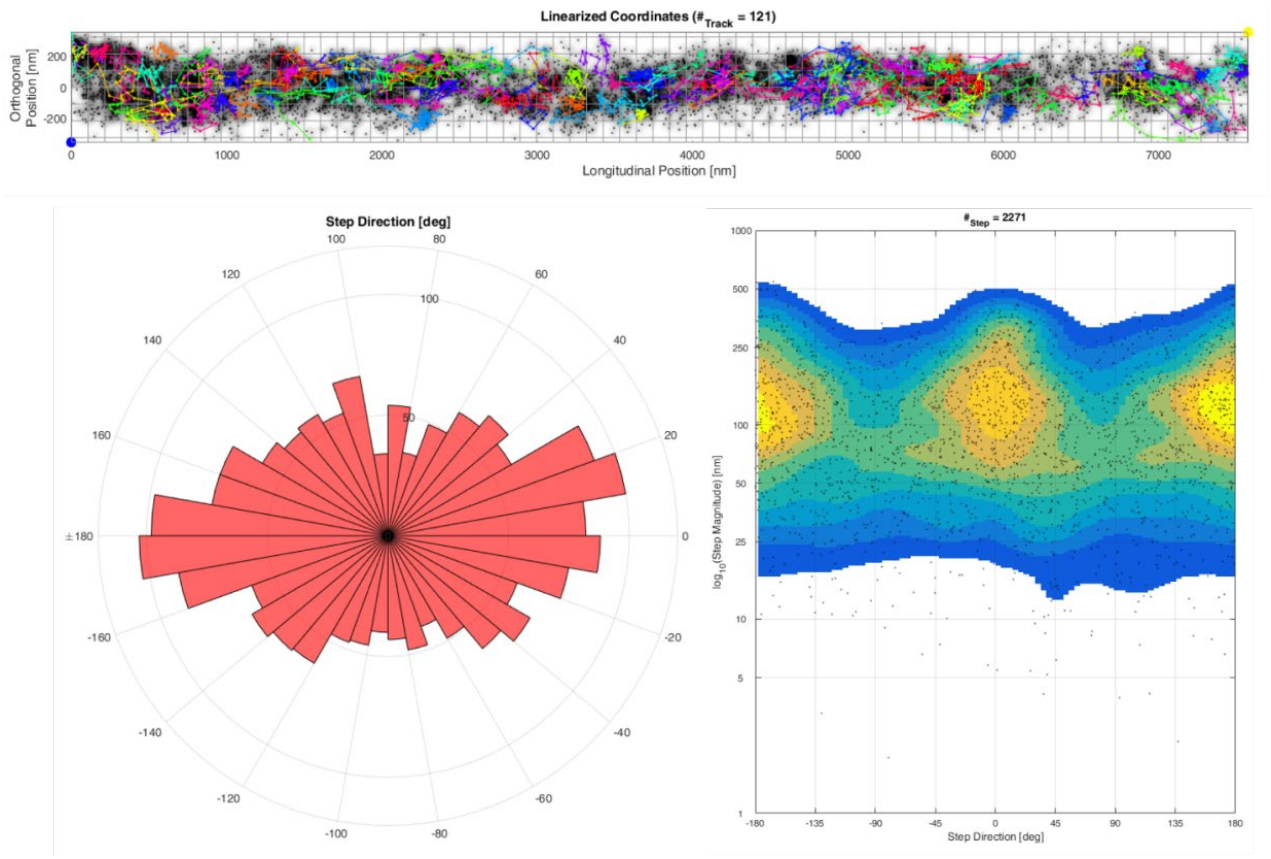

Figure **37**B illustrates the dominant longitudinal movement of CV-SUγ in starvation of the analyzed mitochondrion. Here, the amount of longitudinal directions between -20° to 30° and between -160° to 170° is twice as large as the number perpendicular oriented trajectories. Additionlly, the heatmap in

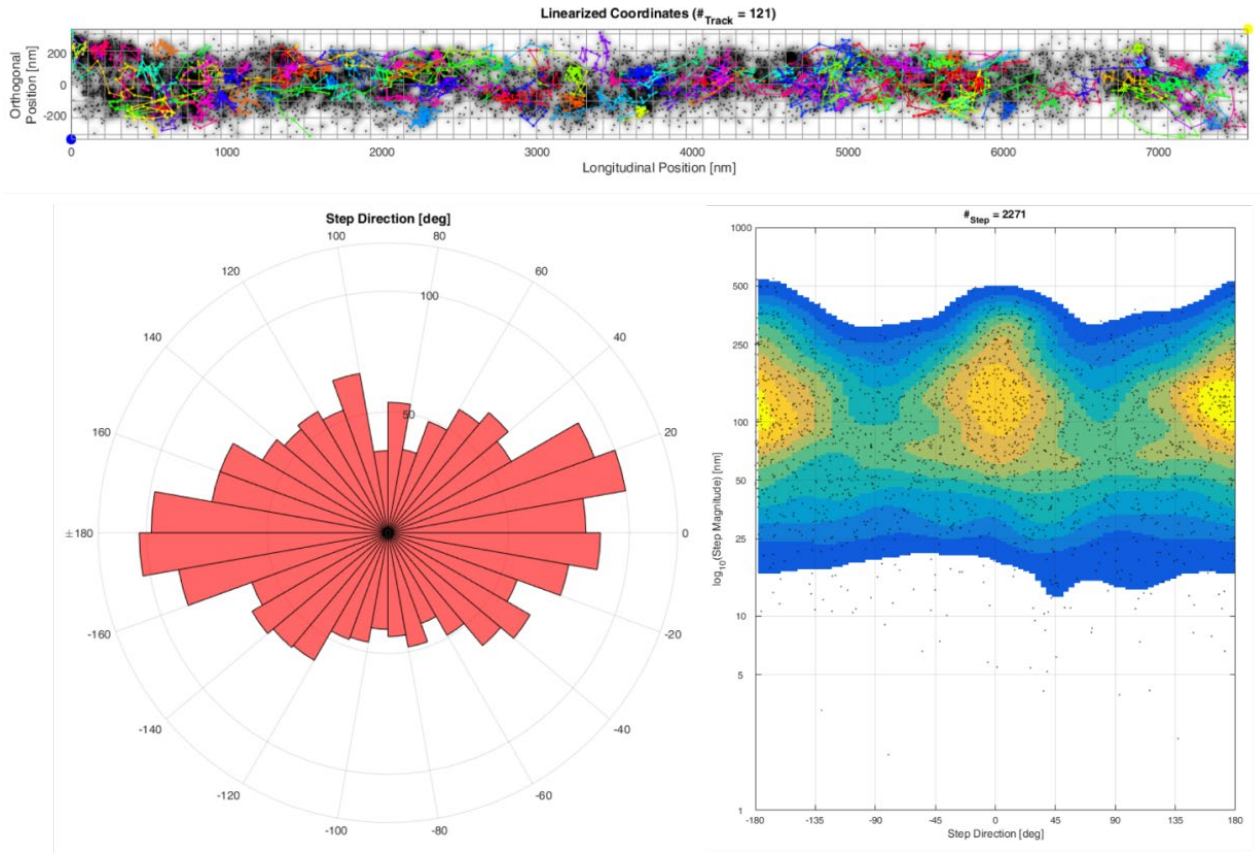

Figure **37**C shows that steps along the longitudinal axis can reach a larger jumpsize than steps in the perpendicular direction. However, this may be influenced by the 3D morphology of mitochondria. Here, jumpsizes in the perpendicular direction can be scaled down stronger than jumpsizes along the longitudinal direction. The trajectory directionality in starvation was compared to the trajectory directionality in control experiments (Figure 38). In the case of the control, 10784 binned steps were taken into account (Figure 38A, C). The analysis of trajectory directionality during starvation was performed on 59743 binned steps (Figure 38B, D).

Table 4 Jumpsize of CV-SUγ in control experiments and during starvation

Protein	Number of steps	Median jumpsize	Maximal. jumpsize	Minimal. jumpsize
CV-SUγ control	20124	96.94 nm	1117 nm	0.58 nm
CV-SUγ starvation	7491	175.70 nm	1211 nm	1.79 nm

Figure 36B, dark blue trajectories) rather show a tendency sticking to the CM. In contrast to this, trajectories of the mobile fraction were interpreted as trajectories in the IBM as mostly none of them showed a perpendicular directionality. This was not observed during starvation. In CV-SUγ in the control and under starving conditions directly differentiate, obviuosly in their directionality (**Fehler! Ungültiger Eigenverweis auf Textmarke.**B, D). This indicates either a shift of a longitudinal orientation of cristae or a shift of CV-SUγ into the IBM or even a lost ofcristae. The transition of CV-SUγ into the IBM can result from avoided diffusion in the CM and a dominant diffusion in the IBM or by a reduction of the CM. In order to analyze the directionality of mobility and to quantify for this, the directionality of trajectories was analyzed with MitoOrientedDynamics. Here, the4-step binning procedure was

used. As described, the longitudinal axis of each mitochondria was marked, which was used to interpolate it to a straight mitochondrion and the angle of binned steps to the longitudinal axis was measured. Shown in

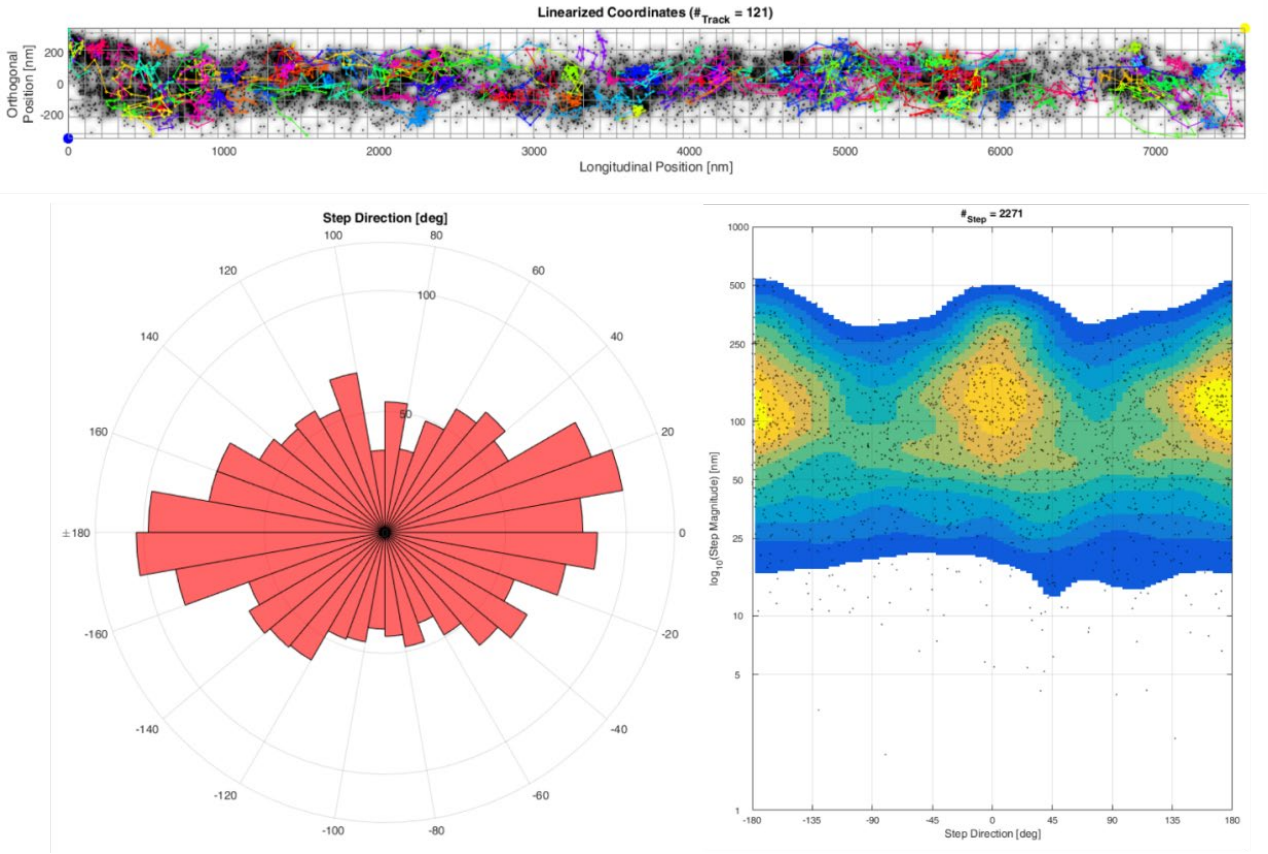

Figure **37** is an example of a straightened mitochondrion in starving conditions and its analysis of the trajectory directionality. In the shown mitochondrion the directionalities of 121 individual trajectories were analyzed (

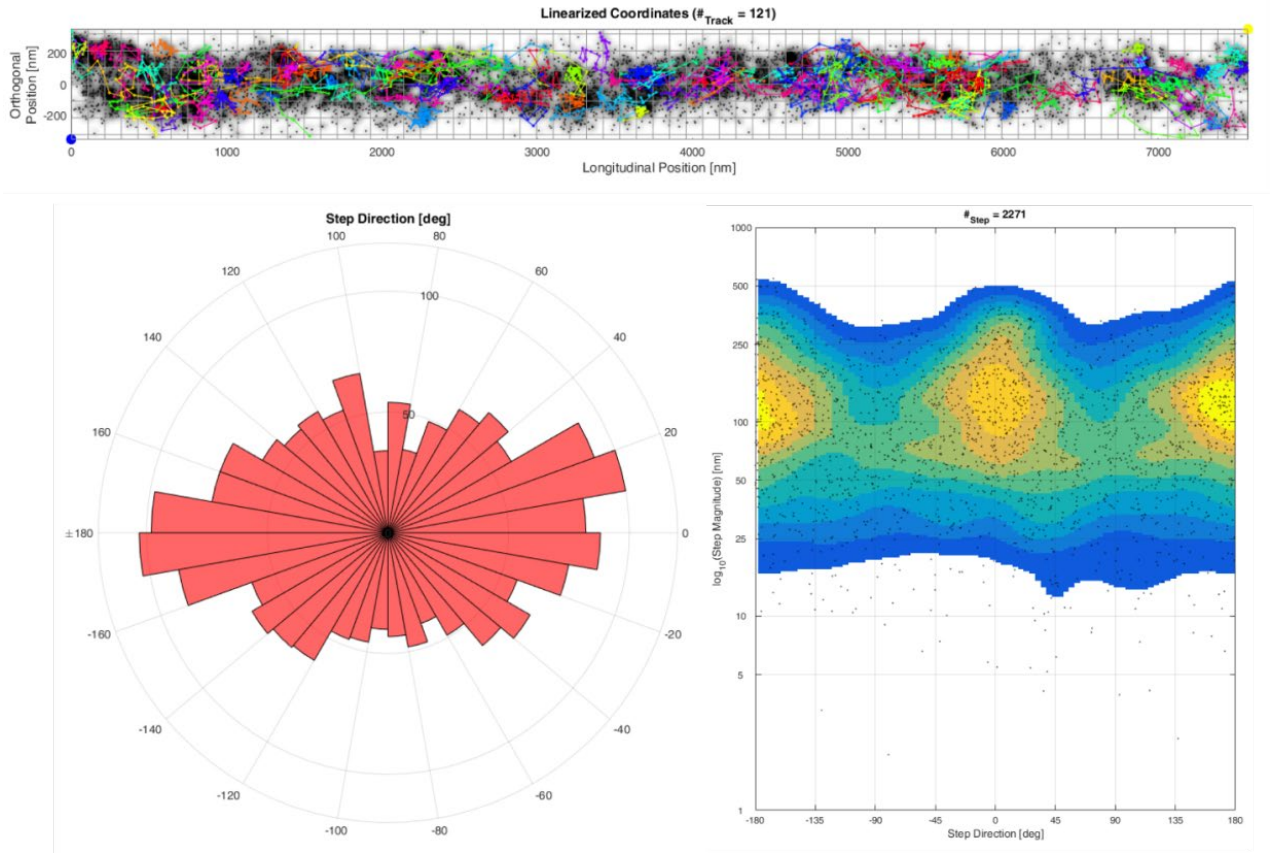

Figure **37**A). The majority of them is oriented along the longitudinal axis (

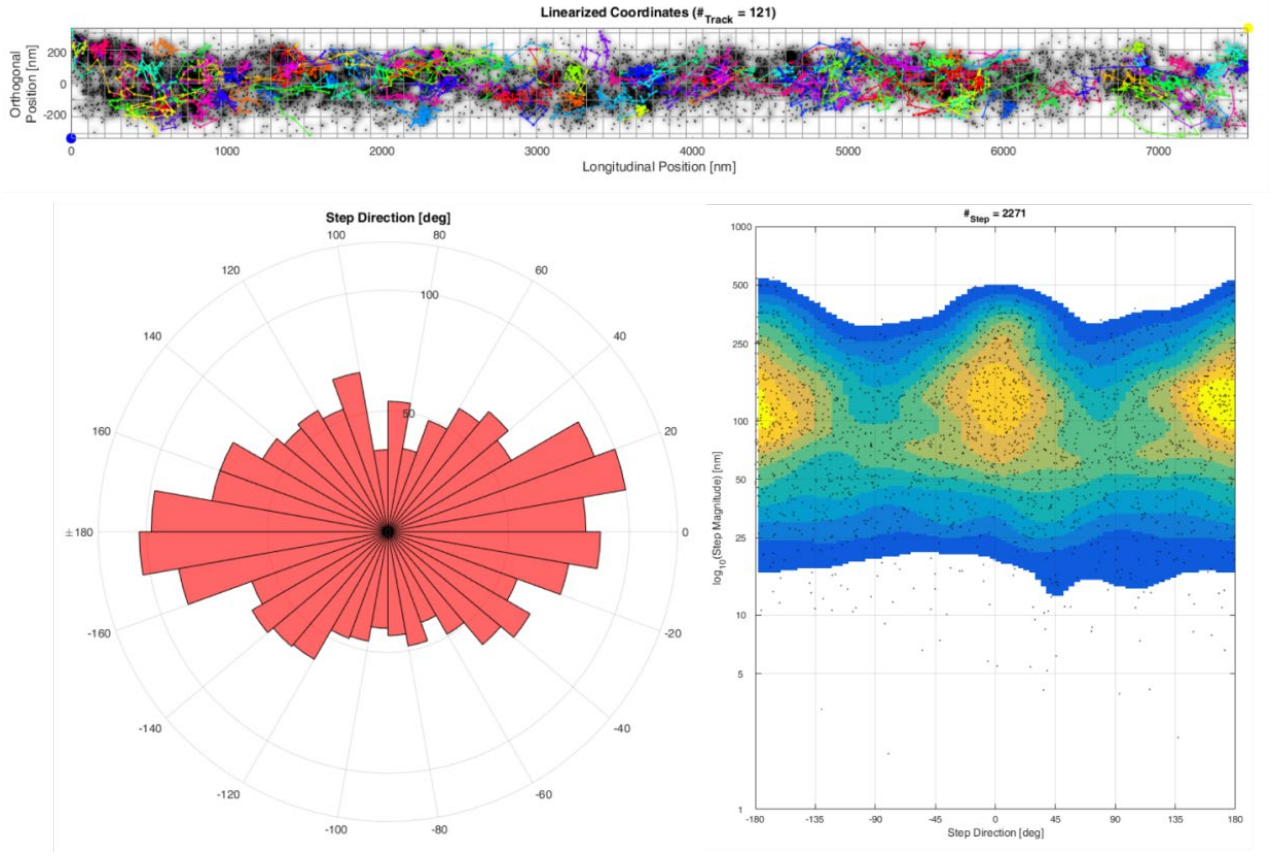

Figure **37**B, C). The pie chart diagram in

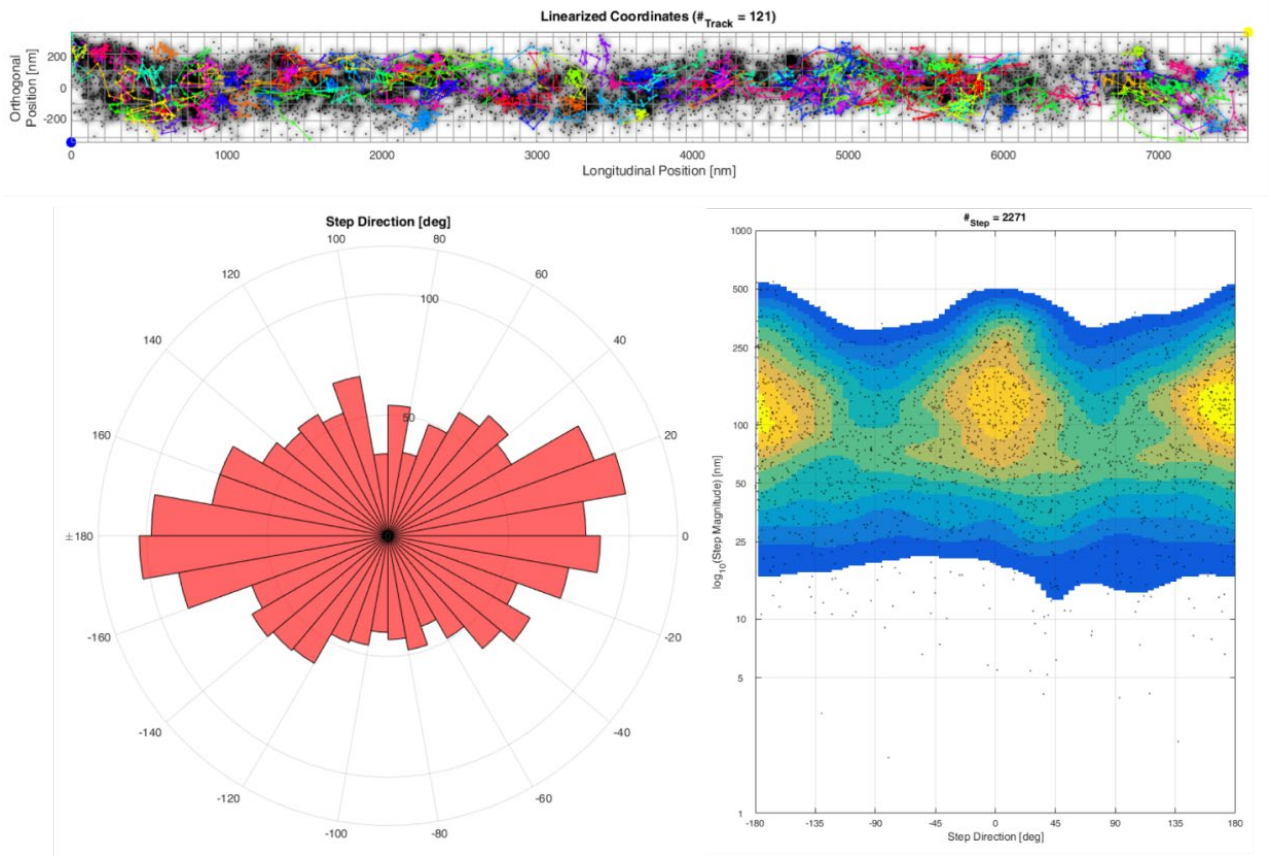

Figure **37**B illustrates the dominant longitudinal movement of CV-SUγ in starvation of the analyzed mitochondrion. Here, the amount of longitudinal directions between -20° to 30° and between -160° to 170° is twice as large as the number perpendicular oriented trajectories. Additionlly, the heatmap in

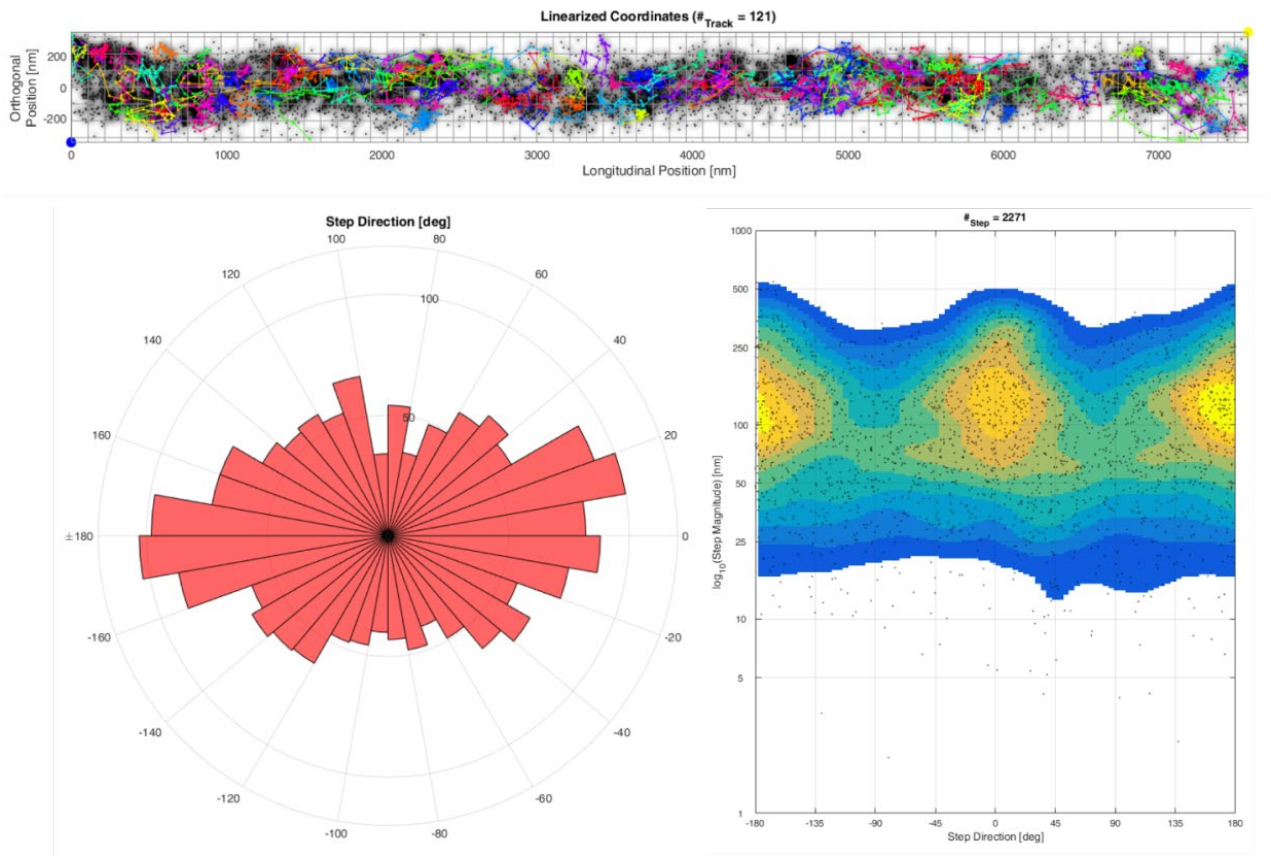

Figure **37**C shows that steps along the longitudinal axis can reach a larger jumpsize than steps in the perpendicular direction. However, this may be influenced by the 3D morphology of mitochondria. Here, jumpsizes in the perpendicular direction can be scaled down stronger than jumpsizes along the longitudinal direction. The trajectory directionality in starvation was compared to the trajectory directionality in control experiments (Figure 38). In the case of the control, 10784 binned steps were taken into account (Figure 38A, C). The analysis of trajectory directionality during starvation was performed on 59743 binned steps (Figure 38B, D).

Table 4 Jumpsize of CV-SUγ in control experiments and during starvation

Protein	Number of steps	Median jumpsize	Maximal. jumpsize	Minimal. jumpsize
CV-SUγ control	20124	96.94 nm	1117 nm	0.58 nm
CV-SUγ starvation	7491	175.70 nm	1211 nm	1.79 nm

Figure 36D no trajectory at all showed a perpendicular movement. The D_{app} of CV-SUγ were measured in both conditions. The D_{app} was fitted by three subpopulations and their D_{app} was compared (Figure 39). The D_{app} of the mobile fraction increased significantly by a factor of 1.48, from 0.079 ± 0.009 µm²/s in the control to 0.117 ± 0.0035 µm²/s in starvation (Figure 39,

Table 5). Similar to this, the D_{app} of the slow mobile fraction increased significantly by a factor of 1.8, from 0.02 ± 0.006 µm²/s to 0.035 ± 0.002 µm²/s. If cells starved for longer than two hours in PBS the mobility of these two sub-

Protein and condition	D_{app} mobile [µm²/s]	relativ amount [%]	D_{app} slow mobile [µm²/s]	relativ amount [%]	D_{app} confined mobile [µm²/s]	relativ amount [%]
CV-SUγ control (N = 63)	0.079 ± 0.009	35 ± 5	0.020 ± 0.006	47.0 ± 3	0.005 ± 0.002	18 ± 3
CV-SUγ starvation (N = 45)	0.117 ± 0.032	31 ± 2	0.036 ± 0.001	47 ± 2	0.010 ± 0.001	22 ± 3
Tom20 control (N = 11)	0.168 ± 0.043	43 ± 5	0.046 ± 0.007	47 ± 7	0.006 ± 0.000	10 ± 3

fractions increased even stronger (Figure 39). The D_{app} of the confined mobile fraction did not increased significantly in any kind of condition. As a reference the D_{app} of the slow mobile and mobile fraction of Tom20 as a protein of the OM are shown (Figure 39,

Table 5). The mobile fraction here showed a D_{app} of 0.168 ± 0.0043 µm²/s, which is significantly higher than CV-SUγ in the control and in starving conditions. The slow mobile fraction of Tom20 shows a D_{app} of 0.046 ± 0.007 µm²/s.

Protein and condition	D_{app} mobile [µm²/s]	relativ amount [%]	D_{app} slow mobile [µm²/s]	relativ amount [%]	D_{app} confined mobile [µm²/s]	relativ amount [%]
CV-SUγ control (N = 63)	0.079 ± 0.009	35 ± 5	0.020 ± 0.006	47.0 ± 3	0.005 ± 0.002	18 ± 3
CV-SUγ starvation (N = 45)	0.117 ± 0.032	31 ± 2	0.036 ± 0.001	47 ± 2	0.010 ± 0.001	22 ± 3
Tom20 control (N = 11)	0.168 ± 0.043	43 ± 5	0.046 ± 0.007	47 ± 7	0.006 ± 0.000	10 ± 3

There was still a significant difference between this value and the D_{app} of the slow mobile subpopulation of CV-SUγ. Starvation over 20 h led to an equal D_{app} of the slow mobile fraction of CV-SUγ compared to Tom20. The confined mobile fraction showed a similar D_{app} in all conditions and of all proteins tracked.

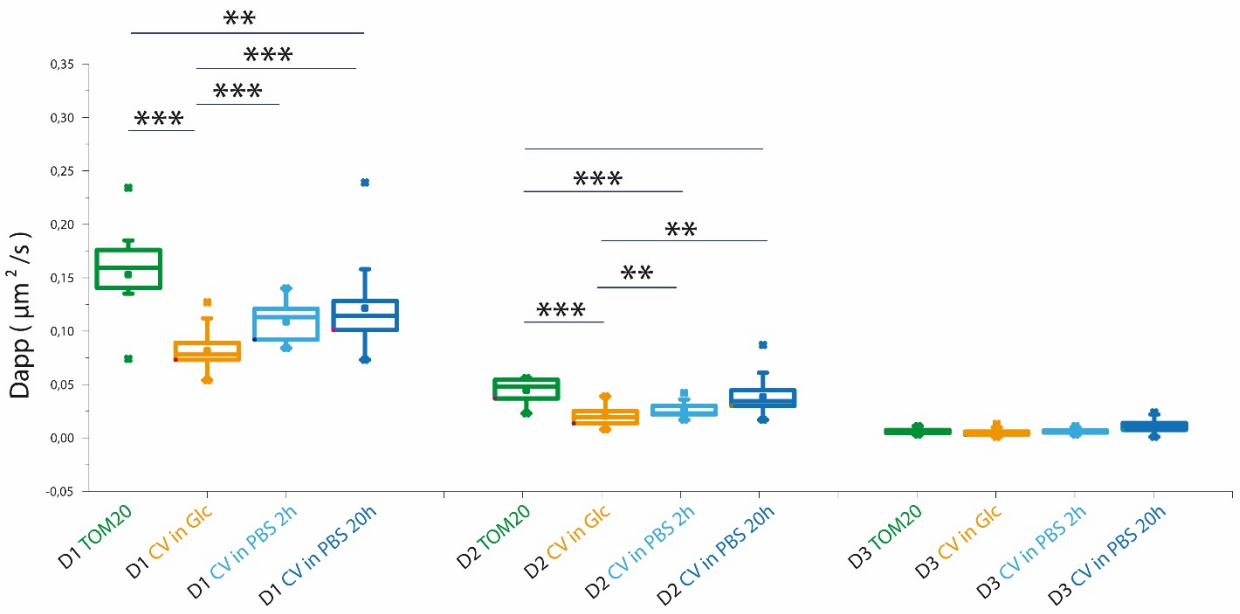

Figure 39 Subfraction fit of the apparent diffusion of F_1F_O ATP synthase subunit-γ in cells in the control and during starvation conditions

The tracked mobility of single proteins allows subfractioning into 3 subpopulations. The mobile fraction (D1) of CV-SUγ proteins speeds up to 0.117 ± 0.0035 µm²/s in mean. Also, the slow mobile fraction (D2) increaseed its mobility. Confined mobility (D3) remained unchanged. Significance levels were determined by a one-way ANOVA: P ≤ 0.01 denoted with **; P ≤ 0.001 denoted with ***.

Table 5 Sub-fractions diffusion coefficients of Tom20, CV-SUγ and CV-SUγ in 2 hours of starvation shown in Figure 39
Datasets of CV-SUγ proteins in control, after 2 hours of starvation and as a reference Tom20 proteins in control conditions. The percentage of the three sub-fraction mobile, slow mobile and confined mobile stayed similar. However, the D_{app} of the mobile and slow mobile fraction show a significant increase. N = number of cells in 3 independent assays

Protein and condition	D_{app} mobile [µm²/s]	relativ amount [%]	D_{app} slow mobile [µm²/s]	relativ amount [%]	D_{app} confined mobile [µm²/s]	relativ amount [%]
CV-SUγ control (N = 63)	0.079 ± 0.009	35 ± 5	0.020 ± 0.006	47.0 ± 3	0.005 ± 0.002	18 ± 3
CV-SUγ starvation (N = 45)	0.117 ± 0.032	31 ± 2	0.036 ± 0.001	47 ± 2	0.010 ± 0.001	22 ± 3
Tom20 control (N = 11)	0.168 ± 0.043	43 ± 5	0.046 ± 0.007	47 ± 7	0.006 ± 0.000	10 ± 3

9.3 Dual-color TALM of mitochondrial membrane proteins

Functional proteins are interacting with their reaction partners. In order to study the interplay of two or more proteins in a living cell dual-color microscopy can be used. Dual-color microscopy can also be used to reveal if two proteins belong to the same microcompartment e.g. dendritic spins, mitochondrial subcompartments or cytosolic vesicles. Furthermore, performing dual-color TIRF microscopy allows to localize each protein seperatly and colocalization analysis can be carried out. Co-localization of proteins allows to study a functional relation of two or more proteins on single molecule level. Co-localization analysis is the backbone for co-locomotion studies. Here, true protein-prrotein interaction can be studied over time.
In order to investigate the spatiotemporal organization and dynamic of two mitochondrial proteins at the same time dual-color TALM was conducted. However, in order to correlate SML and SPT tracking data in living cells simultaneously recording of both POIs is needed, like in dual-color TALM (Wilmes et al., 2015). Furthermore, performing dual-color single molecule microscopy requires a pair of fluorescent probes with well separated emission spectra. As a matter of fact, dual-color TALM with substoichiometric, posttranslational labeling of mitochondrial proteins requires two membrane permeable dyes. HeLa cells stably expressing with CV-SUγ:HaloTag were transfected with the plasmid encoding for the POI, which was genetically fused to the fSnapTag. However, transient transfection leads to different amounts of plasmid in the cells and thereby to different expression levels of the POI. As mentioned previously, the two different tags have different binding kinetics to their ligands. Therefore, the best labeling concentration had to be determined and the labeling degree needed to be adapted to each experiment. In the case of dual-color TALM of mitochondrial proteins only combinations of several dyes fulfill the mentioned criteria. In this study SiR^{HTL} and TMR^{star} were used.

9.3.1 Adaptation of labeling concentrations in dual-color experiments

In Dual-Color experiments with substoichiometric, posttranslational labeling, the labeling degree of the used tags was in the range of single molecules and equal. By this no pre-imaging bleaching needed to be done and a similar amount of single particle localizations and trajectories was expected. This sets the base line for reliable statistics when comparing both channels. However, the used dyes SiR^{HTL} and TMR^{star} have different binding affinities to their tags (Beinlich et al., 2015) (Figure 40, Figure 41). In order to compensate for this and to achieve a similar labeling degree, different final labeling concentrations were used (Figure 41). Furthermore, in previous experiments it turned out that SiR^{HTL} was sensitive for illumination with 561 nm, and with 488 nm (data not shown). Thus, in dual-color experiments, illumination of sample with 561 nm and 642 nm caused a stronger bleaching of SIR (data not shown). Beside this, it is important to note that TMR^{star} was used to label the transiently transfected POI fused to the fSnapTag. Thus, a different concentration of fSnapTags in each experiment was used for labelling inside the transfected cells. Taken together the finally used SiR^{HTL} / TMR^{star} ratio was between 0.0667 and 0.6667.

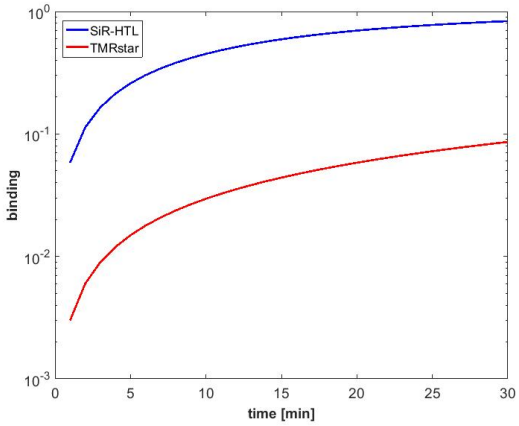

Figure 40 Calculated binding for HaloTag and fSnapTag dyes with the same labeling concentration
The HaloTag can be labeled more efficiently with SiR^{HTL} (blue) due to the higher binding affinity of the HaloTag to its ligand. In contrast to binding of TMR^{star} (red) via the fSnapTag ligand to the fSnapTag.

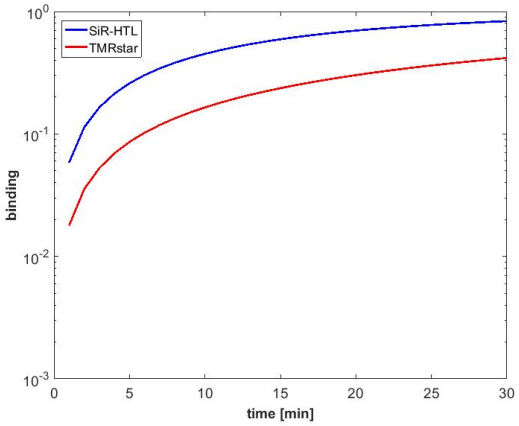

Figure 41 Calculated binding for HaloTag and SnapTag dyes labeling concentration of a ratio 1/15
Binding of SiR^{HTL} (blue) to the HaloTag versus binding of TMR^{star} to the fSnapTag (red). Higher labeling concentrations of the SnapTag ligand can compensate the lower affinity.

9.3.2 Dual-color TALM of Tom20:HaloTag:fSnapTag

In order to investigate if dual-color TALM using posttranslational, substoichimetric labeling with SiR^{HTL} and TMR^{star} can be used for colocalization and co-locomotion anaylsis, the fusion protein Tom20:HaloTag:fSnapTag was labeled with SiR^{HTL} and TMR^{star}. The used labeling concentrations were 15 nM SiR^{HTL} and 30 nM TMR^{star} as well as 1 nM SiR^{HTL} and 15 nM TMR^{star}. The high labeling concentrations were used in order to compensate the different binding affinities of the HaloTag and the fSnapTag and to increase the chance for colocalization and co-locomotion events. In total 353593 signals for SiR^{HTL} were localized. The mean calculated localization precision of SiR^{HTL} was 17.69 ± 3.51 nm. In the case of TMR^{star} 572770 signals were localized. The mean localization precision of TMR^{star} was 15.56 ± 3.42 nm (Figure 42).

Dual-Color TALM of Tom20 revealed the typical accumulations of localizations for an OM-protein (Figure 43A, B).

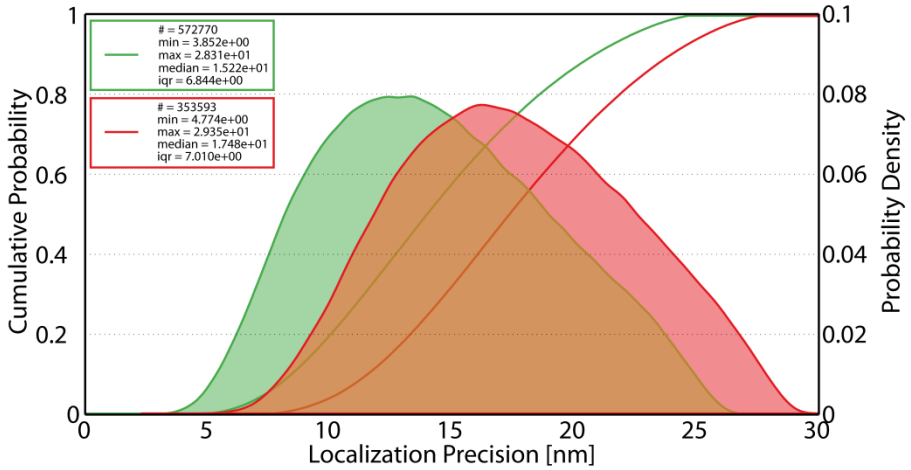

Figure 42 Localization precision of SiR^{HTL} and TMR^{star} signal bound to Tom20
Localization precision of TMR^{star} shown in green. Histogram of the SiR^{HTL} localization precision shown in red.

Thus, in most mitochondria the localizations are found at the outline of mitochondria. These accumulations of localizations were obtained independently of the used dye and tag. In the shown mitochondrial network 54510 localizations of SiR^{HTL} were obtained (Figure 43A). In the case of TMR^{star} 129882 signals were localized (Figure 43B). Co-localization was analyzed using a maximal nearest neighborhood radius of 100 nm. Non-colocalized single molecule localizations were excluded (Figure 43C). In the shown example 1845 co-localized signals were measured (Figure 43C).

Co-locomotion was done by tracking the colocalized particles and ignoring all trajectories with less than 10 steps of co-locomotion. This way, false-positive co-locomotion events were excluded. As an example: In the mitochondria of the cell shown in

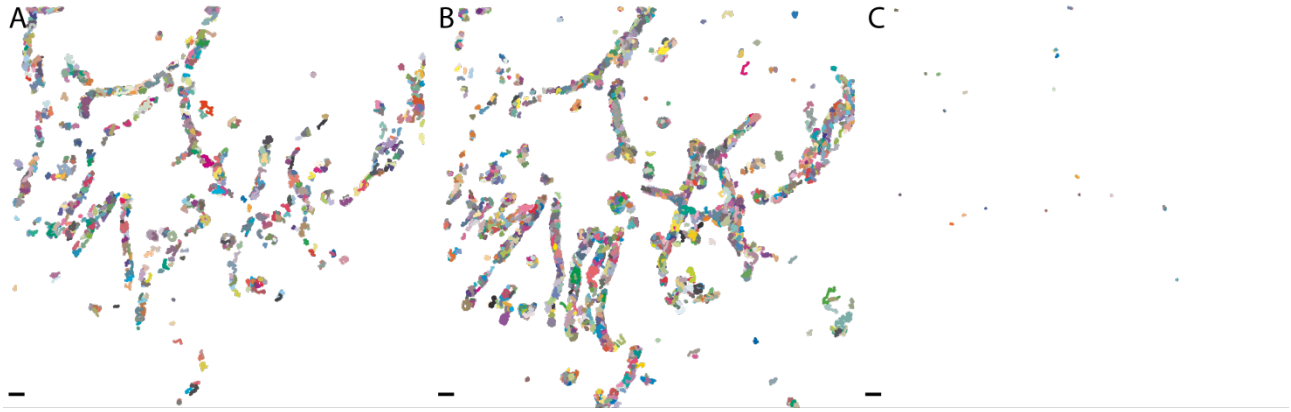

Figure **44**, 2278 single trajectories for Tom20:HaloTag:fSnapTag-SiRHTL were obtained. In the case of Tom20:HaloTag:fSnapTag-TMRstar, tracked in the same cell, resulted in the absolute value of 2187 trajectories (

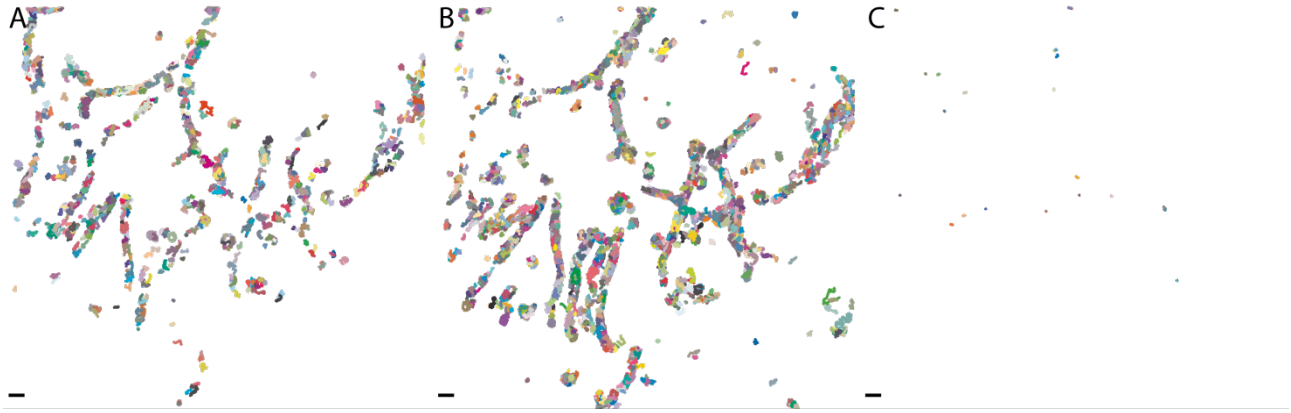

Figure **44**A, B). The similar number of trajectories shows that labeling and imaging resulted in a matching amount of trajectories. However, the total number of co-locomotion trajectories events, without false-positive events, was 18 trajectories (

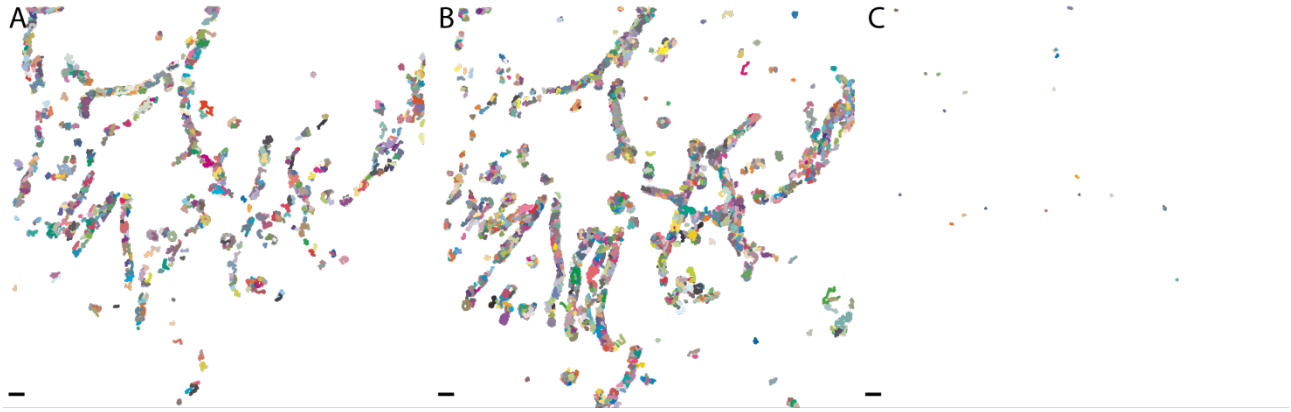

Figure **44**C). Relaxing the nearest neighborhood radius to 150 nm resulted in 24 trajectories of co-locomotion. So only 0.403 % co-locomotion events, 0.538 % respectively were obtained.

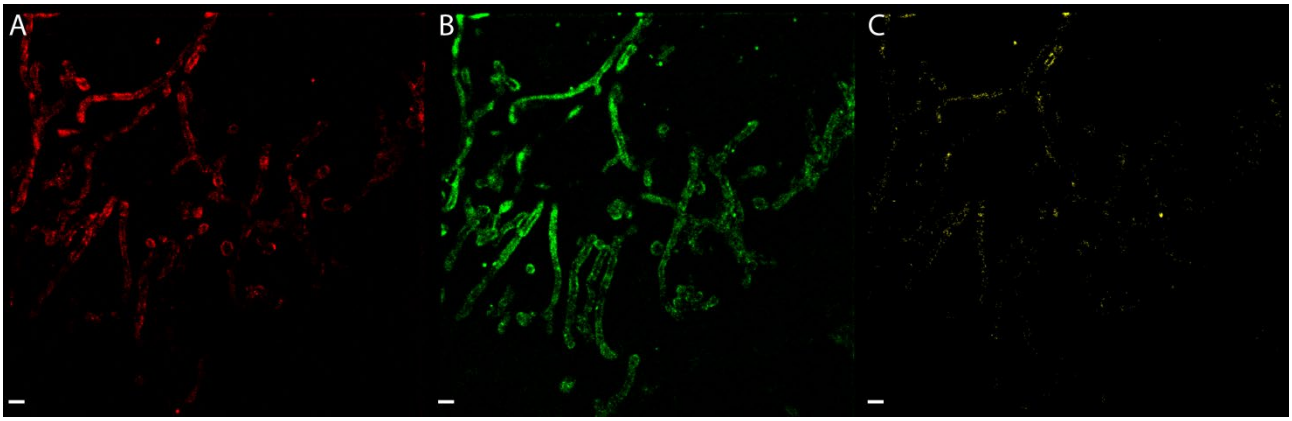

Figure 43 Colocalization of SiR^{HTL} and TMR^{star} bound to Tom20 fused with the HaloTag and the fSnapTag **A** Single molecule localization map of SiR^{HTL} with a used labeling concentration of 15 nM. **B** Single molecule localization map of TMR^{star} with a used labeling concentration of 30 nM. **C** Colocalization map of SiR^{HTL} and TMR^{star}. The nearest neighborhood radius was 100 nm. Scale bars: 1 µm

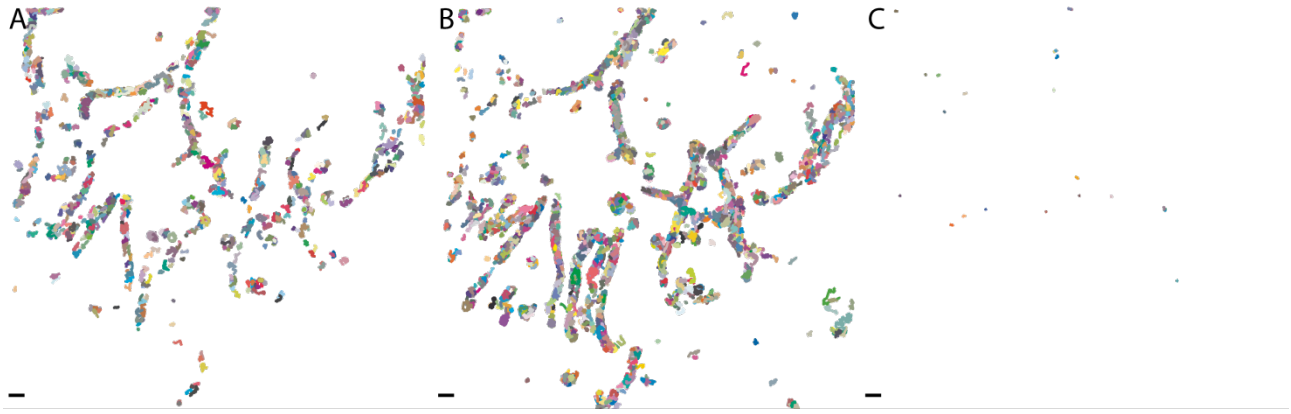

Figure 44 Co-locomotion trajectories of SiR^{HTL} and TMR^{star} bound to Tom20 fused with the HaloTag and the fSnapTag Trajectories from dual/color TALM of Tom20, recorded simultaneously. **A** Trajectory map of SiR^{HTL} trajectories with a minimal track length of 4 frames. **B** Trajectory map of TMR^{star} trajectories with a minimal track length of 4 frames. **C** Co-locomotion trajectories. Scale bars: 1 µm

Single particle tracking of the construct Tom20:HaloTag:fSnapTag labeled with SiRHTL and TMRstar should result in the same D_{app} for both dyes. However, different dyes have different sensitivities regarding brightness and

photostability. Especially a difference in photostability can influence the number of trajectories and the trajectory lifetime. All of these factors can influence the calculation of the D_{app}. The D_{app} of SiR^{HTL} and TMR^{star} bound to Tom20 were analyzed and compared (Figure S6, Figure S7, Table 6). The D_{app} and the percentages of the subpopulations revealed equal values for both dyes (Table 6). Thus, different fluorescent dyes were not altering TALM analysis. Nevertheless, different amounts of trajectories were obtained. For the entire analysis 32 cells were imaged in three independent experiments, resulting in 31625 trajectories of SiRHTL and 51909 trajectories of TMRstar. The amount of co-locomotion trajectories for all cells was 164, which relates to 0.196 % of detected co-locomotion events. The rare colocalization events showed that posttranslational, substoichiometric labeling with dyes was not suitable for the investigation of mitochondrial protein colocalization on single molecule level. Additionally, the low amount of co-locomotion trajectories showed that co-locomotion analysis in order to investigate a protein-protein interaction cannot be performed with this type of labeling. However, this does not exclude the use of dual-color TALM to investigate the colocalization of different proteins in the same mitochondrial microcompartment, especially for proteins localized in the IM with its small subcompartments. Likewise, dual-color TALM may also be useful to investigate if mitochondrial proteins affect the IM architecture and the spatiotemporal organization and dynamics of CV. These experiments will be described in the chapters 9.3.3 and 9.3.4.

Table 6 Diffusion coefficients of SiR^{HTL} and TMR^{star} bound to Tom20 fused with the HaloTag and the fSnapTag

Protein	D_{app} mobile [µm²/s]	relativ amount [%]	D_{app} slow mobile [µm²/s]	relativ amount [%]	D_{app} confined mobile [µm²/s]	relativ amount [%]
Tom20 SiR^{HTL}	0.129 ± 0.001	49.5 ± 0.8	0.45 ± 0.001	36.2 ± 0.7	0.008 ± 0.000	14.4 ± 1.0
Tom20 TMR^{star}	0.120 ± 0.002	49.5 ± 1.0	0.37 ± 0.001	36.7 ± 0.9	0.005 ± 0.000	13.8 ± 1.4

9.3.3 Dual-color TALM of F_1F_O ATP synthase subunit-γ and F_1F_O ATP synthase subunit-e

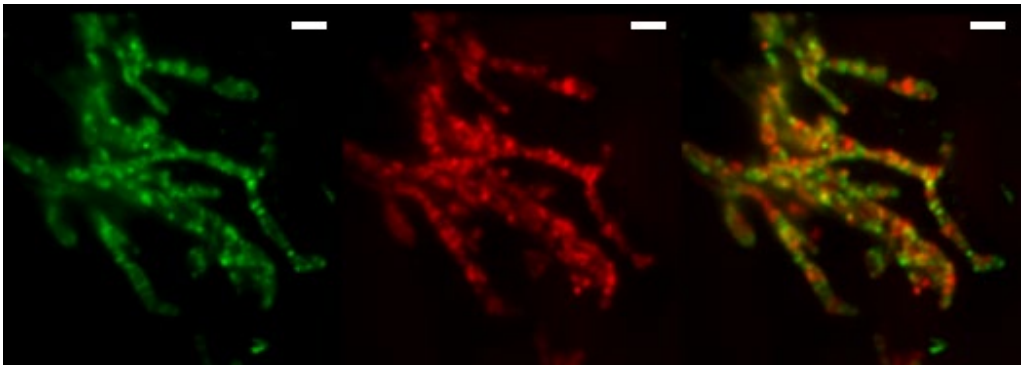

Figure 45 Diffraction limited image of mitochondria via the F_1F_O ATP synthase subunit-γ and the F_1F_O ATP synthase subunit-e
Dual-color microscopy of CV-SUγ (red) and CV-SUe (green) labeled with SiR^{HTL} and TMR^{star}. Both proteins are localized in mito-chondria.

CV-SUγ is a central subunit of CV. CV-SUγ connects the F_1 part with the F_O part of CV. TALM of CV-SUγ:HaloTag in cells allows to reveal the protein organization and to distinguish between trajectories in cristae and trajectories in the IBM. TALM also allows to study the mean trajectory directionality. It has also been shown that starvation switches the predominant diffusion to a longitudinal trajectory directionality.

One of the next questions was, what influences the destination of CV inside the IM. Recent studies have shown that CV dimerizes inside the cristae membrane and also forms oligomers (Allen et al., 1989; Davies et al., 2011; Davies et al., 2012, Dudkina et al., 2005; Habersetzer et al., 2013). These oligomers form the cristae rim (Blum et al., 2018, Davies et al., 2011, Davies et al., 2012, Hahn et al., 2016, Mühleip et al., 2016, Paumard et al., 2002). CV-SUe induces dimerization of CV. This raised the question, if an overexpression of CV-SUe leads to a change in the protein organization of CV and result in an increase of cristae trajectories and thereby a changing in average trajectory directionality. Therfore, a transfection of CV-SUe:fSnapTag into a HeLa cell line stably transfected with CV-SUγ:HaloTag was performed. As described previously SiR^{HTL} and TMR^{star} were used for labeling the POIs covalently. Labeling of these proteins was done with 2 nM SiR^{HTL} and 3 nM TMR^{star}. Then dual-color TALM of both proteins was performed. Both constructs were successfully expressed and imported into mitochondria (Figure 45). No false localizations in the cytosol were observed. Both constructs showed an inhomogeneous distribution along the mitochondrial networks (Figure 45). Remarkably, the accumulated signals of CV-SUe did not reflect the localization of the accuulated signals of CV-SUγ (Figure 45C).

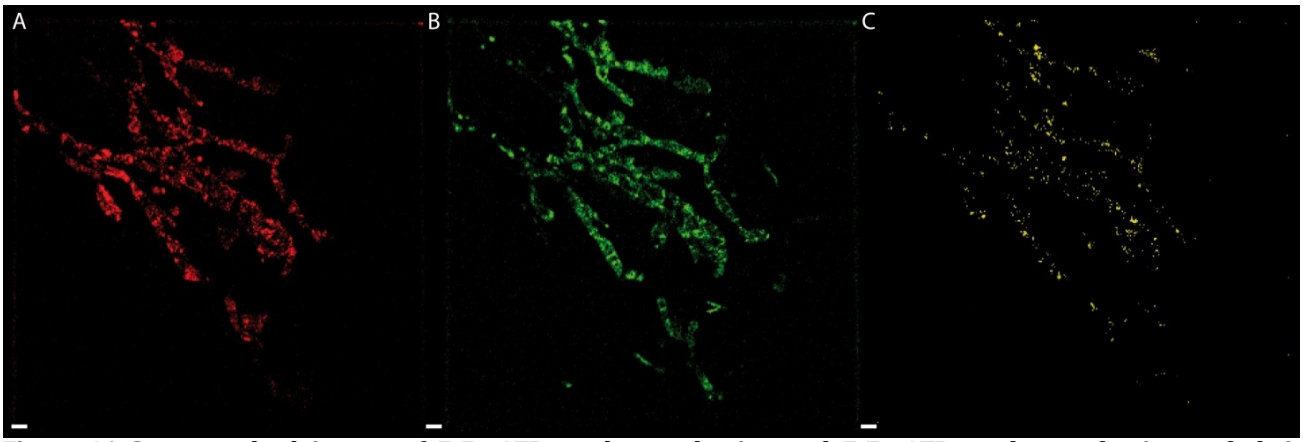

Figure 46 Super-resolved images of F_1F_O ATP synthase subunit-γ and F_1F_O ATP synthase subunit-e and their colocalization

A Super-resolved image of CV-SUγ. **B** Single particle localization of CV-SUe. **C** Co-localization map of CV-SUγ and CV-SUe with a nearest neighborhood radius of 150 nm.

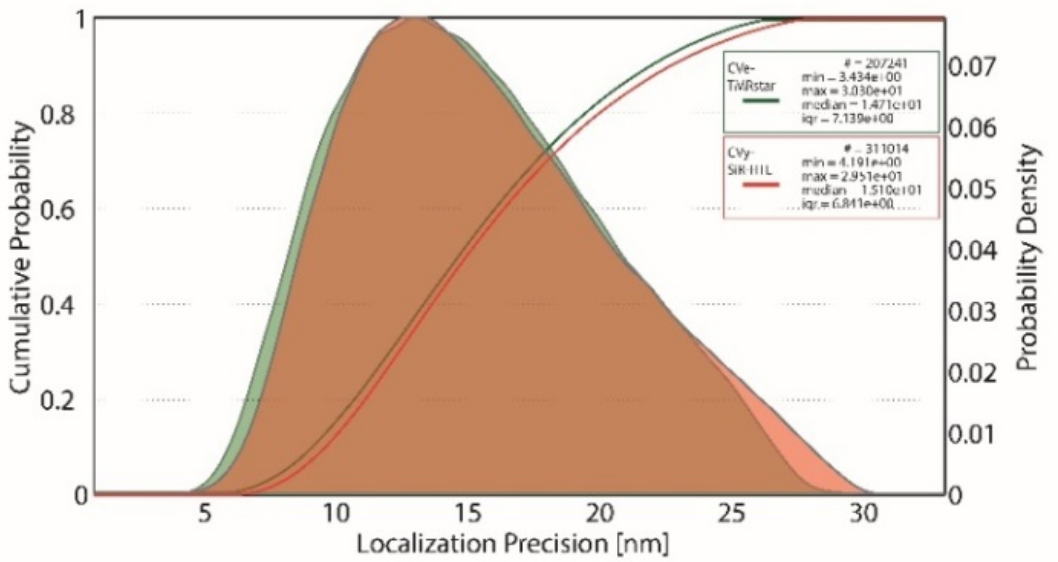

Figure 47 Localization precision of F_1F_O ATP synthase subunit-γ and F_1F_O ATP synthase subunit-e in dual-color experiments
Here a histogram of all localizations of both protein is plotted. The calculated localization precision of CV-SUγ was 15.57 nm. The caculated localization precision of CV-SUe was 14.89 nm.

Dual-color TALM allows localizing two signals of simultaneously recorded channels. This results in a super-resolved image of CV-SUγ and CV-SUe (Figure 46). The super-resolved images revealed that both proteins were not homogenously distributed in the IM, which was expected from the diffraction limited image. Additionally, the typical accumulations of localizations of proteins which are predominantly localized in the CM and thus showing a perpendicular orientation were observed (Figure 46). Especially in the channel of CV-SUe localizations appeared in accumulations which show an orthogonal orientation to the longitudinal axis of the mitochondria (Figure 46B). SML of the CV-SUγ and CV-SUe resulted in a mean calculated localization precision of 15.57 nm ± 3.42 nm for CV-SUγ:HaloTag - SiR^{HTL} and 14.89 nm ± 3.56 nm for CV-SUe:fSNAP-Tag - TMR^{star} (**Fehler! Verweisquelle konnte nicht gefunden werden.**).

Dual-color TALM was used in order to analyze if CV-SUγ and CV-SUe diffuse in the same mitochondrial microcompartment, espacially in the same CM. Therefore, the signals in each channel were tracked individually. Shown in Figure 48 and Figure 49 are trajectory maps gained by SPT of CV-SUγ and CV-SUe in the same mitochondria. First of all, the nonrandom movement of both proteins is obvious. The trajectories of the shown datasets were often confined independent of their location along the mitochondrial network. Confined tracks followed the outline of mitochondria and were also found in the middle of mitochondria (Figure 48, Figure 49, black arrow heads). Additionally, trajectories which reveled diffusion of CV-SUγ and CV-SUe in the IBM were observed; as they continuously followed the outline with a longitudinal directionality (Figure 48, Figure 49, blue arrow heads). Furthermore, cristae trajectories of CV-SUγ and CV-SUe were tracked (Figure 48, Figure 49, red arrow heads). The best criteria for this was a trajectorie orthogonal oriented to a trajectory with a longitudinal orientation in the IBM. Thus, in some mitochondrial parts trajectories in the IBM and cristae trajectories together revealed the shape of the IM architecture. In contrast to this, in other areas confined trajectories and trajectories in the IBM were found at the outline of the mitochondria. Unfortunately, TALM cannot reveal if confined trajectories were localized at the tip

of cristae, which expand the whole mitochondria or if those confined trajectories were localized in the IBM, likely at the CJs or if small cristae confined the movement of CV-SUγ and CV-SUe. However, in order to analyze if CV-SUγ and CV-SUe diffuse in the same CM or IBM an overlay of both trajectory maps was made (Figure 50). Beside single cases were trajectories were found in the same CM, both proteins traveled in different areas of mitochondria. However, in areas where CV-SUγshows a dominant localization in the IBM CV-SUe still showed cristae trajectories. Vice versa in some areas only trajectories of CV-SUγ were obtained. This raises the question, if a selective diffusion barrier for mitochondrial proteins exists.

Protein	Number of steps	Median jumpsize	Maximal. jumpsize	Minimal. jumpsize
CV-SUγ control	20124	96.94 nm	1117 nm	0.58 nm
CV-SUγ	274295	63.34 nm	302.8 nm	0.35 nm
CV-SUe	172253	59.21 nm	723.7 nm	0.21 nm

The gained jumpsizes were plotted in a diagram (Figure 51). Additionally, the median-, maximal- and minimal jumpsize are shown in

Table 7. Remarkably, the mean- and median jumpsize of CV-SUγ and CV-SUe were similar, while the maximal jumpsize of CV-SUe was twice the distance than the maximal jumpsize of CV-SUγ. Furthermore, the minimal jumpsize of CV-SUe measured only two third of the minimal jumpsize of CV-SUγ. Interestingly, the median jumpsize of CV-SUγ in these dual-color experiments compared to the control was decreased by 34.66 %. Also, the maximal jumpsize compared to the control experiments decreased by 27.11 % (

Table 7). Both indicate an increase in the confinement of CV-SUγ compared to the control.

Figure 48 Trajectory map of F_1F_0 ATP synthase subunit-γ
Trajectory map of CV-SUγ. The trajectory map was gained by tracking the single particle localization data of CV-SUγ shown in Figure 46A. The trajectories reveal the trafficking of CV-SUγ in the IM. Trajectories along mitochondria, respectively in the IBM as well as perpendicular oritented trajectories can be seen. Scale bar: 1µm

Figure 49 Trajectory map of F_1F_0 ATP synthase subunit-e
Trajectory map of CV-SUe. The trajectory map was gained by tracking the single particle localization data of CV-SUe shown in Figure 46A. The trajectories reveal the trafficking of CV-SUe in the IM. Trajectories in the IBM (longitudinal oriented) and in the CM (perpendicular oriented) can be observed. Scale bar: 1µm

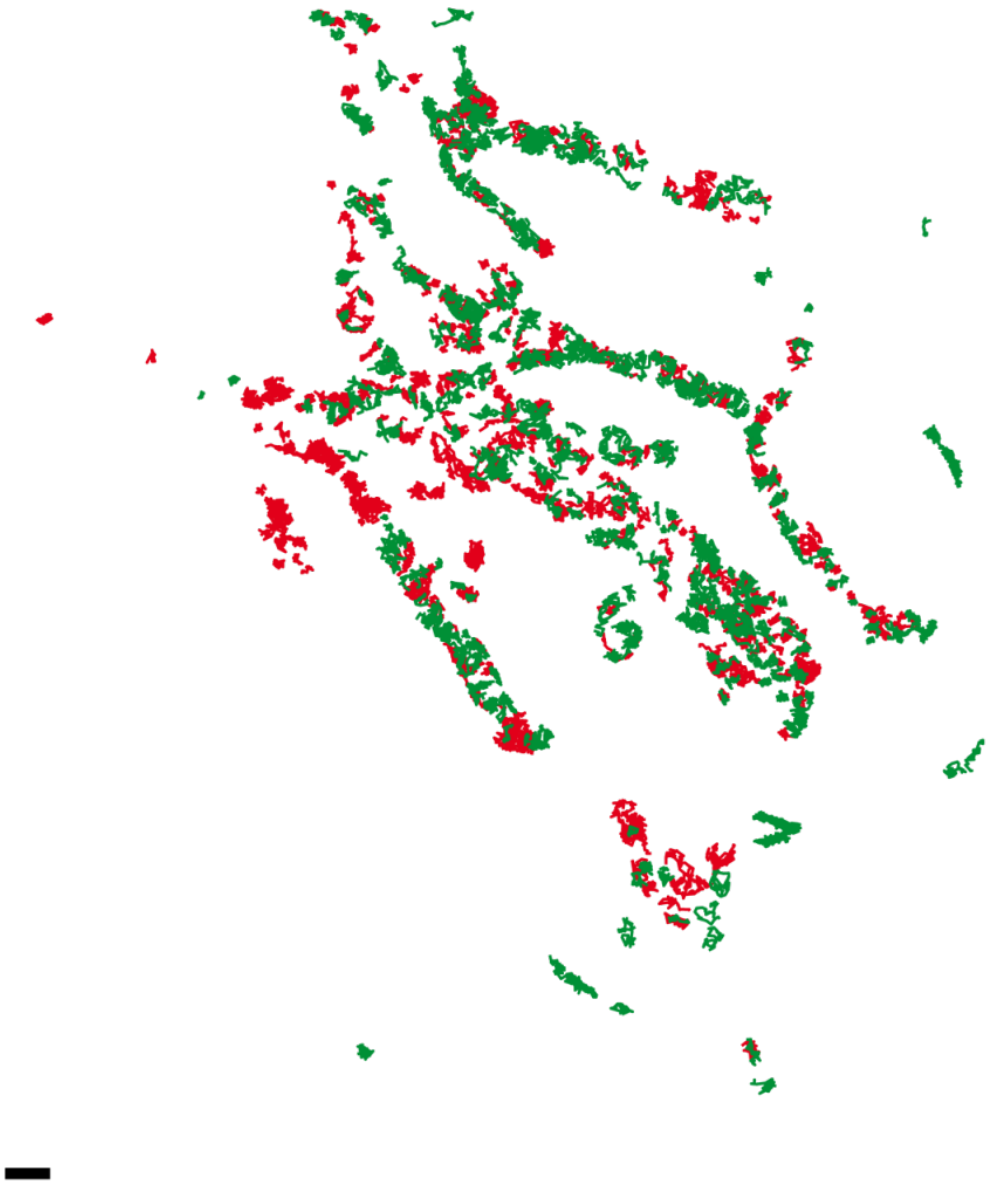

Figure 50 Overlay of trajectory maps from F_1F_O ATP synthase subunit-γ and F_1F_O ATP synthase subunit-e
Overlay of a trajectory map of CV-SU γ (red trajectories) and a trajectory map of CV-SUe (green trajectories) recorded simultanously in the same mitochondrial network. The trajectories do not indicate a diffusion in the same microcompartment at the same time. Scale bar: 1µm

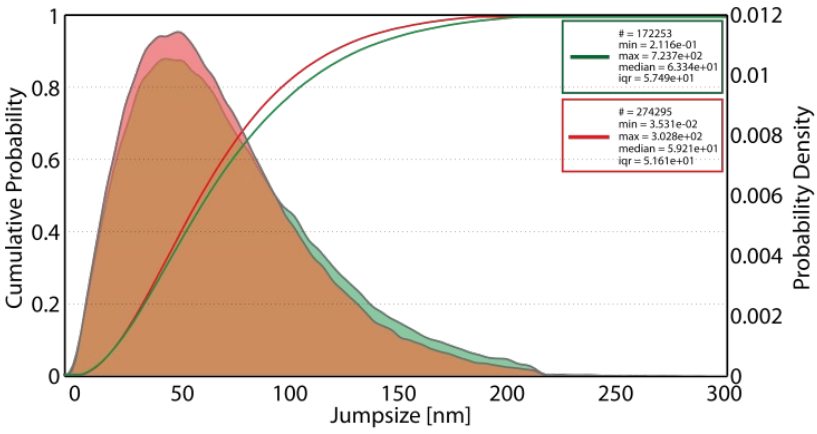

Figure 51 Jumpsize distribution of F_1F_O ATP synthase subunit-γ and F_1F_O ATP synthase subunit-e in dual-color TALM
In the histogram of all steps lengths CVγ are plotted in red, CVe steps are shown in green. The mean jumpsize of CVγ was 153.42 nm. And the mean jumpsize of CVe was 188.99 nm.

Table 7 Jumpsize of the F_1F_O ATP synthase subunit-γ and the F_1F_O ATP synthase subunit-e

Protein	Number of steps	Median jumpsize	Maximal. jumpsize	Minimal. jumpsize
CV-SUγ control	20124	96.94 nm	1117 nm	0.58 nm
CV-SUγ	274295	63.34 nm	302.8 nm	0.35 nm
CV-SUe	172253	59.21 nm	723.7 nm	0.21 nm

Dimers and oligomers of CV are involved in the bending of the CM at the cristae rim (Blum et al., 2018, Davies et al., 2011, Davies et al., 2012, Hahn et al., 2016, Mühleip et al., 2016, Paumard et al., 2002). It can be assumed that these protein super-complexes are quite immobile in the CM. As CV-SUe is needed for dimerization of CV it is possible that it is part of CV dimers and oligomers. If an overexpression of CV-SUe increases recruitment of CV-SUγ into the dimers and oligomers of CV it can influence the mobility of CV-SUγ. Therefore, the D_{app} of CV-SUe and CV-SUγ in the dual-color experiments were measured. Again, a subpopulation test for 3 fractions was successfully performed. The D_{app} of the different fractions of CV-SUe are plotted in

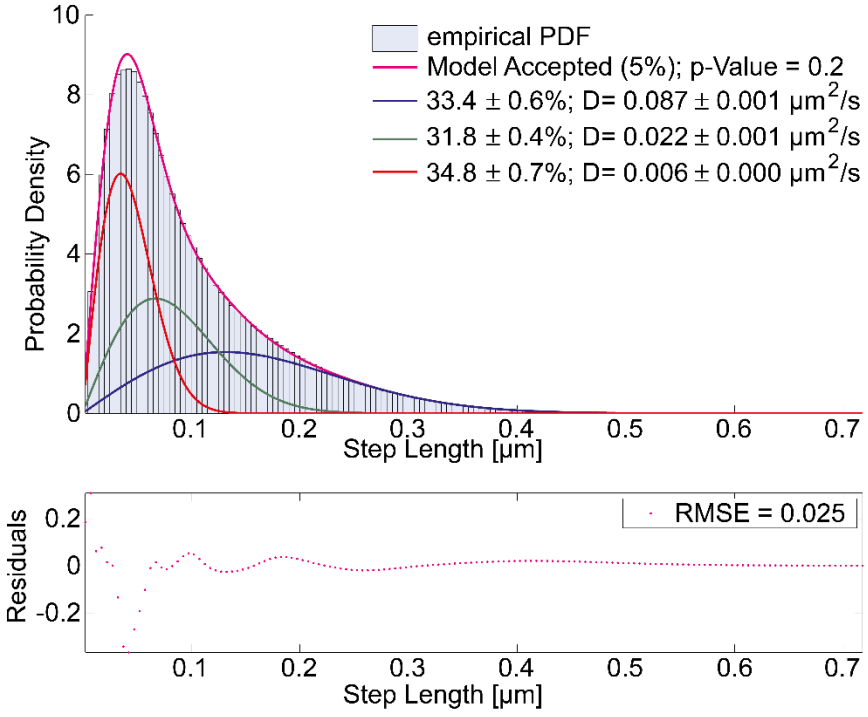

Figure **S8** and listed in Table 8. The D_{app} of CV-SUγ in cells co-transfected with CV-Sue, were also fitted succesfully

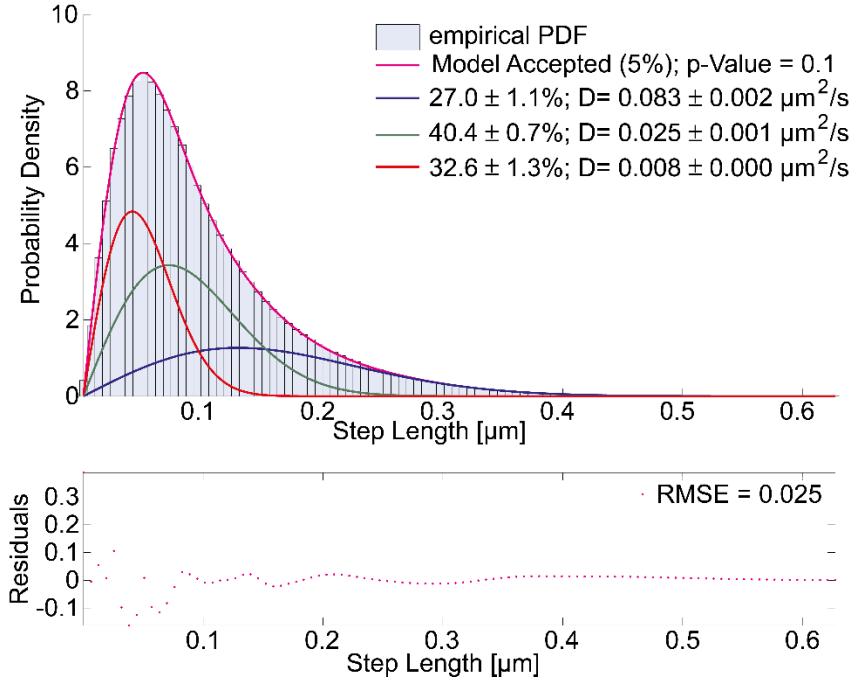

by a three population fit (

Figure **S**9, Table 8). The D_{app} of all fractions of CV-SUγ and CV-SUe were similar. In the case of CV-SUe all fractions have a similar percentage of around 33 %. In the case of CV-SUγ the mobile fraction was around 27 %. The slow mobile fraction amounted to around 40 % and the slow mobile fraction to around 33 %. Compared to the control the D_{app} of CV-SUγ did not changed significantly (Table 8). However, the percentages of the fraction changed. In co-transfection experiments of CV-SUγ together with CV-SUe the percentage of the mobile fraction of CV-SUγ was reduced by over 10% compared to the control. The percentage of the slow mobile fraction was reduced by around 5 %. Meanwhile the percentage of the confined mobile fraction was increased by approximately 15 %. This indicates that co-expression of CV-SUe influences the mobility of CV-SUγ in a manner, that it switches the mobility of CV-SUγ from mobile and slow mobile to a rather confined mobility. On the one hand, this can be interpreted as an induced super-complex formation of CV and thereby dimerization and oligomerization of CV, including CV-SUγ as one of the central subunits of CV. On the other hand, an upregulation of dimers and oligomers of CV by overexpression of CV-SUe may influence the ultra-

Table 8 Diffusion coefficients of the F_1F_0 ATP synthase subunit-γ and the F_1F_0 ATP synthase subunit-e in contransfected cells

Protein	D_{app} mobile [µm²/s]	relativ amount [%]	D_{app} slow mobile [µm²/s]	relativ amount [%]	D_{app} confined mobile [µm²/s]	relativ amount [%]
CV-SUγ control	0.079 ± 0.009	35 ± 5	0.020 ± 0.006	47.0 ± 3	0.005 ± 0.002	18 ± 3
CV-SUγ	0.083 ± 0.002	27.0 ± 1.1	0.025 ± 0.001	40.4 ± 0.7	0.008 ± 0.000	32.6 ± 1.3

CV-SUe	0.087 ± 0.001	33.4 ± 0.6		0.022 ± 0.001	31.8 ± 0.4		0.006 ± 0.000	34.8 ± 0.7

structure in a way that more cristae were formed leading to an increased confinement of CV-SUγ in the CM. However, without blue-native gels this stays unknown. Nevertheless, if more CV-SUγ diffuses in the CM or if more cristae were formed the proportion of perpendicular orientated CV-SUγ-trajectories should be increased. This could be measured with the software MitoOrientedDynamic.

In the case of CV-SUγ, 9558 binned steps were taken into account to analyze the trajectory directionality, using the 4-step binning procedure. The directionality of CV-SUγ-trajectories and CV-SUe-trajectories was mostly perpendicularly (Figure 52). The pie chart diagram illustrates the orthogonal directionality of CV-SUγ-trajectories by an elliptic shape of the pie chart. Here peaks between -50° and -130° as well as between 70° and 120° were observed, representing a perpendicular directionality of the CV-SUγ trajectories caused by diffusion of CV in the CM (Figure 52A). The trajectory directionality analysis of CV-SUe also showed an elliptic shape with perpendicular expansion (Figure 52B). Here the extrema of the pie chart are between 60° and 110° as well as between -70° and -130°. The heatmap of step direction analysis delivered a similar result (Figure 52C, D). The jumpsize of perpendicular steps of CV-SUγ trajectories was between 50 and 100 nm (Figure 52C). Trajectory directionality analysis of CV-SUγ and CV-SUe in the heatmap also showed a perpendicular directionality (Figure 52C, D). The jumpsize of the perpendicular steps of CV-SUe was around 100 nm (Figure 52D). These results show that CV-SUe diffused mostly perpendicular in mitochondria. This means CV-SUe diffuses predominantly in the CM. Furthermore the overexpression of CV-SUe leads to an increase of the perpendicular directionality of CV-SUγ trajectories shown in Figure 52A compared to the trajectorie directionality of the control, shown in Figure 33B. Taken together overexpression of CV-SUe leads to an increase of cristae trajectories of CV-SUγ and of the confined mobility. Thus CV-SUe influences the spatiotemporal organization of CV and mys also influence the IM architecture.

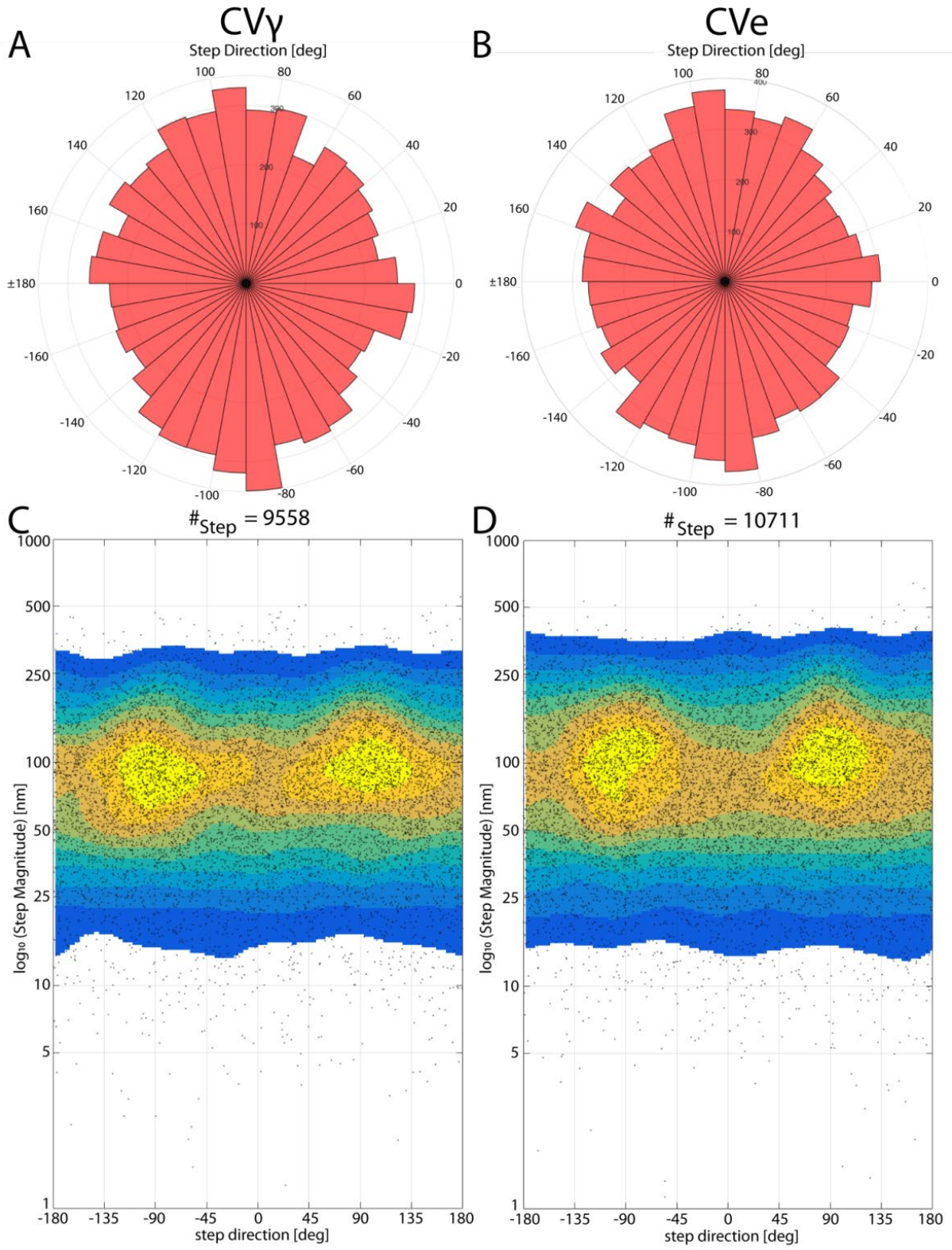

Figure 52 Directionality analysis of the F_1F_0 ATP synthase subunit-γ trajectories and trajectories of F_1F_0 ATP synthase subunit-e

A The directionality of CVγ-trajectories in degree in a pie chart depicts a dominant directionality between -45° and -130° as well as between 70° and 120°. **B** Trajectory directionality of CVe-protein movement. This diagram shows a predominant trajectory directionality between 60° and 110° as well as between -70° and -130°. **C** The step magnitude plot shows that the majority of steps of the CVγ proteins have a size between 50 nm and 100 nm with larger accumulations between -45° and -130° and 70° to 135°. **D** The predominant directionality of trajectories of CVe proteins in the step magnitude plot with showing only a small amount in the longitudinal axis of the analyzed mitochondria. Here, most of the steps are between -45° and 45° and -135° and 135°.

9.3.4 Dual-color TALM of F_1F_O ATP synthase subunit-γ and MINOS/MICOS subunit-10

Dimers of CV and compounds of the MINOS/MICOS complex have cristae shaping functions. Mic10 bends the IM by oligomerization at the CJ (Barbot et al., 2015, Bohnert et al., 2015). Overexpression of the Mic10 leads to an altered ultrastructure (Bohnert et al., 2015). While dimers of CV are mainly found at the rims of cristae in negatively curved membranes, Mic10 is localized at the CJs. It was therefore surprising, that Mic10 apparently interacts with the dimeric form of CV promoting the formation of larger CV oligomers (Rampelt et al., 2017). Furthermore, Mic10 mediates a functional crosstalk between the MINOS/MICOS complex and CV (Rampelt et al., 2017). These interactions, if direct, would require at least a temporarily colocalization. In order to test for colocalization of Mic10 and CV in the same mitochondrial microcompartment, was conducted using dual-color TALM (Appelhans et al., 2018, Beinlich et al., 2015). Furthermore, dual-color TALM was used to investigate if Mic10 influences the IM architecture. If so the spatiotemporal organization of CV-SUγ should be altered compared to results from CV-SUγ TALM data without co-transfection of Mic10. For dual color imaging, a HeLa cell line stably transfected with CV-SUγ-HaloTag was used and transiently transfected with Mic10:fSnapTag. The transfected cells were labeled with concentrations of 2 nM SiR^{HTL} and 6 nM TMR^{star} (Figure 53). The diffraction limited image in Figure 53A,B is a summed image of 1861 frames. The used exposure time was 32 ms. Already, Figure 53A shows an inhomogeneous accunulation of CV-SUγ, indicating localization in mitochondrial sub-compartments. Mic10 showed a rather punctuate distribution along the mitochondrial network (Figure 53B). A merged image was generated (Figure 53C). The overlay of the CV and Mic10 signal shows that both proteins obviously occupy different sub-compartments (Figure 53C). The raw data was further processed by SML and SPT. In the entire experiment, 972440 localizations of CVγ:HaloTag-SiR^{HTL} were recorded. The calculated mean localization precision of CV-SUγ was 14.25 ± 3.15 nm. In the case of Mic10 608822 single molecules were localized with a calculated mean localization precision of 13.72 ± 3.54 nm(Figure 54).

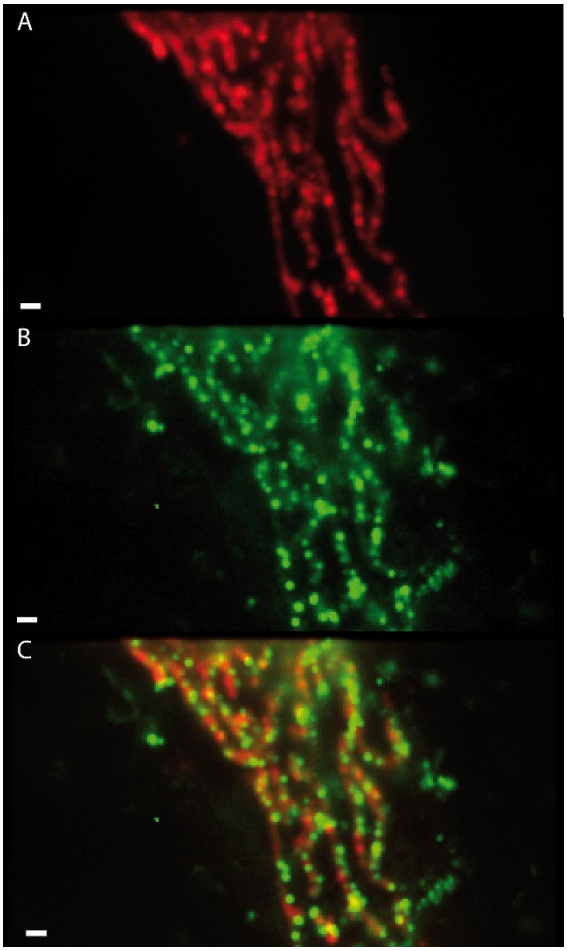

Figure 53 Diffraction limited image of mitochondria via the F_1F_O ATP synthase subunit-γ and MINOS/MICOS subunit-10
A CV-SUγ stained with SiR^{HTL} shown in red. B Mic10 stained with TMR^{star} shown in green. **C** Merge channel shows co-staining of the same mitochondrial network with both constructs. Both proteins show certain spots of increased signal. Additionally, these spots do not overlap.

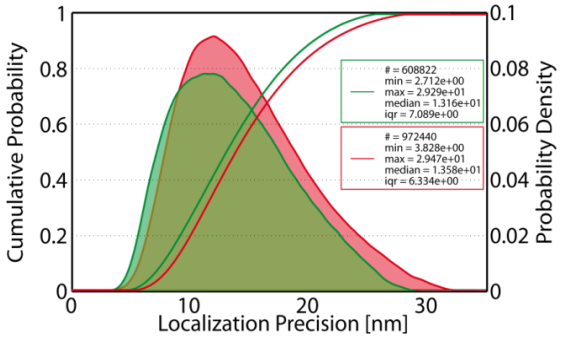

Figure 54 Localization precision of F_1F_O ATP synthase subunit-γ and MINOS/MICOS subunit-10
The mean calculated localization precision of CVγ (red) was 14.25 nm. Mic10 (green) was localized with a precision of 13.72 nm in mean.

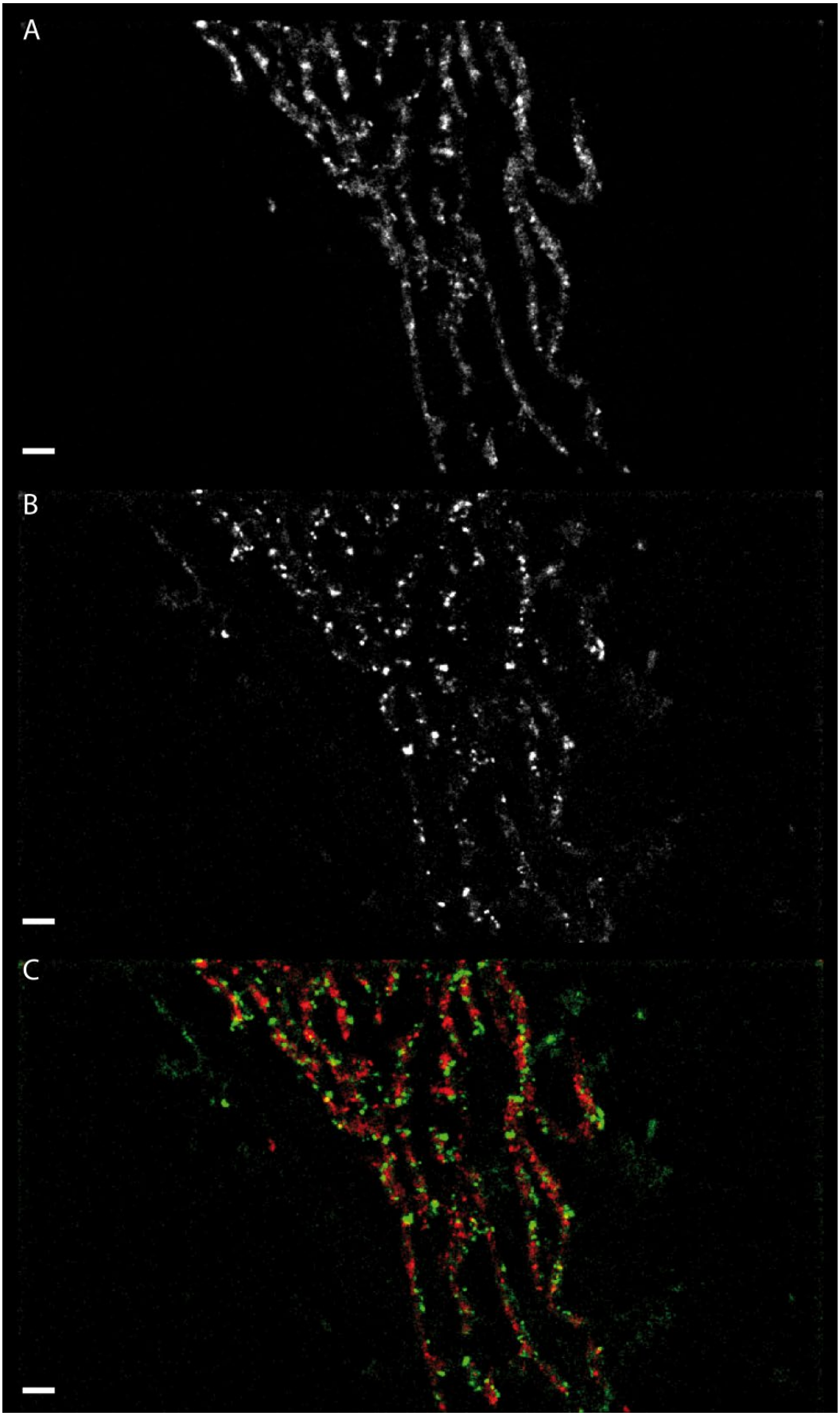

Figure 55 Single molecule localization image of F_1F_O ATP synthase subunit-γ and MINOS/MICOS subunit-10 signals **A** SML image of CV-SUγ-SiR^{HTL}. **B** SML image of Mic10-TMR^{star}. C Merge channel shows the different localizations of CV-SUγ (red) and Mic10 (green). Obviously, CV-SUγ and Mic10 were not localized in the same mitochondrial subcompartment.

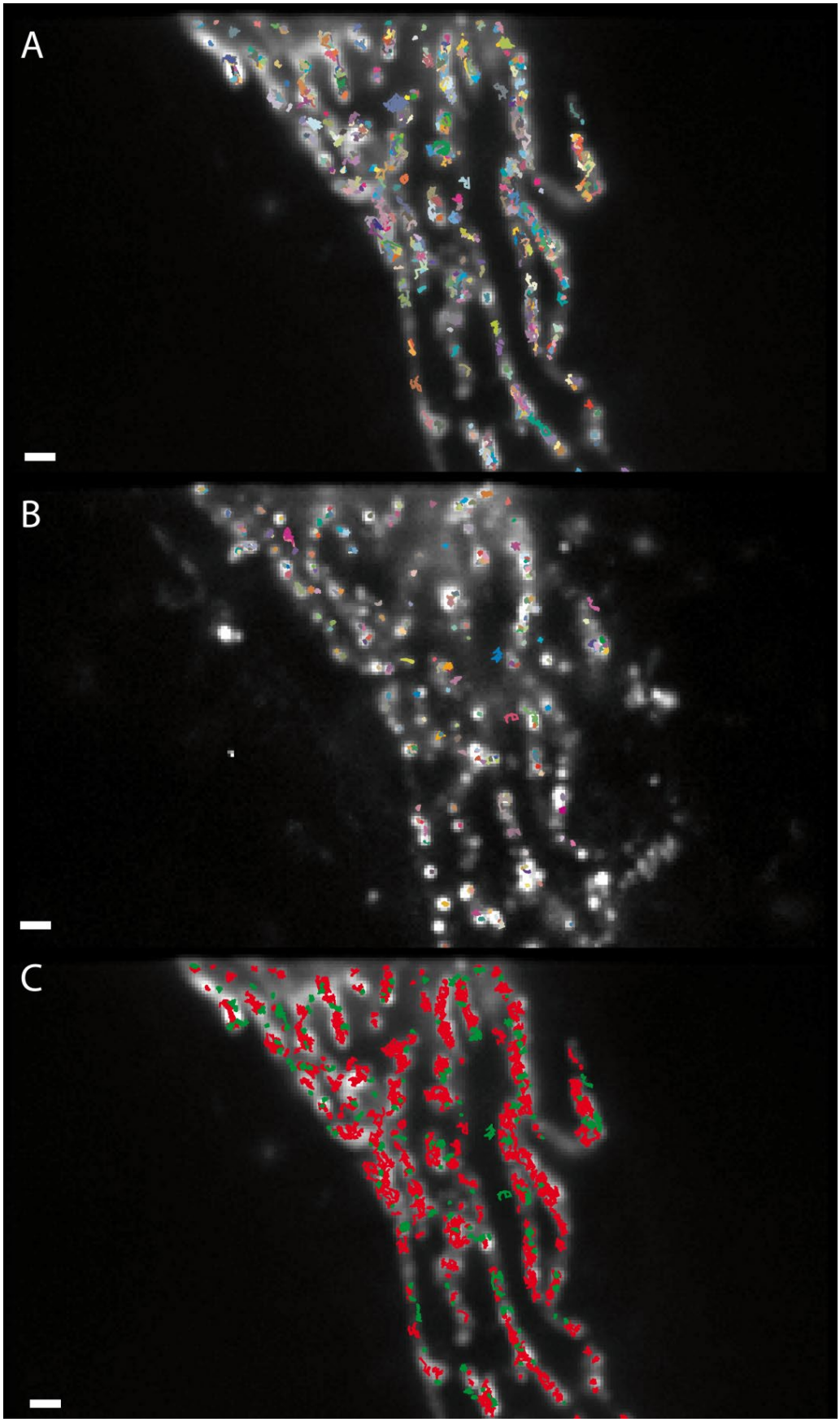

Figure 56 Trajectory maps of F_1F_O ATP synthase subunit-γ and MINOS/MICOS subunit-10
A Trajectory map of CV-SUγ-SiR^{HTL} overlayed with a diffraction limited imag of the SiR^{HTL} signal. **B** Trajectory map of Mic10-TMR^{star} overlayed with the summed signales of TMR^{star}. **C** Combination of both trajectory maps, demonstrating the trafficking of both proteins. CV-SUγ (red) and Mic10 (green) diffuse in different mitochondrial sub-compartments.

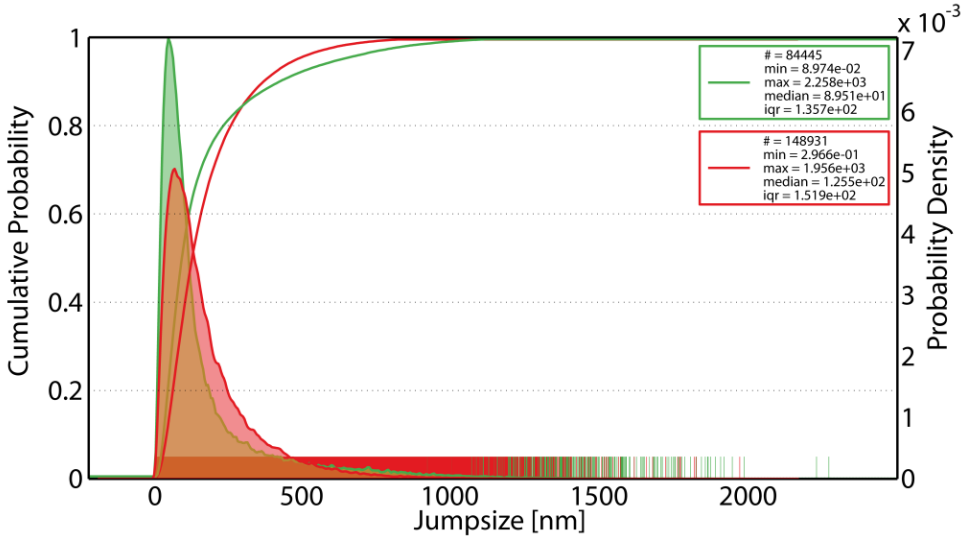

Figure 57 Histogram of the jumpsizes of F_1F_O ATP synthase subunit-γ and MINOS/MICOS subunit-10 The jumpsize of CV-SUγ (red) were a larger than jumpsizes of Mic10 (green).

Table 9 Jumpsize of the F_1F_O ATP synthase subunit-γ and MINOS/MICOS subunit-10

Protein	Number of steps	Median jumpsize	Maximal. jumpsize	Minimal. jumpsize
CV-SUγ control	20124	96.94 nm	1117 nm	0.58 nm
CV-SUγ	148931	125.5 nm	1956 nm	0.30 nm
Mic10	84445	89.51 nm	2258 nm	0.09 nm

In the shown expample, 5123 CV-SUγ localizations and 3562 localizations of Mic10 were obtained (Figure 55). Comparing the localization map of CV-SUγ and Mic10 revealed the localization in distinct sub-compartments as the diffraction limited image had already implied. Althought, CV-SUγ and Mic10 preferentially occupy distinct sub-compartments, an antagonistic interplay in shaping the IM architecture is still possible without interaction. Thus, Mic10 would induce the positive membrane curvature and CV dimers acting as an antagonist inducing the negative membrane curvature or vice versa, respectively. If so, Mic10 would occupy the CJs and result in confined trajectories. In contrast to this CV-SUγ should be found in the CM and at the tip of cristae. Furthermore, as both proteins were overexpressed in the analyzed cell the question raised if either MINOS/MICOS or CV has a stronger influence on the IM architecture.

The trajectorie maps of CV-SUγ and Mic10 in an examplary cell as well as an overlay of both is shown in Figure 56. Directly obvious was a confinced mobility of Mic10 in ach mitochondrion. In contrast to this, trajectories of CV-SUγ reflected a larger mobility along the IM. The overlay of both trajectorie maps shows that CV-SUγ and Mic10 do not diffuse in the same area. Even more CV-SUγ and Mic10 seem to avoid each other as CV-SUγ diffuses around spots where Mic10 diffuses in a confined manner (Figure 56C). Comparing the jumpsize of the proteins, CV-SUγ, in cells co-transfected with Mic10, showed a larger jumpsize than Mic10 and than CV-SUγ in the control without co-transfection of Mic10 (Table 9). Nevertheless, trajectories of CV-SUγ showed confined mobility, cristae trajectories and random movement in the IM (Figure 56A). This fits with the three subpopulations of the D_{app} of CV-SUγ (Figure S10, Table 10). The mobile fraction was interpreted as unhindered diffusion of CV-SUγ. The confined mobile fraction

Table 10 Diffusion coefficients of F_1F_O ATP synthase subunit-γ and MINOS/MICOS subunit-10 in contransfected cells

Protein	D_{app} mobile [µm²/s]	relativ amount [%]	D_{app} slow mobile [µm²/s]	relativ amount [%]	D_{app} confined mobile [µm²/s]	relativ amount [%]
CV-SUγ	0.060 ± 0.004	25.6 ± 0.5	0.013 ± 0.001	47.0 ± 0.5	0.004 ± 0.000	27.3 ± 0.7
Mic10	0.078 ± 0.003	14.5 ± 0.2	0.014 ± 0.001	39.5 ± 0.2	0.003 ± 0.000	46.0 ± 0.3

was interpreted as CV-SUγ proteins, which were hindered in diffusion by e.g. dimerization of CV, which fixes CV at the rim of cristae or hindered diffusion in small cristae resulting from Mic10 overexpression and possible homo-oligomers. Mic10 diffusion was also fitted by three subpopulations (Figure S11, Table 10).The relaitv amount of the mobile and the confined mobile fraction of CV-SUγ and Mic10 differed strongly. Thus, the mobile fraction of CV-SUγ had a percentage of 25.6 ± 0.5 % and the mobile fraction of Mic10 only 14.5 ± 0.2 %. In contrast to this, diffusion of Mic0 was nearly to 50 % confined as the confined fraction had a percentage of 46.0 ± 0.3 %. While the confined fraction of CV-SUγ was determined by 27.3 ± 0.7 %. This was expected from the trajectory maps were Mic10 mostly shows confined trajectories. Furthermore, these results match to the 'behaior' of a protein, which builds up CJs and builds homo-dimers and homo-oligomers and is part of the MINOS/MICOS compex. Therefore, confined trajectories of Mic10 were interpreted as possible locations of CJs (Figure 56B). It was expected that trajectories of CV-SUγ decorate these spots with cristae trajectores, so CV-SUγ trajectories orthogonal to the longitudinal axis of the mitochondrion and starting or ending at confined trajectories / spots of CJs – confined trajectories of Mic10. However, neither the classical trajectory directionlity of CV-SUγ with trajectories along the IBM and trajectories in

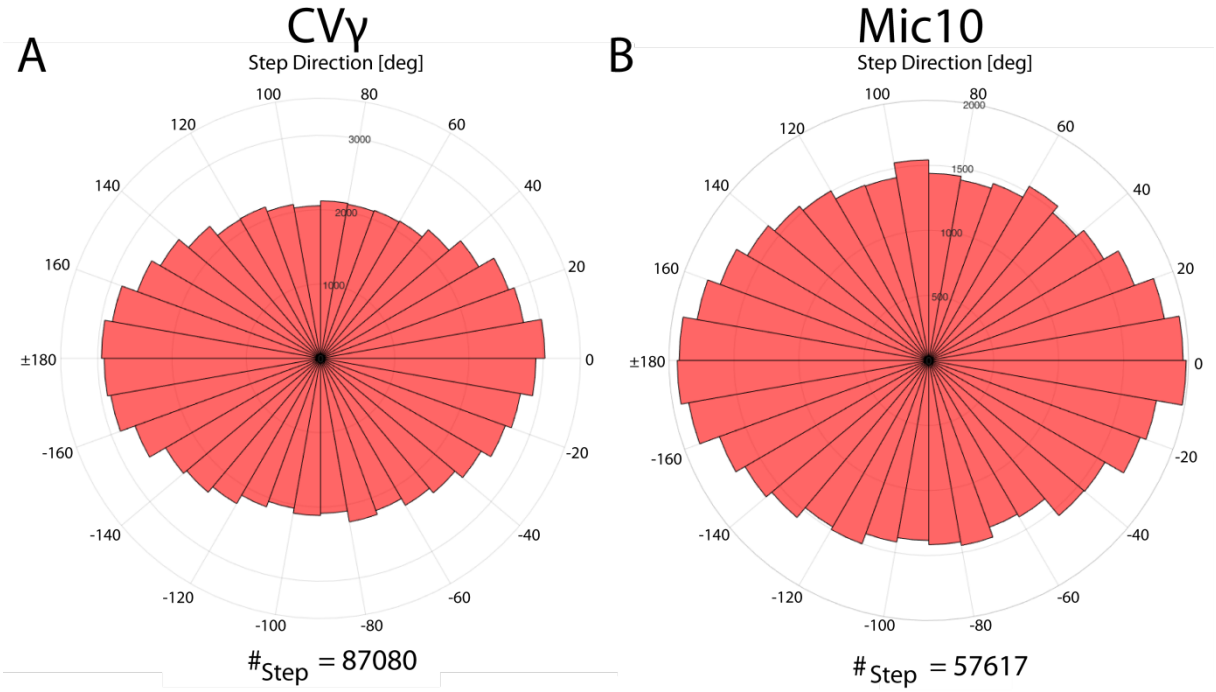

Figure 58 Directionality analysis of the F_1F_O ATP synthase subunit-γ trajectories and trajectories of MINOS/MICOS subunit 10
A The pie chart diagram of the CVγ-trajectories directionality shows an elliptic shapewith extrema between -30° to 40° and -160° to 160°. **B** The pie chart diagram of Mic10-trajectories directionality shows an elliptic shape with peaks between -130° to 140° and -50° to 40°.

The CM, somewhere in the mitochondria nor cristae trajectories decorating confined trajectories of Mic10 were found when Mic10 was co-transfected (

Figure 58A). The trajectories of CV-SUγ even occurred in a rather random oriented way. Interestingly, the overlay of the trajectories of both proteins, shown in Figure 56C indicated that Mic10 seemed to hinder CV-SUγ diffusion. Mic10 and CV-SUγ showed a distinct different localization and trajectory appearance (Figure 55, Figure 56). This, on the one hand, led to the suggestions that Mic10 acts as a diffusion barrier for CV and on the other hand strongly rules the shape of the IM as cristae trajectories vanished by co-transfection of Mic10. Taken together Mic0 has a large impact of the spatiotemporal organization of CV. In order to analyze this further, the trajectory diretionalitywas determined. The software Mito OrientedDynamic was used to investigate the trajectory directionality of CV-SUγ and Mic10 trajectories. Here 87080 binned steps of CV-SUγ and 57617 binned steps of Mic10 were analyzed. The pie chart diagram of the CV-SUγ trajectory directionality and Mic10 trajectory directionality show a dominant longitudinal movement direction of both proteins (

Figure 58A). The pie chart diagram shows an elliptic shape with extrema between -30° to 40° and -160° to 160°. In the pie chart diagram of Mic10, steps show over 1500 steps with an angle between -130° to 140° and -50° to 40° (

Figure 58B, Figure S12). These results demonstrate that Mic10 changes the shape of the IM and thereby the directionality of CV-SUγ and its spatiotemporal organization. The heat maps of the trajectory directionalites support these results and show a longitudinal orientation of the trajectories with an average jumpsize of around 100 nm for both proteins, in this cotransfection experiment (Figure S12).

9.4 Transmission electron microscopy of HeLa cells stably expressing F_1F_O ATP synthase subunit-γ:HaloTag in different metabolic conditions

9.4.1 Transmission electron microscopy of HeLa cells stably expressing F_1F_O ATP synthase subunit-γ:HaloTag

TEM was used in order to investigate the given ultrastructure in HeLa cells stably expressing CV-SUγ:HaloTag qualitatively. In the control, the cells were grown in growth medium containing glucose (MEM^{++}(1)). The mitochondria differ in length (Figure 59). However, in the cell periphery long mitochondria can be seen (Figure 59A). The mitochondria show a regular alternation of cristae and matrx. Most of the cristae have a perpendicular orientation to the longitudinal axis. Cristae which had a curved shape or even start and end at the same site of the IBM are rarely seen (Figure 59A, B, C).

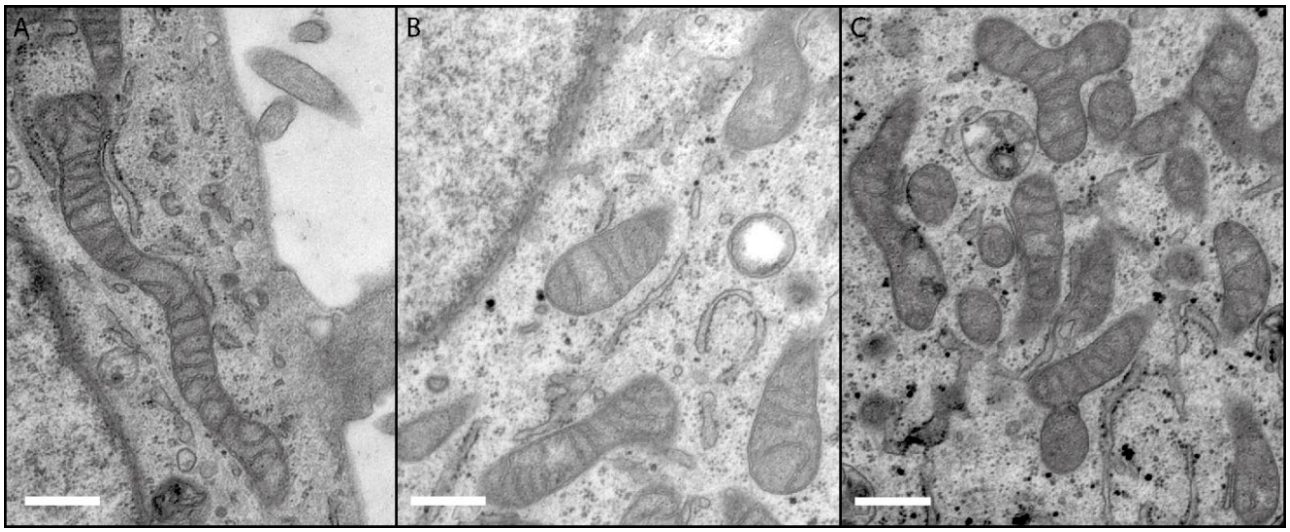

Figure 59 Transmission electron microscopy images of HeLa cells stable transfected with F_1F_O ATP synthase subunit-γ:HaloTag
A An elongated mitochondria in the cell periphery. **B** Short mitochondria in the perinuclear region. **C** Short and fragmented mitochondria as well as branched mitochondria. (Scale bars: 500 nm, figures shown with the permission of Katharina Psathaki)

9.4.2 Transmission electron microscopy of of HeLa cells stably expressing the F_1F_O ATP synthase subunit-γ:HaloTag after 2 hours of starvation

TEM of HeLa cells stably expressing CV-SUγ:HaloTag were kept in starving conditions for 2 hours. Here the same clone as in the control experiment was used. Thus, a potential ultrastrucural difference between mitochondria after 2 hours of starvation and mitochndira in the control experiment can be analyzed qualitatively. In starvation the mitochondria kept their generaldshape (Figure 60). Directly obvious is an ultrastructural change(Figure 60A, B). In mitochondria kept 2 hours in starving conditions the IM becomes tubular. Most of the CM vanishes and became part of the IBM. This can only be explained by a regression of the CM. Furthermore single cristea can be seen but mostly do not show the conserved perpendicular orientation as in the control cells.

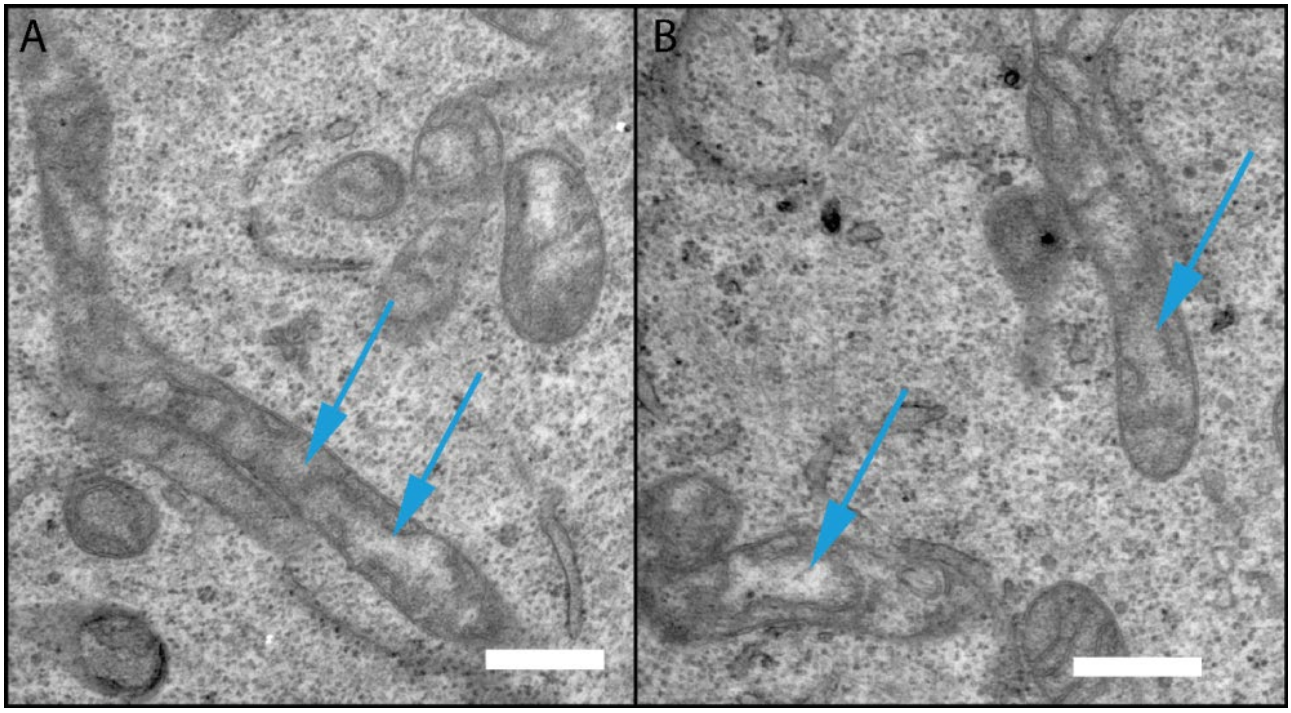

Figure 60 Transmission electron microscopy images of HeLa cells stably transfected with F_1F_0 ATP synthase subunit-γ:HaloTag during starvation condition
A Mitochondria in starving conditions the IM changes its ultrastructure and becomes tubular like the OM (blue arrows). **B** Another example of mitochondria in starving conditions. (Scale bars: 500 nm, figures shown with the permission of Katharina Psathaki))

9.4.3 Transmission electron microscopy of of HeLa cells stably transfected with F_1F_O ATP synthase subunit-γ:HaloTag during improved respiration

In order to investigate the ultrastructure in conditions of improved respiration TEM was performed. Therefore the same clone of the HeLa cell line stably transfected with CV-SUγ:HaloTag was used and grown in the same conditions used for TALM experiments. In these conditions the mitochondria kept their general shape. Long mitochondria in the cell periphery were obtained (

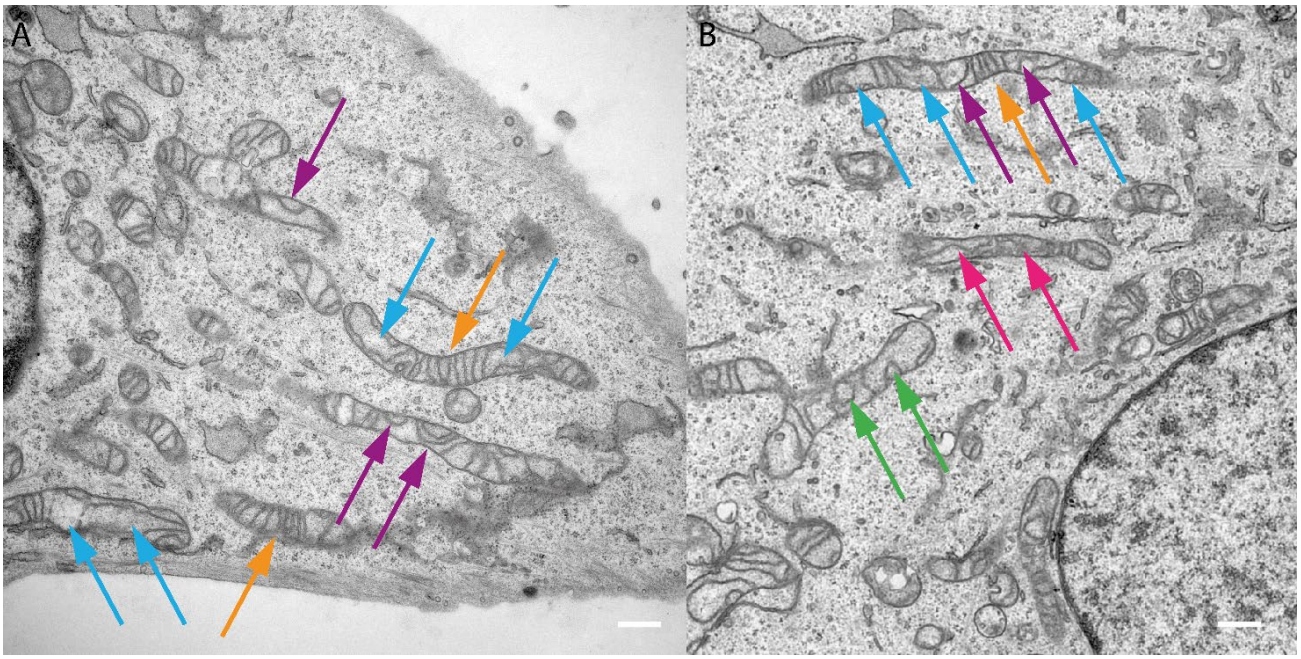

Figure 61). In the perinuclear region the mitochondria appeared rather short, this was due to the orientation of the mitochondria in the axial direction of the image. However, the ultrastructure of mitochondria in conditions of improved respiration was altered. In some areas of the mitochondria the perpendicular orientation of the cristae was kept (

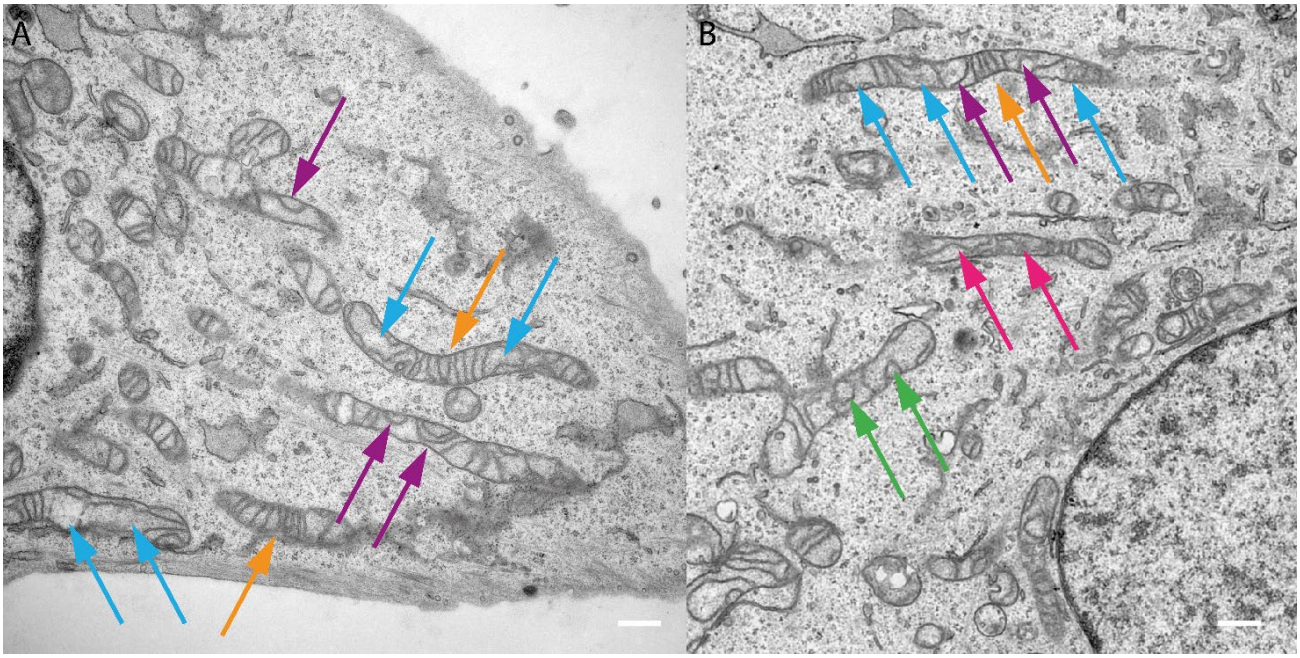

Figure 61A, B, orange arrows). Beside this the IM also became tubular like in starving conditions in some areas (

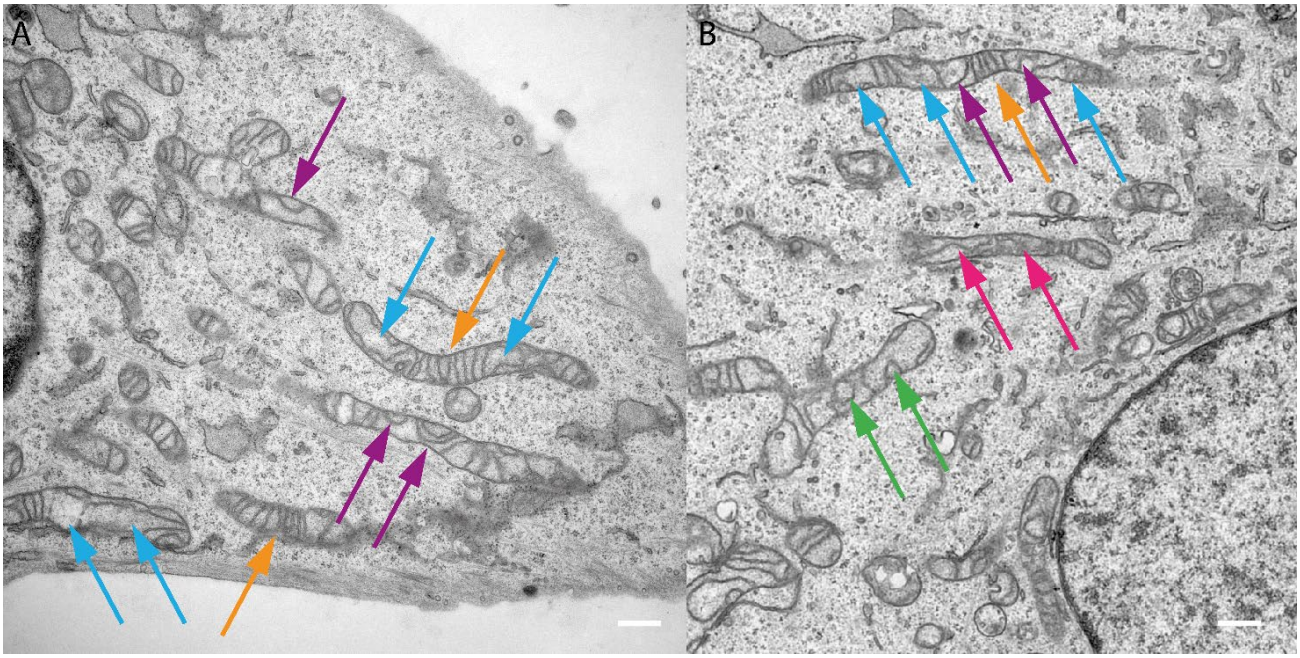

Figure 61A, B, blue arrows). Additionally, in some parts of the same mitochondria cristae occured, which had a curved shape starting and ending at the same site of the IBM (

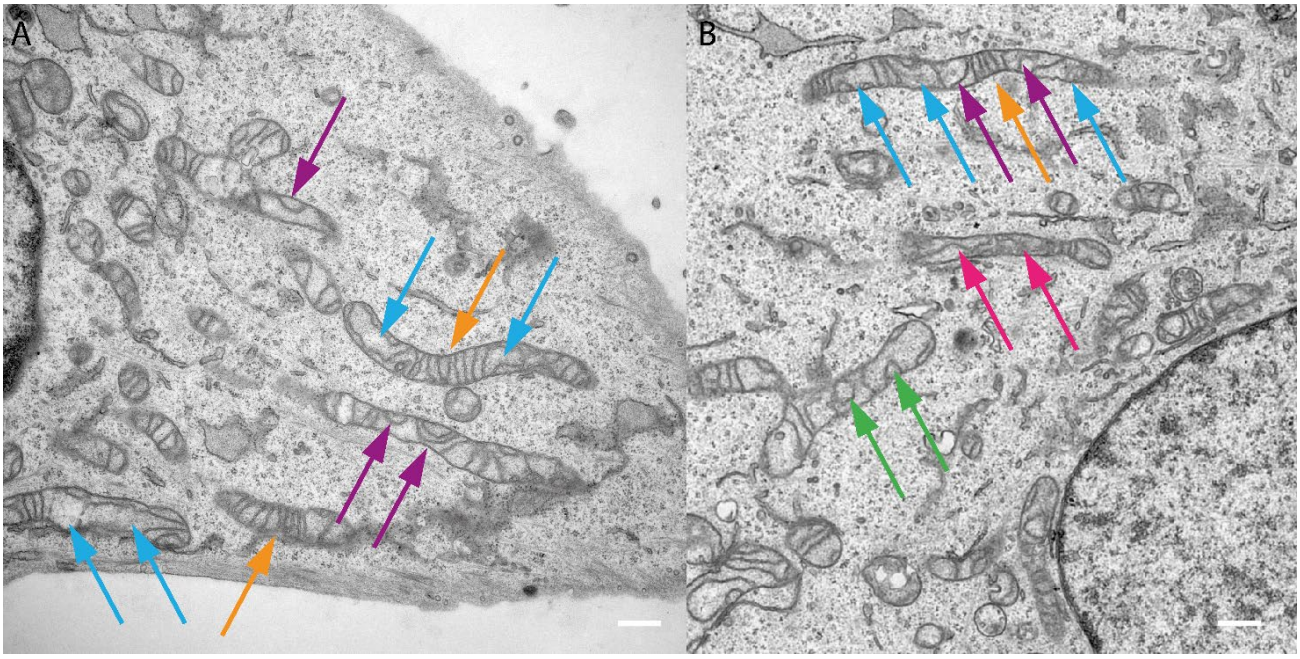

Figure 61A, B, purple arrows) or even occurred in circular / spherical structures (

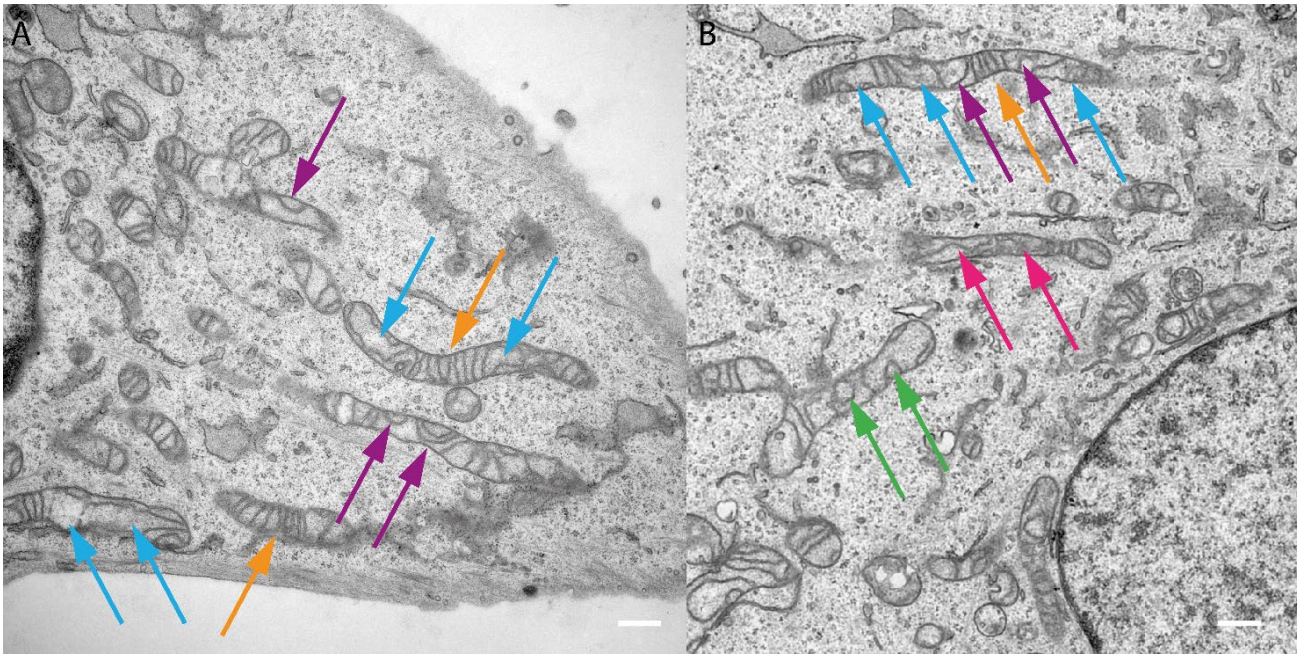

Figure 61A, B, green arrows). In very rare cases cristae followed the longitudinal axis in the middle of a mitochondrion (

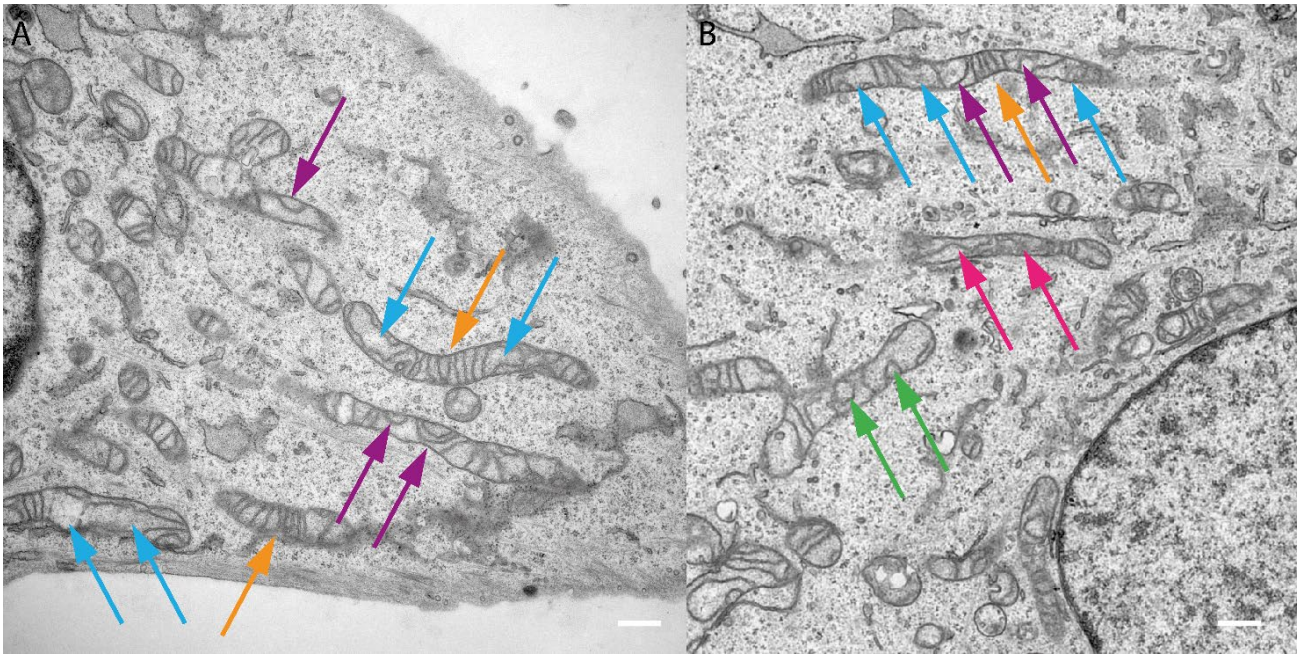

Figure 61A, B, pink arrows).

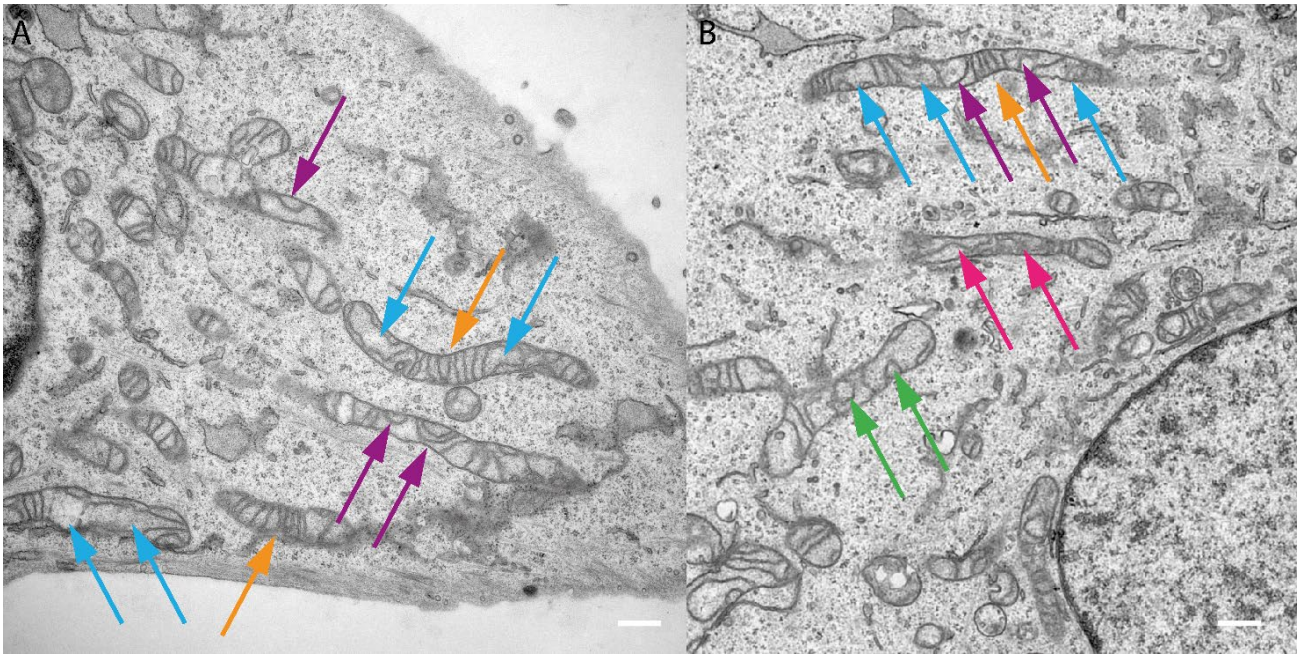

Figure 61 Transmission electron microscopy images of HeLa cells stable transfected with F_1F_O ATP synthase subunit-γ:HaloTag in improved respiration condition
A Mitochondria in improved respiratory conditions. In some parts the regular cristae structure is conserved (orange arrows). In other parts bended and rainbow-like cristae are existent (purple arrows). Additionally, tubular IM shapes can be seen (blue arrows). **B** Another example of mitochondria in improved respiratory conditions. Beside the mentioned cristae shapes in A circular/spherical cristae (green arrows) and cristae following the longitudinal axis (pink arrows) occur, too. (Scale bars: 500 nm, figures shown with the permission of Katharina Psathaki)

9.5 3D TALM of mitochondrial membrane proteins

Mitochondria are 3D cell organelles. In the past, only two-dimensional SPT of mitochondrial proteins has been done. Two-dimensional tracking of proteins in a 3D organelle underestimates the true spatiotemporal protein dynamics especially when proteins diffuse rather fast (Appelhans et al., 2012, Appelhans and Busch, 2017b). In order to overcome this problem, astigmatic distortion of the PSF combined with TALM (3D TALM) was used to reveal the true protein organization of Tom20 and CV-SUγ. The 3D trajectory of a protein is limitd by the 3D space in which the protein moves. In mitochondria this space is predicted by the microcompartments. Thus, a protein diffusing in the OM should result in a trajectory following the tubular shape of the OM. A protein diffusing in the CM should have a trajectory showing a movement along the x. y, and z-axis but being confined by a disc like space - the cristae. Thus, a disc like trajectory could be assumed with most steps following the orientation of the cristae. A protein in the IBM should result in a trajectory reflecting the tubular shape of the IBM. Potentially, 3D TALM should allow to reveal the OM and even the IM shape. If so, 3D TALM should allow to investigate the changes of the IM architecture in living cells due to metabolic switches of cells, as it has been shown by TEM for fixed cells (9.4). In order to analyze the spatiotemporal protein organization and trafficking, only trajectories with a minimal track length of 8 frames were taken into account.

3D TALM of CV-SUγ was analyzed in correlation to the metabolic state. As previously shown starvation of cells led to a switch of CV-SUγ protein organization and trafficking along the IBM due a tubular IM as revealed by TEM images. 3D TALM was used to analyze the spatiotemporal protein organization and trafficking of CV-SUγ during starvation. 3D TALM was tested for its potential to reval changes in the ultrastructural. Tracking CV-SUγ in all three dimensions during starvation should result in a tubular IM if an ultrastructural change of the IM architecture is fullfield. Here, 3D TALM of Tom20 in the tubular OM acted as a control.

Furthermore, 3D TALM was also performed in improved respiration conditions. TEM showed that this metabolic switch leads a re-organization of the ultrastructure. However, TEM uses fixed cells, and analyzing the IM architecture in living cells by SML or SPT was yet not done in 3D. Additionally, the mobility of mitochondrial proteins is underestimated in 2D tracking. 3D TALM allows measuring the true mobility by the 3D D_{app} (D_{3D}). If metabolic switches lead to different D_{3D} will be investigated in chapter 9.5.9.

The used fusion protein constructs were substoichiometrically and posttranslationally labeled with a final concentration of 1 nM TMR^{HTL}. As a control, 3D TALM of mitochondrial proteins in living cells was done in MEM^{++}(1L). In order to investigate mitochondrial protein organization and trafficking during starvation the cells were grown in MEM^{++} and seeded two days before imaging in MEM^{++}(1L). Before imaging the medium was replaced by pure PBS and the cells were incubated at 37° and 5 % CO_2 for 2 h. A metabolic switch of cells to improved respiration conditions was done by growing cells three weeks in the described MEM^{++}(2). Cells grwon in MEM^{++}(2) were seeded in MEM^{++}(2L) two days before imaging in order reduce the background signal. The exposure time in 3D TALM experiments was 16 ms.

9.5.1 Calibration of the astigmatic distortion

The astigmatic distortion of the PSF needed to be calibrated in order to localize and track single molecules in all three dimensions. Here, a sample with monochromatic fluorescent beads was imaged in a z-scan of 4 µm. Only the central 3 µm of the z-scan were used later and the shift of the PSF in focus to the central axial position was corrected (data not shown). The width of the PSF changes with increasing distance to the focal plane (Figure 62, red and black dots). The gained signals were fitted exponential (Figure 62, red and black curves). The resulting fit allowed to calibrate for the distortion of the PSF in dependence of the z-position of the signal to the focal plane. Thus, the axial position of single fluorescent signals could be determined.

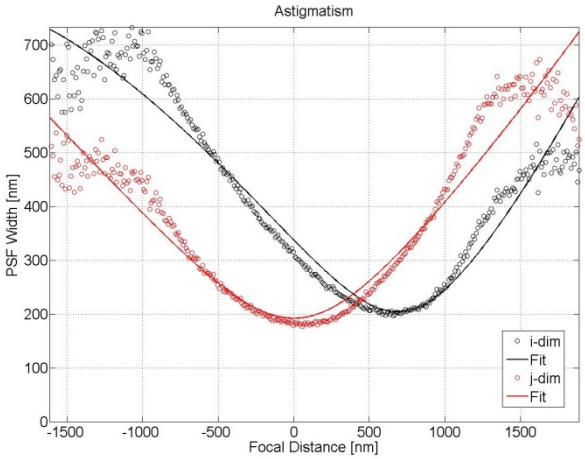

Figure 62 Calibration of the astigmatic point spread function
The astigmatic distortion produces a width of the PSF along the y- and x-axis of the camera which can be calibrated. In the shown diagram a z-scan over 4 µm was performed. Shown here are the central 3 µm. The width of the PSF along the x-axis (i-dim) and the y-axis (j-dim) increase homogenous with distance to the focal plane.

9.5.2 3D axial localization range

3D SML by astigmatic distortion of the PSF results in a spread of the fluorescent signal. Thus, the photons of a signal are redirected so that an elliptic shape of single signals is obtained. The gained PSF can be localized and by the extent of the distortion the relative position of the fluorescent molecule to the focal plane can be calculated. However, the error of localization depends on the signal to background ratio and of the possibility to fit the elliptical shape of the resulting PSF. Thus, a limit of correct localization of fluorescent signals is given. If the photons of one signal are to widely spread the signals is to low in contrast to the background signal to be identified. The 3D axial range a_r of an astigmatic distortion, in which signals can be localized can be calculated, when the distortion is aligned to the lateral axes of the camera, by subtracting the distortion of the PSF along the y-axis δ_y from the distortion of the PSF along the x-axis δ_x:

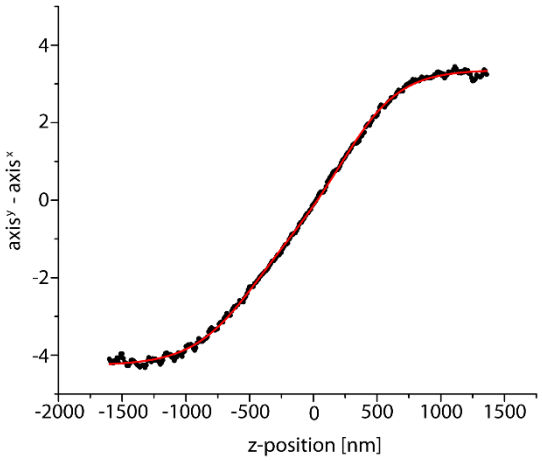

Figure 63 Ideal 3D axial localization range
Astigmatic distortion of the point spread function in the used setup results in a homogenous distortion along the the lateral axis in a z-range of about 500 nm above and below the focal plane. This allows a total axial localization range of 1 µm.

$$a_r = \delta_y - \delta_x \quad (17)$$

In the focal plane this value is 0, with increasing distance to the focal plane this value changes. The resulting data can be plotted in relation to the axial position (

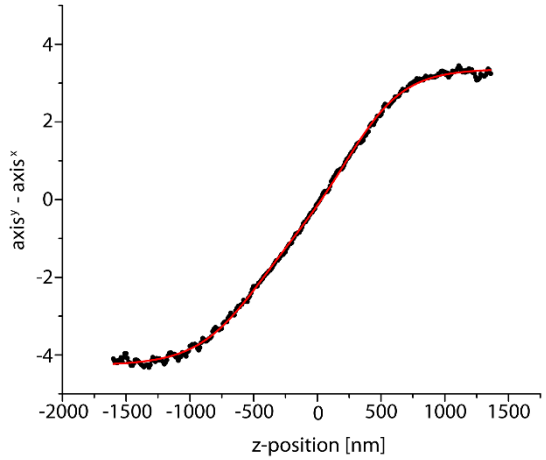

Figure 63). The data was fitted with a sigmoidal function (

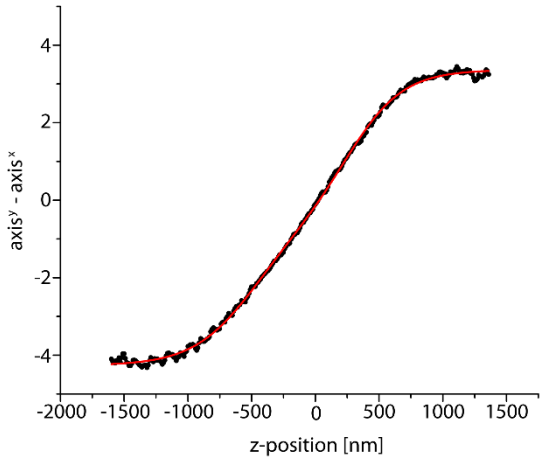

Figure 63, red line). The axial range in which a correct localization could be expected was estimated by this function. The used astigmatic distortion showed an equal distortion along both axes 500 nm above and below the focal plane. This resulted in a total z-range of 1 µm. Healthy mitochondria have a diameter of ≤ 1 µm. Thus, the axial range allowed to image whole mitochondria when the focal plane was set to the middle of the mitochondria. In the cell periphery, mitochondria were oriented nearly parallel to the focal plane. For this reason, mitochondria and mitochondrial networks were imaged only in the cell periphery reducing false localizations of signals in mitochondria above or below the ideal axial range. The certainty if mitochondria were imaged in this range could only be proven after reconstructing the 3D localized signals. Thus, single molecule signals of separated mitochondria showing no overlap were recorded and the localized signals were reconstructed. The resulting reconstruction of the individual mitochondria was used as a quality control. Here, mitochondria which had too curved a shape along the z-axis of a reconstruction and / or extending the ideal range and mitochondria which had too large a diameter were excluded from further analysis.

9.5.3 3D localization precision

The localization precision in each dimension was directly extracted from the data by equation (16). In order to calculate the ith dimensional localization precision the ith dimensional MSD of 87227 individual trajectories of 161 cells was plotted over time and the resulting lateral and axial localization precisions of each experiment were

averaged. The histograms of localization precisions are plotted in

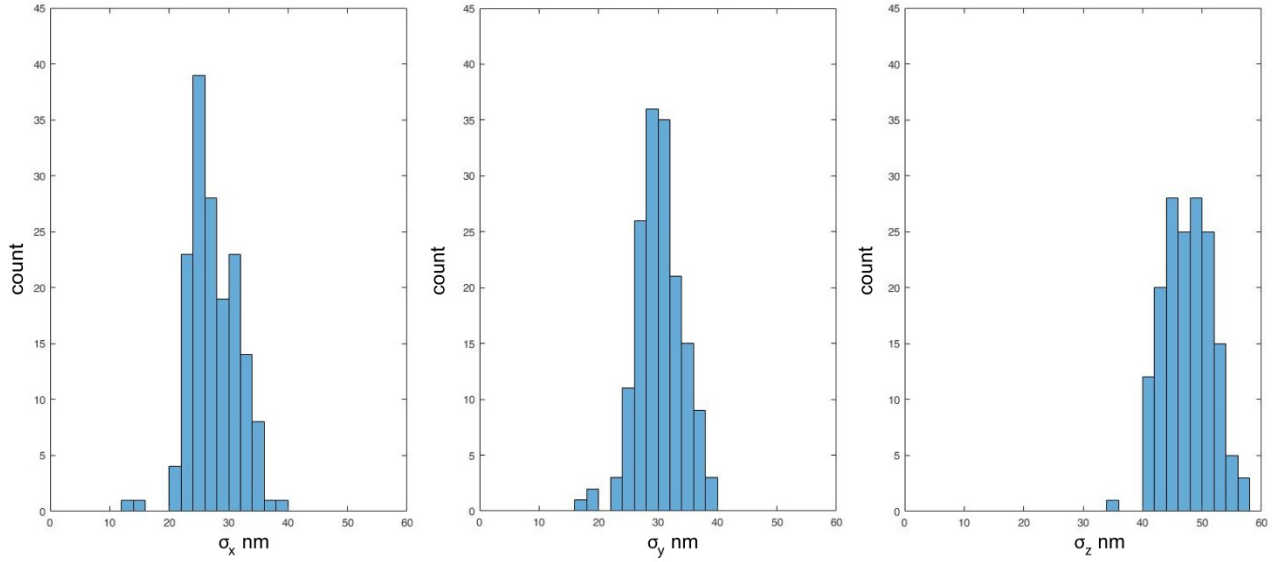

Figure 64. The mean lateral localization precision in x (σ_x) was 27.44 ± 4.04 nm, the mean lateral localization precision in y (σ_y) was 30.23 ± 3.70 nm and the mean axial localization precision (σ_z) was 47.54 ± 4.05 nm. Those values were used in all 3D reconstrcutions in the following chapters.

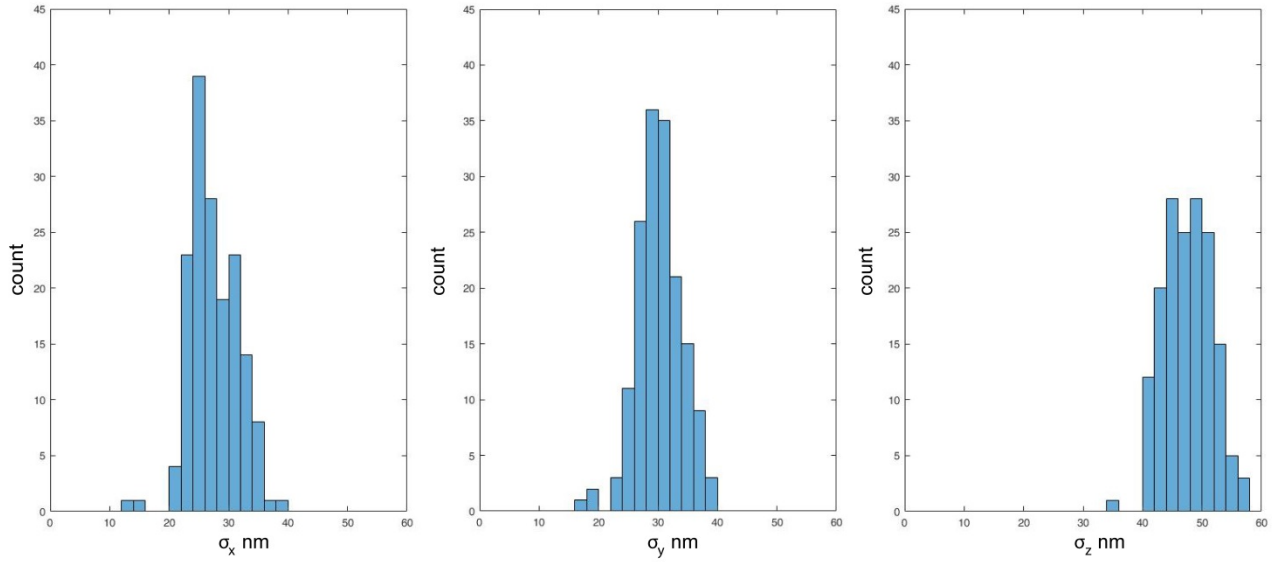

Figure 64 Localization precision in all three dimensions
3D TALM experiments reach a mean localization precision of σ_x = 27.44 ± 4.04 nm (left panel), σ_y = 30.23 ± 3.70 nm (central panel) and σ_z = 47.54 ± 4.05 nm (right panel). The values were extracted from 87227 single trajectories in 161 cells.

9.5.4 3D TALM of Tom20

9.5.4.1 3D reconstruction of mitochondria by 3D single molecule localization of Tom20

Tom20 is localized in the OM of mitochondria. The OM is a tubular membrane. 3D SML of Tom20 should allow to reconstruct the tubular shape of the OM.

Shown Fehler! Verweisquelle konnte nicht gefunden werden. is a large mitochondrial network resulting from the reconstruction of 26060 3D SML of Tom20. The imaged area is about 400 µm². The 3D reconstruction of the mitochondrial network imaged in the cell periphery measured 1.33 µm z-range (Fehler! Verweisquelle konnte nicht gefunden werden.C). Thus, only the localization in the axial center fitted in the ideal imaging range. However, in Fehler! Verweisquelle konnte nicht gefunden werden.A,B a top view of a mitochondrial network is shown. At several mitochondria an accumulation of localizations along the outline of mitochondria can be seen. Here, localizations in the OM of mitochondria lay above each other. However, these areas show a perfect match of the focal plane to the axial middle of a imaged nd reconstructed mitochondrion. This indicates that also large areas in living cells can be successfully imaged and reconstructed in all three dimensions. Nevertheless, small areas, where a perfect alignment of the focal plane to mitochondria was successful, makes it easier to analyze the spatiotemporal organization of proteins in all three dimensions qualitatively. Areas which show a clear accumulation of Tom20 to the outside of mitochondria directly reveal the tubular shape of the OM, but often lack enough localizations above and below the

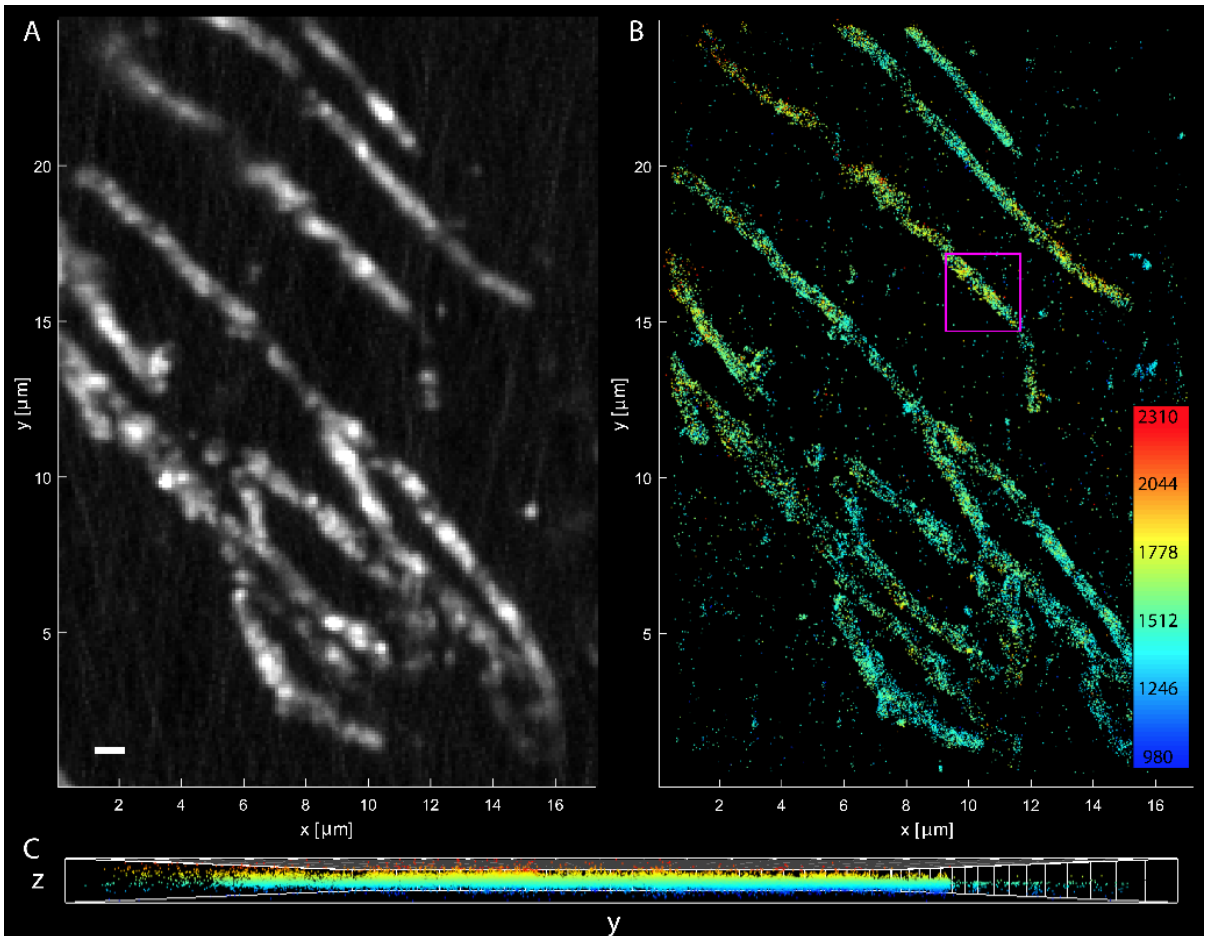

Figure 65 3D reconstruction of a mitochondrial network by Tom20 localizations
A Summed signal of the raw data. Scale bar: 1 µm **B** 3D reconstruction of the imaged mitochondria. The shown reconstruction consists of 26060 localizations. The whole area measured about 400 µm² and measured 1.33 µm in z. **C** Y, z-view of the 3D reconstruction

focal plane to reconstruct the tubular OM structure completely. In order to test if areas without accumulations at the outside of the mitochondrion can be used to reconstruct the tubular OM a region of interest (ROI) was picked out (Fehler! Verweisquelle konnte nicht gefunden werden**.,** pink square, **Fehler! Verweisquelle konnte nicht gefunden werden.**). In this area localizations from the bottom to the top of the mitochondrion were obtained and the middle of the reconstruction lies in the middle of the mitochondrion (**Fehler! Verweisquelle konnte nicht gefunden werden.**B, C). This area included 574 single localizations. However, the 3D reconstruction of the ROI did not allow to reveal the hollow tube that the OM alone is (**Fehler! Verweisquelle konnte nicht gefunden werden.**D). Nevertheless, to demonstrate that areas with accumulations at the outside of mitochondria and enough localizations above and below the focal plane another mitochondrial network is in Figure 67 3D reconstruction of the OM by 3D single molecule localization of Tom20

A Summed signals of raw data. Scale bar: 1 µm B 3D reconstruction of 6956 single localizations. The color code shows a strong curved mitochondrion in axial direction. The top view shows also a strong lateral curvature s. A single part of the mitochondrion is perfectly aligned to the focal plane (purple square) C The 200 nm slice in the middle of the ROI (purple square) demonstrates that 3D reconstruction allows to reveal the hollow shape of the OM in living cells.. Shown in Figure 67 3D reconstruction of the OM by 3D single molecule localization of Tom20

A Summed signals of raw data. Scale bar: 1 µm B 3D reconstruction of 6956 single localizations. The color code shows a strong curved mitochondrion in axial direction. The top view shows also a strong lateral curvature s. A single part of the mitochondrion is perfectly aligned to the focal plane (purple square) C The 200 nm slice in the middle of the ROI (purple square) demonstrates that 3D reconstruction allows to reveal the hollow shape of the OM in living cells.A is a diffraction limited image. The imaged area measured about 31.5 µm^2. The 3D reconstruction of 6956 single localizations is shown (Figure 67 3D reconstruction of the OM by 3D single molecule localization of Tom20

A Summed signals of raw data. Scale bar: 1 µm B 3D reconstruction of 6956 single localizations. The color code shows a strong curved mitochondrion in axial direction. The top view shows also a strong lateral curvature s. A single part of the mitochondrion is perfectly aligned to the focal plane (purple square) C The 200 nm slice in the middle of the ROI (purple square) demonstrates that 3D reconstruction allows to reveal the hollow shape of the OM in living cells.B). This reconstruction shows the power of 3D reconstruction of 3D TALM data. In the top left part the mitochondrion gets out of focus. This can be seen by the dim intensity in Figure 67 3D reconstruction of the OM by 3D single molecule localization of Tom20

A Summed signals of raw data. Scale bar: 1 µm B 3D reconstruction of 6956 single localizations. The color code shows a strong curved mitochondrion in axial direction. The top view shows also a strong lateral curvature s. A single part of the mitochondrion is perfectly aligned to the focal plane (purple square) C The 200 nm slice in the middle of the ROI (purple square) demonstrates that 3D reconstruction allows to reveal the hollow shape of the OM in living cells.A and the z-position of the localizations in Figure 67 3D reconstruction of the OM by 3D single molecule localization of Tom20

A Summed signals of raw data. Scale bar: 1 µm B 3D reconstruction of 6956 single localizations. The color code shows a strong curved mitochondrion in axial direction. The top view shows also a strong lateral curvature s. A single part of the mitochondrion is perfectly aligned to the focal plane (purple square) C The 200 nm slice in the middle of the ROI (purple square) demonstrates that 3D reconstruction allows to reveal the hollow shape of the OM in living cells.B, C. Here, the color code turns to the blue which are localizations at the lower reconstructed axial

position. However, the purple square shows a ROI with typical OM enrichment of signals at the outside of the mitochondrion. Although many localizations can be obtained at the top and bottom side of the 3D reconstruction (Figure 67 3D reconstruction of the OM by 3D single molecule localization of Tom20

A Summed signals of raw data. Scale bar: 1 µm B 3D reconstruction of 6956 single localizations. The color code shows a strong curved mitochondrion in axial direction. The top view shows also a strong lateral curvature s. A single part of the mitochondrion is perfectly aligned to the focal plane (purple square) C The 200 nm slice in the middle of the ROI (purple square) demonstrates that 3D reconstruction allows to reveal the hollow shape of the OM in living cells.B, purple square). In order to reveal a hollow OM tube a z-slice of 200 nm has been chosen leaving 1580 single localizations (Figure 67 3D reconstruction of the OM by 3D single molecule localization of Tom20

A Summed signals of raw data. Scale bar: 1 µm B 3D reconstruction of 6956 single localizations. The color code shows a strong curved mitochondrion in axial direction. The top view shows also a strong lateral curvature s. A single part of the mitochondrion is perfectly aligned to the focal plane (purple square) C The 200 nm slice in the middle of the ROI (purple square) demonstrates that 3D reconstruction allows to reveal the hollow shape of the OM in living cells.C). The strong accumulation of signals, at the outline of the mitochondrion against the few signals in the inside demonstrates the hollow shape of the OM in the imaged mito chondria. This indicates that focusing on single mitochondria in order to reveal the structure by 3D reconstruction can beneficial.

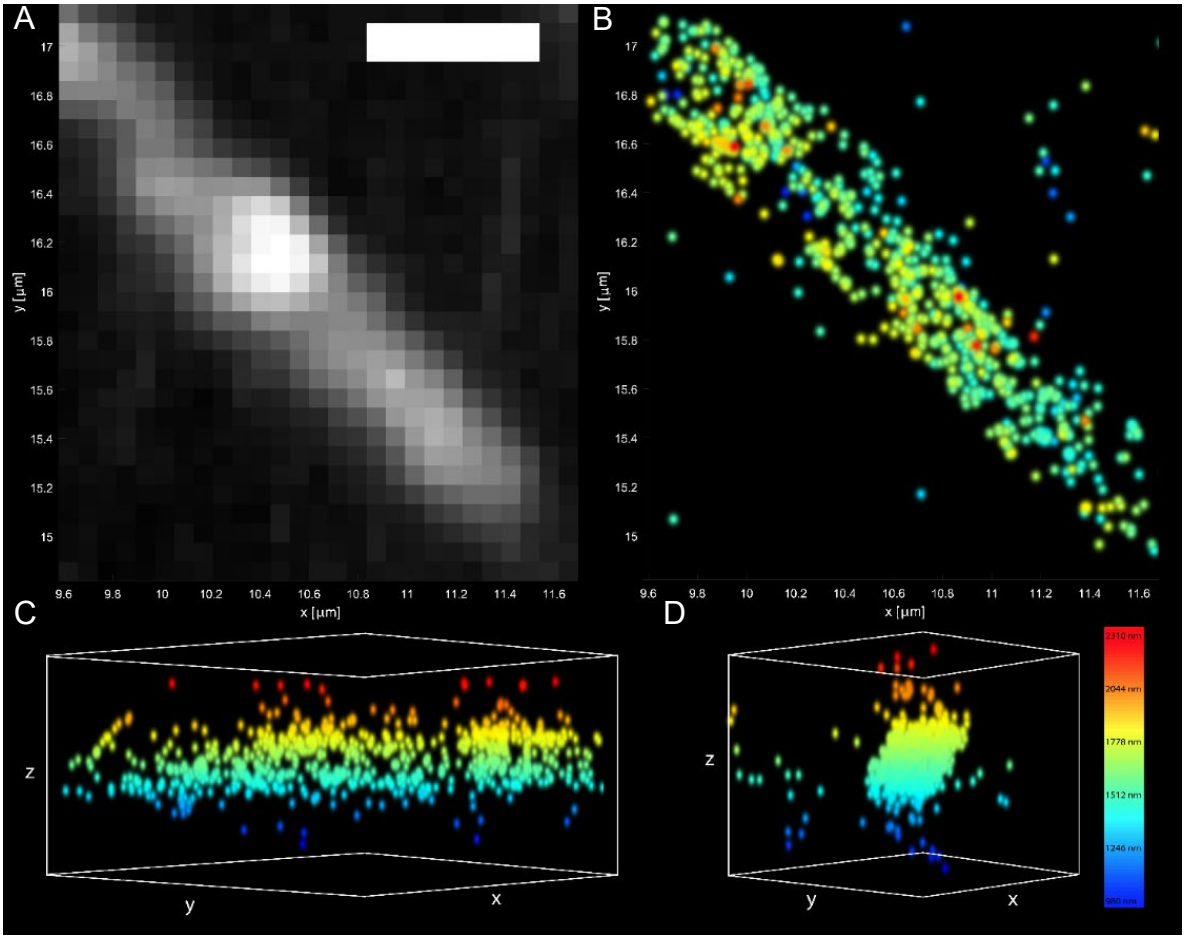

Figure 66 3D reconstruction of a single mitochondrion by 3D single molecule localization of Tom20
A Diffraction limited image of the mitochondrion in the ROI of **Fehler! Verweisquelle konnte nicht gefunden werden.** by summed signals of the data. Scale bar: 1 µm **B** X, y-view of the 3D reconstruction of the imaged mitochondrion in the ROI. The shown reconstructions consist of 574 localizations. **C** X, y, z-view of the 3D reconstruction from the side of the mitochondrion. **D** X, y, z-view of the 3D reconstruction along the longitudinal axis of the mitochondrion.

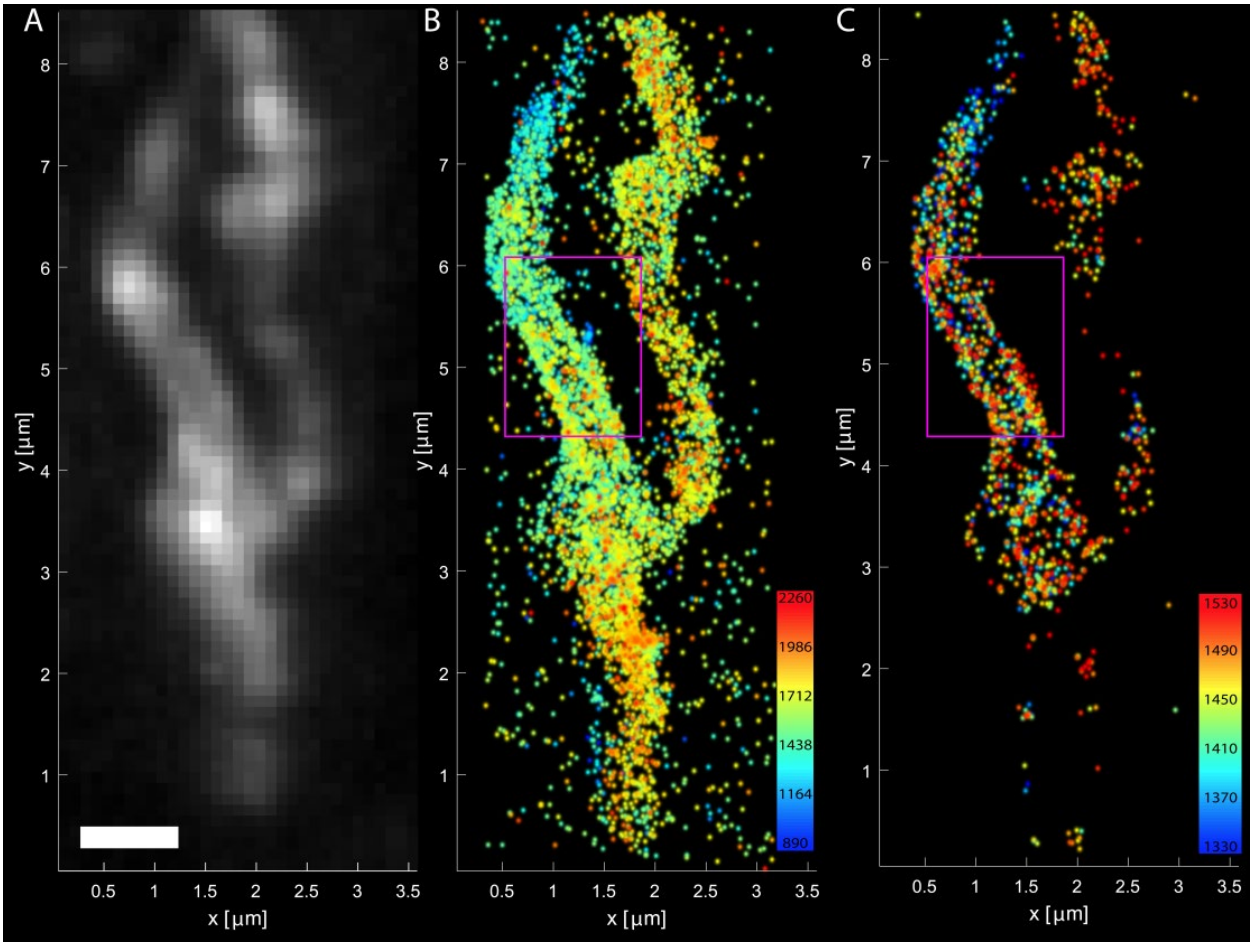

Figure 67 3D reconstruction of the OM by 3D single molecule localization of Tom20
A Summed signals of raw data. Scale bar: 1 µm **B** 3D reconstruction of 6956 single localizations. The color code shows a strong curved mitochondrion in axial direction. The top view shows also a strong lateral curvature s. A single part of the mitochondrion is perfectly aligned to the focal plane (purple square) **C** The 200 nm slice in the middle of the ROI (purple square) demonstrates that 3D reconstruction allows to reveal the hollow shape of the OM in living cells.

9.5.4.2 3D single particle tracking of Tom20

The focus of 3D SPT relied on the parts of the mitochondrial network which were in focus. The previously show dataset (Fehler! Verweisquelle konnte nicht gefunden werden.) of Tom20, where hardly no tubular structure was obtained in the reconstruction, was analyzed by 3D SPT. 3D SPT of proteins excludes single localization events as a trajectory consists of multiple localizations and the steps in between. As mentioned previously only trajectories with a minimal length of 8 frames / lifetime of 128 ms were taken into account. The shown dataset in Figure 68 consists of 355 trajectories. The axial color code shows that the lower right part of the trajectory map is slightly below the focal plane because mostly cyan colored trajectories are seen. The rest of the image is in focus or slightly above the focal plane. However, in order to clarify if 3D SPT allows to reveal the hollow shape of mitochondria where 3D reconstruction failed to reveal the tubular shape of the OM (Fehler! Verweisquelle konnte nicht gefunden werden., pink square, **Fehler! Verweisquelle konnte nicht gefunden werden.**) 3D SPT data of this ROI was performed (Figure 69). Here 24 trajectories in a ~ 2.82 µm long mitochondrial segment are plotted. 3D SPTallowed to reveal the tubular shape of the mitochondrion demonstration the power and possibilities of 3D TALM by astigmatic distortion of the PSF. However, the trajectories of Tom20 in Figure 69B show a random diffusion along

the mitochondrion. In Figure 69C the 3D trajectory map is turned to a y, z-view demonstrating that the mitochondrion was nearly parallel to the focal plane. Furthermore, the trajectories are in a z-range of approximately 500 nm. This showed that the OM of this mitochondrial part has a diameter of approximately 500nm. In Figure 69D the 3D trajectory map is turned to a x, y, z-view with the line of sight along the longitudinal axis of the mitochondrion. This view reveals that trajectories of Tom20 trace the tubular OM and reveal the hollow shape of the OM. This shows that 3D SPT is beneficial in order to draw conclusions of the shape of sub-compartments like the OM in living cells. Furthermore, in short mitochondria only a small number of trajectories is enough to reveal the OM shape. The same procedure was performed of the previously shown 3D TALM data in Figure 67 3D reconstruction of the OM by 3D single molecule localization of Tom20

A Summed signals of raw data. Scale bar: 1 µm B 3D reconstruction of 6956 single localizations. The color code shows a strong curved mitochondrion in axial direction. The top view shows also a strong lateral curvature s. A single part of the mitochondrion is perfectly aligned to the focal plane (purple square) C The 200 nm slice in the middle of the ROI (purple square) demonstrates that 3D reconstruction allows to reveal the hollow shape of the OM in living cells. (Figure 70). In the trajectory map the upper left corner again shows a mitochondrial part getting out of focus as the number of blue trajectories / trajectories below the focal plane increased. Simultaneously the other branch of the mitochondrion stayed in focus (Figure 67 3D reconstruction of the OM by 3D single molecule localization of Tom20

A Summed signals of raw data. Scale bar: 1 µm B 3D reconstruction of 6956 single localizations. The color code shows a strong curved mitochondrion in axial direction. The top view shows also a strong lateral curvature s. A single part of the mitochondrion is perfectly aligned to the focal plane (purple square) C The 200 nm slice in the middle of the ROI (purple square) demonstrates that 3D reconstruction allows to reveal the hollow shape of the OM in living cells.**Fehler! Verweisquelle konnte nicht gefunden werden.**B, Figure 70). However, the focus of interest lies again on the region where accumulations of localizations at the outline of the mitochondria were found in the reconstruction of Figure 67 3D reconstruction of the OM by 3D single molecule localization of Tom20

A Summed signals of raw data. Scale bar: 1 µm B 3D reconstruction of 6956 single localizations. The color code shows a strong curved mitochondrion in axial direction. The top view shows also a strong lateral curvature s. A single part of the mitochondrion is perfectly aligned to the focal plane (purple square) C The 200 nm slice in the middle of the ROI (purple square) demonstrates that 3D reconstruction allows to reveal the hollow shape of the OM in living cells. (Figure 70, pink square). This ROI is enlarged in Figure 71A showing the top view of the obtained 3D trajectory map. In Figure 71B the sight of view follows again the longitudinal axis of the mitochondrion. Again, the hollow shape of the tubular OM in a living cell could be revealed by the trajectories of Tom20 proteins. 3D TALM allowed to investigate the true D_{3D} of a protein. TALM predicted a 3D corrected value of the D_{app} of 0.215 $\mu m^2/s$ in

dependence of the mitochondrial diameter (Appelhans et al., 2012). 3DTALM of Tom20 resulted in an D_{3D} of 0.231 ± 0.056 µm²/s, fitting the corrected value of the D_{app} in TALM.

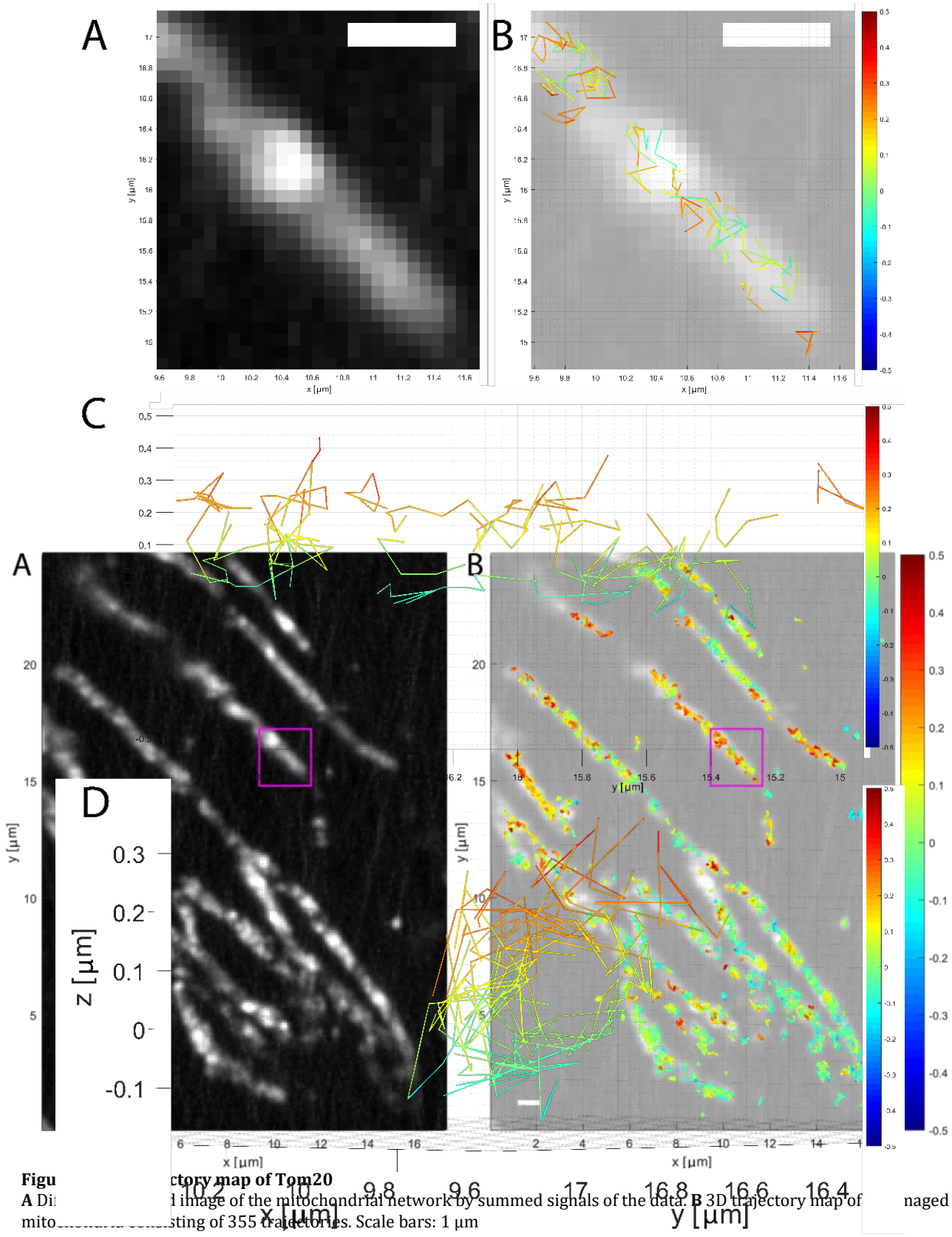

Figu **ctory map of Tom20**
A Di l image of the mitochondrial network by summed signals of the data. **B** 3D trajectory map of naged mito sting of 355 trajectories. Scale bars: 1 µm

Figure 69 Enlarged trajectory map of the of the ROI in Fehler! Verweisquelle konnte nicht gefunden werden.
A Diffraction limited image of the ROI from Figure 68 of the summed signals. Scale bar: 1 µm. **B** Overlay of the trajectory map of

the ROI from Figure 68 with the diffraction limited image from A. Scale bar: 1 µm. **C** Y, z-view of the trajectory map shown in B. Most of the trajectories are in the range of -100nm to 350 nm so slightly above the focal plane. **D** X, y, z-view of the trajectory map shown in A. The line of sight follows the longitudinal axis of the mitochondrion. This view reveals the tubular shape of the OM. The trajectory traces the hollow shape of the OM.

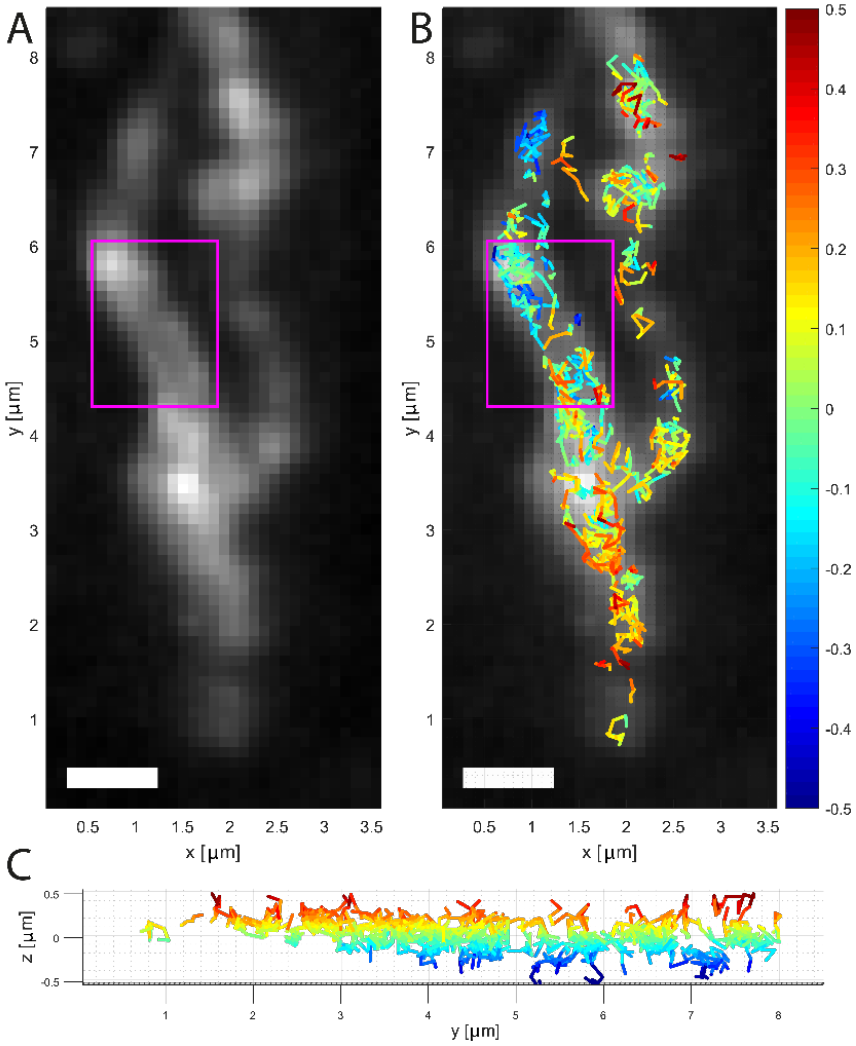

Figure 70 3D trajectory map of Tom20
A Diffraction limited image of the ROI from **Fehler! Verweisquelle konnte nicht gefunden werden.** of the summed signals. **B** X, y-view of the trajectory map of Tom20 proteins tracked in the mitochondria shown in A. **C** Y, z-view of the tractor map shown in B. Scale bars: 1 µm

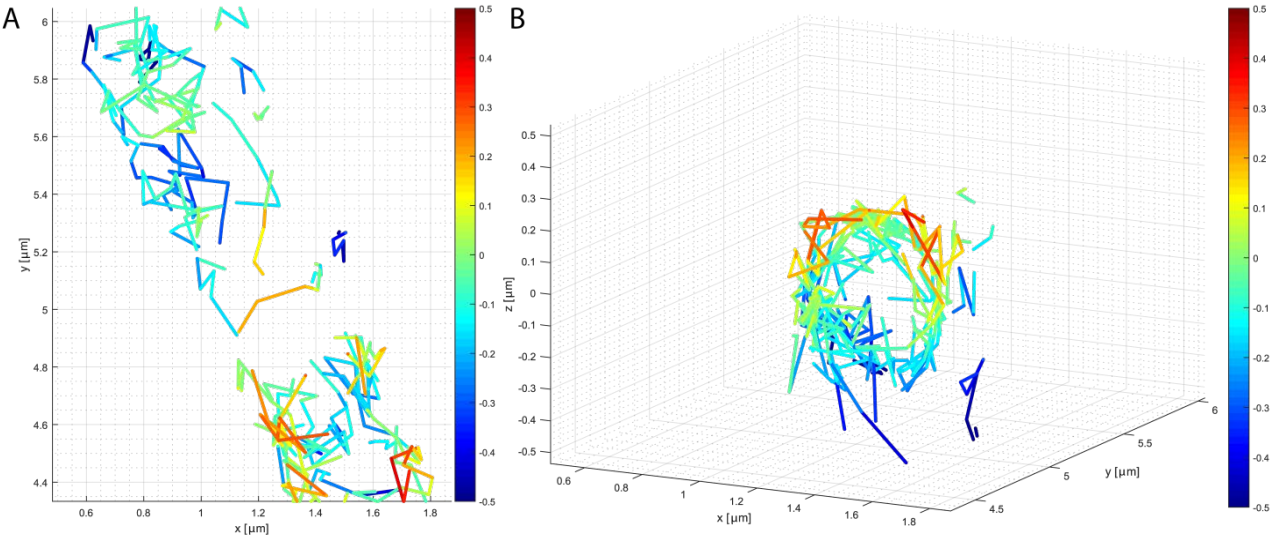

Figure 71 Enlargement of the ROI in Figure 70 Fehler! Verweisquelle konnte nicht gefunden werden.
A Top view of the ROI. **B** Side view with the line of sight along the longitudinal axis of the imaged mitochondria. Here the hollow shape of the OM is revealed. The trajectories of Tom20 trace the tubular OM and allow to draw the shape of the microcompartment, the OM.

9.5.5 3D TALM of F_1F_O ATP synthase subunit-γ

9.5.5.1 3D reconstruction of the inner membrane by 3D single molecule localization of the F_1F_O ATP synthase subunit-γ

The OM shape could be revealed by 3D TALM. The next challenge was to investigate if the IM, with its multiple invaginations and complex shape could also be revealed by 3D TALM. Therefore CV-SUγ 3D TALM was performed as before.

Shown in

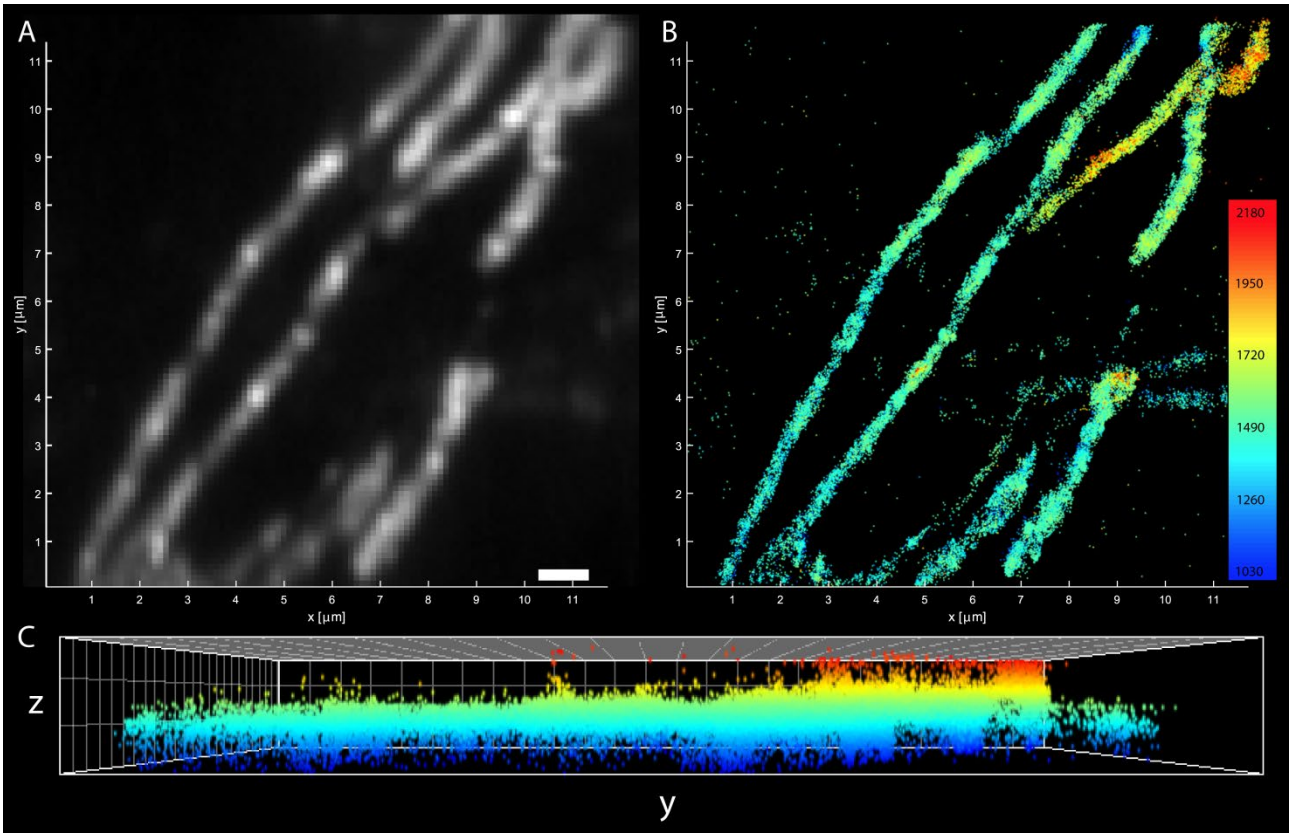

Figure 72 is large area of ~ 144 µm2 in the cell peripherie. In this area a network of elongated mitochondria was imaged. The reconstruction in

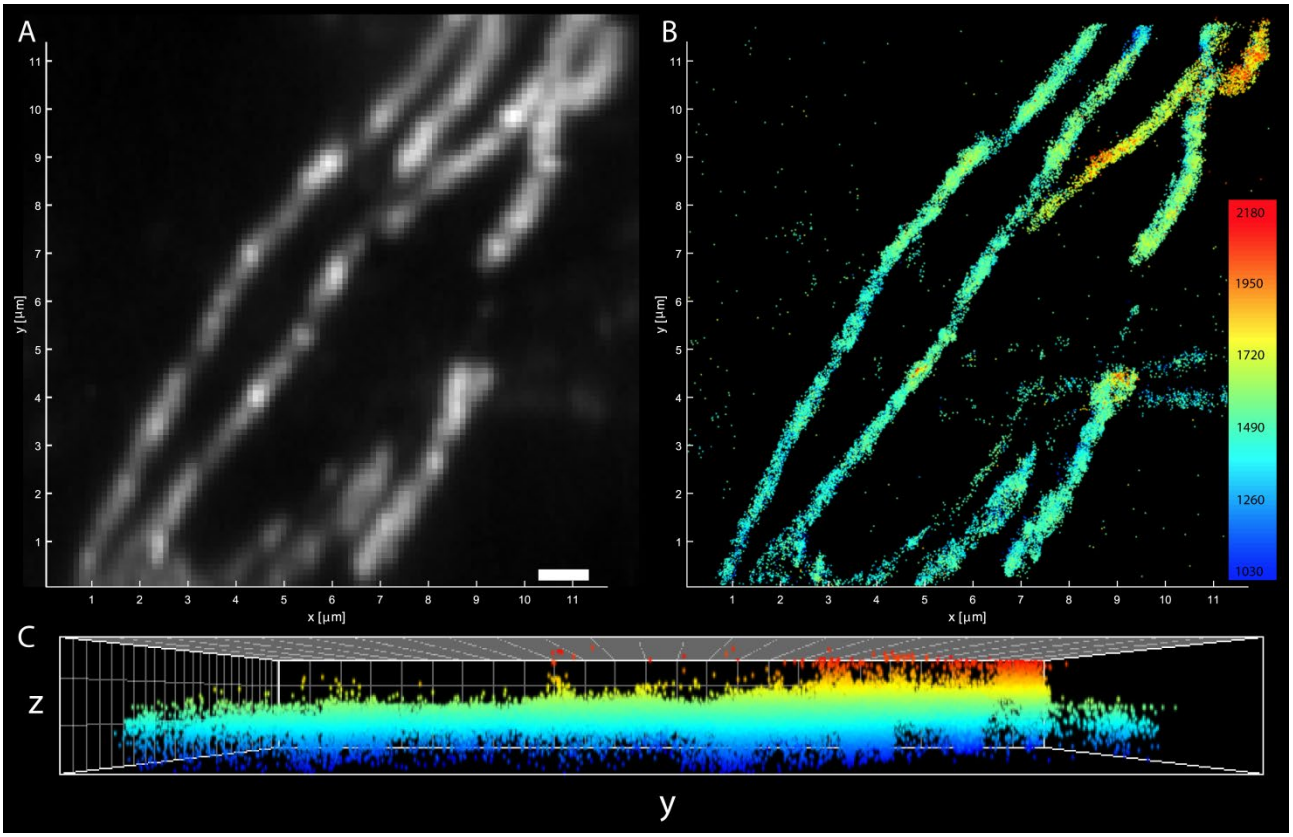

Figure 72B consist of 37652 3D localizations. As the reconstruction in

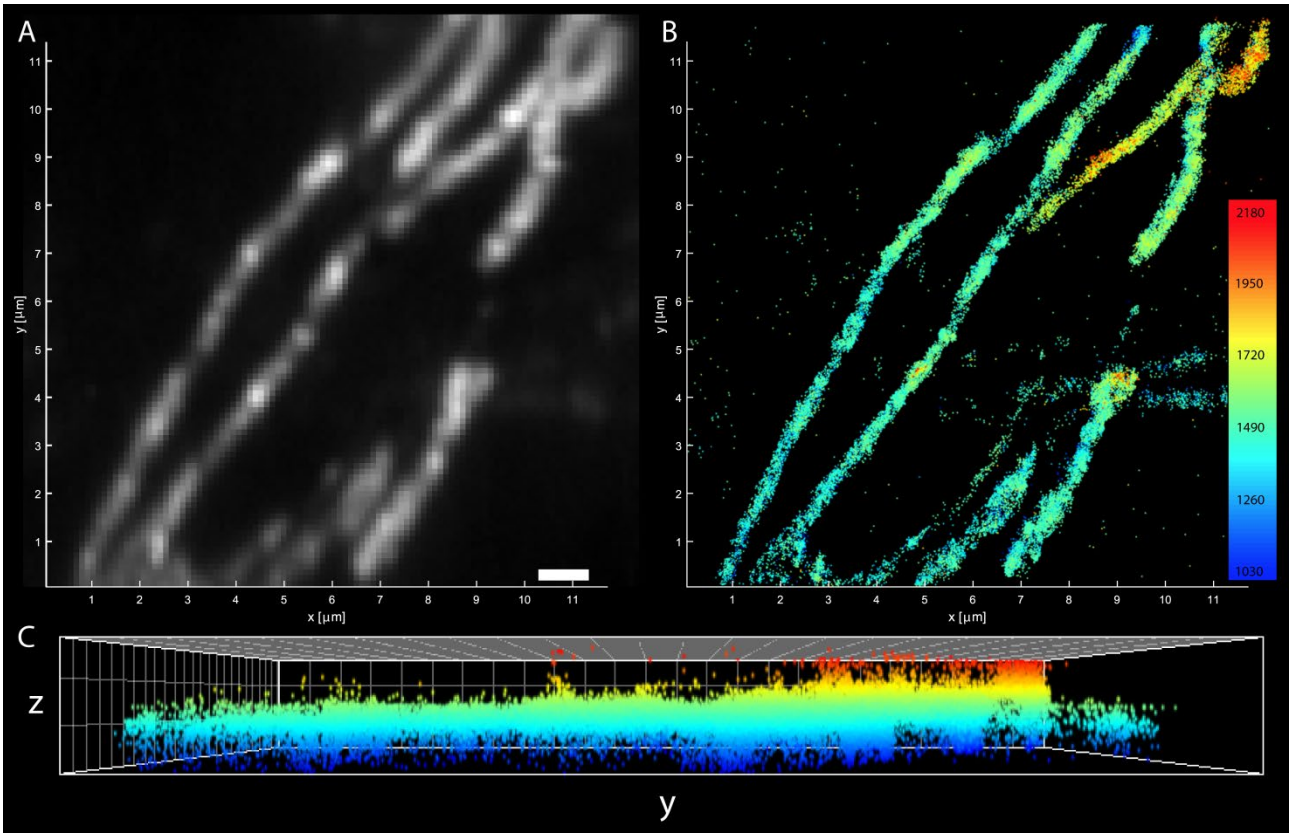

Figure 72B and C shows most of the mitochondrial network is oriented parallel to the focal plane. In the upper right corner of the reconstruction two mitochondria lie above each other. Beside this, this 3D reconstructions of a mitochondrial network via 3D localization of CV-SUγ do not show accumulations at the outline of mitochondria , as

expected (Figure 72B). Localizations of CV-SUγ are found in all mitochondria. However, the distribution of localizations is not homogenous along the mitochondrial network. In some part only a few localizations can be seen. In other parts localizations seem so be enriched. This indicates parts of the IM with less cristae, thus less localizations of CV-SUγ and vice versa. Focussing on single mitochondria allows to take a closer look on the spatiotemporal organization of CV-SUγ in detail (Figure 73). The reconstruction in Figure 73A shows the localization of CV-SUγ in the IM. Here, 17097 localizations were used the reconstruction. In some cases, accumulations of CV-SUγ localizations with a per-

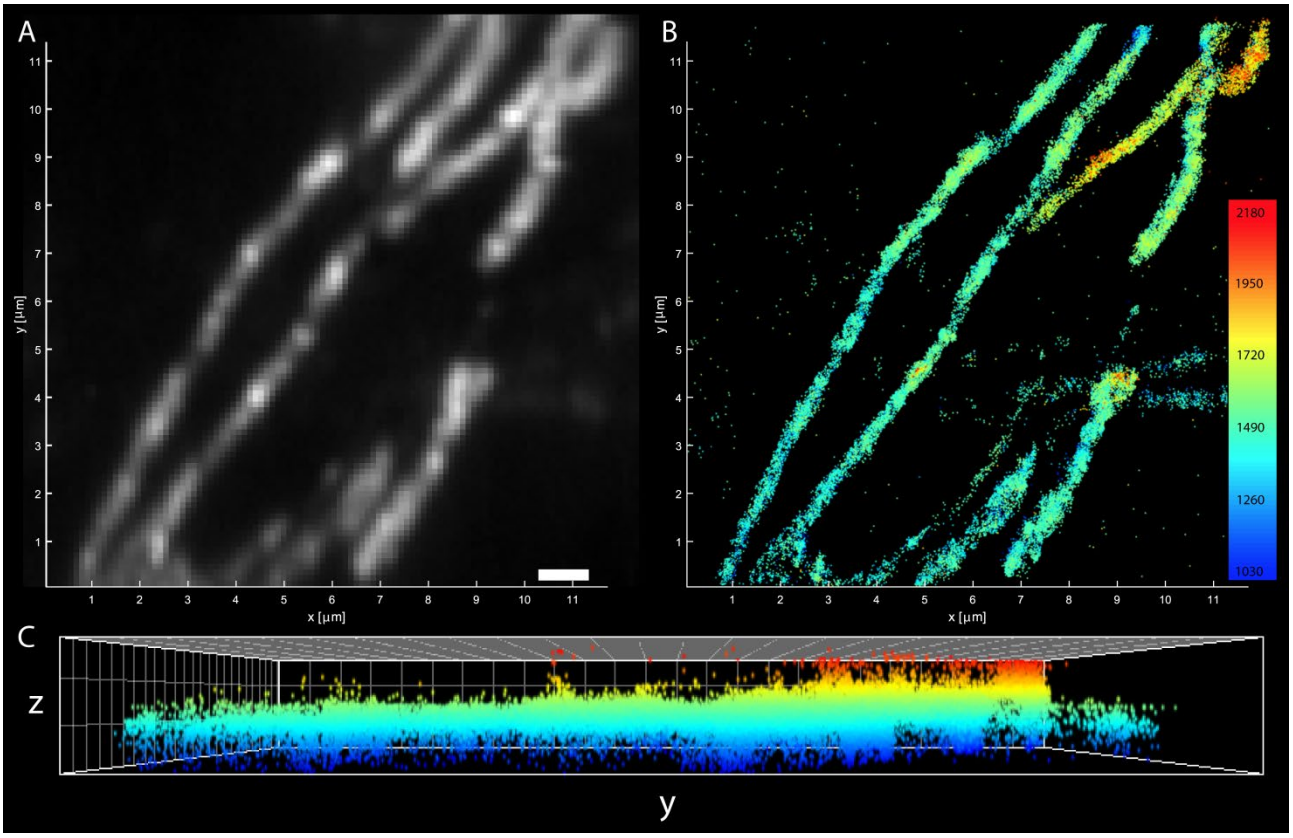

Figure 72 3D reconstruction of a mitochondrial network via 3D localized F_1F_0 ATP synthase subunit-γ
A Summed raw data image of CV-SU. The mitochondrial network was imaged in the periphery of a cell. Scale bar: 1 µm. **B** 3D reconstruction of the mictochondrial network shown in A. Most of the mitochondria lie parallel to the focal plane. In the upper right corner, some mitochondria lie above each other. **C** Y, z-view of the imaged mitochondria.

pendicular orientation and / or crossing the hole reconstrcution can be seen. In order to investigate if the mitochondrion has a non-hollow shape as expected for the IM in control experiments and whether the accumulations also occur in the middle of mitochondria a 200 nm slice in the middle of the reconstruction was taken (Figure 73B). The reconstruction of the slice includes 8356 localizations of CV-SUγ. This slice of the reconstruction reveals a non-hollow shape of the IM in the control experiments. Furthermore, it shows that the accumulations seen in Figure 73A expand through the entire mitochondrion. These accumulations reflect localizations in the CM. The y, z-view of the reconstruction shows that the mitochondria lay perfect in focus and have no curvy structure along the z-axis (Figure 73C). Unfortunately, 3D TALM did not reveal the IM architecture in detail, as a lot of localizations were between the described accumulations. Here, a quality sorting of 3D localizations can be a development for the future. However, 3D SPT is also a way to select certain localizations, as localizations of proteins which occurred only in single frame are not taken into account.

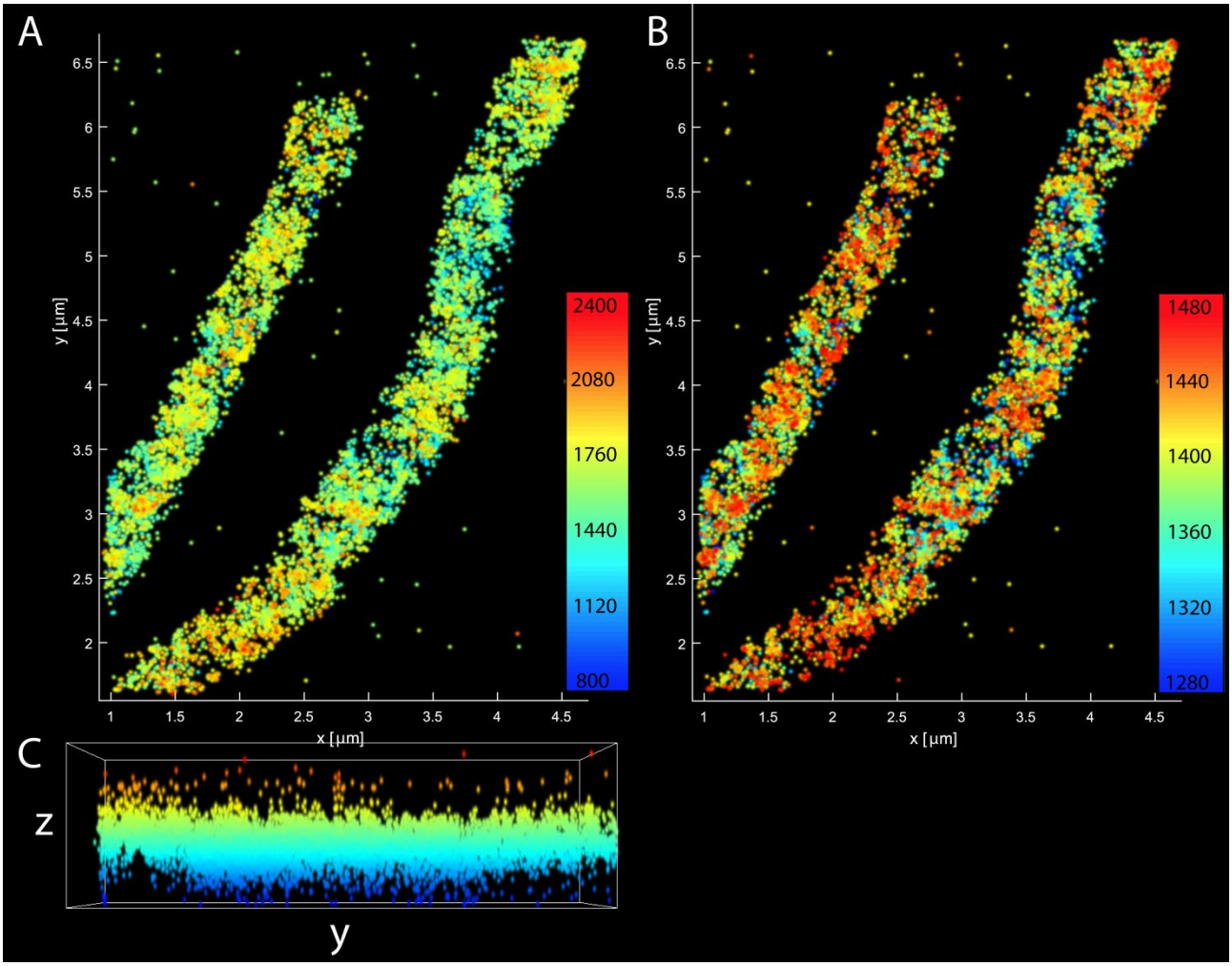

Figure 73 3D reconstruction of mitochondria by 3D single molecule localization of the F_1F_0 ATP synthase subunit-γ
A Reconstruction of two single mitochondria by CV-SUγ localizations. **B** 200 nm slice of the reconstruction shown in A. **C** Y,z-view of the reconstruction shown in A.

9.5.5.2 3D single particle tracking of the F_1F_O ATP synthase subunit-γ

3D SPT of CV-SUγ in the control experiments shows that CV-SUγ is non-homogenously organized in the IM (Figure 74). In this trajectory map trajectories with a minimal lifetime of 8 frames / 128 ms are shown. Some parts show a large number of trajectories. In contrast to this, other parts do completely lack trajectories of CV-SUγ (Figure 74B). So, CV-SUγ seemed to stick to certain areas in the mitochondria and or even were hindered in diffusion along the entire mitochondrial network. .

However, in order to examine the 3D spatiotemporal protein organization of CV-SUγ a focus on single mitochondria is necessary. As an example, the 3D tracking result of the small mitochondrion shown in Figure 73 was performed (

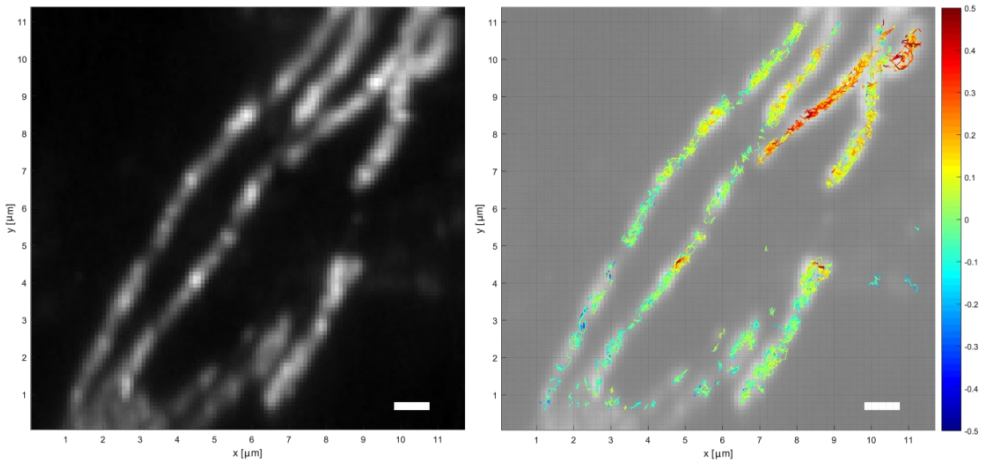

Figure 74 3D trajectory map of the F_1F_O ATP synthase subunit-γ
A Summed raw data image of CV-SU. **B** Trajectory map of CV-SUγ. The color code shows again that in the upper right corner mitochondria lie above each other. The other mitochondria are well separated. Scale bars: 1 µm.

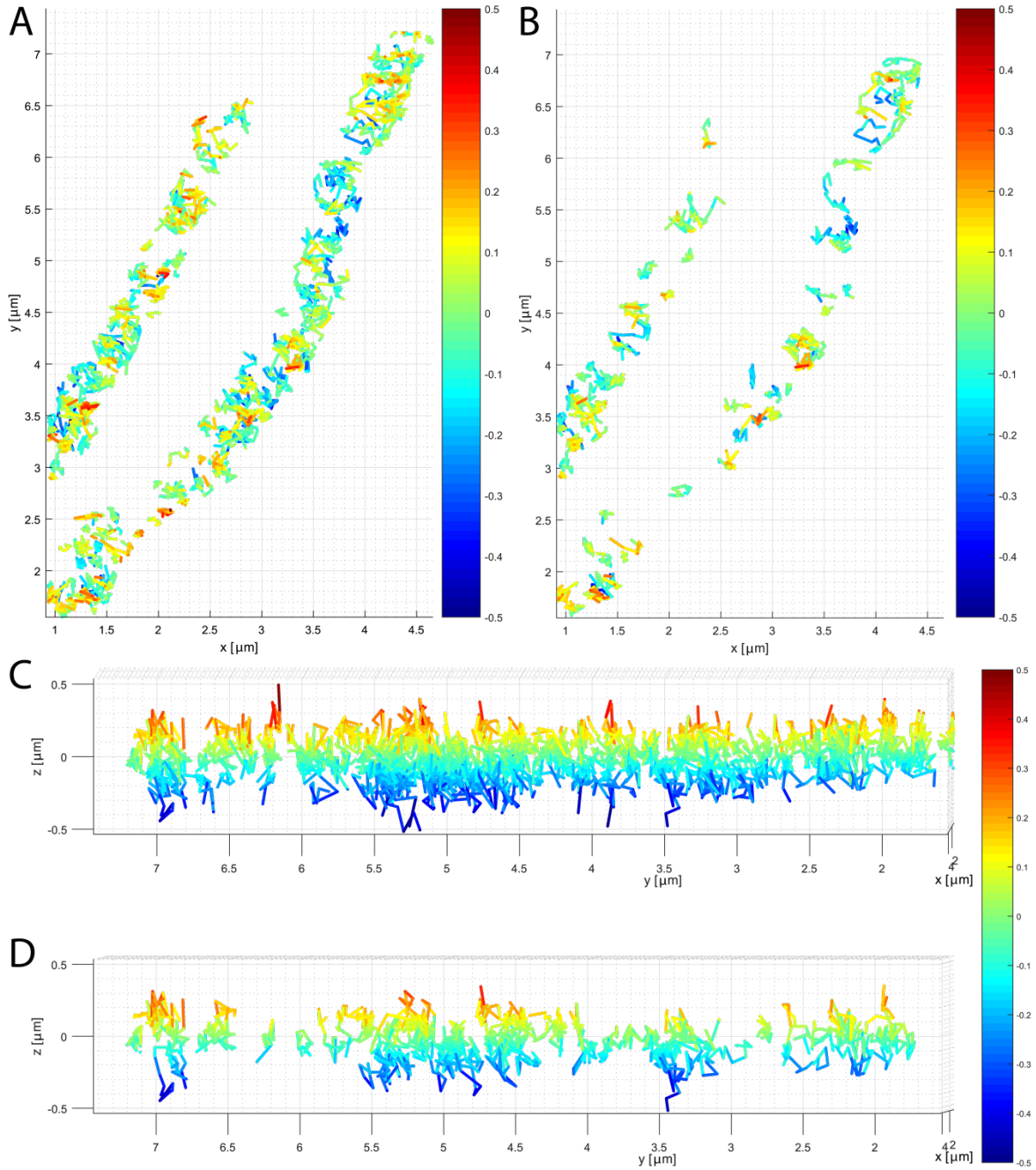

Figure 75). In

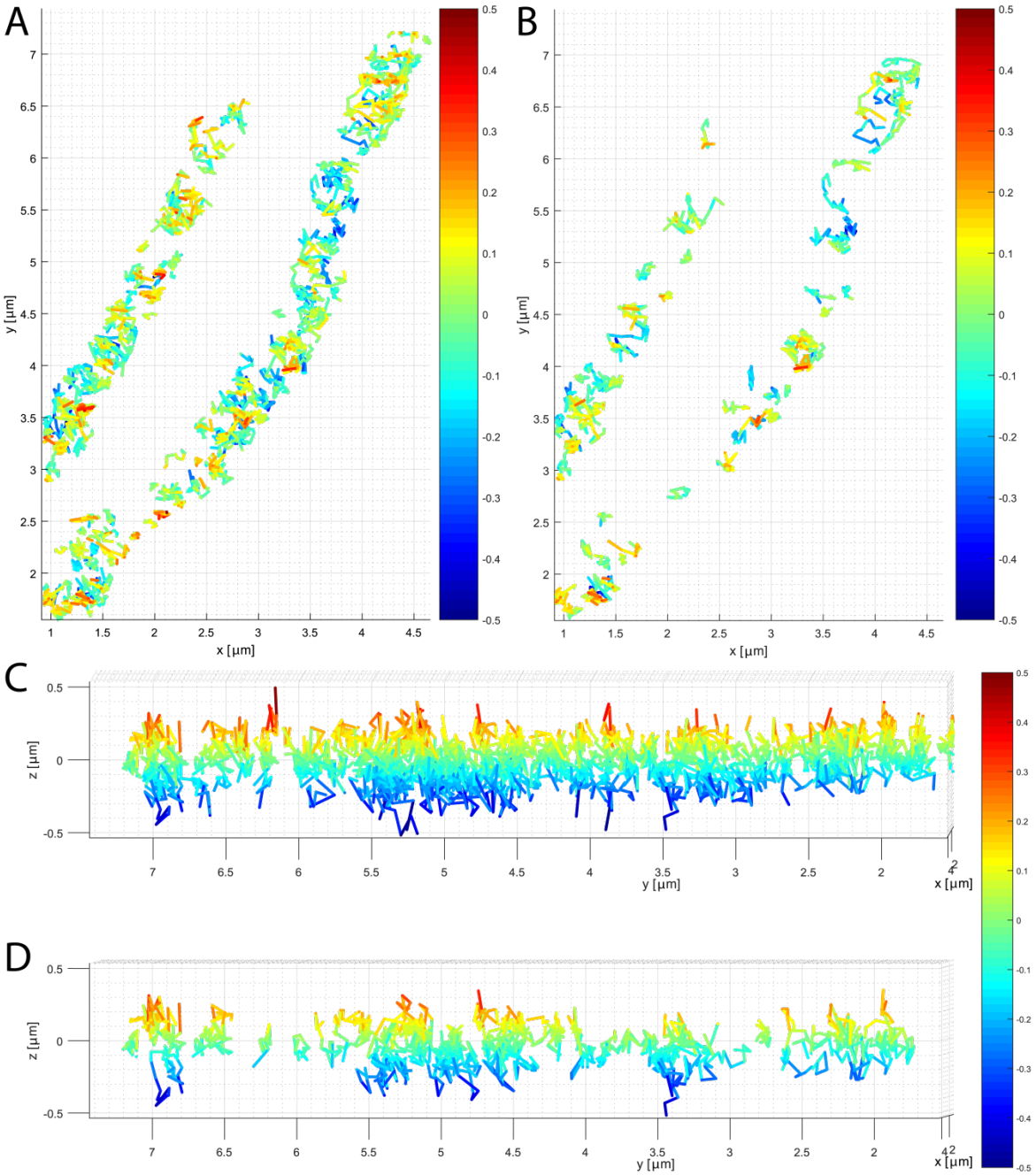

Figure 75A trajectories with a minimal lifetime of 128 ms are shown. Directly obvious is that CV-SUγ did not diffuse randomly along the IM, as expected from results for the control experiments from two-dimesnional TALM. Furthermore, in most areas the trajectories traced a complex structure and revealed that CV-SUγ trajectories showed a perpendicular directionality as well as a lateral confined movement. In order to clarify this only the trajectories with a lifetime of 240 ms were plotted (

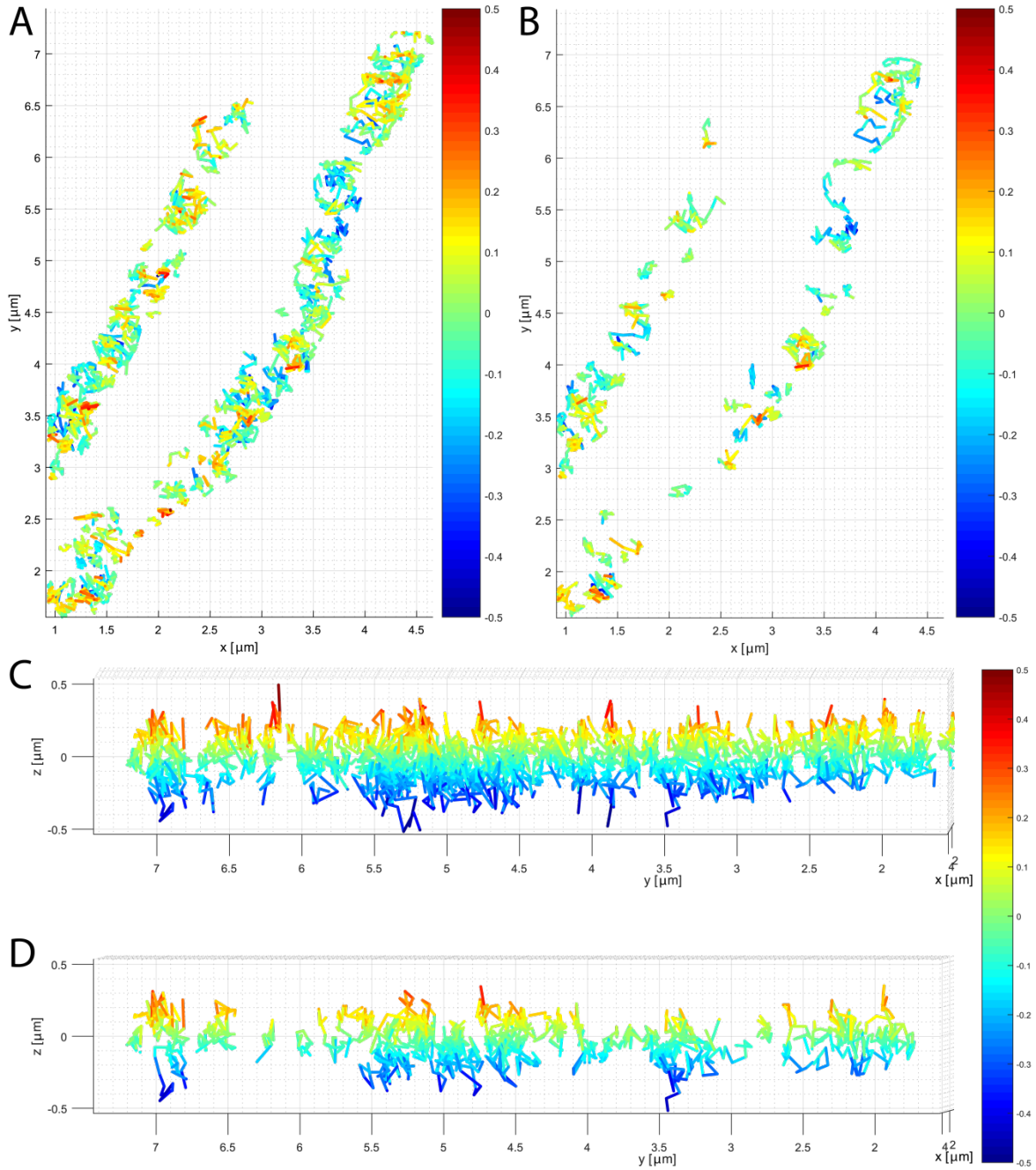

Figure 75B). Here, these events are evident. In the lower left and upper right corner of

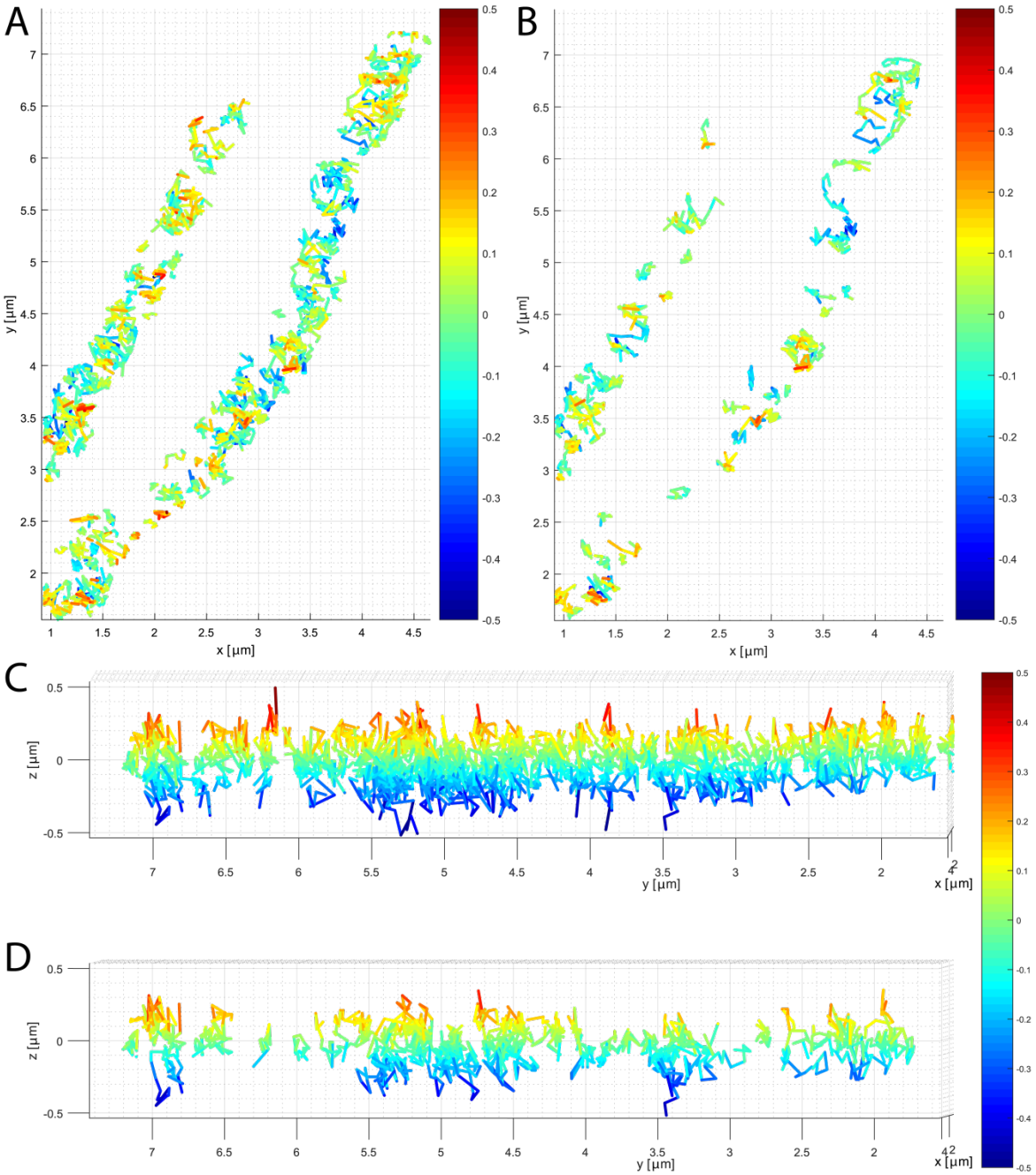

Figure 75B 3D cristae trajectories can be seen. Additionally, the trajectories also trace the IBM and show perpendicular shifts within single trajectories. This demonstrates the entrance or exit events into or out of cristae. Furthermore, the side view of the trajectory maps (

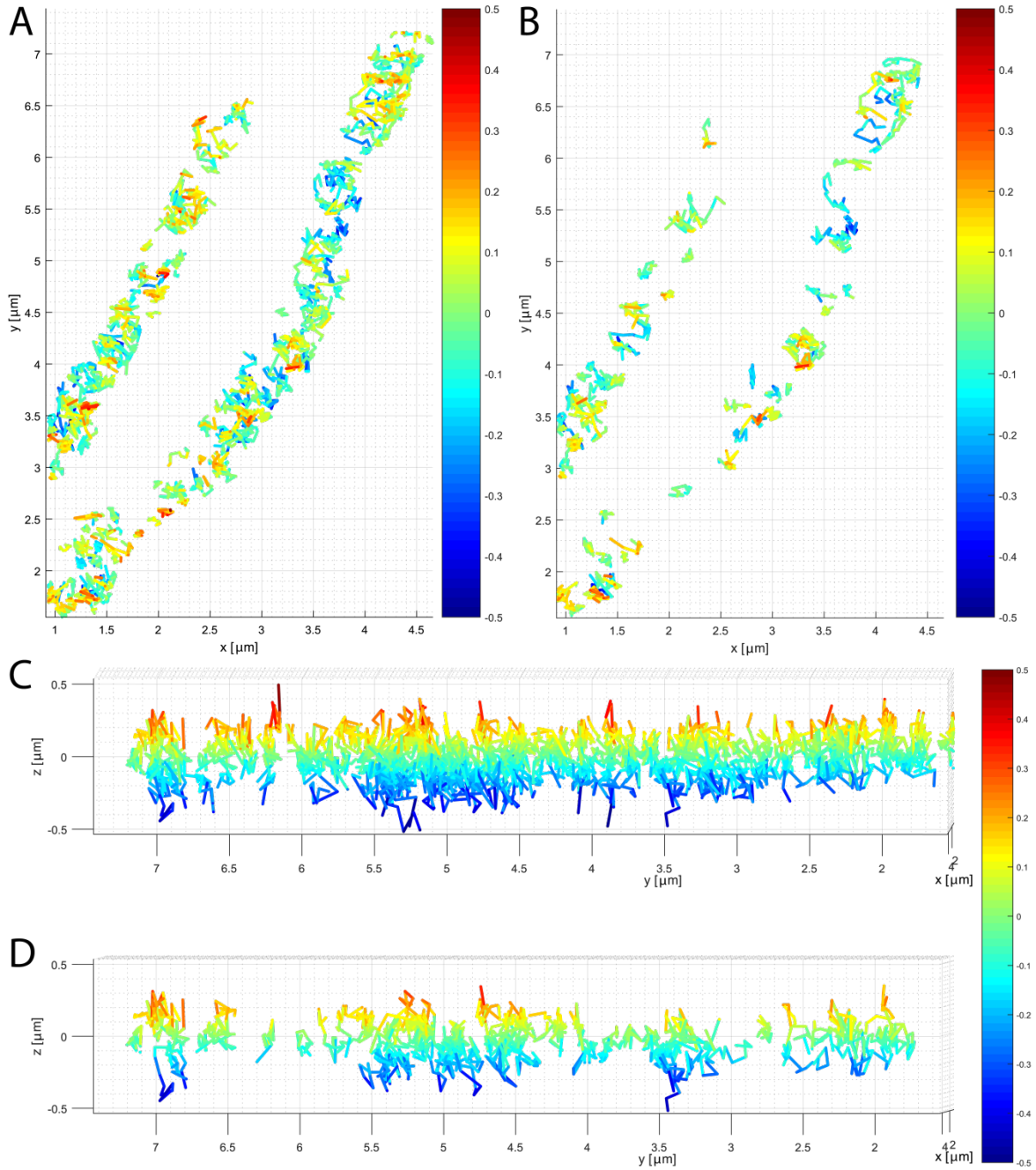

Figure 75C, D) shows that CV-SUγ diffuses up and down / in the axial direction often without lateral displacement, as expected for a protein diffusing in the CM. Additionally no hollow shape of the IM can be traced by the trajectories, demonstration a dominant localization of CV-SUγ the CM (Figure S 13). In order to demonstrate that 3D TALM reveals the spatiotemporal trafficking of CV-SUγ in the IM and especially in the CM the trajectory map from

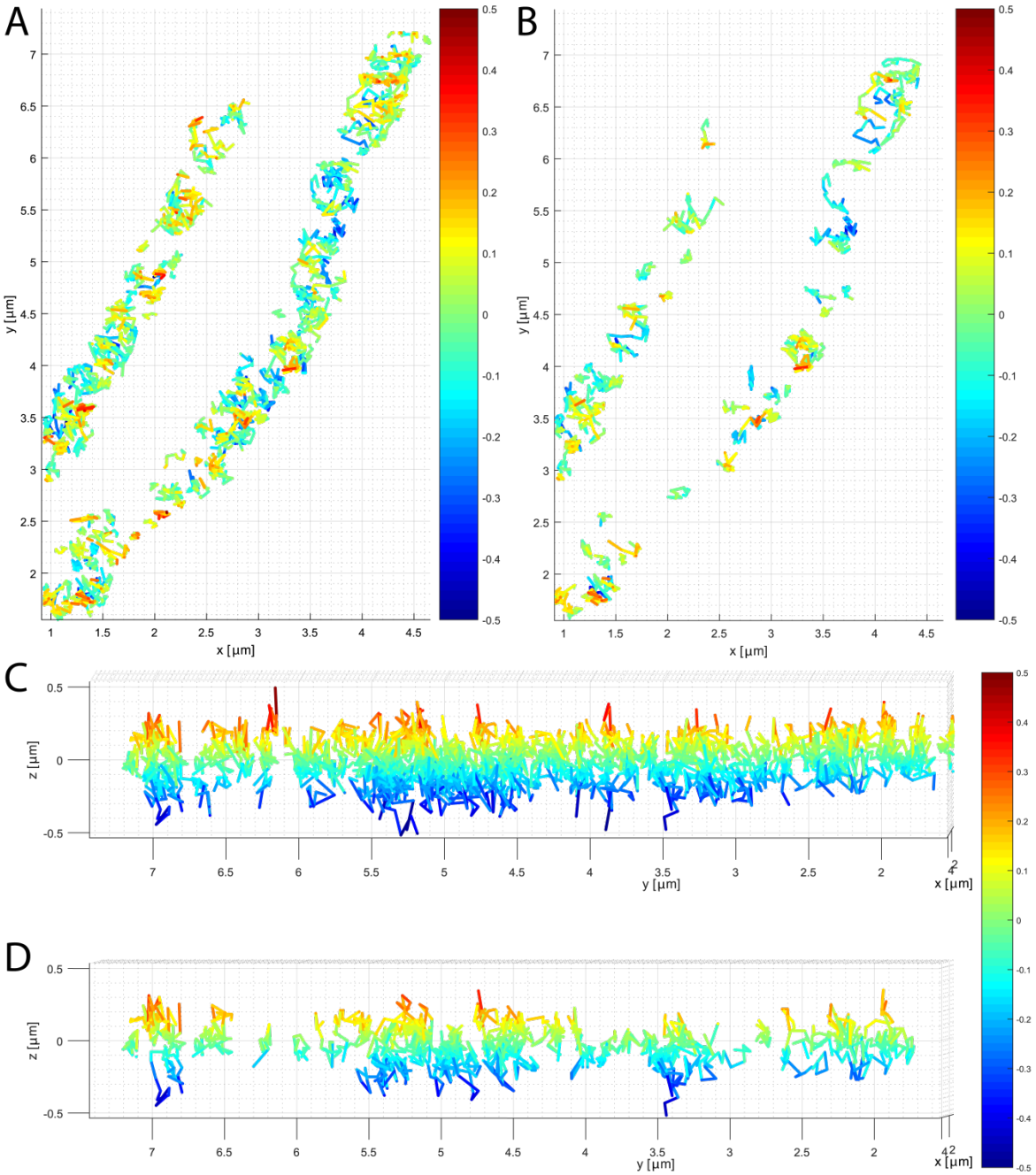

Figure 75B was tilted to an approximately 45° angle (Figure 76). In this angle of view the axial and lateral movement of single CV-SUγ can be understood. Now the lateral confined movement shows an axial diffusion (Figure 76, orange arrowheads). Other trajectories are identified as confined in all three dimensions (Figure 76, red arrowheads). In addition, trajectories which reveal the trafficking of CV-SUγ inside the CM are identified as true cristae trajectories (Figure 76, black arrowheads). These cristae trajectories sometimes also show a back and forward movement in the CM.

Taken together, in the control experiments CV-SUγ is localized in the IBM and CM, but showed a dominant localization in the CM. The reconstruction of CV-SUγ localizations demonstrate the IM is non-hollow and localization in cristae were obtained. Furthermore CV-SUγ diffuses in and out of the CM and seems to be unhindered in this behavior in many cases. In contrast to this lateral confinement can show axial movement or is confined in all three

dimensions. Whether this results from confined diffusion at the rim of a single cristae or from CV-SUγ proteins which try to enter the CM could not be revealed. However, the 3D confinement has to be induced by interaction of CV-SUγ with other proteins, like the MINOS/MICOS or results from dimerization and oligomerization of CV itself. As a third explanation the ultrastructure may also hinder the diffusion of CV-SUγ when small microcompartments / cristea are existent. Of course, these ultrastructural obstacles need to be induced by structure influencing proteins like CV and MINOS/MICOS for example and are thereby speculative.

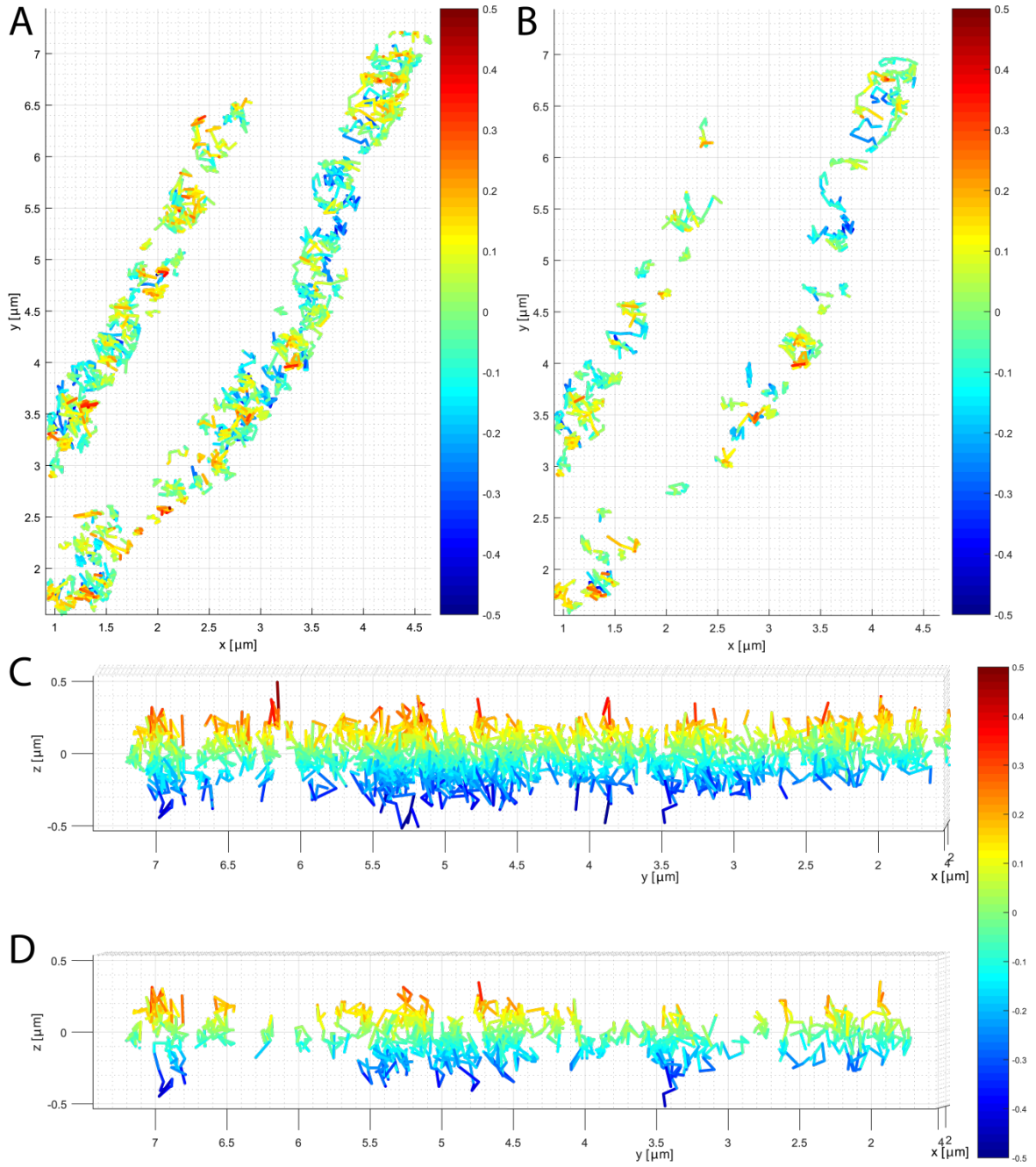

Figure 75 3D trajectories of the F_1F_O ATP synthase subunit-γ in single mitochondria
A Trajectory map of CV-SUγ in two single mitochondria with a minimal track length of 8 frames. **B** Trajectory map of the data shown in A with a minimal track length of 15 frames. **C** Y,z-view of the trajectory map shown in A. **D** Y,z-view of the trajectory map shown in B.

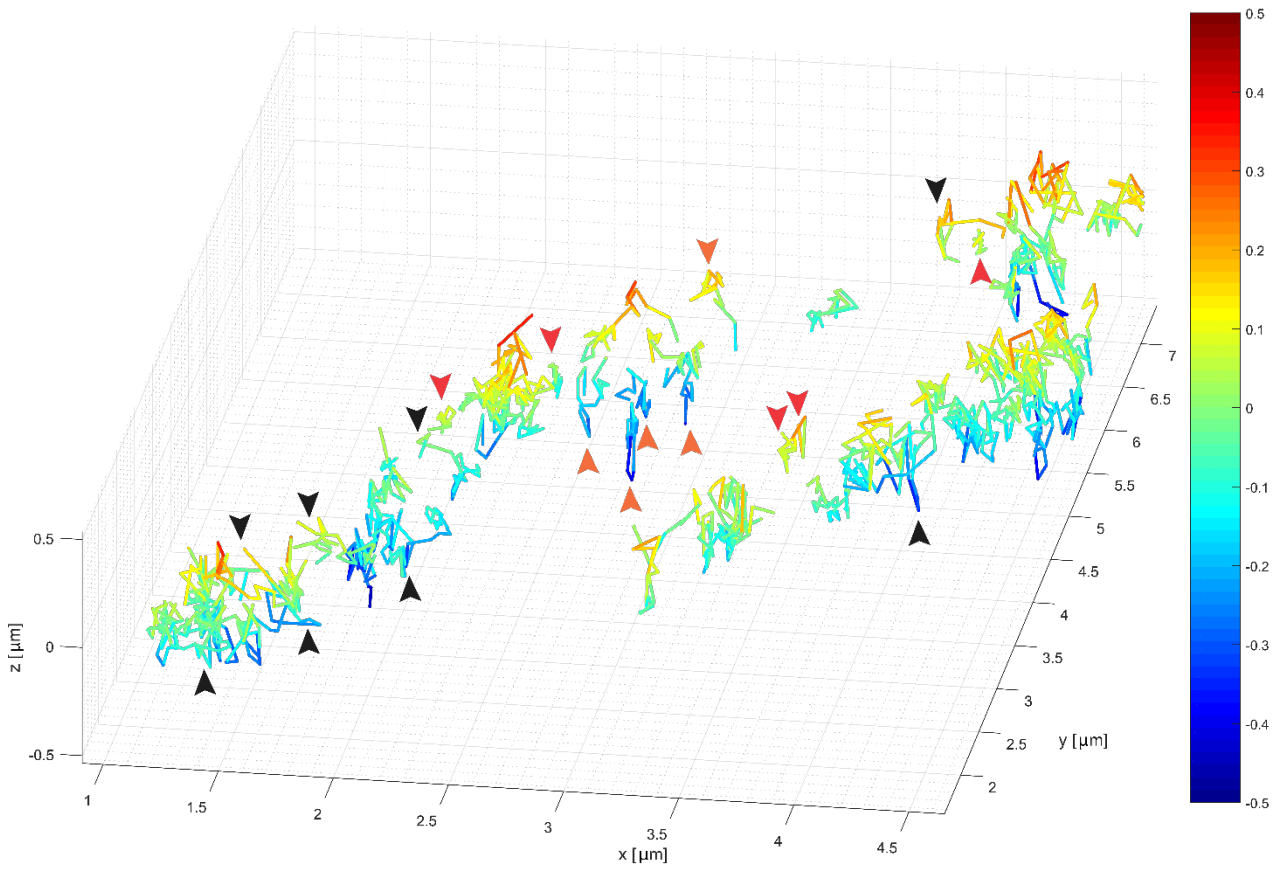
z [µm]
0.5
0
-0.5
x [µm]
1
1.5
2
2.5
3
3.5
4
4.5
y [µm]
2
2.5
3
3.5
4
4.5
5
5.5
6
6.5
7
0.5
0.4
0.3
0.2
0.1
0
-0.1
-0.2
-0.3
-0.4
-0.5

Figure 76 Tilted view of the trajectory map of the F_1F_O ATP synthase subunit-γ in single mitochondria shown in

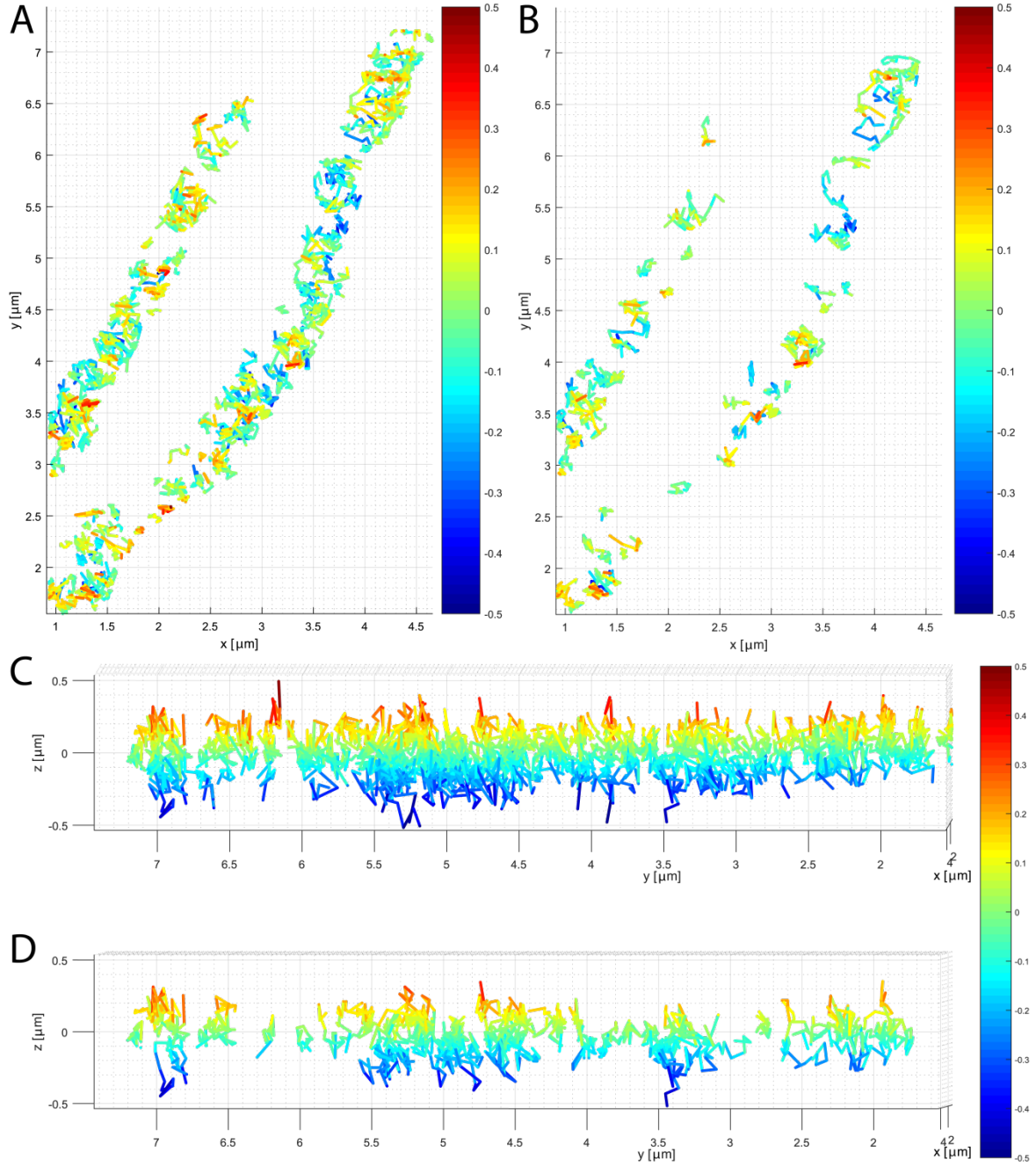

Figure 75
The trajectory map from

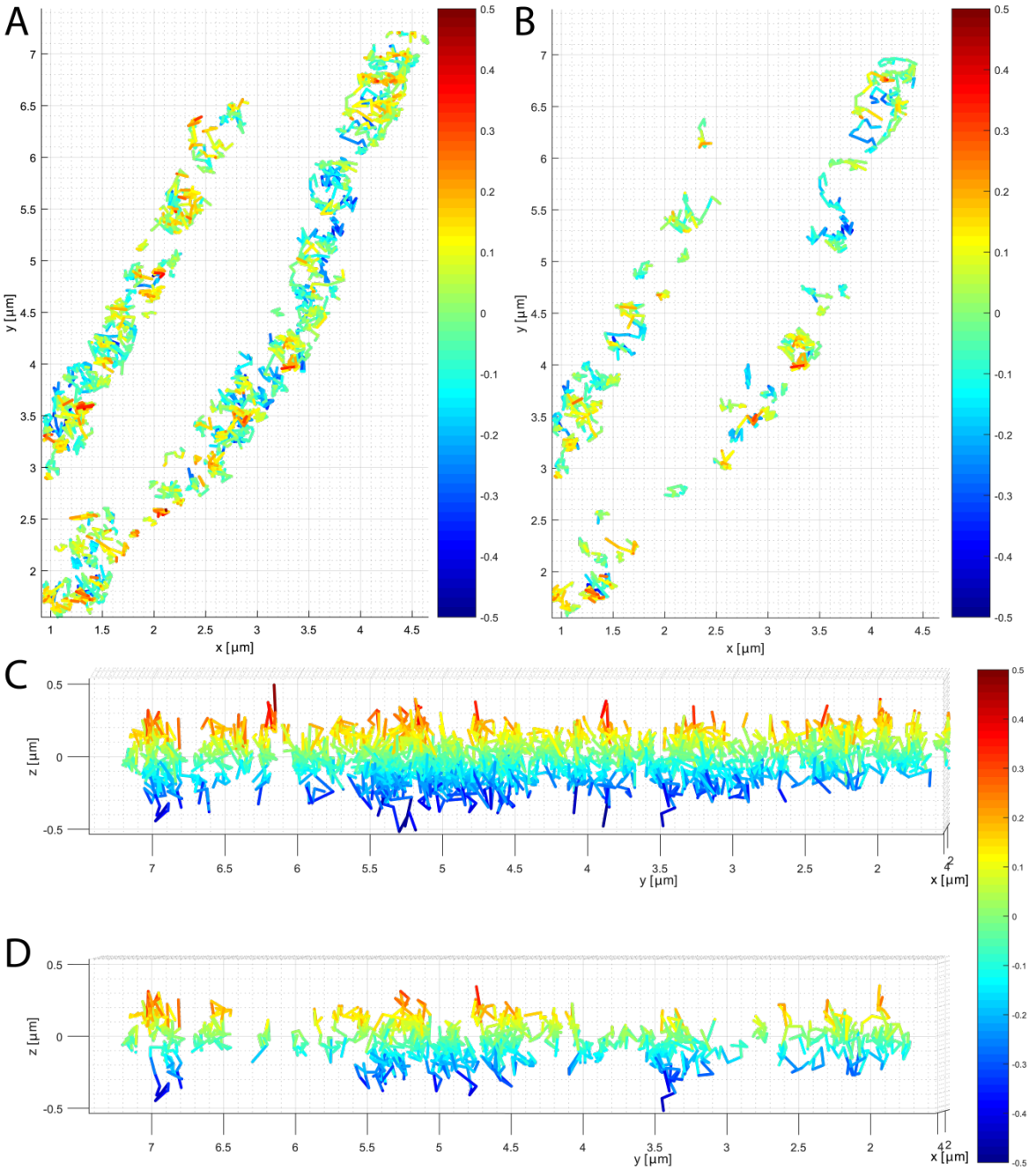

Figure **75**B was tilted by ~ 45°. Here the axial and lateral movement of CV-SUγ is visible. The diffrerent arrowheads mark threedimensional confined (red arrow heads), lateral confined (orange arrow heads) and cristea tracks of CV-SUγ (black arrowheads).

9.5.6 3D TALM of the F_1F_O ATP synthase subunit-γ in cells during starvation

9.5.6.1 3D reconstruction of the inner membrane by 3D single molecule localization of the F_1F_O ATP synthase subunit-γ in cells during starvation

In two-dimensional TALM it has already been shown that a shift to starvation leads to a change of the trajectory direction to the longitudinal axis and no cristae tracks were obtained. However, it is still unknown if either a change of the ultrastructure with cristae orientated parallel to the outline of mitochondria or a lack of cristae and consequently a diffusion of CV-SUγ in the IBM is the reason for this. Therefore, starvation experiments have been repeated with 3D TALM. If the IM becomes tubular during starvation a 3D reconstruction similar to the OM should be the result. On the other hand, if cristae change their alignment to the longitudinal direction of mitochondria 3D reconstruction would not show tubular shapes of the IM.

In fFigure 77 the 3D localizations of CV-SUγ in a single mitochondrion were reconstructed. The 3D reconstruction shown in Figure 77B consists of 4020 localizations. A minor amount of the localizations resulted from detection of unbound dyes in the cytosol. The regions of interest (Figure 77B, C, yellow and purple square) show accumulations at the outline of mitochondria known from 3D TALM of Tom20. However, here CV-SUγ a protein of the IM was recorded. Additionally, a 220 nm slice in the middle of the regions of interest was created (Figure 77C). In the regions of interest, a strong accumulation of localizations at the outline of the mitochondrion was obvious. The side

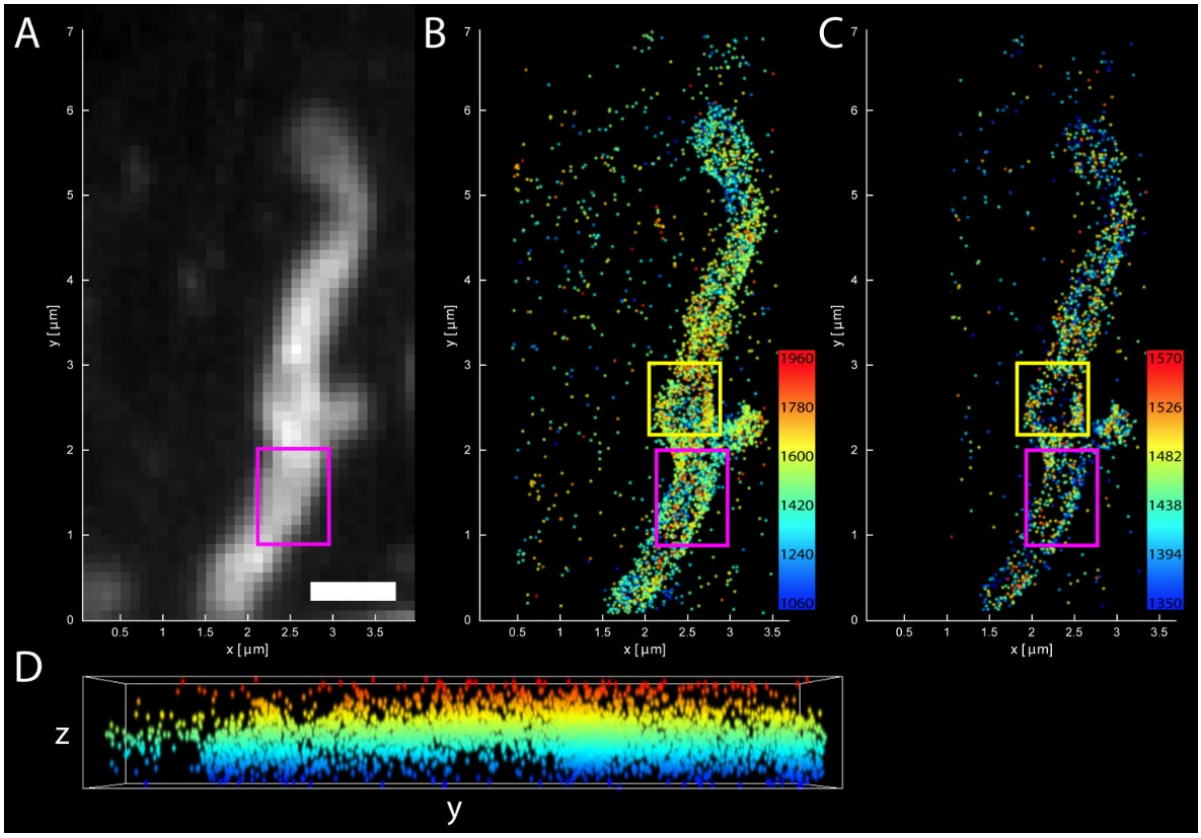

Figure 77 3D reconstruction of mitochondria by 3D localization of the F_1F_O ATP synthase subunit-γ
A Summed raw data of the imaged mitochondria. The imaged region was 28 µm2. Scale bar: 1 µm. **B** 3D loclizations of CV-SUγ. Here, 4020 single signals were localized. False localizations resulted from unbound dyes in the cytosol. In the ROI (yellow and purple square) accumulations at the outline of the mitochondrion were obtained. Indicating a tubular IM. **C** 3D reconstruction of a 220 nm z-slice consisting of 1959 localizations of the data shown in B. In the ROI (yellow and purple square) a hollow shape of the IM was revealed. Demonstrating a lack of cristae in these regions. **D** Y, z-view of the imaged mitochondrion.

view of the reconstruction shows that the imaged mitochondrion lay completely in focus during imaging (Figure 77D). The reconstruction already indicates a tubular structure of the IM.

9.5.6.2 3D single particle tracking of F_1F_O ATP synthase subunit-γ in cells during starvation

Previous two-dimensional TALM experiments showed a switch of the trajectory directionality of CV-SUγ. However, TALM could not reveal if the change in trajectory directionality results from a change in the orientation of the cristae or from a lack of cristae and a following exclusive diffusion of CV-SUγ in the IBM. In order to investigate if either a change of the orientation of cristae or vanished cristae and a tubular IM structure are the reason for this altered trajectory directionality 3D SPTof CV-SUγ in cells during starvation was performed. In Figure 77 a partially tubular mitochondrion was reconstructed. Figure 78 shows the trajectory map of CV-SUγ in the same mitochondrion. The trajectory map shows neary no trajectories oriented perpendicular to the longitudinal axis of the mitochondrion. Furthermore, an accumulation of trajectories at the outline of the mitochondrion was obtained (Figure 78, purple square). This ROI is enlarged in Figure 78C,D. The trajectory map of the ROI demonstrates that orthogonal movement still exist but now the trajectories seem to mark the end of a hollow part of the IM. Figure 78D shows the same ROI but with the line of sight along the longitudinal axis of the mitochondrion. Here, the hollow shape of the IM in this part gets clear. The trajectories trace the IBM revealing that indeed the IM becomes tubular during starvation. Taken together the trajectory maps indicate that the IM becomes partially tubular during stavation. Furthermore, an existence of cristae parallel to the IBM was excluded, as only trajectories at the end of this hollow sub-compartment of the IM move perpendicular to the longitudinal axis of mitochondria. The existence of a tubular IM reveals that during starvation a rearrangement of the ultrastructure occurs. The cristae disappear and the CM becomes part of the IM. Proteins which were predominantly localized in the CM are now localized in the IBM.

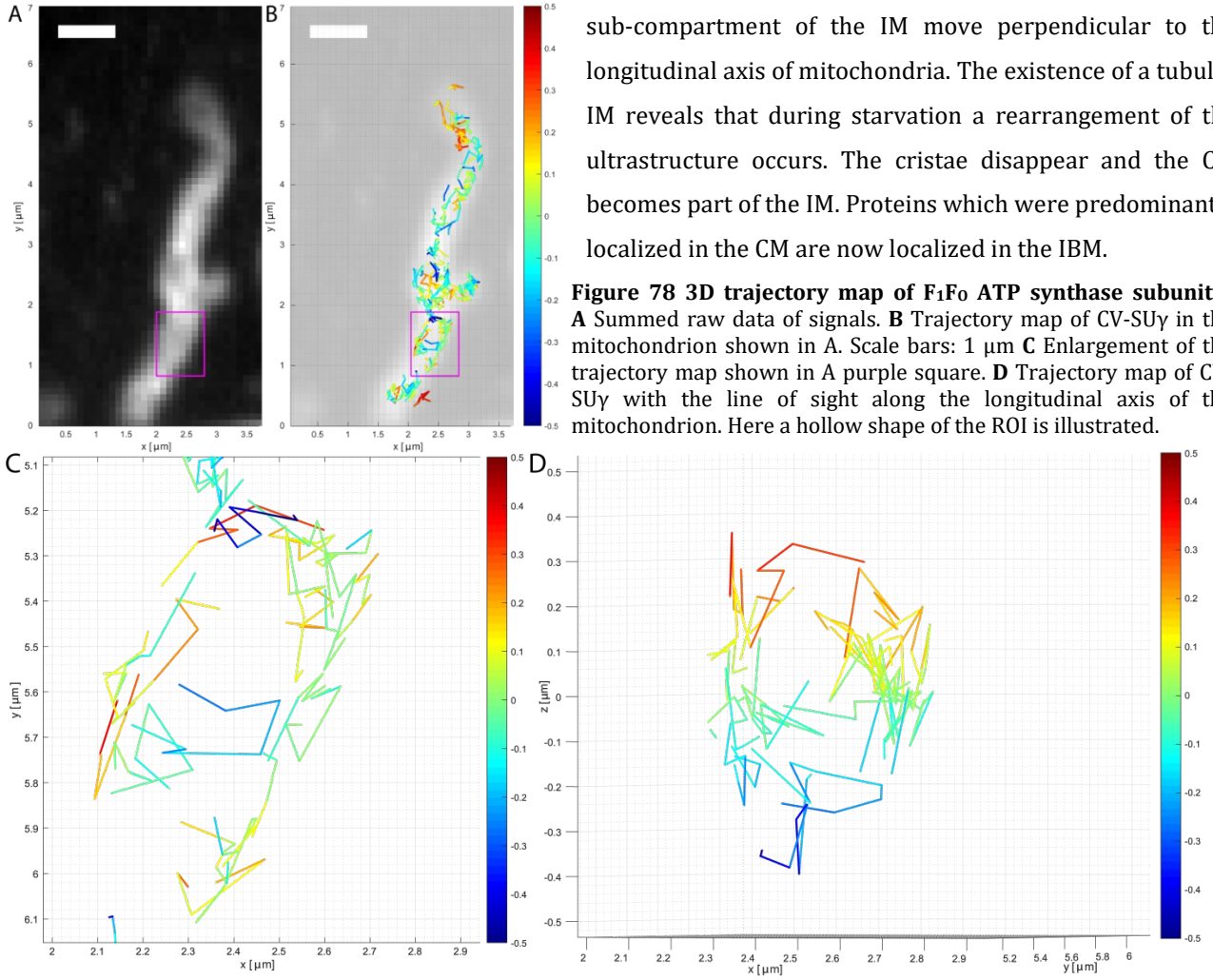

Figure 78 3D trajectory map of F_1F_O ATP synthase subunit-γ **A** Summed raw data of signals. **B** Trajectory map of CV-SUγ in the mitochondrion shown in A. Scale bars: 1 µm **C** Enlargement of the trajectory map shown in A purple square. **D** Trajectory map of CV-SUγ with the line of sight along the longitudinal axis of the mitochondrion. Here a hollow shape of the ROI is illustrated.

9.5.7 3D TALM of F_1F_O ATP synthase subunit-γ in improved respiring conditions

9.5.7.1 3D reconstruction of the inner membrane by 3D single molecule localization of F_1F_O ATP synthase subunit-γ in cells during improved respiration conditions

Starvation has an effect on the membrane potential, oxygen consumption rate and the formation of cristae. Cells grown in medium containing galactose instead of glucose (Table 1) show an increased membrane potential, an increased oxygen consumption rate and a decreased extracellular acidification rate (Bettina Rieger personal communication). This raised the questions if an improved respiration had an opposite effect on the spatiotemporal organization of CV, compared to starvation and the control. Furthermore, it was inverstiagted if the ultrastructural results of TEM can be revealed by 3D TALM. Therefore, HeLa cells were incubated over three weeks in galactose medium (Table 1). Afterwards 3D TALM experiments were performed as previously described. Compared to cells in starvation the mitochondrial networks did show smaller mitochondria (Figure 79A). Beside the smaller size the ends of mitochondria in this image show a larger diameter than the rest of the mitochondrial network. A reason for this shape is unknown and was not quantified. However, the reconstruction shown in Figure 79B consists of 41436 single localizations. Furthermore, the reconstructions already indicate a hollow shape of the ends of mitochondria. This can often be seen in any kind of mitochondria but the size of the hollow ends seems to be enlarged. In order to analyze the spatiotemporal organization and dynamics of CV-SUγ as well as structural features of mitochondria during improved respiration the focus lied again on elongated and separated mitochondria (Figure 79, purple square). In the ROI (Figure 79, purple square) the diameter of mitochondria changes and shows slightly swollen

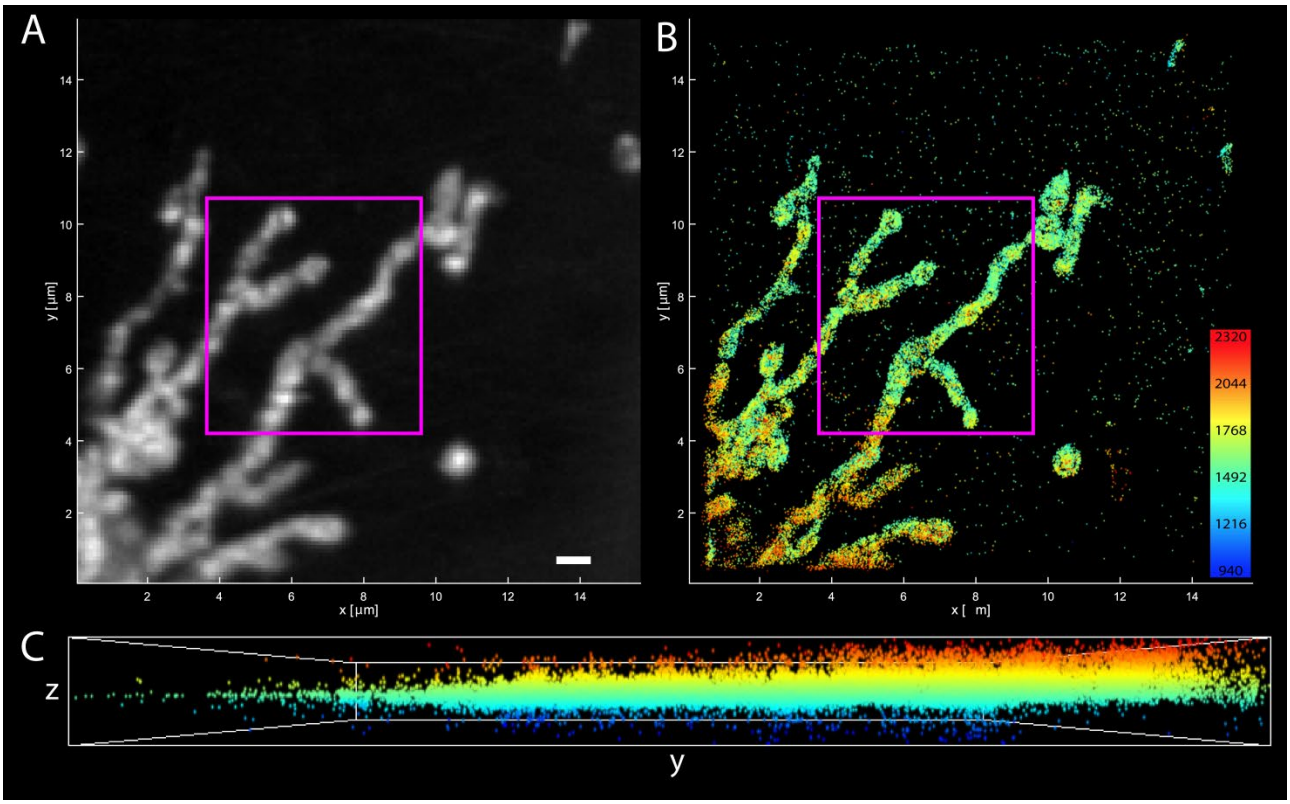

Figure 79 3D reconstruction of the inner membrane in a mitochondrial network by 3D single molecule localizations of F_1F_O ATP synthase subunit-γ in cells during improved respiring conditions
A Raw data image of summed CV-SUγ signals in a cell grown in glactose medium. Scale bar: 1 µm **B** 3D reconstruction of the mitochondrial network by 3D localizations of CV-SUγ. **C** Y, z-view of the 3D reconstruction shown in B.

parts. Interestingly an accumulation of localizations in these parts of mitochondria can be seen.

Next the ROI in Figure 79, where elongated and separated mitochondria were reconstructed was investigated further (

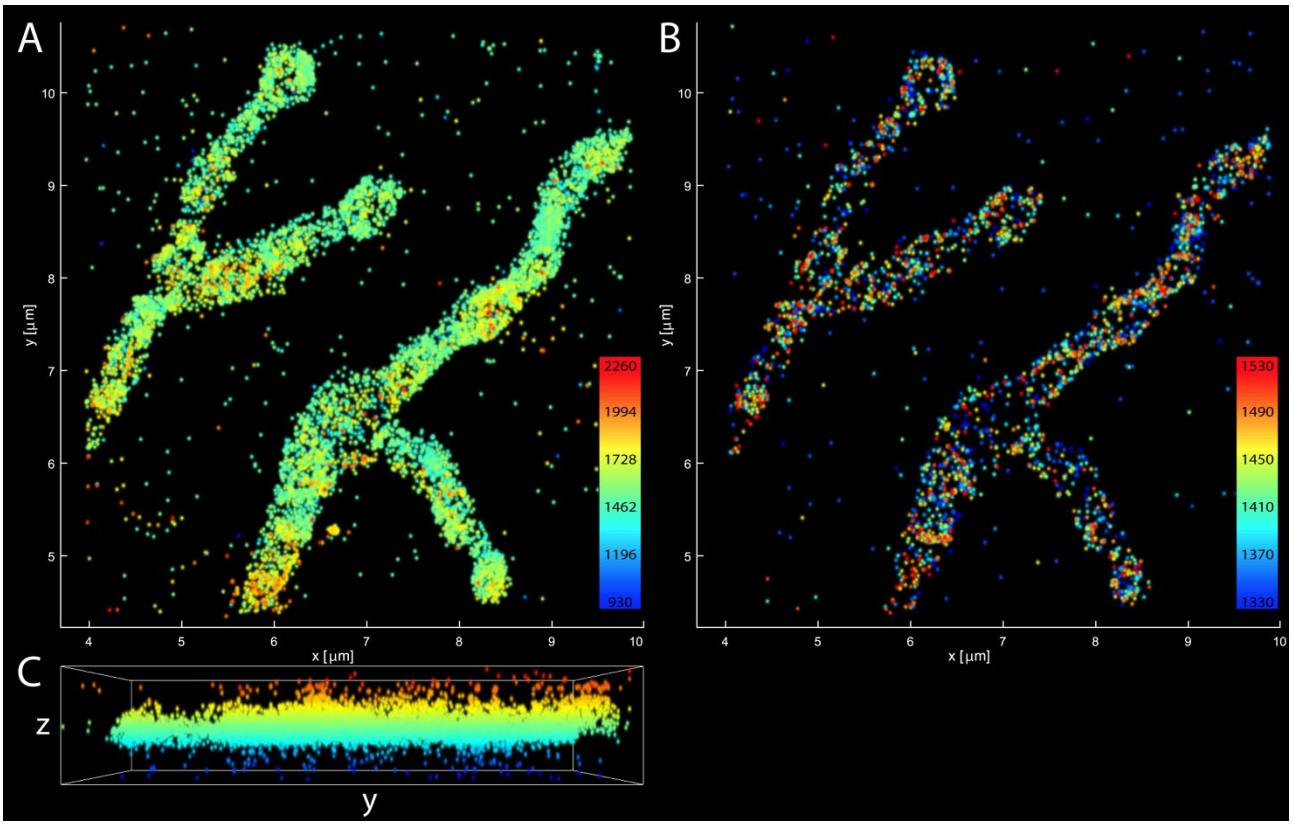

Figure **80**). The ROI was ~ 42 µm2 large. The reconstruction shown in

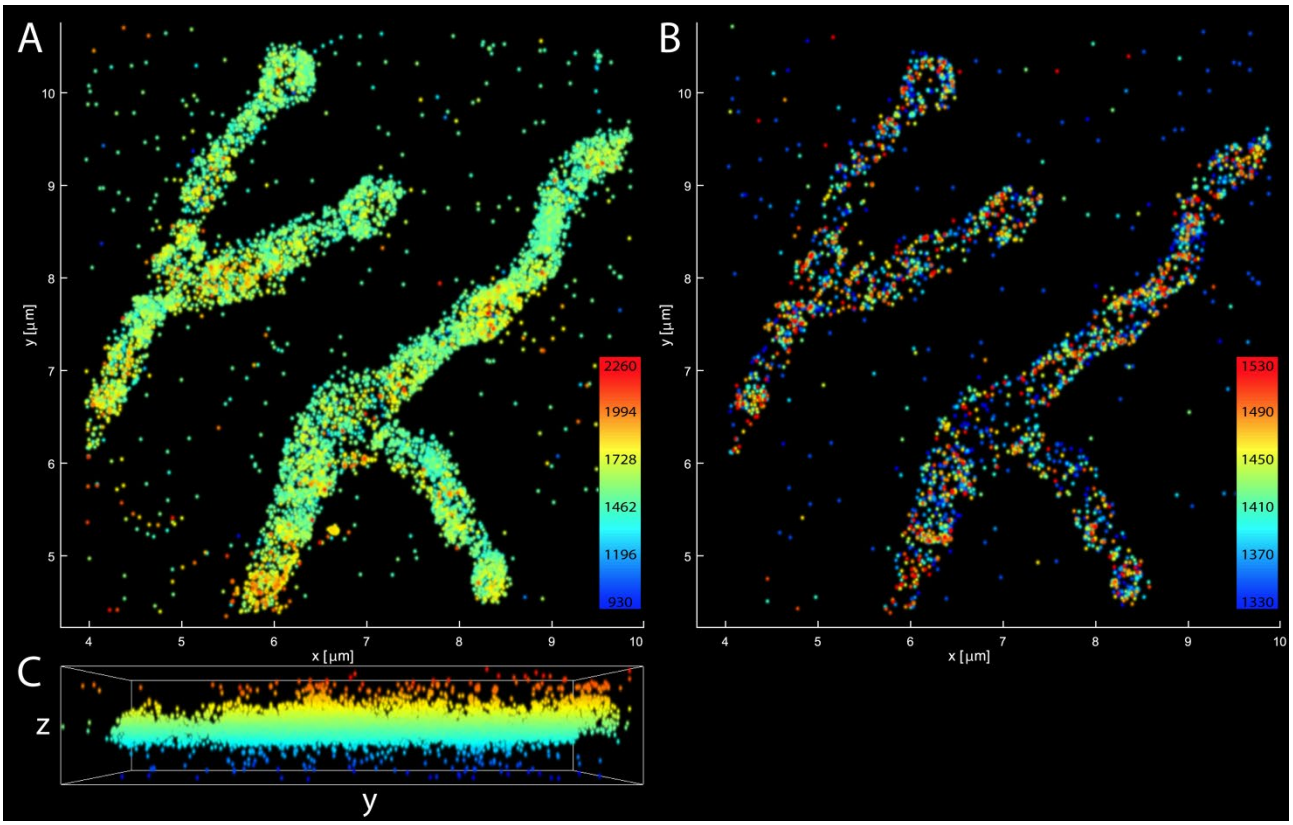

Figure **80**A consists of 8532 localizations. Shown in

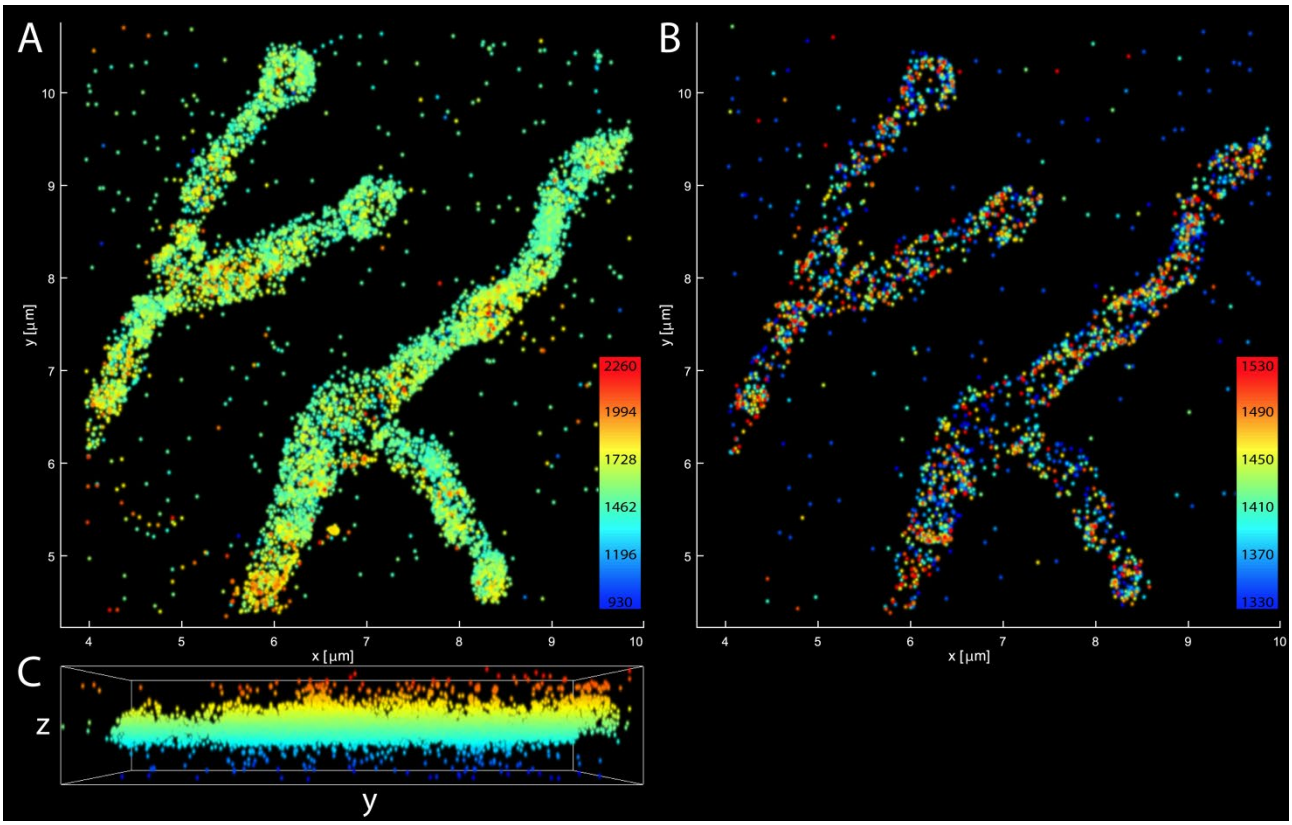

Figure **80**B is a 200 nm slice in the middle of the mitochondrial network. The slice of the reconstruction consists of 2753 localizations. It reveals an accumulation of localizations at the outline of the IM in the slightly swollen regions. Also, the ends of the reconstructed mitochondria show these accumulations at the outline of the IM. This indicates a hollow shape of the IM in these regions. The y, z-view of the reconstruction shown in

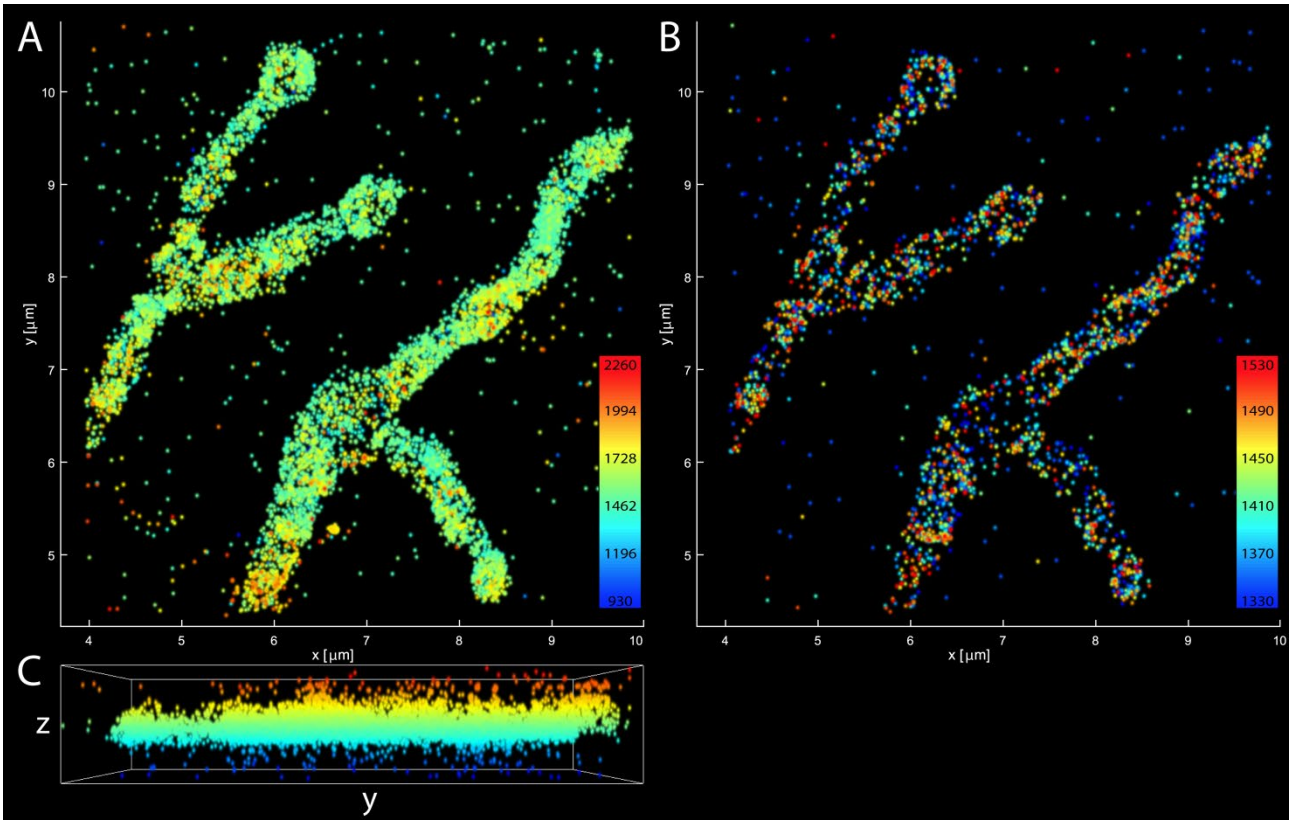

Figure **80**C demonstrates that the entire mitochondrion in the ROI lay parallel to the focal plane.

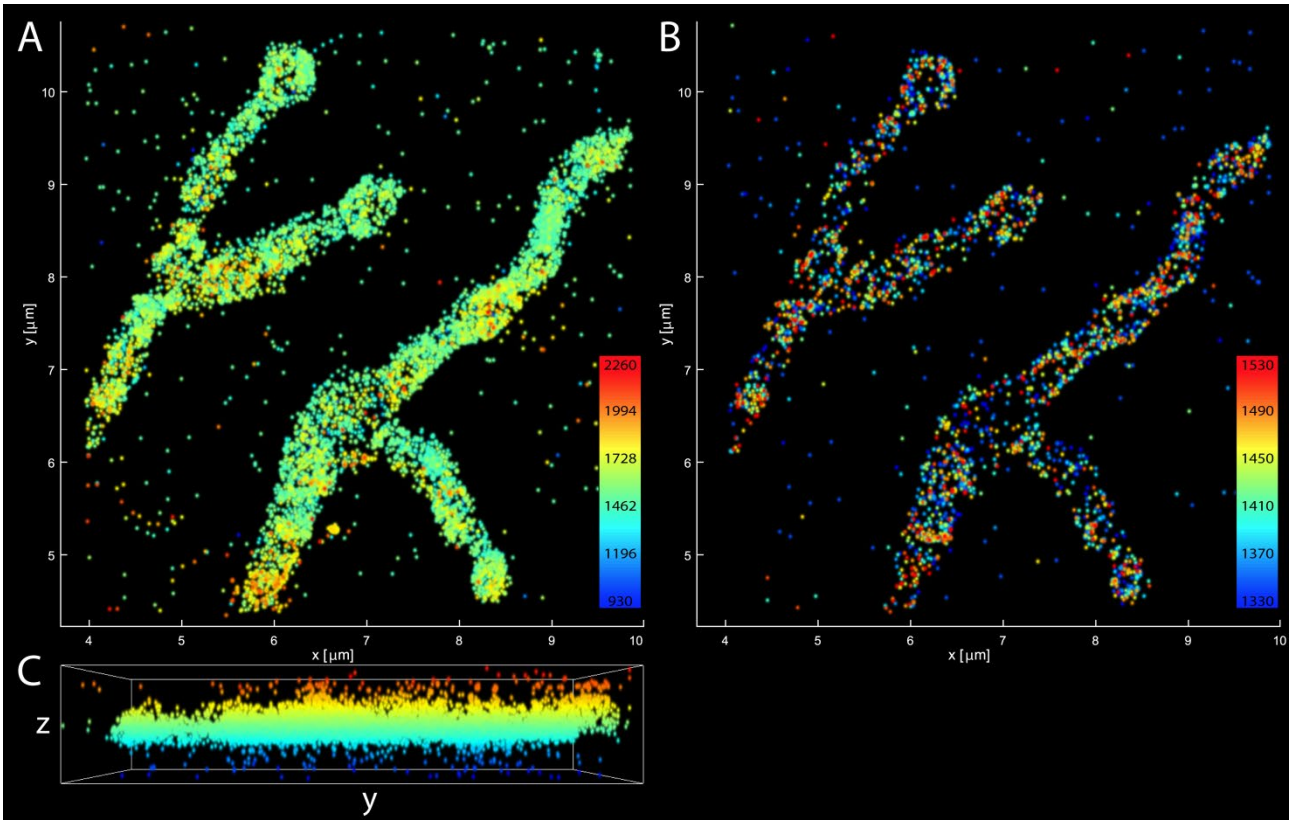

Figure 80 Enlargement of the ROI in the 3D reconstruction shown Figure 79
A 3D reconstruction of the ROI from Figure 79 (purple square). **B** An axial slice of 200 nm thickness in the middle of the reconstruction shown in A. **C** Y, z view of the reconstruction shown in A. This view shows that the reconstruction was in the

middle of the focal plane and the mitochondria were oriented parallel to the focal plane.

9.5.7.2 3D single particle tracking of the F_1F_O ATP synthase subunit-γ in active respiring conditions

As previously explained a 3D reconstruction is not enough to investigate the spatiotemporal dynamics of a protein within the reconstructed structure. Therefore, 3D TALM provides SPT data of the imaged protein. The trajectories of CV-SUγ allow to reveal the IM architecture including its dynamic. Furthermore, 3D SPT allows to investigate if cristae exist and which orientation they had. Therefore, focusing on single mitochondria was obligatory. Whether improved respiratory conditions have an influence on the spatiotemporal protein organization and trafficking of CV-SUγ was investigated by 3D TALM. Shown in Figure 81 is a mitochondrial network. Here, only some mitochondria were in focus (Figure 81B, C). The trajectories were reduced and only the long trajectories with a minimal lifetime of 304 ms were plotted (Figure 81C, D, E). The lateral view of the ROI in Figure 81C was enlarged in Figure 81D. Here, trajectories with a perpendicular directionality reveal the position of cristae (Figure 81D, E, black arrowheads). Comparable to previous results by TALM (Appelhans et al, 2012, Appelhans and Busch, 2017b). One advantage of 3D TALM was to investigate the trafficking of CV in all three dimensions. 3D TALM of trajectories in the CM revealed that CV travels along the entire CM of a disc like cristae and allowed to monitor the IM architecture of certain IM parts. Additionally, longitudinal trajectories were obtained, which marked the IBM (Figure 81D).

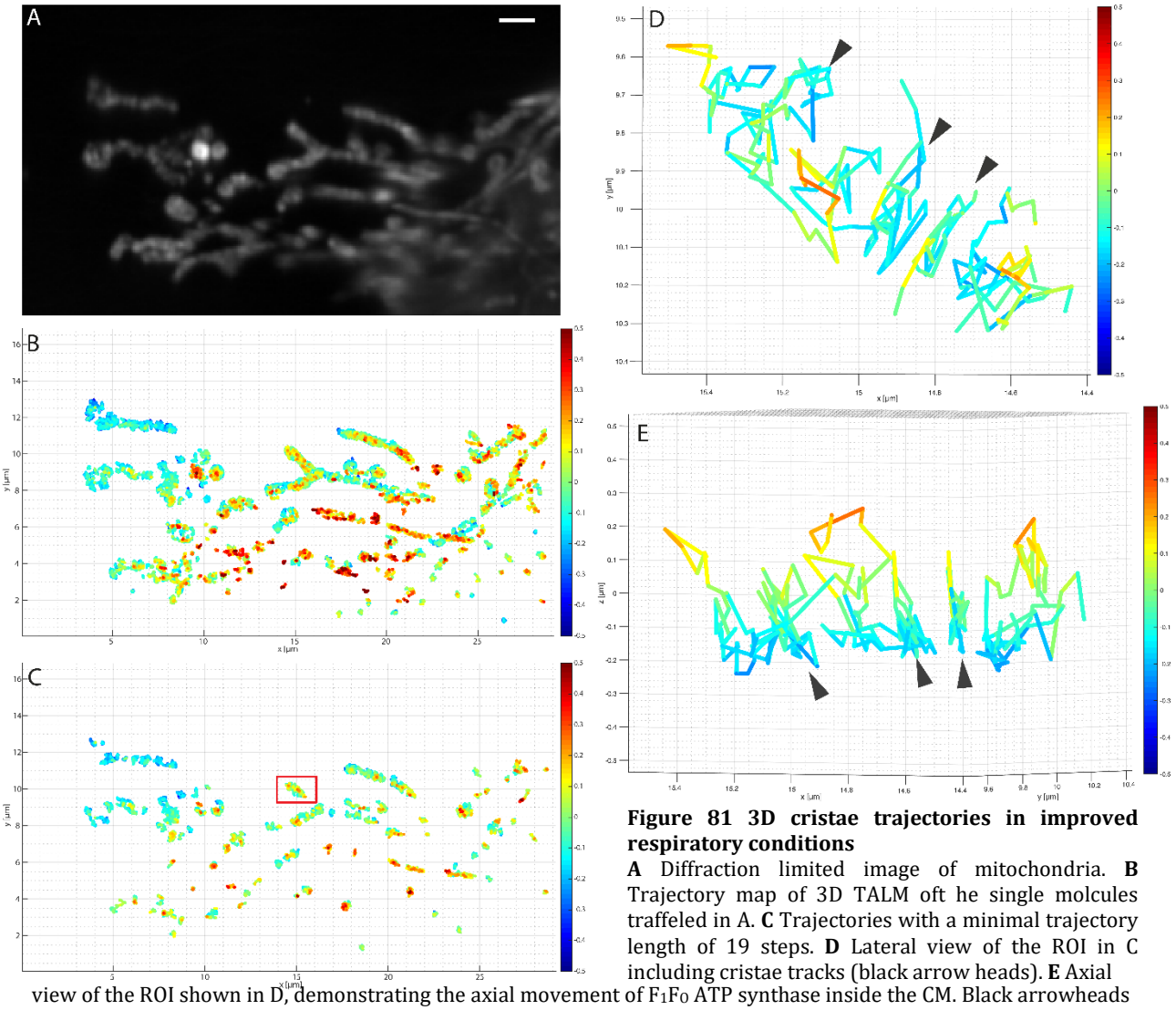

Figure 81 3D cristae trajectories in improved respiratory conditions
A Diffraction limited image of mitochondria. **B** Trajectory map of 3D TALM oft he single molcules traffeled in A. **C** Trajectories with a minimal trajectory length of 19 steps. **D** Lateral view of the ROI in C including cristae tracks (black arrow heads). **E** Axial view of the ROI shown in D, demonstrating the axial movement of F_1F_O ATP synthase inside the CM. Black arrowheads mark the cristae tracks. The trajectories reveal the ultrastructural shape oft he IM inside the ROI.

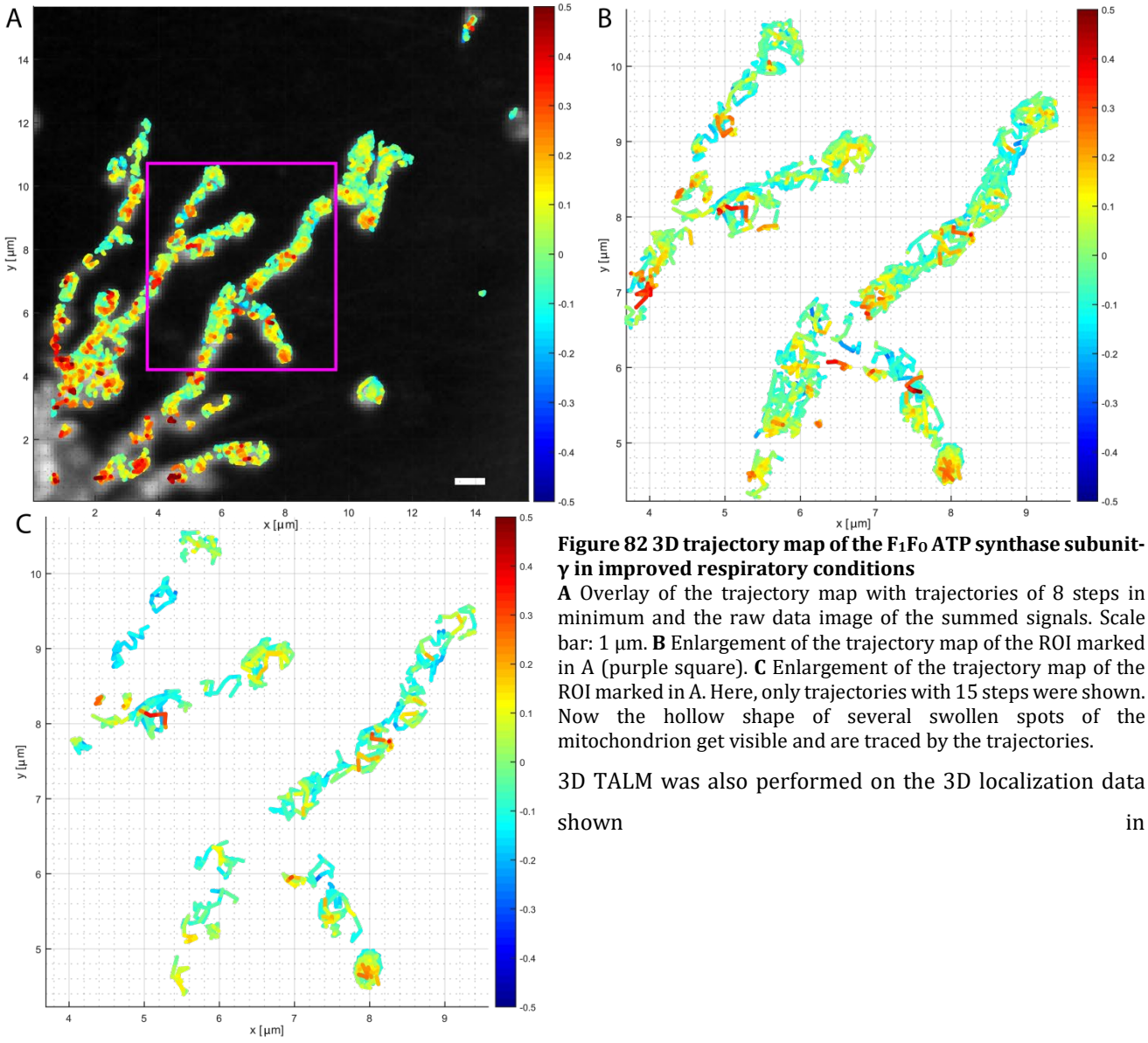

Figure 82 3D trajectory map of the F_1F_0 ATP synthase subunit-γ in improved respiratory conditions
A Overlay of the trajectory map with trajectories of 8 steps in minimum and the raw data image of the summed signals. Scale bar: 1 µm. **B** Enlargement of the trajectory map of the ROI marked in A (purple square). **C** Enlargement of the trajectory map of the ROI marked in A. Here, only trajectories with 15 steps were shown. Now the hollow shape of several swollen spots of the mitochondrion get visible and are traced by the trajectories.

3D TALM was also performed on the 3D localization data shown in

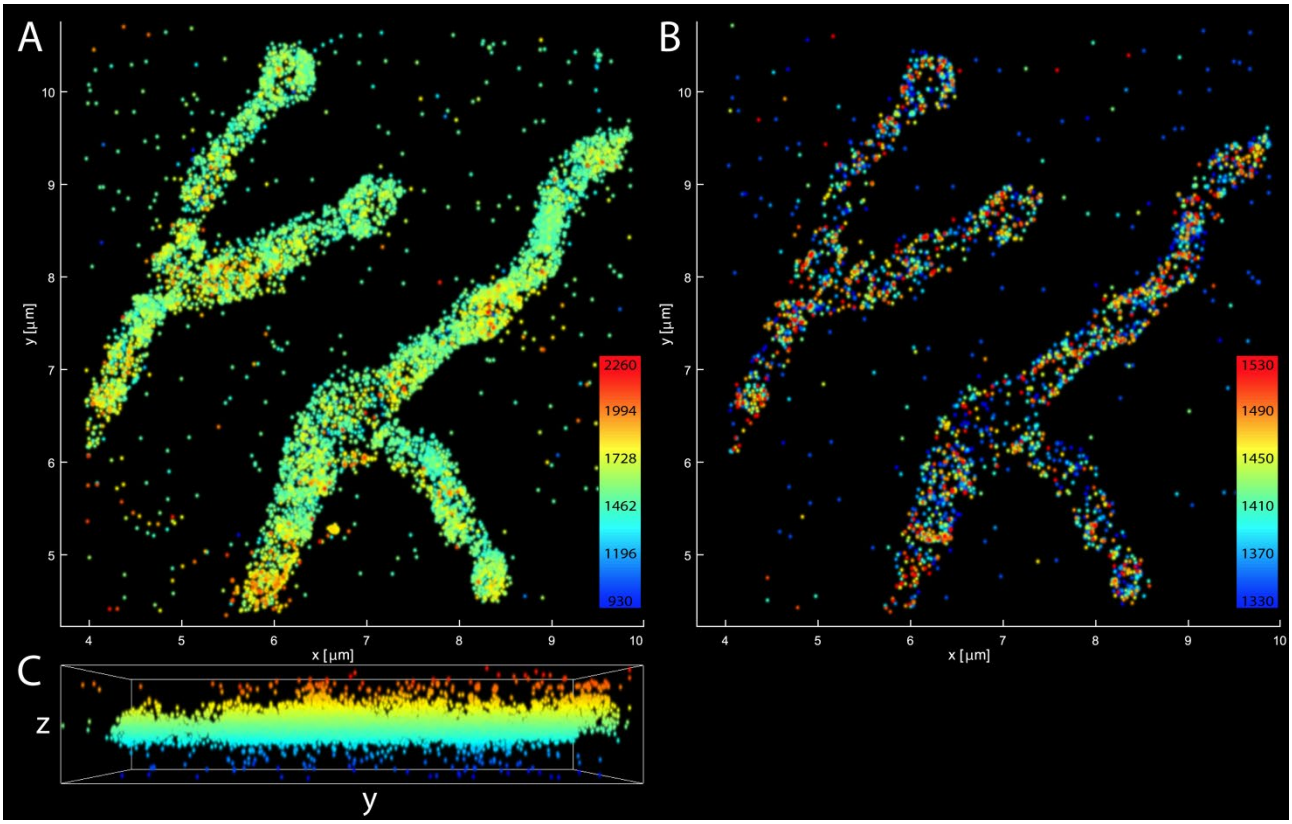

Figure **80** (Figure 82). The enlargement of the trajectory map is shown in Figure 82B. The trajectories have a minimal track length of 8 frames / 128 ms lifetime. However, there were still too many trajectories to reveal the IM shape in a top view. In order to reveal possible changes in the IM shape the minimal trajectory length was set to 15 frames leading to trajectories with a minimal lifetime of 240 ms (Figure 82C). Now the shape of the IM can be traced by the trajectories of CV-SUγ. In order to investigate the trafficking of CV-SUγ further two exemplarily events of trajectories were picked out (

Figure 83). Here, the trajectory map shows trajectories with a minimal lifetime of 240ms. The purple squares mark areas with and without a slightly swollen IM. The top view of ROI1 shows a random diffusion along the IM with no predominant direction of trafficking (

Figure 83, 1 top view). The side view of ROI1 pictures a line of sight along the longitudinal axis of the imaged mitochondrion (

Figure 83, 1 side view). This view reveals the hollow shape of the IM in a slightly swollen area of the mitochondrial network. In contrast to this the ROI2 was picked (

Figure 83). Here an area with a non-swollen part of the mitochondrion was found. In this part the top view shows several trajectories with different characteristics. Most of the trajectories show mobility below the focal plane and are depicted in blue color. However, right in the middle of the trajectory map of ROI2 a trajectory shows a protein, which stayed in focus depicted in a green and yellow trajectory until the signal was bleached (

Figure 83, 2 top view). The trajectory was oriented in a perpendicular angle to the longitudinal axis and moved back and forward. The top view and side view (

Figure 83, 2 top view and 2 side view) together explain how this single CV-SUγ diffused in the IM. At first the CV-SUγ diffused along the IBM and then went into the CM and stayed confined mobile in the CM.

Taken together 3D TALM in improved respiratory conditions revealed unexpected shapes of the IM. Here, the IM showed hollow parts and parts where cristae trajectories were found. The trajectory directions become highly heterogeneous, but spherical traced areas can be seen in every mitochondrion. Whether the rearrangement of the IM shape has an influence on the mobility was investigated in the following by calculating the mean D_{3D}. In order to quantify the trajectory directionality MitoOrientedDynamics was used for 3D TALM data.

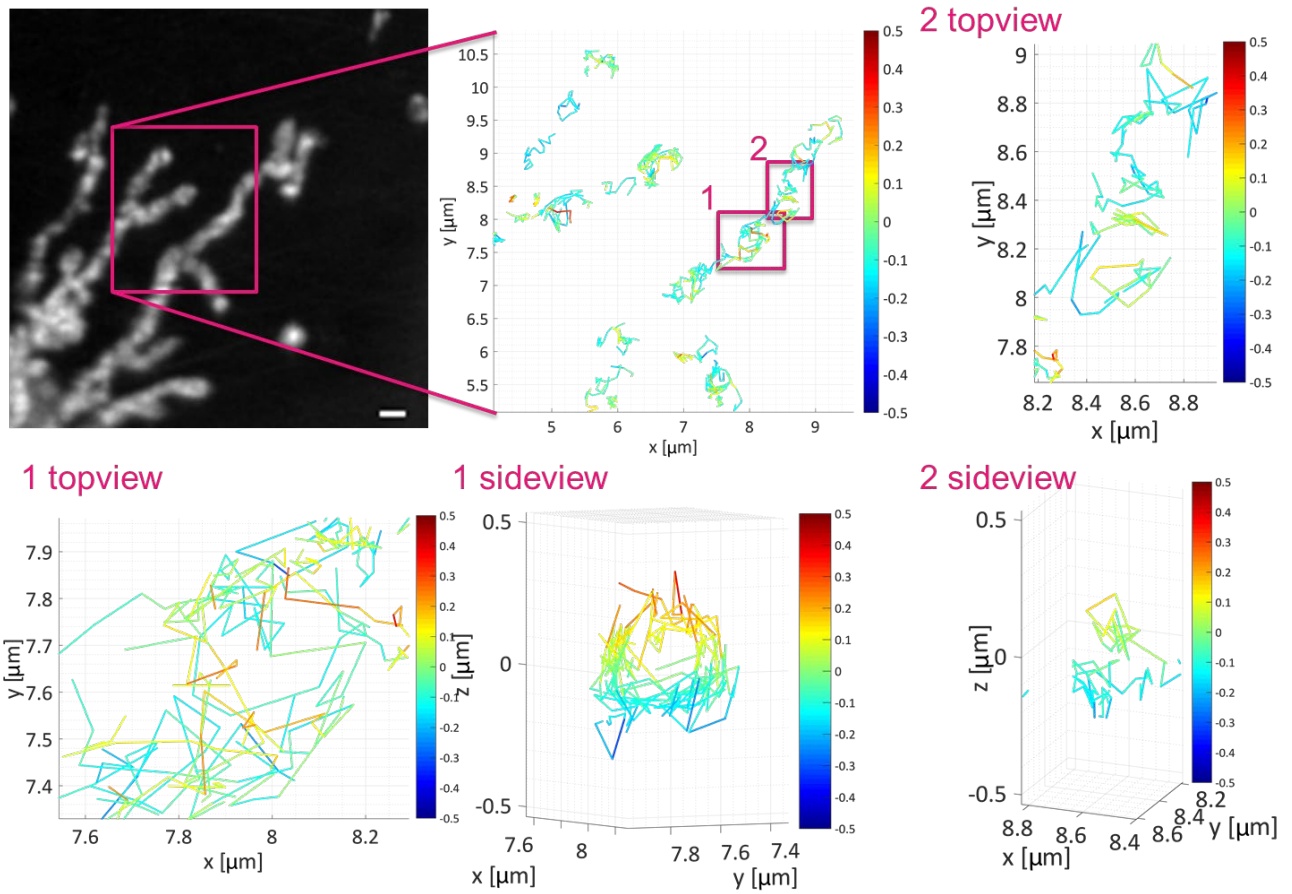

Figure 83 3D trajectory maps of the F_1F_O ATP synthase subunit-γ in improved respiring conditions, in swollen and non-swollen sections of a single mitochondrion

A Raw data image of the summed signals of CV-SUγ. Scale bar: 1 µm. **B** Trajectory map of the ROI with trajectories showing a lifetime above 240 ms. Purple square mark two exemplarily events in a swollen section of the mitochondrion (1) and a non-swollen section of the mitochondrion (2). **1 Topview** Trajectories of CV-SUγ trace the circular shape of the swollen mitochondrial part lateraly. **1 Sideview** The line of sight along the longitudinal axis of ROI 1 reveals the hollow shape of the IM in this region. **2 Topview** Trajectories in a non-swollen part also show circular shape lateraly. Additionally, a perpendicular movement of a protein was obtained. **2 Sideview** The side view of ROI2 indicates that the perpendicular trajectory results from a single CV-SUγ which diffuses from the IBM inside a CM and stays confined mobile inside the CM until the fluorophore is bleached.

9.5.8 Trajectory directionality analysis in 3D tracking and localization microscopy of the F_1F_O ATP synthase subunit-γ in cells in different metabolic conditions

The trajectory directionality can be used to quantify the predominant direction in which mitochondrial membrane proteins diffuse. Thereby conclusions on the spatiotemporal organization and dynamics of CV-SUγ as well as structural features of mitochondria and changes of those during starvation and improved respiration can be drawn. The focus lied again on elongated and separated mitochondria (, marked mitochondrion 1 and 2). As mentioned before the ends of mitochondria and branching points were not taken into account for analysis of the trajectory directionality (Figure 24A). As describes previously the 4-step binning procedure was used to analyze the trajectory directionality.

9.5.8.1 Trajectory directionality analysis of the F_1F_O ATP synthase subunit-γ in cells in the control

In exemplary mitochondria in the control are shown. The longitudinal axis of the mitochondria was marked and their trajectory maps shown in B were interpolated to straightened trajectory maps (C). The gained pie chart diagram shows the directionality and the number of steps with a binning of 5°. The pie chart diagram of the mitochondrion No.1 shows a random directionality of the CV-SUγ trajectories. The pie

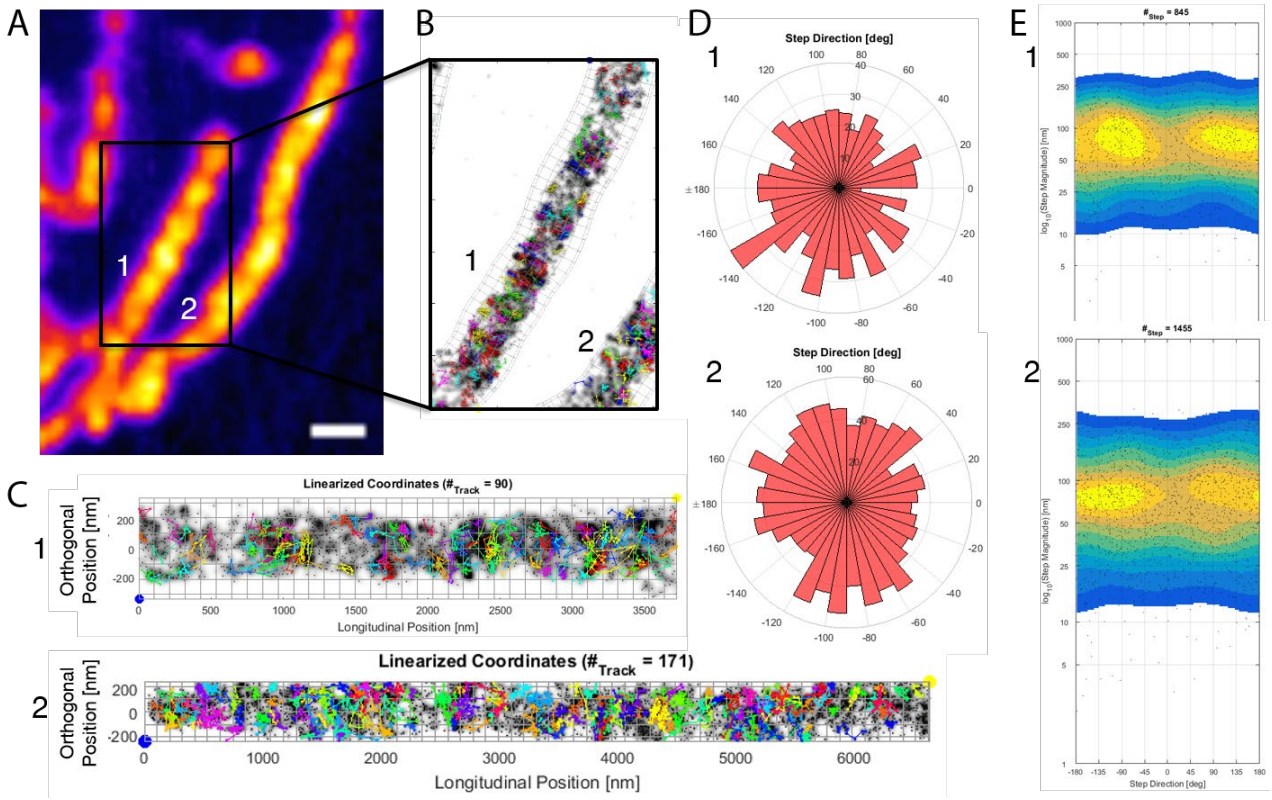

Figure 84 Trajectory directionality analysis of the F_1F_O ATP synthase subunit-γ in two exemplary mitochondria in the control condition
A Raw data image of the summed signals of CV-SUγ, with two mitochondria in a mitochondrial network (1, 2) Scale bar: 1 µm. **B** Trajectory map of a single mitochondrion. **C** Straighten trajectory maps of the two mitochondria shown in A. **D** Pie chart diagrams of the straighten trajectory maps shown in C. Pie chart diagram 1 shows a rather equal orientation of the trajectory directionality. Pie chart diagram 2 shows slight dominant directionality between -45° and -120° as well as between 40° and 120° but also between -160° and 150°. **E** Heat map of the data shown in D. The first diagram shows peaks around -90° and 110°. The second diagram around -110 and ± 180°.

chart diagram of the mitochondrion No.2 shows directionality of the CV-SUγ trajectories, with maxima between -60° to -120° but also maxima of directionalities in the longitudinal direction (D). However, the heat map shows different results (E). Here, both heat maps show that a majority of trajectories had a perpendicular trajectory directionality. The average step size of the perpendicular oriented trajectories was between 50 nm and 100 nm. In the heat map of mitochondrion No.1 the peaks are around -90° and 110°. In the heat map of the second mitochondrion the peaks are around 110° and ±180°. In the control experiments analysis of the trajectory directionality was performed on 22070 binned steps in total after the 4-step binning (Figure 85). In Figure 85A another trajectory map of CV-SUγ in the control experiments is shown. The trajectories occur accumulated in certain regions. In the straightened trajectory map of Figure 85B also cristae trajectories of CV-SUγ can be seen between the longitudinal positions of 4 µm to 5 µm. In total the 22070 binned steps of CV-SUγ trajectories showed a slight dominant direction to the orthogonal axis (Figure 85C). Plotting the data in a heat map showed a similar result (Figure 85D). Here the peaks are around 90° and -90° with a small shift to -45°. However, the pie chart diagram and the heat map also show many values in all other directions. This was expected from two-dimensional TALM experiments shown in chapter 9.2.3, these directionalities resulted from random diffusion in the IBM and confined mobility of CV-SUγ.

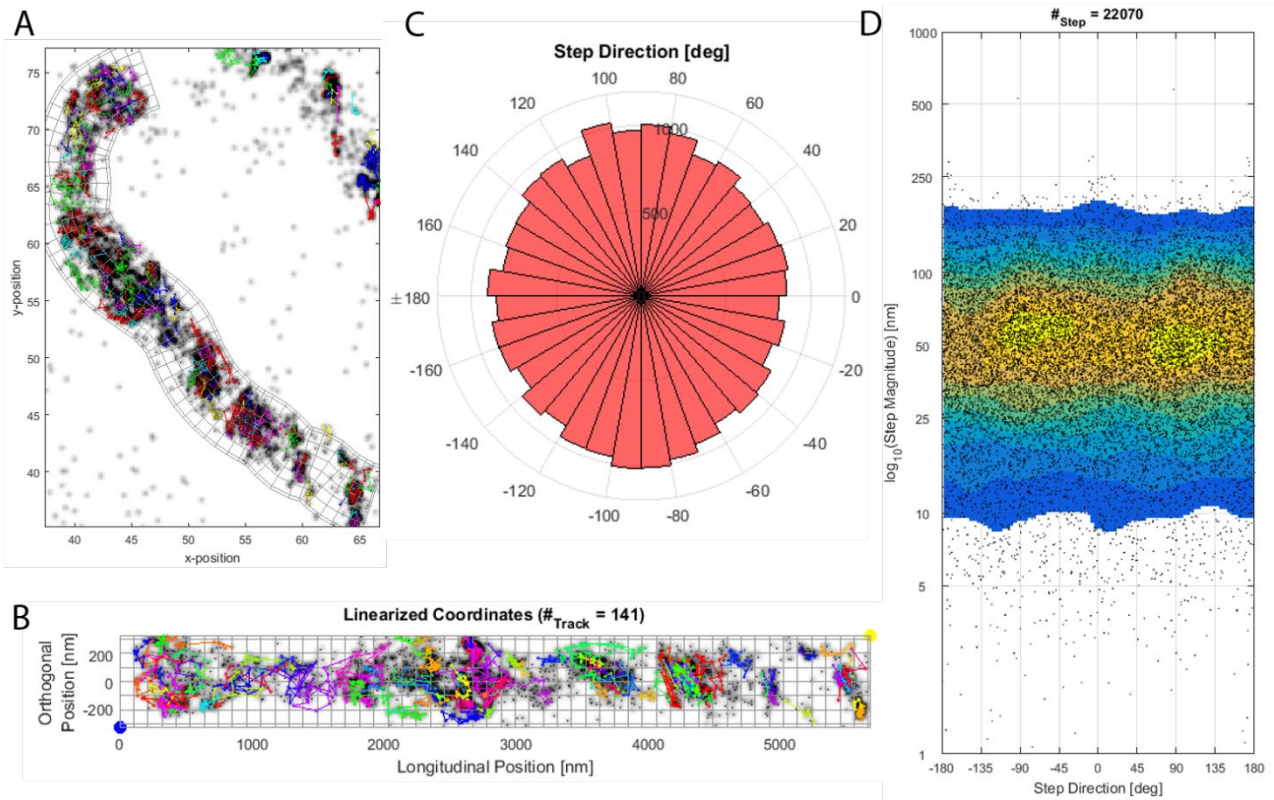

Figure 85 Trajectory directionality analysis of the F_1F_O ATP synthase subunit-γ in the control
A Exemplary trajectory map of a mitochondria. **B** Straighten trajectory map of the mitochondria shown in A. **C** Pie chart diagram of the trajectory orientation of 22070 steps after the 4-step binning procedure. **D** Heat map of the data shown in C. Peaks were obtained at an angle of 90° and -90°and around 50 nm step size.

9.5.8.2 Trajectory directionality analysis of the F_1F_O ATP synthase subunit-γ in cells during starvation

In order to analyze a possible change of the IM shape caused by starvation as it was shown by TEM, the trajectory directionality was analyzed again by MitoOrientedDynamics in mitochondria of cells kept in starving conditions. Similar to before the 4-step binning procedure was used. In the trajectory map mitochondria were again marked and the data was interpolated to a straightened trajectory map of each mitochondria (

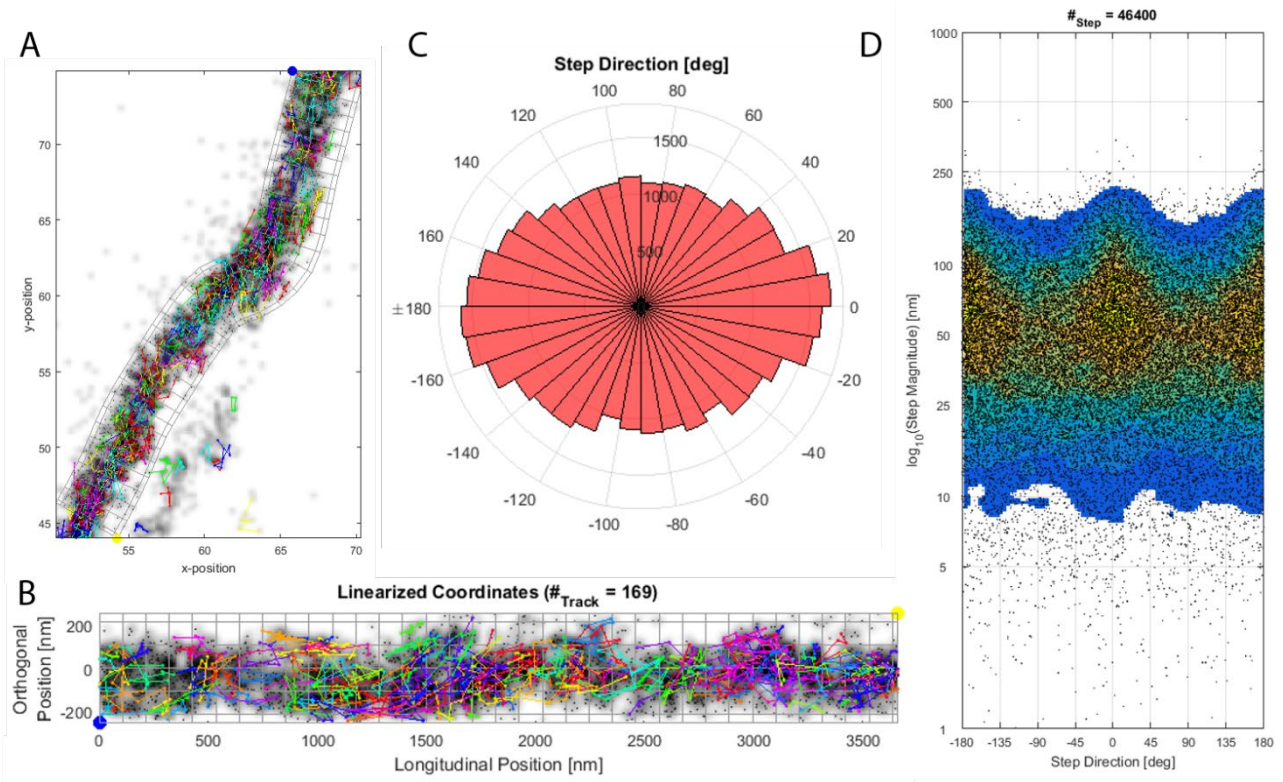

Figure 86A,B). In the exemplary shown mitochondrion, the trajectorie are homogenously distributed along the mitochondrion (

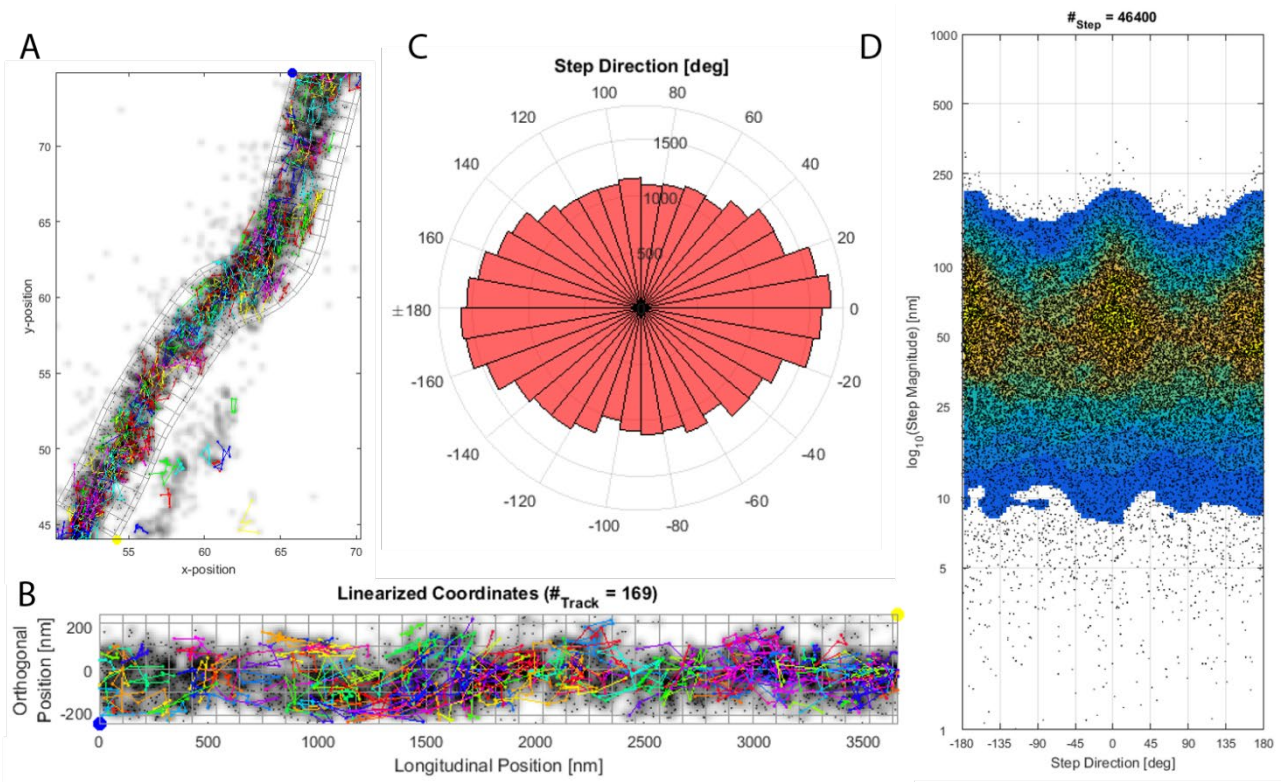

Figure 86A,B). In the straightened trajectory map no accumulation of trajectories at any position was observed (

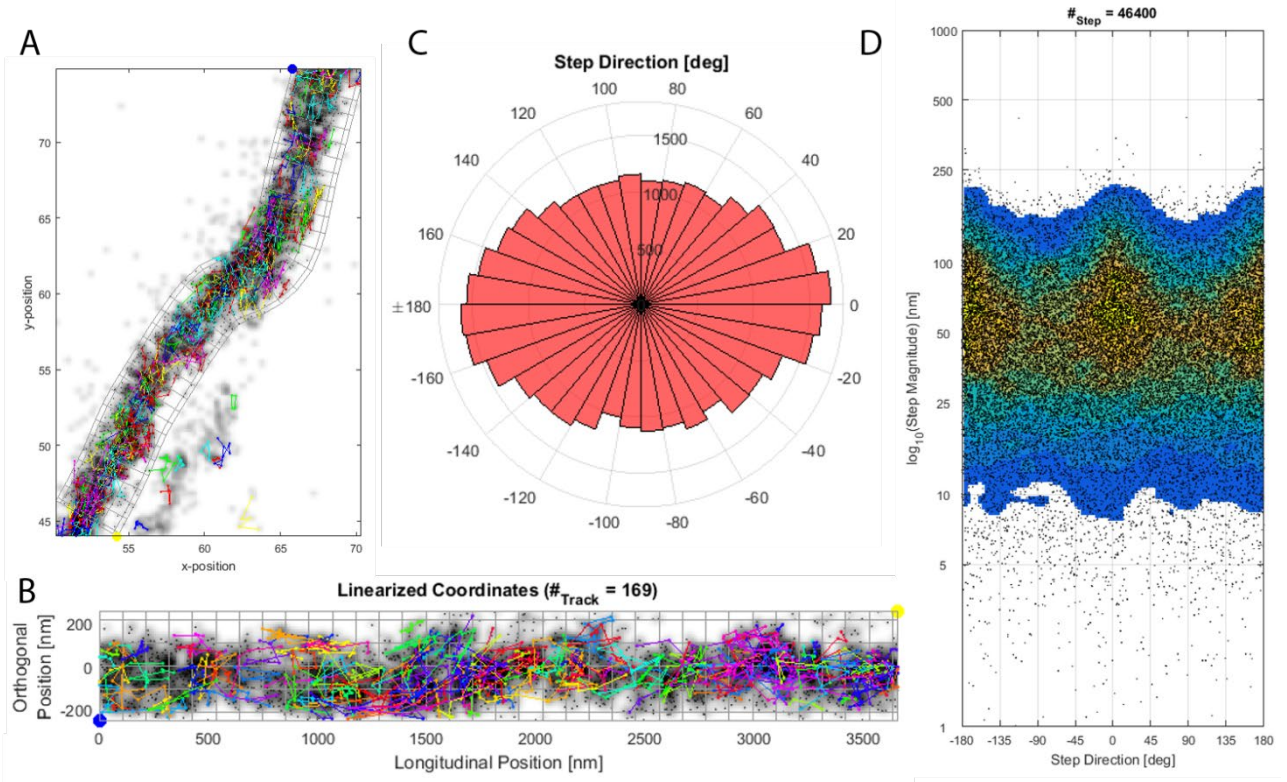

Figure 86B). In total 46400 binned steps after the 4-step binning of CV-SUγ trajectories were analyzed. The pie chart diagram of the trajectory direction of CV-SUγ in starvation showed a strong longitudinal directionality (

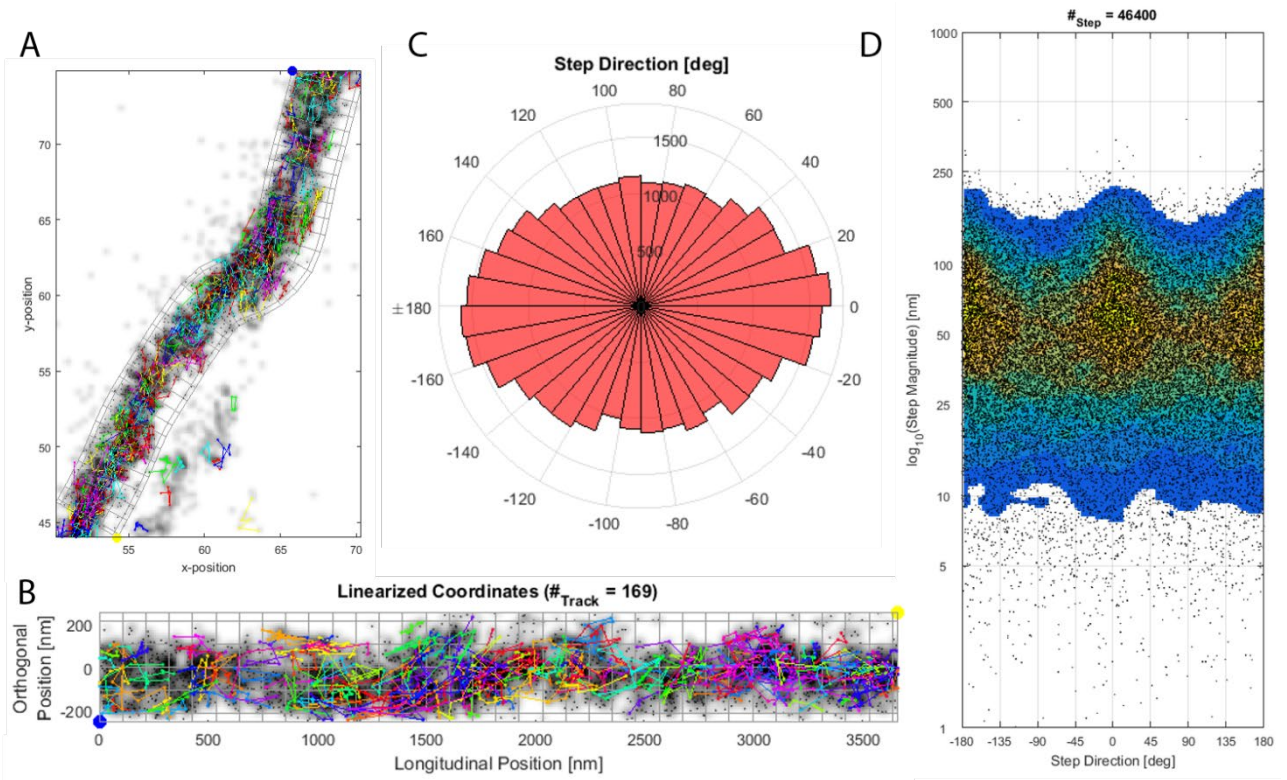

Figure 86C). The number of binned steps in the longitudinal direction reached the 1.5-fold of the number of binned steps along the perpendicular direction. The result in the heat map showed that most of the trajectories were oriented longitudinal in the ± 180° or in the 0° direction (

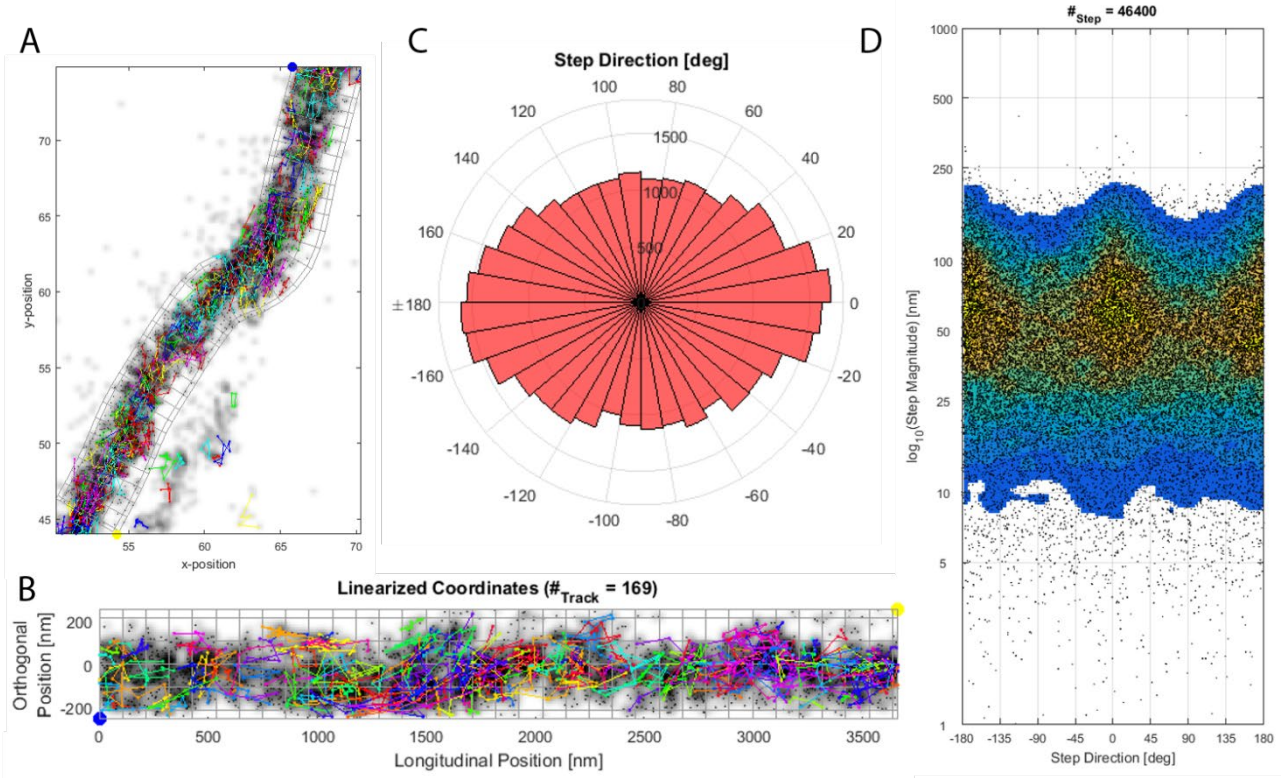

Figure 86D). Additionally, the step magnitude in the longitudinal direction reached larger maximal values. Together these results indicate a lack of the CM and the accompanied longitudinal movement of CV-SUγ in the IBM. 3D TALM already revealed the change of the IM shape due to starvation by 3D SPT of CV-SUγ. Furthermore, 3D TALM of CV-

SUγ in starving conditions illustrates that the spatiotemporal organization of CV-SUγ and an altered IM architecture were coupled to the metabolic state of the cell.

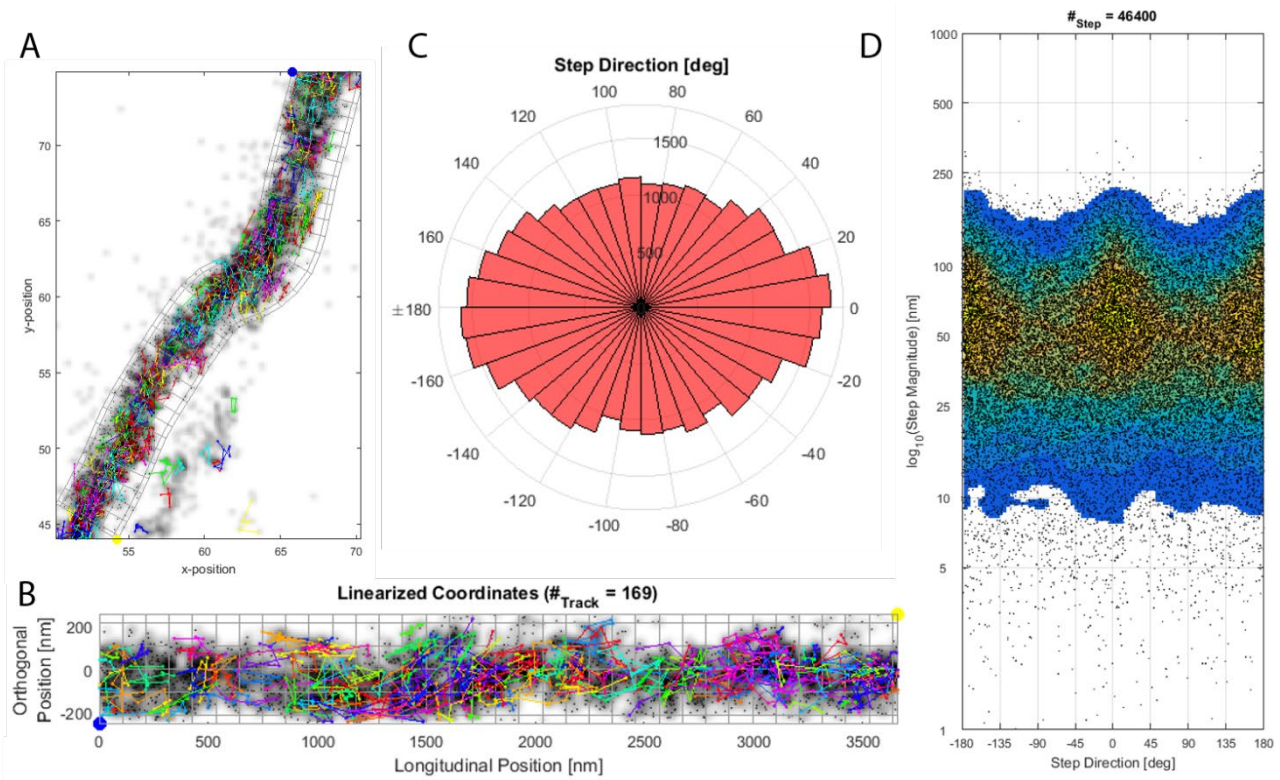

Figure 86 Trajectory directionality of F_1F_0 ATP synthase subunit-γ in cells during starvation conditions
A Exemplary trajectory map of a mitochondrion during starvation. **B** Straighten trajectory map of the mitochondria shown in A. **C** Pie chart diagram of 46400 steps after the 4-step binning. **D** Heat map of the data shown in C. The peaks are at an angle of 0° and ±180°.

9.5.8.3 Trajectory directionality analysis of the F_1F_O ATP synthase subunit-γ in cells during improved respiration

In order to quantify the trajectory directionality in improved respiratory condition the software MitoOrientedDynamics was used again. TEM and trajectories of CV-SUγ gained by 3D TALM already showed qualitatively that circular / spherical IM parts exist. The 4-step binning procedure was used as before. In Figure 87A an exemplary mitochondrion is shown. The marked mitochondrion was again interpolated to a straightened trajectory map. Directly obviously was a heterogeneous distribution of trajectories along the mitochondrion (Figure 87A,B). Between the longitudinal position 500 nm and 1.5 µm more trajectories can be seen than in the following 1 µm (Figure 87B). This indicates an influence of sub-compartmentation on the spatiotemporal protein organization of CV-SUγ, because CV-SUγ was enriched in some parts of the mitochondria, while other parts nearly lack CV-SUγ. Interestingly, performing trajectory directionality analysis of this mitochondrion depicted in the pie chart diagram showed an directionality of the trajectories to the perpendicular direction (Figure 87C). This gets even clearer in the heat map of the trajectory directionality analysis (Figure 87D). Here an accumulation of trajectory directionalities between 45° to 135° and -45° to -135° was visible. The step magnitude of the trajectories stays between 50 nm to 100 nm and equal compared to the control.

In

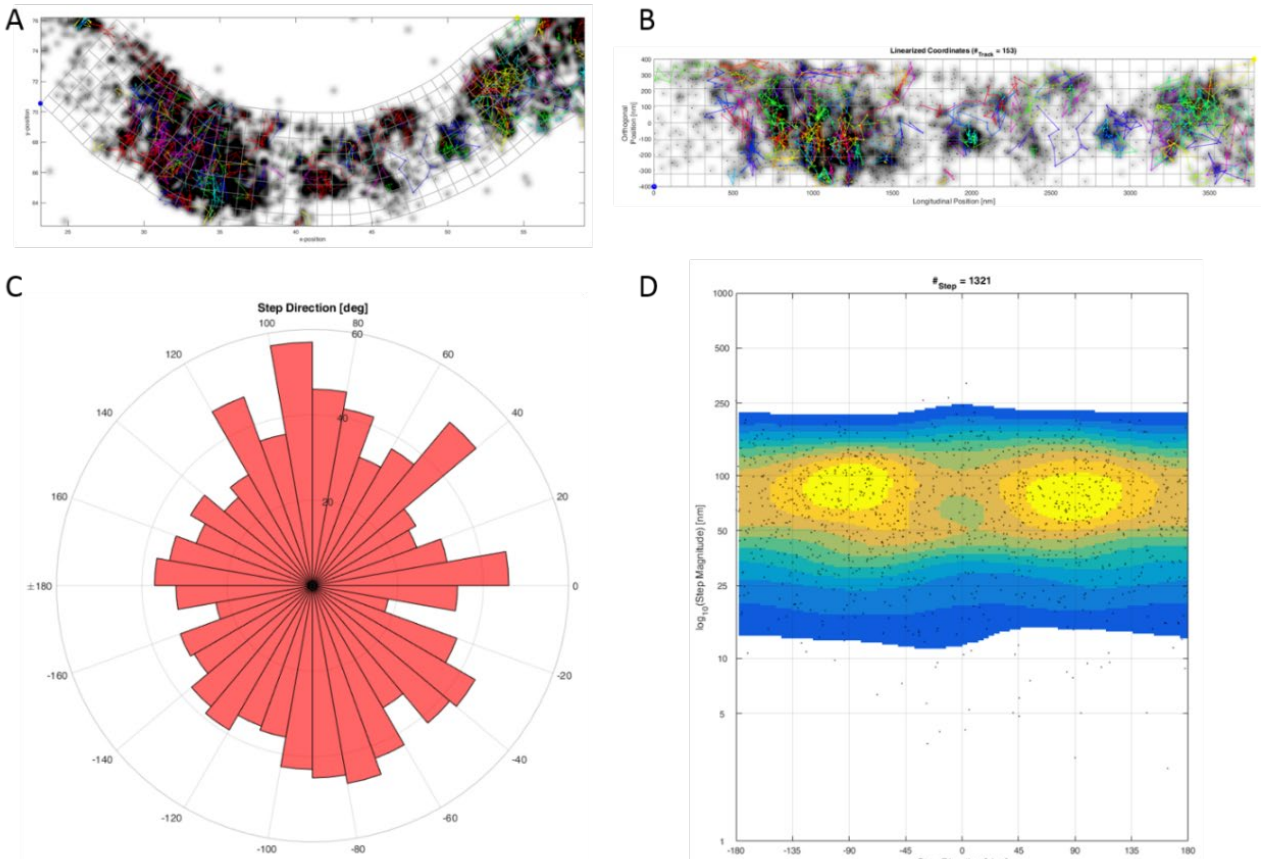

Figure 87 Trajectory directionality analysis of the F_1F_0 ATP synthase subunit-γ in a cell during improved respiration conditions

A Exemplary trajectory map of a mitochondrion in improved respiration. **B** Straighten trajectory map of the mitochondria shown in A. **C** Pie chart diagram of 46400 steps after the 4-step binning. **D** Heat map of the data shown in C. The peaks are at an angle of 0° and ±180°.

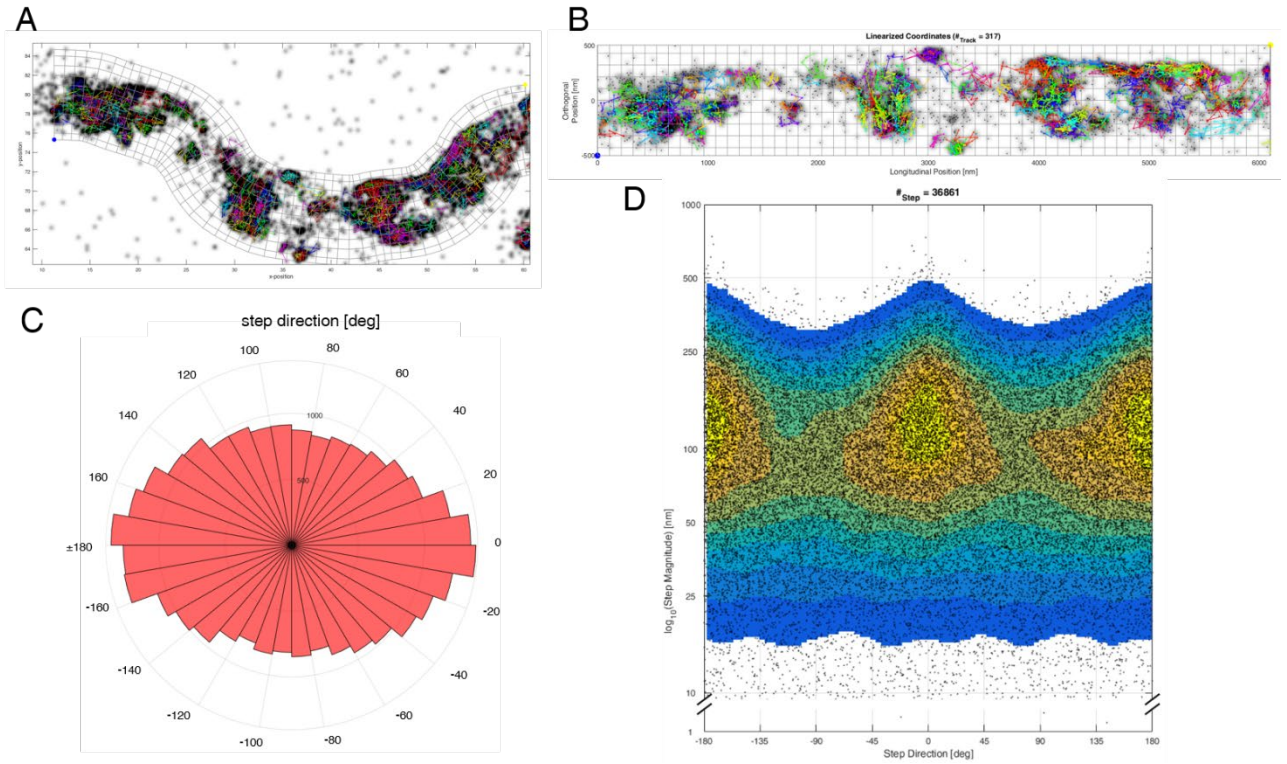

Figure 88A,B another exemplary trajectory map of a single mitochondrion is shown. The trajectory map supports the results from the mitochondrion shown before in Figure 87. The trajectories in

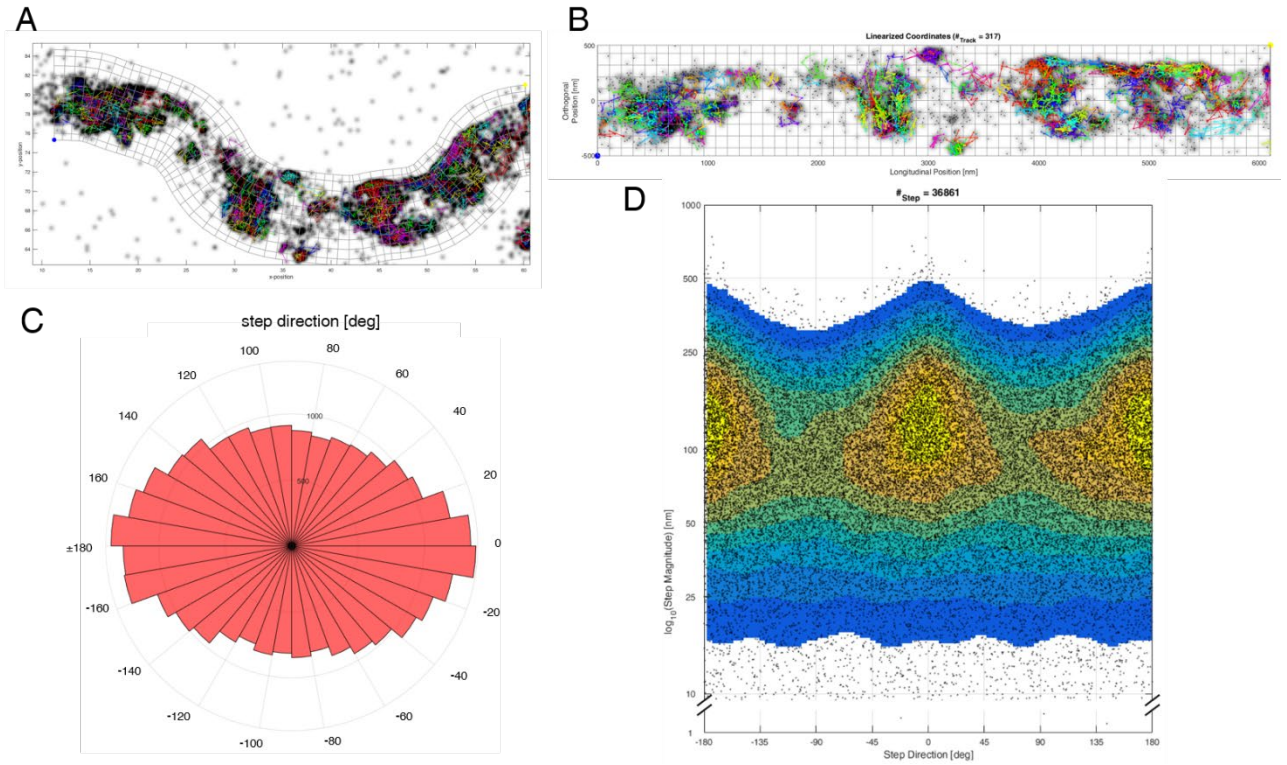

Figure 88 were again heterogeneously distributed and appeared accumulated in circular structures. In the straightened trajectory map of

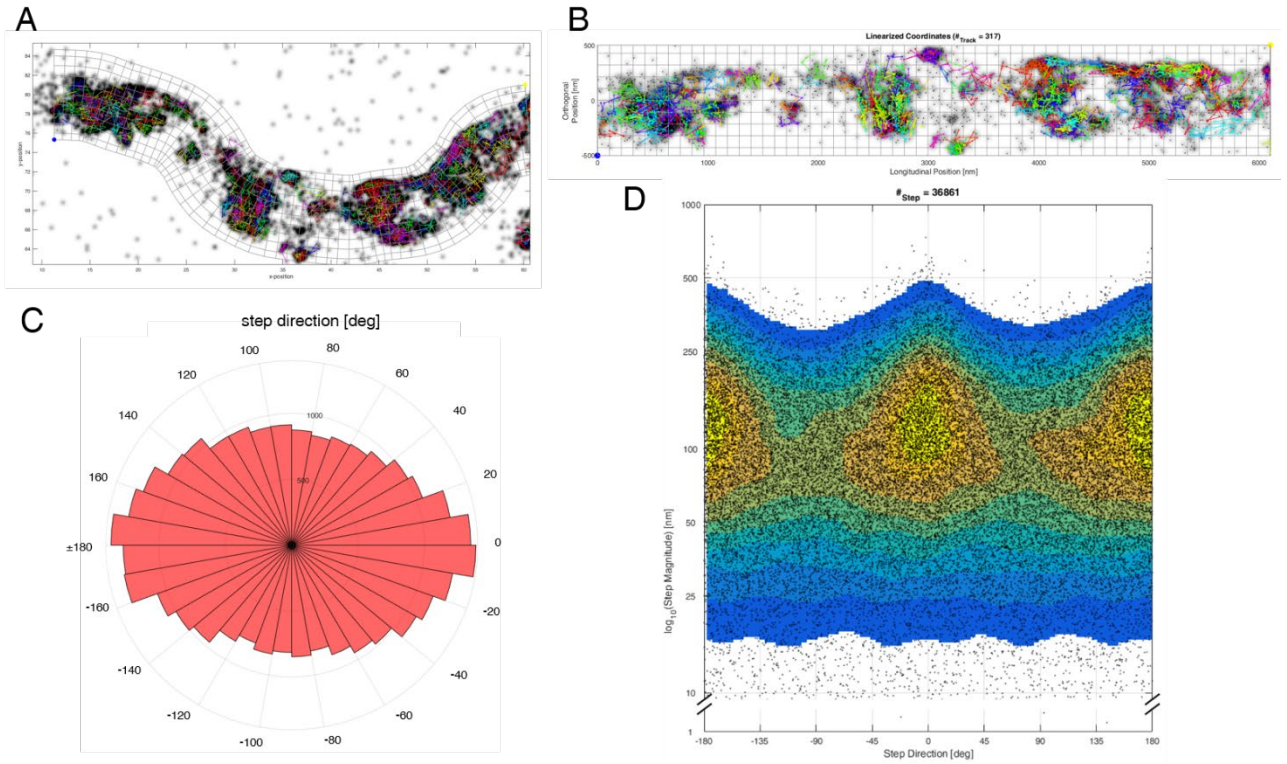

Figure 88B, at the longitudinal position of 4 µm a trajectory (red colored) traced the IM in a small circle. Such structural features of the IM in improved respiration was revealed before by TEM (

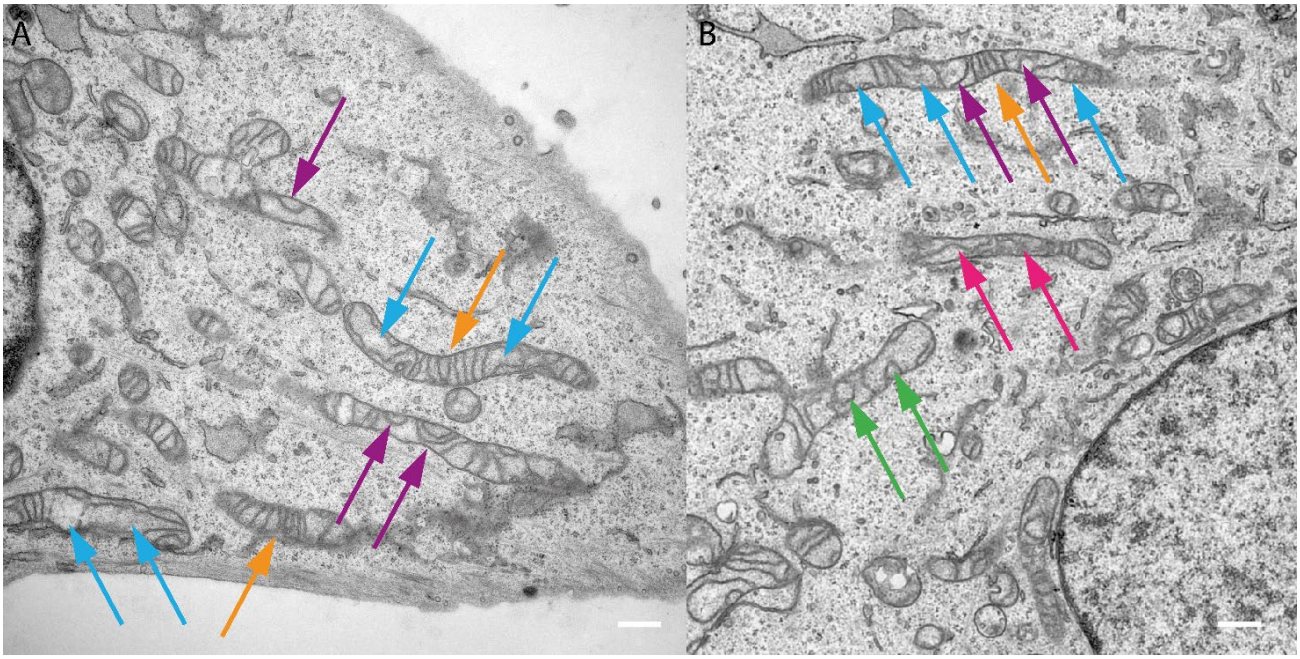

Figure 61). Thus, it was assumed that such trajectories follow a CM with a spherical shape. Additionally, in the longitudinal region between 4 µm and 5 µm a large spherical area was revealed. Those IM shapes were also obtained in TEM.

In experiments with an improved respiration in total 36861 binned steps after the 4-step binning procedure were analyzed. The pie chart diagram of the trajectory directionality analysis of all binned steps showed a dominant longitudinal movement of CV-SUγ (

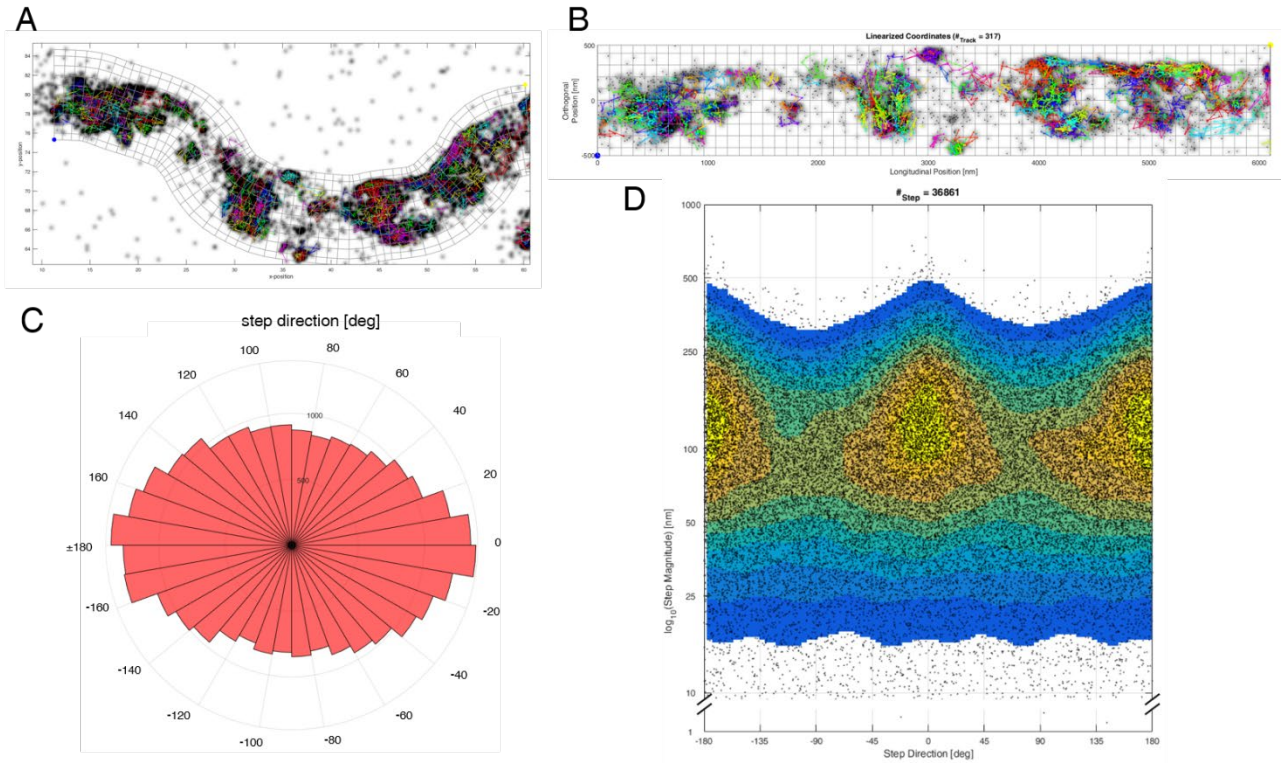

Figure 88C). This demonstrates a spatiotemporal and ultrastructural reorganizations caused by improved respiratory conditions. The amount of longitudinal oriented binned steps reachesd 1.5-fold of the binned steps in the perpendicular direction of starving conditions. This result was supported by the heat map (

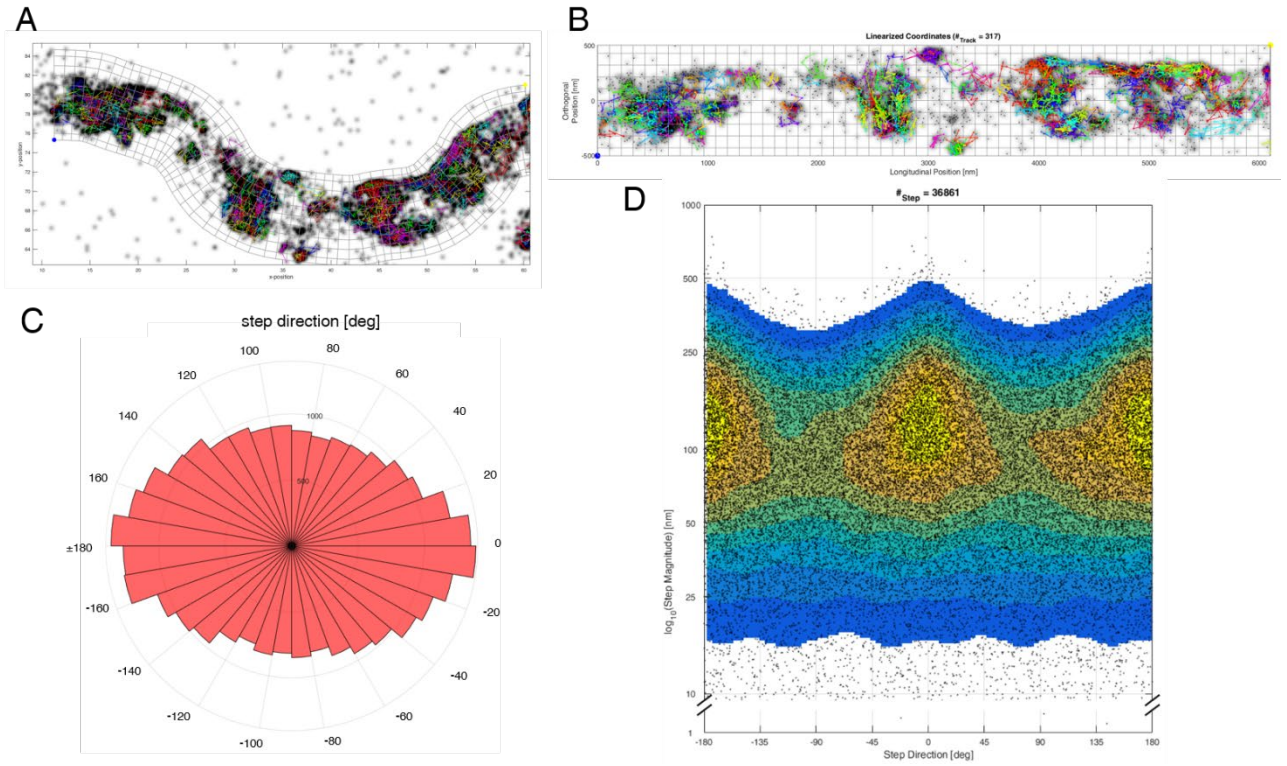

Figure 88D). The heat map also showed the dominant longitudinal movement. Additionally, it showed an increase of the jumpsize up to 500 nm in the longitudinal direction and that steps along the mitochondria showed a larger maximal step magnitude than perpendicular steps. The step magnitude of all direction increased compared to the

control and to the starvation condition.

Taken together the spatiotemporal organization of CV altered in improved respiratory conditions. Now circular trajectories occur revealing structural features like IM spheres, which were already obtained by TEM. Furthermore, the changes in the IM architecture influence the spatiotemporal organization of CV in such a manner that accumulations of CV in certain regions appear or vice versa. However, 3D TALM allowed to reveal these dynamics in living cells just by 3D SPT of CV-SUγ.

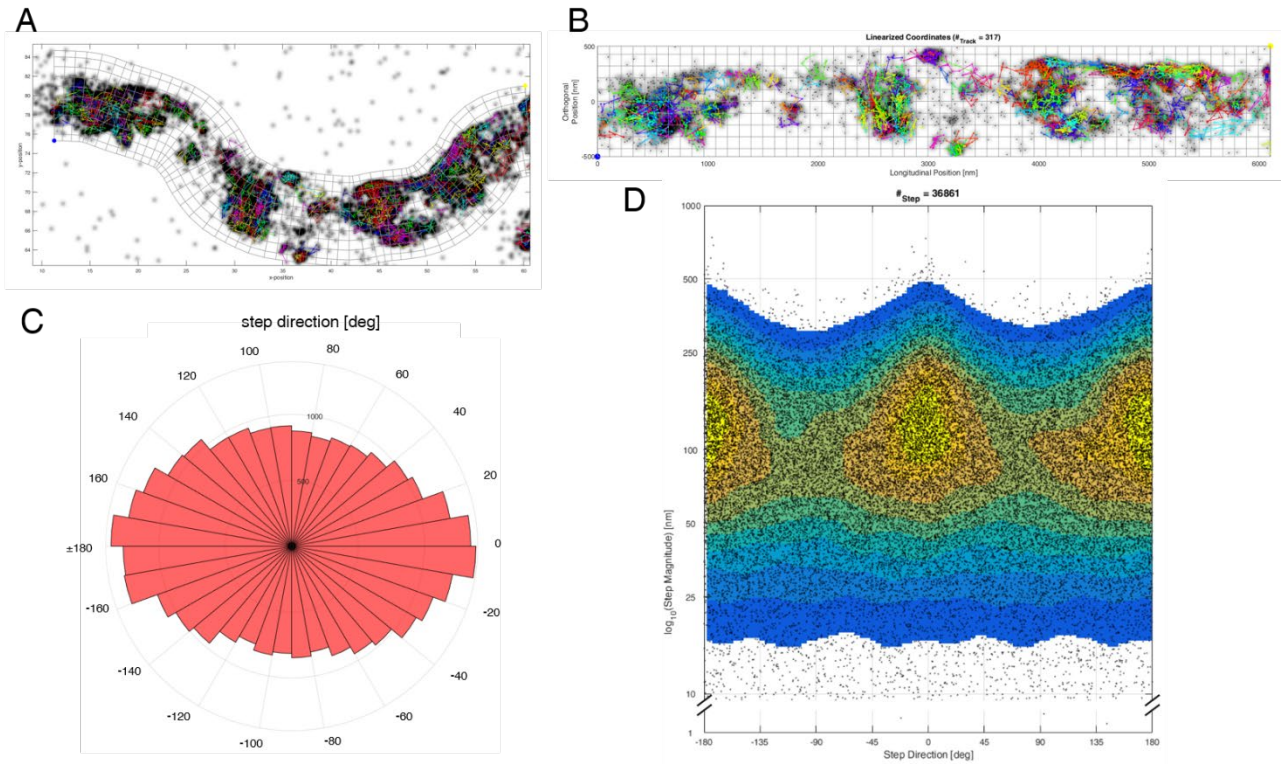

Figure 88 Trajectory directionality analysis of the F_1F_O ATP synthase subunit-γ in all cells imaged during improved respiration conditions

A Exemplary trajectory map of single mitochondrion during improved respiration. **B** Straighten trajectory map of the mitochondrion shown in A. **C** Pie chart diagram of 36861 binned steps by the 4-step binning. **D** Heat map of the binned steps supporting the longitudinal movement of CV-SUγ.

9.5.9 3D diffusion of the F_1F_O ATP synthase subunit-γ in cells during different metabolic conditions

The changes in the IM architecture, spatiotemporal protein organization and trafficking possibly affect the mobility of CV-SUγ. The predominant localization of CV-SUγ was changed due to starvation, because the CM vanishes in large areas of mitochondria and the IM got tubular. Thus, CV-SUγ diffuses mostly in the IBM. Here a possible change in the mobility needed to be investigated. 3D SPT allowed investigating the 3D mobility. The MSD of the proteins was measured and the mean D_{3D} (D_{3Dmean}) was calculated as described previously.

In all conditions only trajectories of CV-SUγ with a minimal jumpsize of 8 frames have been taken into account. In the case of the control experiments 30769 trajectories were obtained. In starving conditions 29255 trajectories of CV-SUγ were analyzed. In experiments of active respiring cells 27203 CV-SUγ-trajectories were taken into account. Figure 89 shows a histogram and a boxplot diagram of the D_{3D} CV-SUγ in all three conditions. Addtionally, the D_{3Dmean} values are shown in Table 11. CV-SUγ in the control experiment showed a D_{3Dmean} of 0.0404 ± 0.0115 µm²/s. The D_{3D} maximal value (D_{3Dmax}) 0.0603 µm²/s. The D_{3D} minimal value (D_{3Dmin}) was 0.0180 µm²/s (Figure 89, yellow dataset). In the case of starving conditions, the D_{3Dmean} was 0.0403 ± 0.0175 µm²/s. D_{3Dmax} in starving conditions increased to 0.0893 µm²/s. D_{3Dmin} in starving conditions was 0.0159 µm²/s (Figure 89, blue dataset). In improved respiring conditions the D_{3Dmean} increased significantly to 0.0554 ± 0.0113 µm²/s compared to the other conditions. D_{3Dmax} in improved respiring conditions was 0.0777 µm²/s. D_{3Dmin} in this condition increased to 0.0394 µm²/s (Figure 89, purple dataset). The mean D_{3Dmean} in starving condition did not changed significantly. However, the

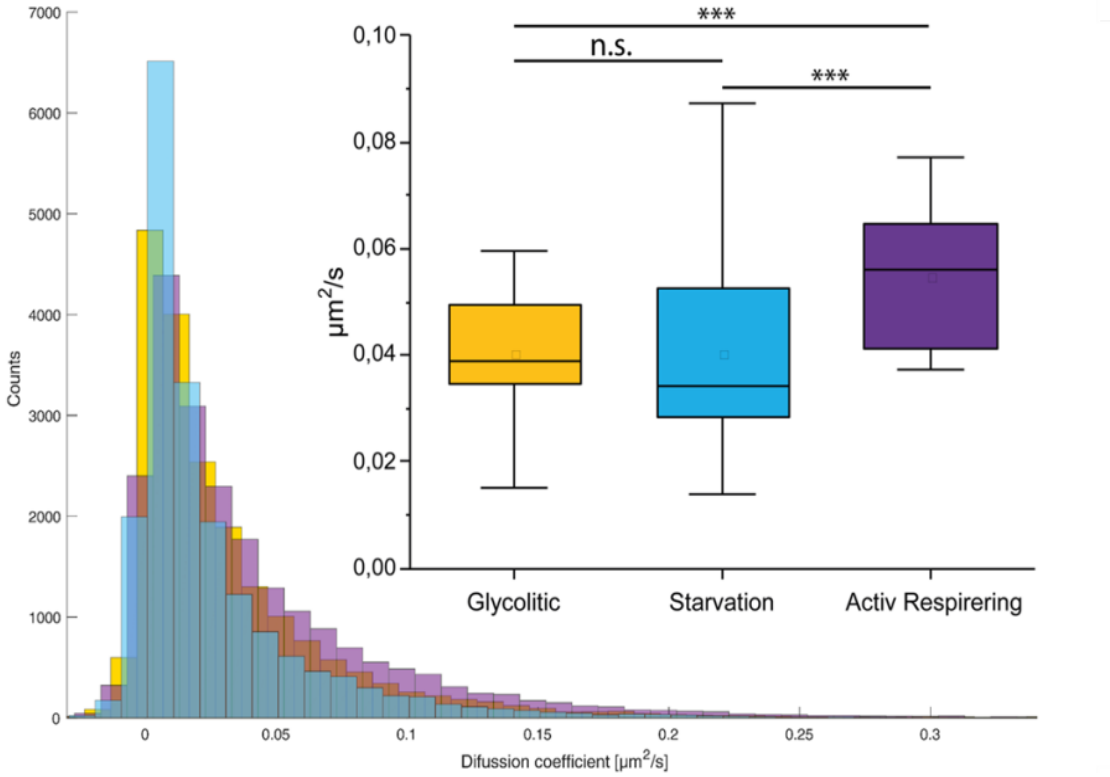

Figure 89 Diffusion coefficient of the F_1F_O ATP synthase subunit-γ in cells during different metabolic conditions

In the histogram the D_{3D} of all tracked CV-SUγ in the different metabolic conditions were plotted (Yellow hitogram = D_{3D}, control; blue histogram = D_{3D}, starvation; purple histogram = D_{3D},improved respiration). **B** Box-plot of the data shown in A. The mean value between CV-SUγ and CVγ in starving conditions is not significantly different. While the maximal value of CV-SUγ in starving conditions increases to 0.0893 µm²/s. CV-SUγ in improved respirering conditions shows a significant increased D_{3Dmean}. Significance levels were determined by a one-way ANOVA: $P \leq 0.001$ denoted with ***.

D_{3Dmax} increased due to starvation while the D_{3Dmin} stayed similar. 3D TALM of CV-SUγ in different metabolic conditions showed that starvation led to alarger spreading of the D_{3D}. Together with the trajectory directionality this showed that a faster mobility was coupled to a longitudinal directionality of the trajectories and thus by a reorganization of the IM shape like a loss of microcompartmentation by vanished cristae. But on the other hand, 3D TALM revealed that starvation did not increase the mobility of CV-SUγ in mean. Furthermore, the mobility of CV in improved respiration increased significantly compared to the D_{3Dmean} in the control and starvation. Taken the trajectory directionality into account this increased mobility was also coupled to a dominant trajectory directionality along the longitudinal axis of mitochondria. However, why the mobility in improved respiration in mean was significantly higher and in starvation not, although two-dimesnional TALM revleaed this stays unclear. Possibliy the lack of a subpopulation fit of the D_{3D} is an explanation. The IM architecture was drastically changed in improved respiratory conditions as trajectorie maps and TEM showed. Thus, the changed IM architecture once more seems to influence the mobility of CV.

Table 11 3D apparent diffusion coefficient of the F_1F_O ATP synthase subunit-γ in the three metabolic conditions

	CV-SUγ (control)	**CV-SUγ (starvation)**	**CV-SUγ (improved respiration)**
D_{3Dmean} [µm²/s]	0.0404 ± 0.0115	0.0403 ± 0.0175	0.0554 ± 0.0113
D_{3Dmin} [µm²/s]	0.0180	0.0159	0.0394
D_{3Dmax} [µm²/s]	0.0603	0.0893	0.0777

9.5.10 Summary of 3D TALM of the F_1F_O ATP synthase subunit-γ in cells during different metabolic conditions

Taken together 3D TALM experiments reveal the 3D spatiotemporal protein organization of Tom20 and CV-SUγ, *in situ*. The localization precision reached lateral resolution of σ_x = 27.44 ± 4.04 nm and σ_y = 30.23 ± 3.70 nm. The axial localization precision was σ_z = 47.54 ± 4.05 nm. Reconstructions of the 3D SML data of the different proteins including the localization precision allowed to reconstruct the mitochondrial shape with a high precision in all three dimensions. Reconstructions of the OM by Tom20 resulted in super-resolved images of the OM in living cells. Here, the tubular OM could partially be reconstructed. However, taking the 3D SPT data into account, trajectories of Tom20 allowed to trace the shape of the OM.

In the case of CV-SUγ the spatiotemporal protein organization in connection to different metabolic conditions could be revealed. In control experiments 3D SML of CV-SUγ resulted in super-resolved images of the IM. These images revealed that the CM expands through the entire mitochondria as 3D accumulations localizations could be seen in small z-slices of mitochondria. However, the IM architecture in the control was not clearly revealed by 3D SML. Nevertheless, 3D SPT allowed to reveal diffusion in cristae and partially the IM architecture. 3D TALM in starvation revealed that the IM lacks cristae and became partially tubular like the OM. Again, this tubular shape was revealed even clearer by using the 3D SPT data. Here, the trajectories of CV-SUγ once more traced the shape of the IM, in which they moved within. Same was true for improved respiratory conditions, where the complex altered

ultrastructure was revealed by 3D TALM of CV-SUγ. Here, spherical IM sub-comparmtnes were revealed in all three dimensions by accumulations of trajectories and circular trajectories. However, also orthogonal trajectories were found in improved respiratory conditions, here 3D TALM revealed that perpendicular movement of CV-SUγ resulting from diffusion in the CM of disc like shape of cristae. Furthermore, trajectory directionality analysis revealed a tendency to the orthogonal movement of CV-SUγ in the control, resulting from a dominant localization in the CM. Here, movement of CV-SUγ in the IBM lowered this tendency.

3D TALM in starvation showed that cristae were reduced or vanished and the CM became part of the IBM forcing the proteins to diffuse in the IBM. 3D SPT and analyzing the trajectory directionality of CV-SUγ demonstrated a spatial unhindered and longitudinal movement along the IBM. As no confined trajectories were obtained and the trajectory directionality was dominantly longitudinal. This resulted in a dominant longitudinal movement of CV-SUγ. In contrast to this improved respiration led to a different spatiotemporal protein organization in the IM. Here the trajectory maps showed circular sub-compartments of the IM, indicating a complex rearrangement of the IM.

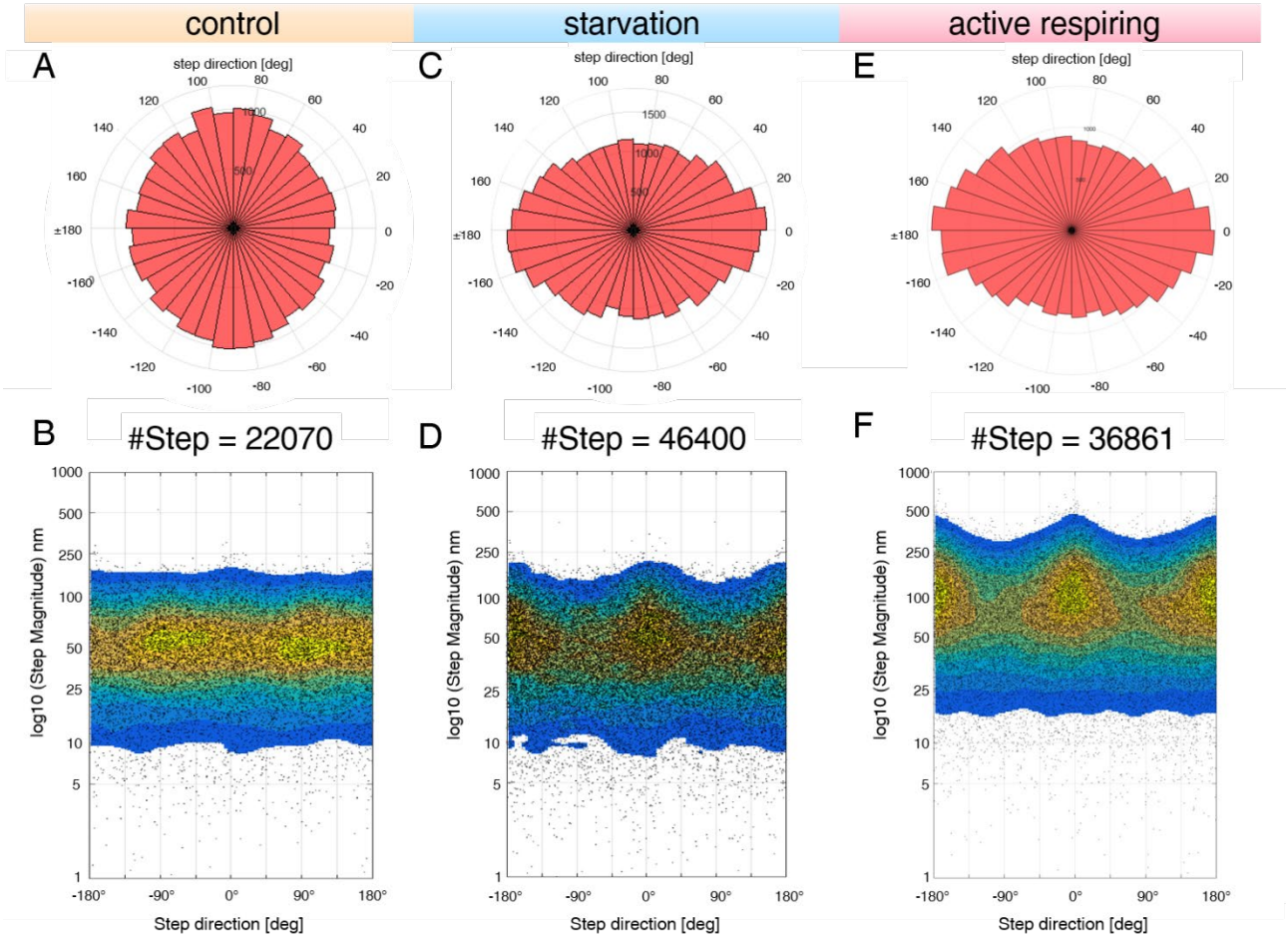

Figure 90 Shift of trajectory directionality in all three metabolic conditions
A Trajectory directionality of CV-SUγ in control experiments plotted in a pie chart diagram. CV-SUγ trajectories are oriented in a dominant perpendicular direction. **B** The heat map of the data shown in A reflects the same result. An accumulation of binned steps at ~±90° was obtained. **C** In starvation the trajectory directionality is altered and follows the longitudinal direction. **D** The heat map shows a large number of longitudinal steps, while the perpendicular oriented steps get less. **E** The trajectory directionality of CV-SUγ in improved respiratory conditions is also longitudinal but still perpendicular movement occurs. **F** The heat map of the data shown in E shows a larger amount of perpendicular movement compared to the trajectory directionality in starving conditions.

Additionally, the spatiotemporal trafficking of CV-SUγ seemed to stick to the spherical sub-compartments as most of the localizations and trajectories accumulated in those IM areas. This points to large and active sub-compartments in the IM. The comparison of the shift of the trajectory directionalitys in the three different metabolic conditions is shown in

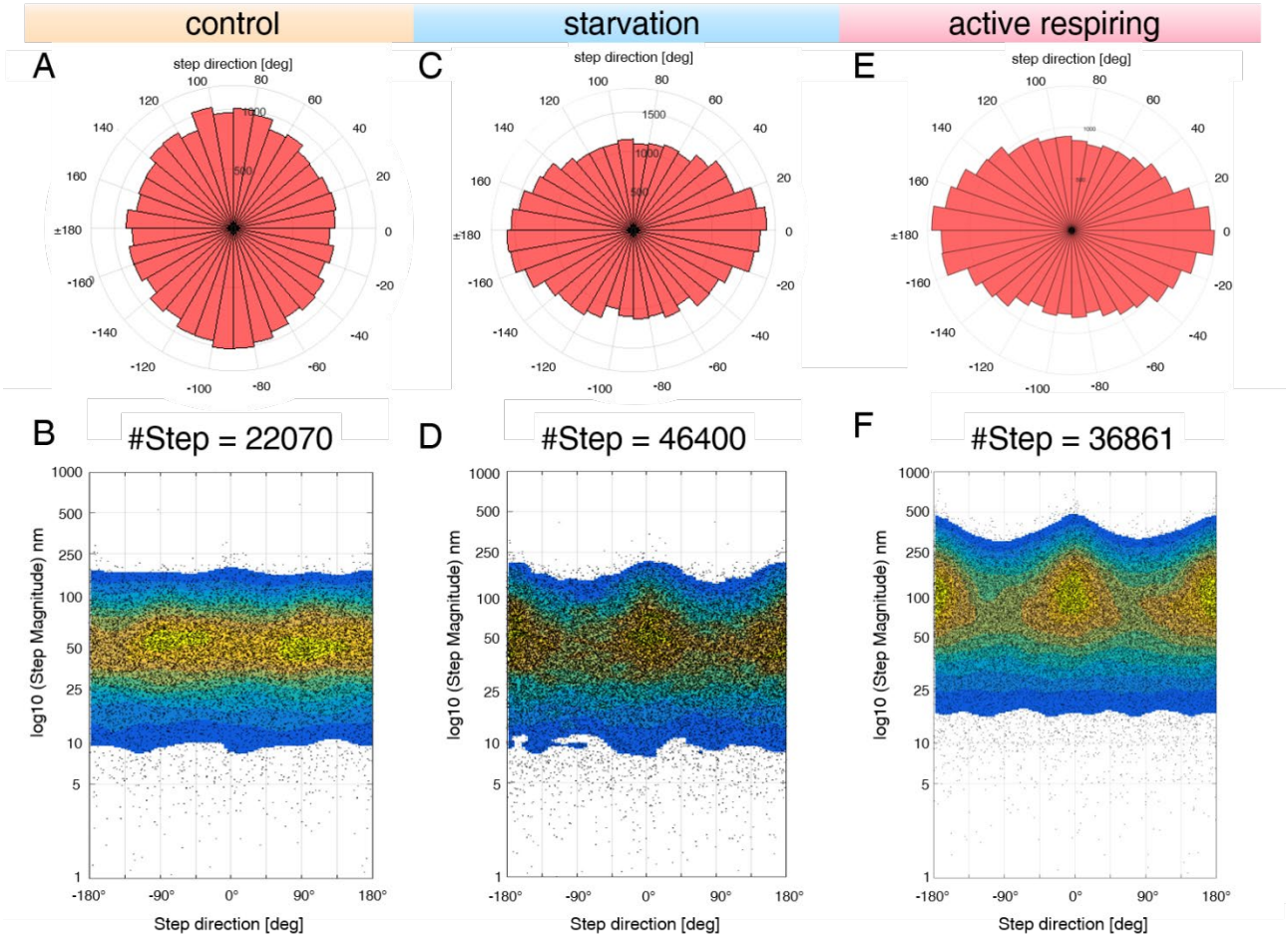

Figure 90.

Finally, 3D TALM proved itself a simple and cost-efficient method to investigate the spatiotemporal protein organization, the dynamics of proteins within sub-compartments and as an analytic tool of structural features of mitochondrial membranes, in living cells. Furthermore, 3D TALM was the first technique, which revealed the OM and parts of the IM by 3D SPT.

10 Discussion and Conclusion

10.1 TALM of mitochondrial proteins

10.1.1 TALM allows to determine the spatiotemporal organization of mitochondrial proteins and to detect mitochondrial subcompartments

The present results of mitochondrial proteins demonstrate TALM allows to investigate the spatiotemporal mitochondrial protein organization in living cells. Using TALM on different mitochondrial proteins allows to reveal their dominant localization, *in situ*. TALM was compared to fluorescent recovery after photobleaching (FRAP) and fluorescent correlation spectroscopy (FCS) (chapter 9.2.1). In FRAP experiments an area of the membrane is bleached and the D_{app} of the mobile proteins diffusing into the bleached area is calculated. Thus FRAP can only distinguish the mobility of mobile proteins and their relative amount. Detecting confined / immobile proteins cannot be done by FRAP. FRAP studies show higher D_{app} than TALM experiments. Two reasons are important for this: 1) FRAP is diffraction limited and by this a coarse technique. 2) In FRAP experiments slow and confined molecules do not contribute to the recovery of the fluorescence.

FCS depends on diffusion of molecules in the confocal volume. The diffusion time (τ_D) through the confocal volume can be determined by the decrease in the (auto)-correlation function. However, FCS is always in average of many molecules.

In contrast, SPT methods like TALM allows to investigate the dynamics of single proteins, the averaged D_{app} and to detect subpopulations in the D_{app} like confined mobilities and mobile proteins. Furthermore, TALM allows to reveal the localization of proteins in mitochondrial sub-compartments and their mobility within those microcompartments (Appelhans et al., 2012, Appelhans and Busch, 2017b). By the combination of accumulations of localizations / localization patterns and trajectories of CV-SUγ conclusions on the shape of the IM can be drawn (Appelhans et al., 2012). Here, the perpendicular trajectories of CV-SUγ result from diffusion in the CM. In contrast longitudinal movement reflects diffusion in the IBM. Furthermore, certain

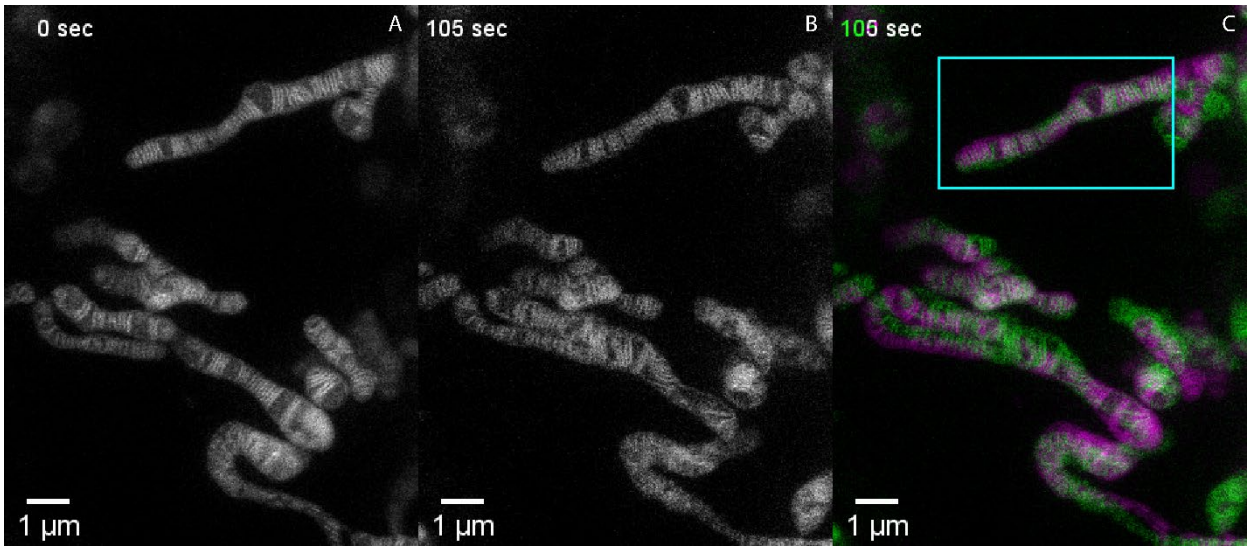

Figure 91 Live-cell time-lapse STED nanoscopy of mitochondria
Time laps image of mitochondria via STED microscopy. Here, STED nanoscopy allows to reveal the morphology of mitochondria and its ultrastructure in a living cell over time. **A** Start of the time-lapse. **B** Image after 105 seconds of the mitochondrial network shown in A. **C** Merged image of A and B. (Adapted from: Stephan et al., 2019)

proteins were localized only in the IBM (Appelhans and Busch, 2017b). Thus, TALM can also be used to distinguish between different membranes and subcompartments of the IM. If the mitochondria itself did not move, fused with other mitochondria or fragmented during imaging a conserved ultrastructure was assumed. Live cell STED nanoscopy of mitochondria proved that the IM architecture of mitochondria which did not move or undergow fusion or fission events is conserved for short time periods of 100 seconds (Stephan et al., 2019) (

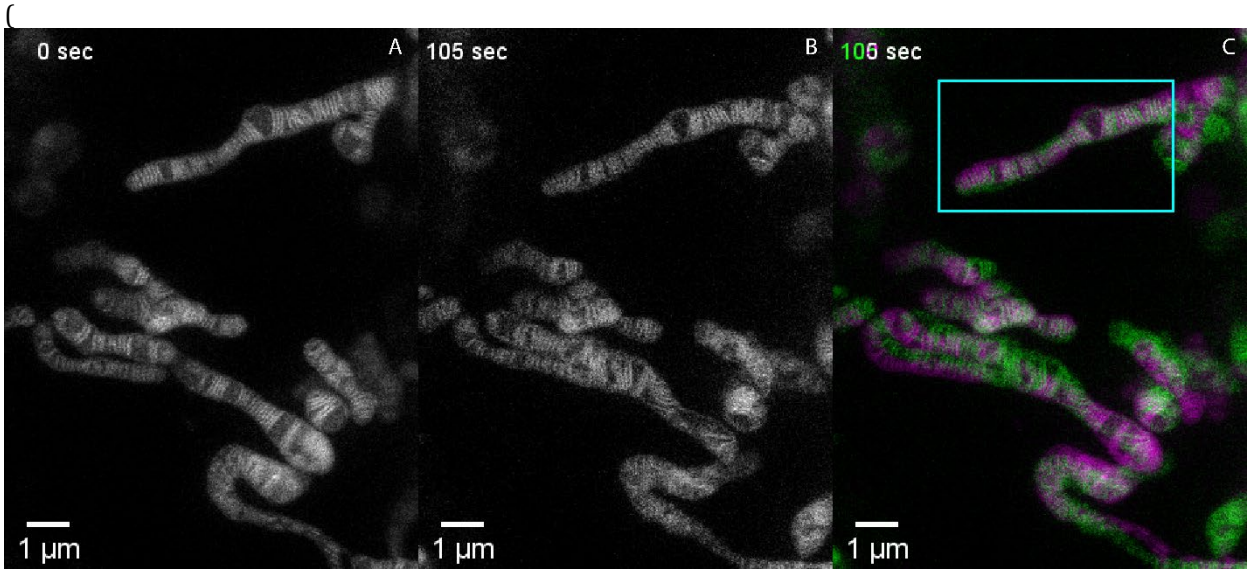

Figure 91). Here, the ultrastructure of mitochondria was revealed in living cells. Comparing the shape of the IM of the mitochondrion in the blue square over time in contrast to the other mitochondria, which undergo fission and fusion events, it gets clear that the ultrastructure is strongly affected by fusion and fission. However, the mitochondriom in the blue square which did not undergo those events stayed at its position and even the ultrastructure was conserved over more than 100 seconds (

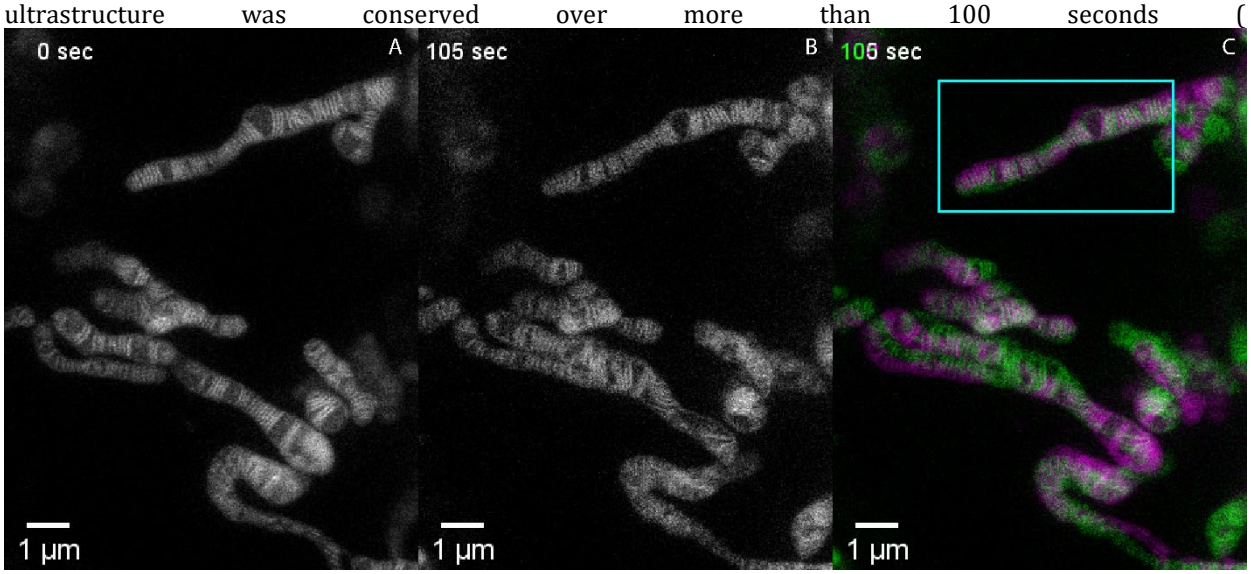

Figure 91). In TALM experiments 3000 to 4000 frames were recorded with either 16 ms or 32 ms exposure time. In maximum this results in an imaging time of 128 s for 32 ms exposure time and 64 s for 16 ms exposure time respectively. Thus, TALM trajectories which reveal the perpendicular mobility of proteins were not affected by the mobility of mitochondria or rearrangement of the IM, if the mitochondria did not move or undergo fusion or fission events during recording. Therefore, a mobility of the imaged mitochondria was

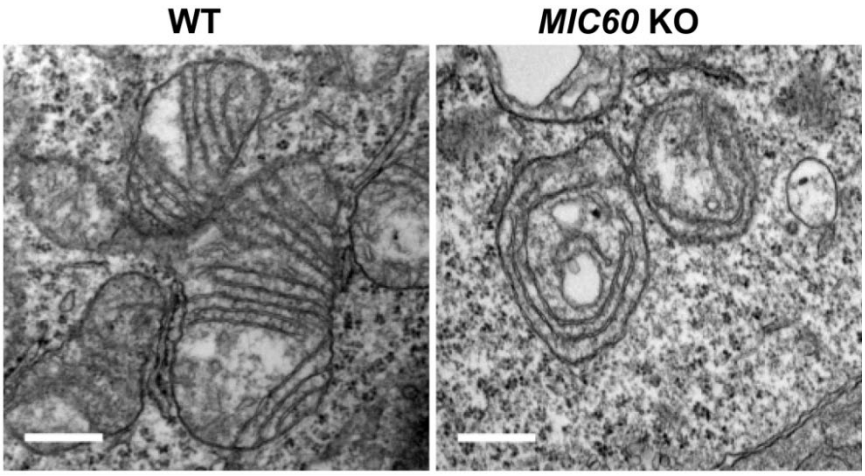

Figure 92 Representative transmission electron microscopy images of mitochondria in wilde-type, MIC60 knock-out HAP1 cells.
TEM image of mitochondria in HAP1 cells. Mitochondria in HAP1 cells wild-type (wt) show regular cristae (left panel). Knock-ou (KO)t of Mic60 leads circular cristae. Scale bar: 0.5 µm (Figure adapted from Kondadi et al., 2020)

excluded by comparing the localization data of the first 500 frames to the last 500 frames (Appelhans and Busch, 2017a) (chapter 13.5.1).

In TALM experiments, hFis1, Tom7, Tom20 and Tom40 were imaged as examples of proteins diffusing in the OM (chapter 9.2.1). Trajectory maps of hFis and Tom20 show a rather unhindered and random oriented dynamic in the OM. The D_{app} of the mobie fraction (D_{mobile}) were $D_{mobile, hFis}$ = 0.17 µm²/s for of hFis and $D_{mobile, Tom20}$ = 0.142 µm²/s for Tom20. So, both proteins show a quite similar mobility. Additionally, 14% of hFis and Tom20 had a D_{app} < 0.009 µm²/s indicating confined mobility for this fraction. A confinement in the OM cannot be based on a structural obstacle of the OM, rather by interaction with other proteins. Thus, it can be suggested that inactive proteins in the OM move relatively fast and undirected in the OM, while functional active proteins, which need to stick to a certain position to fulfill their function become confined mobile. In the case of Tom20 this can be explained by interaction of the Tom-complex in the OM with the Tim-complex in the IM.

As the maximal D_{app} of hFis and Tom20 is underestimated due to the tubular structure of the OM it needs to be corrected. A correction which takes the geometry of the OM into account results in an increase of the D_{app} to the corrected D_{app} ($D_{appcorr}$). In the case of hFis this results into a $D_{appcorr}$ = 0.410 µm²/s and for Tom20 into a $D_{appcorr}$ = 0.215 µm²/s (Appelhans et al, 2012, Appelhans and Busch, 2017b). These values are still lower than those obtained from FRAP experiments (D= 0.6 µm²/s and D= 0.7 µm²/s, respectively) (Appelhans and Busch, 2017b, Sukhorukov et al, 2009). On the one hand this shows that unhindered diffusion of proteins in the OM differs a lot. On the other hand, this demonstrates once more the power of TALM against FRAP, as FRAP does not allow to calculate for the geometric corrected mobility of proteins. Furthermore, SPT of mitochondrial proteins is so far the only way to reveal whether a single protein is mobile or confined mobile. A confined mobility of a protein always indicates an interplay with other proteins, which often is relevant for its function. SPT methods like TALM are so far the only way to identify and discriminate the spatiotemporal organization and trafficking of proteins as other techniques like FRAP and FCS cannot detect confined mobility and therefore do not take these spatiotemporal events of proteins into account.

The ultrastructure of mitochondria is influenced by the MINOS/MICOS complex. Here Mic60 and Mic10 play an important role. A knockout of Mic60 leads to an onion like structure of the IM (Figure 92) (Kondadi et al., 2020). TALM revealed the spatiotemporal protein organization of Mic60 (Appelhans and Busch, 2017b) (chapter 9.2.1) in a pearl-like arrangement along both sides of the IBM. This can only be explained by the function of Mic60 in CJs formation. Indicating that TALM experiments of Mic60 allow to distinguish positions

of the CJs. Thus, confined mobile proteins of Mic60 are a validate candidate as a marker for the CJs. The diffusion of the mobile fraction of Mic60 measured by TALM resulted in a $D_{app,\ mobile,\ Mic60}$= 0.063 µm²/s (Appelhans and Busch, 2017b, chapter 9.2.1). Similar results were found by SPT of Mic60 in HeLa cells using the Fiji plugin Trajectory classifier (Kondadi et al., 2020) (Figure 93). Here, Mic60 also showed a confined mobility along the IBM.

Tim23 also diffuses in the IM (chapter 9.2.1). Trajectory maps of Tim23 demonstrate a dominant diffusion in the IBM as the trajectories were rather oriented longitudinal at both sides of the IBM. In some datasets confined trajectories in a neckless like disposition along the IBM were obtained similar to Mic60 and Mic10 (for Mic10 see chapter 9.3.4). This shows a clear organization of Tim23 in the IM as no perpendicular trajectories were obtained/ diffusion in the CM was not obtained. Thus, Tim23 diffuses only in the IBM, but the confined mobility of Tim23 rather results from interaction with the Tom-complex. Tim23 showed a D_{app} = 0.057 µm²/s (Appelhans and Busch, 2017b). Diffusion analysis by TALM of other proteins in the IM like Cox and CV-SUγ ,resulted in D_{app} = 0.056 µm²/s and D_{app} = 0.070 µm²/s, respectively (Appelhans and Busch, 2017b). Furthermore, the trajectory maps of Cox and CV-SUγ indicate a restricted diffusion of those specific IM proteins in cristae. Interestingly the IM proteins: Tim23, Mic60, Cox and CV showed similar D_{app} of their mobile fraction, although their specific localization was clearly different. This different localization of mitochondrial proteins in the IM allows to use certain membrane proteins like Mic60, Mic10, Tim23 and CV-SUγ as markers for mitochondrial sub-compartments. Thus, proteins of the MINOS/MICOS complex allow to discriminate where CJs were localized. Tim23 allows to determine the IBM, while the TALM data of CV-SUγ allows to reveal the IM shape and the localization of cristae. Finally, TALM allows to distinguish if single molecules show different spatiotemporal dynamics. Thus, Mic60 is mostly confined mobile, while other proteins of the IM like Tim23 and CV did not show this conserved confinement. Tim23 interacts with the Tom-complex in order to import proteins in the IM amd matrix. Thus, a higher mobility allows the protein to search for its interaction partner. In the case of CV, it makes sense that a diffusion of monomeric CV allows the cell to reorganization the distribution of CV to allow this enzyme to function most efficiently and use the PMF all over the IM. However, it was shown that CV reorganization along the IM happens in larger time scales (Wilkens et al., 2013) In contrast the MINOS/MICOS complex is an exclusively structure building protein complex. Thus, it was not surprising that tracking Mic60 resulted in mostly confined trajectories.

The different localization of mitochondrial IM proteins allows to reveal the subcompartments of mitochondria by TALM, in living cells. Thus, trajectorie maps of Tim23 can be used to visualize the IBM (Appelhans and Busch, 2017b) (chapter 9.2.1), while trajectories of Mic10 and Mic60 allow to reveal the localization of CJs (chapter 9.2.1 and 9.3.4) (Figure 55, Figure 56). The CM can be detected by TALM of CV-SUγ (CV-SUγ in the control and under starving conditions directly differentiate, obviuosly in their directionality (**Fehler! Ungültiger Eigenverweis auf**

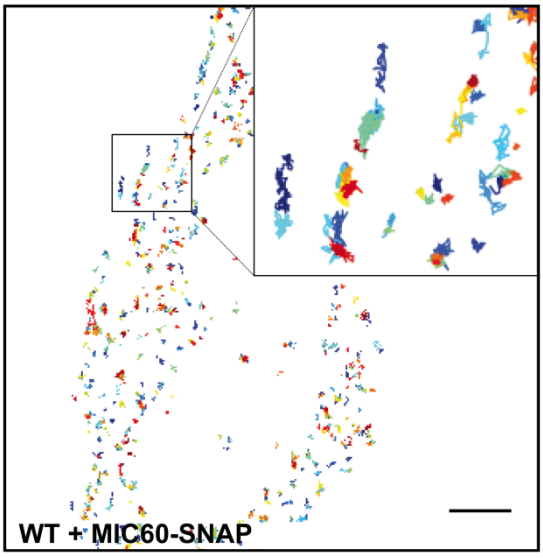

Figure 93 Single particle tracking of Mic60 in HeLa cells using the Fiji plugin Trajectory classifier (Figure adapted from Kondadi et al., 2020).

Textmarke.B, D). This indicates either a shift of a longitudinal orientation of cristae or a shift of CV-SUγ into the IBM or even a lost ofcristae. The transition of CV-SUγ into the IBM can result from avoided diffusion in the CM and a dominant diffusion in the IBM or by a reduction of the CM. In order to analyze the directionality of mobility and to quantify for this, the directionality of trajectories was analyzed with MitoOrientedDynamics. Here, the4-step binning procedure was used. As described, the longitudinal axis of each mitochondria was marked, which was used to interpolate it to a straight mitochondrion and the angle of binned steps to the longitudinal axis was measured. Shown in

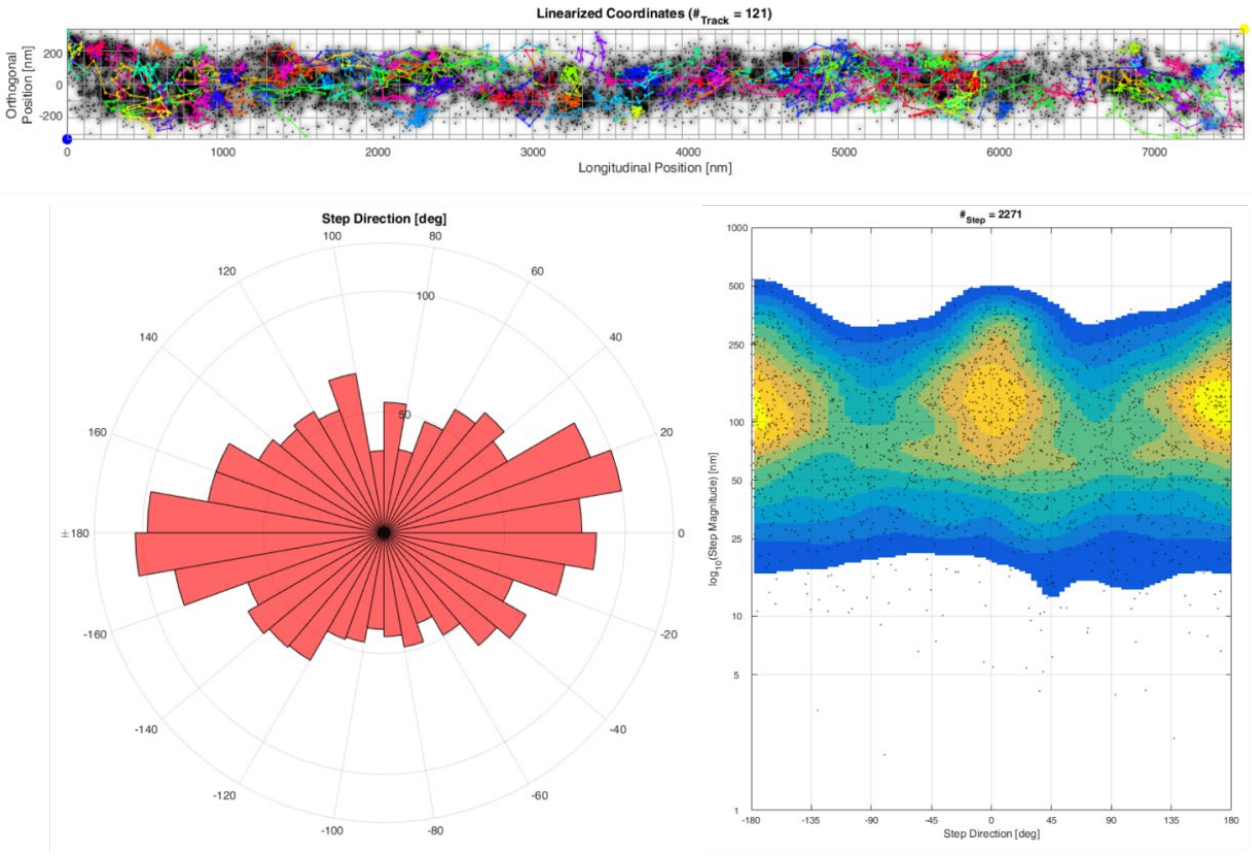

Figure **37** is an example of a straightened mitochondrion in starving conditions and its analysis of the trajectory directionality. In the shown mitochondrion the directionalities of 121 individual trajectories were analyzed (

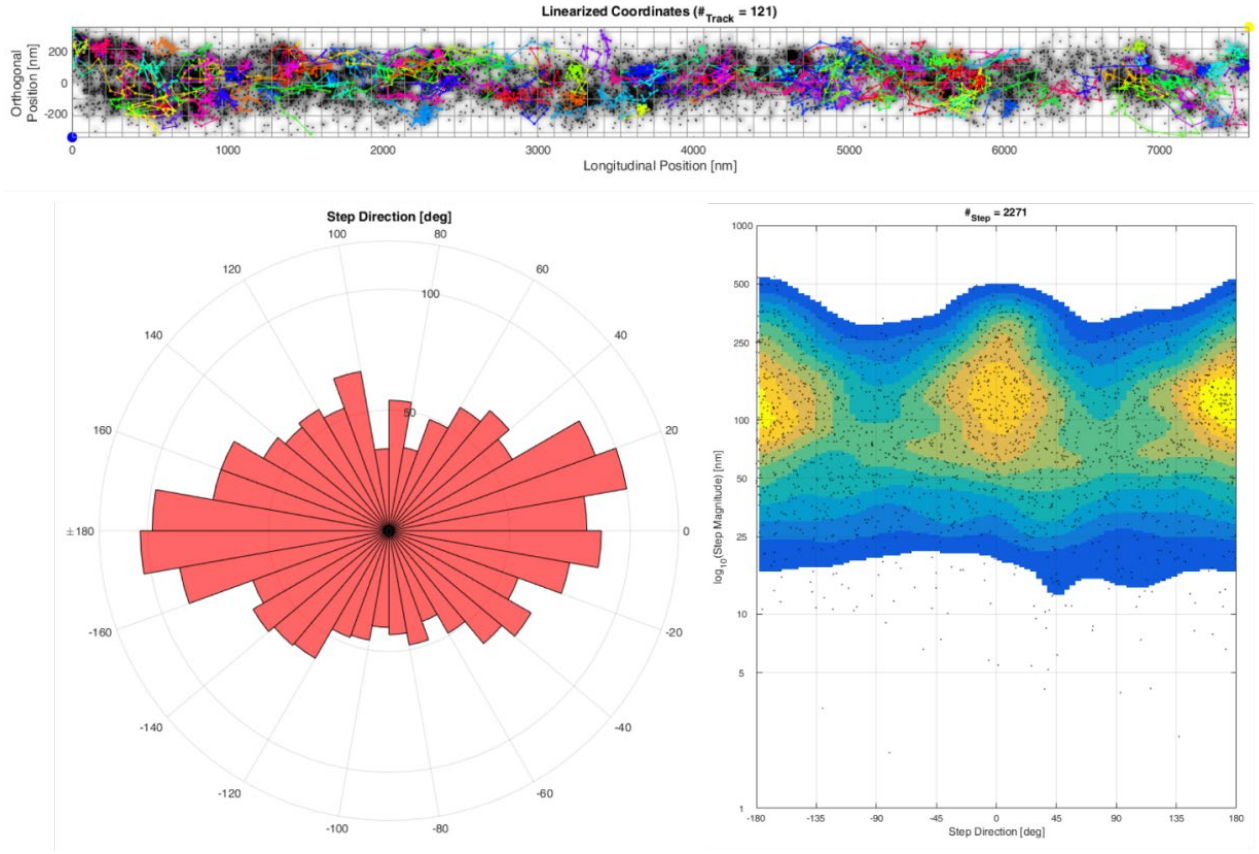

Figure **37**A). The majority of them is oriented along the longitudinal axis (

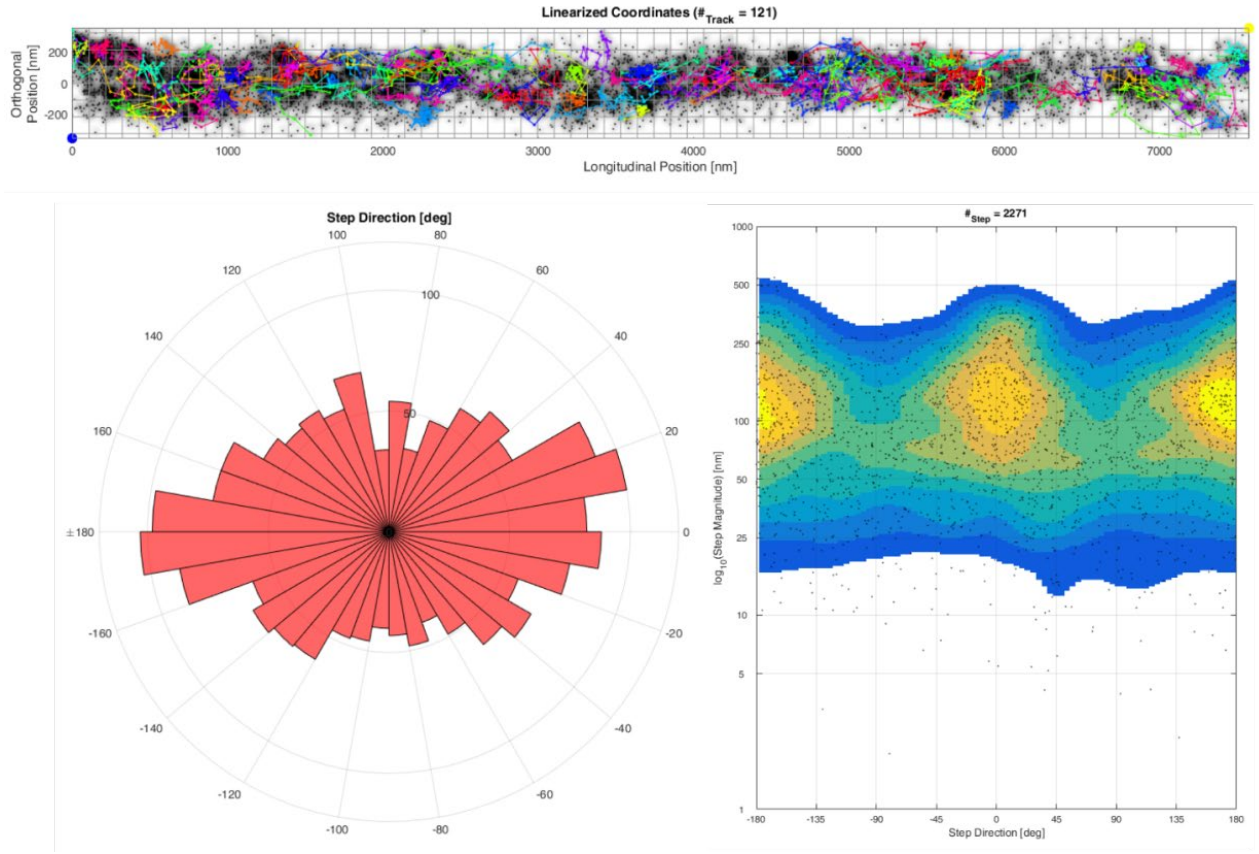

Figure **37**B, C). The pie chart diagram in

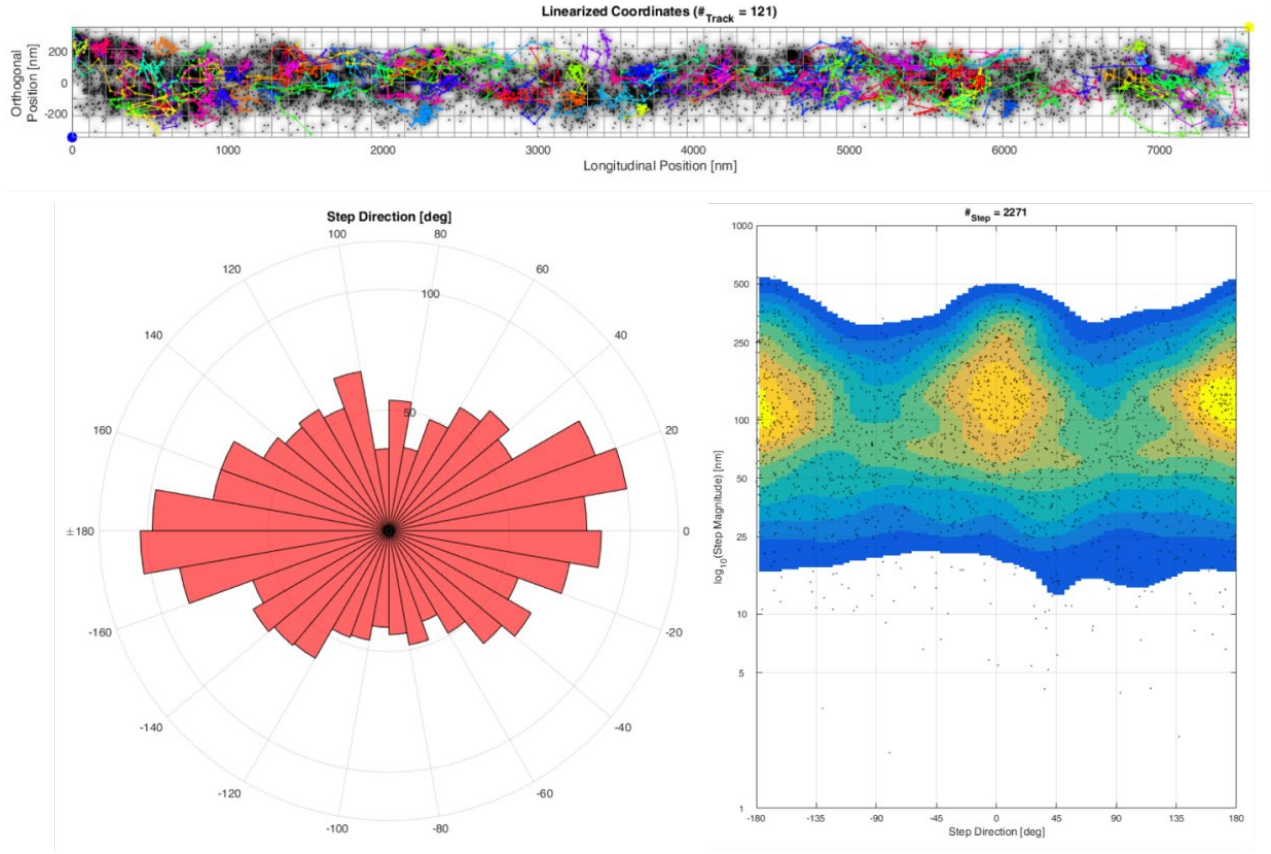

Figure **37**B illustrates the dominant longitudinal movement of CV-SUγ in starvation of the analyzed mitochondrion. Here, the amount of longitudinal directions between -20° to 30° and between -160° to 170° is twice as large as the number perpendicular oriented trajectories. Additionlly, the heatmap in

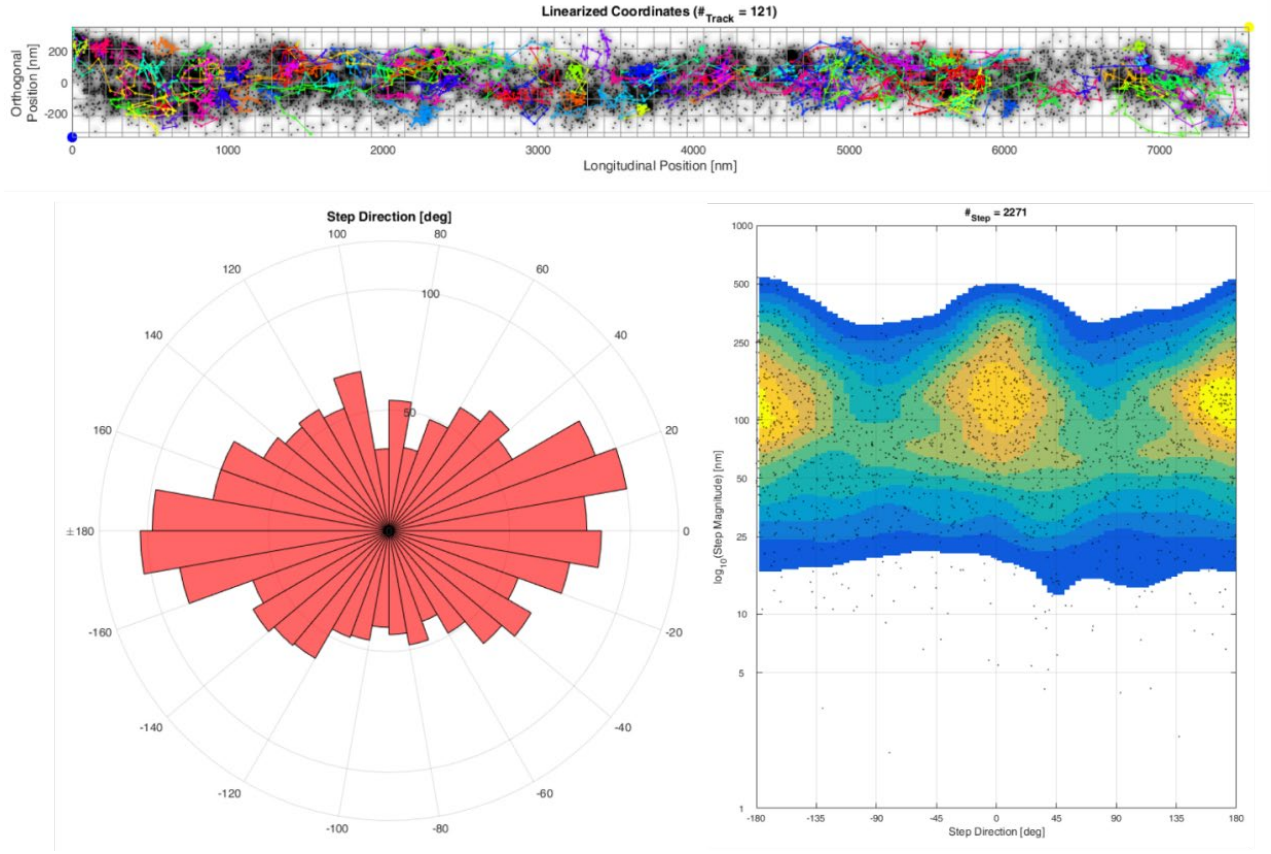

Figure **37**C shows that steps along the longitudinal axis can reach a larger jumpsize than steps in the perpendicular direction. However, this may be influenced by the 3D morphology of mitochondria. Here, jumpsizes in the perpendicular direction can be scaled down stronger than jumpsizes along the longitudinal direction. The trajectory directionality in starvation was compared to the trajectory directionality in control experiments (Figure 38). In the case of the control, 10784 binned steps were taken into account (Figure 38A, C). The analysis of trajectory directionality during starvation was performed on 59743 binned steps (Figure 38B, D).

Table 4 Jumpsize of CV-SUγ in control experiments and during starvation

Protein	Number of steps	Median jumpsize	Maximal. jumpsize	Minimal. jumpsize
CV-SUγ control	20124	96.94 nm	1117 nm	0.58 nm
CV-SUγ starvation	7491	175.70 nm	1211 nm	1.79 nm

Figure 36B). Finally the OM can be revealed by TALM of Tom20 (Appelhans et al., 2012, Appelhans and Busch, 2017b) (chapter 9.2.1).

10.1.2 Spatiotemporal protein organization of the F_1F_O ATP synthase is coupled to its functionality

The ATP synthesis of CV can be inhibited by addition of oligomycin. In order to investigate if the spatiotemporal protein organization of CV and its functionality are coupled TALM experiments of CV-SUγ have been performed during addition of oligomycin. The localization precision was not influenced by inhibition of ATP-synthesis (Figure 28). However, the jumpsize increased by a factor of 1.28 compared to the control (Table 2). An increase of the jumpsize revealed an altered dynamic due to the inhibited function of CV to synthesize ATP. In contrast to this, the D_{app} of CV-SUγ were not changed (

Table 3). On the other hand, trajectory maps record during inhibition of ATP synthesis lacked trajectories following the CM. The so called cristae trajectories vanished completely after addition of oligomycin (Figure 30, Figure 31, Figure 32). It can be concluded that the ultrastructure changed due to inhibition of the ATP synthesis. Leading to larger jumpsizes but not influencing the mobility. This could only be explained by a hindered movement of CV-SUγ. So, the steps between two frames increased but the area traveled is reduced by an altered ultrastructure of more complexity. Unfortunately, TEM images of mitochondria during addition of oligomycin, which may answer this question, are missing. However, the trajectory maps alone clearly demonstrated the changes in spatiotemporal organization of CV-SUγ during inhibition of the ATP synthesis. This revealed a context between the functionality of CV and its spatiotemporal organization. Leading to the conclusion that a functional active CV sticks to the CM and stabilizes this structure by dimerization and oligomerization. Once the catalytic function of CV is inhibited, it starts to diffuse out of its sub-compartment / the CM leading to a loss of cristae tracks and possibly to a loss of the conserved IM architecture. Albeit, the spatiotemporal organization was altered with regard to the trajectories the mobility was hardly influenced (

Table 3). CV-SUγ still showed a mobile fraction of 28.2% with D_{app} = 0.087 ± 0.002 µm²/s. This fraction was measured with a D_{app} = 0.079 ± 0.009 µm²/s and a percentage of 35% ± 5% in the control. The slow mobile fraction during inhibition included 42.3% ± 0.2% with a D_{app} = 0.027 ± 0.001 µm²/s. In the control this fraction consisted of 47% ± 3% and a D_{app} = 0.02 ± 0.006 µm²/s. The third and confined fraction during inhibition of ATP synthesis had a percentage of 29.5% ± 0.4% and showed a D_{app} = 0.010 ± 0.000 µm²/s. In the control this fraction of 18% ± 3% was measured with a D_{app} = 0.005 ± 0.002 µm²/s. Thus, the confined fraction showed an increased D_{app} and a slight increase in the percentage. However, as the D_{app} was still ≤ 0.010 µm²/s and thus showed a mobility of a confined fraction.

10.1.3 Spatiotemporal protein organization of the F_1F_O ATP synthase is coupled to the metabolic state of the cell

Nutrient-deficient simulated in the starvation experiments, where cells starved in PBS for 2 hours, showed a drastic reorganization of CV. This revealed the fast and direct reaction of the protein organization to nutrient depletion. In starvation the trajectory maps revealed that most of CV-SUγ diffused with a random directionality and confined mobile proteins were still found (CV-SUγ in the control and under starving conditions directly differentiate, obviuosly in their directionality (**Fehler! Ungültiger Eigenverweis auf Textmarke.**B, D). This indicates either a shift of a longitudinal orientation of cristae or a shift of CV-SUγ into the IBM or even a lost ofcristae. The transition of CV-SUγ into the IBM can result from avoided diffusion in the CM and a dominant diffusion in the IBM or by a reduction of the CM. In order to analyze the directionality of mobility and to quantify for this, the directionality of trajectories was analyzed with MitoOrientedDynamics. Here, the4-step binning procedure was used. As described, the longitudinal axis of each mitochondria was marked, which was used to interpolate it to a straight mitochondrion and the angle of binned steps to the longitudinal axis was measured. Shown in

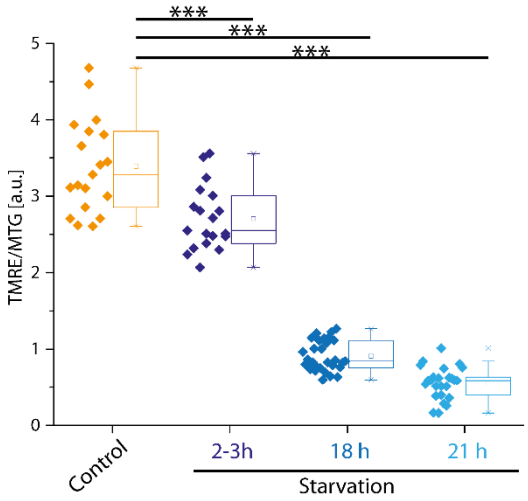

Figure 94 Drop of the mitochondrial membrane potential during starvation
The membrane potential drops due to starvation over 2 hours significantly. Starvation over 18 hours leads to a complete collapse of the $\Delta\Psi m$. (shown with the permission of Bettina Rieger)

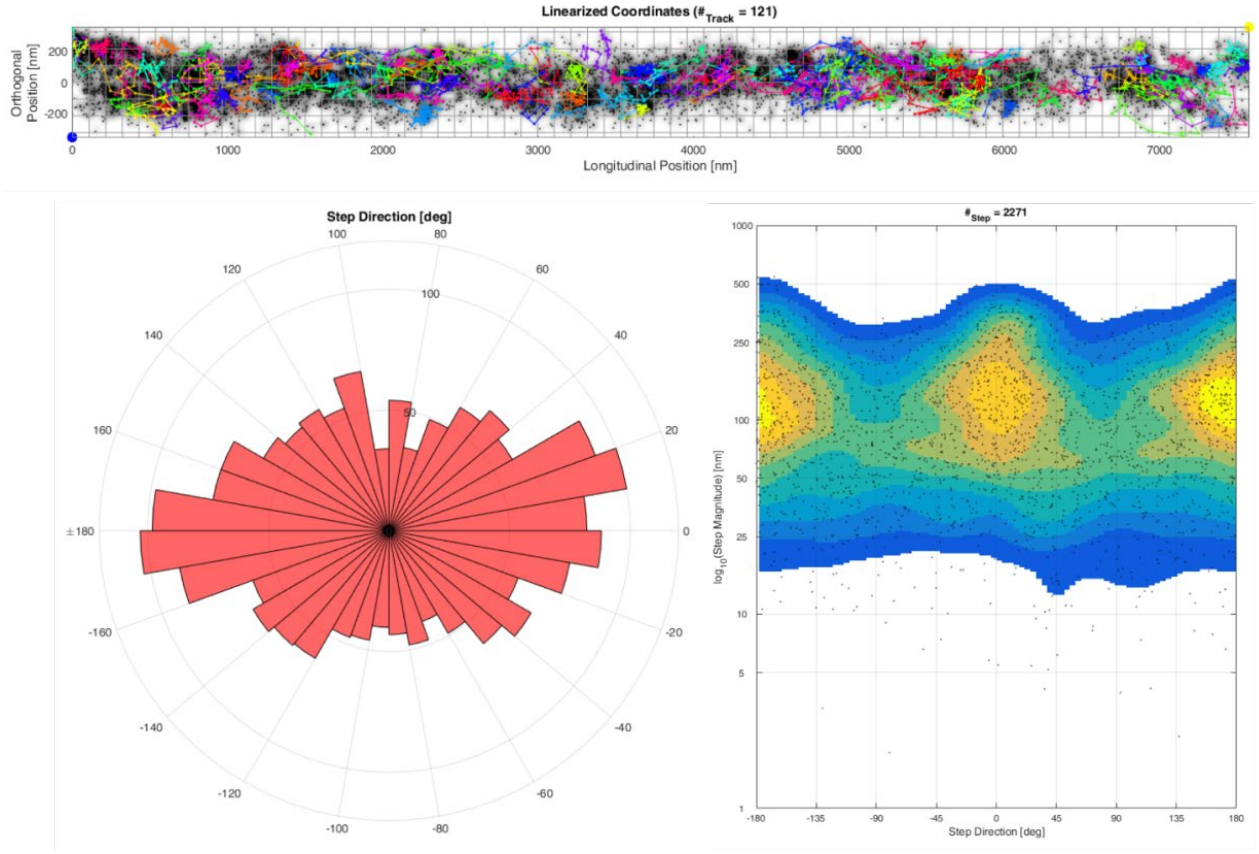

Figure **37** is an example of a straightened mitochondrion in starving conditions and its analysis of the trajectory directionality. In the shown mitochondrion the directionalities of 121 individual trajectories were analyzed (

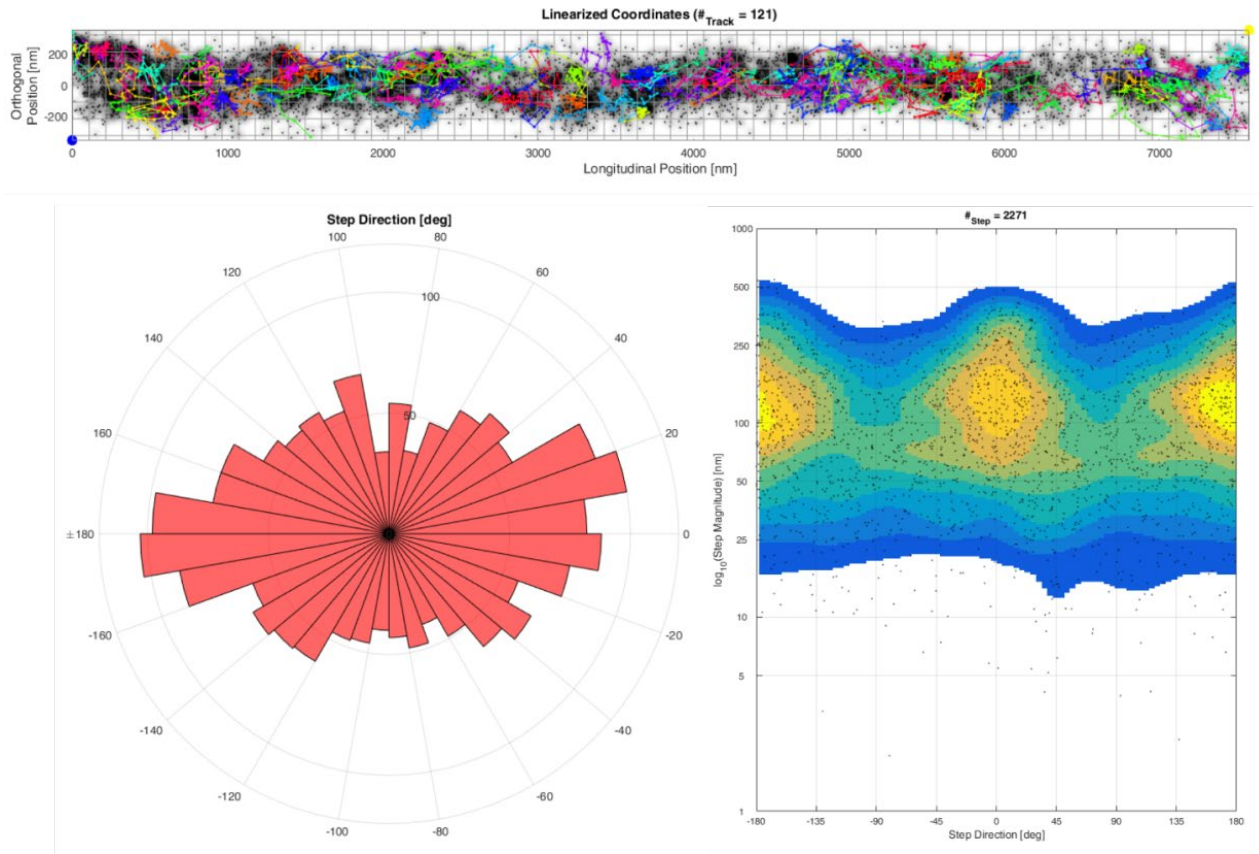

Figure **37**A). The majority of them is oriented along the longitudinal axis (

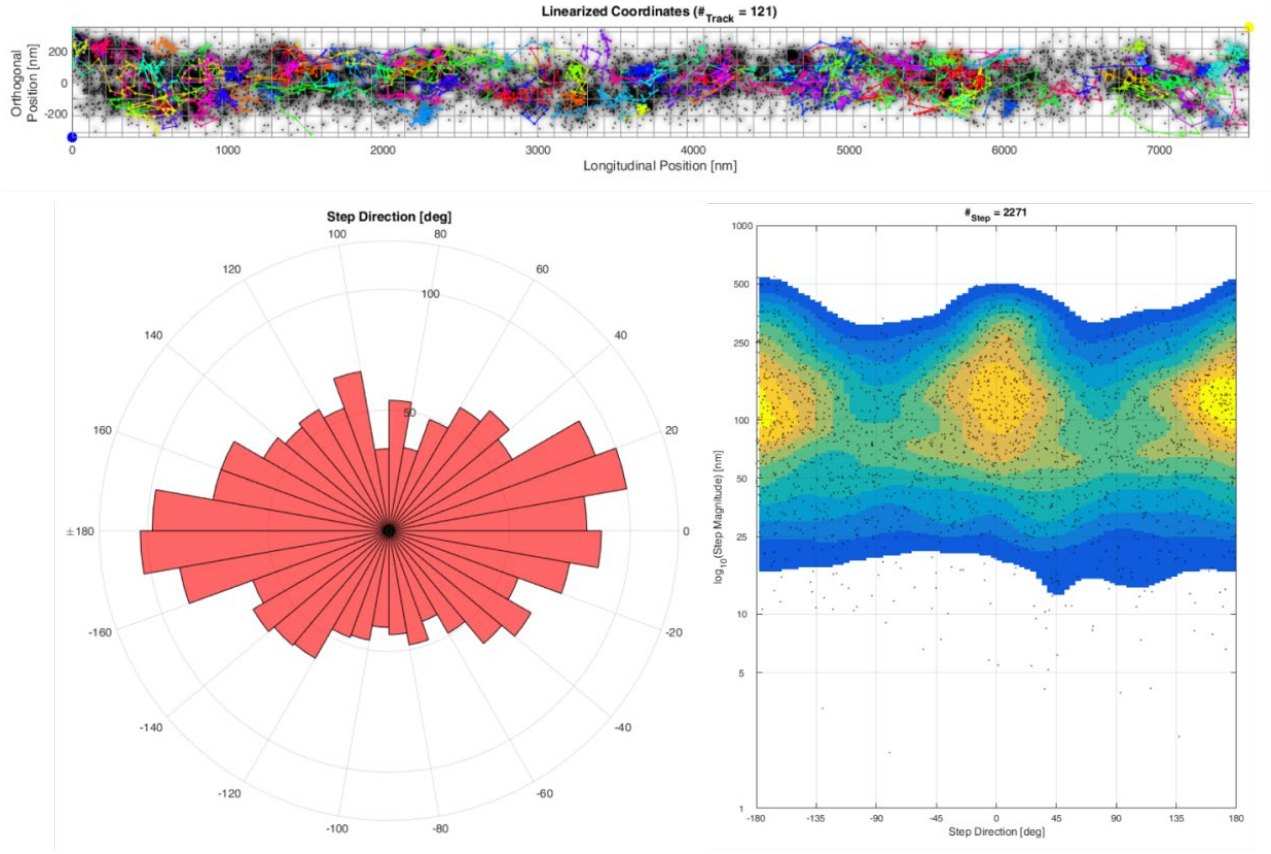

Figure **37**B, C). The pie chart diagram in

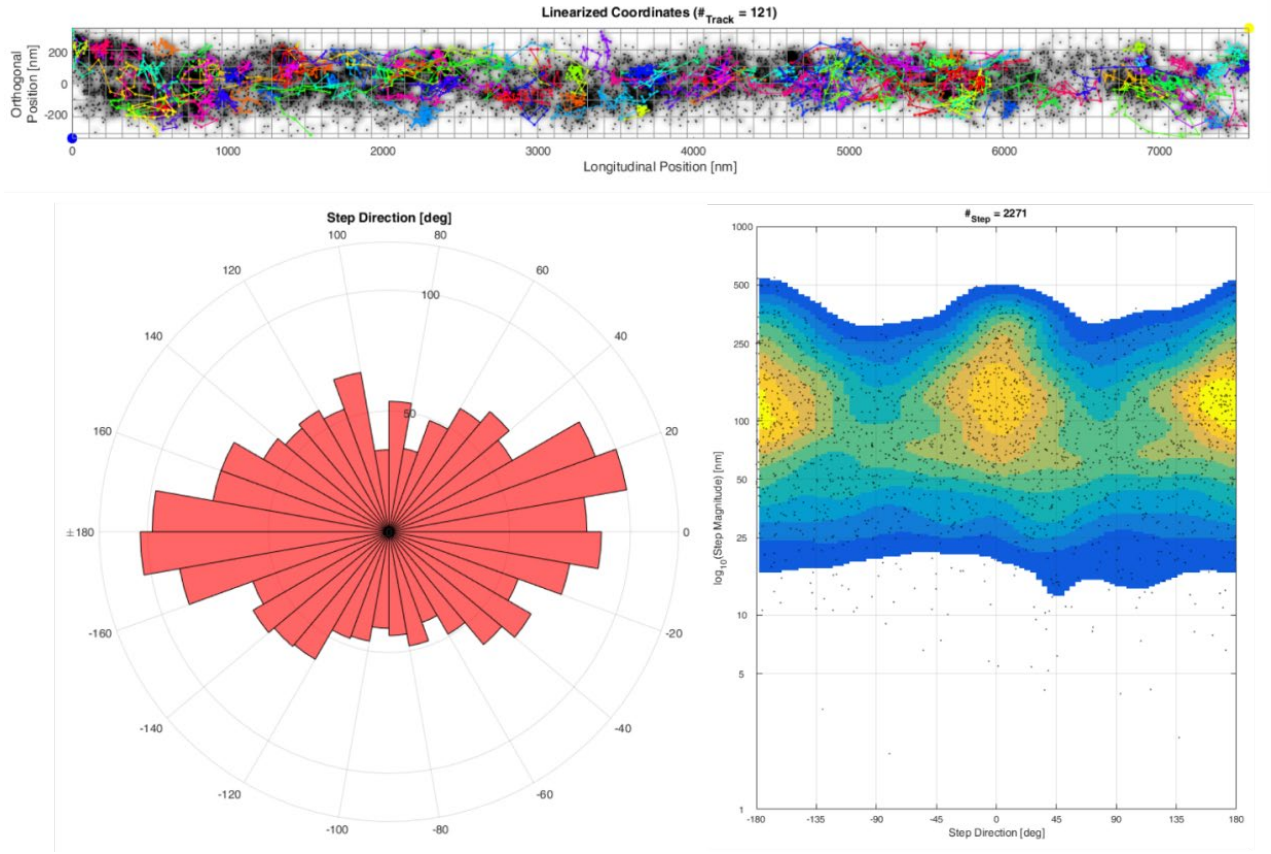

Figure **37**B illustrates the dominant longitudinal movement of CV-SUγ in starvation of the analyzed mitochondrion. Here, the amount of longitudinal directions between -20° to 30° and between -160° to 170° is

twice as large as the number perpendicular oriented trajectories. Additionlly, the heatmap in

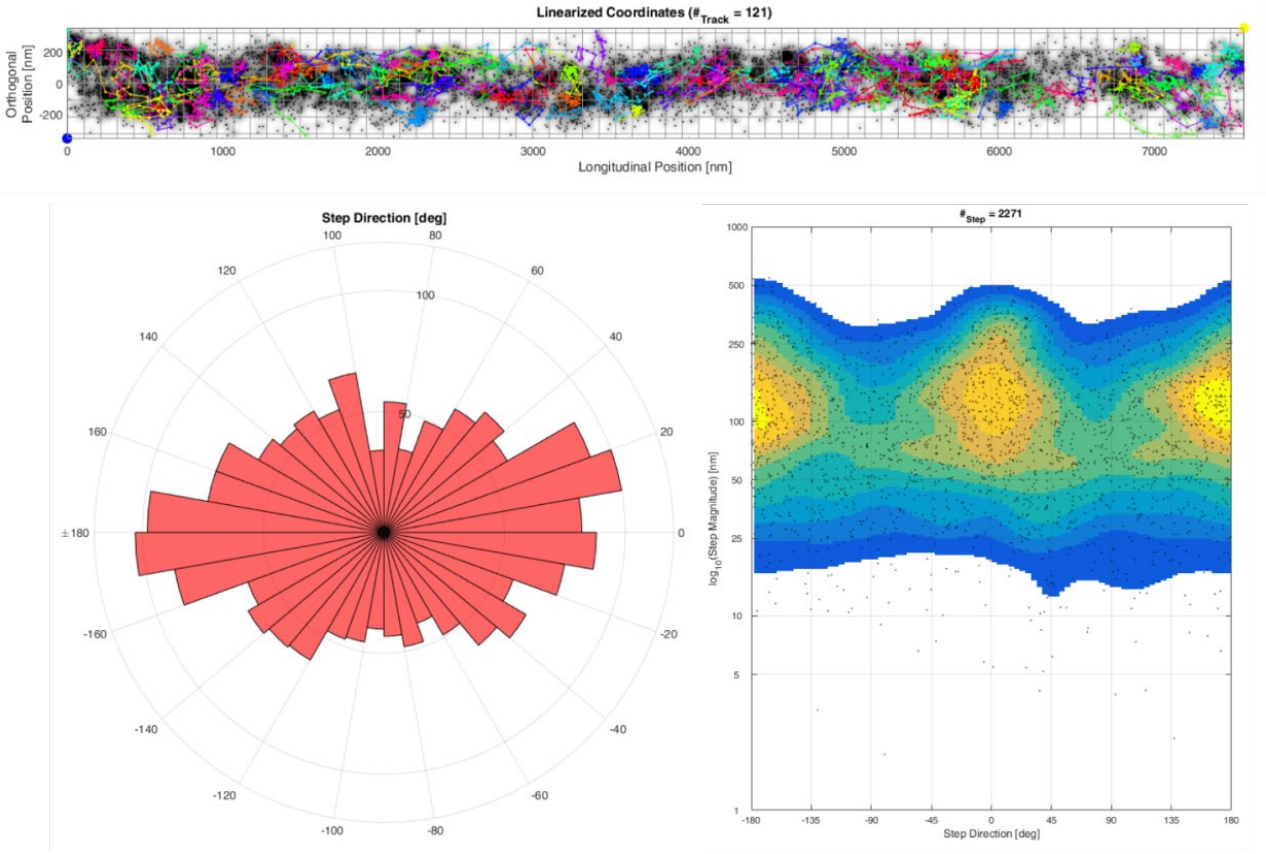

Figure **37**C shows that steps along the longitudinal axis can reach a larger jumpsize than steps in the perpendicular direction. However, this may be influenced by the 3D morphology of mitochondria. Here, jumpsizes in the perpendicular direction can be scaled down stronger than jumpsizes along the longitudinal direction. The trajectory directionality in starvation was compared to the trajectory directionality in control experiments (Figure 38). In the case of the control, 10784 binned steps were taken into account (Figure 38A, C). The analysis of trajectory directionality during starvation was performed on 59743 binned steps (Figure 38B, D).

Table 4 Jumpsize of CV-SUγ in control experiments and during starvation

Protein	Number of steps	Median jumpsize	Maximal. jumpsize	Minimal. jumpsize
CV-SUγ control	20124	96.94 nm	1117 nm	0.58 nm
CV-SUγ starvation	7491	175.70 nm	1211 nm	1.79 nm

Figure 36). The trajectory directionality revealed a change in the direction of diffusion due to starvation (Figure 38). CV-SUγ diffuseed now longitudinal - in the IBM. Whether this resulted from longitudinal oriented cristae or by a dissolution of the cristae and the CM could not be resolved by two-dimensional TALM. Here, TEM images showed that the cristae were reduced or even vanished (Figure 60). Furthermore, TALM revealed an increase of the mobility of CV-SUγ, but confined mobility was still present (Figure 39). Interestingly the percentage of the fractions of the three subpopulations stayed equal in the control and in starvation (

Table 5). The D_{app} of the mobile fraction (D_{mobile},) of CV-SUγ increased due to starvation from 0.079 ± 0.009 µm²/s to 0.117 ± 0.032 µm²/s, while the percentage stayed similar at 31 ± 2 % compared to the control at 35

Protein and condition	D_{app} mobile [µm²/s]	relativ amount [%]	D_{app} slow mobile [µm²/s]	relativ amount [%]	D_{app} confined mobile [µm²/s]	relativ amount [%]
CV-SUγ control (N = 63)	0.079 ± 0.009	35 ± 5	0.020 ± 0.006	47.0 ± 3	0.005 ± 0.002	18 ± 3
CV-SUγ starvation (N = 45)	0.117 ± 0.032	31 ± 2	0.036 ± 0.001	47 ± 2	0.010 ± 0.001	22 ± 3
Tom20 control (N = 11)	0.168 ± 0.043	43 ± 5	0.046 ± 0.007	47 ± 7	0.006 ± 0.000	10 ± 3

± 5 %. Same is true for the slow mobile fraction, here the D_{app} changed from 0.02 ± 0.006 µm²/s to 0.036 ± 0.002 µm²/s, while the percentage stayed at 47 ± 2 % similar to the control of 47 ± 2 %. These findings were accompanied by a drop of the membrane potential during starvation (personal communication with Bettina Rieger, Figure 94). Starvation led to a reduced activity of the proton pumps CI, CIII and CIV. This is shown in **Fehler! Verweisquelle konnte nicht gefunden werden.** in a metabolic assay, which demonstrates that the oxygen consumption rate decreased already after 2h of starvation, as the basal respiration was lower after 2 h of starvation and decreased significantly after 6 h of starvation (**Fehler! Verweisquelle konnte nicht gefunden werden.**A, B). Espacially, after adding of Carbonylcyanid-*p*-trifluoromethoxyphenylhydrazon (FCCP) the maximal respiration was lower than in the control (**Fehler! Verweisquelle konnte nicht gefunden werden.**A, B). This demonstates that CI, CII and CIV did not reach their maximal activity during starvation. However, after 2h of starvation a tendency of a lower glycolytic activity was obtained (Figure 96). After 20 h of starvation a significant decrease of the glycolytic activity was measured. Meanwhile the activity of the citric acid cycle changed not significantly over 2h and 20h (Figure 96). Interestingly the oxidation of fatty acids increased significantly after 20h of starvation (Figure 96). Already after 2h of starvation a tendency to a higher dependency on oxidation of fatty acids was obtained (Figure 96). Together with a loss of the membrane potential, an equal activity of the citric acid cycle in control conditions and starving conditions and an increased oxidation of the fatty acids caused by starvation, it can be assumed that the metabolic switch caused by starvation leads to an inactive glycolysis and a lowered OXPHOS as well as a shift of the metabolism to oxidation of fatty acids. Thus the PMF is not build by CI, CII and CV and used up by CV. Interestingly, this metabolic shift was accompanied by the spatiotemporal reorganization of CV-SUγ. Taking into account that the functionality of CV and its spatiotemporal organization are coupled shown by TALM experiments during inhibition of CV activity, leads to the assumption that starvation has a similar effect. This was supported by the increased mobility during starvation and the altered trajectory orientation. Additionally, TEM images of mitochondria in starving conditions showed a loss of CM and a tubular IM. CV is involved of the IM curvature as a dimer or oligomer, thus also this function seems to be coupled to its functionality and the metabolic state.

The cristae rim is built dimers and oligomerization of CV (Blum et al., 2018, Davies et al., 2011, Davies et al., 2012, Hahn et al., 2016, Mühleip et al., 2016, Paumard et al., 2002). Taking this model into account starvation should result into more monomeric CV. More monomers and less dimers of CV would reduce the number of cristae and in extreme cases lead to a complete dissolution of the CM. A lack of cristae results in a tubular IM, without microcompartments hindering the diffusion, as it was shown in the TEM images (Figure 60). This effect was visualized by the trajectory maps (CV-SUγ in the control and under starving conditions directly differentiate, obviuosly in their directionality (**Fehler! Ungültiger Eigenverweis auf Textmarke.**B, D). This indicates either a shift of a longitudinal orientation of cristae or a shift of CV-SUγ into the IBM or even a lost ofcristae. The transition of CV-SUγ into the IBM can result from avoided diffusion in the CM and a dominant diffusion in the IBM or by a reduction of the CM. In order to analyze the directionality of mobility and to quantify for this, the directionality of trajectories was analyzed with MitoOrientedDynamics. Here, the4-step binning procedure was used. As described, the longitudinal axis of each mitochondria was marked, which was used to interpolate it to a straight mitochondrion and the angle of binned steps to the longitudinal axis was measured. Shown in

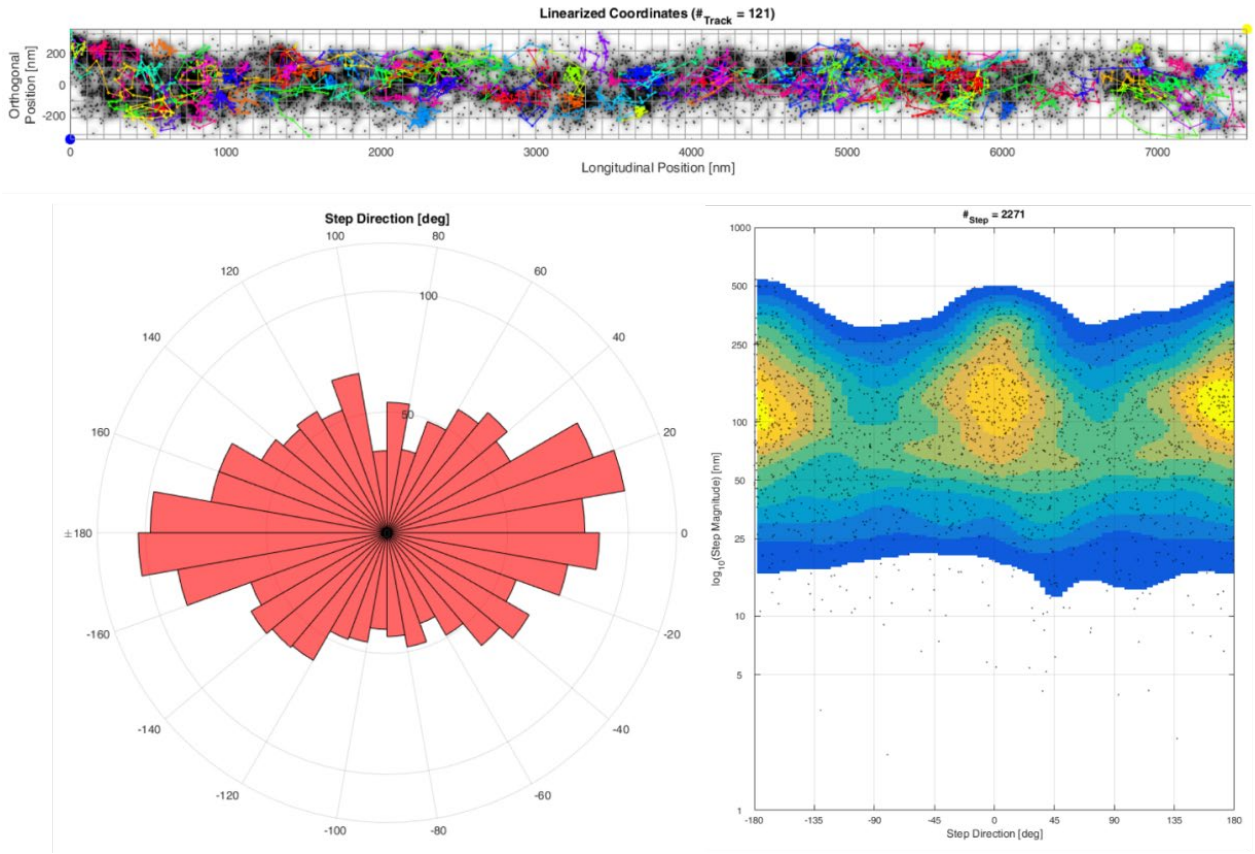

Figure **37** is an example of a straightened mitochondrion in starving conditions and its analysis of the trajectory directionality. In the shown mitochondrion the directionalities of 121 individual trajectories were analyzed (

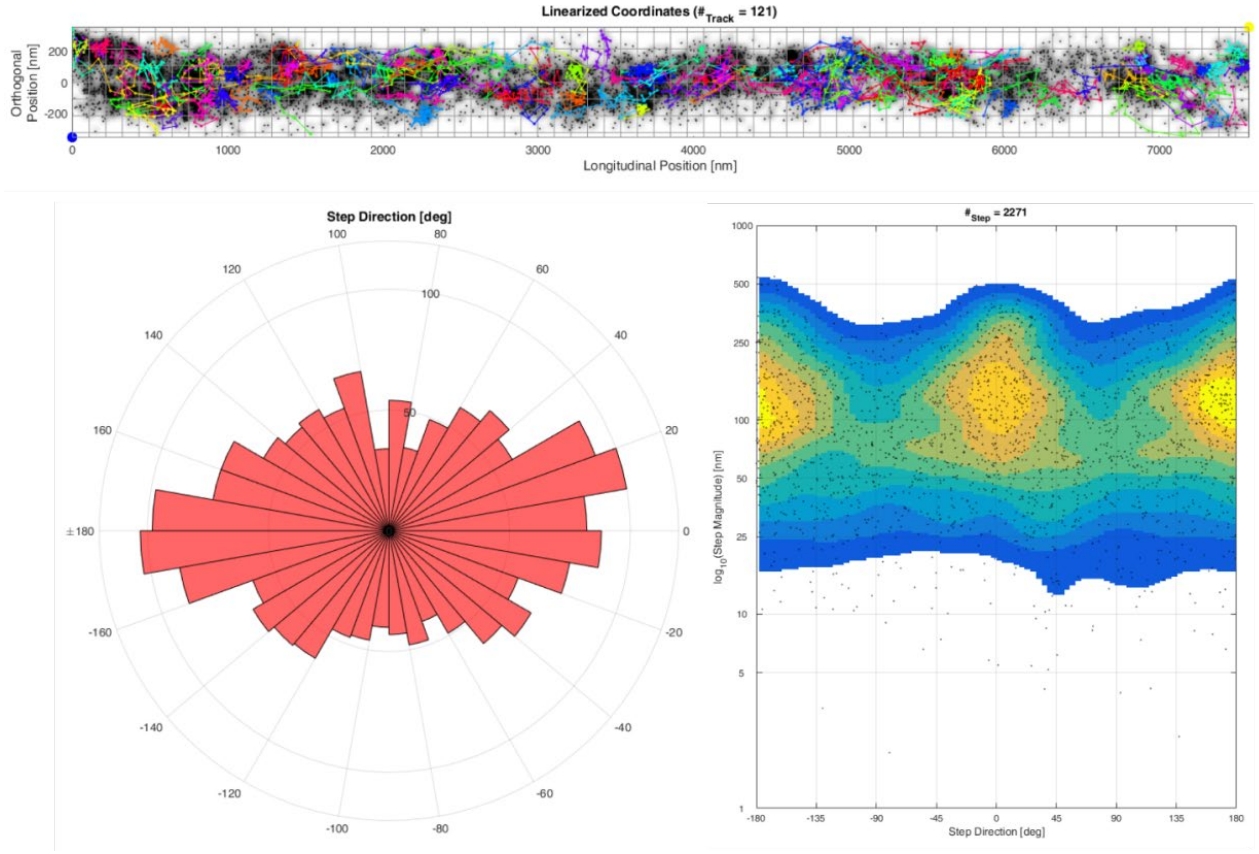

Figure **37**A). The majority of them is oriented along the longitudinal axis (

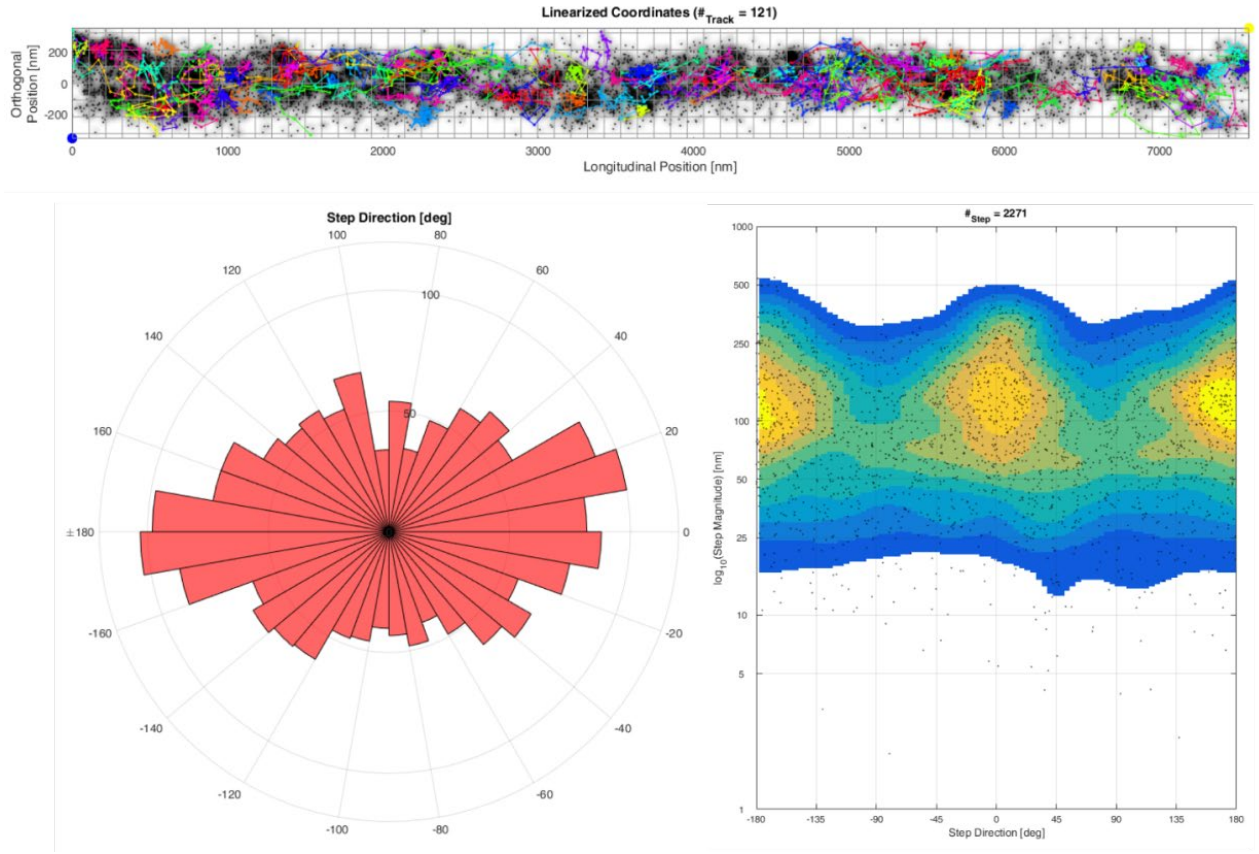

Figure **37**B, C). The pie chart diagram in

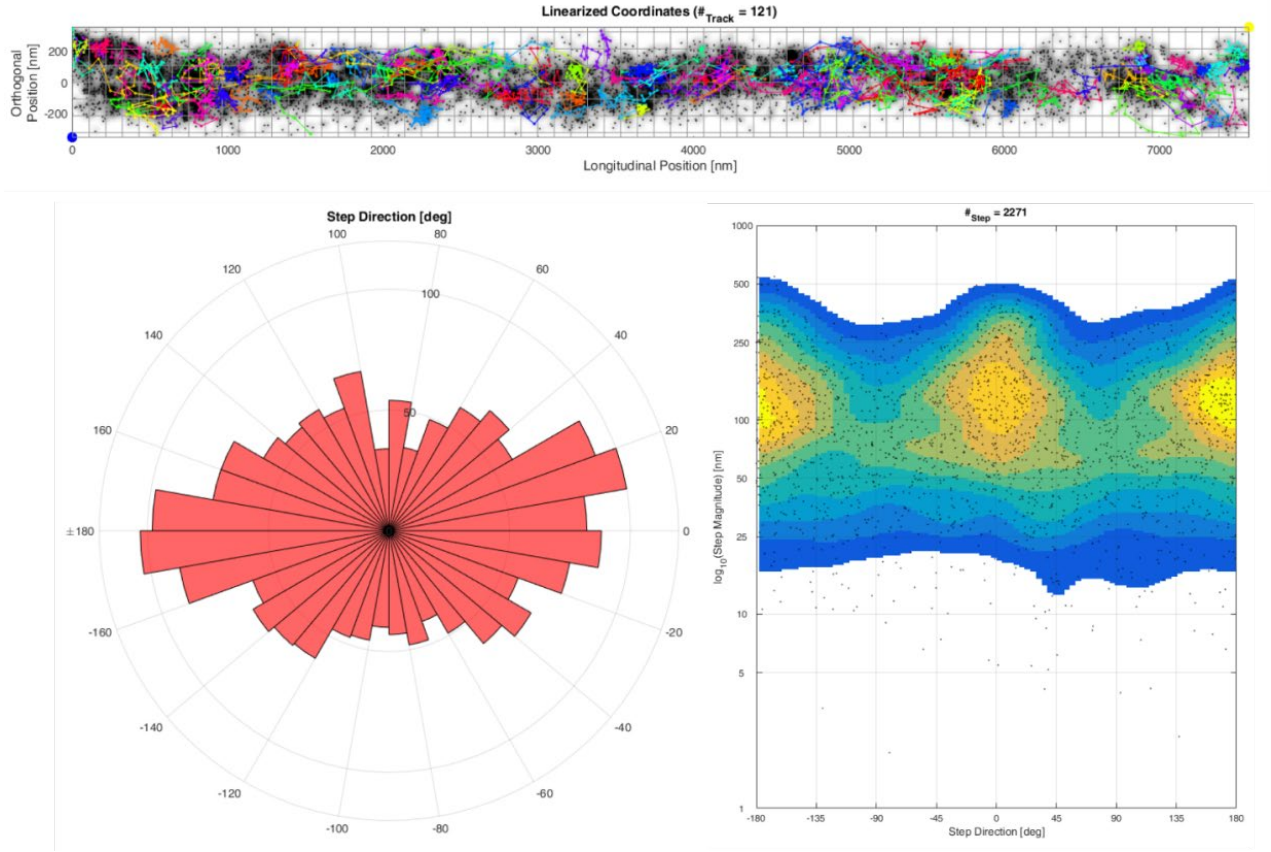

Figure **37**B illustrates the dominant longitudinal movement of CV-SUγ in starvation of the analyzed mitochondrion. Here, the amount of longitudinal directions between -20° to 30° and between -160° to 170° is twice as large as the number perpendicular oriented trajectories. Additionlly, the heatmap in

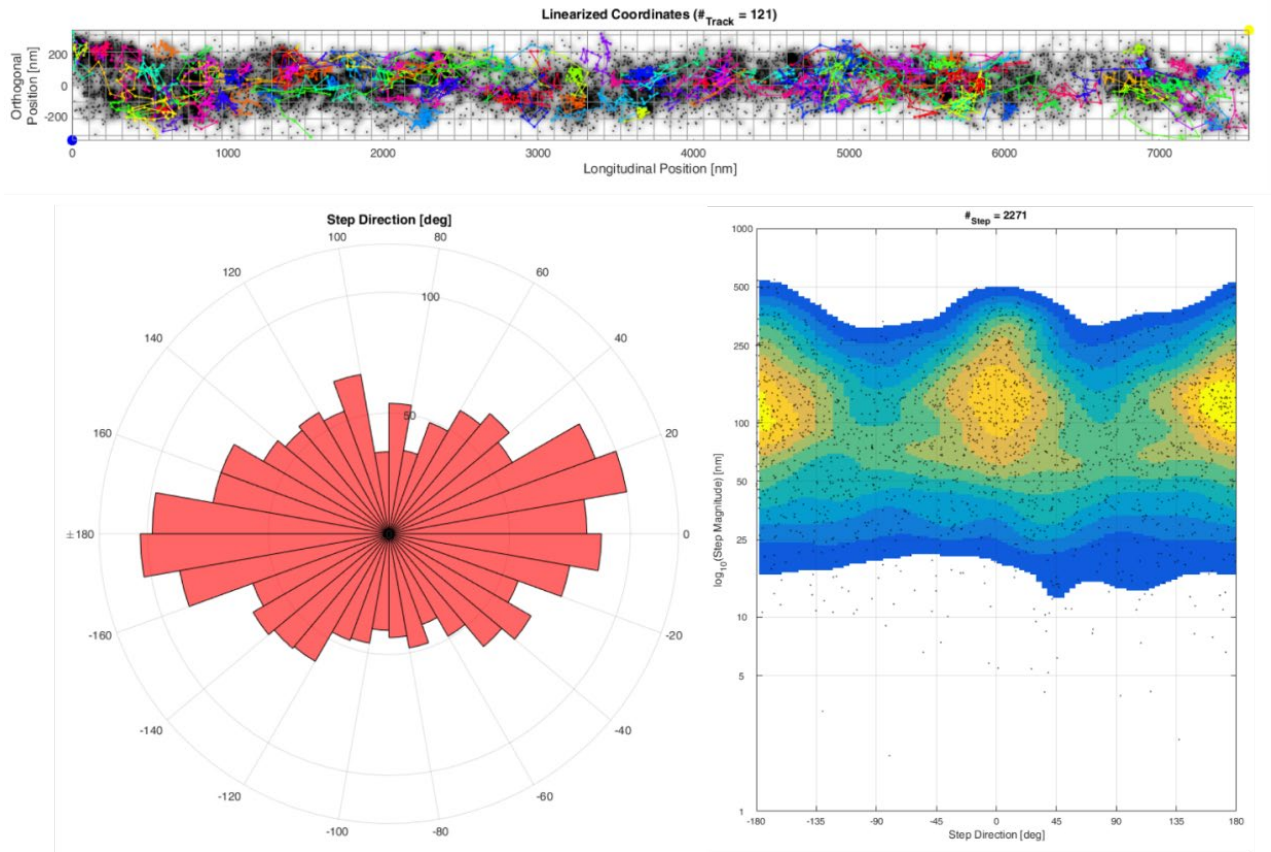

Figure **37**C shows that steps along the longitudinal axis can reach a larger jumpsize than steps in the perpendicular direction. However, this may be influenced by the 3D morphology of mitochondria. Here, jumpsizes in the perpendicular direction can be scaled down stronger than jumpsizes along the longitudinal direction. The trajectory directionality in starvation was compared to the trajectory directionality in control experiments (Figure 38). In the case of the control, 10784 binned steps were taken into account (Figure 38A, C). The analysis of trajectory directionality during starvation was performed on 59743 binned steps (Figure 38B, D).

Table 4 Jumpsize of CV-SUγ in control experiments and during starvation

Protein	Number of steps	Median jumpsize	Maximal. jumpsize	Minimal. jumpsize
CV-SUγ control	20124	96.94 nm	1117 nm	0.58 nm
CV-SUγ starvation	7491	175.70 nm	1211 nm	1.79 nm

Figure 36,

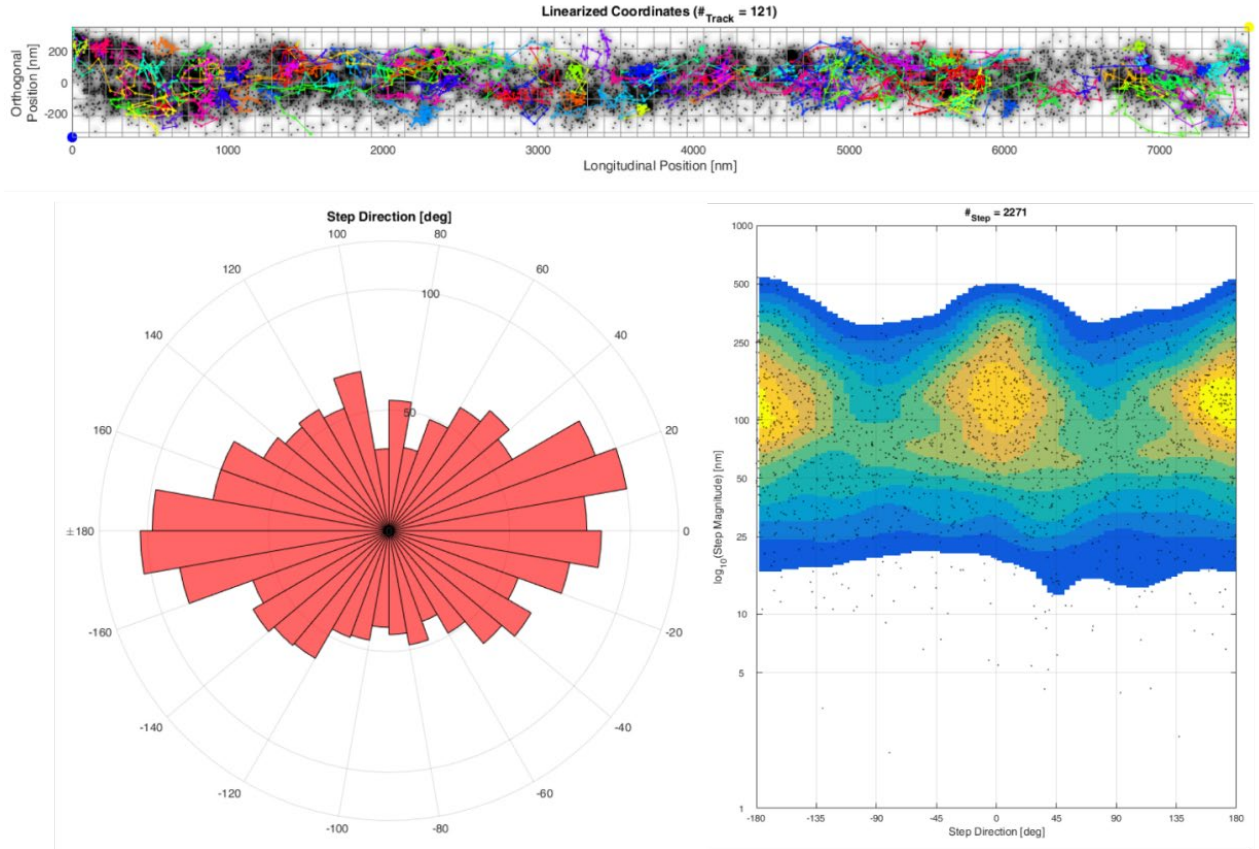

Figure **37**) – no perpendicular trajectories were obtained, reporting the dissolution of the CM. The longitudinal trajectory directions increased and the perpendicular trajectory directions decreased (Figure 38). Furthermore, less dimers and oligomers of CV and a dissolution of the CM resulted in an increase of the mobility of CV. Especially the D_{app} of the mobile fraction increased drastically (Figure 39,

Table 5).

Taken together TALM analysis showed a coupled and rapid adaptation of the spatiotemporal organization of

Protein and condition	D_{app} mobile [µm²/s]	relativ amount [%]	D_{app} slow mobile [µm²/s]	relativ amount [%]	D_{app} confined mobile [µm²/s]	relativ amount [%]
CV-SUγ control (N = 63)	0.079 ± 0.009	35 ± 5	0.020 ± 0.006	47.0 ± 3	0.005 ± 0.002	18 ± 3
CV-SUγ starvation (N = 45)	0.117 ± 0.032	31 ± 2	0.036 ± 0.001	47 ± 2	0.010 ± 0.001	22 ± 3
Tom20 control (N = 11)	0.168 ± 0.043	43 ± 5	0.046 ± 0.007	47 ± 7	0.006 ± 0.000	10 ± 3

CV to the metabolic state of the cell. The results indicate that the spatiotemporal organization is coupled to the membrane potential. Furthermore, a reorganization of the IM architecture took place, as TEM images of mitochondria cells during starvation demonstrate (Figure 60). Due to the structural influence of CV on the shape of the IM (Blum et al., 2018, Davies et al., 2011, Davies et al., 2012, Hahn et al., 2016, Mühleip et al., 2016, Paumard et al., 2002) an influence of the reorganization of CV on the ultrastructure is assumable, as the specific localization of CV changed under starvation. However, TALM analysis showed that SPT is a suitable tool to investigate the dynamic of spatiotemporal organization of CV caused by a metabolic switch. Furthermore,

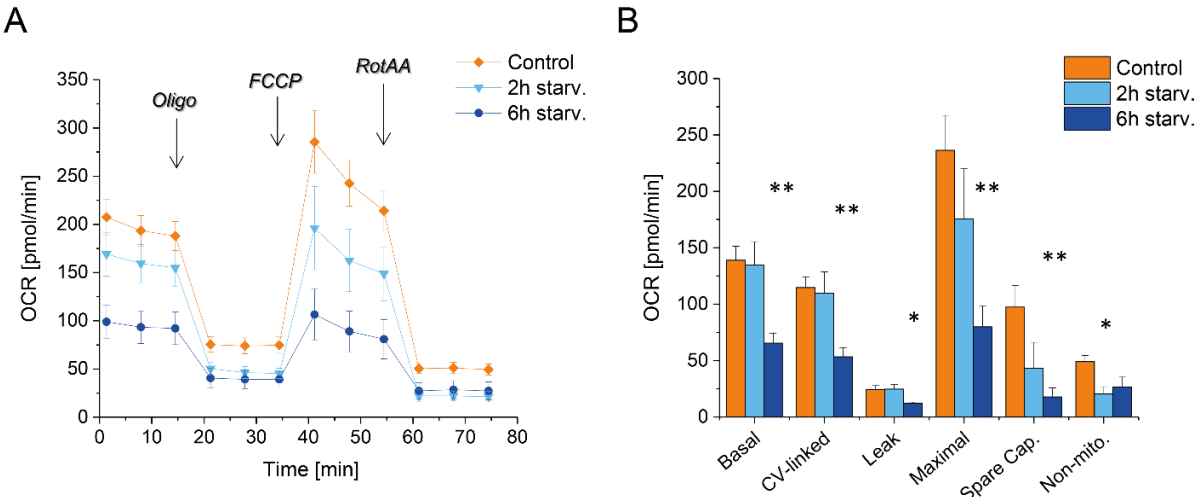

Figure 95 Mitochondrial stress test of HeLa cells in glucose and under starvation conditions
A Diagram of the oxygen consumption rate measured over time in the control and in short-term (2 h) and long-term starvation (6 h). **B** Bioenergetic parameters of the mitochondrial stress test data shown in A. (shown with the permission from Bettina Rieger)

TALM can be used to investigate changes in the sub-compartmentation of mitochondria by visualizing the trajectories of proteins and their directionality.

10.2 Dual-color TALM of mitochondrial membrane proteins

10.2.1 Colocalization and co-locomotion events of mitochondrial proteins cannot be revealed by posttranslational and substoichimetric labeling

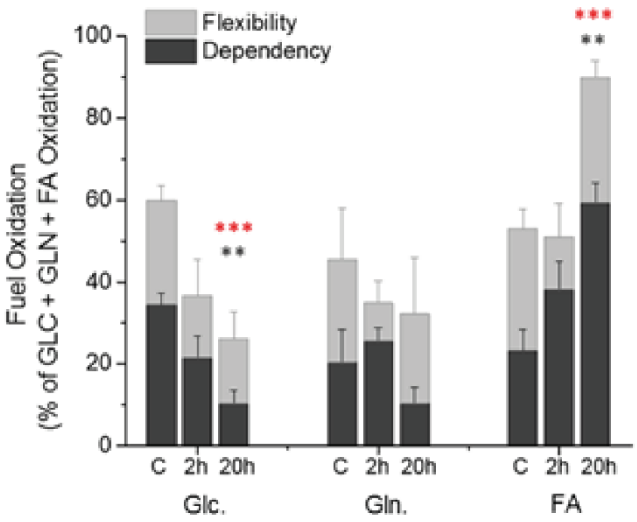

Figure 96 Agilent Seahorse XF Mito Fuel Flex test with HeLa cells kept in glucose and under starving conditions.
Cells can switch their dependency, flexibility and capacity to oxidize glucose/pyruvate (Glc.), long-chain fatty acids (FA), and glutamine/glutamate (Gln). Here the relative mitochondrial dependency of HeLa wildtype cells on the fuels is shown in dark grey and their relative mitochondrial flexibility for the fuels is shown in light grey, respectively, in the control (C = control = Glc) and starving conditions (2 h and 20 h PBS). Fuel capacity is the sum of dependency and flexibility. Data are mean ± SEM (N=4 independent assays). Significance levels were determined by a one-way ANOVA: $P \leq 0.01$ denoted with **; $P \leq 0.001$ denoted with ***. Dark grey stars = significance levels of dependency, red stars = significance levels of capacity. (Figure shown with the permission of Bettina Rieger)

Dual-color TIRF microscopy allows to localize and to track two proteins in the same area of a cell at the same time. It was shown that dual-color TIRF microscopy allows to study protein-protein colocalizations and co-locomotion of proteins in the plasma membrane and/or in the cytosol (Wilmes et al., 2015, You et al., 2016,). Colocalization of mitochondrial proteins on single molecule level was used for proteins of the Parkinson's disease (Beinlich et al, 2012). However, dual-color TIRF microscopy was so far not used for protein co-locomotion of mitochondrial membrane proteins. The main reason for this could be that TIRF microscopy of single molecules in mitochondria is limited by the labeling method. The use of one protein tagged with the HaloTag and the fSnapTag, allowed on the one hand, to test the right labeling concentrations, as both tags have different affinities and on the other hand increased the chance to colocalize both dyes independent of effects of protein-protein interaction. Therefore, dual-color TALM was tested on the Tom20:HaloTag:fSnapTag construct in order to evaluate the potential of posttranslational, substoichiometric labeling for colocalization and co-locomotion of mitochondrial proteins. The used construct dealed as a positive control for colocalization and co-locomotion on single mitochondrial proteins. Therefore a HeLa cell line stable transfected with the Tom20:HaloTag:fSnapTag construct was labeled with SiR^{HTL} and TMR^{star} and TALM experiments were performed as described.

Unfortunately, percentage of colocalization events was 0.01 %. Thus substoichimetric, postrantaltional labeling of mitochondrial proteins on single molecule level did not allow to perform colocalization analysis. Colocomotion was not possible either as the percentage of co-locomotion events was less than 0.2 %. Nevertheless, dual-color TALM could stilled be used to inverstigate the impact of one protein to the spatiotemporal organization of another protein.

10.2.2 Spatiotemporal protein organization of the F_1F_O ATP synthase is influenced by dimerization inducing subunit-e

The F_1F_O ATP synthase forms dimers and oligomers (Allen et al., 1989; Davies et al., 2011; Davies et al., 2012, Dudkina et al., 2005; Habersetzer et al., 2013). These dimers and oligomers can induce membrane curvature (Blum et al., 2018, Davies et al., 2011, Davies et al., 2012, Hahn et al., 2016, Mühleip et al., 2016, Paumard et al., 2002) being localized at the rim of cristae (Blum et al, Davies et al., 2012, 2019, Hahn et al., 2016, Mühleip et al., 2016) (Figure 97). The dimersization of CV is triggered by binding of subunit-e and subunit-g (Fronzes et al., 2006, Wagner et al., 2009). Both subunits are found in dimers, but not in monomers of CV (Arnold et al., 1998, Esparza-Perusquía et al., 2017). In order to investigate if the spatiotemporal organization of CV-SUγ was influenced by overexpression of the dimerization inducing CV-SUe, it was co-transfected in a HeLa cell line stable transfected with CV-SUγ. Afterwards dual-color TALM experiments of CV-SUγ and CV-SUe were performed (Figure 46, Figure 48, Figure 49). First of all, SML of both proteins at the same time was possible. Surprisingly, the both constructs did not colocalized in the same cristae. However, typical cristae localization patterns occurred in all images taken (Figure 45) and were revealed with a localization precision of ~15 nm (**Fehler! Verweisquelle konnte nicht gefunden werden.**). Cristae trajectories of both proteins by were obtained (Figure 46). In addition, the D_{app} of CV-SUγ

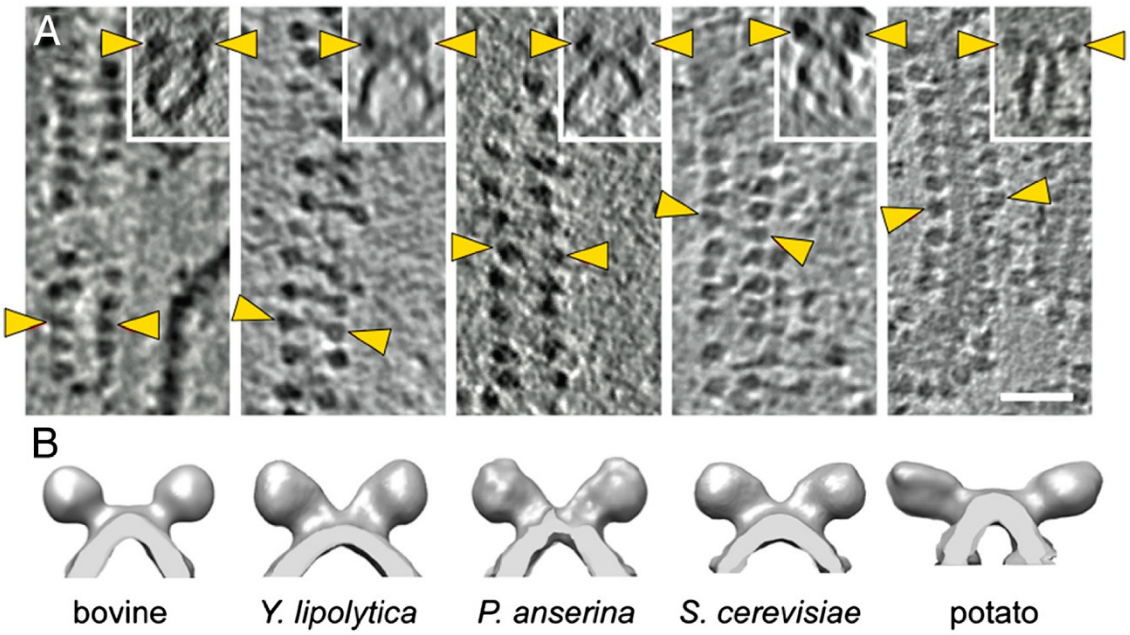

Figure 97 F_1F_O ATP synthase dimers oriented in rows
A Dimers of CV can be found in different species. Here shown are tomographic slices demonstrating the row like orientation of CV dimers in CM of bovine heart, *Yarrowie lipolytica*, *Podospora ansernia*, *Saccharomyces cerevisiae* and potato. The yellow arrowheads mark F_1 heads of CV. Scale bars: 50 nm **B** Surface rendered representations of subtomogram averages. (Figure adapted from Davies et al., 2011)

stayed unaffected by co-transfection of the CV-SUe:SnapTag construct (

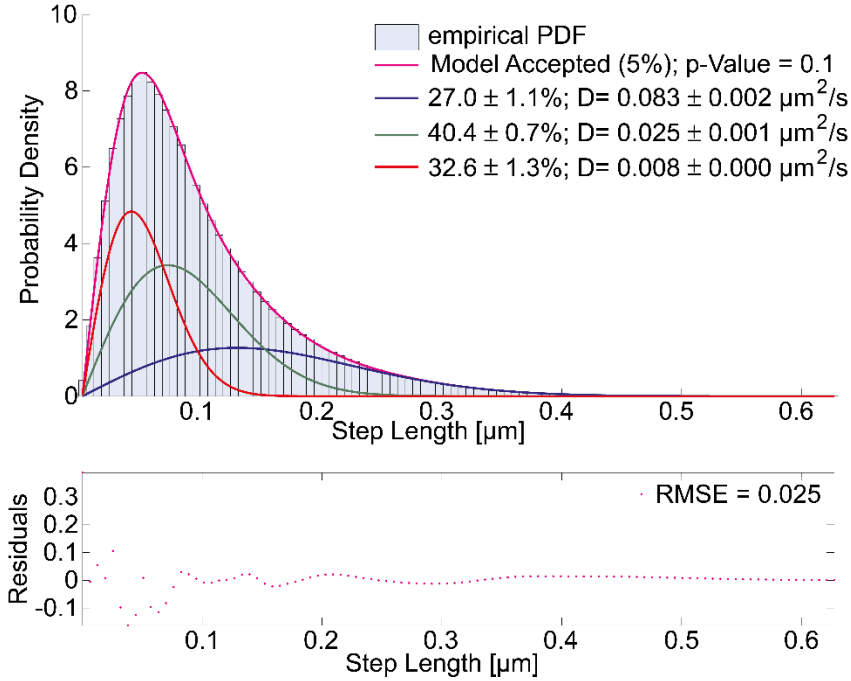

Figure S9, Table 8). So, the mobile fraction of CV- SUγ was measured with 0.087 ± 0.001 µm²/s, and a percentage of 33.4 % ± 0.6 %. The slow mobile fraction of 31.8 ± 0.4 % was measured with 0.022 µm²/s ± 0.001 µm2/s. Thus, the percentage of the slow mobile fraction decreased from 47 ± 3% to 31.8 ± 0.4 %. The confined mobile fraction stayed at 0.006 ± 0.000 µm²/s. But the percentage of the confined fraction increased from 18 ± 3 % to 34.8 ± 0.7 %. Thus, the confined fraction increased by co-transfection of CV-SUe. On the one hand, this demonstrates a slow down of CV diffusion, which can be caused by a higher value of CV dimers being confined mobile at the cristae rim. On the other hand, if CV-SUe stabilizes dimers of CV, this could influence the IM shape and led to a stronger sub-compartmentation, which also would result in an increase of the confined fraction of CV-SUγ due to a multiple bended CM. Here, TEM of cells stable transfected with CV-SUγ and cotransfected with CV-SUe shell answer this question, but were missing. Nevertheless, the mobile and slow mobile fraction did not lower their mobility, this can be interpreted as an indication that the ultrastructure was not influenced by a stronger bending of the IM, otherwise the D_{app} of the mobile and slow mobile fraction should also show a decrease caused by a stronger compartmentation of the IM. However, a lack of subunit-e and subunit-g leads to a reduction of cristae tip numbers (Rabl et al., 2009). An overexpression of subunit-e therefore allowed to record the maximal amount of CV-SUγ bound to CV.

10.2.3 MINOS/MICOS regulates the shape of the IM and influences the spatiotemporal organization of the F_1F_O ATP synthase

The MINOS/MICOS complex consist of several subunits. It is postulated that especially the function of Mic10 is crucial for CJ formation, as a knockout of Mic10 results in a lack of cristae (Barbot et al., 2015, Bohnert et al., 2015, Harner et al., 2011, Jans et al., 2013, von der Malsburg et al. 2011, Rampelt et al., 2018) (**Fehler! Verweisquelle konnte nicht gefunden werden.**). Additionally, Mic10 is involved in bending the IM by homo-dimerization depending on the GxGxGxG motif (Bohnert et al., 2015). Additionally, an overexpression of Mic10 does not influence the level of Mic10 in the MINOS/MICOS complex but leads to more homo-dimerization (Bohnert et al., 2015)**.** Dimers of CV were found at the rim of cristae and bent the IM in the opposite direction (Blum et al, Davies et al., 2012, 2019, Hahn et al., 2016, Mühleip et al., 2016). Therefore, CV dimers can be seen as an antagonist of Mic10 in influencing the IM curvature (Rampelt et al., 2018). As the spatiotemporal organization of CV was well investigated in this thesis, the question raised which protein had a stronger influence on shaping the IM. Furthermore, could a co-transfection of Mic10 be used to mark the CJ of cristae in which CV diffuses in the CM and/or does an overexpression of Mic10 alter the spatiotemporal organization and mobility of CV.

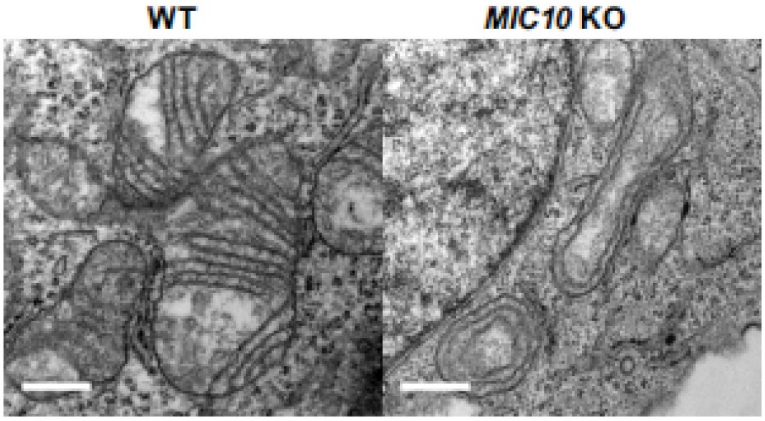

Figure 98 Transmission electron microscopy images of WT, *MIC10* knock out HAP1 cells.
TEM image of mitochondria in HAP1 cells. Mitochondria in HAP1 cells wild-type show regular cristae (left panel). Knock-out of Mic10 leads to a tubular IM or even circular cristae. Scale bar: 0.5 µm (Figure adapted from Kondadi et al., 2020)

HeLa cells using the Fiji plugin Trajectory classifier (Figure adapted from Kondadi et al., 2020)

First of all, the mitochondrial networks seemed not to be influenced by transfection of Mic10:fsnapTag and its overexpression. Mitochondria in the cell periphery occured in their known elongated shape (Figure 53). The calculated localization precision of CV-SUγ and Mic10 was below 15 nm. Remarkably, the diffraction limited image already showed an alternating localization of Mic10 and CV-SUγ (Figure 53C, Figure 55C). Mic10 showed a confined mobility revealed by SPT (Figure 56B), as it was shown for Mic60 (Appelhans and Busch, 2017b, chapter 9.2.1). The same result was gained by SPT of Mic10 in HeLa cells using the Fiji plugin Trajectory classifier (Kondadi et al., 2020) (Figure 99). Here, Mic10 also shows a confined mobility. STED images of Mic10 in HAP1 cells also revealed a dominant localization of Mic10 at CJs (Kondadi et al., 2020). Interestingly, QIL1/Mic13 the orthologue of Mic12 (fungi) in metazoa promotes the connection of the Mic10, Mi26, Mic27 complex with the Mic60, Mic19 complex (Guarani et al., 2015, Huynen et al., 2016) . Here, an interesting TALM experiment may answer the question how the MINOS/MICOS complex formation is regulated, by investigating these proteins in a multi-color TALM experiment.
However, as the level of Mic10 in the MINOS/MICOS complex is not altered by its overexpression (Bohnert et al., 2015) the trajectories of Mic10 resulted either from homo-dimers of Mic10 or from intact MINOS/MICOS complexes. Assuming that QiL1/Mic13 is present in the performed TALM experiments a functional

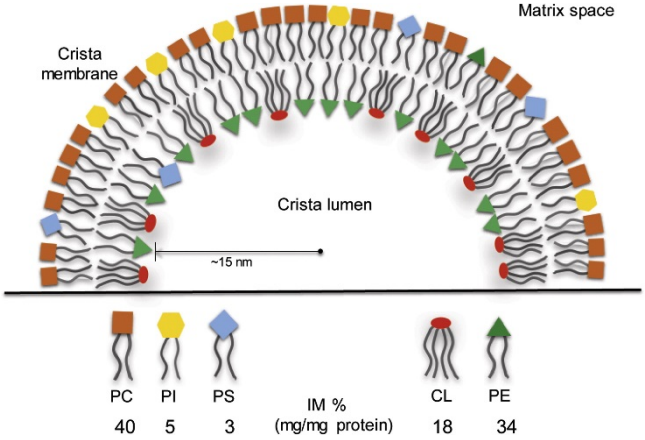

Figure 101 Asymmetry of phospholipids in the cristae membrane
Cardiolipin (CL) and phosphatidylethanolamine (PE) are localized in the negatively curved leaflet. (Figure adapted from Ikon et al., 2017)

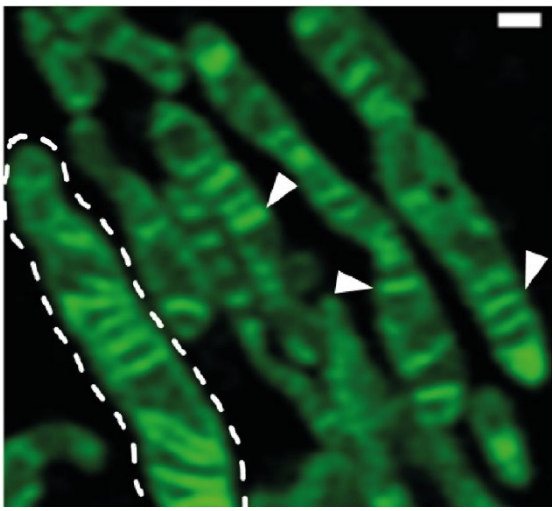

Figure 101 High resolution image of the IM via Airyscan technology
NAO staining of cardiolipin in the IM of mitochondria. Arrowheads mark cristae. NAO signal intensity shows an enrichment of cariolipin in the CM. Scale bar: 500 nm (Figure adapted from Wolf et al. 2019)

MINOS/MICOS complex is one explanation for confined mobility of Mic10 and Mic60. Another explanation would be that Mic10 homo-dimers stick to bended IM parts, which they evoke. An additional factor of IM shaping is the asymmetry of phospholipids. Here, phosphatidylcholine, phosphatidylinositol (PI) and phosphatidylserine segregate into the positively curved leaflet while cardiolipin and phosphatidyl-ethanolamine (PE)are localized in the negatively curved leaflet of the IM (Ikon et al., 2017) (Figure 101). 10-N-nonyl acridine orange (NAO) is a fluorescent dye, which preferentially binds to cardiolipin and shows a low affinity for other phospholipids found in mitochondria, such as PE and PI (Wolf et al., 2019, Leung et al, 2014). Furthermore, cardiolipin is enriched in the CM as staining with NAO shows a higher intensity in CM, than in the IBM (Wolf et al., 2019) (Figure 101). However, cardiolipin stabilizes Mic10 oligomers at the CJs (Ramplet et al., 2018). Cardiolipin also binds tightly to OXPHOS proteins (Szeto et al., 2014).

However, as Mic10 trajectories mark the CJs it was expected that dual-color TALM of Mic10 and CV-SUγ results in a combation of trajectories where CM tracks of CV-SUγ will be found nearby confined trajectories of Mic10. Unfortunately, co-transfection of Mic10 in a HeLa cell line already overexpressing CV-SUγ did not resulted in trajectory maps of confined Mic10 trajectories marking CJs of cristae in which CV-SUγ diffused. Additionally, the D_{app} of CV did not changed compared to the control. Furthermore, the mobile subpupultion of CV-SUγ was reduced by about 10% and meanwhile its confined fraction increased by 10%. Interestingly, about 15 % of Mic10 were found in the mobile subpopulation with a D_{app}= 0.078 $\mu m^2/s$ ± 0.003 $\mu m^2/s$, while nearly 40 % of Mic10 showed a diffusion with a D_{app}= 0.014$\mu m^2/s$ ± 0.001 $\mu m^2/s$ and over 45% of Mic10 showed a confined diffusion with a D_{app}= 0.003 ± 0.000 $\mu m^2/s$. Together with the trajectories this once more shows strongly that Mic10 remains confined monile at a certain position in the IM - the CJs. An explanation for this behavior of Mic10 could be an interaction of MICOS complex across the CJs with another MICOS complex.

Dual-color TALM analysis revealed that Mic10 overexpression altered the spatiotemporal organization of CV-SUγ. Trajectory maps of CV-SUγ did not show the typical cristae trajectores with their perpendicular directionality anymore. The quantification of the trajectory directionality, shown in f

Figure 58 demonstrates a strong influence of Mic10 to the sub-compartmentation of the IM and thereby to the spatiotemporal protein organization of the proteins within. Here, shown by the resulted dominant longitudinal directionality of CV-SUγ trajectories. The reason for this altered organization can be explained by the possible large amount of Mic10 homo-dimers when overexpressed. Thus homo-dimers of Mic10 induce an altered ultrastructure. This was already shown by surface rendering of isolated mitochondria from yeast (Bohnert et al., 2015) (Figure 102). However, the influence of Mic10 on the ultrastructure was not compensated by CV-

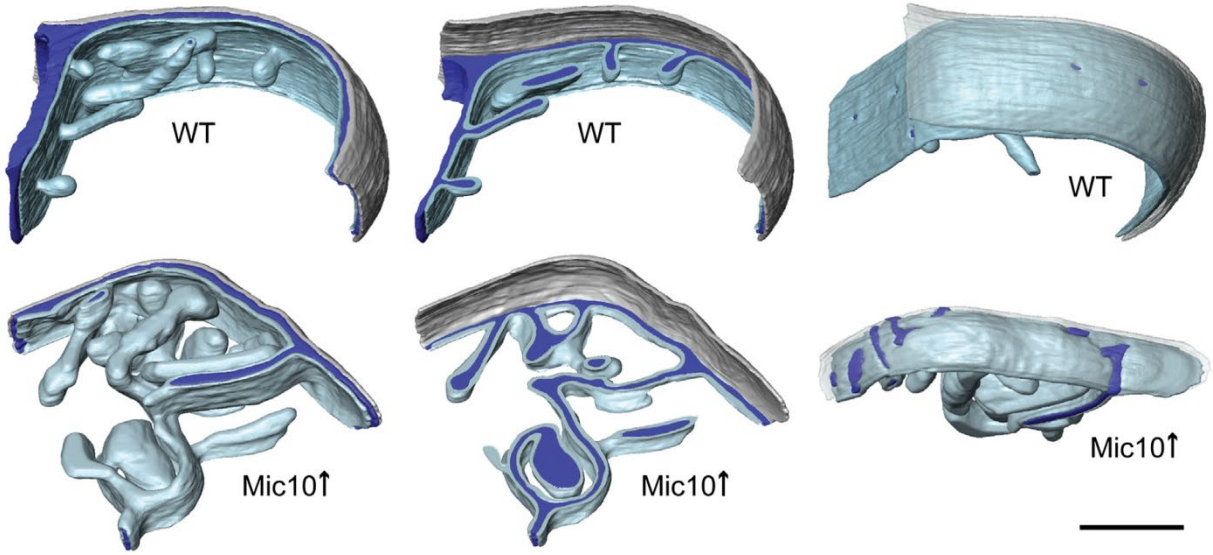

SUγ overexpression in the same cells, as expected because CV-SUγ is not involved in triggering the dimerization of CV, and that the MINOS/MICOS complex seems to be the major player in shaping the IM. This assumption is supported by the trajectory directionality of CV-SUγ compared to the control. Nevertheless, TALM experiments of CV-SUγ with co-transfection of Mic10 and CV-SUe may give a detailed view about this antagonistic interplay btween MINOS/MICOS and CV dimers. However, it can be assumed that MINOS/MICOS would be needed to induce cristae formation and the dimers and oligomers of CV structurally only come into play when the cristae formation is present to bend the CM back to the IBM. Interestingly both protein complexes are stabilized by cardiolipin which than acts as a cofactor for IM bending.

Taken together dual-color TALM by SPT of an IM protein like CV-SUγ allows to reveal changes of the IM architecture evoked by overexpression of Mic10. Thus dual-color TALM can be used to analyze the effects of mitochondrial proteins on the shape of the IM and the spatiotemporal organization of proteins within, in living cells. Here, SPT and in especially TALM is today the only method, which allows to investigate such interplays, *in situ*. The possibility to analyze the trajectory directionality of proteins, allows to draw back conclusions of the ultrastructure. Thus TALM, once more demonstrates its role as a cutting-edge method in the field of SPT.

Figure 102 Segmented surface-rendered representation of a mitochondrion isolated from wt yeast or a Mic10-overexpressing strain
Left: view from matrix; middle: cut view showing crista junctions; right: view from outer membrane. Gray, outer membrane (transparent in the right panels); light blue, inner membrane; dark blue, intermembrane space (intracristal space in the right panels). The cristae volume was 1.85% (WT) and 12.2% (Mic10[) of the volume enclosed by the inner boundary membrane. Scale Bar: 200 nm. (Figure adapted from Bohnert et al., 2015)

10.3 3D tracking and localization microscopy compared to 3D super-resolution techniques

Today, 3D SPT is state of the art. There are different ways to reveal the third dimension in microscopy. Here, three different methods are presented shortly and compared to 3D TALM.

First of all, DH-PSF uses an engineered PSF (Gustavsson et al., 2018). Here, the addition of a spatial light modulator (SLM) in combination with a 4*f* relay system in the emission pathway of a microscope creates a PSF containing the 3D information of the single fluorescent molecule. The most prominent one is a DH-PSF, where the PSF consist of two dots, which show a spiral shape along the z-axis formed like a double-helix. DH-PSF microscopy has also been combined with light sheet microscopy resulting in tilted light sheet microscopy with 3D PSFs (TILT3D) (Gustavsson et al., 2018).

Secondly 4Pi microscopy has been established and is based on confocal microscopy with two juxtaposed objectives (Hell and Stelzer, 1992, Hell et al. 1998). The excitation light results in constructive and deconstructive interference, which reduces the possible axial resolution to approximately 80 nm (Gugel et al., 2004). However, in the past 4Pi microscopy has been developed further to whole-cell 4Pi single-molecule switching nanoscopy (W-4PiSMSN) (Huang et al. 2016). W-4PiSMSN allows volumetric reconstruction with 10 nm to 20 nm isotropic resolution of a ~10 µm thick sample. W-4PiSMSN has been used to reconstruct mitochondria (Huang et al. 2016). In dual-color experiments also with microtubule networks (Huang et al. 2016). Unfortunately, it has so far not been used for imaging mitochondria in living cells. Additionally, it does not allow SPT.

Thirdly astigmatic distortion of the PSF established in 3D STORM can be used to reveal the position of proteins in all three dimensions and allows to reconstruct cell structures and cell organelles (Huang et al. 2007, Huang et al., 2008), but lacks information of the dynamics and mobility of proteins because of fixed samples. Furthermore, 3D STORM has been used for dual-color imaging (Huang et al., 2008). Here, mitochondrial networks of whole cells together with microtubule networks in fixed cells have been reconstructed.

In contrast, 3D TALM opens up the field for 3D SPT when using astigmatic distortion of the PSF. It combines HILO illumination and astigmatic distortion of the PSF together with posttranslational, substoichiometric labeling of fusion proteins with membranepermable dyes. Thus, 3D SML and 3D SPT of fluorescent signals in living cells was possible. Additionally, a reconstruction of small mitochondrial networks was possible. Furthermore, 3D TALM is the most cost-efficient way to upgrade a TIRF microscope to perform 3D SML and 3D SPT.

3D SML of mitochondrial proteins in living cells was not done before. Thus, 3D TALM provides a new method to localize and track mitochondrial proteins in living cells with nanometer resolution. The lateral localization precision reached was σ_x=27.44 ± 4.04 nm and σ_y=30.23 ± 3.70 nm and an axial localization precision σ_z=47.54

± 4.05 nm (

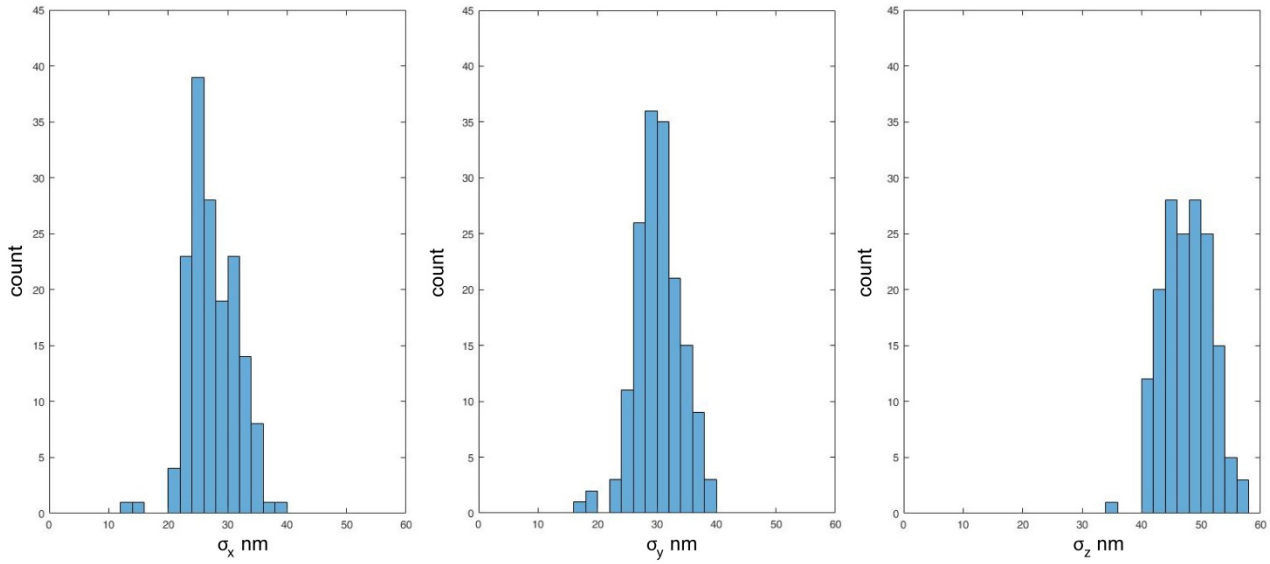

Figure 64). Demonstrating that 3D super-resolution in living cells is possible with a high accuracy. In contrast to 3D STORM similar resolutions were achieved. In 3D STORM of mitochondrial poroteins, the lateral localization precision reached was 20 - 30 nm, while the axial localization precision was 60 to 70 nm (Bo Huang et al. 2008). In TILT3D the lateral localization precision was 13 nm and the localization precision 20 nm for Tom20 and a lateral localization precision of 3 nm and 7 nm axial localization precision for fiducial bead detection using the 6-µm tetrapod PSF. Thus TILT3D reached a nearly isotropic localization precision (Gustavsson et al., 2018). Using W-4PiSMSN resulted in an isotropic resolution of 10 nm – 20 nm as well (Huang et al. 2016). However, 3DSTORM, TILT3D and W-4PiSMSN allow to image and reconstruct larger z-ranges in the sample due to cell fixation and scanning through the sample but have only been used for imaging mitochondrial proteins / mitochondria in fixed cells. In 3D TALM the maximal z-range of the used cylindrical

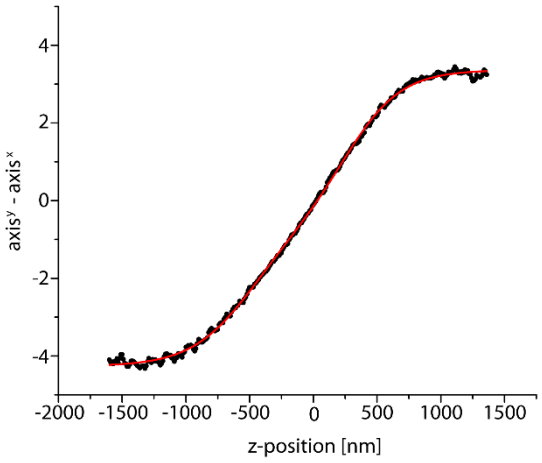

lens was 1 µm (Figure 63). DH-PSF microscopy has already been used for 3D SPT of mRNA particles with 25 nm localization precision in the lateral direction and 50 nm precision in the axial direction. However, 3D TALM is the next step for imaging mitochondria and mitochondrial proteins, because it allows to track mitochondrial proteins with similar localization precisions as in DH-PSF and to investigate the shape of mitochondria and their membranes, in living cells.

In the case of Tom20 imaging of single mitochondria over a timescale of less than 48 seconds provided enough

data points to reconstruct the tubular OM. At the same time 3D TALM allows to investigate the spatiotemporal organization of Tom20 by the same data.

10.3.1 The outer mitochondrial membrane revealed by 3D TALM compared to 3D STORM and TILT3D

3D TALM of Tom20 allowed to investigate the 3D shape of mitochondrial networks in the cell periphery. Compared to results reached by 3D STORM, 3D TALM was lacking the possibility to reconstruct complete mitochondrial networks of a cell. However, the reconstructions of single mitochondria are comparable. Here, 3D TALM allowed to reconstruct the tubular OM by 3D SML of Tom20 in living cells with a localization precision similar to 3D STORM (
Figure 103). The microscopy setup in 3D TALM and 3D STORM was similar and included a cylindrical lens with a focal length of 1 m, in the emission pathway of the microscope. In both cases the 3D position of the signal was obtained by localizing the astigmatic PSF. 3D STORM used fixed cells. Thus, the cell could be optically scanned. This allowed to scan a large axial range like a whole mitochondrial network (
Figure 103A). Additionally, slices containing localization scan be selected (

Figure 103D). However, as 3D STORM was performed in fixed cells it did not allow to track the proteins. Here, 3D TALM provides important advantages in order to investigate the spatiotemporal dynamics of mitochondrial proteins. Additionally, 3D TALM reached similar localization precisions and also allowed to reconstruct the hollow shape of the tubular OM. A comparable technique, which allows 3D SPT is DH-PSF microscopy. The development of DH-PSF to TILT3D uses a tilted light sheet. Thus, 3D TALM with the use of HILO illumination is comparable to this technique and both allow 3D SPT. Nevertheless, TILT3D reached a localization precision of 13 nm in x and y and 20 nm in z for Tom20, and this is twice as precise as 3D TALM. However, the results with TILT3D on mitochondria were done in fixed cells. Nevertheless, 3D reconstruction of mitochondria by localization of Tom20 resulted in similar results compared to 3D TALM (Figure 104). Important to note is that some mitochondria imaged by TILT3D did not show the tubular shape similar to 3D TALM (Figure 104A). Thus, TILT3D dealed with similar challenges of mitochondria like their orientation in the cell and enough localizations per mitochondria. Results of DH-PSF in living cells compared to 3D TALM can be done by setting

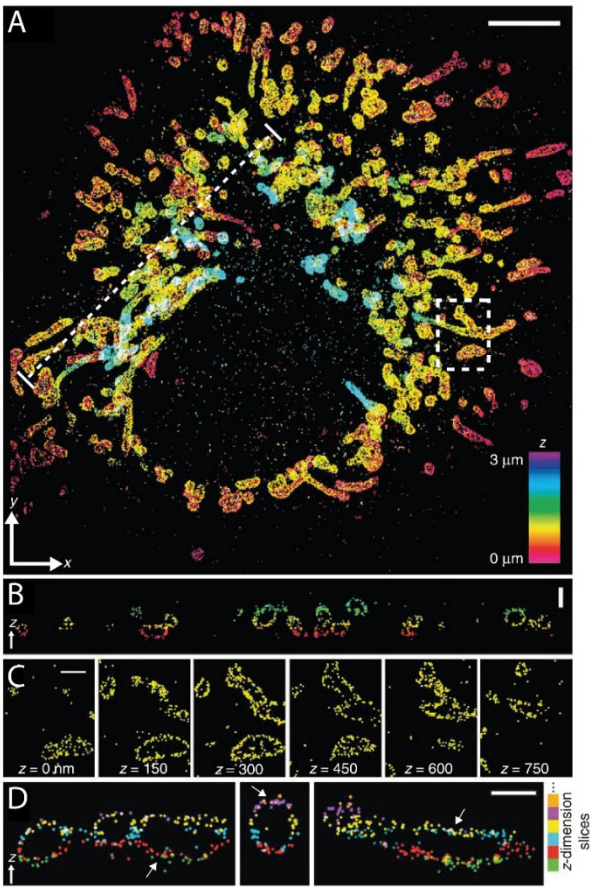

Figure 103 3D STORM image of mitochondria in a BS-C-1 cell
A 3D reconstruction of a mitochondrial network in a BS-C-1 cell by 3D localization of Tom20 in optical slices. **B** Cross-section along the dotted line in A. The hollow OM was visualized. **C** X, y sections oft he boxed region in A at different z-positions. D Vertical cross-sectionsof different region in A. The color code refers to six different slices. Again, the tubular shape of the OM was reconstructed. (Figure adapted from Huang et al., 2008)

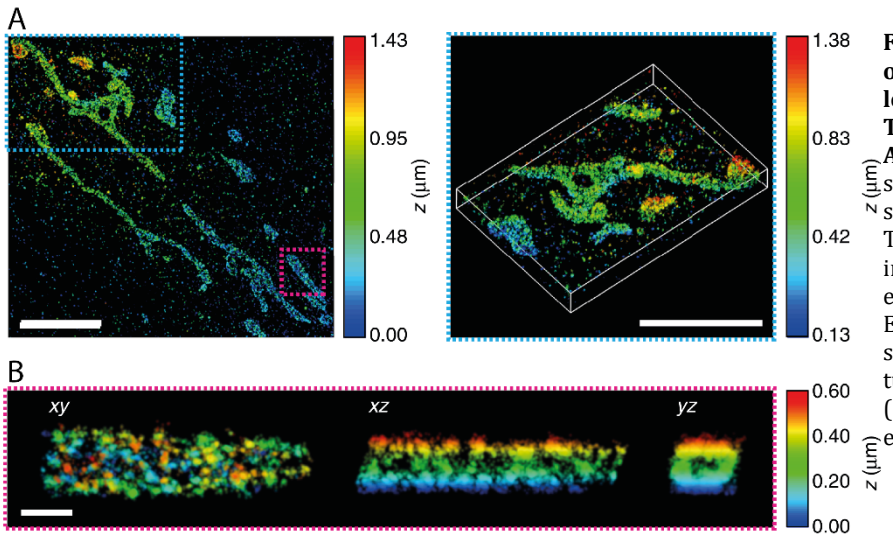

Figure 104 3D reconstructions of mitochondria by 3D localizations of Tom20 via TILT3D
A 3D Super-resolution reconstruction of mitochondria by single molecule localization of Tom20 in a HeLa cell with TILT3D imaging. The blue squarewas enlarged in the right panel. **B** Enlargement of the magenta square. The yz-view revealed the tubular structure of the OM. (Figure adapted from Gustavsson et al., 2018)

tracking of mRNA-proteins via DH-PSF (Thompson et al., 2007) in contrast to 3D TALM SPT data. Here, a localization precision of 24.7 nm in x, 27.9 nm in y and 49.5 nm in z were reached. Remarkably, these values are totally similar than the localization precisions reached by 3D TALM. However, now the advantage of DH-PSF to track signals over a large axial range comes into play. DH-PSF allowed to track mRNA-proteins over more than 1.5 µm (Thompson et al., 2007).

However, 3D TALM is still the only method challenging 3D SPT of mitochondrial proteins in order to investigate their spatiotemporal organization. It was published that the D_{app} of mitochondrial proteins in two-dimensional TALM is underestimated (Appelhans et al., 2012) The D_{app} of Tom20 via TALM is 0.140 µm²/s and was corrected mathematically in dependence of the mitochondrial diameter to 0.215 µm²/s (Appelhans et al., 2012). However, the diameter can change along a mitochondrion and differs between mitochondria. 3D TALM overcomes the problem of underestimating the mitochondrial protein mobility. The gained D_{app} of Tom20 in 3D TALM was 0.231 µm²/s ± 0.056 µm²/s. Thus, reached a similar value to the predicted one by two-dimensional TALM.

Especially 3D SPT allows to reveal the shape of the OM by tracing the structure with the gained trajectories. Taken together 3D TALM sets the basis for tracking mitochondrial proteins, in living cells. The possibility to reconstruct mitochondria, without fixation of the cell, opens new possibilities for analyzing the spatiotemporal protein organization of proteins in cell organelles.

10.3.2 3D TALM of F_1F_O ATP synthase subunit-γ revealed IM structure in living cells in different metabolic conditions

10.3.2.1 3D TALM of F_1F_O ATP synthase subunit-γ

3D TALM of CV-SUγ in the control allowed to localize CV in living cells. 3D reconstructions of the localizations showed that CV was localized in the IBM and CM. Furthermore, CV-SUγ accumulated in certain regions of the IM. These accumulations were mostly oriented in a perpendicular direction to the longitudinal axis and expanded through whole mitochondria as the 200nm slice of the reconstruction in Figure 73 showes. This were interpreted as localization in the CM. Regarding to literature CV is organized in dimers and oligomers along the rim of cristae which bend the CM at the rim (Blum et al, Davies et al., 2012, 2019, Hahn et al., 2016, Mühleip et al., 2016). Surprisingly the localizations did not reveal an organization of CV in a row like organization of localizations of different proteins. Here the resolution of 3D TALM seems to avoid this. Additionally, confined trajectories were not accumulated in a neckless like arrangement along the CM, as it would be expected for CV dimers. This could have been an effect of the overexpression of the CV-SUγ:HaloTag construct, so that not all CV-SUγ were bound in CV or even CV dimers. However, this also showed that CV-SUγ was localized in the flat membrane part of the cristae, since cristae trajectories were obtained as mobile trajectories but still longitudinal confined and diffusing up and down in an area perpendicular to the longitudinal axis (Figure 76, Figure 81).

3D SPT of CV-SUγ revealed that CV-SUγ diffused along the IBM and in the CM. This was revealed by trajectories which showed a longitudinal direction, respectively a perpendicular direction to the longitudinal axis of the imaged mitochondrion (

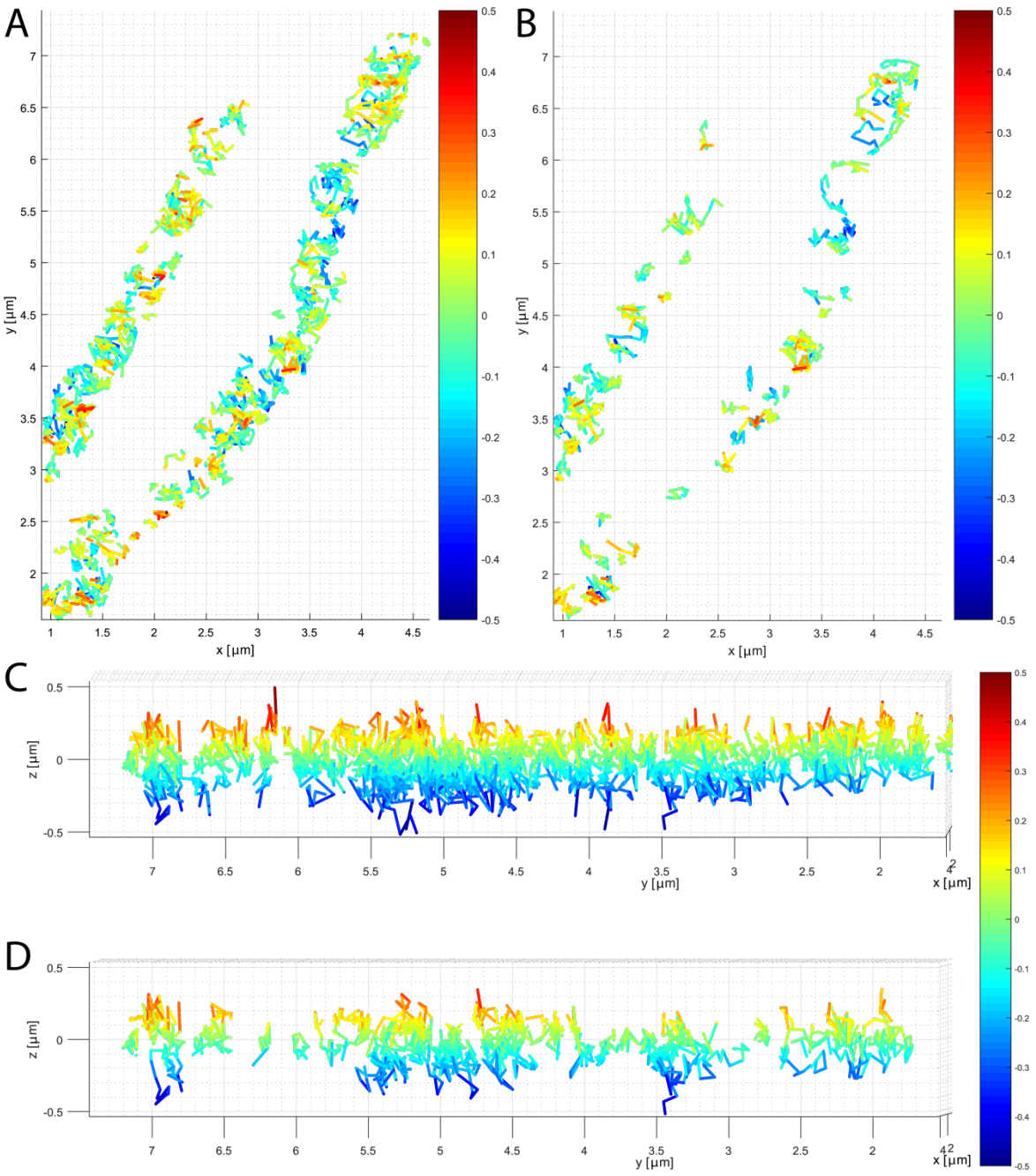

Figure 75). Here, for the first time 3D information of the spatiotemporal organization of CV was provided. Additionally, confined mobility of CV in cristae, respectively in the CM was observed. This demonstrated the standalone criteria and revolutionary position of 3D TALM in fluorescent microscopy.

10.3.2.2 Altered inner mitochondrial membrane architecture caused by starvation

TEM images of mitochondria in starvation revealed that cristae vanished nearly completely and a tubular shape of the IM (Figure 60). 3D TALM of CV-SUγ:HaloTag labeled with TMR^{HTL} was used to investigate if this tubular IM shape could be revealed by 3D reconstruction and 3D trajectories, in living cells. The cells were starved for 2 hours. 3D TALM allowed to reconstruct the IM shape of mitochondria in cells exposed to starving conditions partially. In several areas of the 3D reconstructions of the IM a tubular shape was visible (Figure

77). Limiting was the overall shape of the mitochondria in reference to the focal plane. Again, the 3D SPT results showed a clearer view of the IM architecture. Here, trajectories of CV-SUγ traced the IM shape (Figure 78). Remarkably no cristae trajectories were found (Figure 78), as expected from two-dimesnional TALM data in the same conditions (CV-SUγ in the control and under starving conditions directly differentiate, obviuosly in their directionality (**Fehler! Ungültiger Eigenverweis auf Textmarke.**B, D). This indicates either a shift of a longitudinal orientation of cristae or a shift of CV-SUγ into the IBM or even a lost ofcristae. The transition of CV-SUγ into the IBM can result from avoided diffusion in the CM and a dominant diffusion in the IBM or by a reduction of the CM. In order to analyze the directionality of mobility and to quantify for this, the directionality of trajectories was analyzed with MitoOrientedDynamics. Here, the4-step binning procedure was used. As described, the longitudinal axis of each mitochondria was marked, which was used to interpolate it to a straight mitochondrion and the angle of binned steps to the longitudinal axis was measured. Shown in

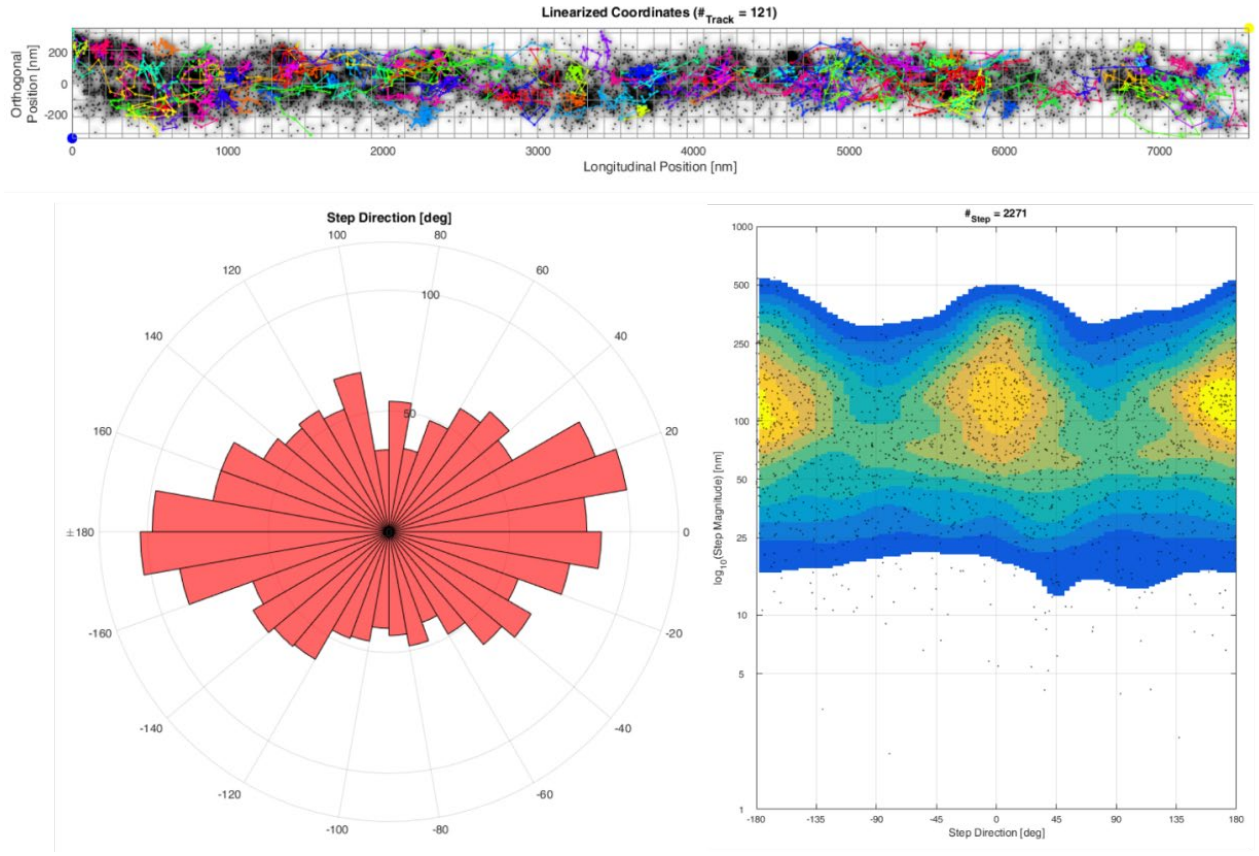

Figure **37** is an example of a straightened mitochondrion in starving conditions and its analysis of the trajectory directionality. In the shown mitochondrion the directionalities of 121 individual trajectories were analyzed (

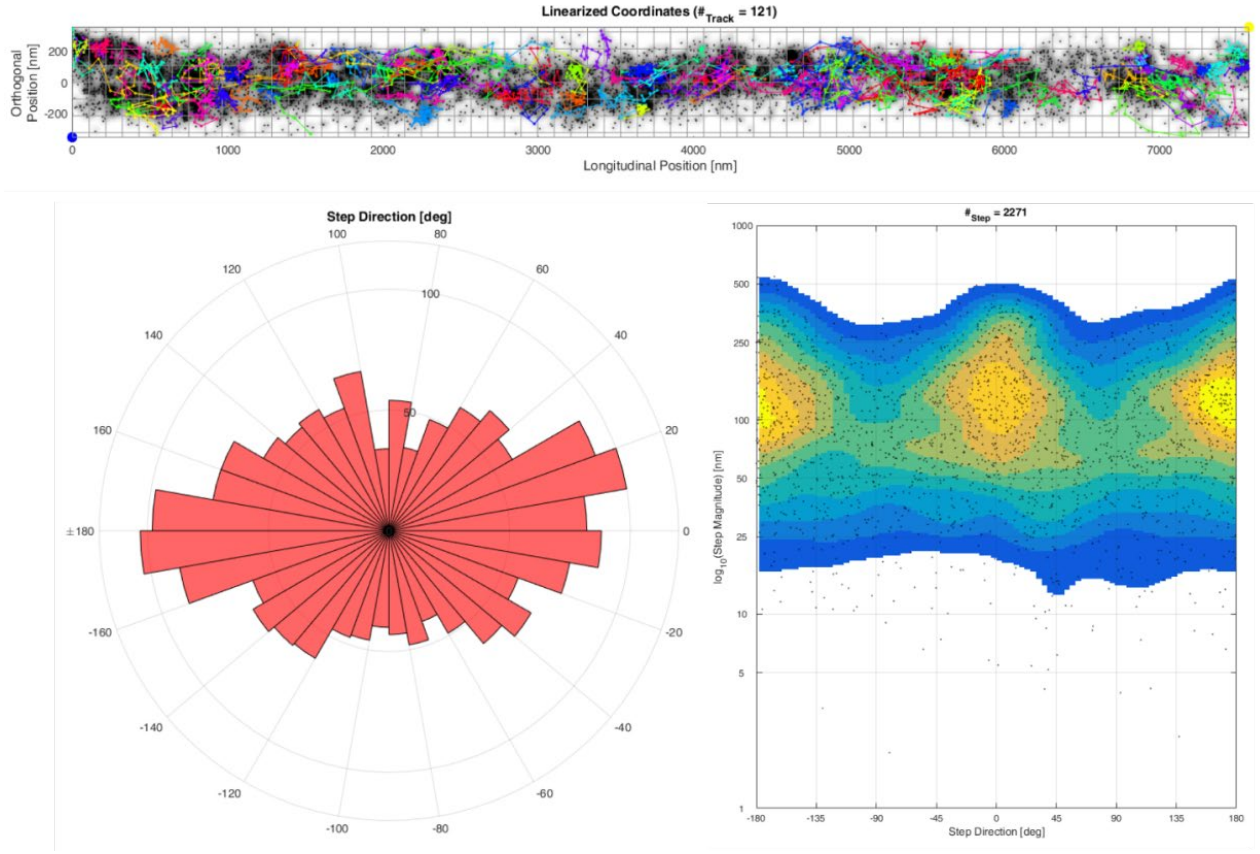

Figure **37**A). The majority of them is oriented along the longitudinal axis (

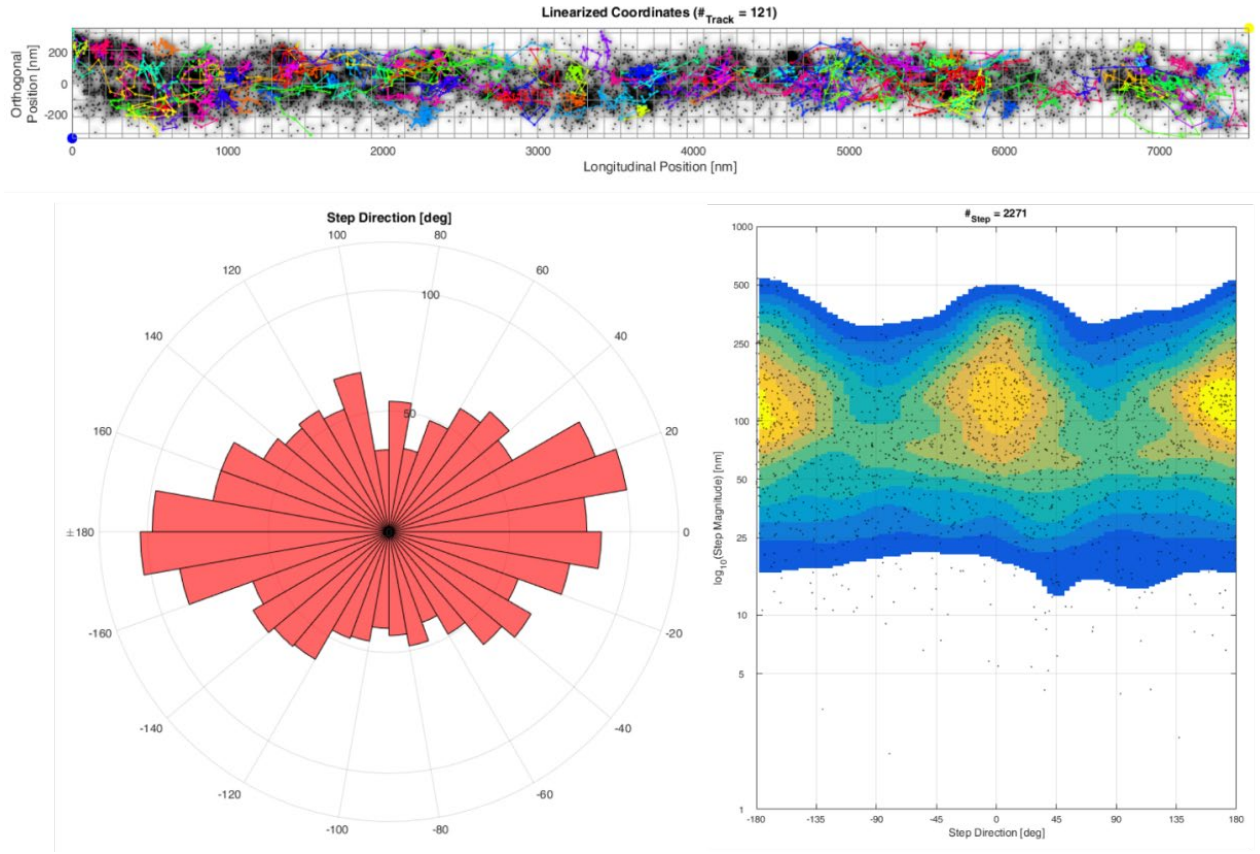

Figure **37**B, C). The pie chart diagram in

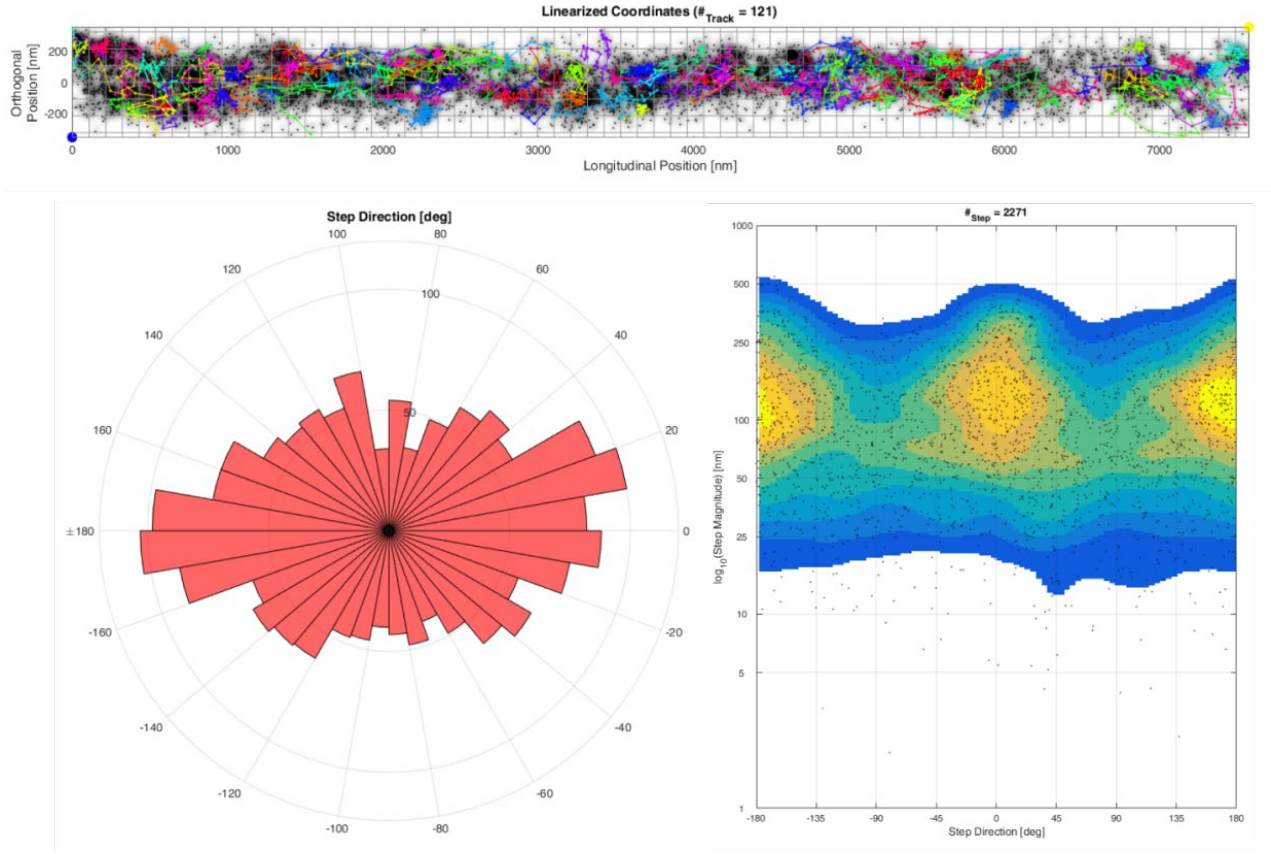

Figure **37**B illustrates the dominant longitudinal movement of CV-SUγ in starvation of the analyzed mitochondrion. Here, the amount of longitudinal directions between -20° to 30° and between -160° to 170° is twice as large as the number perpendicular oriented trajectories. Additionlly, the heatmap in

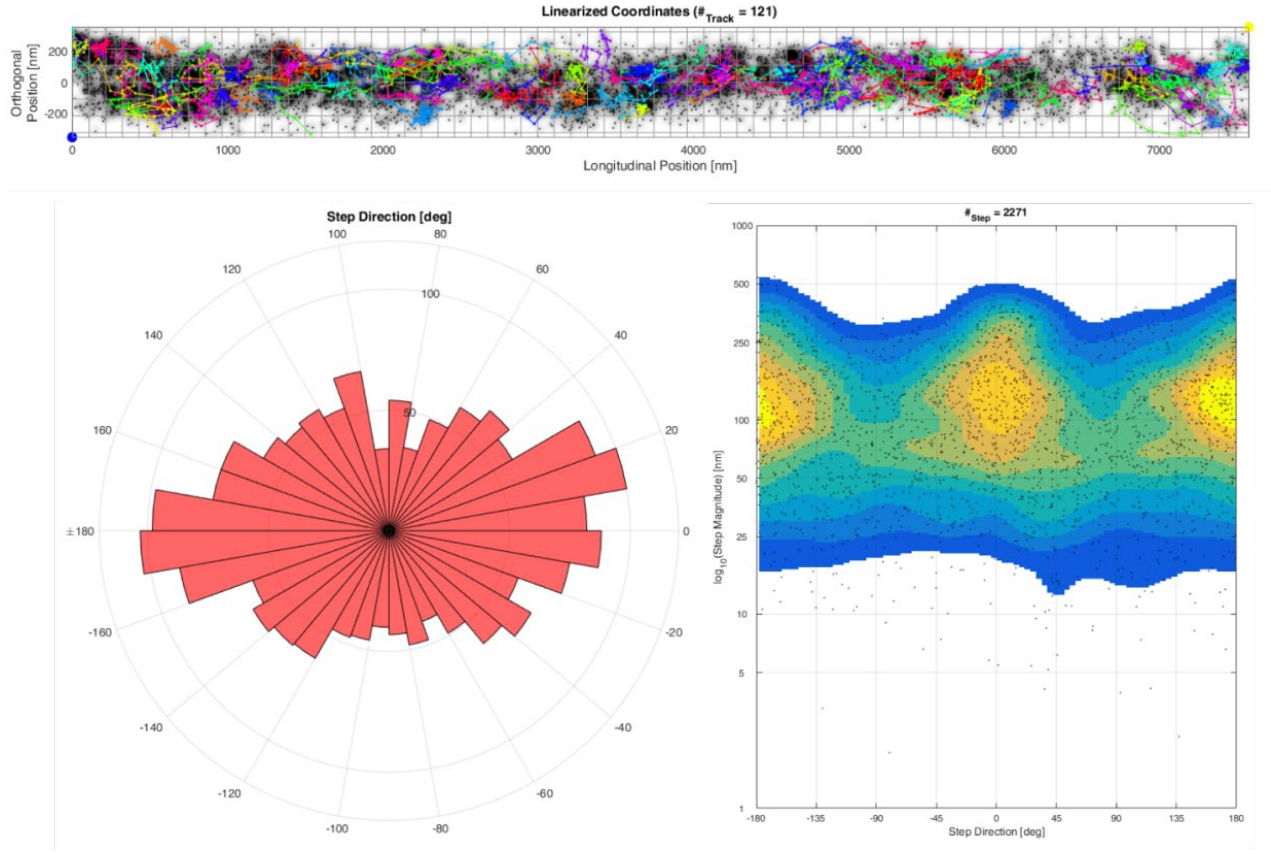

Figure **37**C shows that steps along the longitudinal axis can reach a larger jumpsize than steps in the perpendicular direction. However, this may be influenced by the 3D morphology of mitochondria. Here, jumpsizes in the perpendicular direction can be scaled down stronger than jumpsizes along the longitudinal direction. The trajectory directionality in starvation was compared to the trajectory directionality in control experiments (Figure 38). In the case of the control, 10784 binned steps were taken into account (Figure 38A, C). The analysis of trajectory directionality during starvation was performed on 59743 binned steps (Figure 38B, D).

Table 4 Jumpsize of CV-SUγ in control experiments and during starvation

Protein	Number of steps	Median jumpsize	Maximal. jumpsize	Minimal. jumpsize
CV-SUγ control	20124	96.94 nm	1117 nm	0.58 nm
CV-SUγ starvation	7491	175.70 nm	1211 nm	1.79 nm

Figure 36). The directionality of CV-SUγ trajectories performed in 3D TALM showed again a longitudinal orientation (

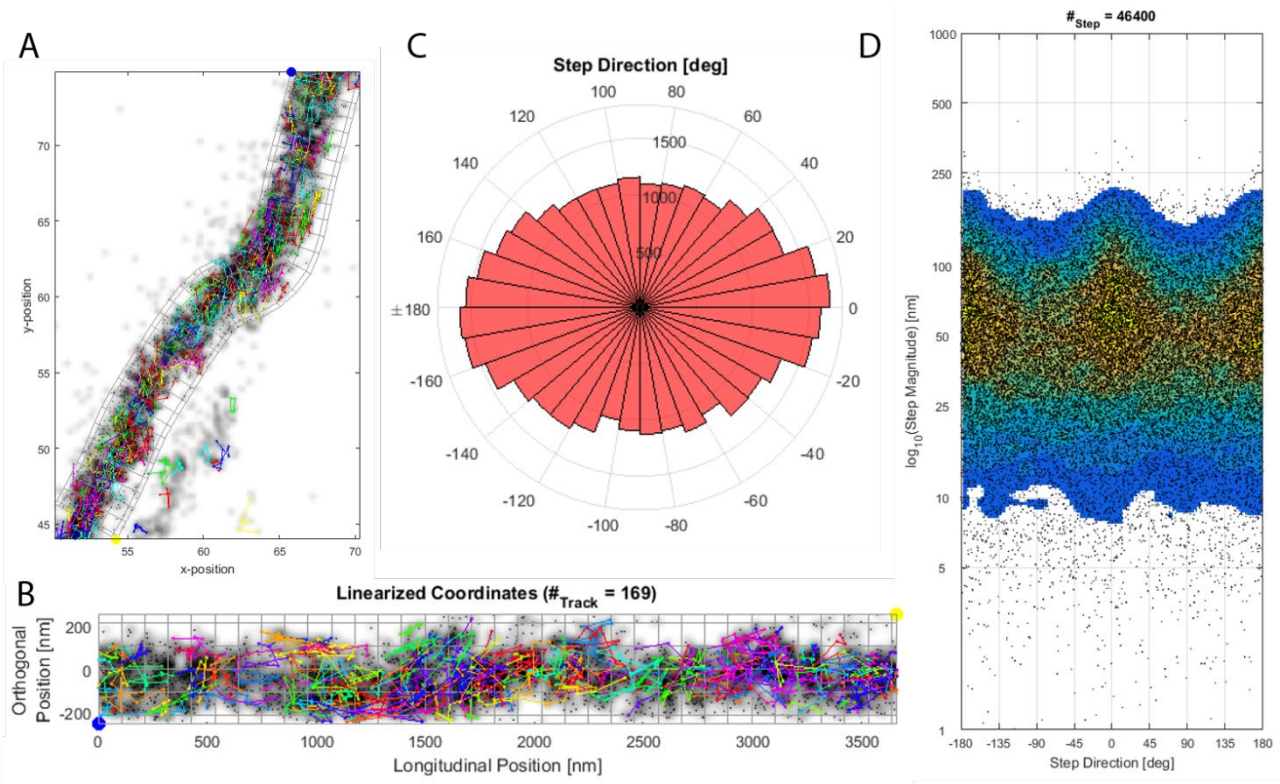

Figure 86), which was also expected and seen in two-dimensional TALM experiments (Figure 38).

The results demonstrated that 3D TALM has the potential to uncover tubular regions of single mitochondria and to reveal the altered IM shape best by 3D SPT. Together with TEM tomography of HeLa cells exposed to starving conditions the altered architecture of the IM gets clear (

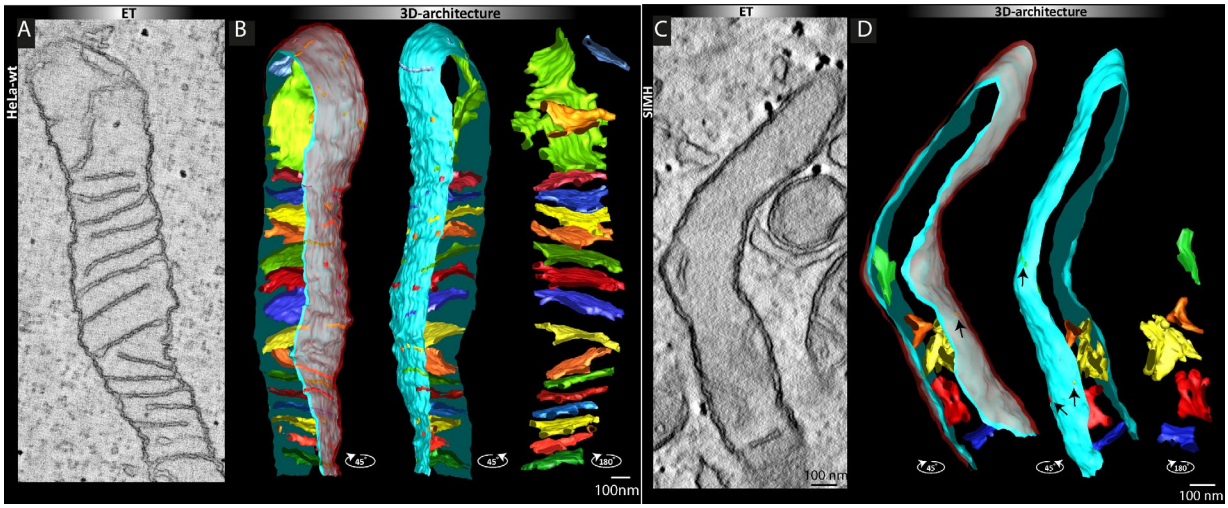

Figure 105 3D tomography reconstruction of mitochondria by surface rendered transmission electron microscopy

A Mitochondrion in a HeLa cell in control conditions. A regular cristae arrangement was obtained. **B** 3D reconstruction of TEM images by surface rendering resulted in a tomographic view of the ultrastructure. Cristae appear in a disc like shape with multiple CJs. **C** Mitochondrion in a HeLa cell in starving conditions. Cristae vanished and the IM became tubular. **D** 3D reconstruction of TEM images by surface rendering resulted in a tomographic view of the IM. A large area without cristae was obtained and cristae appeared in an unregularly shape. (Figure adapted from Verena Wilkens, 2012 (Dissertation))

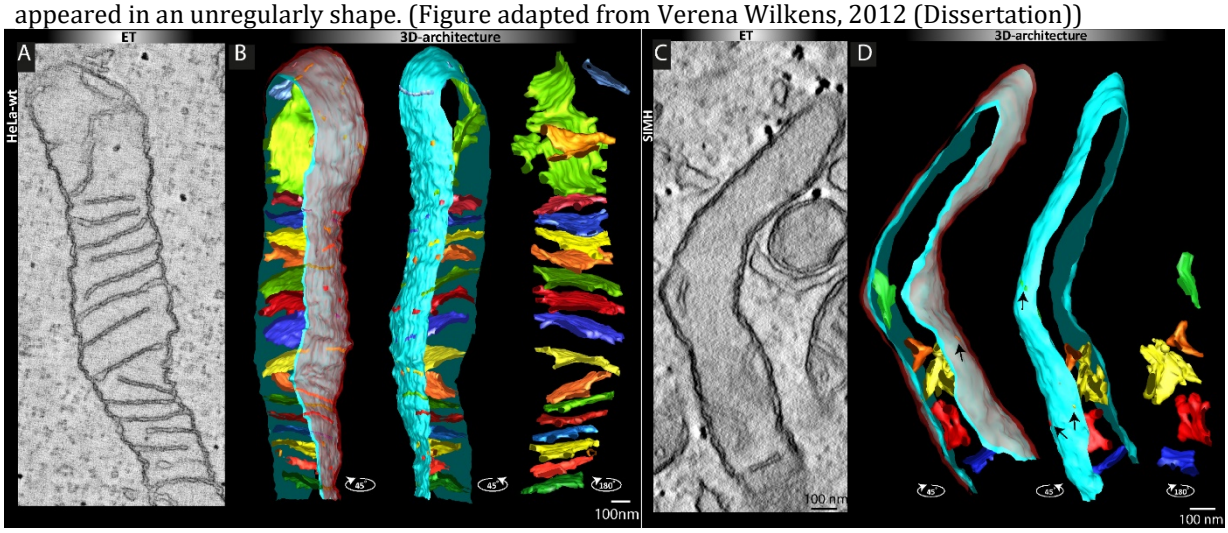

Figure 105). Cristae vanish during starvation. Although, TEM images revealed areas with regular cristae and/or unregularly cristae alternating with areas which showed no cristae at all (Wilkens V., Dissertation 2012) (Data not shown). The power of 3D TALM becomes obvious, as 3D TALM allowed to reveal the heterogeneous IM shape, in living cells during starvation with an IM partially tubular. Additionally, the spatiotemporal organization and dynamics of a mitochondrial protein could be observed. Unfortunately, 3D TALM was yet not combined with dual-color microscopy.

10.3.2.3 Altered inner mitochondrial membrane architecture caused by improved respiration conditions

As starvation led to an altered IM shape with loss of the cristae or unregularly arrangement of cristae and a partially tubular IM, the opposite metabolic switch of cells was investigated by 3DTALM of CV-SUγ in improved respiratory conditions. Here, TEM images revealed a heterogeneous and complex shape of the IM (

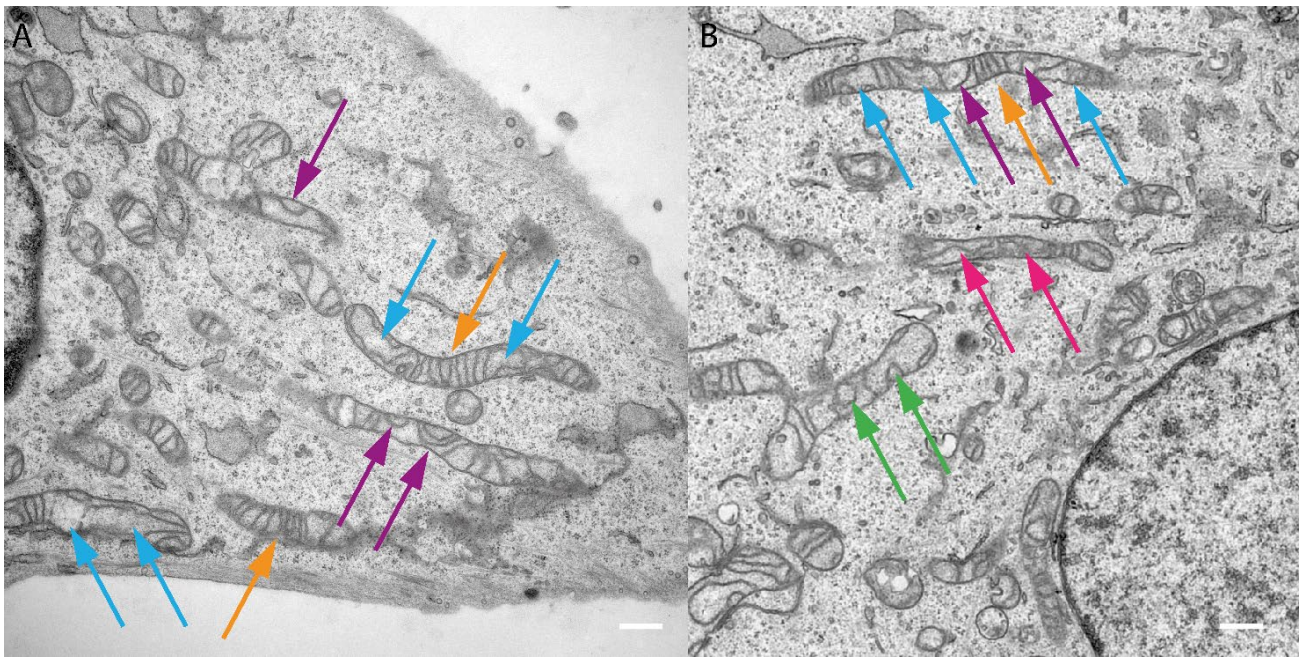

Figure 61). Beside areas of regular cristae arrangements, areas with no cristae, areas with longitudinal oriented cristae, and strongly bended cristae in a rainbow shape or even with a circular / spherical shape occurred. 3DTALM of CV-SUγ delivered trajectory maps in which all kind of shapes were visible. Beside areas containing cristae trajectories (Figure 81), trajectories with a longitudinal directionality were found (Figure 82). Additionally, areas with accumulation of trajectories were obtained (Figure 87,

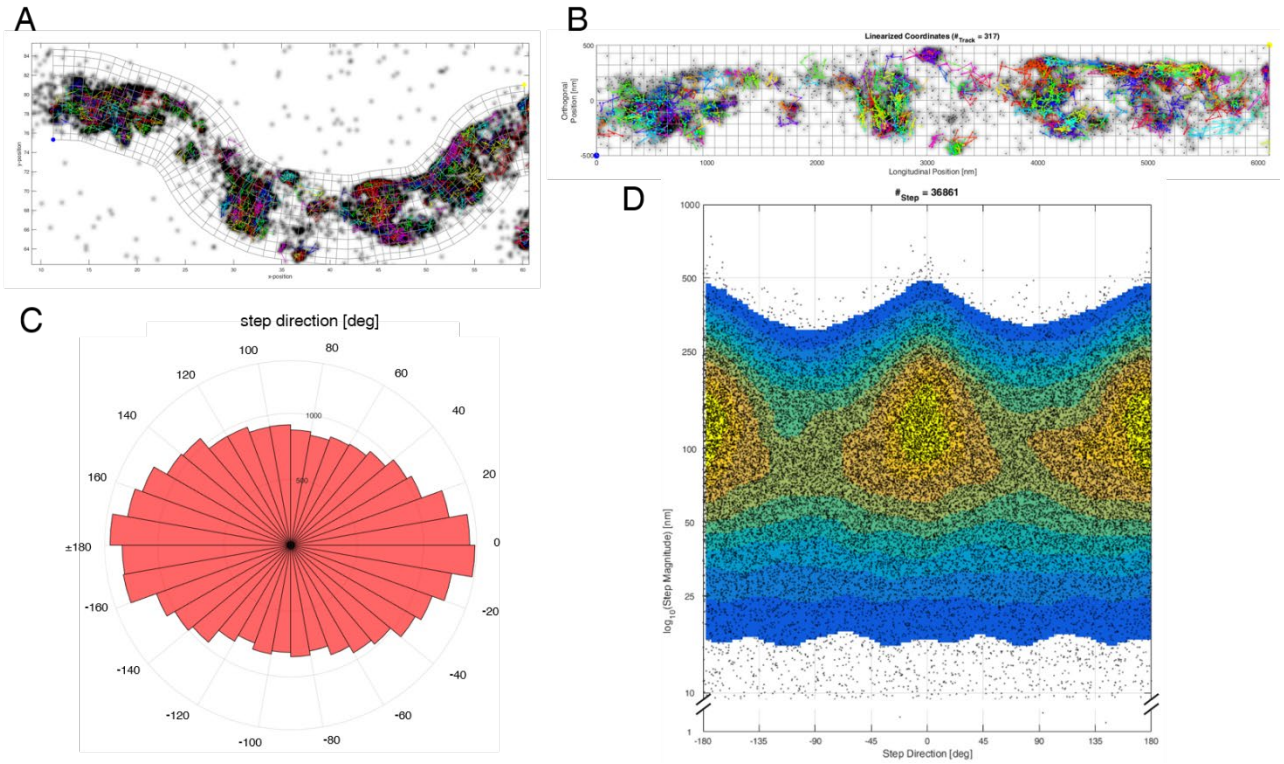

Figure 88). These could result from cristae having a rainbow shape or large spherical cristae. 3DTALM did not allow to distinguish between those structures. However, in some cases single trajectories clearly showed a circular route, here a spherical IM architecture was assumed (Figure 88). Thus, 3DTALM allowed to resolve the morphology of mitochondria by 3D trajectories tracing the IM architecture. However, unfortunately a reference of the true IM shape was missing. Additionally, and influence of the overexpression of CV-SUγ:HaloTag together with improved respiration conditions cannot be excluded, as the medium for improved respiration did not contained glucose, but instead galactose. Cell used for 3DTALM were grown in medium containing glucose and then transferred to galactose medium and grown in improved respiratory conditions for at least three weeks. Comparable TEM images of mitochondria were done in human bone osteosarcoma epithelial (U2OS) cells, grown in high glucose conditions (25 mM) and then switched to galactose growth conditions and imaged by after TEM 24 h and 48 h (Figure 106) (Balsa et al., 2019). Here the cristae abundance increased after 24 h and 48 h of growing in improved respiratory conditions (Figure 106B). Additionally the cristae density also increased significantly, while the maximal width of the cristae (Figure 106C, D) and the mitochondrial mass stayed similar (Balsa et al., 2019). Thus, it would be interesting to repeat 3D TALM in HeLa cells and U2OS cells under the same conditions.

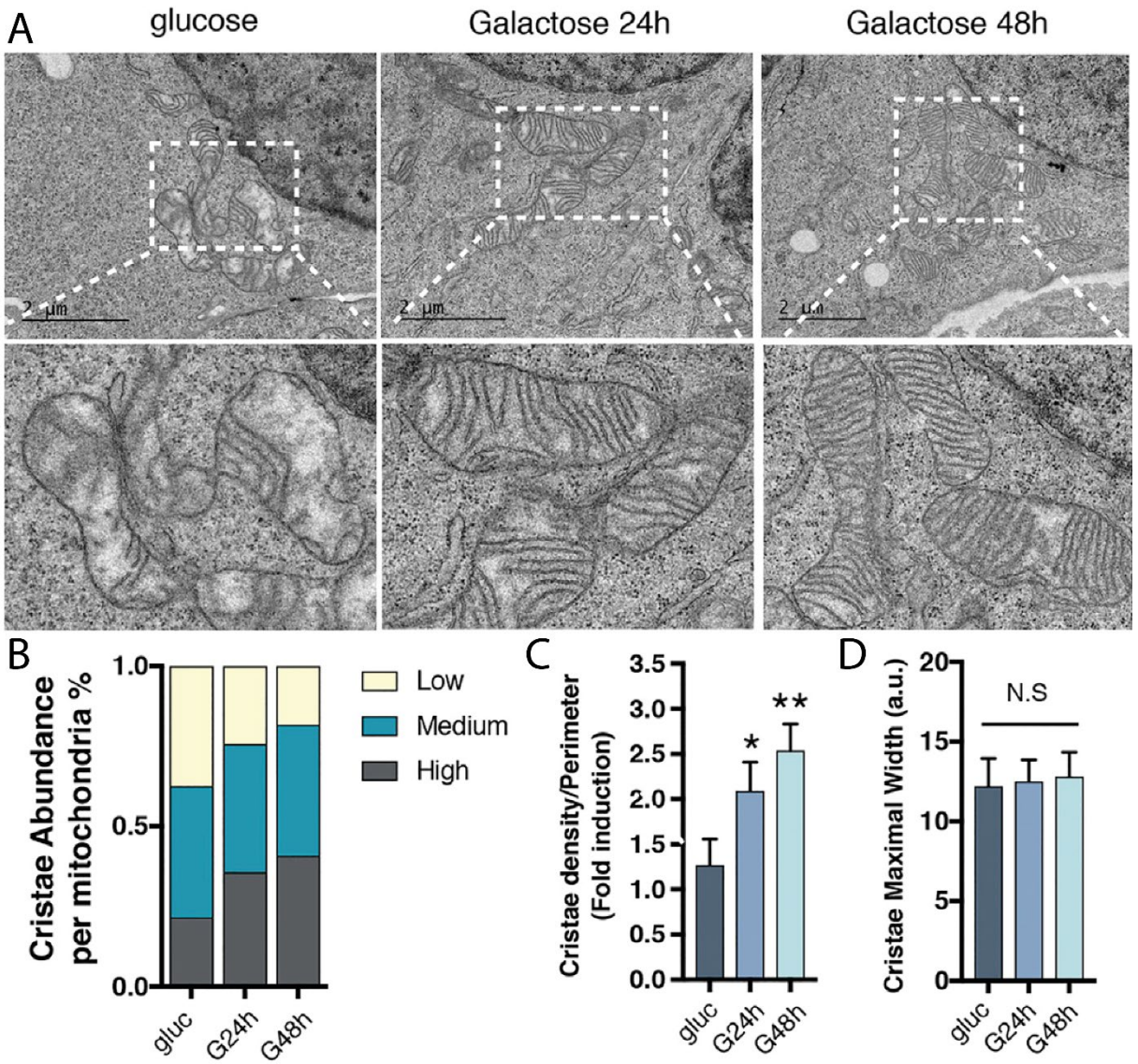

Figure 106 Cristae morphology of U2OS cells grwon in glucose and galactose growth conditions
A TEM image of mitochondria in U2OS cell line, grown in high glucose and 24 h, 48h in improved respiratory condition. **B** Abundance of cristae in the analyzed mitochondria. **C** Cristae density per perimenter of mitochondria increased after 24 h and 48 h of cells grwon in glactose medium. **D** Cristae maximal width stayed similar in the different growth conditions. (Figure adapted from Balsa et al., 2019)

10.3.2.4 The inner mitochondrial membrane architecture is influenced by the metabolic state of the cell

Taken together TEM and TEM tomography of mitochondria in the control and starvation revealed an altered ultrastructure. TALM and 3D TALM allowed to reveal these changes of the IM in living cells. Thus, two-dimensional TALM and 3D TALM proved itself to be a suitable technique to investigate changes in the structure and sub-compartmentation of the IM. Furthermore, 3DTALM allowed to reveal the structural features of single mitochondria, when perfectly aligned to the focal plane in all three dimensions, in living cells. Furthermore, TEM showed heterogeneous IM shapes and orientations of cristae. 3DTALM allowed to recognize and reveal those structural features of the IM. 3DTALM showed that a metabolic switch of cells and the IM architecture are strongly coupled. Thus, 3DTALM put the frontier in 3D SPT further and is today the only method in the field of 3D SPT which was tested to reveal the IM architecture and it changes due to metabolic conditions, in living cells. Nevertheless, Airyscan technology and STED microscopy allow to investigate the IM architecture directly, in living cells (Stephan et al., 2019Wolf et al. 2019). The future will show how microscopy of the IM and SPT of mitochondrial proteins can be performed simultaneously, *in situ*. Then it would be even more important to analyze the spatiotemoral organization of mitcohonrial OXPHOS proteins together with bioenergetic parameters like the $\Delta\Psi m$. However, still it is unknown if mitochondria adapt to the changed metabolic state themselves by rearranging their ultrastructure or if the cell triggers this ultrastructural change. Latest results demonstrate that the protein kinase: R-like ER kinase (PERK) has a regulatory effect on the mitochondrial ultra-structure. PERK increases the cristae formation and thus influences the ultrastructure (Balsa et al., 2019). Furthermore, it finally activates the super complex assembly factor 1 (SCAF1), which leads to an increased supercomplex formation of CI, CIII and CV (Balsa et al., 2019). Interestingly cardiolipin is supposed to have a similar effect (Bazán et al., 2013). Both, SCAF1 and cardiolipin thus design a more efficient coupling of the ETC in OXPHOS. PERK gets activated by an ER stress signal induces by glycosylation based on low concentrations of glucose (Balsa et al., 2019).

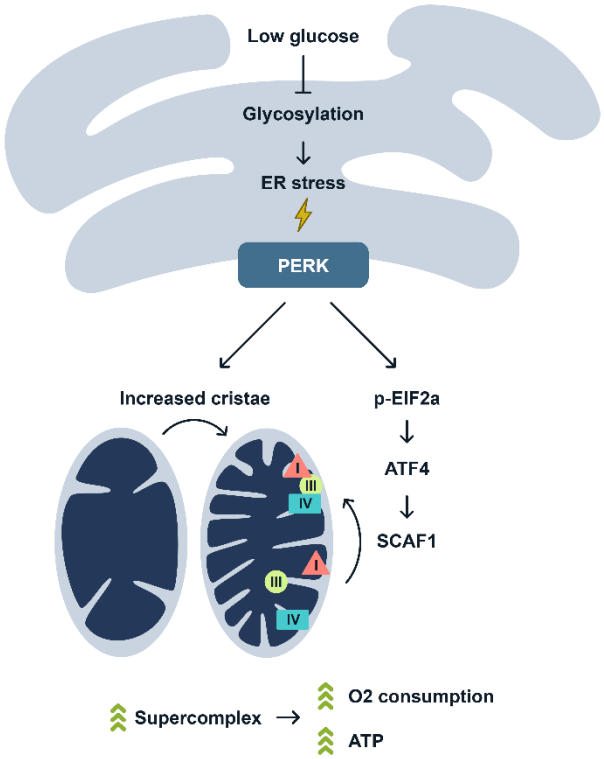

Figure 107 Influence of PERK on cristae formation and supercomplex assembly
PERK gets activated by an ER stress signal caused by low concentrations of glucose and an inhibited glycosylation. Finally, PERK upregulates the formation of cristae and supercomplex SCAF1. (Figure adapted from Balsa et al., 2019)

10.3.2.5 3D TALM of F_1F_O ATP synthase revealed its altered spatiotemporal organization in starvation and improved respiration

Two-dimesnional TALM already revealed an altered spatiotemporal organization of CV-SUγ caused by starvation. TEM, TEM tomography and 3D TALM proved that indeed the IM becomes tubular during starvation. TEM and 3D TALM also revealed that the ultrastructure of mitochondria showed a complex shape with spherical cristae, cristae parallel to the OM and large areas without cristae in improved respiratory conditions. 3D TALM revealed that an altered IM shape influences the spatiotemporal organization of CV and vice versa that the changes of the IM architecture can be monitored by 3D TALM. As a consequence of the altered IM architecture the directionality of trajectories changed. Here, analysis with the tool MitoOrientedDynamic revealed those changes by analysis of all trajectories recorded. However, beside the complete loss of cristae trajectories in the tubular parts of the IM, mitochondria during starvation were still heterogeneously in their phenotype. Thus, beside trajectories following the IBM, with a longitudinal or random like directionality confined trajectories could be seen in all metabolic conditions. However, cristae trajectories and a perpendicular directionality of the trajectories was most common in the control, and still existed in improved respiratory conditions. Nevertheless, in improved respiration the overall analysis by MitoOrientedDynamics showed a shift to the longitudinal direction. Areas with clear cristae trajectories and areas with circular trajectories marking sperical cristae were obtained. Additionally, often areas with accumulations of random oriented trajectories were found. Taking the TEM images into account it seems that these accumulations of random oriented trajectories and also trajectories running in a circle resulted from IM sub-compartments such as spherical cristae, in which CV seemed to be enriched. Furthermore, the accumulation of CV-SUγ trajectories in those spherical cristae suggest the assumption that these cristae possesed a diffusion barrier for CV-SUγ. As areas nearby those accumulations nearly lack CV-SUγ trajectories completely.

However, it cannot be excluded that the ultrastructural changes obtained by TEM and 3DTALM in improved respiratory condition were an effect of overexpression of the CV-SUγ:HaloTag together with the improved respiratory conditions in galactose growth medium. As HeLa wildtype cells exposed to improved respiratory conditions did not show these circular IM microcompartments (personal communication with Bettina Rieger). Next the D_{3Dmean} of CV-SUγ in the three different metabolic conditions was altered (Figure 89). In starvation mitochondria lose their CM, and the diffusion was not hindered structural. This result was obtained in two-dimesnional TALM and 3D TALM experiments. A loss of the functionality, as caused by inhibition of CV performed in two-dimensional TALM experiments also increased the mobility of CV and was accompanied by a loss of cristae trajectories. Together with the loss of the $\Delta\Psi m$ caused by starvation. It can be assuemed that metabolic activity and a healthy $\Delta\Psi m$ are as importnant for the correct spatiotemporal organization of CV as its functionality. Or vice versa, the spatiotemporal organization of CV depends on a healthy $\Delta\Psi m$ and its correct functionality. Additionally, either the spatiotemporal organization of CV or bioenergetic parameters, like the $\Delta\Psi m$ or both influence the IM architecture.

Interestingly, during improved respiration the D_{app} increased significantly, compared to the control and to starvation. This matches the strong changes of the IM architecture in the improved respiratory condition with accumulations of random diffusing CV in spherical cristae and less perpendicular trajectory directionality. Thus, the altered IM architecture caused by the improved respiratory conditions effects the mobility of CV. Or

vice versa, improved respiratory conditions reorganizes the spatiotemporal organization of CV, which than effects the IM architecture. However, 3DTALM of CV allows to reveal the changes in the IM architecture and the spatiotemporal organization of CV, in living cells. Therfore 3D TALM provides a new insight into the dynamic of mitochondrial membrane proteins and allows to determine the spatiotemporal organization and the IM architecture, in living cells.

11 Outlook

It is still unkown to what extend the investigated CV-SUγ is part of CV. Here, blue native electrophoresis would provide data to what extend CV-SUγ:HaloTag is part of the fully assembled CV. Furthermore, the relative amount of dimers and oligomers in the different metabolic conditions need to be investigated. In order to perform TALM experiments of the endogenous CV-SUγ CRISPR/CAS can provide a possibility. Here, CRISPR/CAS can be used to insert the HaloTag gen into the gen of CV-SUγ in order to produce an endogenous encoded CV-SUγ:HaloTag fusion protein. Therfore a haploid cell line like HAP1 cells would simplify this method.

Beside this, still less is known about the assembly of the Tom-complex and of the Tom-Tim machinery, *in situ*. Here, the interaction of Tom20 and Tom22 with the Tom core-complex as well as the interaction of the Tom-complex with the Tim-complex via Tim23 are attractive targets for dual-color TALM of mitochondrial proteins. Using other labeling methods than posttranslational, substoichiometric labeling in order to record co-locomotion of Tom and Tim proteins would be a fascinating experiment. This would open up the field for mitochondrial protein-protein interaction studies in living cells. Using Förster resonance energy transfer (FRET) allows to investigate protein-protein interaction, in living cells. In order to localize and track interacting proteins in mitochondria on single protein level, single molecule FRET (smFRET) can be used. SmFRET should allow to investigate longterm protein interactions such as CV dimers, subunits of the Tom-complex and proteins of the MINOS/MICOS complex. Performing smFRET-SPT shell allow to study protein-complexes like the mentioned ones and to record their spatiotemporal dynamics. A good FRET pair would be mNeon-green and mCherry. Thus, testing FRET pairs for their possibility to be a smFRET pair can become one

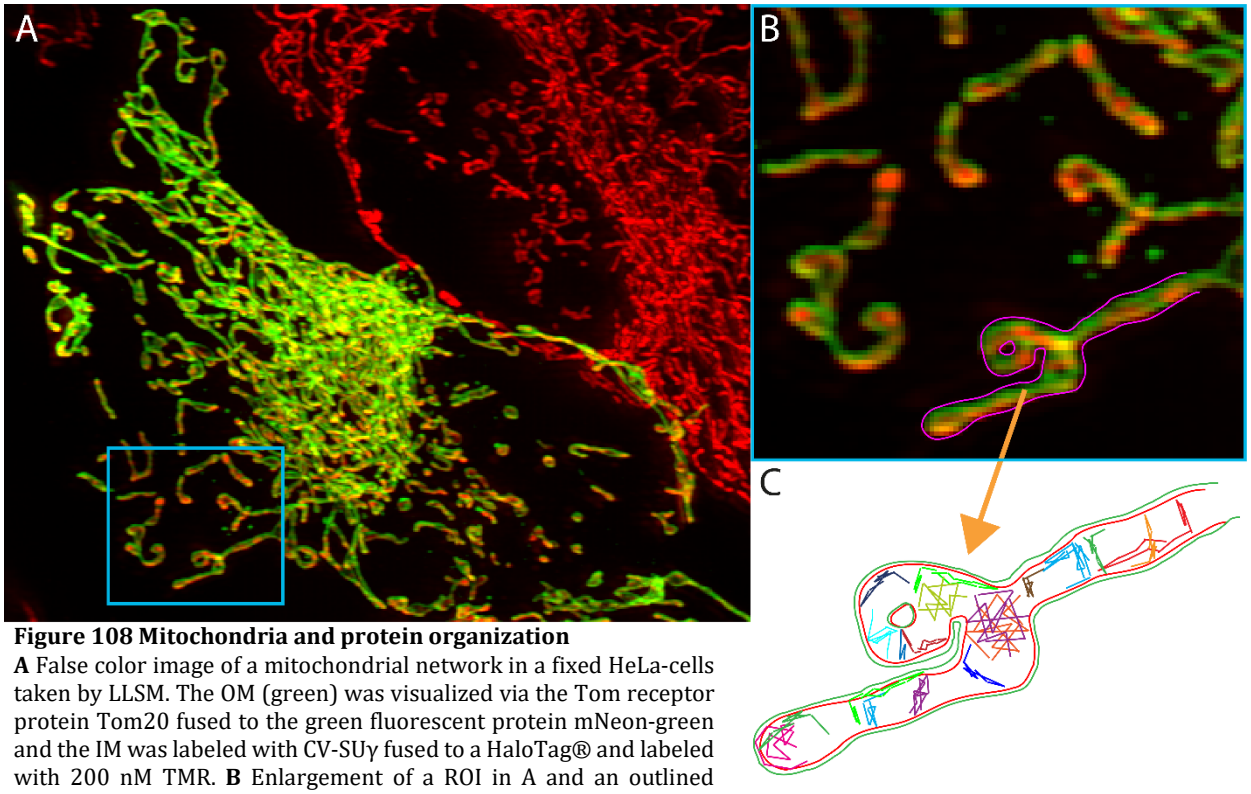

Figure 108 Mitochondria and protein organization
A False color image of a mitochondrial network in a fixed HeLa-cells taken by LLSM. The OM (green) was visualized via the Tom receptor protein Tom20 fused to the green fluorescent protein mNeon-green and the IM was labeled with CV-SUγ fused to a HaloTag® and labeled with 200 nM TMR. **B** Enlargement of a ROI in A and an outlined mitochondrion. **C** Illustration of the OM (green line) and IBM (red line) with possible single mitochondrial protein trajectories.

of the next challenges of TALM on mitochondrial proteins.

This work has given a small inside on the confined proteins localization of Mic10 and Mic60. However, it is unknown what triggers the behavior of Mic10 and the MINOS/MICOS complex to remain at a certain position in the continuous IM. Multi-color TALM of Mic10, Mic60 or other proteins of the MINOS/MICOS complex together with stained cardiolipin can address this question. However, revealing the localization of the MINOS/MICOS complex in reference with the IM architecture in living cells will be an interesting challenge. The localization, assembly and function of MINOS/MICOS complex in dependence on several of its subunits like Mic10, Mic60, Mic27, Mic26 as well as phospholipids like cariolipin can be addressed by multi-color LLSM. LLSM allows to visualize the OM and IM at the same time (Figure 108A,B). Here, the OM was revealed by the fusion protein Tom20:mNeon-green and the IM by CV-SUγ:HaloTag stained with 200 nM TMR^{HTL}, in fixed HeLa cells. A HeLa cell line stably transfected with CV-SUγ:HaloTags was transiently transfected with Tom20:mNeon-green. LLSM was performed with the combination of LLSM and structure illumination microscopy (SIM). Due to the heterogenous distribution of CV-SUγ:HaloTag different intensities of TMR occurred. In AiryScan microscopy the IM architecture was revealed by using MitoTrackerGreenFM (MTG) (Wolf et al. 2019). Next the possibility to stain the IM with MitoTrackerGreen should be tested in LLSM. Thus, also the localization of certain proteins of the MINOS/MICOS complex or proteins of the OXPHOS complex can be revealed inside the IM and with knowledge of the IM architecture. Furthermore, LLSM and SIM combined with SPT may provide a technique to investigate IM protein dynamics in reference to the ultrastructure (Figure 108C).

In order to enlarge the axial range for 3D SPT of mitochondrial proteins, 3DSPT by DH-PSF may allow to image a larger z-range in living cells without losing accuracy in the localization precision and therefore gain more information about the POI and its spatiotemoral organization. However, here 3D TALM in a LLSM should also perform better, because the rapid scanning with the light sheet can make the alignment of the focal plane to mitochondria obsolete.

12 Supplements

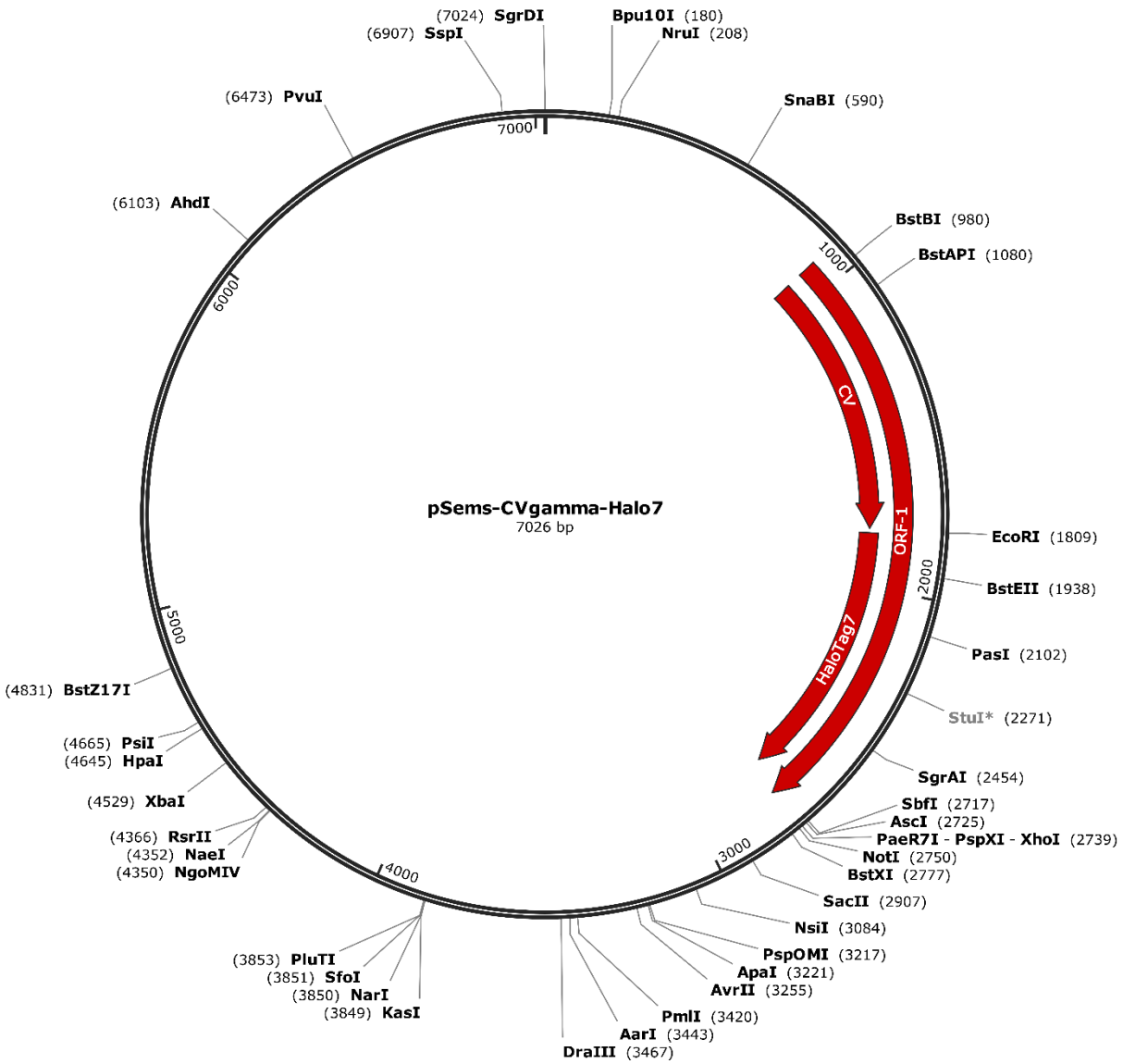

Figure S1 Plasmid map of F_1F_0 ATP synthase subunit-γ:HaloTag

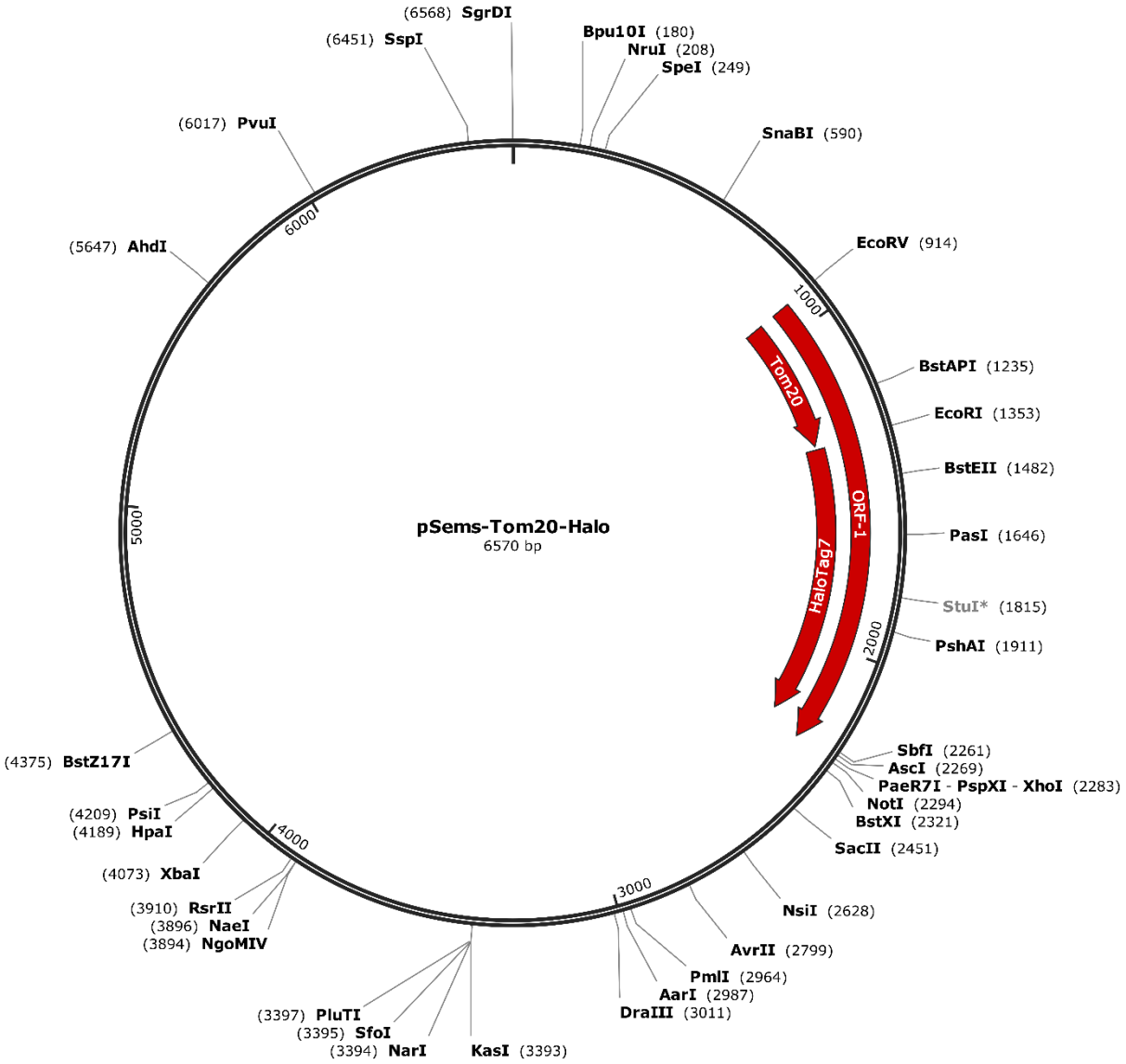

Figure S2 Plasmid map of Tom20:HaloTag

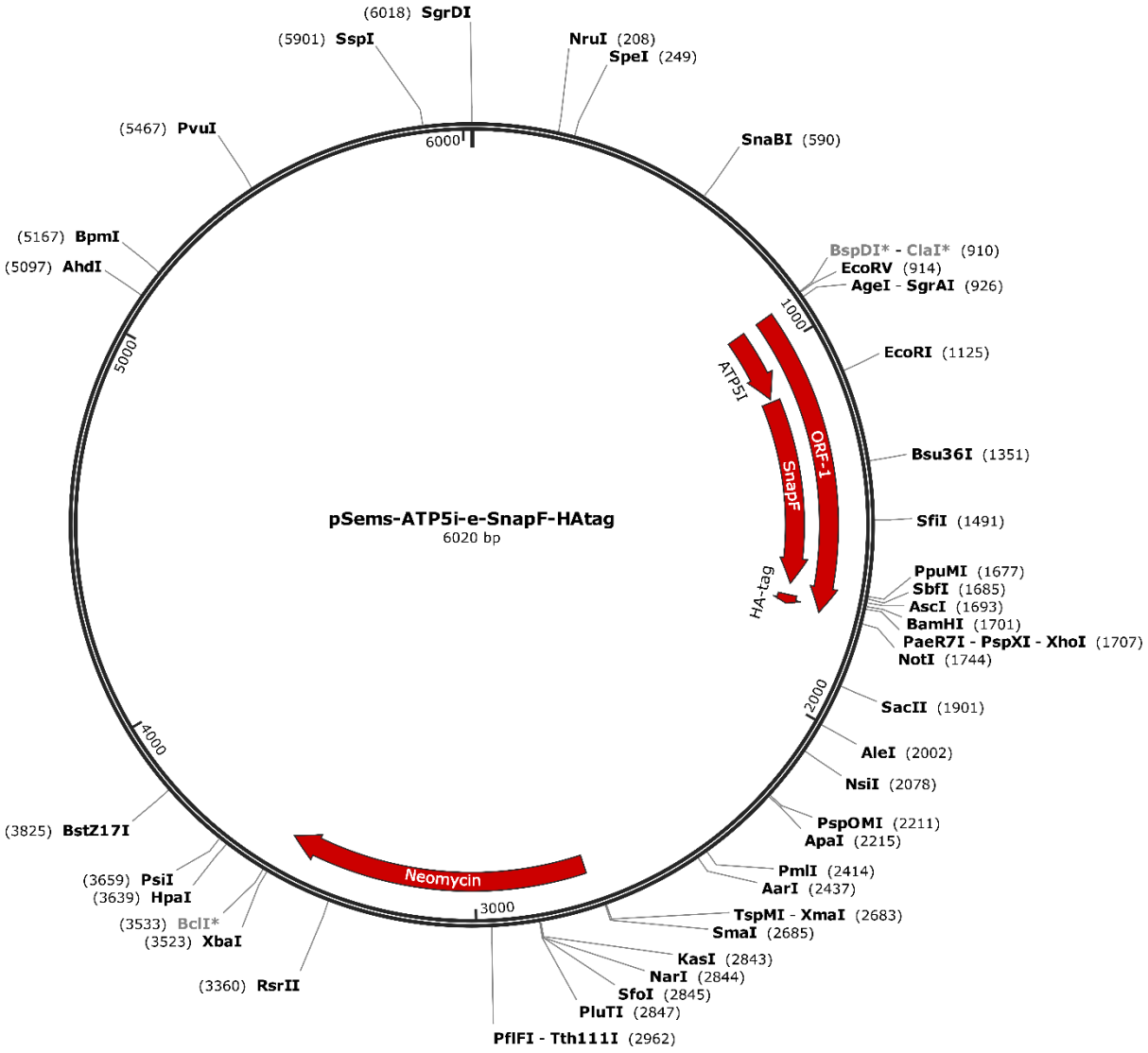

Figure S3 Plasmid map of F_1F_O ATP synthase subunit-e:fSnapTag

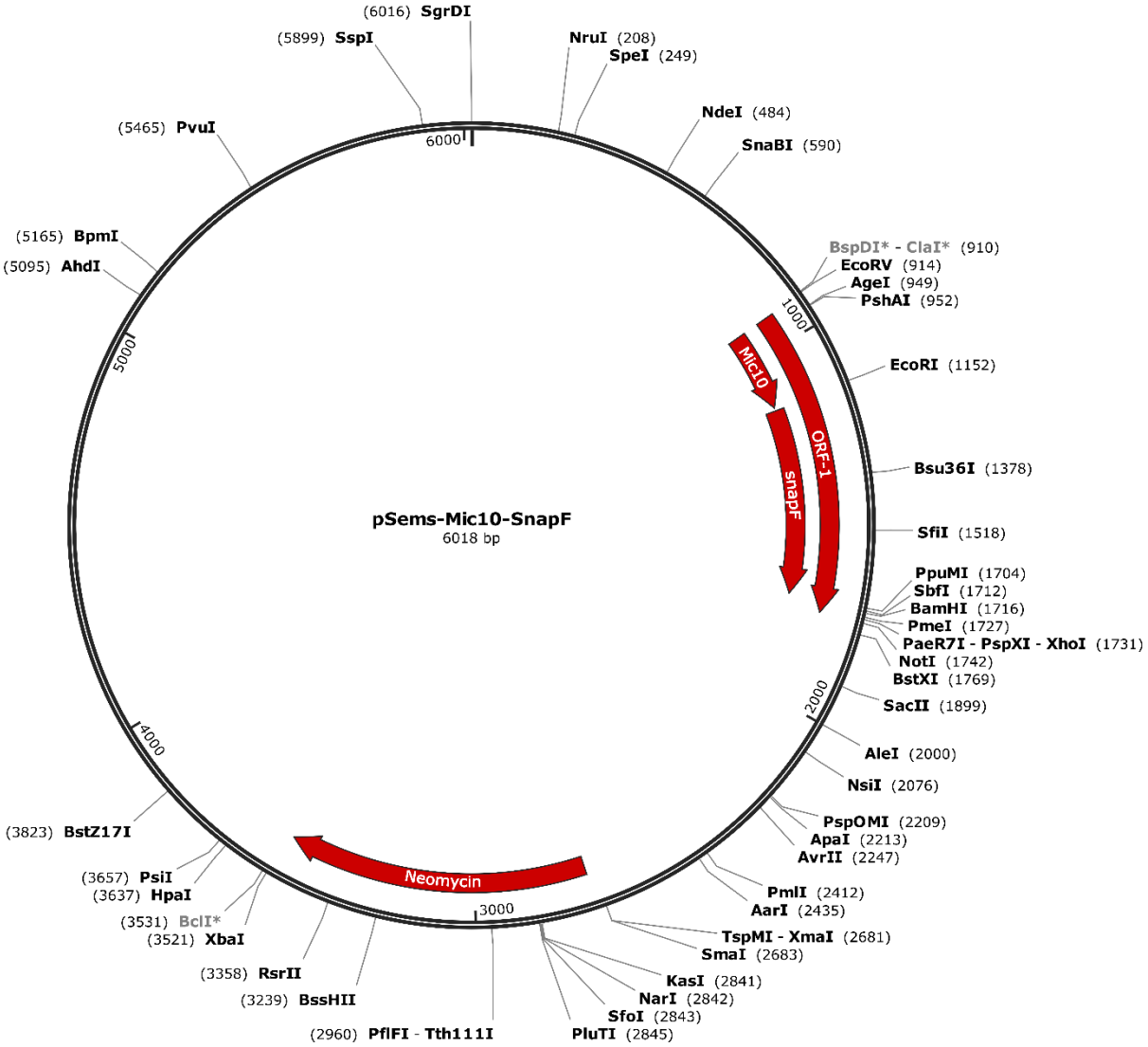

Figure S4 Plasmid map of Mic10:fSnapTag

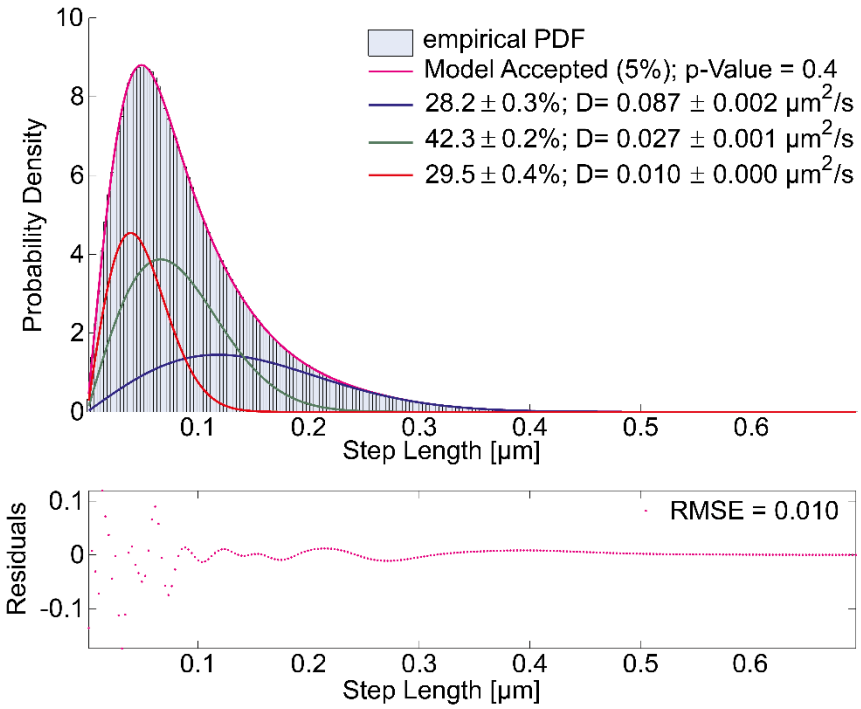

Figure S5 Apparent diffusion coefficients of F_1F_0 ATP synthase during inhibition of ATP synthesis

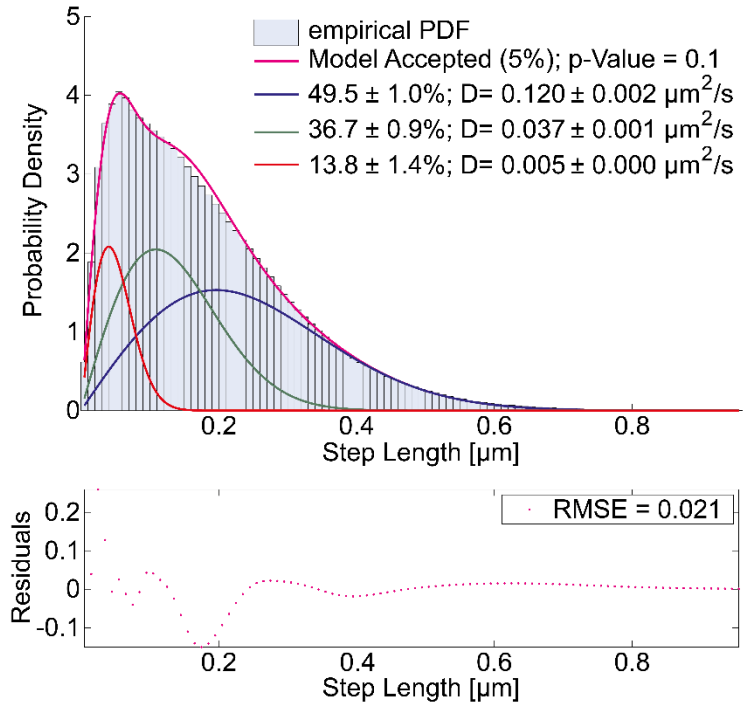

Figure S6 Apparent diffusion coefficients of Tom20 in dual-color experiment labeled with TMR^{star}

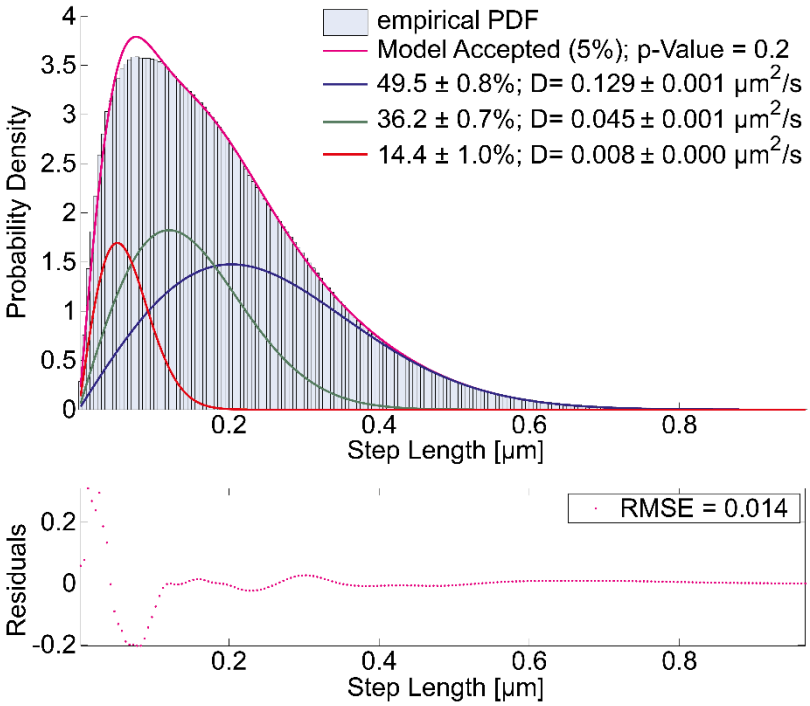

Figure S7 Apparent diffusion coefficients of Tom20 in dual-color experiment labeled with SiR^{HTL}

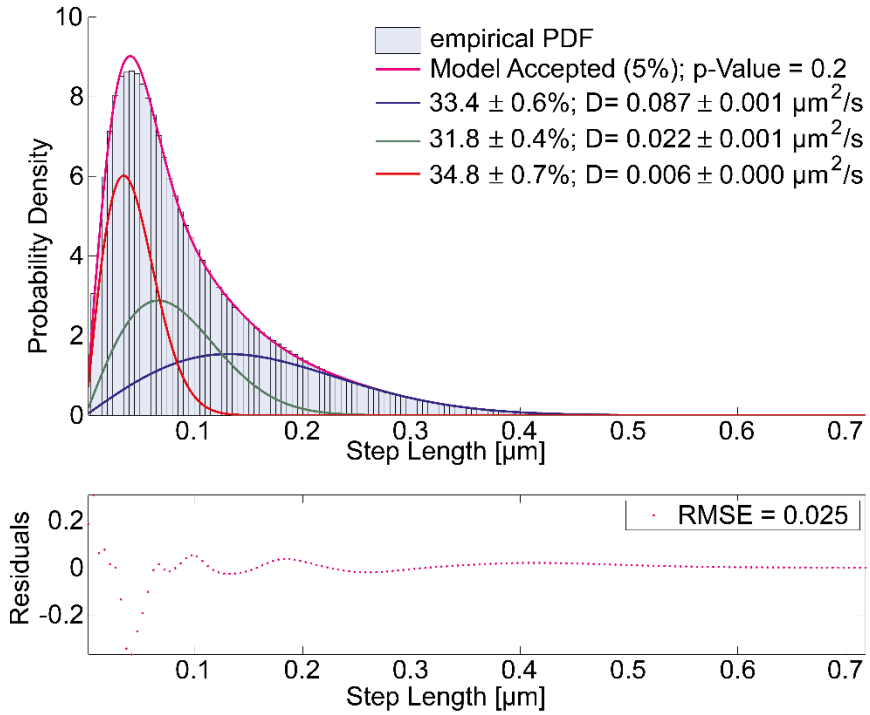

Figure S8 Apparent diffusion coefficients of F_1F_0 ATP synthase subunit-e in dual-color experiment with F_1F_0 ATP synthase subunit-γ

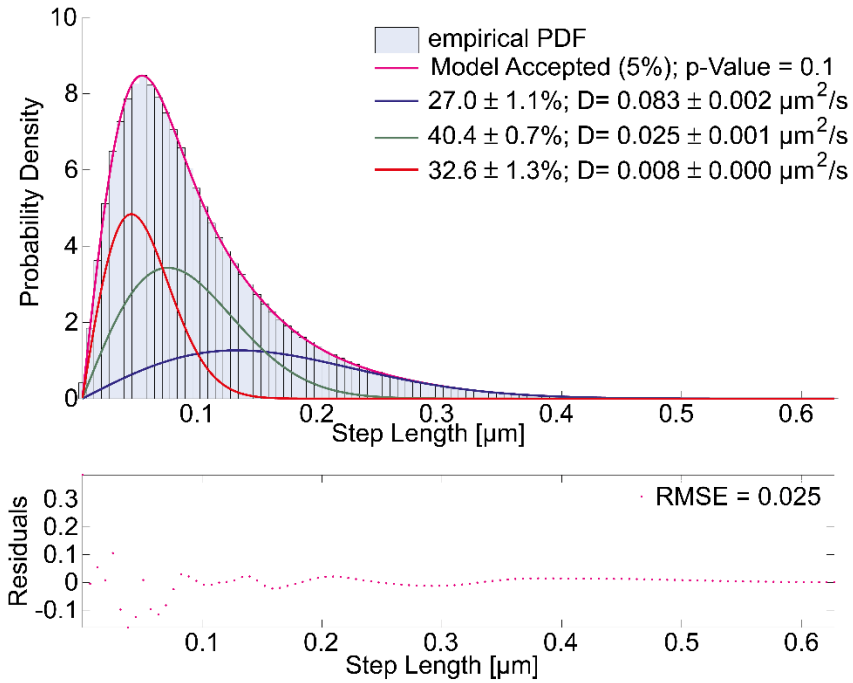

Figure S9 Apparent diffusion coefficients of F_1F_0 ATP synthase subunit-γ in dual-color experiments with F_1F_0 ATP synthase subunit-e

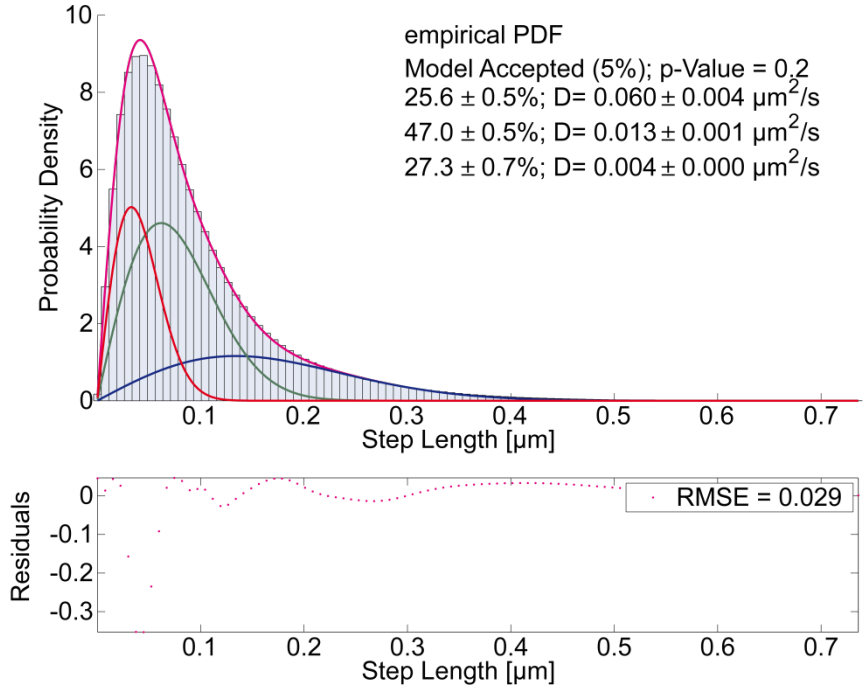

Figure S10 Apparent diffusion coefficients of F_1F_0 ATP synthase subunit-γ in dual-color experiments with MINOS/MICOS subunit-10

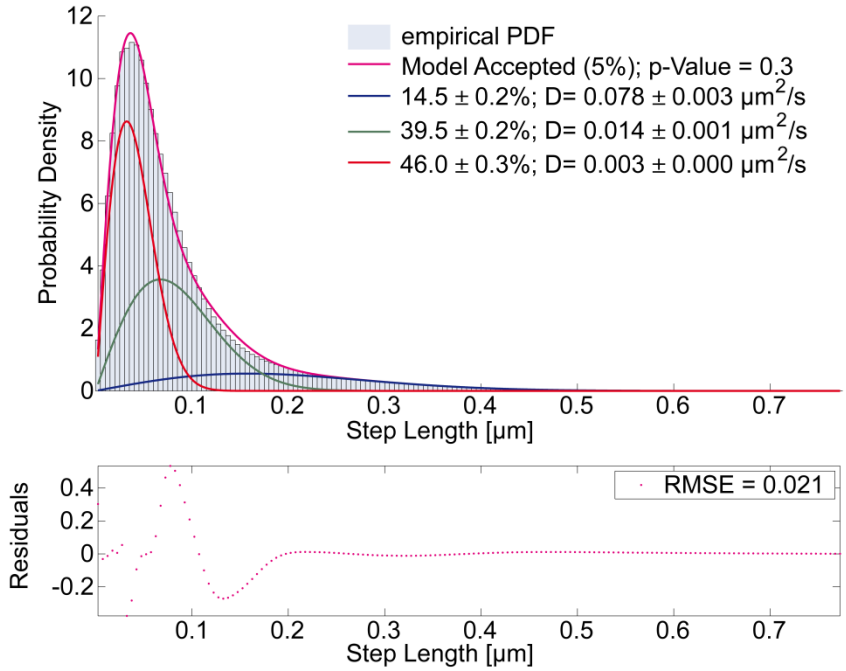

Figure S11 Apparent diffusion coefficients of MINOS/MICOS subunit-10 in dual-color experiment F_1F_O ATP synthase subunit-γ

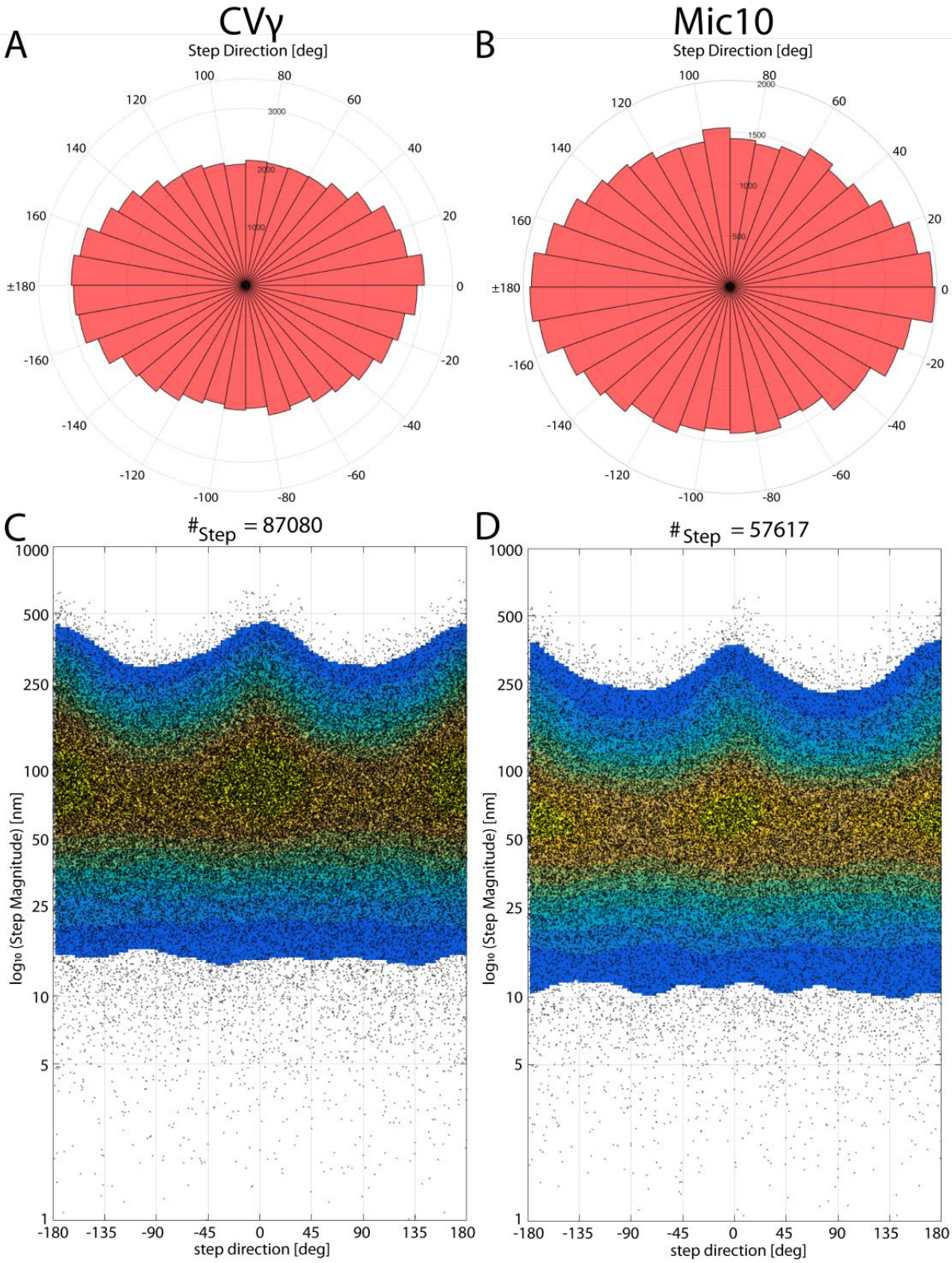

Figure S12 Analysis of trajectory directionality of the F_1F_0 ATP synthase subunit-γ and MINOS/MICOS subunit 10
A The pie chart diagram of CVγSU-trajectory directionalities shows an elliptic shape with extrema between -30° to 40° and -160° to 160°. **B** The pie chart diagram of Mic10-trajectory directionalities shows an elliptic shape with peaks between -130° to 140° and -50° to 40°. **C** The step magnitude plot of CV-SUγ supports the result in A, demonstrating a longitudinal directionality of CV-SUγ trajectories. The longitudinal steps show a jumpsize around 100 nm. **D** The dominant directionality of Mic10 trajectories gets clear in the step magnitude plot with showing only a small amount of perpendicular directionality. Here, an accumulation of the steps in a longitudinal direction was measured.

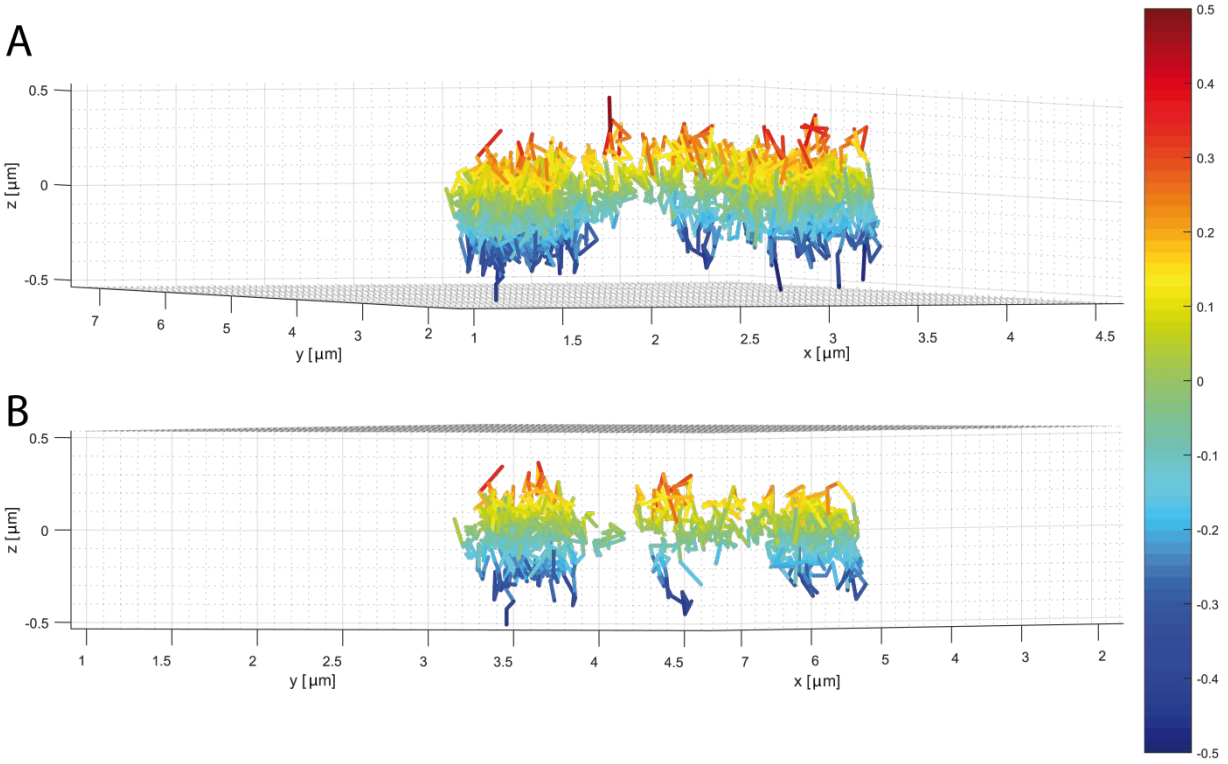

Figure S 13 Trajectory map of F_1F_0 ATP synthase subunit-γ
A Side view of the trajectory map from

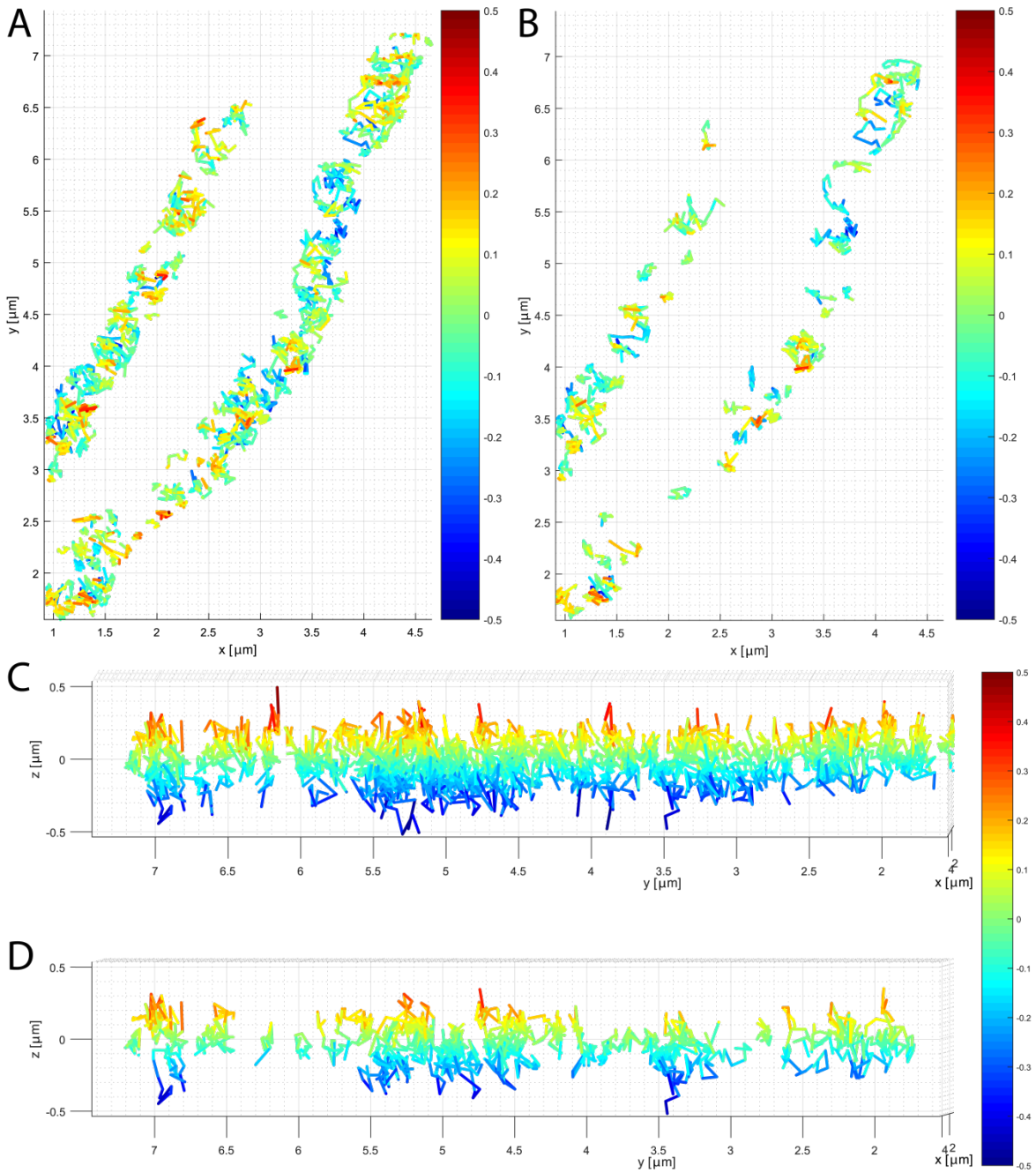

Figure **75** **A** with the line of sight along the longitudinal axis of the mitochondria. No hollow shape of the IM can be seen. **B** Side view of the trajectory map from

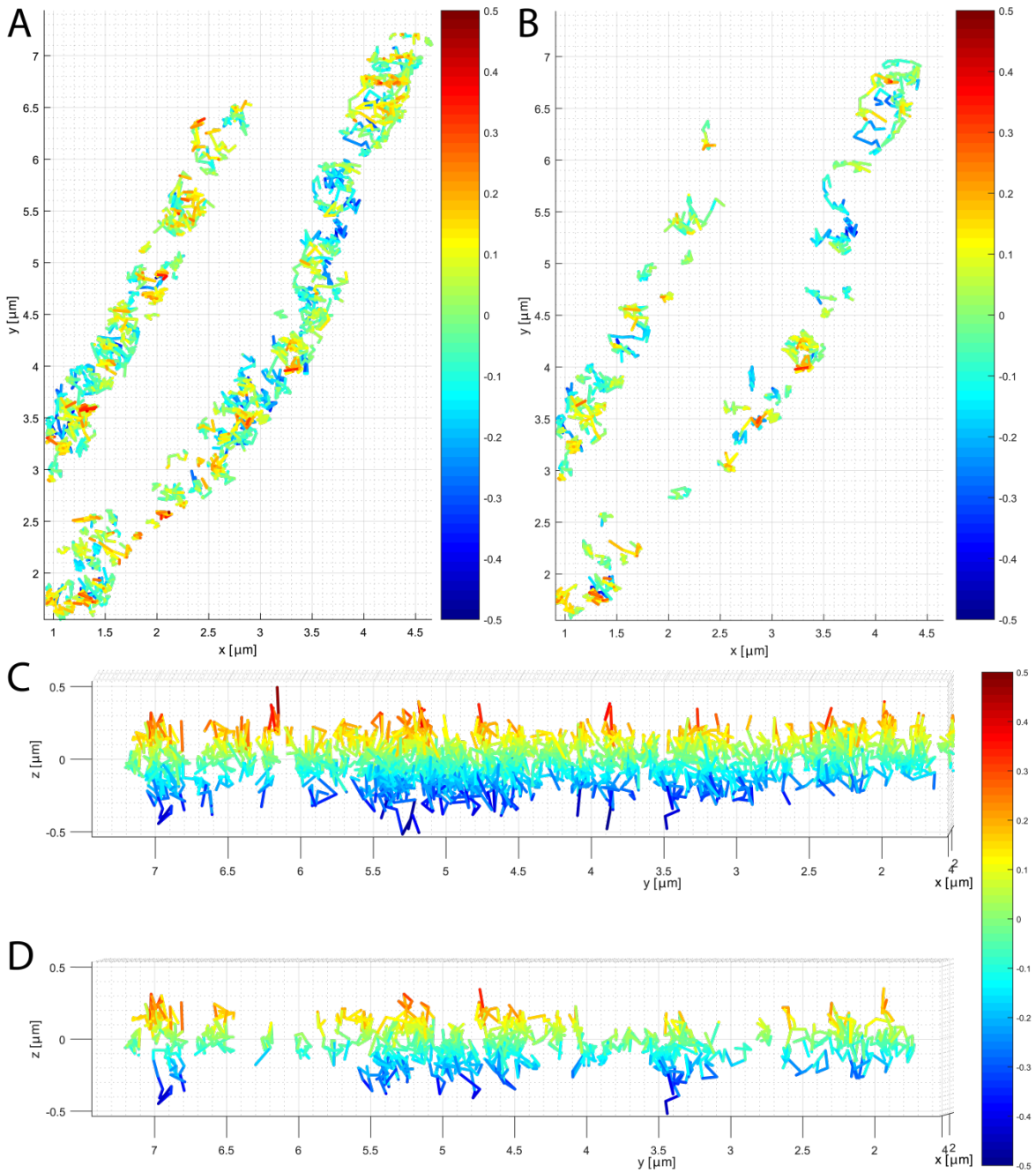

Figure **75**B with the line of sight along the longitudinal axis of the mitochondria. Here also no hollow shape of the IM can be seen.

13 Appendix

13.1 Additional figure

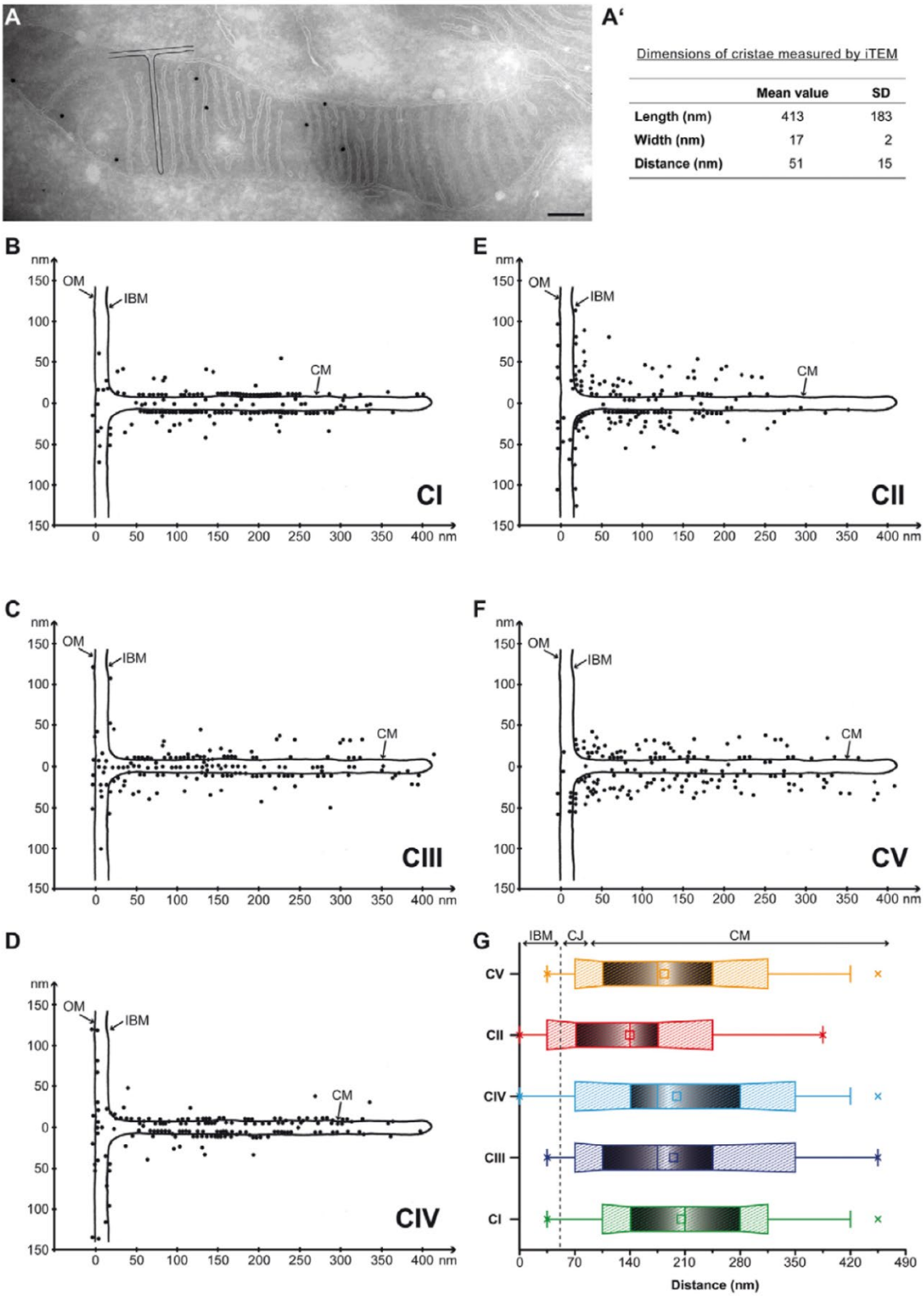

Figure A1 Distribution of OXPHOS proteins along the IM
Distribution of OXPHOS proteins in the IM. Revealed by IEM. CI, CIII, CIV and CV are predominatly localized inn the CM, while CII is also found in the IBM (Figure adapted from Wilkens et al., 2013)

13.2 Figure legend

Figure 1 Mitochondria and their structure 23

Figure 2 Distributions of OXPHOS complex V in the IM subcompartments of mitochondria in a mammalian cell 24

Figure 3 Distances between outward and inward cristae membranes of two adjacent cristae 25

Figure 4 The mitochondrial F_1F_0 ATP synthase 26

Figure 5 ATP synthesis and hydrolisis 27

Figure 6 Cryogenic electron microscopy images and models of F_1F_0 ATP synthase dimer 28

Figure 7 Source and sink model of hydrogen proton flow 31

Figure 8 Metabolic switch of cells grown in galactose containing medium 32

Figure 9 Mic10 oligomerization and MINOS/MICOS formation 33

Figure 10 Shape of the inner membrane depends on the interplay of Mic60 and F_1F_0 ATP synthase dimers 34

Figure 11 The Tom-Tim machinery of mitochondria and the import pathways for precursor proteins 35

Figure 12 Scheme of a multi-color TIRF microscope setup 44

Figure 13 PLL-PEG-RGD layer on a coverslip PLL-PEG-RGD was used to coat the upside of a coverslip to avoid unspecific binding of dyes to the coverslip. 48

Figure 14 Posttranslational and substoichiometric labeling of fusion proteins 50

Figure 15 Microscopy chamber for 24 mm diameter coverslips 51

Figure 16 Channel aligment with fluorescent beads 51

Figure 17 Imaging mitochondria in the cell periphery 52

Figure 18 Schematic representation of single molecule localization and single particle tracking 53

Figure 19 Determination of diffusion constants and diffusion properties 54

Figure 20 Alignment of the astigmatic distortion to the axis of the camera 55

Figure 21 Screenshot of the AstigAxisCalibration-Class software 56

Figure 22 Error in distortion in reference to the depth from the interface 57

Figure 23 3D TALM setup and astigmatic distortion of the PSF of a single fluorescent signal 58

Figure 24 Directionality analysis by MitoOrientedDynamics 60

Figure 25 Trajectory orientation by 4-step binning 61

Figure 26 Critical cell density in samples 62

Figure 27 Mitochondrial network 60 min after addition of olygomycin 72

Figure 28 Localization precision of F_1FO ATP synthase subunit-γ during oligomycin treatment 72

Figure 29 Jumpsize of F_1F_0 ATP synthase subunit-γ during inhibition of ATP synthesis 72

Figure 30 Trajectory map of F_1F_0 ATP synthase subunit-γ during inhibition of ATP-synthesis 75

Figure 31 Quantification of trajectory directionality of the F_1F_0 ATP synthase subunit-γ of a representative mitochondrion during inhibition of ATP synthesis 75

Figure 32 Quantification of trajectory directions of the F_1F_0 ATP synthase subunit-γ of a representative mitochondrion during inhibition of ATP-synthesis 76

Figure 33 Quantification of step directions of the F_1F_0 ATP synthase subunit-γ of all imaged mitochondria during inhibition of ATP synthesis compared to the control 76

Figure 34 Localization precision of F_1F_0 ATP synthase subunit-γ in starving conditions 77

Figure 35 Jumpsize distribution of F_1F_0 ATP synthase subunit-γ in glycolytic and starving conditions 78

Figure 36 Single trajectories of F_1F_0 ATP synthase subunit-γ in control and starving conditions 91

Figure 37 Directionality analysis of the F_1F_0 ATP synthase subunit-γ of a single mitochondrion in starvation 99

Figure 38 Quantification of trajectory directionalities of the F_1F_0 ATP synthase subunit-γ of all tracked proteins in the control- and starving conditions 100

Figure 39 Subfraction fit of the apparent diffusion of F_1F_0 ATP synthase subunit-γ in cells in the control and during starvation conditions 117

Figure 40 Calculated binding for HaloTag and fSnapTag dyes with the same labeling concentration 120

Figure 41 Calculated binding for HaloTag and SnapTag dyes labeling concentration of a ratio 1/15 120

Figure 42 Localization precision of SiR^{HTL} and TMR^{star} signal bound to Tom20 120

Figure 43 Colocalization of SiR^{HTL} and TMR^{star} bound to Tom20 fused with the HaloTag and the fSnapTag 122

Figure 44 Co-locomotion trajectories of SiR^{HTL} and TMR^{star} bound to Tom20 fused with the HaloTag and the fSnapTag 122

Figure 45 Diffraction limited image of mitochondria via F_1F_0 ATP synthase subunit-γ and F_1F_0 ATP synthase subunit-e 124

Figure 46 Super-resolved images of F_1F_0 ATP synthase subunit-γ and F_1F_0 ATP synthase subunit-e and their colocalization 124

Figure 47 Localization precision of F_1F_0 ATP synthase subunit-γ and F_1F_0 ATP synthase subunit-e in dual-color experiments 125

Figure 48 Trajectory map of F_1F_0 ATP synthase subunit-γ 127

Figure 49 Trajectory map of F_1F_0 ATP synthase subunit-e 128

Figure 50 Overlay of trajectory maps from F_1F_0 ATP synthase subunit-γ and F_1F_0 ATP synthase subunit-e 129

Figure 51 Jumpsize distribution of F_1F_0 ATP synthase subunit-γ and F_1F_0 ATP synthase subunit-e in dual-color TALM 129

Figure 52 Directionality analysis of the F_1F_0 ATP synthase subunit-γ trajectories and trajectories of F_1F_0 ATP synthase subunit-e 133

Figure 53 Diffraction limited image of mitochondria via F_1F_0 ATP synthase subunit-γ and MINOS/MICOS subunit-10 134

Figure 54 Localization precision of F_1F_0 ATP synthase subunit-γ and MINOS/MICOS subunit-10 134

Figure 55 Single molecule localization image of F_1F_0 ATP synthase subunit-γ and MINOS/MICOS subunit-10 signals 135

Figure 56 Trajectory maps of F_1F_0 ATP synthase subunit-γ and MINOS/MICOS subunit-10 136

Figure 57 Histogram of the jumpsizes of F_1F_0 ATP synthase subunit-γ and MINOS/MICOS subunit-10 137

Figure 58 Directionality analysis of the F_1F_0 ATP synthase subunit-γ trajectories and trajectories of MINOS/MICOS subunit 10 138

Figure 59 Transmission electron microscopy images of HeLa cells stable transfected with F_1F_0 ATP synthase subunit-γ:HaloTag 140

Figure 60 Transmission electron microscopy images of HeLa cells stably transfected with F_1F_0 ATP synthase subunit-γ:HaloTag during starvation condition 141

Figure 61 Transmission electron microscopy images of HeLa cells stable transfected with F_1F_0 ATP synthase subunit-γ:HaloTag in improved respiration condition 145

Figure 62 Calibration of the astigmatic point spread function 148

Figure 63 Ideal 3D axial localization range 148

Figure 64 Localization precision in all three dimensions 150

Figure 65 3D reconstruction of a mitochondrial network by Tom20 localizations 151

Figure 66 3D reconstruction of a single mitochondrion by 3D single molecule localization of Tom20 153

Figure 67 3D reconstruction of the OM by 3D single molecule localization of Tom20 154

Figure 68 3D trajectory map of Tom20 156

Figure 69 Enlarged trajectory map of the of the ROI in figure 68 156

Figure 70 3D trajectory map of Tom20 157

Figure 71 Enlargement of the ROI in Figure 70 158

Figure 72 3D reconstruction of a mitochondrial network via 3D localized F_1F_O ATP synthase subunit-γ 161

Figure 73 3D reconstruction of mitochondria by 3D single molecule localization of the F_1F_O ATP synthase subunit-γ 162

Figure 74 3D trajectory map of the F_1F_O ATP synthase subunit-γ 163

Figure 75 3D trajectories of the F_1F_O ATP synthase subunit-γ in single mitochondria 170

Figure 76 Tilted view of the trajectory map of the F_1F_O ATP synthase subunit-γ in single mitochondria shown in figure 75 172

Figure 77 3D reconstruction of mitochondria by 3D localization of the F_1F_O ATP synthase subunit-γ 174

Figure 78 3D trajectory map of F_1F_O ATP synthase subunit-γ 175

Figure 79 3D reconstruction of the inner membrane in a mitochondrial network by 3D single molecule localizations of F_1F_O ATP synthase subunit-γ in cells during improved respiring conditions 176

Figure 80 Enlargement of the ROI in the 3D reconstruction shown figure 79 179

Figure 81 3D cristae trajectories in improved respiratory conditions 181

Figure 82 3D trajectory map of the F_1F_O ATP synthase subunit-γ in improved respiratory conditions 182

Figure 83 3D trajectory maps of the F_1F_O ATP synthase subunit-γ in improved respiring conditions, in swollen and non-swollen sections of a single mitochondrion 184

Figure 84 Trajectory directionality analysis of the F_1F_O ATP synthase subunit-γ in two exemplary mitochondria in the control condition 185

Figure 85 Trajectory directionality analysis of the F_1F_O ATP synthase subunit-γ in the control 186

Figure 86 Trajectory directionality of F_1F_0 ATP synthase subunit-γ in cells during starvation conditions 190

Figure 87 Trajectory directionality analysis of the F_1F_0 ATP synthase subunit-γ in a cell during improved respiration conditions 191

Figure 88 Trajectory directionality analysis of the F_1F_0 ATP synthase subunit-γ in all cells imaged during improved respiration conditions 195

Figure 89 Diffusion coefficient of the F_1F_0 ATP synthase subunit-γ in cells during different metabolic conditions 196

Figure 90 Shift of trajectory directionality in all three metabolic conditions 198

Figure 91 Live-cell time-lapse STED nanoscopy of mitochondria 201

Figure 92 Representative transmission electron micros-copy images of mitochondria in wilde-type, MIC60 knock-out HAP1 cells. 203

Figure 93 Single particle tracking of Mic60 in HeLa cells using the Fiji plugin Trajectory classifier (Figure adapted from Kondadi et al., 2020). 204

Figure 94 Drop of the mitochondrial membrane potential during starvation 209

Figure 95 Mitochondrial stress test of HeLa cells in glucose and under starvation conditions 218

Figure 96 Agilent Seahorse XF Mito Fuel Flex test with HeLa cells kept in glucose and under starving conditions. 219

Figure 97 F_1F_0 ATP synthase dimers oriented in rows 220

Figure 98 Transmission electron microscopy images of WT, *MIC10* knock out HAP1 cells. 222

Figure 99 Single particle tracking of Mic10 in HeLa cells using the Fiji plugin Trajectory classifier 222

Figure 101 Asymmetry of phospholipids in the cristae membrane 223

Figure 101 High resolution image of the IM via Airyscan technology 223

Figure 102 Segmented surface-rendered representation of a mitochondrion isolated from wt yeast or a Mic10-overexpressing strain 224

Figure 103 3D STORM image of mitochondria in a BS-C-1 cell 227

Figure 104 3D reconstructions of mitochondria by 3D localizations of Tom20 via TILT3D 228

Figure 105 3D tomography reconstruction of mitochondria by surface rendered transmission electron microscopy 235

Figure 106 Cristae morphology of U2OS cells grwon in glucose and galactose growth conditions 238

Figure 107 Influence of PERK on cristae formation and supercomplex assembly 239

Figure 108 Mitochondria and protein organization 243

Figure S1 Plasmid map of F_1F_O ATP synthase subunit-γ:HaloTag 245

Figure S2 Plasmid map of Tom20:HaloTag 246

Figure S3 Plasmid map of F_1F_O ATP synthase subunit-e:fSnapTag 247

Figure S4 Plasmid map of Mic10:fSnapTag 248

Figure S5 Apparent diffusion coefficients of F_1F_O ATP synthase during inhibition of ATP synthesis 249

Figure S6 Apparent diffusion coefficients of Tom20 in dual-color experiment labeled with TMR^{star} 249

Figure S7 Apparent diffusion coefficients of Tom20 in dual-color experiment labeled with SiR^{HTL} 250

Figure S8 Apparent diffusion coefficients of F_1F_O ATP synthase subunit-e in dual-color experiment with F_1F_O ATP synthase subunit-γ 250

Figure S9 Apparent diffusion coefficients of F_1F_O ATP synthase subunit-γ in dual-color experiments with F_1F_O ATP synthase subunit-e 251

Figure S10 Apparent diffusion coefficients of F_1F_O ATP synthase subunit-γ in dual-color experiments with MINOS/MICOS subunit-10 251

Figure S11 Apparent diffusion coefficients of MINOS/MICOS subunit-10 in dual-color experiment F_1F_O ATP synthase subunit-γ 252

Figure S12 Analysis of trajectory directionality of the F_1F_O ATP synthase subunit-γ and MINOS/MICOS subunit 10 253

Figure S 13 Trajectory map of F_1F_O ATP synthase subunit-γ 254

13.3 Table legend

Table 1: Growth and Imaging Media The total volume of the prepared Media was 80 ml. 47

Table 2 Jumpsize of CV-SUγ in control experiments and during inhibition of ATP synthesis 73

Table 3 Diffusion coefficients of F_1F_O ATP synthase subunit-γ during inhibition of ATP-synthesis 74

Table 4 Jumpsize of CV-SUγ in control experiments and during starvation 90

Table 5 Sub-fractions diffusion coefficients of Tom20, CV-SUγ and CV-SUγ in 2 hours of starvation shown in figure 39 118

Table 6 Diffusion coefficients of SiR^{HTL} and TMR^{star} bound to Tom20 fused with the HaloTag and the fSnapTag 123

Table 7 Jumpsize of the F_1F_O ATP synthase subunit-γ and the F_1F_O ATP synthase subunit-e 130

Table 8 Diffusion coefficients of the F_1F_O ATP synthase subunit-γ and the F_1F_O ATP synthase subunit-e in contransfected cells 131

Table 9 Jumpsize of the F_1F_O ATP synthase subunit-γ and MINOS/MICOS subunit-10 137

Table 10 Diffusion coefficients of F_1F_O ATP synthase subunit-γ and MINOS/MICOS subunit-10 in contransfected cells 138

Table 11 3D apparent diffusion coefficient of the F_1F_O ATP synthase subunit-γ in the three metabolic conditions 197

13.4 Material

13.4.1 Cells

E. coli (DH5α)	
Cervix Cancer Cells - HeLa Cells (Tissue Culture)	Leibniz Institute DSMZ-German Collection of Microorganisms and Cell Cultures

13.4.2 Cell Culture

40 mL Bottle	Schott
80 mL Bottle	Schott
Alanyl-L-Glutamine (200 mM)	Biochrom AG
Cellstar® Tissue Culture Dish, 35 mm Cat. No. Ref.83.3900, Lot. No. 7023811	Greiner Labortechnics
Dulbecco´s Phosphate-Buffered Saline (PBS) 1x (w/o Ca & Mg)	PAA lab. GmbH
Dulbecco´s Phosphate-Buffered Saline (PBS) 1x (w/w Ca & Mg)	Sigma-Aldrich & Co
HBS-Buffer (HEPES 50 mM, NaCl 280 mM, Na_2HPO_4 1.5 mM)	
Earle´s Minimum Essential Media (MEM) (w/ Phenol red, stable L-Gln, 2.2 g/l $NaHCO_3$)	Biochrom AG
Earle´s Minimum Essential Media (MEM) (w/o Phenol red, w/o L-Gln, w/o $NaHCO_3$)	Biochrom AG
Fetal Bovine Serum Superior (FBS) (10x) Cat. No. S0615, Lot. No. 0513C	Biochrom AG
HEPES (1 M) 2-(4-(2-Hydroxyethyl)-1-Piperazinyl)-Ethanesulfonic Acid	Carl Roth GmbH
Sterile Disposable Pipettes (2, 5, 10, 25 mL)	Greiner Labortechnik
Non-Essential Amino Acids (NEAA)	PAA lab. GmbH

Sodium Hydrogen Carbonate ($NaHCO_3$ 0.75g/l)	PAA lab. GmbH
Trypsin- Ethylene Diamine Tetraacetic Acid (EDTA) (1x)	PAA lab. GmbH
Eppendorf Safe-Lock Tubes (0.2 mL, 1.5 mL and 2 mL)	Sarstedt AG & Co.
Pipette tips (20 µL, 200 µL, 1000 µL)	Sarstedt AG & Co.
TC Flask T25, standard Cat. No. Ref.83.3910.002	Sarstedt AG & Co.

13.4.3 Chemicals

Ethanol (70 % v/v)	Carl Roth GmbH
Ethidiumbromide (0.5 %)	Carl Roth GmbH
Glycerin	Carl Roth GmbH
Isopropanol	Carl Roth GmbH
Methanol	Carl Roth GmbH
PEG 800 (Polyethylglycole) 10 %	Carl Roth GmbH
TAE-Puffer	Carl Roth GmbH
RGD Peptide (Ac-CGRGDS-COOH)	Coring System Diagnostix GmbH, Gernsheim
Agar-Agar	Gibco BRL
NHS-PEG-MAL, Rapp Polymer	Rapp Polymere GmbH Tübingen
Agarose	Sigma Chemicals & Co.
Calcium Chloride ($CaCl_2$)	Sigma-Aldrich & Co.
Cycloheximide (CHX) (100 mg/mL)	Sigma-Aldrich & Co.
Poly-L-lysine (1.2 mg/mL)	Sigma-Aldrich & Co.
Sucrose	Sigma-Aldrich & Co.
Water H_2O (MQ)	Sigma-Aldrich & Co.

13.4.4 Equipment

Centrifuge Allegra 25R	Beckmann Coulter
Plasma Cleaner, Femto - Variante A	Diener electronic GmbH + Co. KG
BD Falcon™ Express Pipet-Aid	Falcon
Pipettes (0.1-2 µL, 0.5-10 µL, 0.5-20 µL, 20-200 µL, 100-1000 µL)	Gilson, Inc.
Incubator (Cell Culture) HERAcell 240 (5 % CO_2, 37 °C)	Heraeus
Table Centrifuge Fresco 21 Centrifuge	Heraeus
Thermo Scientific Microbiological Safety Cabinets HERAsafe™	Heraeus
Freezer	Liebherr
Fridge	Liebherr
Waterbath U16	Medingen
Microscopy-Chamber	Optomechanics – University of Osnabrück
Microscales Sartorius Extend	Sartorius
Vortexer	Scientific Industries
Precision cover slips (0.17 ± 0.005 mm, Ø 24 mm) Cat. No. PK26.1	Carl Roth GmbH & Co. KG

13.4.5 Experimental Setups

Cobolt Jive™	Cobolt, Inc.
Inverted Microscope „WILOVERT Standard”	Hund Wetzlar
150x Oil Immersion Objective (NA: 1.45)	Olympus
Cell^TIRF MITICO System	Olympus
TIRF-Microscope body „IX73”	Olympus
NanoScanZ Piezo Stage System, NZ100	Prior Scientific
Mounted Plano-Convex Round Cylindrical Lens, UV Fused Silica (LJ4530RM - f = 1000 mm, Ø1", UVFS)	THORLABS

13.4.6 Fluorescent Dyes and Beads

MitoTracker® Deep Red FM	Invitrogen
MitoTrackerGreen™	Invitrogen
PS-Speck™ Microscope Point Source Kit	Invitrogen
Tetramethylrhodamine bound to HaloTag® Ligand (TMR^{HTL})	Promega

13.4.7 Plasmids

CVγ-Halo7-psems	
Tom20-link-Halo7-psems	
CVe-fSnap-psems	
Mic10-fSnap-psems	
HaloTag®	Promega
fSnapTag®	New England Biolabs

13.4.8 Software/Algorithms

Matlab-Algorithm: AstigAxisCalibrationClass	Biophysics, University of Osnabrück
Imaris v7.1.1	Bitplane – Oxford Instruments
SlimFastNextGen v16c	C.P. Richter, Biophysics, University of Osnabrück, Osnabrück, Germany
ViSP v1.0	El Beheiry et al., 2013, Laboratoire Physico-Cimie Curie, Institut Curie, Centre National de la Recherche Scientifique Unité Mixte de Recherche 168, Paris, France
QuickPALM ImageJ Plugin	Henriques et al., 2010
Matlab-Algorithm: FPALM	Labor Samuel Hess
ImageJ	MacBiophotonics
Microsoft Office 2019, Word	Microsoft
CellSens v2	Olympus

Clone Manager v9	Scientific & Educational Software
Matlab R2013a	TheMathWorks
Matlab R2014b	TheMathWorks
Matlab R2016b	TheMathWorks
u-track 2.1.3	Danuser Lab

13.5 Additional publications

13.5.1 Single Molecule Tracking and Localization of Mitochondrial Protein Complexes in Live Cells

Single molecule tracking and localization of mitochondrial protein complexes in live cells

Timo Appelhans[1], and Karin Busch[1,2]

[1] Mitochondrial Dynamics Group, School of Biology, University of Osnabrück, Germany

[2] Institute of Molecular Cell Biology, Department of Biology, Westphalian Wilhelms-University Münster, Germany

Summary

Mitochondria are the power plant of most non-green eukaryotic cells. An understanding of their function and regulation is only possible with the knowledge of the spatiotemporal dynamics of their proteins. Mitochondrial membrane proteins involved in diverse functions like protein import, cell respiration, metabolite transport and mitochondrial morphology are mobile within membranes. Here, we provide a protocol for a superresolution fluorescence technique, tracking and localization microscopy (TALM) that allows for diffusion analysis of single mitochondrial membrane proteins *in situ* in cell cultures. This non-invasive imaging technique is a useful tool to reveal the spatiotemporal organization of proteins in diverse mitochondrial membrane compartments in living cells. Proteins of interest are tagged with the HaloTag® and specifically labeled with functionalized rhodamine dyes. The method profits from low abundance of proteins and therefore works better with substoichiometric labeling of Halo-tagged proteins. In particular, the use of photostable bright rhodamine dyes enables the specific tagging and localization of single molecules with a precision below 20 nm and the recording of single trajectories.

Keywords: superresolution microscopy, mitochondria, membrane protein dynamics, single molecule localization and tracking, live cell imaging, Tom20, ATP synthase

Introduction

Owing to their evolutionary origin, mitochondria possess two membranes of different structure and composition. The tubular outer mitochondrial membrane (OMM) envelopes the organelle, while the intensely folded inner mitochondrial membrane (IMM) provides two sub-compartments: the inner boundary membrane (IBM) and the cristae membranes (CM), with probably different functions. Biochemical analysis gave insights in the composition of OMM and IMM, but already the dissection of the

IBM and the CM as two sub-compartments of the one continuous membrane has been challenging. However, metabolic adaptation, functional optimization and also failure of mitochondrial performance cannot be understood without knowledge of the composition and spatiotemporal organization of the proteins in the respective sub-compartments. Membrane proteins are mobile and their diffusion is determined by the architecture of their respective sub-compartment, its lipid composition, and possible interactions with other proteins. To reveal protein dynamics, analysis has to be done *in situ* and in a non-invasive manner in living cells. In the recent years, superresolution microscopy provided techniques for localizing single proteins. Here, we extend this toolbox and provide a protocol that allows also for tracking of single membrane proteins in mitochondria in live cells (1) (Fig. 1; Fig. 2). Our technique is based on the general feature that membrane proteins have a reduced mobility compared to soluble proteins and thus can be tracked. During recording time, mobile proteins occupy different positions at different time points, limited by their specific functional and structural microcompartment (Fig. 1b, c; Fig. 2b, d). Thus, the localization and trajectory map of a recorded protein represents the spatiotemporal dynamics of this particular protein in its membrane microcompartment. As the mobility and localizations of individual molecules is followed over some time, the number of single molecules required to pinpoint the structure of a certain microcompartment is much lower than with other techniques. This is an advantage, especially when proteins with low expression levels are analyzed. Low labelling degree also reduces the danger of phototoxic effects and allows for prolonged live cell imaging. The mobility analysis reveals different trajectory maps and diffusion coefficients for outer and inner membrane proteins (Fig. 1c, 2d), clearly related to the underlying structure of the membrane (1).

In order to visualize specific proteins, these are tagged by genetic fusion to the HaloTag®. The HaloTag®-Protein (2) is a "suicide" protein that covalently reacts with its substrate, the HaloTag®-Ligand (^{HTL}). Cells are transfected with the according plasmid and the expressed tagged protein of interest is posttranslationally labeled with a fluorescent dye linked to the HaloTag®-Ligand (^{HTL}). Today, several suitable fluorescent dyes for labeling of HaloTag® proteins are available, however, for intracellular labeling membrane-permeable dyes are required. In this protocol, tetramethylrhodamine-HaloTag®-Ligand (TMR^{HTL}) is used. The bright TMR fluorescence enables localization of single molecules with high precision (Fig. 2c). Correct mitochondrial localization of labeled proteins can be controlled by co-staining with MitoTracker® Deep Red FM or MitoTracker®Green.

Materials

TIRF microscope setup

For single molecule tracking and localization, a commercially available inverse total internal reflection fluorescence (TIRF) microscope (Olympus IX71), equipped with a TIRF-condensor (Olympus), a diode pumped solid-state laser (excitation 561 nm, 200 mW, Cobolt Jive 561, Cobolt) and a back-illuminated electron multiplying charged coupled device EMCCD camera (Andor iXON 897, pixel size 16 μm^2) was used. The TIRF-microscope otherwise has no specific or special fabrication. In order to perform single molecule tracking and localization microscopy (TALM) with high signal to noise (S/N) ratio within living cells, a highly inclined and laminated optical sheet (HILO) is used for excitation (3). Therefore, an incident beam

angle is chosen just below the critical angle for TIRF-mode. The fluorescence-labeled specimen is excited through the objective. For excitation of tetramethylrhodamine, a diode pumped solid-state laser (excitation 561 nm, 200 mW, Cobolt Jive 561, Cobolt) is coupled into a single mode fiber (Qioptiq) connected to the motorized integrated TIRF illumination combiner (MITICO, cell^TIRF, Olympus) with laser light. The MITCO system enables the user to couple up to four laser lines into the microscope. For each illumination pathway an individual angle for illumination between Epi and TIRF illumination can be chosen. The MITICO software allows a simple and precise identification of the appropriate objective to adjust the angle of illumination and thereby the penetration depth of the excitation light reproducibly. The microscope is equipped with an apochromatic 150x oil immersion objective designed for TIRF microscopy (150 x TIRF objective numerical aperture N.A.=1.45, Olympus, UAPO). With the 150x objective, a pixel size of 107 nm is obtained fulfilling the Nyquist-Shannon theorem for diffraction limited imaging (4, 5). The high magnification and N.A. is needed to achieve high laser power densities in the focal plane (maximum 1-2 kW/cm^2). For single molecule tracking, the power density is adjusted to one-tenth (100 W/cm^2) to reduce photobleaching and blinking to obtain longer trajectories. Laser light reflected from a dichroic mirror (OBS-U-M3TIR 405/488/561, Semrock) passes through the 150 x objective. The fluorescence is filtered by a HC Quadband pass filter, 446/523/600/677 (F72-866 from AHF analysentechnik AG) installed in the U-MF2 filter cube. Image acquisition is performed with a back-illuminated EMCCD camera (iXon Ultra 897), providing high quantum efficiency of > 90 % between 500 nm and 700 nm and a maximal frame rate of 56 frames per second (fps) at full resolution (512 x 512 pixel, each 16 µm x 16 µm in size). Under the settings used, the pixel to photon conversion factor (EM gain 300) is 9.2.

Buffers

1. 1 M HEPES buffer, pH 7.5
2. 100 mM HEPES buffer, pH 7.5
3. 100 mM HEPES buffer, 1 mM EDTA, pH 7.5
4. PBS buffer, pH 7.4 without Ca^{2+} and Mg^{2+}

Chemicals

1. 10 % PEG 800 (Polyethylene glycol)
2. 30 % H_2O_2
3. 70 % v/v Ethanol
4. 98 % sulfuric acid
5. Acetyl-CG-RGD-S-COOH (Sigma Aldrich, Germany)
6. Ethylendiaminetetraacetic acid (EDTA)
7. Isopropanol
8. Immersion Oil - Immersoil™ 518 F (n_e = 1.518, v_e = 45)

9. N_2 gas
10. NHS-PEG-MAL, Rapp Polymer (Rapp Polymere GmbH Tübingen)
11. PLL-PEG-RGD-Peptide
12. Poly-L-lysine (PLL)
13. Tris(1-chloroethyl) phosphate (TCEP)

PLL-PEG-RGD preparation

PLL-PEG-RGD is a short name of Poly-*L*-Lysine-*g*(3)-PEG_{2k}-RGD. '*g*' means graft modification on Poly-*L*-Lysine. '3' means 33 % of side chain lysine groups (NH2) were coupled with PEG so that the ratio of total L-lysine to the coupled one is 3. 'PEG_{2K}-RGD' denotes that the graft PEG has an average molecule weight of 2 KDa with a terminal RGD peptide.

1. Dissolve 7.6 mg Acetyl-CG-**RGD-**S-COOH in 0.1 ml 100 mM HEPES buffer containing 1 mM EDTA, pH 7.5
2. Dissolve 3 mg TCEP in 0.1 ml 1M HEPES buffer , pH 7.5, check the pH to be 6 - 7
3. Incubate for 10 minutes at RT
4. Dissolve 7.5 mg Poly-L-Lysin (PLL) in 0.25 ml 1M HEPES, pH 7.5
5. Dissolve 36 mg M(alemeid)-PEG-NHS (3000Da) in 0.05 ml 1M HEPES, pH 7.5
6. Mix Acetyl-CG-**RGD-**S solution with M(alemeid)-PEG-NHS solution and incubate at RT for 5 minutes, check the pH to be 6 - 7
7. Add dissolved PLL to the mixture, adjust pH to 7 – 8.3
8. Place the mixture on a shaker overnight
9. Lyophilise the mixture the next day 12 to 20 h

Consider note 1.

Plasmids

For tracking mitochondrial membrane proteins, we used Tom20, an outer mitochondrial membrane protein, and complex V (F_1F_0 ATP synthase, CV) as an inner membrane protein, predominantly found in the cristae membranes. In principle, it is possible to use any other membrane protein as well. Please note that for most inner membrane proteins the mitochondrial targeting sequences is at the N-terminus. Mitochondrial localization can be checked by GFP constructs, before starting single molecule experiments with Halo7-fusion proteins.

1. TOM20-link-Halo7-psems (1), generated from $pSNAP_f$-Tag® New England Biolabs® by substitution of the SNAPf-ORF with Halo7-ORF
2. CVγ-Halo7-psems (see above)

Cells

Cervix Cancer Cells - HeLa Cells (Tissue Culture) (Leibniz Institute DSMZ-German, Collection of Microorganisms and Cell Cultures)[1]

Media

1) Growth medium

1. Minimal Essential Medium with Earle's salts and Phenolred
2. 10 x Fetal Bovine Serum Superior (FBS) (Biochrom AG, Cat. No. S0615, Lot. No. 0513C)
3. 1 % (v/v) HEPES (4-(2-Hydroxyethyl)piperazine-1-1ethanesulfonic acid
4. 1 % (v/v) nonessential amino acids NEA
5. 1 % (v/v) stable Alanyl-L-Glutamine
6. 2.2 g/l $NaHCO_3$

2) Selective growth medium

1. Growth medium
2. 0.8 mg/ml Neomycin

3) Imaging medium

1. Earle´s Minimum Essential Media (MEM) (w/o Phenol red)
2. 10 x Fetal Bovine Serum Superior (FBS) (Biochrom AG, Cat. No. S0615, Lot. No. 0513C)
3. 1 % (v/v) HEPES (4-(2-Hydroxyethyl)piperazine-1-1ethanesulfonic acid
4. 1 % (v/v) nonessential amino acids NEA
5. 1 % (v/v) stable Alanyl-L-Glutamine
6. 2.2 g/l NaHCO3

4) Transfection medium

1. 2.5 M CaCl2 solution

[1] Further PC12 cells (a pheochromocytoma of the rat adrenal medulla), 143b cells (human boneosteocarcinoma), and MEF (mouse embryonic fibroblast cells) were also used for TALM in different experiments.

2. HBS Buffer
3. 50 mM HEPES
4. 280 mM NaCl
5. 1.5 mM Na2HPO4

5) Detaching medium

1. 0.025 % (w/v) Trypsin
2. 2.5 mM EDTA
3. 1x PBS

Fluorescent Dyes

Store fluorescent dyes as stock solutions in dry Dimethylsulfoxid (DMSO). Later dilute with imaging medium to appropriate concentrations. Do not keep diluted dyes.

1. 1 µM Tetramethylrhodamine-HaloTag®-Ligand (TMR^{HTL})
2. 1 mM MitoTracker® Deep Red FM

Software/Algorithms

1. Andor IQ3 (Andor Technology)
2. ImageJ (MacBiophotonics)
3. Matlab R2013b (TheMathWorks)
4. Matlab-Algorithm: FPALM localization gui (Labor Samuel T. Hess (6,7,8)
5. Matlab-Algorithm MultiTargetTracer (Serge et al., 2008)

Consider note 2.

Specific Equipment

1. Coverslip (0.15 mm, Ø 24 mm) (VWR)
2. Microscopy-Chamber (Fig. 3) Optomechanics – University of Osnabrück
3. Plasma Cleaner, Femto - Variante A, Diener electronic GmbH & Co. KG

Methods

1) Cell Culture

1.1) Cultivation

Cultivate HeLa cells in T25 cell culture flasks, with 5 ml Growth medium at 37 °C and 5 % CO_2. Passage cells when reaching confluence.

1.2) Passaging (1:5)

1. Remove the old medium from confluent cells grown in T25 flasks
2. Wash the cells thoroughly with 4 ml PBS
3. Remove the PBS
4. Add 1 ml Detaching medium to remove cells from the flask surface
5. Incubate the flask at 37 °C and 5 % CO2 until the cells are removed from the bottom (1 to 2 minutes)
6. Stop the reaction when all cells are solute by adding 4 ml fresh medium
7. Pipette up and down to homogenize the cell solution
8. Transfer 1 ml to a new T 25 flask and fill up to 5 ml with fresh culture medium

1.3) Cell transfection

Mammalian HeLa cells for transient transfection and direct imaging are grown in a 35 mm Cellstar® tissue culture dish on coverslips (0.15 mm, Ø 24 mm). For transfection, the calcium phosphate method (9) is used.

9. Seed 2 x 103 to 5 x 103 cells into a 35 mm Cellstar® tissue culture dish containing a coverslip and 2 ml Growth medium.
10. Pipette 10 µl plasmid solution, containing 5 µg pure DNA in an Eppendorf Cup
11. Add 20 µl CaCl2 solution (2.5 M)
12. Mix by carefully pipetting up and down once
13. Wait for 30 second
14. Add 170 µl milliQ H_2O
15. Pipette 200 µl c (pH 7 ± 0.04) in another Eppendorf Cup
16. Vortex the HBS Buffer in the Eppendorf Cup
17. Add the 200 µl buffered DNA / $CaCl_2$ solution by dropping it into the HBS Buffer during vortexing
18. Replace the Growth medium of the HeLa cells in the 35 mm Cellstar® tissue culture dishes with 1 ml fresh Growth medium

19. Pipette the DNA solution in single drops into the 35 mm Cellstar® tissue culture dishes filled with 1 ml medium. Increase the height of pipetting to avoid "dancing" of drops onto the medium surface, which can lead to inhomogeneous DNA concentration in the sample.
20. Incubate the transfected HeLa cells at 37 °C and 5 % CO_2 overnight
21. Replace the Growth medium after 12 h
22. Let the cells grow for 24 h after replacing the Growth medium
23. In order to have good expression levels of your protein of interest image transfected cells 36 to 48 h after transfection.

At day of imaging:

1. Wash each dish with 2 ml PBS twice
2. Wash each dish with 2 ml Imaging medium once
3. Keep the cells at 37 °C and 5 % CO_2 in 2 ml fresh Imaging medium until mounting on stage
4. Replace the medium before imaging with 1 ml fresh Imaging medium

1.4) Generation of stable transfected cell lines

For generation of a stable cell line the transfected plasmid has to be integrated into the target cell genome. The advantage is a stable, long-term expression of the protein of interest with usually uniform and moderate expression levels.

1. Seed 5 x 10^3 cells into a 60 mm Cellstar® tissue culture dish
2. Transfect cells 1 day after seeding at 60-80 % confluency as described under 3.2
3. Wash cells with 4 ml PBS, 18 h after transfection
4. Wash cells with 4 ml Selective growth medium
5. Incubate cells with 5 ml Selective growth medium
6. During a period of 10 to 14 days change Selective growth medium every day
7. Colonies (visible by eye) which grow in the selective medium are from stable transfected cells and are isolated as following
8. Incubate cells with detaching solution until cells round and start to detach
9. Pick colonies with 200 µl pipette and transfer into separate 35 mm Cellstar® tissue culture dish
10. Add 2 ml Selective growth medium
11. Incubate at 37 °C and 5 % CO_2
12. Continue proliferation in selective growth medium in T25 flask until confluency reached, then split and freeze leftovers

13. Check stable transfection by imaging cells after staining with 500 nM TMR^{HTL}-substrate for 20 min and subsequent washing: all stable transfected cells shall be fluorescent.

Consider note 3.

2) Surface cleaning of coverslips

Usually, coverslips contain dirt that is enhances the background of single molecule imaging. In order to get a clean coverslip, plasma cleaning or cleaning with Piranha solution is performed. Alternatively, coverslips can be put it into freshly prepared Piranha solution. During the procedures particles on the glass surface are oxidized which destroys the fluorescence. To avoid re-contamination, always wear gloves when performing cleaning procedures. The freshly cleaned coverslips are used for coating immediately.

2.1) Piranha cleaning

1. Prepare Piranha solution by mixing 98 % sulfuric acid into 30 % H_2O_2 in a 2:1 volume ratio. (Cautious!! It is very corrosive).
2. Put coverslips it into freshly prepared Piranha solution for more than 1 hr
3. Afterwards, the glass substrate should be washed by enough MiliQ water
4. Dry by nitrogen steam

2.2) Plasma cleaning

1. Wash each coverslip in pure water to remove dust from the coverslip
2. Blow coverslips dry with nitrogen gas
3. Scratch an achiral symbol on the topside of each coverslip
4. Place the coverslips topside up into a shallow beaker without overlapping one another
5. Set plasma cleaning time to 15 minutes
6. Set the power to 40 W
7. Open the plasma cleaner
8. Place the open shallow beaker in the middle of the glass tray of the plasma cleaner
9. Evacuate the plasma cleaner for 2 minutes
10. Start the generator, plasma cleaning will stop automatically after 15 minutes
11. Turn on the ventilation for approximately 30 sec
12. Switch off the pump
13. Continue to ventilate the chamber for approximately 15 sec
14. Remove the lid with two hands and turn off the main switch
15. Place each cleaned coverslip topside up into a 35 mm Cellstar® tissue culture dish

Consider note 4.

3) PLL-PEG-RGD - coverslip coating

To prevent unspecific binding of fluorescent molecules to the coverslip surface and to reduce background signals, coverslips are coated with Poly-L-Lysine - Polyethylene Glycol - Arginine Glycine Aspartate (PLL-PEG-RGD). PLL-PEG-RGD is a poly-L-Lysine (PLL) derivative attached with a polyethylene glycol 3000 Da and a Cysteine-Glycine-Arginine-Glycine-Aspartate-Serine (CGRGDS) peptide. The RGD motif is a signal peptide of the integrin receptor.

1. Add 15 µl PLL-PEG-RGD (0.8 mg / ml) on a plasma cleaned coverslip
2. Slowly place another plasma cleaned coverslip upside down on the first one
3. The PLL-PED-RGD gets soaked between the coverslips
4. Avoid bubbles between the coverslips. If bubbles occur you may slightly push on the upper coverslip
5. Incubate the coated coverslips below the hood for 1 h
6. Wash the coverslips 3 times with milli Q water
7. Blow coverslips dry with nitrogen gas
8. Place a single coverslip in a 35 mm Cellstar® tissue culture dish, the coated site up

Consider note 5 and 6.

4) Preparation of cells for imaging

1. Cells for transient transfection should be seeded on coated coverslips 1 day for transfection and 2 days before imaging. Stable transfected cells can be seeded 1 day before imaging on coated coverslips.
2. Coated coverslips are incubated at 37 °C for 5 minutes, if previously stored at -20 °C.
3. Add 2 ml imaging medium in a 35 mm Cellstar® tissue culture dish containing a coated coverslip
4. Remove the Growth medium from the T25 culture flask containing the cells to be seeded.
5. Add 3 ml PBS and slightly shake the flask
6. Remove the PBS
7. Add 1 ml Detaching medium
8. Incubate the flask at 37 °C and 5 % CO_2 until the cells are removed from the bottom (1 to 2 minutes)
9. Add 4 ml Growth medium
10. Pipette up and down gently to avoid cell clusters
11. Passage 2 x 10^3(for imaging after 36 h to49 h) to 5 x 10^3 (for imaging the next day) into the provided 35 mm Cellstar® tissue culture dish, containing 2 ml Imaging medium
12. Slightly shake the culture dish to homogenize the cell suspension
13. Incubate the samples at 37 °C and 5 % CO_2
14. Change the Imaging medium the next day
15. Incubate the cells before imaging with 2 ml fresh Imaging medium for 1 h at 37 °C and 5 % CO_2

5) Posttranslational labeling

It is necessary to adapt the right labeling concentration for every cell line and specific tagged protein of interest. Therefore, different labeling concentrations need to be tested to achieve an optimum of as much as possible distinct single molecules[2]. The correct mitochondrial localization of labeled proteins is confirmed by co-staining of mitochondria with MitoTracker®DeepRed FM.

1. Use cells grown on glass coverslips when confluency of 60-80 % is reached
2. Warm up the imaging medium to 37 °C
3. Pipette 1 ml pre-warmed, fresh imaging medium into an Eppendorf Cup
4. Add 0.5-1 µl TMR^{HTL} 1 µM stock solution for final concentration: 0.5 - 1 nM) and
5. Vortex gently
6. Remove the medium from the cells in the 35 mm Cellstar® tissue culture dish. Make sure that medium is removed completely, but do not touch the coverslip in the imaging area
7. Add the imaging solution with TMR^{HTL} prepared in steps 1-3.
8. Incubate the cells at 37 °C and 5 % CO_2 for 20 minutes
9. Wash twice with 2 ml PBS
10. Wash once with 2 ml Imaging medium
11. Add 1 ml fresh Imaging medium
12. Incubate the samples at 37 °C and 5 % CO_2 for 1 h
13. Replace the Imaging medium before imaging
14. Labeled cells should be imaged on the same day.

Consider note 7 and 8.

6) Specimen clamping

The coverslips from the 35 mm dishes with the labeled cells, prepared as described under 3.7, are mounted on imaging chambers for inverse microscopy (Fig. 3). Prepared specimen chambers can be stored for 2 h at 37 °C and 5 % CO_2 but the imaging medium should be renewed 1 h before microscopy. Storage of empty chambers is in 70 % ethanol.

1. Perform a final check on the sample checking that cell confluency is ~ 60 % and dead detached cells are removed by washing with PBS.
2. Prepare the microscopy chambers (non-sterile)
3. Use tissues to dry the chamber, the Teflon® ring and the rubber band

[22] Note: Take care that the DMSO concentration does not exceed 10 % for reasons of cell toxicity.

4. Place a Teflon® ring in the notch of the lower chamber part
5. Transfer the coverslips from the 35 mm dishes on the Teflon® ring in the notch of the lower chamber part
6. Put the rubber band above the coverslip
7. Put the upper chamber part on to it
8. Screw the chamber carefully and make sure the chamber is sealed and the coverslip is not broken
9. Dry and clean the undersurface of the coverslip and the chamber with a tissue
10. Add 800 µl imaging medium at the rim of the coverslip
11. The samples are ready for imaging
12. After imaging take the chamber apart and wash the individual parts with 70 % ethanol solution

Imaging

1. Switch on the microscope, the Acousto Optic Tunable Filter (AOTF), and the laser(s)
2. Start the Computer
3. Start the TIRF controller
4. Start the Camera
5. Launch the manufacturer software
6. Control hardware via software
7. Clean the objective with a KIMTECH Science Precision Wipe and Isopropanol
8. Place a small droplet of immersion oil on the pupil of the objective
9. Clean the undersurface of the coverslip in the microscopy chamber with a KIMTECH Science Precision Wipe soaked in isopropanol and then rub the undersurface dry with a new dry KIMTECH Science Precision Wipe
10. Prepared specimen are placed in a microscopy chamber (Fig. 3)
11. Pre-adjust the objective position / the focal plane
12. Adjust the electron multiplier gain (EM-gain) to 300
13. Set for frame transfer
14. Image at full frame (512 x 512 px^2) with 32 ms exposure time
15. monitor live via the camera, and find the cells
16. Searching for cells is done using a laser power of < 1 mW (appropriate for TMR^{HTL})
17. If possible, take an image of the entire cell (Fig. 4a)
18. Adjust the focal plane, the inclination angle and the laser power
19. Find an area in the cell periphery with distinct, elongated mitochondria (Fig. 4a framed, Fig. 4b, c)

20. Adjust imaging area to the area of the separated, elongated mitochondria (e.g. 200 px x < 200 px) (Fig. 4b, c). A reduced imaging area allows for the increase of imaging frame rates (Hz). The higher the frame rate, the more accurate the step length determination (but in parallel the signal decreases due to reduced exposure and emission time, which lowers the localization precision) (see Tab. 1)
21. Adjust the HILO inclination angle to the specific region of interest, if necessary
22. Adjust the laser power to 3.5 - 5.2 mW
23. Start recording
24. Image at least 3000 frames

Consider note 9, 10, 11, 12 and 13.

Evaluation

Single molecule localization and tracking are post imaging processes which reveal a non-diffraction limited view of proteins localizations and their dynamic organizations. However, single fluorescent molecules need to fulfill the Rayleigh criterion *R* to be seen as single signals.

$$R = \frac{0.61\lambda}{NA}$$

Where λ is the emission wavelength of the used fluorophore and *NA* is the numerical aperture of the used objective. Localization based methods circumvent the diffraction barrier (6). In addition, TALM takes advantage of single, fluorescently labeled and mobile proteins, which travel along a biological structure emphasizing why the right labeling degree and exposure time are crucial. For localization of single emitters, a modified 2D Gaussian mask for approximation is used (5,6,7,) to determine the peak of single point spread functions in front of the cellular background. Localization data are rendered using Thompson blurring (10). The localization precision σ_{xy} for each localized signal is given by:

$$\sigma_{xy}^2 = \frac{s^2 + q^2/12}{N} + \frac{8\pi s^4 b^2}{q^2 N^2}$$

Where *s* is the standard deviation of the PSF, *N* is the number of recorded photons of the signal, *q* is the pixel size of the EMCCD camera chip dived by the total magnification and *b* is the background noise per pixel of the illuminated region. In order to localize fluorescent signals a pixel conversion factor of the used setup needs to be handover to the software. Be aware that the EM gain influences the pixel conversion factor. The positions of individual fluorescence emitters are determined with sub-pixel precision in a two-step process, which is developed for high-density single particle tracking as described previously in detail (1). Initial emitter positions are identified using a pixel-wise statistical test limiting the rate of false-positive detection to 10^{-6} per pixel. These initial positions are refined to sub-pixel accuracy in a second step by maximum likelihood estimation modeling the microscope´s PSF as a two-dimensional Gaussian profile. From the localization data, single particle tracking is performed by using the multiple-target tracing (MTT) algorithm

(11). Several parameters like the exposure time, the image pixel size *q*, the *NA* of the used objective and the emission wavelength of the fluorophore have to be handover to the software. Additionally parameters like the size of the detection box, the error rate, the performed deflation loops and the particle offtime have to be selected. In order to track proteins with the MTT a maximal diffusion coefficient has to be set. To avoid false connections of localized emitters, the maximal diffusion coefficient has to be set as small as possible. Therefore the value has to be approximated to the lowest possible value and has to be adapted to the crowding level. This is an iterative process and needs some experience. The maximal diffusion coefficient in the MTT stands for the maximal step size in all lateral directions and is not the mean diffusion coefficient of a single trajectory of a protein. Most of the mitochondrial proteins can be tracked with a maximal expected diffusion coefficient between 0.2 $\mu m^2/s$ and 0.3 $\mu m^2/s$. Nevertheless, some small proteins may be faster and need higher D_{max} values. Step-length distributions are obtained from single molecule trajectories (5 steps, ~160 ms for exposure time of 32 ms). Average diffusion constants are finally determined by the slope in mean square displacement analysis (2-10 steps).

Consider notes 14, 15 and 16.

Notes

Note 1: Lyophylisation is done like standard protocol with a Lyophilisator Alpha 1-2 LDplus

Note 2: Localization and tracking procedure are described in 1,6,7,8

Note 3: Stable transfected cells are easier to handle and show more homogenous expression levels. Avoid fragmentation of mitochondria by any stress

Note 4: Coverslips should be plasma cleaned at the day of use for cell seeding or coating.

Note 5: Coating of coverslips improves results by increasing the signal to noise ratio.

Note 6: Coated coverslips can be stored at -20 °C for a few days in cell culture dishes, sealed with parafilm.

Note 7: Compare different fluorescent ^{HTL} and check specificity of labeling by co-staining with MitoTracker®. For co-staining, add 0.5 µ 1 mM MitoTracker®DeepRed FM per ml medium to final concentration 500 nM.

Note 8: Optimize labeling degree (0.5 nM to 20 nM), excitation power and angle of incidence to obtain single molecule signals

Note 9: Choose a region in the periphery of a cell, where a mitochondrial network with elongated mitochondria is seen.

Note 10: Exposure time needs to be set as low as possible to avoid photon blur and as high as possible to increase the SNR.

Note 11: Use frame transfer mode when using an EMCCD camera.

Note 12: The given laser power refers to the used fluorescent dye TMR. Adapt the laser power to the used fluorophores if necessary.

Note 13: Avoid phototoxic effects by not going beyond 10.000 frames per region of interest.

Note 14: Check mitochondrial movement at any time by generating an overlay of rendered images from first < 30 s of the time series to the following < 30s interval until the last < 30 s. No shift of the mitochondrial shape should be seen (Fig. 5).

Note 15: Adapt evaluation parameters, e.g. the maximal expected diffusion coefficient is dependent on the investigated membrane protein, the structure and composition of the membrane, possible supercomplex formation etc. In general, free diffusing molecules are faster than molecules with anomalous diffusion. For outer membrane proteins a higher diffusion coefficient is expected than for

inner membrane proteins. Diffusion coefficients are in general slower than expected from FRAP experiments which exclusively determine the diffusion coefficients from mobile molecules.

Note 16: FPALM and MTT allow for watching the data processing. Use this feature to be sure that your chosen parameters are correct. Test different parameters on the same data sets and optimize parameters iteratively.

References

1. Appelhans, T., Richter, C. P., Wilkens, V., Hess, S. T., Piehler, J., and Busch, K. B. (2012) Nanoscale organization of mitochondrial microcompartments revealed by combining tracking and localization microscopy, *Nano Letters 12*, 610-616.
2. Los, G. V., Encell, L. P., McDougall, M. G., Hartzell, D. D., Karassina, N., Zimprich, C., Wood, M. G., Learish, R., Ohana, R. F., Urh, M., Simpson, D., Mendez, J., Zimmerman, K., Otto, P., Vidugiris, G., Zhu, J., Darzins, A., Klaubert, D. H., Bulleit, R. F., and Wood, K. V. (2008) HaloTag: a novel protein labeling technology for cell imaging and protein analysis, *ACS Chem Biol 3*, 373-382.
3. Tokunaga, M., Imamoto, N., and Sakata-Sogawa, K. (2008) Highly inclined thin illumination enables clear single-molecule imaging in cells, *Nature Methods 5*, 159-161.
4. Shannon, C. E. (1949) Communications in the presence of noise, *Proc. IRE 37*, 10-21.
5. Nyquist, H. (1928) Certain topics in telegraph transmission theory, *AIEE Trans. 47*, 617-644.
6. Gould, T. J., Verkhusha, V. V., and Hess, S. T. (2009) Imaging biological structures with fluorescence photoactivation localization microscopy, *Nat Protocols 4*, 291-308.
7. Hess, S. T., Girirajan, T. P. K., and Mason, M. D., (2006) Ultra-High Resolution Imaging by Fluorescence PhotoactivationLocalization Microscopy, *Biophysical Journal* 91, 4258–4272.
8. Hess S. T., Gould T. J., Gunewardene M., Bewersdorf J., and Mason M. D. (2009) Ultrahigh Resolution Imaging of Biomolecules by Fluorescence Photoactivation Localization Microscopy, Micro and Nano Technologies in Bioanalysis, Springer Protocols 544 of the Series: Methods in Molecular Biology™, chapter 32, 483-522.
9. Graham, F. L., and van der Eb, A. J. (1973) A new technique for the assay of infectivity of human adenovirus 5 DNA, *Virology 52*, 456-467.
10. Thompson, R. E., Larson, D. R., and Webb, W. W. (2002) Precise nanometer localization analysis for individual fluorescent probes, *Biophys J 82*, 2775-2783.
11. Serge, A., Bertaux, N., Rigneault, H., and Marguet, D. (2008) Dynamic multiple-target tracing to probe spatiotemporal cartography of cell membranes, *Nat Methods 5*, 687-694.
12. Lin Shao L., Peter Kner P., Rego E. H., Gustafsson M. G. L. (2011) Super-resolution 3D microscopy of live whole cells using structured illumination, *Nat Methods 8*, 1044–1046

Figure legends

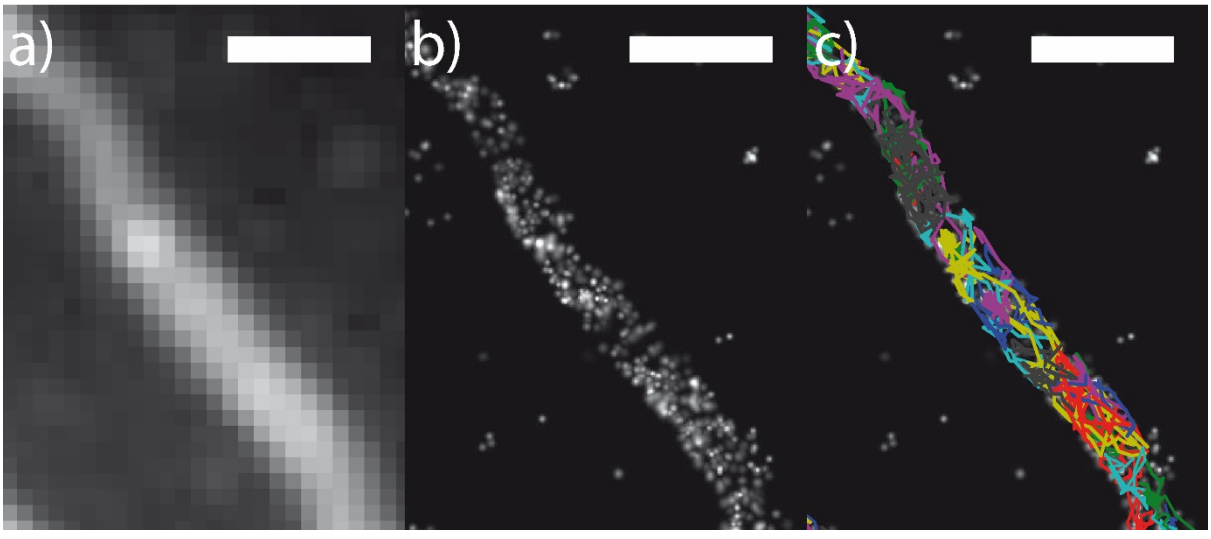

Fig. 1 TALM analysis of single TOM20-HaloTag® / TMR^{HTL} in a living HeLa cell
a) Diffraction limited view of summed fluorescent signals from TOM20:HaloTag®/TMR^{HTL} in the outer mitochondrial membrane. **b)** FPALM image of localized TOM20 proteins in the OMM in a movie of 112 s with 32 ms exposure time. **c)**

Trajectories of individual TOM20 proteins with at least 15 steps in sequence (single trajectories with different colors). Scale bars: 5 μm (a), 1 μm (b-d).

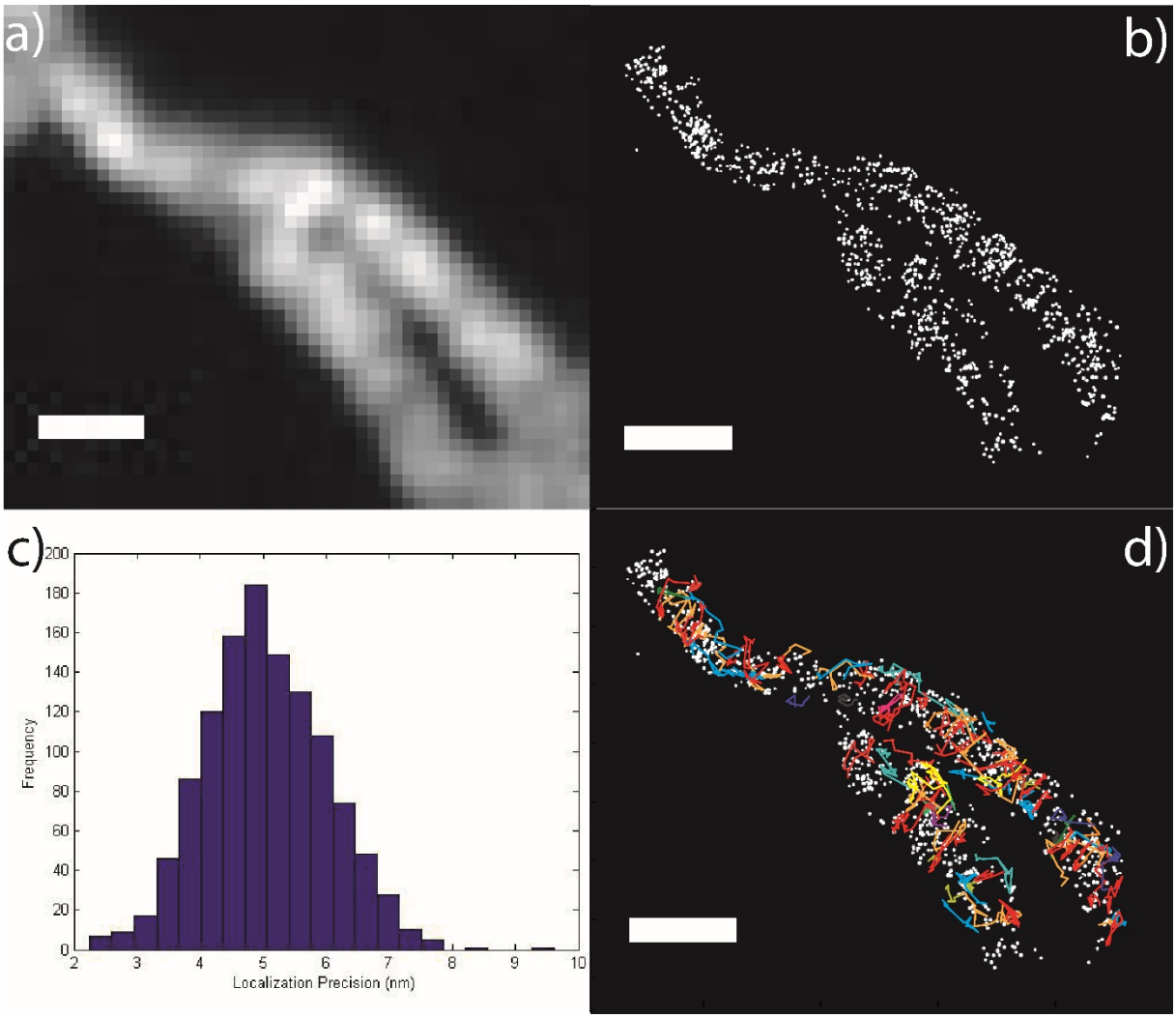

Fig. 2 TALM analysis of single F_1F_0 ATP-Synthase: HaloTag® / TMR^{HTL}
a) Diffraction limited view of summed fluorescent signals from ATP-Synthase:HaloTag®/TMR^{HTL} in the inner mitochondrial membrane. **b)** Localization map of ATP-Synthase:HaloTag®/ TMR^{HTL} proteins. Localization patterns reflect distribution of ATP synthase in cristae microcompartments. **c)** Calculated localization precision of the localized proteins shown in b). **d)** Trajectory map of ATP Synthase:HaloTag®/TMR^{HTL} proteins. Most red and orange trajectories demonstrate the diffusion of ATP-Synthases in the cristae and reveal the orthogonal cristae membrane (CM) orientation while blue trajectories demonstrate the likely diffusion of ATP-Synthase:HaloTag®/ TMR^{HTL} proteins along the inner boundary membrane (IBM). Scale bars: 1 µm (a, b and d).

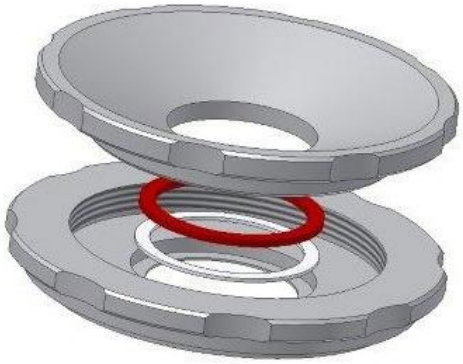

Fig. 3 Microscopy chamber for live cell imaging
The coverslip with an appropriate cell layer is mounted between the top and bottom part of the homemade chamber (developed by J. Bereiter-Hahn), which is connected by a screwed joint. A Teflon® ring (white ring) and a rubber ring (red ring) seal the system. The buffer reservoir is open and allows exchange of imaging medium (figure from H. Heine, Optomechanics - University of Osnabrück).

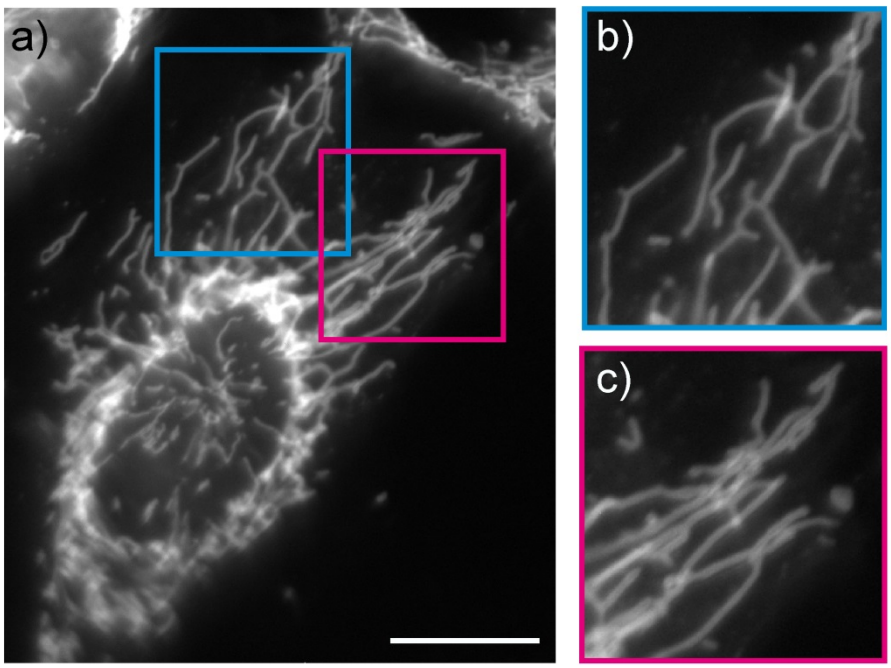

Fig. 4 Selection of adequate regions of interest with elongated, separated mitochondria
a) Morphology of mitochondria throughout mammalian cells shows some diversity. Focus on cells with elongated, clearly separated mitochondria and select adequate regions of interest (ROIs, blue and magenta frames) from the mitochondrial network for TALM image series. **b** and **c)** ROIs with separated mitochondria as in b) are preferred. Avoid recording ROIs with overlapping mitochondria as shown in c). Also, set small imaging regions for fast recording with short frame rates (~30 Hz) needed in single molecule tracking experiments. Scale bar: 10 µm

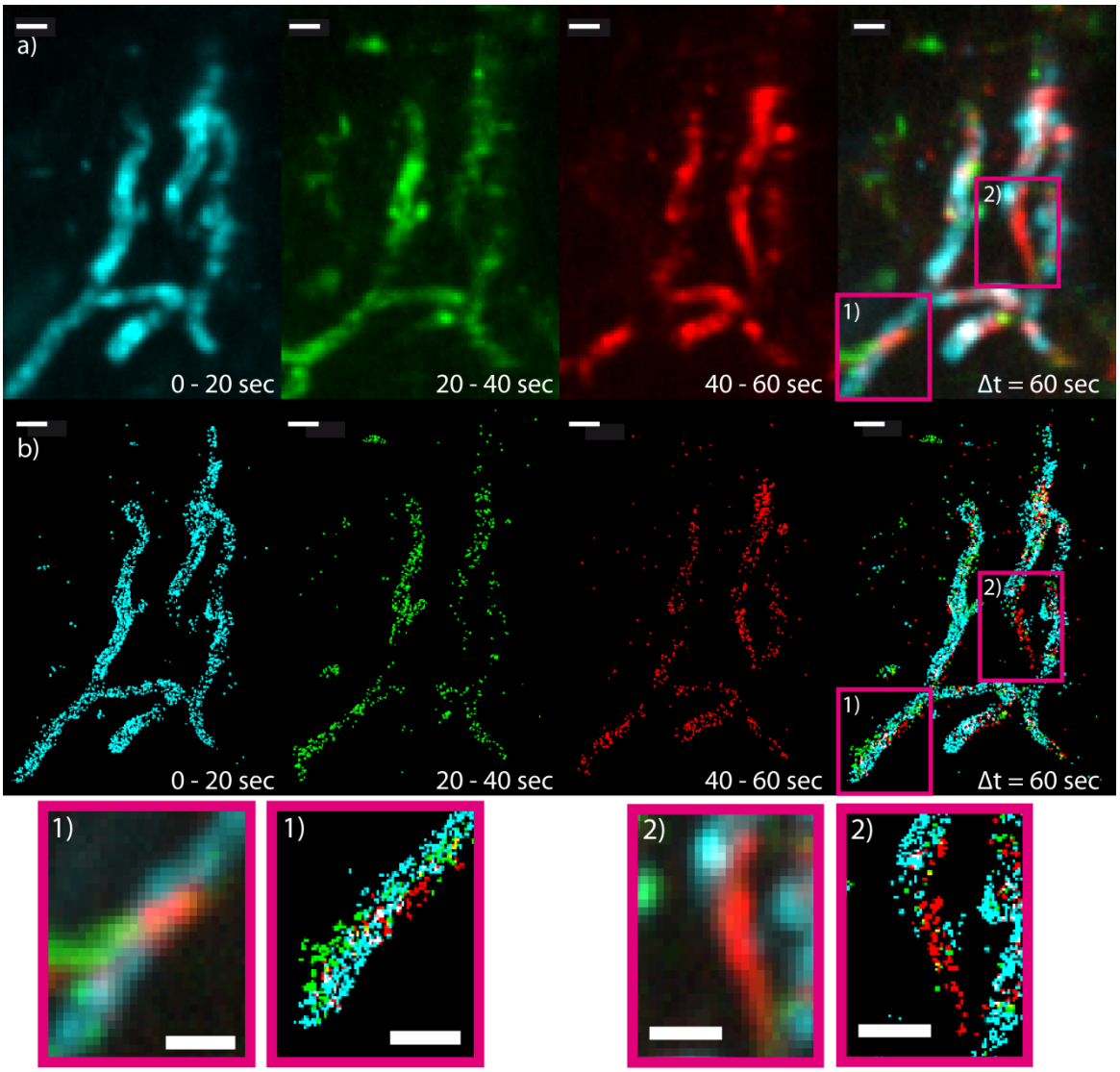

Fig. 5: Investigation of Lateral Drift with FPALM
a) Superimposed non-rendered signals from 1250 binned frames each color. Some parts of mitochondria moved (frame 1), 2)). Other parts of the mitochondrial network did not move during recording and are suitable for single molecule localization and single molecule tracking analysis. **b)** Same signals after localization and rendering. **1) &2**) Enlarged view of the areas where mitochondrial movement occurs. Meanwhile demonstrating that SML in small time scales of ~20 seconds is enough to excluded possible movement (1,). In general absolute time series of a movie of ~150 s can be used to image mitochondria without movement. (12). Scale bars: 1 µm.

Table 1: Used Frame Rates

Smaller imaging areas allow for reduction of the exposure time

Imaging area (pixel, x,y)	Exposure time (ms)	Frame rate (Hz)
512 x 512	32	30.42
512 x 512	24	40.15
256 x 256	16	59.17
200 x < 200	8	112
125 x 125	8	112

13.5.2 Multi-color Localization Microscopy of Single Membrane Proteins in Organelles of Live Mammalian Cells

Multi-color Localization Microscopy of Single Membrane Proteins in Organelles of Live Mammalian Cells

Timo Appelhans, Felix R.M. Beinlich, Christian P. Richter, Rainer Kurre, Karin B. Busch

Abstract

Knowledge about the localization of proteins in cellular subcompartments is crucial to understand their specific function. Here, we present a super-resolution technique that allows for the determination of the microcompartments that are accessible for proteins by generating localization and tracking maps of these proteins. Moreover, by multi-color localization microscopy, the localization and tracking profiles of proteins in different subcompartments are obtained simultaneously. The technique is specific for live cells and is based on the repetitive imaging of single mobile membrane proteins. Proteins of interest are genetically fused with specific, so-called self-labeling tags. These tags are enzymes that react with a substrate in a covalent manner. Conjugated to these substrates are fluorescent dyes. Reaction of the enzyme-tagged proteins with the fluorescence labeled substrates results in labeled proteins. Here, Tetramethylrhodamine (TMR) and Silicon Rhodamine (SiR) are used as fluorescent dyes attached to the substrates of the enzymes. By using substrate concentrations in the pM to nM range, sub-stoichiometric labeling is achieved that results in distinct signals. These signals are localized with ~15–27 nm precision. The technique allows for multi-color imaging of single molecules, whereby the number of colors is limited by the available membrane-permeable dyes and the repertoire of self- labeling enzymes. We show the feasibility of the technique by determining the localization of the quality control enzyme (Pten)-induced kinase 1 (PINK1) in different mitochondrial compartments during its processing in relation to other membrane proteins. The test for true physical interactions between differently labeled single proteins by single molecule FRET or co-tracking is restricted, though, because the low labeling degrees decrease the probability for having two adjacent proteins labeled at the same time. While the technique is strong for imaging proteins in membrane compartments, in most cases it is not appropriate to determine the localization of highly mobile soluble proteins.

Video Link

The video component of this article can be found at https://www.jove.com/video/57690/

Introduction

The goal of this protocol is to provide an imaging method to localize and track single membrane proteins inside live cells. We call this method Tracking and Localization Microscopy (TALM)[1,2]. Like Stochastic Optical Reconstruction Microscopy (STORM)[3] and Fluorescence Photoactivation Localization Microscopy ((F)PALM)[4,5], TALM is a single molecule-based fluorescence localization technique. However, it is distinct in the way that the mobility of membrane proteins in combination with repetitive imaging of the same labeled molecule at different positions reveals the microcompartment that is accessible for the mobile protein. In other words, the possible localizations of the protein are set by the architecture of the organelle and by the mobility of the protein[1]. The method is complementary to various other super-resolution techniques[6,7,8] because it reveals localization and trajectory maps by imaging mobile proteins. The labeling is based on using genetically engineered fusion proteins that are per se non-fluorescent. These fusion proteins are self-labeling enzymes that react covalently with a substrate conjugated to a dye. This procedure has the advantage that the labeling degree can be controlled by the amount of added substrate. Furthermore, it allows to vary the color of fluorescence, depending on the chosen conjugated dye. Several self-labeling enzyme-tags are available[9]. Another advantage of using self-labeling enzyme-tags is, that the conjugated dyes usually are more stable and brighter than

fluorescent proteins[1] and individual proteins therefore can be recorded longer and more precisely until they are bleached. This allows for the recording of trajectories of mobile proteins and the extraction of diffusion coefficients[10,11]. Here, we demonstrate the feasibility of TALM with mitochondrial membrane proteins, but it can also be applied for other intra- and extra-cellular membrane proteins, including different cell types[12,13]. We show that multi-color TALM further allows for the simultaneous distinction of proteins in different subcompartments in complementation to existing super-resolution fluorescence microscopy techniques[14,15,16]. TALM is compatible with live cell imaging[17]. The photo-physics of the chosen rhodamines Tetramethylrhodamine (TMR) and Silicon-Rhodamien (SiR), in particular their brightness and stability, allows to record single membrane proteins over multiple frames providing localization (and trajectory) maps. However, TALM is limited for the localization of soluble proteins with high diffusion coefficients since the motion blur is too high and the collected photons per frame are too low for proper localization. Besides, TALM requires less excitation power than for example STORM or Stimulated Emission Depletion (STED) microscopy[6,7], reducing phototoxic effects. This is important, since phototoxic stress often affects organellar morphology[18] and thus mobility analysis[19]. In sum, we present multi-color TALM in living cells as a technique that fills a gap between the localization microscopy methods STORM/STED/(F)PALM and techniques that analyze protein mobility such as fluorescence recovery after photobleaching (FRAP)[20,21], fluorescence correlation spectroscopy (FCS)[22], and fluorescence cross correlation spectroscopy (FCCS)[11,23].

Protocol

The following protocol follows the guidelines of the local institution research ethics committee.

Method

1) Cell culture

1. Cultivate cells, for example HeLa cells (human cervix carcinoma), in a T25 cell culture flask containing 5 mL of growth medium at 37 °C and 5% CO_2.
   NOTE: For imaging, split the cells onto prepared coverslips (see steps 1.3 and 1.4) and keep in imaging medium.

2) Cell transfection

NOTE: Use cell lines that stably express the tagged proteins whenever possible[24] to avoid strong overexpression. For transient transfection, adapt the amount of plasmid DNA used for transfection. For example, when Ca^{2+} phosphate transfection[25] is used, transfect cells (80–90% confluency) in a 3.5 cm cell culture dish with 2.5–5 µg of plasmid DNA. When performing double transfection, use 2.5 µg per each plasmid construct.

1. For dual color experiments, use a cell line with stable expression of one self-labeling protein and transiently transfect with the plasmid encoding the other self-labeling protein[17].
   NOTE: Here, for dual color experiments, HeLa cells were used that stably expressed the self-labeling proteins PINK1-Halo-Tag and Tom20-fSNAP-Tag.

3) Cleaning of coverslips

1. Place the coverslips in a beaker. Add 30 mL of H_2O into the beaker containing the coverslips and gently shake to remove dust from their surface.
2. Gather the coverslips with tweezers and dry them with a stream of nitrogen.
3. Remove any organic contamination on the surface of the coverslips, *e.g.*, by plasma cleaning.
   NOTE: To avoid further contamination of the glass material, wear gloves during handling of the

coverslips.
CAUTION: When coverslips are cleaned by plasma cleaning, only the upper side of the coverslips is cleaned; use this side for coating with poly-L-Lysine-polyethylene glycol-arginine-glycine-aspartate (PLL-PEG-RGD) (section 1.4) and cell seeding (section 1.5).

4) Coverslip coating with PLL-PEG-RGD

NOTE: PLL-PEG-RGD is a poly-L-Lysine (PLL) derivative attached with a polyethylene glycol (3,000 Da) and a cysteine-glycine-arginine- glycine-aspartate-serine (CGRGDS) peptide. PLL binds to the negatively charged glass surface and forms a PEG brush. This drastically reduces unspecific binding of charged fluorescent dyes. In addition, the RGD motif mimics the signal peptide of the integrin receptor and thereby promotes integrin-mediated adherence of cells that otherwise do not easily adhere.

1. Prepare PLL-PEG-RGD as previously described[26]. In short, dissolve 0.8 mg of PLL-PEG-RGD in 1 mL of PBS. Add 10 µL of the PLL- PEG-RGD solution on the upper side of a clean coverslip.
2. Take a second coverslip and place it with its clean surface upside down onto the first coverslip (that has the PLL-PEG-RGD drop on top); this results in sandwiching the PLL-PEG-RGD solution between two coverslips.
3. Carefully place the sandwiched coverslips in a beaker and incubate for 1 h at room temperature in a dust-free dry environment.
4. After 1 h, add 30 mL of H_2O to the beaker to fully cover the coverslips with water.
5. Gently shake the beaker until the coverslips detach from each other.
6. Use tweezers to gather the coverslips out of the water and dry them under a stream of nitrogen gas. NOTE: The coated coverslips can be stored in a dry, sterile glass Petri dish with lid for a couple of days.

5) Preparation of specimen for imaging

1. Transfer the single coated coverslips into a 35 mm cell culture dish, with the PLL-PEG-RGD coated surface facing upward and add 2 mL of imaging medium on top.
2. Add ~500,000 trypsinized cells (200–500 µL) that express the self-labeling tags at the respective membrane proteins to the 2 mL imaging medium in the cell culture dish with the coated coverslip. Shake gently by hand to ensure a homogenous distribution of the cells to obtain a uniformly cell layer.
3. Incubate cells at 37 °C and 5% CO_2 until 80% confluency is reached.
   NOTE: Cell samples should be seeded 3 days before imaging and 1 day before transfection. Cells, which stably express the protein of interest, can be seeded 2 days before imaging. Later, only cells grown on the coverslip are imaged.

6) Labeling of tagged proteins

NOTE: Most fluorescent substrates have to be dissolved in water-free DMSO. We advise to use stock solutions of 1 µM fluorescent substrate when the final labeling concentration is 0.2–30 nM[17]. For imaging membrane proteins inside cells, use membrane permeable fluorescent substrates.

1. Warm up the imaging medium to 37 °C in a water bath.
2. Pipette 1 mL of the pre-warmed imaging medium into a 2 mL tube with lid. Add 0.2–30 µL of fluorescent substrates from 1 µM stock solutions to prepare the final labeling solution (final concentration: 0.2–30 nM).
3. Vortex the labeling solution for 10 s.
4. Substitute the medium in the 35 mm culture dish with the cells on a coverslip (see step 1.5) by 1 mL of prepared labeling solution.
5. Incubate the cells in the labeling solution at 37 °C and 5% CO_2 for 20–30 min.
6. Wash the cells with 2 mL of PBS once, then with 2 mL of imaging medium twice. Finally, pipette

1 mL of fresh imaging medium to the cell dish and put the sample back into the incubator at 37 °C and 5% CO_2 for at least 1 h. Before imaging, exchange the imaging medium once more.
NOTE: When running the experiment for the first time, confirm correct targeting of self-labeled proteins to organellar membranes by staining the organelles with commercially available organelle specific dyes[27,28]. In this case, also use 100–200 nM of substrate for the self-labeling enzymes to produce strong signals.

7) Preparation of a fluorescent bead sample

NOTE: In order to determine the optical drift and to align images of the different channels, multi-color fluorescent beads (0.1 µm) are used. With the recorded images, an affine transformation matrix for the two emission channels will be generated.

1. Dilute the solution of beads to 1% with pure H_2O.
2. Place 5 drops of the prepared solution with the fluorescence beads at five different positions on a cleaned coverslip (see step 1.3).
3. Let the fluorescent bead sample dry on a clean bench.
   NOTE: The sample can be re-used; therefore, cover the sample with aluminum foil to avoid contamination and keep it at a 4 °C.

Microscopy

1) Experimental setup

NOTE: A basic microscopy system for dual-color single molecule imaging is based on an inverted microscope: it is equipped with two lasers coupled via a multi-mode-optical polarization maintaining monomode fiber into a single total internal reflection (TIR) condenser, an oil immersion objective designed for TIRF, a polyband emission filters, an image splitter, and a highly-sensitive camera (**Figure 1**). A TIR condenser is needed that allows for continuous tuning of the incident angle to switch between the epi-, highly inclined and laminated optical sheet (highly inclined thin illumination (HILO)[29]), and the TIRF excitation mode with optimized penetration depth. Images are acquired with a highly-sensitive cooled detector system, *e.g.,* a back-illuminated electron multiplying charged coupled device (EMCCD) camera (quantum efficiency QE >90%) or a sCMOS camera (QE >80–90%).

1. Determine the optical drift by imaging fluorescent beads (see step 2.2) under the same conditions as those that will be later used for the experiment, *e.g.*, when 10,000 frames are recorded in the experiment, record also 10,000 frames with the bead sample. For the determination of the optical drift, compare the position of the beads in the first frame and the last acquired frame (**Figure 1B**). If necessary, later correct the image series for optical drift[30] and/or use drift stable environments.
2. Equip the filter cube with the appropriate dichroic beam splitter, *e.g.*, for orange and red fluorescence plus the adequate emission filters for orange fluorescence and red fluorescence. Equip the image splitter with the suitable filters. Check for the possible leak of signals from one channel into the other channel by recording single color samples in both channels (**Figure 1C**).

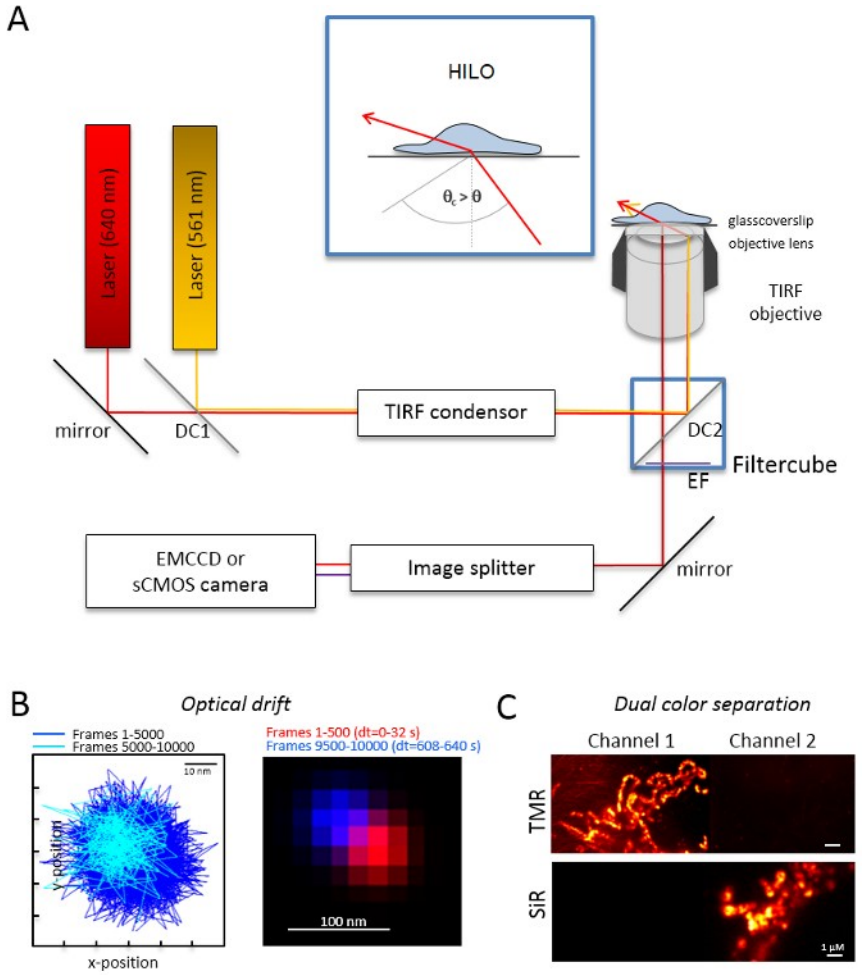

Figure 1: Optical layout for multi-color tracking and localization microscopy (TALM) with orange and red emitters.
(A) Inverted microscope setup with at least two excitation lasers, a TIRF condenser, a TIRF suitable objective, an image splitter, and a sensitive camera. Inset: to excite organelles inside cells, the angle of the incident beam must be set smaller than the critical angle for TIRF to achieve highly inclined and laminated optical sheet illumination (HILO). DC1: Dichroic mirror 1; DC2: Dichroic mirror 2. EF: emission filter. **(B)** Test on optical drift by imaging positions of a fluorescent bead for 10,000 frames with the same frame rate as of the following experiments (here: 15 Hz).
Connected positions of the first 500 frames and the last 500 frames show the drift. Also, a merged image with the position of the first and the last frame in red and blue show a minimal drift. The drift is the distance between the centre of the signals divided by the total recording time, here 125 pm/s. **(C)** Check on the clear separation of signals, here TMR and SiR. For both channels, cumulative sum images from 3,000 frames (TMR in Channel 1 and SiR in Channel 2) were generated. SiR^{HTL} was attached to Tom20-HaloTag and TMR^{HTL} to OxPhos complex V-HaloTag. Colors are false colors. Scale bars = 100 nm (B) and 1 µm (C).

2) Physical alignment of image splitter generated images

NOTE: For mounting the specimen prepared on a coverslip, a self-made sample-holder can be used (**Figure 2A**). To avoid dust, *etc.* falling into the sample, place the lid of the culture dish loosely on top of the chamber, when mounted. The same sample-holder can be used to mount the coverslip with fluorescent beads or cells; when cells are imaged, add 0.5–0.8 mL of imaging medium. The image splitter splits the image into two or more spectrally separated channels and projects them side-by-side onto the same camera. This process potentially introduces systematic distortions between the channels due to distinct optical paths traversed and obstructs direct colocalization analysis.

Therefore, first perform physical alignment and second, post-correction alignment with a transformation matrix. For both alignment processes, fluorescent beads should be homogenously distributed throughout the field of view.

1. Mount the prepared sample with the fluorescent beads in the sample-holder between the polytetrafluoroethylene (PTFE)-ring and the red rubber ring (**Figure 2A**).

2. Start the microscope, all hardware components, and all software needed for microscopy.
3. Clean the objective and the bottom of the coverslip with a lint-free tissue wipe wetted with isopropanol. Then dry both items with a fresh lint-free tissue. Place a droplet of immersion oil on the pupil of the objective lens.
4. Place the sample holder with the bead sample onto the microscope stage so that the bottom of the coverslip contacts the oil. Focus on beads by using transmission light or a laser line.
5. Adjust the power of the two excitation lasers to achieve similar signal intensity in the two fluorescence channels. Search for an area with many distinct fluorescent signals.
6. Generate a merged view of the fluorescent channels by using the camera control software. Then use the screws at the image splitter to manually tilt the internal mirrors of the image splitter to achieve the best overlay of the signals from the two fluorescent channels (**Figure 2B**).
   NOTE: Attention! Do not exceed the dynamic range of the camera.

3) Alignment of spectrally separated channels by software performing spatial transformation

NOTE: The following part shows the post-correction alignment and localization procedure with our software plugin (available upon request).

1. Start the TIRF microscope controlling software and choose to display individual channels in the live stream mode. Take a snapshot image exciting fluorescence in all channels (**Figure 2C**).
2. Use this snapshot image to produce the transformation matrix (see **Figure 2**).
   NOTE: The transformation matrix is used for a spatial transformation, typically an affine one, that corrects for translation (divergence of signals from a single point source between two channels).
3. Start the software analysis plugin (can be obtained upon request from our lab, see **Figure 2C**).
4. Load the previously recorded dual color images (see step 2.2) of fluorescent beads into the software. Choose the used orientation of the fluorescent channels. Then click 'yes' when asked for 'calibrate images' and select the previously taken snapshot.
5. Open the "UNIT MANAGER" to define unit conversion factors (pixel size, frame rate, photon conversion factor).
6. Open the "LOCALIZATION MANAGER". Determine the point spread function (PSF) first. Press the button: “PSF radius”. In the "PSF Estimator" window that opens, define the numerical aperture and the emission maximum. Start “Estimate PSF radius” by clicking.Accept the obtained experimental PSF. Define the evaluation box, number of deflation loops, and how many cores of the computer are used for calculation. Press "localize" to start fitting the intensity distribution of single particles by a 2D symmetric Gaussian function (**Figure 2C**).
7. “Accept” the obtained experimental PSF. Define the evaluation box, number of deflation loops, and how many cores of the computer are used for calculation. Press “localize” to start fitting the intensity distribution of single particles by a 2D symmetric Gaussian function (**Figure 2C**).
8. Open the "CALIBRATION MANAGER". In the rendered merged image of the two channels, the original signals and the localized centers are shown. Choose the "affine" mode. Manually connect the corresponding pairs of localized centers in the two channels that have originated from the same fluorescent bead by drawing a connection line.
9. Connect the corresponding signals distributed all over the field of view. After this, press "accept". Save the calibration.
   NOTE: The spatial transformation is sampled at each fluorescent bead and interpolated in between. The extracted transformation function represents a displacement field $\Delta r(x,y)$ that is used to subsequently correct the experimental dual-color single molecule localizations so that they overlay within their localization precision. The spatial transformation matrix is typically an affine one that corrects for translation, scaling, and rotation between channels with nanometer accuracy, and it can be inferred from this manual one- to-one mapping (**Figure 2C**).

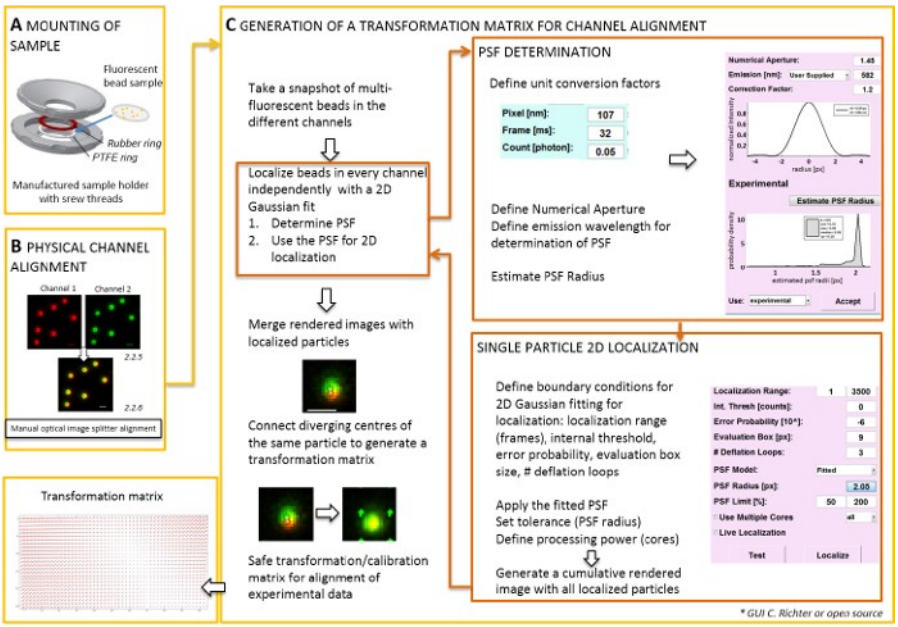

Figure 2: Workflow for dual color alignment.
(A) The coverslip with the fluorescent beads is mounted in a sample holder between a PTFE and a rubber ring. Then the upper and lower part of the chamber are bolted together. **(B)** Physical alignment of the channel views that are generated by the image splitter. Recorded fluorescent signals from beads (0.1 µm) in two channels (green and red, false colors) are merged. The corresponding screws at the optical image splitter are manually turned until the best overlay of the different signals is achieved (yellow color, lower panel). **(C)** Generation of a transformation matrix for post-processive channel alignment. For precise localization of a particle, it is necessary to determine the point spread function (PSF) in dependence on the emission wavelength and the numerical aperture of the objective. The center of a PSF can be determined by its intensity profile analyzed by a symmetric two-dimensional Gaussian fit. The resulting localization of the signal peak is then projected on the original, blurred signals. In a merged image, the localized centers of the signals from the two channels are connected to generate a transformation matrix that is later used for the post-processive alignment of the experimental data. Scale bars = 1 µm (B, C).

4) Single molecule imaging of mitochondrial membrane proteins

NOTE: All experiments are carried out at room temperature. T-cells or non-adherent cells must be immobilized in agarose before imaging[31].

1. Mount the specimen with adherent cells on the coverslip between the rubber and PTFE rings (**Figure 3A**). Fill the chamber with 0.5–0.8 mL imaging medium.
2. Repeat steps 2.2.2–2.2.5**.**
3. Adjust the illumination angle TIRF microscope controlling software to create an incident angle that is smaller than the critical angle for TIR mode to excite the specific region of interest via a HILO sheet[32] (HILO mode, **Figure 1A**).
   CAUTION: Avoid direct eye contact with the laser beam!
4. Set the EM gain and choose an exposure time suitable for the experiment that collects sufficient photons per frame.
5. Set the laser power to achieve a high signal to noise (S/N) ratio (**Figure 3B**), since the localization precision directly corresponds to S/ N[33] (**Figure 3C**).
6. Find an area in the cell periphery with non-overlapping, elongated mitochondria and single molecule signals (**Figure 3D**; **Supplementary Video 1**). If no single molecule signals are visible, wait until bleaching results in the appearance of single molecule signals (**Figure 3E**).
7. Record until the number of signals is too low for reasonable continuation (usually 1,000–10,000 frames depending on the bleaching behavior of the fluorescent dye, **Figure 3F**).
8. Start the imaging processing software and check for mitochondrial structures by generating a cumulative rendered sum image of at least 1,000 recorded frames (**Figure 3G**).
   NOTE: The fastest possible frame rate is dictated by the readout area. The field of view for one

channel is reduced by a dual-color image splitter (512 x 512 pixels) to 256 x 512 pixels, and for a Quad-color to 256 x 256 pixels. Thus, for using an image splitter for two colors, this is 30 Hz. Set the frame transfer mode to achieve the lowest possible readout time.

9. Start software analysis plugin and load raw data. Select the channel orientation and load images. Use the transformation matrix from step 2.3.9 when asked for “Calibrate images”. Channels will be separately displayed.
10. Open the "UNIT MANAGER" as before to define unit conversion factors for each channel. Open the "LOCALIZATION MANAGER" for each channel. Then define the evaluation box, number of deflation loops, add the theoretical PSF for the conditions used and set how many cores of the computer are used for calculation. Finally, press “localize” to get localized single particles (**Figure 3H**; **Supplementary Video 2**).
11. Note that the program will finally generate a cumulative superresolution image showing all localized particles (**Figure 3I**).
12. Perform analysis, *e.g.*, by open source software or our software available upon request.
13. Track the single molecules in both localized channels, *e.g.*, with the multiple-target tracer[10]
NOTE: Step 2.4.13 needs preliminary (experimental) knowledge about the diffusibility of the proteins of interest to set the boundary conditions correctly. Usually, finding the correct boundary conditions is an iterative process.

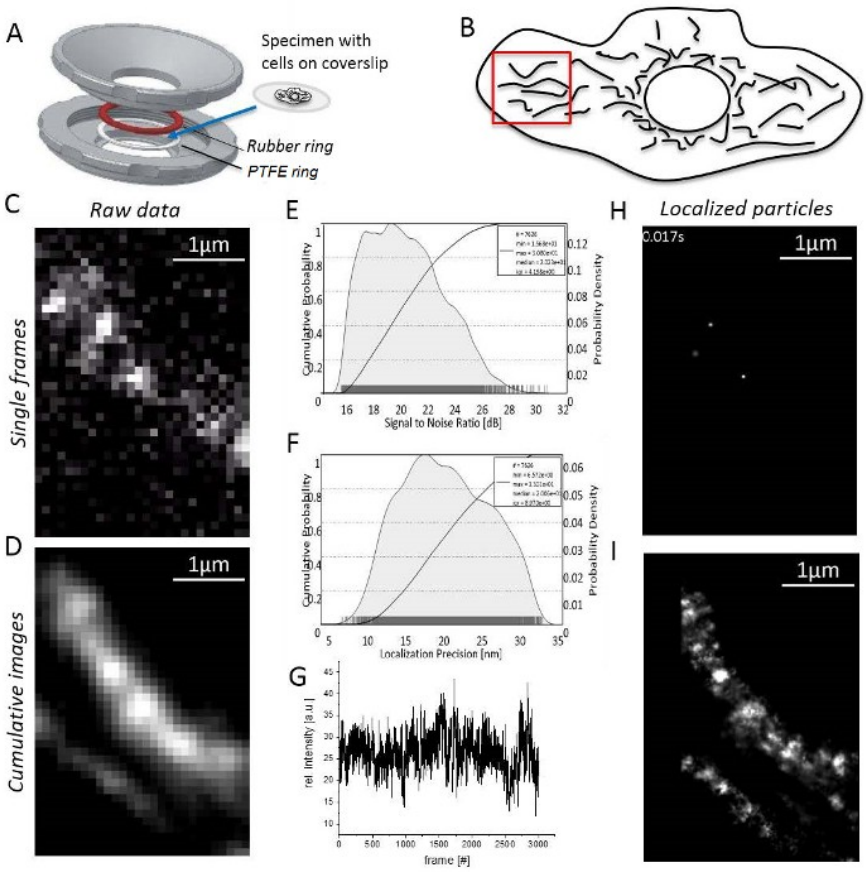

Figure 3: Steps during single molecule localization microscopy.
(A) A coverslip with the specimen is mounted between the top and bottom part (grey) of the homemade sample holder (designed by J. Bereiter-Hahn). A rubber ring (red) and a PTFE ring (white) seal the system from above and below the coverslip, when the sample-holder parts are bolt together. **(B)** Signal to noise ratio of the TMR signal. **(C)** Calculated localization precision histogram for all localized particles. **(D)** Choice of a reasonable region for imaging, here, the cell periphery with clearly separated mitochondria. **(E)** Recording and image processing: a single frame with distinct single molecule signals is shown (here, single molecules of CV-HaloTag/TMR^{HTL} were recorded). **(F)** Intensity of TMR over the recording time. (G) Cumulative sum image of 3,000 frames, unprocessed. **(H**) Particles of CV-HaloTag/TMR^{HTL} localized with a 2D Gaussian function from a single frame. **(I)** Cumulative, rendered sum image showing all localized CV-HaloTag/TMR^{HTL} particles from 3,000 frames.

Representative Results

Multi-color imaging and colocalization analysis can help to determine the sub-organellar localization of proteins. We demonstrated this earlier with the cytosolic phosphatase and tensin homologue, PINK1, that has different sub-mitochondrial locations due to its processing by mitochondrial proteases[17]. PINK1 is an important factor guaranteeing mitochondrial functionality[34,35]. To determine the localization of PINK1 in different mitochondrial compartments in the course of its processing (**Figure 4A**), multi-color super-resolution microscopy with live cells was performed. Therefore, PINK1 was genetically fused to a self-labeling tag (HaloTag). To determine its localization relative to other proteins in functional and dysfunctional mitochondria, Tom20, as part of the translocase of the outer mitochondrial membrane (TOM)[36], was tagged with another self-labeling tag (SNAP-tag). Time series with at least 1,000 frames (96 frames per s) were recorded. The cumulative image of all signals over time from one channel showed that PINK1 was localized in the cytosol and in the mitochondria (**Figure 4B**, left panel) under normal conditions, while it was retained at the outer membrane of depolarized mitochondria (treatment with 10 µM of the uncoupler carbonyl cyanide m- chlorophenyl hydrazine, CCCP, for 20 min). The corresponding trajectory maps also show this difference in the spatio-temporal organization. As the summed images of localized particles reveal, PINK1 is distributed mainly inside polarized mitochondria (**Figure 4C**, left upper panel), while Tom20 is localized in the outer mitochondrial membrane (OM) (**Figure 4C**, left lower panel). This becomes even more clear in the merged image of localized Tom20 and PINK1 particles, where the distribution of the outer membrane protein Tom20 is much broader (**Figure 4C**, right panel). To verify the localization of PINK1 inside mitochondria, a third protein localized in the inner mitochondrial membrane was also imaged. Therefore, the 30 kDa subunit of respiratory complex I (CI) was fused to photoactivable GFP (paGFP) and recorded by FPALM[4]. The cumulative triple color image and the cross-section distribution show the overlay of CI (green) and PINK1 (red) (**Figure 4D**), confirming the import of full-length PINK1. PINK1 has an N-terminal mitochondrial targeting sequence and thus the label was put at the C-terminus of the kinase. Co-localization with CI demonstrates that the full length PINK1 had been imported. The fluorescence distribution along a cross-section shows that a quota of PINK1 particles apparently also colocalized with Tom20 in the outer mitochondrial membrane. Probably, this is PINK1 associated with Tom20, which
is the import receptor. As these data demonstrate, several mitochondrial micro-compartments are occupied by subpopulations of PINK1. To address this question of sub-mitochondrial localization by biochemical methods would be much more difficult, since it would require stringent sub-fractionation of the different membranes and a clear separation of soluble components to exclude cross-contamination.

Supplementary Video 1: Footage of single molecule recording, 100 frames, CV-HaloTag/TMR^{HTL}.

Supplementary Video 2: Localized data.

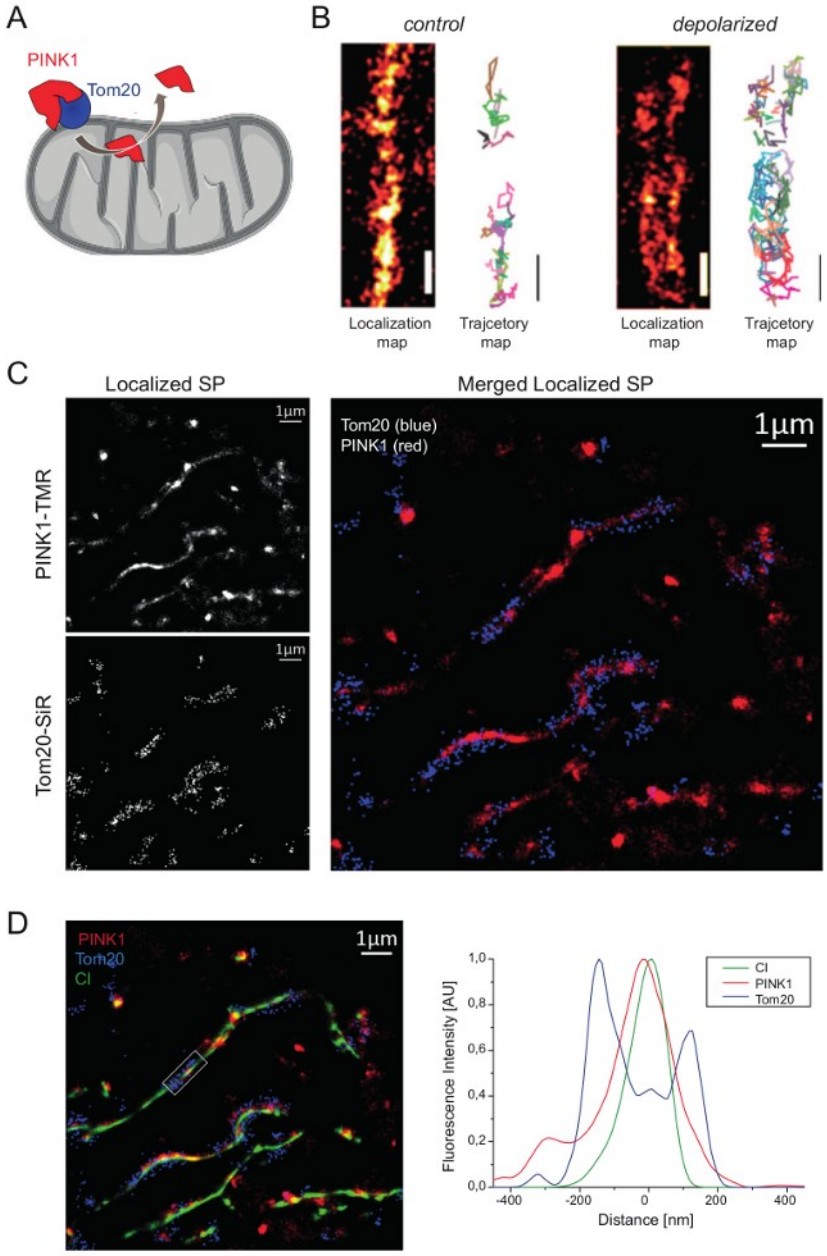

Figure 4: Dual color super-resolution microscopy showing the subcompartmental localization of PINK1 in mitochondria.
(A) Hypothesized PINK1 shuttling and processing in mitochondria. **(B)** Localization and trajectory maps of PINK1 under normal conditions and in depolarized mitochondria. **(C)** Dual-color super-resolution localization microscopy to reveal mitochondrial localization of PINK1 in relation to Tom20. Image series of 1,000 frames recorded with a frame rate of 96 frames per s. Left upper panel: Localization map of PINK1 (labeled via HaloTag with TMR^{HTL}). Left lower panel: localization map of Tom20 (labeled via SNAP-Tag with SiR^{BG}). Right panel: Merge cumulative sum image of PINK1-TMR (red) and Tom20-SiR(blue)localizations. **(D)** Same data plus localizations of respiratory complex I (CI, green) in the inner mitochondrial membrane. CI was fused to paGFP (CI-paGFP). Right: Mean cross section profile of Tom20 (blue), PINK1 (red), and CI (green) fluorescence in the marked region of the merged image. The mean cross section profiles were obtained by averaging up to 30 parallel oriented cross lines (interval 40 nm). Adapted version reprinted with permission from Beinlich *et al.*[16], copyright (2015) ACS chemical biology. All colors are false colors. Scale bars = 1 µm.

Discussion

Here, a technique for dual color single molecule localization of mobile membrane proteins was presented. Following the protocol, membrane proteins are fused to self-labeling proteins that react with the rhodamine dyes TMR and SiR conjugated to their respective substrates.
Rhodamine dyes are bright and photostable and thus allow for repetitive imaging[1]. For successful performance, several conditions and critical topics have to be kept in mind. First, it is important to choose appropriate filters and splitters to separate the signals from TMR and SiR clearly. To reduce background from outside the cell, a precleaning and coating of the coverslip with PLL-PEG-RGD was helpful. The final concentration of the dye-substrate must be tested by considering the affinity of the self-labeling enzyme for its substrate and the accessibility of the enzyme inside the cell. Nano- to picomolar concentrations were sufficient for mitochondrial proteins[17] and stress granules[13]. For other organelles, the required concentrations
need to be tested. If the staining is too strong at the beginning of the recording and no single molecules are distinguishable, it is best to wait until bleaching has reduced the amount of fluorescent dyes so that single particles (SP) can be discerned. We have found that concentrations of dyes higher than 30 nM for BG-substrates and 1 nM for HTL substrates during the staining procedure, or longer staining times in order to increase the number of labeled molecules, are not feasible. For each experiment, the intensity of the excitation laser has to be adapted, since the subcellular location of the dye influences its fluorescence behavior (quantum yield, bleaching, blinking)[5] due to different environmental conditions such as pH and redox state[3]. It further must be mentioned that the background is higher in dual-color experiments when compared to single color imaging.
This influences the precision of localization. Therefore, it is critical to optimize the laser power to achieve good signal to noise (S/N) ratios but low photobleaching rates. Typical laser power densities in HILO microscopy are in the range of 25 ± 8 kW/cm^2. For fine-tuning of excitation power, different sets of neutral density filters can be used if laser diodes are not directly modulated and not modulated via an acousto-optical modulator. It is recommended to use special 2 mm thick mirrors for TIRF to reduce beam distortions. Especially under TIR and HILO conditions,
very efficient blocking of excitation light is needed. For single molecule imaging and localization with subpixel accuracy, a proper spatial sampling frequency (Nyquist-Shannon sampling theorem) is required. This should be twice as high as the maximum spatial frequency defined by the resolution limit of the imaging system[37]. Using an oil immersion objective with a high numerical aperture (NA >1.4), the resolution, $d = \lambda/(2 \times NA)$, is typically at 200-250 nm for orange to far-red dyes. Thus, considering the physical pixel size of the detector, the magnification of the imaging optics should result in an image pixel size of approximately 100 nm. For an EMCCD camera with a pixel size of 16 x 16 µm^2 in combination with a 150X objective, the pixel size is 106.7 nm and thus adequate.
Generally, it is suggested to use stable transfected cells because this has the advantage that a steady amount of tagged proteins is expressed in most of the cells[24]. However, for dual-color localization and tracking experiments, this would require a double transfection and double selection with different antibiotics. Therefore, it is often more feasible to transiently transfect an already stable cell line with a second plasmid encoding the additional tagged protein of interest.
For mitochondria, movement and fragmentation is a critical issue. Fragmented or moving organelles should not be recorded or analyzed. Movement can be checked by overlaying rendered images of localized molecules from the beginning and the end of the experiment, with two different (false) colors. A homogeneous distribution of the signals from the organelles in the overlay indicates that organelles have not moved. Generally, room temperature reduces the movement of cellular compounds and structures.

Disclosures

The authors have nothing to disclose.

Acknowledgements

The authors would like to thank the Biophysics group and Jacob Piehler at the University of Osnabrück for continuous support, Wladislaw Kohl for technical assistance and preparation of material, and the CellNanOs board for providing microscopes for use. The project was funded by the SFB 944.

References

1. Appelhans, T., Richter, C., Wilkens, V., Hess, S., Piehler, J., Busch, K. Nanoscale organization of mitochondrial microcompartments revealed by combining tracking and localization microscopy. *Nano Letters.* 12 (2), 610–6 (2012).
2. Appelhans, T., Busch, K. Single Molecule Tracking and Localization of Mitochondrial Protein Complexes in Live Cells. *Methods Mol Biol.* 1567, 273–291 (2017).
3. Rust, M.J., Bates, M., Zhuang, X. Sub-diffraction-limit imaging by stochastic optical reconstruction microscopy (STORM). *Nat Methods.* 3 (10), 793–5, (2006).
4. Gould, T.J., Verkhusha, V.V., Hess, S.T. Imaging biological structures with fluorescence photoactivation localization microscopy. *Nat Protoc.* 4 (3), 291–308, (2009).
5. Pennacchietti, F., Gould, T.J., Hess, S.T. The Role of Probe Photophysics in Localization-Based Superresolution Microscopy. *Biophys J.* 113 (9), 2037–2054 (2017).
6. Wegel, E., Göhler, A., Lagerholm, B.C., Wainman, A. Imaging cellular structures in super-resolution with SIM, STED and Localisation Microscopy: A practical comparison. *Scientific reports.* At <https://www.nature.com/articles/srep27290?WT.feed_name=subjects_physical- sciences> (2016).
7. Pellett, P.*et al.* Two-color STED microscopy in living cells. *Biomedical Optics Express.* 2 (8) (2011).
8. Ishigaki, M. *et al.* STED super-resolution imaging of mitochondria labeled with TMRM in living cells. *Mitochondrion.* 28, 79–87 (2016).
9. Liss, V., Barlag, B., Nietschke, M., Hensel, M. Self-labelling enzymes as universal tags for fluorescence microscopy, super-resolution microscopy and electron microscopy. *Scientific Reports.* 5, 17740 (2015).
10. Sergé, A., Bertaux, N., Rigneault, H., Marguet, D. Dynamic multiple-target tracing to probe spatiotemporal cartography of cell membranes. *Nat Methods.* 5 (8), nmeth.1233 (2008).
11. Appelhans, T., Busch, K.B. Dynamic imaging of mitochondrial membrane proteins in specific sub-organelle membrane locations. *Biophysical reviews.* 9 (4), 345–352 (2017).
12. Wilmes, S. *et al.* Triple-color super-resolution imaging of live cells: resolving submicroscopic receptor organization in the plasma membrane. *Angewandte Chemie.* 51 (20), 4868–71, (2012).
13. Niewidok, B. *et al.* Single-molecule imaging reveals dynamic biphasic partition of RNA-binding proteins in stress granules. *J Cell Biol.* (2018).
14. Wurm, C.A., Jakobs, S. Differential protein distributions define two sub-compartments of the mitochondrial inner membrane in yeast. *FEBS Lett.* 580 (24), 5628–34 (2006).
15. Schmidt, R., Wurm, C.A., Punge, A., Egner, A., Jakobs, S., Hell, S.W. Mitochondrial cristae revealed with focused light. *Nano Lett.* 9 (6), 2508–10, (2009).
16. Kukat, C., Wurm, C.A., Spahr, H., Falkenberg, M., Larsson, N.G., Jakobs, S. Super-resolution microscopy reveals that mammalian mitochondrial nucleoids have a uniform size and frequently contain a single copy of mtDNA. *Proceedings of the National Academy of Sciences of the United States of America.* 108 (33), 13534–9, (2011).
17. Beinlich, F., Drees, C., Piehler, J., Busch, K. Shuttling of PINK1 between Mitochondrial Microcompartments Resolved by Triple-Color Superresolution Microscopy. *ACS chemical biology.* 10 (9), 1970–6 (2015).
18. Shim, S. *et al.* Super-resolution fluorescence imaging of organelles in live cells with photoswitchable membrane probes. *Proceedings of the National Academy of Sciences.* 109 (35), 13978–83 (2012).
19. Sbalzarini, I., Mezzacasa, A., Helenius, A., Koumoutsakos, P. Effects of Organelle Shape on Fluorescence Recovery after Photobleaching. *Biophysical Journal.* 89 (3), 1482–1492 (2005).
20. Reits, E., Neefjes, J. From fixed to FRAP: measuring protein mobility and activity in living cells. *Nature Cell Biology.* 3 (6), E145–E147 (2001).
21. Goehring, N., Chowdhury, D., Hyman, A., Grill, S. FRAP Analysis of Membrane-Associated Proteins: Lateral Diffusion and Membrane- Cytoplasmic Exchange. *Biophysical Journal.* 99 (8), 2443–2452 (2010).
22. Bacia, K., Haustein, E., Schwille, P. Fluorescence correlation spectroscopy: principles and applications. *Cold Spring Harbor protocols.* 2014(7), 709–25 (2014).
23. Sukhorukov, V., Dikov, D., Busch, K., Strecker, V., Wittig, I., Bereiter-Hahn, J. Determination of protein mobility in mitochondrial membranes of living cells. *Biochimica et biophysica acta.* 1798 (11), 2022–32 (2010).
24. Kim, T.K., Eberwine, J.H. Mammalian cell transfection: the present and the future. *Anal Bioanal Chem.* 397 (8), 3173–8 (2010).
25. Graham, F.L., van der Eb, A.J. A new technique for the assay of infectivity of human adenovirus 5 DNA. *Virology.* 52 (2), 456–67 (1973).
26. Wedeking, T. *et al.* Spatiotemporally Controlled Reorganization of Signaling Complexes in the Plasma Membrane of Living Cells. *Small.* 11 (44), 5912–8 (2015).
27. Mironov, S.L., Ivannikov, M.V., Johansson, M. [Ca2+]i signaling between mitochondria and endoplasmic reticulum in neurons is regulated by microtubules. From mitochondrial permeability transition pore to Ca2+-induced Ca2+ release. *J Biol Chem.* 280 (1), 715–21 (2005).
28. Poot, M. *et al.* Analysis of mitochondrial morphology and function with novel fixable fluorescent stains. *J Histochem Cytochem.* 44 (12), 1363– 72 (1996).
29. Tokunaga, M., Imamoto, N., Sakata-Sogawa, K. Highly inclined thin illumination enables clear single-molecule imaging in cells (vol 5, pg 159, 2008). *Nature Methods.* 5 (5), 455–455 (2008).
30. Elmokadem, A., Yu, J. Optimal Drift Correction for Superresolution Localization Microscopy with Bayesian Inference. *Biophys J.* 109 (9), 1772–80 (2015).
31. Barlag, B. *et al.* Single molecule super-resolution imaging of proteins in living Salmonella enterica using self-labelling enzymes. *Sci Rep.* 6, 31601 (2016).
32. Tokunaga, M., Imamoto, N., Sakata-Sogawa, K. Highly inclined thin illumination enables clear single-molecule imaging in cells. *Nature Methods.* 5 (2), 159–161 (2008).
33. Mortensen, K.I., Churchman, L.S., Spudich, J.A., Flyvbjerg, H. Optimized localization analysis for single-molecule tracking and super- resolution microscopy. *Nat Methods.* 7 (5), 377–81 (2010).
34. Jin, S., Youle, R.J. PINK1- and Parkin-Mediated Mitophagy at a Glance. *Journal of Cell Science.* 125, 795–799 (2013).
35. Yamano, K., Youle, R.J. PINK1 is degraded through the N-end rule pathway. *Autophagy.* 9 (11), 1758–69, (2013).
36. Wiedemann, N. *et al.* Machinery for protein sorting and assembly in the mitochondrial outer membrane. *Nature.* 424 (6948),

565–71 (2003).
37. Thompson, R., Larson, D., Webb, W. Precise Nanometer Localization Analysis for Individual Fluorescent Probes. *Biophysical Journal.* 82 (5), 2775–2783 (2002).

13.5.3 The spatiotemporal organization of mitochondrial F_1F_O ATP synthase in cristae depends on its activity mode

The spatio-temporal organization of mitochondrial F_1F_O ATP synthase in cristae depends on its activity mode

Kirill Salewskij, Bettina Rieger, Frances Hager, Tasnim Arroum, Patrick Duwe, Jimmy Villalta, Sara Colgiati, Christian P. Richter, Olympia E. Psathaki, José A. Enriquez, Timo Dellmann, Karin B. Busch

Abstract

F_1F_O ATP synthase, also known as complex V, is a key enzyme of mitochondrial energy metabolism that can synthesize and hydrolyze ATP. It is not known whether the ATP synthase and ATPase function are correlated with a different spatio-temporal organisation of the enzyme. In order to analyze this, we tracked and localized single ATP synthase molecules *in situ* using live cell microscopy. Under normal conditions, complex V was mainly restricted to cristae indicated by orthogonal trajectories along the cristae membranes. In addition confined trajectories that are quasi immobile exist. By inhibiting glycolysis with 2-DG, the activity and mobility of complex V was altered. The distinct cristae-related orthogonal trajectories of complex V were obliterated. Moreover, a mobile subpopulation of complex V was found in the inner boundary membrane. The observed changes in the ratio of dimeric/monomeric complex V, respectively less mobile/more mobile complex V and its activity changes were reversible. In IF1-KO cells, in which ATP hydrolysis is not inhibited by IF1, complex V was more mobile, while inhibition of ATP hydrolysis by BMS-199264 reduced the mobility of complex V. Taken together, these data support the existence of different subpopulations of complex V, ATP synthase and ATP hydrolase, the latter with higher mobility and probably not prevailing at the cristae edges. Obviously, complex V reacts quickly and reversibly to metabolic conditions, not only by functional, but also by spatial and structural reorganization.

Abbreviations: 2-DG, 2-Deoxy-D-glucose; CM, cristae membranes; EMCCD, electron multiplying charge-coupled device; HK, hexokinase; IBM, inner boundary membrane; ICS, intracristal space; IMM, inner mitochondrial membrane; MSD, mean square displacement; OMM, outer mitochondrial membrane; OXPHOS, oxi- dative phosphorylation; SU, subunit; TALM, tracking and localization microscopy

Introduction

In respiring cells, ATP is mainly provided by oxidative phosphorylation (OXPHOS) involving five membrane protein complexes (CI-CV) in the inner mitochondrial membrane. Their joined task is to oxidize $NADH/H^+$ (complex I) and $FADH_2$ (complex II) to generate a proton motive force across the inner membrane (complexes I, III, IV) and to synthesize ATP (F_1F_O ATP synthase, complex V). Tumor cells, often used in research, usually have a reduced oxidative metabolism and switch to glycolytic energy metabolism – a phenomenon known as the Warburg effect [1,2]. By changing the sugar supply, this can be reversed [3]. Morphology and internal architecture of mitochondria are responsive to mitochondrial function [4–7]. The mitochondrial ultrastructure is modulated by several inner membrane proteins, including the Optic atrophy 1 protein OPA1 [8], compounds of the MICOS complex at the cristae junctions [9–11], and F_1F_O ATP synthase [12]. Moreover, new studies suggest that these main players are functionally coupled, e.g. high OPA1 levels [13] and Mic10/Mic27 [14] apparently stabilize complex V oligomerization. Habitually, F_1F_O ATP synthase assembles into rows of dimers at the small

rims of lamellar or tubular cristae [15,16]. Analysis of distances between complex V by 3D-STORM superresolution suggests that stress conditions affecting respiration also alter complex V dimer organization [17,18]. These observations imply that complex V exhibits specific spatio-temporal dynamics which allows such re-organization. Indeed, single particle tracking and FRAP studies have shown that the complex V is in principal diffusive in the inner membrane [19–21], which suggest that the assembly of complex V into rows of dimers is reversible.

The purpose of this study was to monitor the underlying dynamics of ATP synthase/ATPase organization in response to metabolic switches. We monitored the spatio-temporal organization of complex V with a particular focus on its mobility in the inner membrane. To induce a short-term metabolic switch, the enzyme Hexokinase, which has a key function at the junction between glycolysis and respiration, was inhibited by the non-fermentable sugar 2-Deoxy-$_D$-glucose (2-DG) [22,23]. This resulted in an intermediate depletion of substrate for the respiratory chain, measurable by a decrease in extracellular acidification rate as well as maximal and spare oxygen consumption rate. However, it seems that this decrease did not result in decreased ATP synthesis in mitochondria. On contrary, we found an increased mitochondrial ATP production rate – correlating with a lower mitochondrial membrane potential $\Delta\Psi_m$. As inhibitor studies suggested, ATP hydrolysis - in addition to ATP synthesis - apparently took place before 2-DG treatment. To dissect whether ATPase Inhibitory Factor 1 (IF1) and spatial separation of ATP synthesis and hydrolysis might be a clue, we determined the localization and mobility of complex V molecules
under different conditions. Therefore, we fluorescence-labeled complex V and recorded its localization and dynamics on the single molecule level by means of Tracking and Localization Microscopy (TALM) [19,24]. Trajectories of F_1F_O ATP synthase particles were obtained from single particle tracking experiments with the Multiple-Target Tracing Algorithm (MTT) [25]. We found that increased ATP synthesis in 2-DG treated cells was accompanied by a slight decrease of the dimer/ monomer ratio and a narrowing of cristae. In addition, the complex V showed a different localization pattern in cristae, with decreased diffusion coefficients. When ATP synthesis decreased again, complex V reorganized and showed the same localization and mobility pattern as before. Furthermore, cristae widened again. Moreover, complex V diffusion was decreased upon chemically inhibition of ATP hydrolysis, but increased under conditions where the factor for physiological inhibition of ATP hydrolysis was knocked out. Thus, our data show that spatio-temporal organization of complex V is determined by the specific metabolic setting, which here was given as a reversible inhibition of glycolysis.

Materials and methods

Cell culture and labeling

Stable transfected HeLa cells expressing SU γ-HaloTag® were cultivated in Minimal Essential Medium Earle's Salt (5.6 mM glucose + $_L$- glutamine) supplemented with 10% FBS (Fetal bovine serum), 1% HEPES and 1% NEAA (non-essential amino acids) at 37 °C and 5% CO_2. When confluence was reached, cells were split using 1 mL Trypsin/ EDTA for 5 min at 37 °C (and 5% CO_2). Labeling and preparation of single molecule studies is described in detail elsewhere [19,24].

Metabolic studies

Oxygen consumption rates (OCR) and extracellular acidification rates (ECAR) of intact HeLa cells were recorded with the Seahorse XF^e 96 Extracellular Flux Analyzer (Agilent Technologies). 25.000 cells were seeded per well of a 96-well XF cell culture microplate 24 h before the experiment. Before loading into the XF^e Analyzer, control cells were washed with XF base medium adjusted to pH 7.4 (Minimal DMEM, 0 mM Glucose, 102353-100 from Agilent), placed in fresh XF base medium pH 7.4 with supplements (1 mM pyruvate, 2 mM $_L$-glutamine, and 5.6 mM $_D$-glucose) and shortly incubated at 37 °C. Supplements were from Carl Roth GmbH + Co. KG. To inhibit glycolysis, 30 mM 2- Deoxy-D-glucose (2-DG, Sigma Aldrich) was added to the 5.6 mM glucose MEM and XF base media with supplements. After recording resting respiration in the analyzer, a mitochondrial stress test was performed. Therefore, the following chemicals from Seahorse Biosciences were added sequentially to the cells: oligomycin (1 μM) to inhibit the ATP synthase; trifluoromethoxy carbonylcyanide phenylhydrazone

(FCCP, 0.5 µM) an uncoupler of respiration and ATP synthesis, and inhibitors for complex I (rotenone; 0.5 µM) and complex III (antimycin A; 0.5 µM). In each experiment, three time points with a 6 min interval were recorded for the basal oxygen consumption rate (OCR). In a second experiment analyzing mitochondrial fuel usage, the following chemicals from Agilent (former Seahorse Biosciences) were added sequentially to the cells: UK5099 (2-Cyano-3-(1-phenyl-1H- indol-3-yl)-2-propenoic acid, 2 µM), to inhibit the glucose oxidation pathway by blocking the mitochondrial pyruvate carrier (MPC); BPTES (Bis-2-(5-phenylacetamido-1,3,4-thiadiazol-2-yl) ethyl sulfide, 3 µM),
an allosteric inhibitor of glutaminase (GLS1), to inhibit the glutamine oxidation pathway; Etomoxir (4 µM), to inhibit long chain fatty acid oxidation by blocking the carnitine palmitoyl-transferase 1A (CPT1A). By subsequent addition of the inhibitors of metabolic pathways (glucose, GLC; glutamine, GLU and fatty acid, FA catabolism), fuel dependency was determined. Three measurements were conducted for the resting OCR, five after the first injection and five after the second injection with a 2-min interval of recording followed by 2 min of mixing and 2 min of incubation for each measurement. In a third experiment referred to as ATP rate assay, XF base medium pH 7.4 with additional supplementation of 5 mM HEPES was used. The assays to dissect mitochondrial from glycolytic ATP synthesis rates follows suggestions made by Mookerjee and co-workers [41]. Injections: Oligomycin (1.5 µM) to inhibit the ATP synthase; inhibitors for complex I (rotenone;
0.5 µM) and complex III (antimycin A; 0.5 µM). Inhibitors were purchased from Agilent (Agilent Seahorse XF Real-Time ATP Rate Assay Kit 103592-100). Agilent Seahorse XF technology measures the flux of both H^+ production (ECAR) and O_2 consumption (OCR), simultaneously. By obtaining OCR and ECAR data under basal conditions and after serial addition of mitochondrial inhibitors (oligomycin and rotenone/antimycin A), total cellular ATP Production Rates and pathway-specific mitoATP and glycoATP Production Rates can be measured. The series of calculations used to transform the OCR and ECAR data to ATP Production Rates is performed using the Agilent Seahorse XF Real-Time ATP Rate Assay Report Generator, described in the according user guide. Briefly: Glycolytic ATP Production Rate (pmol ATP/ min) = glycoPER (pmol H^+/min) is associated with the conversion of glucose to lactate in the glycolytic pathway; Mitochondrial ATP production rate: OCR_{ATP} (pmol O_2/min) = OCR (pmol O_2/min) - OCR_{Oligo} (pmol O_2/min) is associated with oxidative phosphorylation in the mitochondria. Total ATP production rate: Glycolytic ATP Production Rate + Mitochondrial ATP Production Rate. Cell counting: Cell number per well was measured after ATP rate assay performance by counting fluorescently labeled nuclei from images captured by Cytation 1 (BioTek). Therefore, cells were stained with 2 µg/mL Hoechst 33342 (Sigma) and the nuclear images were captured using a 4× lens with a DAPI filter. Cells (the individual nuclei) were counted by BioTek Cytation 1 using the XF Cell Imaging and Counting software2 and data was normalized in Wave software.

Generation of IF1-KO cell lines

The IF1-knockout cells were manufactured using the CRISPR/Cas technique. The first step was to find the appropriate targeting sequence for crRNA in the vicinity of the START codon. The crRNA was cloned into the pSpCas9(BB)-2A-GFP (PX458) vector (Addgene). Thus, the resulting vector contained both sgRNA and Cas9 nuclease. To enable selection with Puromycin, the *pac* gene was inserted at the cutting site. For this purpose, a construct was cloned with homologous arms to the right and left of the place where Cas9 is to be cut with the *pac*-gen in between. HeLa cells were cotransfected with both constructs and transformed cells were selected by Puromycin treatment. Positive clones were isolated and the IF1 knockdown tested by qPCR.

ROS measurements

Before staining, culture medium was exchanged to PBS (phosphate buffered saline w/o Ca^{2+} and Mg^{2+}) plus 1% FBS (fetal bovine serum). For ROS detection, cells were stained with 2.5 nM of CellROX™ Deep Red ($\lambda_{ex/em}$~644/665 nm) in PBS for 30 min. After washing twice with PBS, flow cytometry analysis was performed with the adequate laser and band pass filter (exc. 660/10 nm, em. 690/50 nm). For the time course of ROS levels in dependency on 2-DG application, microscopic

analysis was conducted (cLSM, 63× objective). HeLa cells that stable expressed a matrix-targeted GFP were stained with the ROS sensitive
dye MitoTracker®CM-H2XRos Red (200 nm for 30 min) and then washed twice with PBS. MitoTracker Red CM-H2XRos is a reduced, non-fluorescent version of MitoTracker Red (M-7512, Thermofisher) that fluoresces upon oxidation. The emission of MitoTracker Red CM- H2XRos was set to 600–700 nm (exc. 579 nm). For imaging, medium without phenol red was used. Before 2-DG application (30 mM), cells were imaged (t = 0 min). Every 5 min, several images were taken at different positions to minimize photobleaching effects. N = 3 technical replicates. The fluorescence intensities were analyzed with ImageJ (MacBiophotonics). The ROS signal was normalized to the mt-GFP signal.

Measurement of mitochondrial membrane potential

Mitochondrial membrane potential $\Delta\Psi_m$ was measured using the $\Delta\Psi_m$ sensitive dye tetramethylrhodamine ethyl ester (TMRE, 7 nM) [26]. The dye was excited at 561 nm, and the emission recorded between 600 and 700 nm at a fluorescence microscope. For normalization on the mitochondrial mass, mitochondria in addition were stained with MitoTracker™ Green (MTG, 100 nM). The fluorescence of MTG is supposed to be membrane potential independent [27]. MTG was excited at 488 nm, emission was recorded between 510 and 540 nm. *Z*-stacks of 7 slices (step size of 360 nm) were recorded. The fluorescence intensity was analyzed with ImageJ (MacBiophotonics). The ratio of the TMRE/ MTG signal indicates the relative value of the $\Delta\Psi_m$.

Fluorescence microscopy

Fluorescence imaging was carried out with confocal laser scanning microscope (Leica TCS SP8 SMD) equipped with a 63× water objective (N.A. 1.2) and a tunable white light laser. HyD's with GaASP photocathodes were used as detectors. Measurements were performed at 37 °C and 5% CO_2. For determination of fluorescence intensities of fluorescent dyes specifically accumulating in mitochondrial compartments, mean grey values of the whole mitochondrial network are measured after automatic clustering-based image thresholding by application of the Otsu's thresholding in the open source Fiji program.

ATP determination

Relative ATP was determined by using a FRET sensor composed of the ε-subunit of complex V from Bacillus spec. sandwiched betwee Clover and m mRuby2 (Clover-ATeam-mRuby2), modified from the original ATeam [28]. FRET was determined via fluorescence lifetime (τ) decrease of the donor with increasing ATP. τ was determined in the time domain with a time correlated single photon counting device (Piqoquant/Leica) docked to the cLSM. Clover was excited at 488 nm with a pulsed white light laser (40 MHz), emission was recorded from 520 to 560 nm using a BS560, Bandpass filter I BP500-550. For the decay histograms, at least 1000 photons were collected per pixel.

Single molecule tracking and localization microscopy

Single molecule tracking and localization was performed at a room temperature with an inverted microscope (Nikon, Eclipse TE2000) equipped with a TIRF condenser, an oil immersion objective designed for TIRF (100× oil/N.A. 1.49/0.12 Apochromat, Nikon), an EMCCD camera (Evolve™512, Photometrics, 512 × 512 pixel imaging array, 16 µm × 16 µm pixel area). To fulfil the Nyquist-oversampling, a 1.5x magnitude focussing lens was used. A quad line beam splitter (zt405/ 488/561/633–640) was mounted in combination with an emission quadband filter (HC 446 nm/523 nm/600 nm/677 nm). A 561 nm laser (Melles Griot, 20 mW, DPSS) was coupled into the device via a singlemode glass fiber (FC/PC). The measurements were performed as described before [29]. In short, HeLa cells stable transfected with F_1F_O ATP synthase subunit ɣ fused C-terminally to a HaloTag were posttranslationally labeled with TMR^{HTL} (1 nM) for 20 min, washed twice in PBS and once in medium without phenol red before imaging. Assembly and correct intramitochondrial localization were shown earlier with constructs where similar sized EGFP and pHluorin, respectively, were genetically fused to the same position in SU γ as exchange of by the HaloTag7 [30,31]. The TMR^{HTL} concentration was set

for sub-stoichiometric labeling and low enough to visualize single molecule signals. The incident angle was set to achieve a highly inclined laminated optical light sheet [32]. Usually, 3000 frames were recorded. Frame rates were 33 Hz and 50 Hz, respectively. Individual signals with a signal to noise ratio above 5 were fitted with a 2D Gaussian fit for localizing molecules. From all frames, a cumulative localization map was generated after movement of mitochondria during the recording time was excluded. For generating trajectory maps, single molecules in subsequent frames were connected when the following criteria were matched: they must have been within a radius of maximal 2 px (pixel size 107 nm) and the intensity distribution profile must have been identical. Only trajectories with a minimum duration of 160 ms were analyzed.

Theoretical background

Single fluorescent molecules, whose size is below the diffraction limit, project a three-dimensional diffraction pattern onto the image plane, which is defined as the point spread function (PSF). The PSF can be calculated by Abbe's law and used to localize single emitters by a 2D Gaussian fit [33–35]:

$$d = \frac{\lambda}{2NA} = \frac{\lambda}{2n * \sin(\theta)}$$

with d being the diameter of the PSF, λ as the wavelength of the emitted light and NA being the numerical aperture of the microscope's objective. The numerical aperture describes the light gathering capability of an objective and depends on the refractive index n of the medium in which the lens is used and the half angular aperture of the objective θ. The "full width at half maximum" (FWHM) criterion is used to describe a PSF, whereby FWHM is the width at 50% of the intensity maximum. For TMR ($\lambda_{em.} = 582$ nm) and an objective with NA of 1.49, the PSF diameter is approximately 390 nm. According to the Rayleigh criterion, the resolution of the system is:

$$r = \frac{1.22\lambda}{2NA} = \frac{0{,}61\lambda}{n * \sin(\theta)}$$

where r is the minimal distance between the two objects. n is the refractive index of the medium between the objective and sample, λ is the wavelength of the emitted light, θ is the half angular aperture of the objective and NA is the numerical aperture of the microscope objective. Practically, this means that two separate light points can just be distinguished if the intensity maximum of the first point coincides with the first intensity minimum of the second point. Here, the theoretical resolution is ~240 nm. The pixel size was 106.7 nm for an EMCCD camera (512 × 512 px chip) with a pixel area of 16 µm × 16 µm, thus fulfilling the Nyquist-Shannon sampling theorem which demands a 2fold oversampling rate for the desired spatial resolution. In order to probe the spatio-temporal behavior of F_1F_O ATP synthase, the multi-target tracer was used [25]. The first step of single-particle tracking (SPT) involves the localization of the particle by a 2D Gaussian fit. The accuracy of this localization highly depends on the occurrence of discrete signals, the pixel size of the EMCCD/CMOS camera and the photon emission of the molecule as well as the background noise:

$$\sigma_{\mu i} = \sqrt{\left(\frac{s_i^2}{N}\right) + \left(\frac{a^2/12}{N}\right) + \left(\frac{8\pi s_i^4 b^2}{a^2 N^2}\right)}$$

where σ is the standard error of the mean value of photon distribution, N is the number of gathered photons, a is the pixel size of the EMCCD/ CMOS detector, b is the standard deviation of the background and s_i is the standard deviation in dimension i, with i being either x or y dimension.

Single molecule localization and tracking

Single molecules are recorded over several frames and then are localized by a 2D Gaussian mask. The multiple-target tracing algorithm (MTT) [25] is used to generate trajectories. To obtain diffusion data,

the mean square displacement is determined (MSD) and the diffusion coefficient is calculated according to:

$$r^2 = 2n4D\Delta t^{\alpha} + 4\varepsilon^2$$

$$D = \frac{r^2 - 4\varepsilon^2}{2n4\Delta t^{\alpha}}$$

where r^2 is the MSD, D is the lateral diffusion coefficient, Δt is the lag time, n is the dimension and ε is the localization error. The exponent α is a factor that distinguishes modes of diffusion, with $\alpha < 1$ for anomalous diffusion. Anomalous diffusion is expected when the movement of particles is restricted by structural constraints such as physical obstacles or inclusion in micro-compartments. Further details are found in Appelhans et al. [29].

Transmission electron microscopy

For transmission electron microscopy (TEM) HeLa cells from the different conditions were fixed for 2 h at room temperature (RT) in 2.5% glutaraldehyde (Sciences Services, Germany) and in 0.1 M cacodylate buffer pH 7.4 (Sciences Services, Germany), subsequently washed in 0.1 M cacodylate buffer pH 7.4, post-fixed for 2 h at RT in 1% osmium tetroxide/0.8% potassium ferrocyanide in 0.1 M cacodylate buffer pH 7.4, dehydrated stepwise in a graded ethanol series and em- bedded in Epon 812 (Fluka, Buchs, Switzerland). Ultrathin sections (70 nm, ultramicrotome EM UC7, Leica, Wetzlar, Germany) were afterwards stained for 30 min with 1% uranyl acetate (Leica, Germany) and 20 min in 3% lead citrate (Leica, Germany). TEM images were acquired with a 200 kV transmission electron microscope (JEM2100- Plus, Jeol Japan). The cristae width was determined as following: TEM images were inverted. Line plots were perpendicularly placed to the length of cristae (ImageJ™). The line plot intensity profiles showed two peaks corresponding to the intensity of the negative stained membranes. The distance between the peaks was taken as cristae width. Per crista, two to three line plots were drawn for the determination of the crista width.

Blue Native page electrophoresis assays

Mitochondria from the indicated cell lines were isolated as follows.

HeLa cells were cultured in Minimum Essential Medium Eagle (MEM) supplemented with 10% fetal calf serum (FCS); 1% non-essential amino acids (NEAS), 1% HEPES, and 1% glutamine (MEM++) in T175 flask and maintained in 37 °C with 5% CO_2 during the experiment. For starvation, the medium was aspired and exchanged to fresh MEM++ supplemented with 30 mM sterile 2-DG. For mitochondrial isolation we used the cell homogenizer (Isobiotec, Germany) combined with 1 mL Glas syringes (Hamilton, USA) as described in Schmitt et al. [36]. Cells were trypsinized and separated with syringe before homogenization. All steps were performed on ice, the Isolation buffer was freshly prepared, and all materials used were pre-cooled before each isolation. For HeLa cells, the 6 mm Tungsten carbide ball was used. Isolation buffer: 300 mM Sucrose, 5 mM TES, 200 µM EGTA, pH should be adjusted with KOH to 7.2. Protein concentration was determined via the Bradford method using BSA as a standard. 50 µg protein were loaded per pocket. Mitochondria were further processed in the presence of Digitonin 6 g/g Mitochondria [37]. Dimers of ATP synthase were resolved by mean of high resolution Blue Native electrophoresis as described in Witting et al. 2007 [38]. After separation on a 3–13% gel, the proteins were electro-blotted onto Hybond-P-polyvinylidene fluoride (PVDF) membranes (GE Healthcare) and immune-blotted with a primary anti- body against subunit β of ATP synthase (Abcam 14730, mouse mono- clonal). The secondary antibody was anti-mouse dylight 800 from Rockland (610145002) and the signal detected using the Odyssey® In- frared Imaging System (Li-COR bioscience). The densito-metric analysis of the ratio between monomer and dimer of ATP synthase was performed using Gel Eval™ software.

Western blotting

Cells were washed twice in PBS and extracted in sample buffer. Depending on the confluency, 50 µL to 150 µL of SDS sample buffer was added to each well (0.83% SDS; 6.25 mM TRIS; 7.25% Glycerine; 0.0083% MercaptoEtOH; 0.01% Bromphenol blue) plus 0.1 µL Benzonase® nuclease was added to the reaction tubes. The solution was incubated at RT for 10 min. The extracted proteins were separated by SDS-PAGE and then transferred onto a polyvinylidene difluoride (PVDF) membranes by semi-dry blotting. Detection of OXPHOS complexes was done with a total rodent OXPHOS antibody cocktail (Abcam, Ab110413). Subunit β was detected with an anti-ATP5B antibody (proteintech #17247-1-AP), VDAC with an anti-VDAC antibody (Cell signalling #4661), subunit e with an anti-ATP5I antibody (abcam #122241). For the detection of bands, enhanced chemiluminescent substrate consisting of a 1:1 mix of Luminol/Enhancer & Peroxide solution was used.

Statistical analysis

Statistical analysis was performed using OriginPro version 9.6, 2019 (OriginLab Cooperation, Northhampton, MA). Student's *t*-test or ANOVA was used with subsequent post hoc test (Scheffé-Test) or pairwise comparisons if applicable (as indicated). For the calculation of the ratio dimer/monomer ($k = D / M$) the ratio k was treated as a function of two variables k (D, M). According to the error propagation law of Gauss, the partial derivative of each variable must first be formed from this function. Partial derivation to D means, for example, that the function is differentiated to D and M is regarded as a constant. For the calculated value k, the error σ is obtained according to:

$$\sigma = \sqrt{\left(\frac{1}{M}\right)^2 * \sigma_D^2 + \left(-\frac{D}{M^2}\right)^2 * \sigma_M^2}$$

Results

2-DG-caused HK inhibition leads to decreased glycolytic but increased mitochondrial ATP synthesis rates

First, we investigated the effect of glycolysis inhibition on mitochondrial oxidative phosphorylation (OXPHOS) in mammalian cervical carcinoma cells (HeLa). HeLa cells are metabolically flexible and thus a suitable model system [39]. The cells were cultivated with quasi physiological concentrations of glucose (5.6 mM) for several passages. The inhibition of glycolysis was initiated by the addition of 2-Deoxy-D- glucose (2-DG) in 5-fold excess (30 mM) to the carbon source glucose (5.6 mM) for up to 5 h. The mitochondrial respiratory function and aerobic glycolysis were then analyzed with an extracellular metabolic flux analyzer (Agilent/Seahorse). Although 2-DG was present all the time, we found a time-dependent inhibitory effect on respiration that was strongest in the first hour. 30 min after addition of 2-DG, respiration, measured as oxygen consumption rates (OCR) were reduced to 63%, but recovered to 75% in the next 30 min and then showed a continuous decrease (Fig. 1A). The decline was stronger than in the control without 2-DG. In parallel, the extracellular acidification rate (ECAR) as a measure of glycolysis, was recorded. The decrease in ECAR was also strongest in the first 30–60 min after 2-DG addition (Fig. 1B).

In the control, ECAR finally increased in response to rotenone and antimycin A, suggesting that extracellular acidification was mainly caused by glycolysis and not by TCA cycle activity [40]. This was not the case for the 2-DG probe, suggesting TCA cycle activity instead of glycolytic activity under inhibitory conditions.

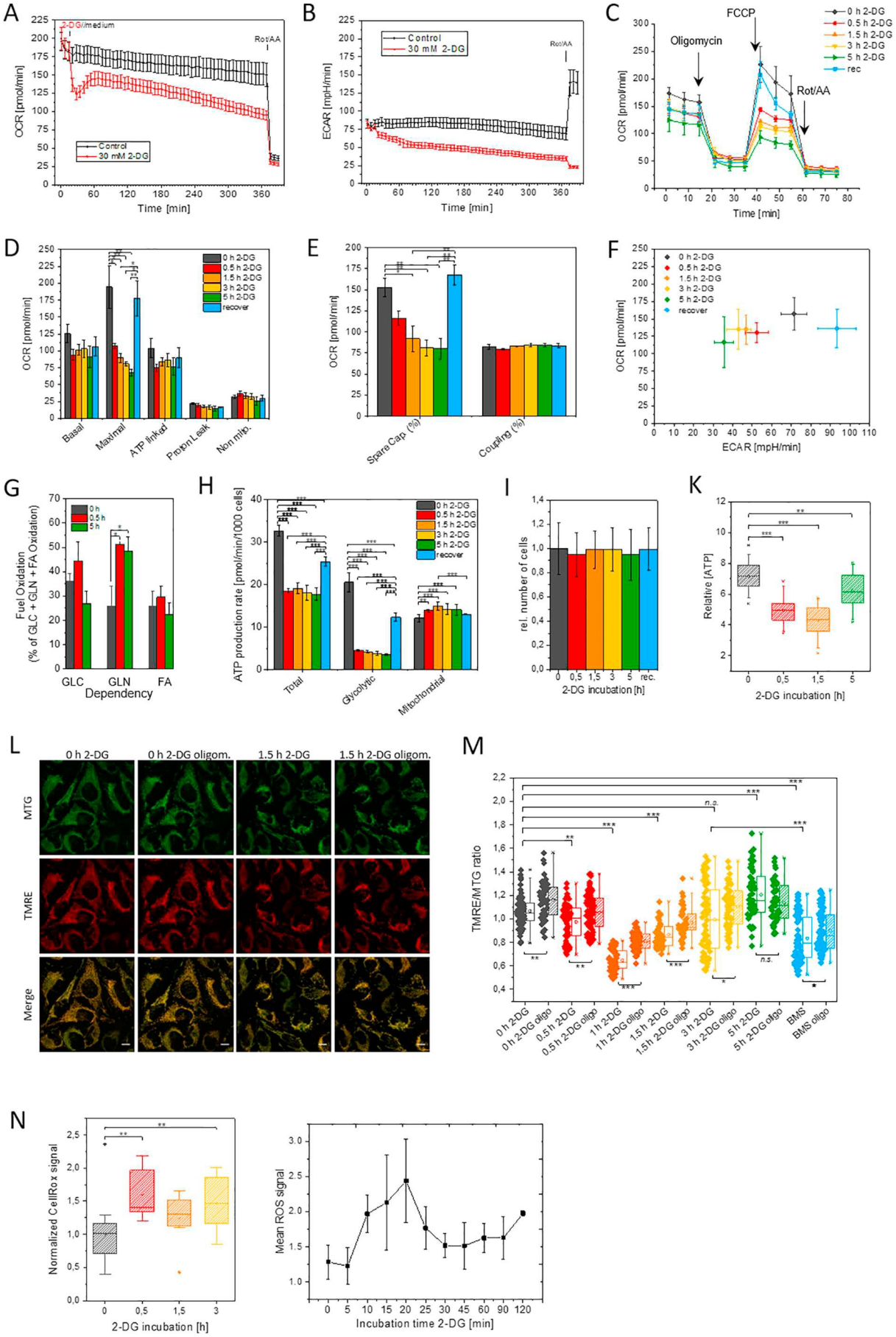
A
2-DG/medium
Rot/AA
Control
30 mM 2-DG
OCR [pmol/min]
Time [min]
B
Control
30 mM 2-DG
Rot/AA
ECAR [mpH/min]
Time [min]
C
FCCP
Oligomycin
Rot/AA
0 h 2-DG
0.5 h 2-DG
1.5 h 2-DG
3 h 2-DG
5 h 2-DG
rec
OCR [pmol/min]
Time [min]
D
0 h 2-DG
0.5 h 2-DG
1.5 h 2-DG
3 h 2-DG
5 h 2-DG
recover
OCR [pmol/min]
Basal
Maximal
ATP linked
Prot.n Leak
Non mit.
E
OCR [pmol/min]
Spare Cap. (%)
Coupling (%)
F
0 h 2-DG
0.5 h 2-DG
1.5 h 2-DG
3 h 2-DG
5 h 2-DG
recover
OCR [pmol/min]
ECAR [mpH/min]
G
0 h
0.5 h
5 h
Fuel Oxidation
(% of GLC + GLN + FA Oxidation)
GLC
GLN
FA
Dependency
H
0 h 2-DG
0.5 h 2-DG
1.5 h 2-DG
3 h 2-DG
5 h 2-DG
recover
ATP production rate [pmol/min/1000 cells]
Total
Glycolytic
Mitochondrial
I
rel. number of cells
0
0,5
1,5
3
5
rec.
2-DG incubation [h]
K
Relative [ATP]
0
0,5
1,5
5
2-DG incubation [h]
L
0 h 2-DG
0 h 2-DG oligom.
1.5 h 2-DG
1.5 h 2-DG oligom.
MTG
TMRE
Merge
M
TMRE/MTG ratio
n.s.
0 h 2-DG
0 h 2-DG oligo
0.5 h 2-DG
0.5 h 2-DG oligo
1 h 2-DG
1 h 2-DG oligo
1.5 h 2-DG
1.5 h 2-DG oligo
3 h 2-DG
3 h 2-DG oligo
5 h 2-DG
5 h 2-DG oligo
BMS
BMS oligo
N
Normalized CellRox signal
0
0,5
1,5
3
2-DG incubation [h]
Mean ROS signal
Incubation time 2-DG [min]

Fig. 1. Effect of glycolysis inhibition on mitochondrial respiration and physiology. (A–B) Mitochondrial oxygen consumption rates (OCR) and extracellular acidification rates (ECAR) when inhibiting glycolysis with 2-DG over an extended period of time ($N = 2$). (A) Effect of 2-DG-induced inhibition of glycolysis on oxygen consumption rate. After 6 h rotenone and antimycin A (Rot: 0.5 μM; AA: 0.5 μM) were added. (B) Parallel determination of ECAR under the same conditions. (C) OCR of HeLa cells under normal conditions (0 h, dark grey), 0.5 h (red) 1.5 h (orange), 3 h (yellow), 5 h (green) after 2-DG application and after recovery (=3 h 2-DG followed by 2 h normal medium, blue) ($N = 3$ independent experiments). Time point 5 h is not shown here. After basal respiration monitoring, oligomycin (1 μM), uncoupler FCCP (trifluoromethoxy carbonylcyanide phenylhydrazone; 0.5 μM), rotenone and antimycin A (Rot, 0.5 μM; AA, 0.5 μM) were added at the indicated times to determine ATP linked respiration, maximum respiration and OXPHOS specific oxygen consumption, respectively. (D) OCR results for all time points including recovery conditions. Statistics were performed on means. (E) Spare capacity and coupling during 2-DG treatment (both in %). Statistics were performed on means. (F) Ratio of oxygen consumption (OCR) to extracellular acidification rate (ECAR) for metabolic phenotyping. (G) Fuel dependency change under 2-DG induced starvation. GLC: glucose, GLN: glutamine, FA: fatty acids ($N = 3$). 2-DG inhibition induces increased glutamine metabolism after 0.5 h. Statistics were performed on means; One Way ANOVA with post hoc Fisher LSD. (H) Dissection of glycolytic and mitochondrial ATP production rates. (I) 2-DG inhibition does not affect the cell number during the measurement time. Fluorescently labeled nuclei from images captured by Cytation 1 were counted. (K) Relative changes in cytosolic ATP levels determined by a modified ATeam, a FRET sensor for ATP [29] ($N = 2$). (L) Effect of 2-DG and oligomycin on mitochondrial membrane potential ($\Delta\Psi_m$), mass and morphology. TMRE (tetramethylrhodaminethyl ester, 7 nM) was used as $\Delta\Psi_m$ sensitive dye and MitoTracker™Green (MTG, 100 nM) as mitochondrial mass indicator [43]. (M) Effect of ATP synthase inhibition by oligomycin and ATPase inhibition by BMS-199264 during 2-DG treatment on $\Delta\Psi_m$. Oligomycin (1 μM), BMS (5 μM), 2-DG (30 mM), medium glucose (5.6 mM). Box and whisker plots: The boxes represent the 25th to 75th percentiles. The vertical lines in the boxes represent the median values, while the square symbols in the boxes represent the respective mean values. The minimum and maximum values are marked with x. Statistics: One Way ANOVA with post hoc Tukey test and Students *t*-test for pairwise comparison. $^{*}P \leq 0.05$; $^{**}P \leq 0.01$; $^{***}P \leq 0.001$. (N) For determination of mitochondrial ROS, cells stained with CellROX Deep Red were analyzed via flow cytometry analysis (left graph). Moreover, MitoTracker Red CM-H2XRos stained cells were analyzed with a fluorescence microscope (right graph). Statistics: One Way ANOVA with post hoc Tukey test (if not stated otherwise) performed on single values (if not stated otherwise). All measurements were performed at 37 °C. Scale bars: 10 μm (L).

Next, the mitochondrial stress test was performed. The maximum respiration was measured in the presence of an uncoupler, here trifluoromethoxycarbonyl cyanide phe- nylhydrazoneane (FCCP), after complex V inhibition with Oligomycin (Fig. 1C). In the time period measured (0.5 h–5 h after initial addition of 2-DG), maximal respiration and spare capacity were reduced (Fig. 1D, E). If 2-DG containing medium was replaced by standard medium for another 2 h after 3 h incubation (=recover), a restoration of maximal respiration to > 90% of the control state was observed. The coupling efficiency was not affected by 2-DG treatment. For metabolic phenotyping, the OCR/ECAR ratio was plotted and revealed a decrease of the extracellular acidification rate as measure for glycolysis due to 2-DG inhibition and as well as attenuation of respiration (Fig. 1F). The fact that there were only slight differences in OCR between 0.5 h and 5 h indicates the use of a different fuel for respiration. In a fuel test, glucose, glutamine and fatty acids were added in combination with inhibitors for the different catabolic pathways (UK5099 for glycolysis; etomoxir for FA oxidation and BPTES for glutamine conversion to glutamate). The result shows that mitochondria became more dependent on glutamine metabolism after glycolysis inhibition, whereas fatty acids were apparently not used as an alternative energy source during measurements (Fig. 1G). This is in accordance to the increased TCA cycle activity observed before (Fig. 1B). To test for ATP synthesis, we included an assay to determine mitochondrial versus glycolytic ATP synthesis as recently established [41]. It revealed that mitochondrial ATP production was increased during 2-DG treatment, while glycolytic ATP production was significantly reduced (Fig. 1H). Notably, 2-DG treatment did not cause a reduction in cell number (Fig. 1I). Next, we determined the cytosolic ATP levels with a genetically encoded fluorescence probe known as ATeam. ATeams consist of the ATP-binding subunit ε of a *Bacillus sp*., which is located between a fluorescent donor and an acceptor protein [28,42]. After ATP-binding, conformational changes increase Förster resonance energy transfer (FRET) and shorten the fluorescence lifetime of the donor. We exchanged the donor for the fluorescence protein Clover, and the acceptor for mRuby2, which resulted in a Clover-SU-ε-mRuby2 ATeam construct. To monitor cytosolic ATP changes, the fluorescence lifetime of the donor was recorded by fluorescence lifetime imaging microscopy (FLIM). The data show that the cellular ATP level decreased significantly between 0.5 and 1.5 h of glycolysis inhibition (Fig. 1K). After 5 h the ATP values had risen again. Although 2-DG was still present, this was not reflected in the glycolytic ATP production rate values, (Fig. 1H).

The mitochondrial membrane potential is reduced during the attenuation of respiration due to ongoing ATP synthesis

The active complexes I, III and IV pump protons into the intra cristae space and generate an electrochemical gradient or membrane potential ($\Delta\Psi_m$). We asked how the decrease in respiratory activity following glycolysis inhibition affected $\Delta\Psi_m$. We used tetramethylrhodaminethyl ester (TMRE) to measure $\Delta\Psi_m$ under normal conditions and during inhibition of glycolysis and respiration. TMRE is distributed in active mitochondria according to the Nernst equation and in dependence on $\Delta\Psi_m$. An increase in TMRE fluorescence suggests an increased electrochemical gradient or $\Delta\Psi_m$. By means of fluorescence microscopy we determined the mean intensity of TMRE stained mitochondria in single cells and normalized the signal on the MitoTracker™Green signal, which is a mitochondrial mass indicator [43]. To check the contribution of ATP synthase/ATPase to the $\Delta\Psi_m$, oligomycin was added after taking a first round of images (Fig. 1L). Oligomycin treatment resulted in increased $\Delta\Psi_m$, as expected when ATP synthesis was performed before inhibition. We found that 2-DG treatment generally resulted in reduced membrane potential with the lowest level 1 h after first addition of 2-DG, but already 0.5 h after 2-DG application, $\Delta\Psi_m$ was decreased ($P \leq 0.01$). The $\Delta\Psi_m$ recovered in the next few hours despite the presence of 2-DG (Fig. 1M). The level of respiratory complexes I, II and V did not change during 2-DG treatment, but the core subunit I of complex IV displayed a lower signal in immune-detection at time point 0.5 h (Fig. S1). Reduced complex IV activity could also explain the increase in mitochondrial ROS increase after 0.5 h 2-DG treatment (Fig. 1N), and would result in a decreased $\Delta\Psi_m$. Except for 5 h 2-DG treatment in the presence of oligomycin, the $\Delta\Psi_m$ was always significantly higher than with 2-DG alone, indicating that ATP synthesis driven by the proton motive force was performed during the treatment with 2-DG. We next tested the effect of the ATPase specific inhibitor BMS-199264 [44] under control conditions. While the oligomycin treatment increased the $\Delta\Psi_m$, the BMS-199264 treatment significantly decreased the $\Delta\Psi_m$ ($P \leq 0.001$). This would mean that ATP hydrolysis in the absence of the inhibitor contributes to $\Delta\Psi_m$ and is stopped in the presence of BMS-199264. Accordingly, the decrease in $\Delta\Psi_m$ during 0.5-1.5 h 2-DG treatment might also be explained by inhibition of ATP hydrolysis. Mitochondrial morphology was not significantly affected by 2-DG treatment (Figs. S2, S3).

Ultrastructural analysis of mitochondria

It has been reported that cristae narrow in response to starvation [45]. In order to test whether glycolysis inhibition has the same effect, TEM microscope images of mitochondria in a monolayer of cells incubated with 2-DG were quantitatively analyzed in order to determine the average mitochondrial width, the average cristae width, the number of cristae per µm mitochondrial length, and the cristae shape (Fig. 2 and Fig. S1). No significant differences were found when mitochondrial diameter, and number of cristae per length unit of rod-shaped mitochondria was analyzed in the time frame of 0–3 h after inhibition of glycolysis. However, the cristae width narrowed ($P = 0.035$) when glycolysis was inhibited by 2-DG for 0.5 h (14.45 $\pm$ 2 nm) compared to control (15.03 $\pm$ 3.6 nm). The effect was reversible and at 1.5 h after 2-DG there was no significant difference between control and 1.5 h 2-DG treatment. So, similar to earlier studies, where cristae thinning was observed under starvation [45], during short term slowdown of respiration an intermediate decrease in the cristae width was detectable (Fig. 2D).

Glycolysis inhibition alters the spatio-temporal organization of single F_1F_O ATP synthase in the mitochondrial inner membrane

Following, we asked whether these slight variations in ultrastructure and changes in complex V activity were correlated with a different spatial organization of the enzyme. F_1F_O ATP synthase is known to be involved in cristae-shaping [12]. Normally, the F_1F_O ATP synthase is located at the tips and rims of cristae [15,16,46]. However, it is not known how strict this localization/organization is and whether it

is influenced by different modes of complex V activity (e.g. ATP synthesis vs. ATP hydrolysis). Since submitochondrial resolution was required to monitor possible changes in the spatio-temporal organization of complex V, a recently introduced fluorescence superresolution technique - Tracking and Localization Microscopy (TALM) [19,47] - was used to localize F_1F_O ATP synthase in sub-compartments of the inner membrane. For fluorescence labeling, the HaloTag® was fused with the C-terminus of complex V subunit γ as previously described [47] and a stable cell line was generated expressing this construct. Tagging of subunit γ at this position had no effect on respiratory parameters in a stable transfected cell line (Fig. S4). For the specific labeling, the Tetramethylrhodamine- HaloTag® Ligand (TMR^{HTL}) was added for 20 min as fluorescent substrate for the self-labeling HaloTag®. Unbound TMR^{HTL} substrate was then washed out. Due to the low TMR^{HTL} substrate concentrations (1 nM), the complex V labeling was substoichiometric and individual molecules could be differentiated in the flat, peripheral part of the cells in which the mitochondria form a 2D network [29]. In order to reduce the background fluorescence of out-of-focus emitters, a highly inclined laminated optical sheet (HILO) illumination was used for excitation [32]. For a comprehensive localization map of the complex V, 1000–3000 images were recorded (frame rate 33 Hz). Fluorescence signals of individual molecules were fitted with a 2D Gaussian distribution using a calculated point spread function as reference to obtain the precise localization for all particles. In this way, we produced localization maps for complex V at different times after glycolysis inhibition (Fig. 3A). Under control conditions, complex V showed a structured distribution along the longitudinal axis of a mitochondrion (Fig. 3A, left panel). During the first 2 h of glyco- lysis inhibition, the distribution profile changed to a more dispersed one. 2.5 h after addition of 2-DG, a regular, striped distribution pattern of the F_1F_O ATP synthase was visible again in certain areas of the mi- tochondria (Fig. 3A, right panel, white arrowhead).

A change in the localization pattern must be associated with a dynamic rearrangement of the F_1F_O ATP synthase. To test this, the dynamics of the fluorescence-labeled F_1F_O ATP synthase in mitochondria in living cells was determined by single molecule tracking microscopy. For this purpose, trajectories of the mobile F_1F_O ATP synthase were generated: Localized particles in subsequent frames were linked if they were found within a defined maximum distance and if they had the same biophysical footprint (such as intensity). The multi-target tracer (MTT) algorithm [48] was used to identify and connect particles. In- dividual trajectories were colored in different colors (Fig. S5A, B). By overlaying trajectories, which were color-coded according to their temporal occurrence, it was possible to determine whether the mitochondria had moved during the recording time. Data from moving mito chondria have not been

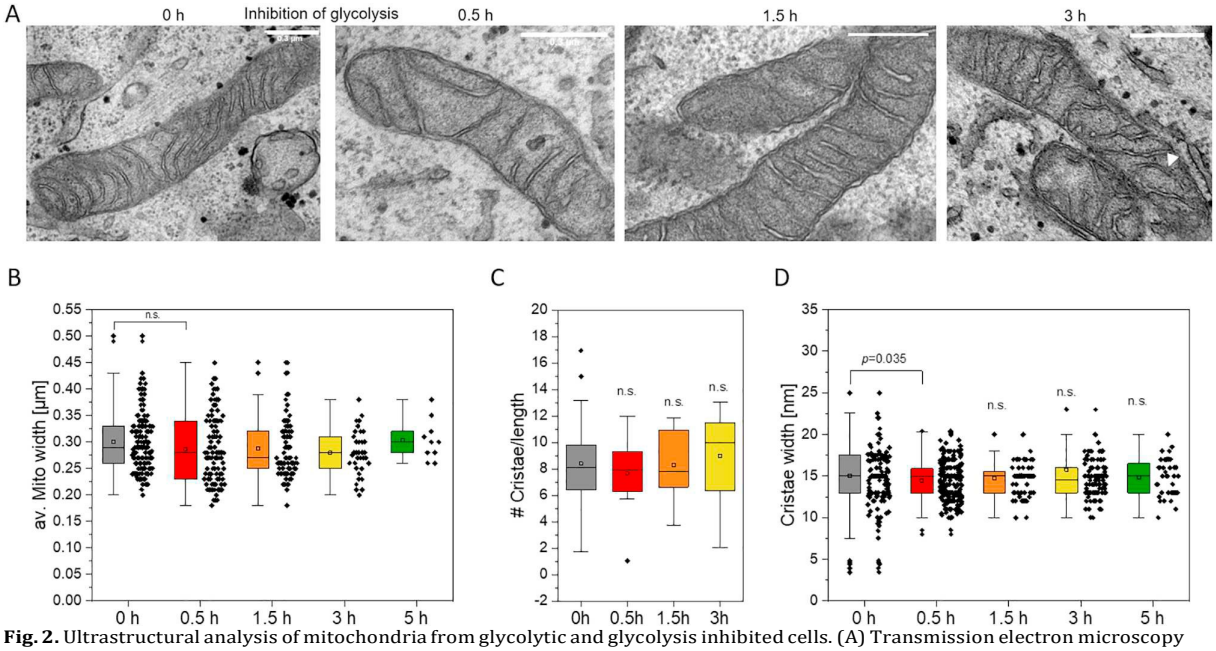

Fig. 2. Ultrastructural analysis of mitochondria from glycolytic and glycolysis inhibited cells. (A) Transmission electron microscopy (TEM) images of single mitochondria at different time points after 2-DG application and metabolic switch. (B) Average mitochondrial width ($N = 2$ independent specimen; $n = 57$ (0 h), $n = 40$ (30 min), $n = 40$ (1.5 h), $n = 36$ (3–5 h) mitochondria). (C) Average cristae width ($n = 224$ cristae, 0 h; $n = 288$ cristae, 0.5 h; $n = 290$ cristae, 1.5 h; $n = 112$ cristae, 3 h), (D) Cristae per length of mitochondrion (μm^{-1}) ($n = 26$, 0 h; $n = 13$, 0.5 h; $n = 19$, 1.5 h; $n = 15$, 3 h). Scale bars: 0.3 µm (A). ANOVA test, $P \leq 0.001^{***}$.

considered (Fig. S5C). The dynamics of the fluorescent F_1F_O ATP synthase particles were recorded over a period of 32 s to 96 s (1000 to 3000 images; 33 Hz) at different times of glycolysis inhibition (0 h, 0.5 h, 1.5 h and 2.5 h) and cumulative trajectory maps were generated. The movement of complex V in tubular single mitochondria is shown in Fig. 4B as a cumulative superposition of recorded trajectories for the times 0 h, 0.5 h and 2.5 h after 2-DG application.

Under normal respiratory conditions, complex V predominatly shows restricted movement in cristae, visible as orthogonal trajectories. This has already been comprehensively analyzed earlier [19,49]. However, within 0.5 h after glycolysis inhibition, the trajectory pattern of the F_1F_O-ATP synthase became more diffuse (Fig. 3B, middle panel). After 2.5 h more orthogonal trajectories appeared again (arrowhead Fig. 3B, right panel). In order to quantify this, mean square displacement diagrams (MSD) were generated (Fig. S6). If only the short-term diffusion (2–5 step sliding intervals) was analyzed, the MSD increased linearly over time for all conditions and time points (Fig. 3C). However, in the presence of 2-DG and glycolysis inhibition, MSD were lower, suggesting reduced complex V movement. When the MSDs were recorded for 2–20 steps, the relation between MSD and time was no longer linear but attenuated, indicating restricted or anomalous diffusion (Fig. 3D). We then calculated the diffusion

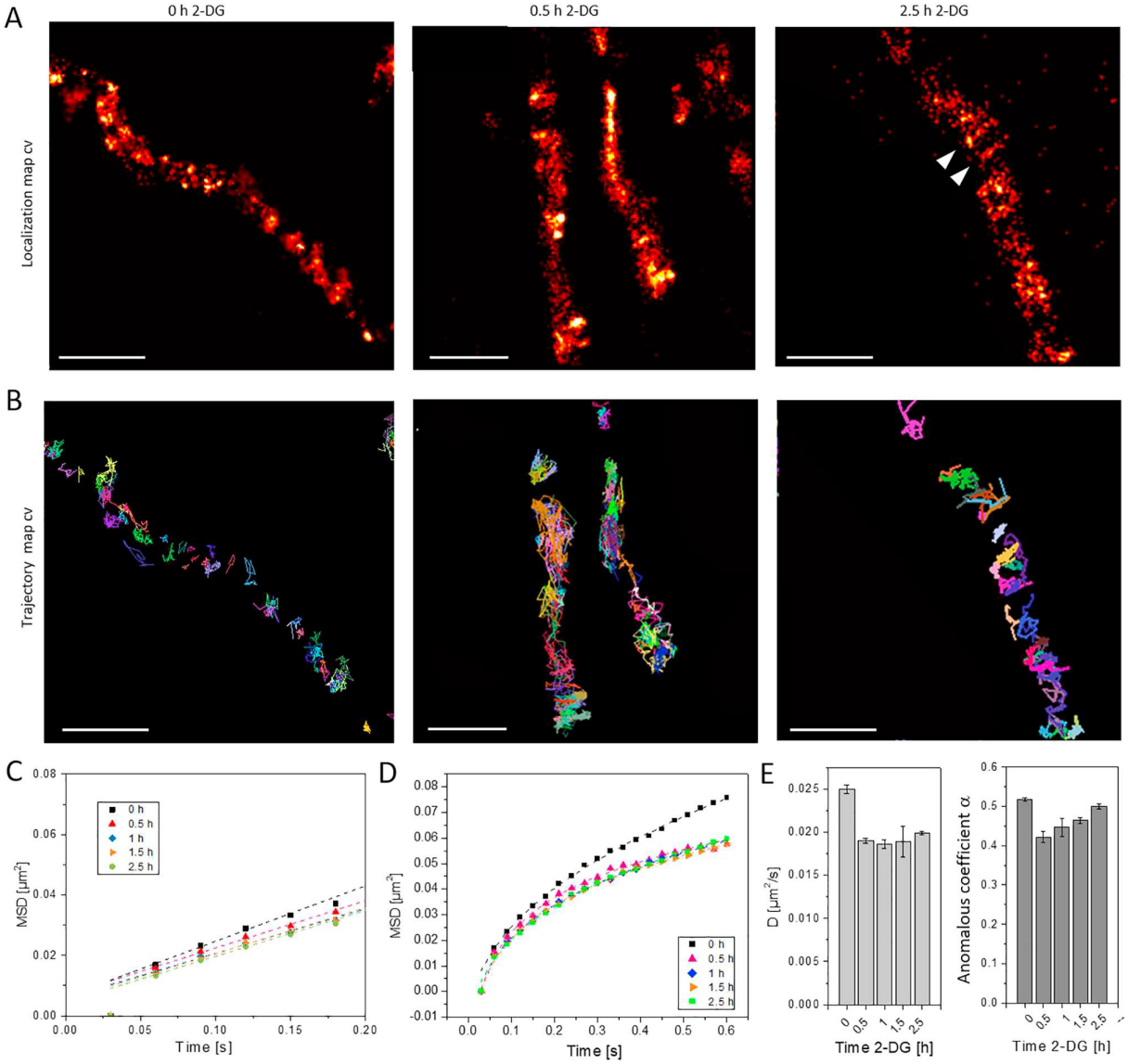

Fig. 3. The localization and dynamics of ATP synthase and ATPase are different. (A) Effects of 2-DG (2-deoxyglucose) on the localization pattern of F_1F_O ATP synthase at different times after 2-DG addition. Localization maps of the single F_1F_O ATP synthase in mitochondria resulting from the summation of up to 3000 images. The application of a Gaussian fit on the PSF of the single molecules resulted in point localized F_1F_O ATP synthase single molecules. Recording rate: 30 fps (33 Hz). Point localizations are false color-coded in *Hot*. (B) Mobility of ATP synthase at different times after onset of glycolysis inhibition with 2-DG. The panels show trajectory maps of the F_1F_O ATP synthase in individual mitochondria resulting from time series between 48 and 96 s (1600–3000 frames), see Movie S1, Movie S2 and Movie S3 in supplementary information. Trajectories of the F_1F_O ATP synthase were generated by using the Multi-Target-Tracing-Tool (MTT). Every single trajectory in one color. (C) Mean square displacement (MSD) diagram showing the linear increase of the MSD in short-term (200 ms) diffusion times. (D) Complete MSD plots covering mean square displacements in the range between 2 and 20 steps (600 ms). (E) Diffusion coefficients and anomalous coefficients calculated from MSD/time diagrams according to Eq. (2). Scale bar: 1 µm (A, B).

coefficients from the MSD according to the formula (2) in section 2.10:
Individual MSD/time diagrams for the different time points of 2-DG inhibition are shown in Fig. S6. The total number of trajectories analyzed per condition is listed in supplementary Table 1.
The calculated diffusion coefficients of complex V in normal cells and in inhibited cells were clearly different and showed a decrease of the average mobility in the latter (Fig. 3E). At the same time, the coefficient α decreased, which correlated with an increased anomalous diffusion. In order to dissect this in detail, we determined the directionality of movement of complex.

Mitochondrial ATPase has a different temporal footprint than ATP synthase

As described earlier, mobile complex V in cristae has a preferred direction of motion orthogonal to the longitudinal axis of the mitochondria [19,]. This is related to the almost exclusive localization of ATP synthase in cristae [49,51,52]. When glycolysis was inhibited and ATPase activity reduced, this motion pattern was clearly changed (Fig. 3B, middle panel). To dissect these changes in more detail, the trajectory map of complex V in mitochondria of an exemplary cell was divided into three areas (#1, blue frame; #2, orange frame; #3, green frame) (Fig. 4A). In area #1 (0s –15 s), trajectories with long step lengths indicate the presence of unrestricted mobile particles, moving in all directions (marked with **m**). In the upper part, a trajectory of an immobile molecule is shown (light blue), marked with **I** (Fig. 4B, left panel, # frame 1). In the lower part, several particles showed an orthogonal direction of motion typical for diffusion in cristae membranes (indicated as **o**). During the next 15 s, further free moving particles appeared in the upper part (**m**), while orthogonally moving (**o**) and immobile molecules (**i**) continued to dominate in the lower part (see Fig. 4B, middle panel, frame #1). Between 30 s and 45 s, mainly orthogonal trajectories were registered in the lower part (Fig. 4B, right panel, frame #1). Next, we quantified the motion in relation to the longitudinal axis of the mitochondria. Therefore, the direction of the successive steps of a moving single molecule was described by a vector. The relative shares of direction were expressed in degree [°] and plotted on a circular disc. The longitudinal axis of a mitochondrion was assigned as covering ± 180° and 0° and the orthogonal axis as −90° and 90°. First, the longitudinal axis of a mitochondrion was drawn manually. Curved mitochondria first required a linearization. For this purpose, the longitudinal axis of a curved mitochondrion was stretched to linearity in order to generate a transformation matrix (Fig. S7C). For the vector analysis, the integrated change of direction between the first and the fifth step was determined and then plotted on the directionality disk (Fig. S7D). This analysis also made it possible to determine the diffusion coefficients *D* for the movement along the longitudinal axis and in the orthogonal direction independently of each other by generating separate MSDs (Fig. S8). The derivation of diffusion coefficients in dependence on time shows that the physical constraint imposed by the cristae architecture reduces the mobility (lower $D_{orthog.}$) compared to movement along the tubular shape of the IBM (Fig. S8E).
The directional analysis of the areas framed in Fig. 4A shows that in the area #1 trajectories with orthogonal direction (−90° and 90°) prevail. This indicates an organization in the cristae sheet. In contrast, the trajectories in the areas #2 and #3 are different with a strong share of steps in the longitudinal direction (Fig. 4C). This would be consistent, for example, with the movement in the tubular IBM, since in a tubular structure the longitudinal direction (±180° and 0°) always prevails due to geometric reasons. Moreover, confined longitudinal trajectories can also represent dimeric complex V at cristae edges. We next performed a global directionality analysis for the motion of ATP synthase/hydrolase under all conditions. The respective trajectory maps that were analyzed are shown in Fig. 5A. Already visible from the maps is the distinct pattern at time point 0.5 h of 2-DG inhibition of glycolysis and respiration corresponding with the metabolic switch. The directionality was quantified as described and results are displayed on directionality discs. As the distribution shows, orthogonal/perpendicular movement dominated at 0 h (Fig. 5B). Between 0.5 h to 1.5 h after 2-DG induced enhanced ATP synthesis, the vector analysis of directionality suggests an increased share of longitudinal movement. After 2.5 h, corresponding with a recovery of mitochondrial physiology and ATP hydrolase activity, the preferential movement of complex V reverted back to an orthogonal orientation. We then performed MSD analysis in the short time range (2–5 frames) for longitudinal and orthogonal movement separately (Fig. 5C). During the first 0.5 h, MSDs in the orthogonal direction was

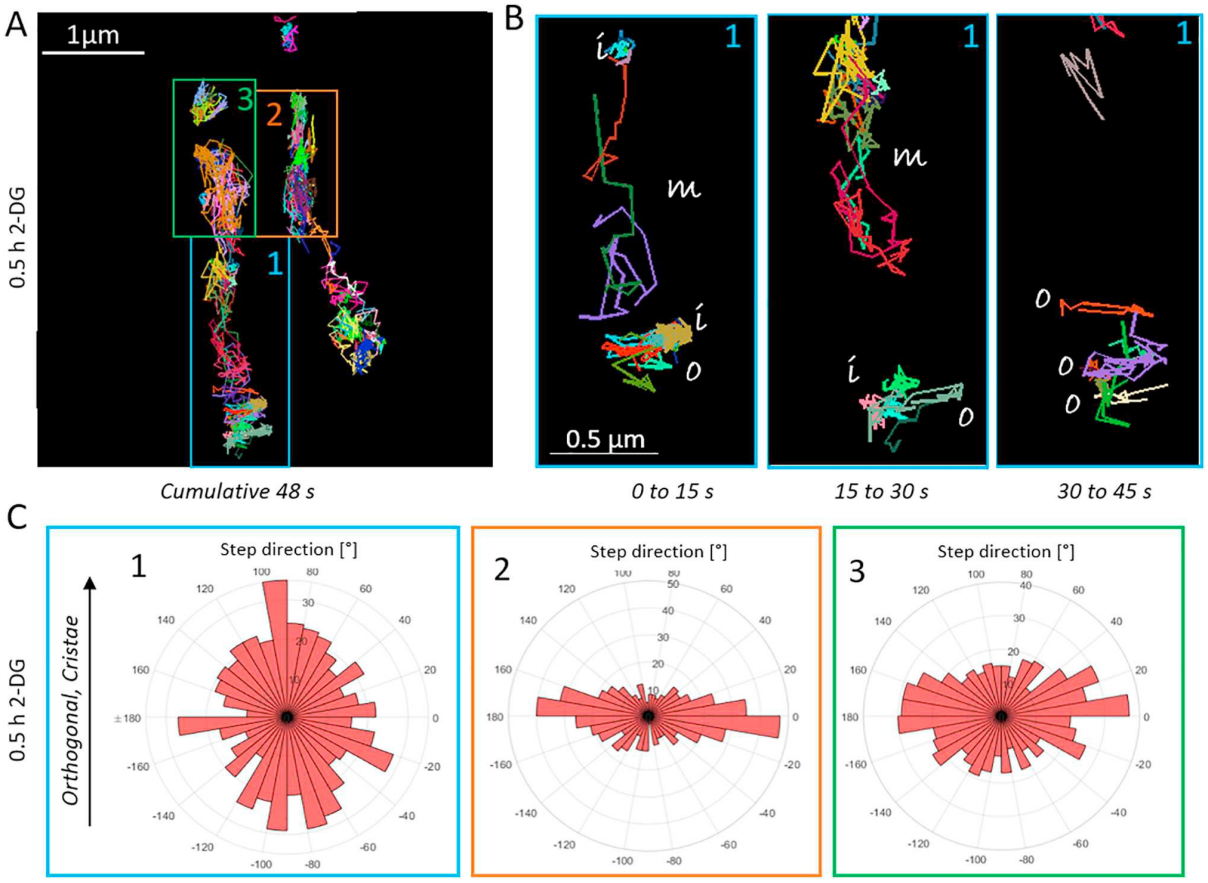

Fig. 4. Quantification of the dynamics and directionality of F_1F_0 ATP synthase. (A) Trajectory map of the F_1F_0 ATP synthase in two mitochondria after 0.5 h incubation with 2-DG. A cumulative image with trajectories from a 1605 image film lasting 48 s is displayed. (B) Detailed view of the individual trajectories from the framed part #1 of (A), each image shows the trajectories of 500 subsequent images (15 s). m: unrestricted movement, o: Diffusion orthogonal to the longitudinal axis of the mitochondrion, i: immobile molecules. Individual trajectories are displayed in different colors; only trajectories with a minimum duration of 180 ms are displayed. (C) Analysis of the step directions with respect to the longitudinal axis (± 180° and 0°) and the orthogonal axis (−90° and +90°) represented on a graduated disk. The direction of the trajectories from the framed areas of interest #1, 2 and 3 of (B) are shown here in the degree window. For the determination of directionality, 5 successive steps were integrated.

lower than mean square displacements in the longitudinal direction. At 2.5 h, the MSD in longitudinal and orthogonal direction did not differ any more (Fig. 5C). The different mobility behavior of ATP synthase and ATPase resulted in different diffusion coefficients D for longitudinal and orthogonal motion (Fig. 5D). The diffusion in the orthogonal direction was lowest at 1 h to 1.5 h corresponding with decreased ATPase activity. The directionality analysis of > 15,000 steps of ATP synthase/hydrolase in mitochondria at different time points ($N = 2$ independent assays) essentially confirmed the results (Fig. S9). The directional diagrams for the movement of ATP synthase were similar before and after 2.5 h of glycolysis inhibition, while at 0.5 h–1.5 h (increased ATP synthase activity) the amount of orthogonal traces was reduced. In our opinion, this clearly indicates a change in the spatio-temporal organization of ATP synthase compared to ATP hydrolase. It appears that the average mobility of complex V in cristae decreased when ATP synthesis was.

ATP synthase dimers display lower mobility than the average pool of ATP synthase

In order to dissect dimeric complex V by its tracking behavior, we tagged complex V at SUg with the HaloTag for labeling. SUg is suggested to trigger ATP synthase dimerization together with SUe [53,54]. Cells were transiently transfected with SUe-HaloTag and labeled with 0.5 nM TMR^{HTL}. We recorded trajectories of ATP synthase labeled at SUg and SUγ in direct comparison (Fig. 6A). The

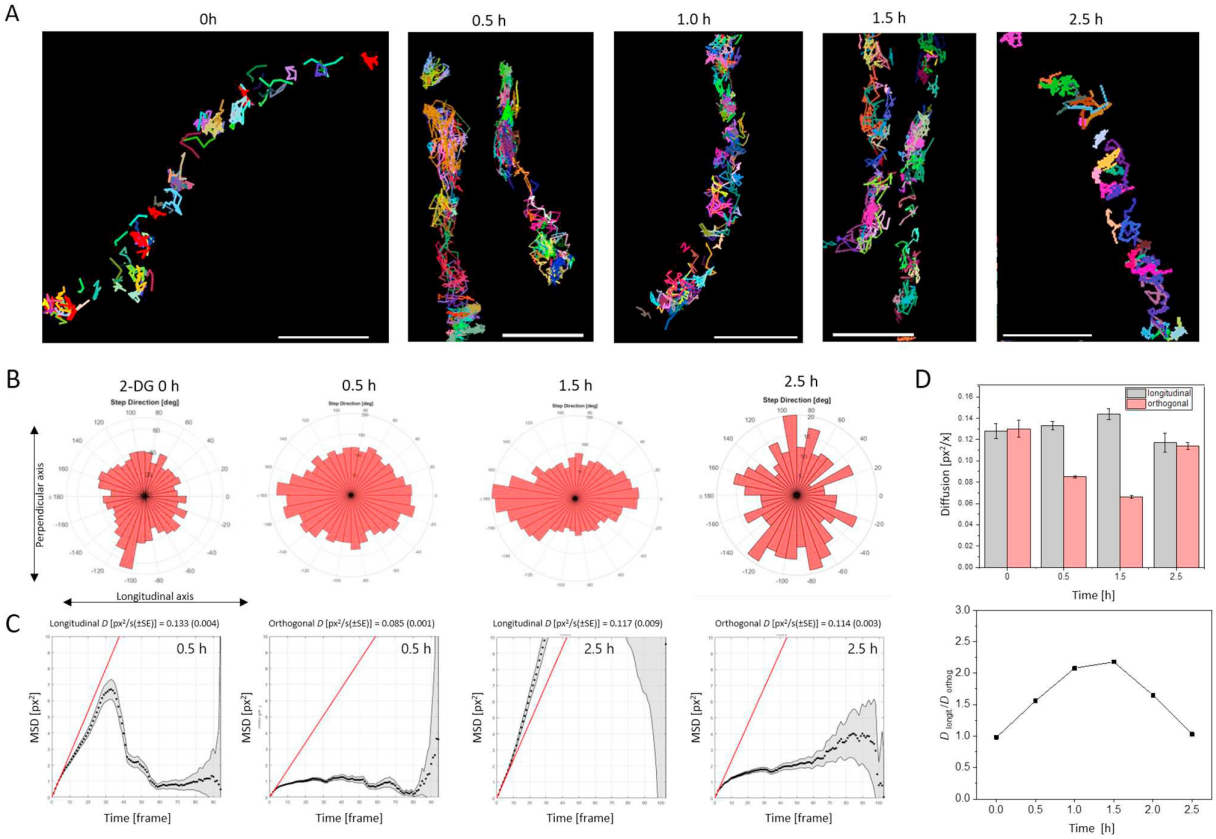

Fig. 5. The diffusion of F_1F_O ATP synthase in cristae is reduced when glycolysis is inhibited. (A) Exemplary cumulative trajectory maps of ATP synthase in mitochondria at different times after starting glycolysis inhibition. Time 0.5–1.5 h corresponds to inhibition of ATPase activity. (B) Directionality of ATP synthase movement in mitochondria shown in (A). (C) Mean square displacements (MSDs) for longitudinal and orthogonal movement at 0.5 h and 2.5 h 2-DG treatment. (D) Diffusion coefficients *D* for longitudinal and orthogonal displacements at different time points. The ratio of the diffusion coefficients $D_{longit.}/D_{orthog.}$ is plotted to demonstrate the difference exemplary.

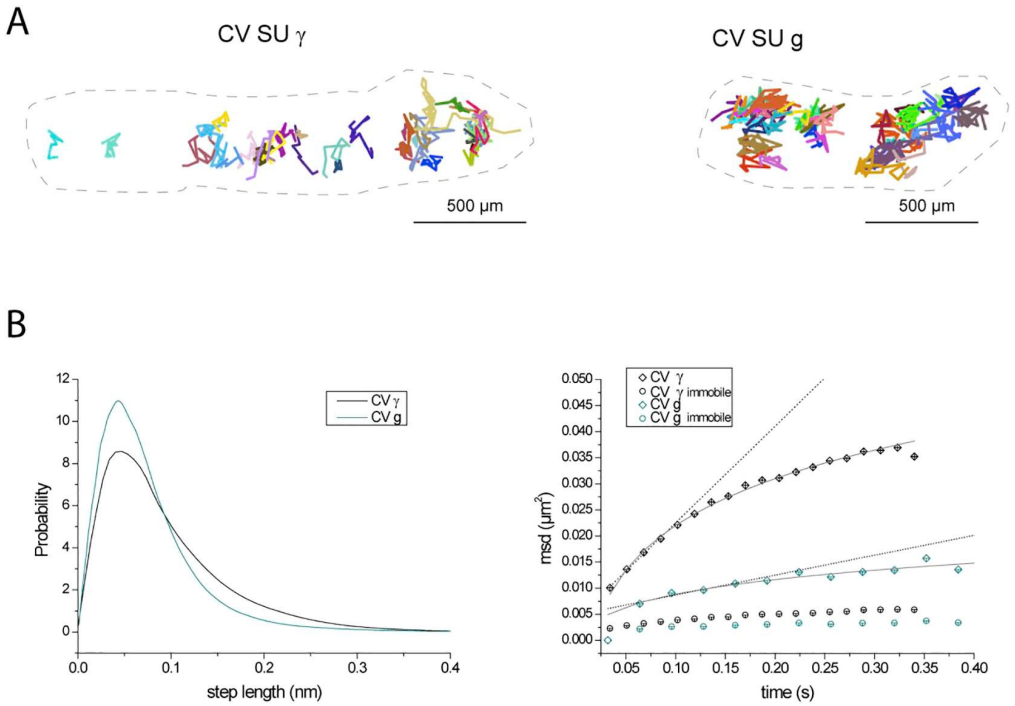

Fig. 6. Dimers of complex V display a very low mobility. (A) Trajectory maps of ATP synthase labeled at subunits γ and g in single mitochondria. The grey line was drawn to indicate the mitochondria. Lines in color represent individual trajectories of single molecules. (B) Step length histograms and means square displacements (MSD) are plotted. The MSD of the long range diffusion was fitted assuming anomalous diffusion (α = 0.069 for CV SU γ and 0.042 for CV SU g). For subunit γ labeled ATP synthase, 12,277 trajectories were analyzed, for subunit g 22,811 trajectories.

trajectory maps of complex V in single mitochondria show a clear difference with more molecules displaying shorter step length and a significantly lower mean square displacement of complex V labeled at SUg (Fig. 6B). For long range diffusion, we calculated $D_{SUg} = 0.054 \pm 0.039$ [SD] μm/s and $D_{SU_\gamma} = 0.033 \pm 0.039$ [SD] μm/s. While complex V labeled at SUγ does not discriminate between monomers, dimers and oligomers and thus represents the entire population, labeling SUg probably will mainly discern dimeric and oligomeric complex V. Short range diffusion analysis revealed that, dimers/oligomers of complex V are almost immobile ($D_{\text{short range}}=0.018 \pm 0.005$ [SD] $\mu m^2/s$ compared to $D_{\text{short range}}=0.046 \pm 0.002$ [SD] μm/s for SUg), localized at the cristae rims.

Inhibition of ATPase activity results in decreased mobility of complex V

In order to test, whether inhibition of ATPase activity affects the mobility of the enzyme, we inhibited ATPase activity with the specific inhibitor BMS-199264 [44]. If inhibition of ATPase activity under 2-DG conditions was the cause for the decrease in diffusion, we would also expect a decrease in mobility upon BMS-199264 treatment. Thus, cells expressing the Halo-Tagged SUγ of ATP synthase were exposed to 5 μM BMS-199264. This treatment caused a decrease in the $\Delta\Psi_m$ (Fig. 1M), which can be explained if ATP synthesis activity continued while ATPase activity stopped. Indeed, we found decreased mobility of ATP synthase when cells were incubated with BMS-199264 alone or together with 2-DG for 0.5 h (Fig. 7A). In parallel, a significant fraction of quasi immobile particles appeared in the trajectory map (Fig. 7B, pink arrowheads, right panel). Thus, inhibition of ATPase activity obviously decreases the overall mobility of the enzyme. The localization map reminds of the map of SUg (Fig. 6A).

Knockdown of inhibitory factor 1 IF1 results in an increase of complex V mobility under normal and 2-DG conditions

We next asked, how ablation of inhibitory factor 1 (IF1) would impact on the mobility of ATP synthase. IF1 binds to ATP synthase dimers in the groove between α-helices of subunits α and β in the F_1 head [55] and likely is involved in dimer/oligomer formation [56]. It can be expected that knockdown of IF1 will result in increased ATP hydrolysis, resulting in increased mobility of the enzyme. If the hypothesis is correct that cells treated with 2-DG are IF1-blocked and possess more oligomeric ATPase, in the absence of IF1 the mobility of the overall complex V population should increase. We first generated IF1-KO knockout cells by the CRISPR/Cas9 technology. Puromycin-resistant clones were subjected to immunoblot analysis to verify knockout of the target gene (Fig. 8A). Four knockout clones were identified, tracking studies were continued with clone #8. IF1-KO cells were transiently transfected with CV-SU γ-Halo Tag, labeled with TMR ^{HTL} and imaged at a TIRF-fluorescence microscope. 4000 frames per region of interest were recorded with a frame rate of 32 ms/frame. The following conditions were compared: control cells with glucose supply (ctrl.), IF1-KO cells and IF1-KO cells treated with 2-DG (30 mM for 0.5 h). The mobility of ATP synthase was determined with the MTT tracker and the cumulative probability of the diffusion coefficients *D* plotted (Fig. 8B). The peaks from left to right indicate ctrl., IF1-KO and IF1-KO + 2-DG conditions. The corresponding median *D* were then plotted for comparison. Clearly, ATP synthase in IF1-KO cells displayed a higher mobility than in control cells. This is expected, either when more complex V monomers are present, respectively less complex oligomers and/or ATPase activity is increased, according to our hypothesis. Interestingly, 2-DG treatment for 0.5 h here further resulted in increased mobility of complex V. We next analyzed the changes in ATP synthase monomers, dimers and oligomers under the different conditions.

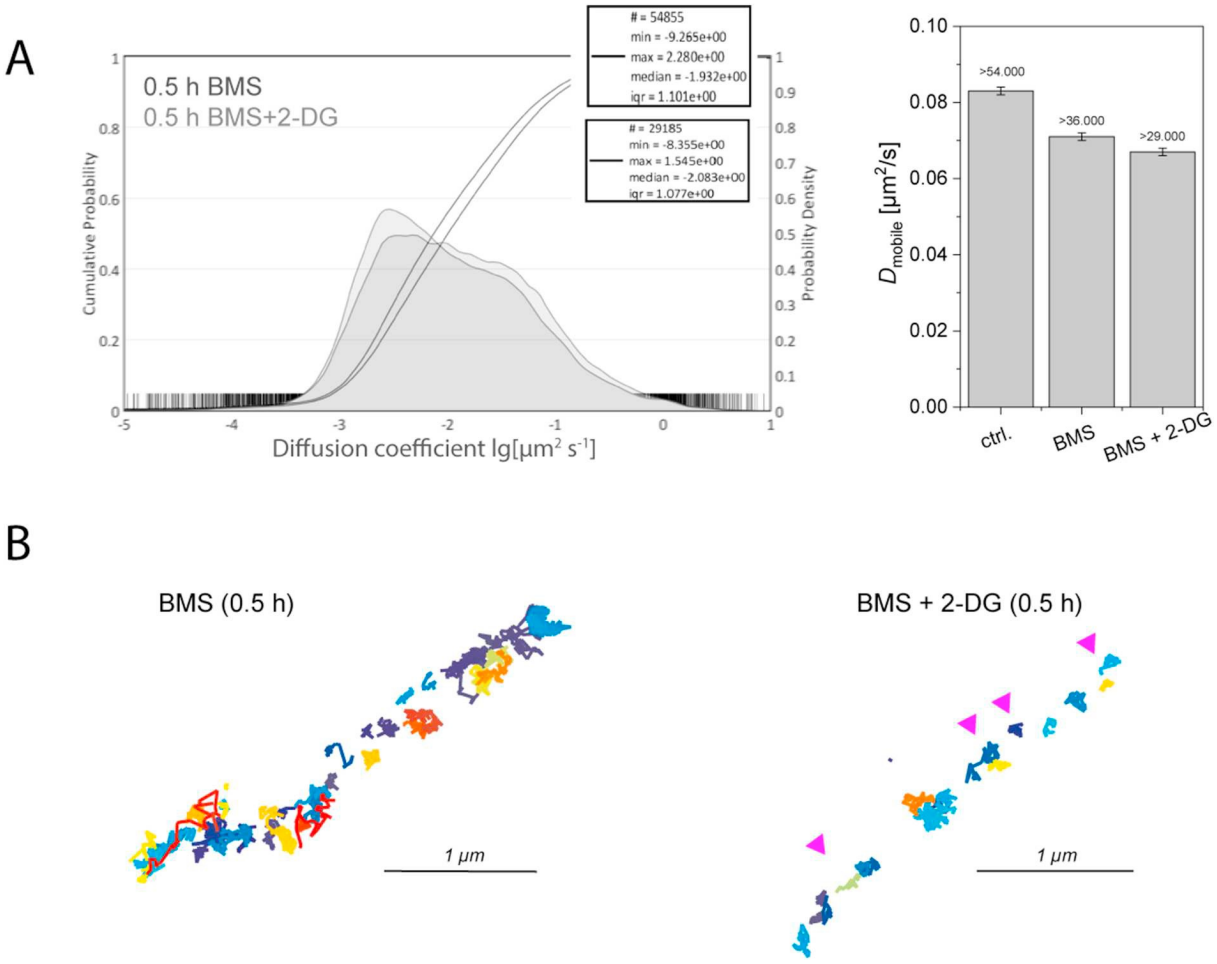

Fig. 7. Inhibition of ATP hydrolysis activity results in decreased mobility of the ATP synthase population. (A) Histogram of diffusion coefficients for ATP synthase under control conditions (5.6 mM Glucose, no inhibition), in the presence of BMS-199264 (5 µM) and BMS-199264 treated in addition with 2-DG for 0.5 h. The cumulative probabilities are plotted. Peaks from left to right: BMS + 2-DG, BMS. Data from $N = 3$ biological replicates. In the right graph, the median diffusion coefficients are plotted. Numbers at the top of the columns indicate the number of analyzed trajectories. No errors are shown, since all trajectories ($N = 3$ biological replicates, > 20 cells) were analyzed in a batch procedure. (B) Trajectory map of mitochondria from an BMS treated cells and a BMS plus 2-DG treated cell, both 0.5 h after application of the inhibitors. Frame rate 32 ms, 4000 frames in total recorded, superimposition of all trajectories during measurement. Red: early trajectories (frames 0–500), dark blue: late trajectories (frames 3500–4000).

Glycolytic inhibition results in a higher proportion of dimer-bound IF1

So far, our data suggested that the spatio-temporal re-organization of complex V observed under inhibitory conditions is due to bioenergetic changes in combination with changes in the molecular assembly.

Therefore, we determined whether the amount of subunit e, which is known to contribute to dimerization of the complex V [57,58] was changed during 2-DG treatment (ATP hydrolyzing conditions). We compared levels of SUe with levels of SUβ. VDAC, an outer membrane protein, was analyzed as a loading control. At 0.5 h, the level of SUe was significantly ($P = 0.0077$) reduced relative to the level of VDAC after inhibition of glycolysis (Fig. 9A). In parallel, levels of subunit β were determined. After 3 h, the relative protein level of complex V appeared to be decreased ($N = 5$, normalization on VDAC), however, this was not confirmed in a different batch of experiments (Fig. S1). When SUe was related to SUβ, the lowest ratio of SUe/SUβ was observed at time point 0.5 h after inhibition of glycolysis.

To complement the results, we performed BN-PAGE to separate oligomers, dimers and monomers of complex V at the different time points after glycolysis inhibition. We found a relative decrease of dimers compared to monomers after 0.5 h of 2-DG treatment (Fig. 9B). Oligomers apparently decreased between 0.5 h and 1.5 h after glyco- lysis inhibition, but quantification was difficult (Fig. S10A). Next, we tested, whether IF1, the inhibitory factor 1 of ATPase which is upregulated in cancer cells [59],

would bind to monomers and dimers during the inhibition of glycolysis. This was indeed the case, we found IF1 associated with monomeric and dimeric ATP synthase. Binding of IF1 obviously is not exclusive to dimers. We then normalized the calculated IF1 dimer/monomer ratio to the SUß dimer/monomer ratio. The proportion of IF1 bound to dimers tended to increase relative to the binding to monomers (Fig. 9B, right panel). Unfortunately, we could not quantify changes in IF1 binding to the oligomeric complex V. Our data suggest that glycolysis inhibition was accompanied by a relative increase in the ratio of dimers/monomers that have bound IF1.

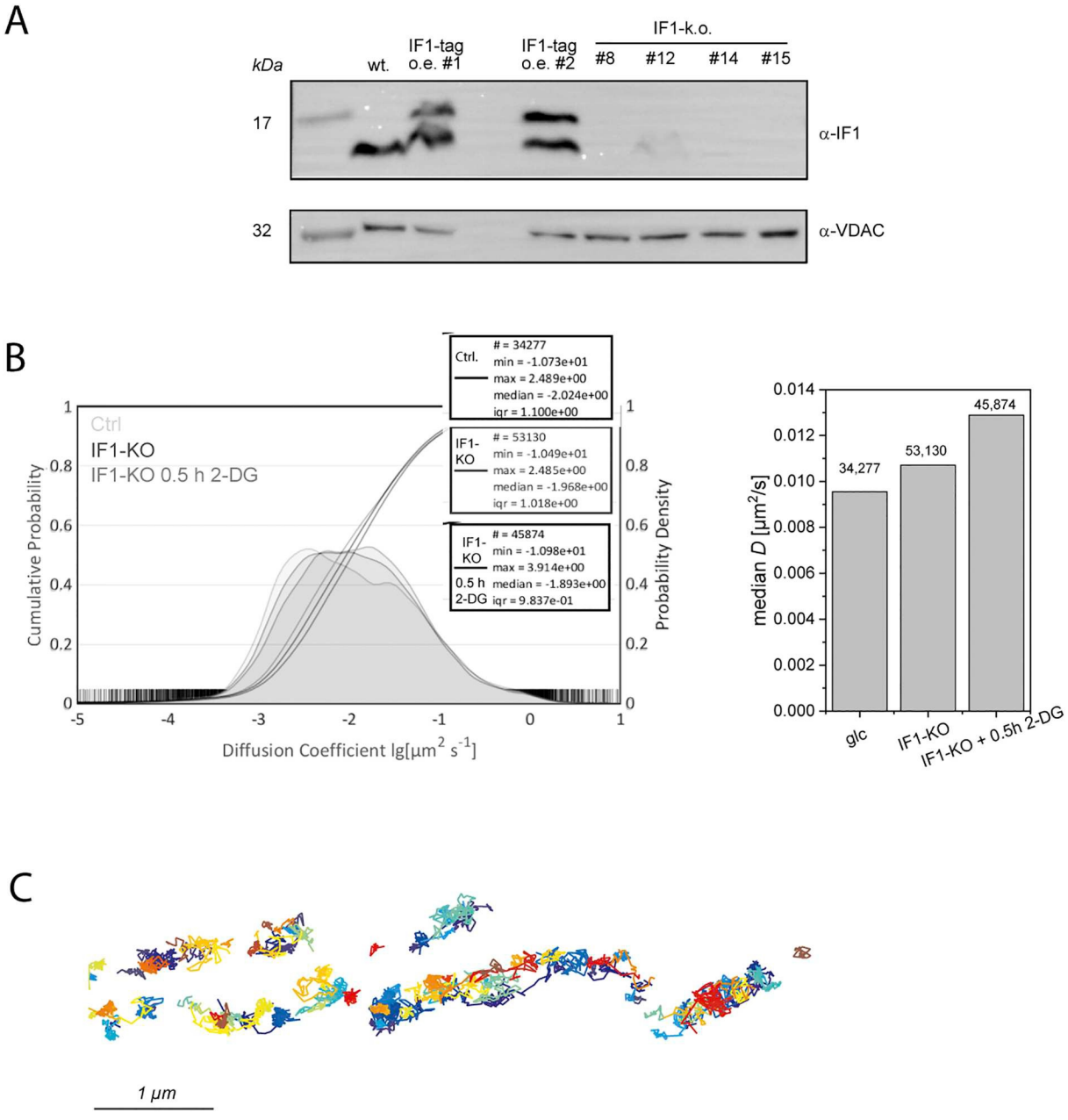

Fig. 8. ATP synthase mobility increases in 2-DG-treated IF1-KO cells. (A) Candidate IF1 knock-out clones of human cervical carcinoma cells were subjected to immunoblot analysis with antibodies against IF1 and the mitochondrial marker protein VDAC. (B) Histogram of diffusion coefficients for ATP synthase under control conditions (5.6 mM Glucose, no inhibition), in IF1-KO cells and in IF1-KO cells treated with 2-DG for 0.5 h. The cumulative probabilities are plotted. Peaks from left to right: ctrl., IF1-KO, IF1-KO + 2-DG. Boxes show the number of trajectories analyzed, and the statistical values (minimal *D*, maximal *D*, median, iqr: interquartile range). Data from $N = 3$ biological replicates. In the right graph, the diffusion coefficients are plotted. Numbers at the top of the columns indicate the number of analyzed trajectories. No errors are shown, since all trajectories ($N = 3$ biological replicates, > 20 cells) were analyzed in a batch procedure. (C) Trajectory map of mitochondria from an IF1-KO cell treated with 2-DG. Frame rate 32 ms, 4000 frames. Red: early trajectories (frames 0–500), dark blue: late trajectories (frames 3500–4000).

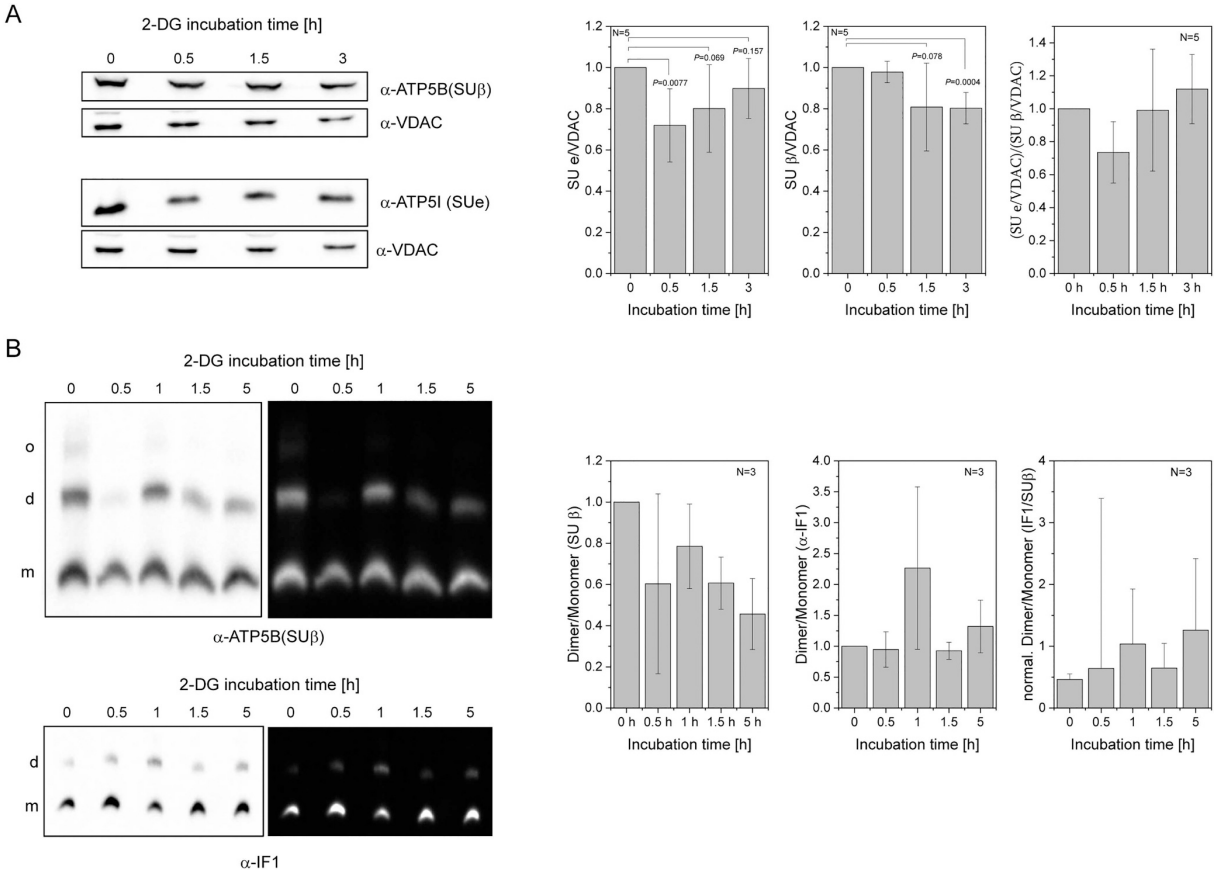

Fig. 9. Glycolytic inhibition results in a relative higher proportion of dimer-bound IF1. (A) Relative protein levels of SUe of ATP synthase/complex V (AB: ATP5I) and SU-β of ATP synthase (AB: ATP5B) and their ratio normalized to VDAC (AB: VDAC) at different times during glycolysis inhibition ($N = 5$). SDS-PAGE with im- munostaining as indicated. Statistics: ANOVA test, SD shown. (B) BN-PAGE separation of complex V oligomers, dimers, and monomers and detection of ATP complexes by immunostaining with α-ATP5B (anti-SU-β) and with α-IF1 (anti-IF1). Abbreviations: o: oligomers d: dimers, m: monomers. Images are also shown in inverse mode (right panel). No oligomers were detected with α-IF1. The dimer/monomer ratio was calculated for each gel and averaged (left and middle graph). Right graph: Relative binding of IF1 to complex V dimers/monomers (normalized to the SU β signal). Mean values of three independent replicates were used. Calculation of error propagation see statistics sections.

Discussion

The aim of this study was to check if the activity mode of mitochondrial complex V, either ATP synthesis or ATP hydrolysis, is associated with a specific spatio-temporal organization. Complex V of oxidative phosphorylation was suggested to work as an ATP synthase under physiological conditions, but under certain circumstances, e.g. under ischemic or in cancer cells, it can function as an ATPase. To alter complex V activity, we decided to inhibit glycolysis with 2-DG treatment. As recently demonstrated, the inhibition of HK by 2-DG had a strong and fast effect on mitochondrial ATP metabolism [42]. Also, one advantage of this strategy was that respiration and ATP synthase were not directly inhibited. Our measurements suggest that before 2-DG administration a subpopulation of the complex V worked in reverse mode. However, most surprisingly, mitochondrial ATP synthesis took place at the same time and continued during 2-DG inhibition as the oligomycin effect suggests. Indeed, a similar transient increase of matrix ATP levels upon 2-DG induced glucose deprivation was observed earlier [42], followed by ATP decrease. During 2-DG treatment, the mitochondrial membrane potential decreased, probably due to reduced proton pumping. BMS-199264, an ATP hydrolase inhibitor, also decreased $\Delta\Psi_m$, suggesting that ATP hydrolysis activity was present before. Based on this data we suggest that two populations of complex V with different function can be present at the same time, probably in different sub-compartments: ATPase in the cristae sheet and ATP synthase in more confined (cristae edges). Reverse proton pumping by ATP hydrolysis function could be physiologically useful to provide a membrane potential, e.g. for import processes [60].

Because mitochondria switched to another fuel source, the effects of glucose depletion on ATP

synthase/hydrolase were only short-term (0.5 to 1.5 h) and reversible. This reversibility enabled us to study the effects of the induced shift on the organization of complex V. We determined the spatio-temporal organization of complex V during the time window for which we had evidence of altered ATPase activity and compared it with the conditions in which ATP hydrolysis was blocked or released. To block ATPase activity, we used the inhibitor BMS-199264 [44] and to study the effect of a release of inhibition of ATPase, we used an IF1- KO cell line. IF1, the inhibitor factor 1 is the physiological master regulator of ATPase activity [56]. It is widely accepted that IF1 blocks the hydrolysis function [61] but more recent data also suggest an inhibitory effect on the ATP synthesis mode [59]. A microscopy method based on single molecule tracking and localization [19] was used to dissect the organization of ATP synthase molecules in mitochondria *in situ* and to generate detailed maps of the localization and dynamics of complex V under different conditions. Under normal conditions, F_1F_O ATP synthase is confined in cristae in terms of localization and mobility [19,49,51,62], which manifests itself in restricted mobility. Significant proportion of complex V displays orthogonal trajectories in the cristae sheet, performing ATP hydrolysis. Here we report that this specific spatio-temporal arrangement has changed with altered complex V activity. A thorough analysis of the mobility patterns including the analysis of the directionality of the movement showed that the confined mobile fraction of the ATP synthase in the cristae increased and the orthogonal directional dependence was lost at the same time. In addition, we found a reduction in cristae width. A narrowing of the cristae in response to starvation has been described earlier [13,45]. The ultrastructural changes under starvation were mainly attributed to the changes in OPA1 levels, whereby the contribution of complex V was not discussed [45]. However, no changes in OPA1 levels were reported for 2-DG-induced metabolic starvation [23], leading us to conclude that an alteration in the complex V dimers/monomer ratio was mainly responsible for the mild and reversible effect on cristae narrowing. Since this would decrease the volume, more efficient coupling is expected [63]. In addition, we found a tendency of more IF1 binding to complex V dimers under this condition. IF1 was shown to promote dimerization of the mitochondrial F_1F_O ATP synthase [61]. In IF1-KO cells, ATP synthase displayed a higher mobility, while in BMS-199264 treated cells (inhibition of ATP hydrolysis), the mobility decreased. Together, this data supports the hypothesis that ATPase activity is associated with a different localization and organizational state in the inner mitochondrial membrane. We suggest that the assembly of ATP synthase that is usually organized in a regular dimer/oligomer structure at the cristae rims [16,52,64–66], thereby shaping the cristae curvature [12,67,68], is associated with ATP synthase. Under 2-DG treatment, the loss of orthogonal trajectories and the decrease of complex V mobility in the cristae sheet suggests that immobile dimeric and oligomeric F_1F_O ATP synthases remained. The observed cristae narrowing is in accordance with this, since a change of the cristae architecture is a frequent outcome when the oligomerization of ATP synthase is altered due
to various conditions [13,14,17,63,69–71]. In this context, we provide for the first time data on the dynamic spatio-temporal organization of F_1F_O ATP synthase in living cells.

In summary, our observations suggest that the specific spatio-temporal organization of complex V in subcompartments of the inner mitochondrial membrane may be essential for its respective function, namely either ATP synthesis or ATP hydrolysis. Obviously, complex V displays a comparable dynamic organization as the respiratory complexes which assemble into supercomplexes for functional adaptation [72,73]. It can be speculated that the arrangement of the complex V dimers in rows that form the cristae, which is obviously advantageous for optimal function as ATP synthase [46], is not necessarily also the typical arrangement for the ATPase function. However, to finally ascertain this, the specific activity of F_1F_O ATP synthase would have to be visualized with submitochondrial resolution *in situ*.

Conclusions

Mitochondrial F_1F_O ATP synthase has several functions: in ATP synthesis, cristae shaping and possibly mitochondrial permeability. By means of high-resolution localization and tracking of single molecules, we have probed the current view of static F_1F_O ATP synthase organization as series of dimers aligned at the edges of cristae. Our results rather suggest that subpopulations of complex V with different distribution and mobility exist in the inner membrane compartments. Under normal respiratory conditions, complex V was mainly localized in cristae, while under metabolic stress and nutrient deprivation with decreased respiration this specific spatio-temporal pattern became intermediately blurred. We suggest that in addition to modification of the metabolic setting, a shift in the ratio of oligomeric/dimeric F_1F_O ATP synthase to monomeric forms is correlated with different distribution and mobility in the inner mitochondrial membrane compartments. Such dynamics would allow the simultaneous existence of ATP synthesis and ATP hydrolysis function, but spatially separated.

Supplementary data to this article can be found online at https://doi.org/10.1016/j.bbabio.2019.148091.

Declaration of competing interest

The authors do not declare any competing financial interests.

Acknowledgments

The authors thank Wladislaw Kohl for excellent technical support.

References

[1] M.V. Liberti, J.W. Locasale, The Warburg effect: how does it benefit cancer cells? Trends Biochem. Sci. 41 (2016) 211–218.
[2] O. Warburg, On respiratory impairment in cancer cells, Science 124 (1956) 269–270.
[3] R. Rossignol, R. Gilkerson, R. Aggeler, K. Yamagata, S.J. Remington, R.A. Capaldi, Energy substrate modulates mitochondrial structure and oxidative capacity in cancer cells, Cancer Res. 64 (2004) 985–993.
[4] G. Benard, N. Bellance, C. Jose, S. Melser, K. Nouette-Gaulain, R. Rossignol, Multi- site control and regulation of mitochondrial energy production, Biochim. Biophys. Acta 1797 (2010) 698–709.
[5] E.P. Bulthuis, M.J.W. Adjobo-Hermans, P. Willems, W.J.H. Koopman, Mitochondrial morphofunction in mammalian cells, Antioxid. Redox Signal. 30 (2019) 2066–2109.
[6] D. Dikov, J. Bereiter-Hahn, Inner membrane dynamics in mitochondria, J. Struct. Biol. 183 (2013) 455–466.
[7] M. Picard, M.J. McManus, G. Csordas, P. Varnai, G.W. Dorn 2nd, D. Williams, G. Hajnoczky, D.C. Wallace, Trans-mitochondrial coordination of cristae at regu- lated membrane junctions, Nat. Commun. 6 (2015) 6259.
[8] C. Frezza, S. Cipolat, O. Martins de Brito, M. Micaroni, G.V. Beznoussenko, T. Rudka, D. Bartoli, R.S. Polishuck, N.N. Danial, B. De Strooper, L. Scorrano, OPA1 controls apoptotic cristae remodeling independently from mitochondrial fusion, Cell 126 (2006) 177–189.
[9] M. Barbot, D.C. Jans, C. Schulz, N. Denkert, B. Kroppen, M. Hoppert, S. Jakobs, M. Meinecke, Mic10 oligomerizes to bend mitochondrial inner membranes at cristae junctions, Cell Metab. 21 (2015) 756–763.
[10] J.R. Friedman, A. Mourier, J. Yamada, J.M. McCaffery, J. Nunnari, MICOS co- ordinates with respiratory complexes and lipids to establish mitochondrial inner membrane architecture, Elife 4 (2015).
[11] F. Wollweber, K. von der Malsburg, M. van der Laan, M. contact site cristae orga- nizing system, A central player in membrane shaping and crosstalk, Biochim. Biophys. Acta, Mol. Cell Res. 1864 (2017) 1481–1489.
[12] K.M. Davies, C. Anselmi, I. Wittig, J.D. Faraldo-Gomez, W. Kuhlbrandt, Structure of the yeast F1Fo-ATP synthase dimer and its role in shaping the mitochondrial cristae, Proc. Natl. Acad. Sci. U. S. A. 109 (2012) 13602–13607.
[13] R. Quintana-Cabrera, C. Quirin, C. Glytsou, M. Corrado, A. Urbani, A. Pellattiero, E. Calvo, J. Vazquez, J.A. Enriquez, C. Gerle, M.E. Soriano, P. Bernardi, L. Scorrano, The cristae modulator optic atrophy 1 requires mitochondrial ATP synthase oligo- mers to safeguard mitochondrial function, Nat. Commun. 9 (2018) 3399.
[14] K. Eydt, K.M. Davies, C. Behrendt, I. Wittig, A.S. Reichert, Cristae architecture is determined by an interplay of the MICOS complex and the F1FO ATP synthase via Mic27 and Mic10, Microb. Cell 4 (2017) 259–272.
[15] N.V. Dudkina, S. Sunderhaus, H.P. Braun, E.J. Boekema, Characterization of di- meric ATP synthase and cristae membrane ultrastructure from Saccharomyces and Polytomella mitochondria, FEBS Lett. 580 (2006) 3427–3432.
[16] R.D. Allen, C.C. Schroeder, A.K. Fok, An investigation of mitochondrial inner membranes by rapid-freeze deep-etch techniques, J. Cell Biol. 108 (1989) 2233–2240.
[17] L. Plecita-Hlavata, H. Engstova, L. Alan, T. Spacek, A. Dlaskova, K. Smolkova, J. Spackova, J. Tauber, V. Stradalova, J. Malinsky, M. Lessard, J. Bewersdorf, P. Jezek, Hypoxic HepG2 cell adaptation decreases ATP synthase dimers and ATP production in inflated cristae by mitofilin down-regulation concomitant to MICOS clustering, FASEB J. 30 (2016) 1941–1957.
[18] A. Dlaskova, H. Engstova, T. Spacek, A. Kahancova, V. Pavluch, K. Smolkova, J. Spackova, M. Bartos, L.P. Hlavata, P. Jezek, 3D super-resolution microscopy re- flects mitochondrial cristae alternations and mtDNA nucleoid size and distribution, Biochim. Biophys. Acta Bioenerg. 1859 (2018) 829–844.
[19] T. Appelhans, C.P. Richter, V. Wilkens, S.T. Hess, J. Piehler, K.B. Busch, Nanoscale organization of mitochondrial microcompartments revealed by combining tracking and localization microscopy, Nano Lett. 12 (2012) 610–616.
[20] V.M. Sukhorukov, J. Bereiter-Hahn, Anomalous diffusion induced by cristae geometry in the inner mitochondrial membrane, PLoS One 4 (2009) e4604.
[21] V.M. Sukhorukov, D. Dikov, K. Busch, V. Strecker, I. Wittig, J. Bereiter-Hahn, Determination of protein mobility in mitochondrial membranes of living cells, Biochim. Biophys. Acta 1798 (2010) 2022–2032.
[22] H. Pelicano, D.S. Martin, R.H. Xu, P. Huang, Glycolysis inhibition for anticancer treatment, Oncogene 25 (2006) 4633–4646.
[23] R. Yamaguchi, E. Janssen, G. Perkins, M. Ellisman, S. Kitada, J.C. Reed, Efficient elimination of cancer cells by deoxyglucose-ABT-263/737 combination therapy, PLoS One 6 (2011) e24102.
[24] T. Appelhans, K. Busch, Single molecule tracking and localization of mitochondrial protein complexes in live cells, Methods Mol. Biol. 1567 (2017) 273–291.
[25] A. Sergé, N. Bertaux, H. Rigneault, D. Marguet, Dynamic multiple-target tracing to probe spatiotemporal cartography of cell membranes, Nat. Methods 5 (2008) 687–694.
[26] R.C. Scaduto Jr., L.W. Grotyohann, Measurement of mitochondrial membrane po- tential using fluorescent rhodamine derivatives, Biophys. J. 76 (1999) 469–477.
[27] W. Pendergrass, N. Wolf, M. Poot, Efficacy of MitoTracker Green and CMXrosamine to measure changes in mitochondrial membrane potentials in living cells and tis- sues, Cytometry A 61 (2004) 162–169.
[28] H. Imamura, K.P. Nhat, H. Togawa, K. Saito, R. Iino, Y. Kato-Yamada, T. Nagai, H. Noji, Visualization of ATP levels inside single living cells with fluorescence re- sonance energy transfer-based genetically encoded indicators, Proc. Natl. Acad. Sci. U. S. A. 106 (2009) 15651–15656.
[29] T. Appelhans, F.R. Beinlich, C.P. Richter, R. Kurre, K.B. Busch, Multi-color locali- zation microscopy of single membrane proteins in organelles of live mammalian cells, JoVE (2018) e57690.
[30] B. Muster, W. Kohl, I. Wittig, V. Strecker, F. Joos, W. Haase, J. Bereiter-Hahn, K. Busch, Respiratory chain complexes in dynamic mitochondria display a patchy distribution in life cells, PLoS One 5 (2010) e11910.
[31] M. Rosselin, J. Santo-Domingo, F. Bermont, M. Giacomello, N. Demaurex, L-OPA1 regulates mitoflash biogenesis independently from membrane fusion, EMBO Rep. 18 (2017) 451–463.
[32] M. Tokunaga, N. Imamoto, K. Sakata-Sogawa, Highly inclined thin illumination enables clear single-molecule imaging in cells, Nat. Methods 5 (2008) 159–161.
[33] E. Betzig, G.H. Patterson, R. Sougrat, O.W. Lindwasser, S. Olenych, J.S. Bonifacino, M.W. Davidson, J. Lippincott-Schwartz, H.F. Hess, Imaging intracellular fluorescent proteins at nanometer resolution, Science 313 (2006) 1642–1645.
[34] T.J. Gould, V.V. Verkhusha, S.T. Hess, Imaging biological structures with fluorescence photoactivation localization microscopy, Nat. Protoc. 4 (2009) 291–308.
[35] S.T. Hess, T.P. Girirajan, M.D. Mason, Ultra-high resolution imaging by fluorescence photoactivation localization microscopy, Biophys. J. 91 (2006) 4258–4272.
[36] S. Schmitt, F. Saathoff, L. Meissner, E.M. Schropp, J. Lichtmannegger, S. Schulz, C. Eberhagen, S. Borchard, M. Aichler, J. Adamski, N. Plesnila, S. Rothenfusser, Kroemer, H. Zischka, A semi-automated method for isolating functionally intact mitochondria from cultured cells and tissue biopsies, Anal. Biochem. 443 (2013) 66–74.
[37] R. Acin-Perez, P. Fernandez-Silva, M.L. Peleato, A. Perez-Martos, J.A. Enriquez, Respiratory active mitochondrial supercomplexes, Mol. Cell 32 (2008) 529–539.
[38] I. Wittig, M. Karas, H. Schagger, High resolution clear native electrophoresis for in- gel functional assays and fluorescence studies of membrane protein complexes, Mol. Cell. Proteomics 6 (2007) 1215–1225.
[39] P.E. Porporato, N. Filigheddu, J.M.B. Pedro, G. Kroemer, L. Galluzzi, Mitochondrial metabolism and cancer, Cell Res. 28 (2018) 265–280.
[40] A.S. Divakaruni, G.W. Rogers, A.N. Murphy, Measuring mitochondrial function in permeabilized cells using the seahorse XF analyzer or a clark-type oxygen electrode, Curr. Protoc. Toxicol. 60 (25 22) (2014) (21–16).
[41] S.A. Mookerjee, A.A. Gerencser, D.G. Nicholls, M.D. Brand, Quantifying in-tracellular rates of glycolytic and oxidative ATP production and consumption using extracellular flux measurements, J. Biol. Chem. 293 (2018) 12649–12652.
[42] M.R. Depaoli, F. Karsten, C.T. Madreiter-Sokolowski, C. Klec, B. Gottschalk, G. Bischof, E. Eroglu, M. Waldeck-Weiermair, T. Simmen, W.F. Graier, R. Malli, Real-time imaging of mitochondrial ATP dynamics reveals the metabolic setting of single cells, Cell Rep. 25 (2018) 501–512 (e503).
[43] J.D. Wikstrom, S.M. Katzman, H. Mohamed, G. Twig, S.A. Graf, E. Heart, A.J. Molina, B.E. Corkey, L.M. de Vargas, N.N. Danial, S. Collins, O.S. Shirihai, beta- Cell mitochondria exhibit membrane potential heterogeneity that can be altered by stimulatory or toxic fuel levels, Diabetes 56 (2007) 2569–2578.
[44] G.J. Grover, J. Malm, Pharmacological profile of the selective mitochondrial F1F0 ATP hydrolase inhibitor BMS-199264 in myocardial ischemia, Cardiovasc. Ther. 26 (2008) 287–296.

[45] D.A. Patten, J. Wong, M. Khacho, V. Soubannier, R.J. Mailloux, K. Pilon-Larose, J.G. MacLaurin, D.S. Park, H.M. McBride, L. Trinkle-Mulcahy, M.E. Harper, M. Germain, R.S. Slack, OPA1-dependent cristae modulation is essential for cellular adaptation to metabolic demand, EMBO J. 33 (2014) 2676–2691.
[46] M. Strauss, G. Hofhaus, R.R. Schroder, W. Kuhlbrandt, Dimer ribbons of ATP syn- thase shape the inner mitochondrial membrane, EMBO J. 27 (2008) 1154–1160.
[47] T. Appelhans, K.B. Busch, Dynamic imaging of mitochondrial membrane proteins in specific sub-organelle membrane locations, Biophys. Rev. 9 (2017) 345–352.
[48] H. Shen, L.J. Tauzin, R. Baiyasi, W. Wang, N. Moringo, B. Shuang, C.F. Landes, Single Particle Tracking: From Theory to Biophysical Applications, Chem. Rev.117 (2017) 7331–7376.
[49] V. Wilkens, W. Kohl, K. Busch, Restricted diffusion of OXPHOS complexes in dy- namic mitochondria delays their exchange between cristae and engenders a tran- sitory mosaic distribution, J. Cell Sci. 126 (2013) 103–116.
[51] S. Stoldt, D. Wenzel, K. Kehrein, D. Riedel, M. Ott, S. Jakobs, Spatial orchestration of mitochondrial translation and OXPHOS complex assembly, Nat. Cell Biol. 20 (2018) 528–534.
[52] K.M. Davies, M. Strauss, B. Daum, J.H. Kief, H.D. Osiewacz, A. Rycovska, V. Zickermann, W. Kuhlbrandt, Macromolecular organization of ATP synthase and complex I in whole mitochondria, Proc. Natl. Acad. Sci. U. S. A. 108 (2011) 14121–14126.
[53] K. Wagner, P. Rehling, L.K. Sanjuan Szklarz, R.D. Taylor, N. Pfanner, M. van der Laan, Mitochondrial F1Fo-ATP synthase: the small subunits e and g associate with monomeric complexes to trigger dimerization, J. Mol. Biol. 392 (2009) 855–861.
[54] I. Arnold, K. Pfeiffer, W. Neupert, R.A. Stuart, H. Schagger, Yeast mitochondrial F1F0-ATP synthase exists as a dimer: identification of three dimer-specific subunits, EMBO J. 17 (1998) 7170–7178.
[55] J.R. Gledhill, M.G. Montgomery, A.G. Leslie, J.E. Walker, How the regulatory protein, IF(1), inhibits F(1)-ATPase from bovine mitochondria, Proc. Natl. Acad. Sci. U. S. A. 104 (2007) 15671–15676.
[56] M. Campanella, E. Casswell, S. Chong, Z. Farah, M.R. Wieckowski, A.Y. Abramov, A. Tinker, M.R. Duchen, Regulation of mitochondrial structure and function by the F1Fo-ATPase inhibitor protein, IF1, Cell Metab. 8 (2008) 13–25.
[57] P.D. Gavin, M. Prescott, R.J. Devenish, F1F0-ATP synthase complex interactions in vivo can occur in the absence of the dimer specific subunit e, J. Bioenerg. Biomembr. 37 (2005) 55–66.
[58] I. Wittig, J. Velours, R. Stuart, H. Schagger, Characterization of domain interfaces in monomeric and dimeric ATP synthase, Mol. Cell. Proteomics 7 (2008) 995–1004.
[59] L. Sanchez-Cenizo, L. Formentini, M. Aldea, A.D. Ortega, P. Garcia-Huerta, M. Sanchez-Arago, J.M. Cuezva, Up-regulation of the ATPase inhibitory factor 1 (IF1) of the mitochondrial H+-ATP synthase in human tumors mediates the metabolic shift of cancer cells to a Warburg phenotype, J. Biol. Chem. 285 (2010) 25308–25313.
[60] M. Pelosse, C. Cottet-Rousselle, C.M. Bidan, A. Dupont, K. Gupta, I. Berger, U. Schlattner, Synthetic energy sensor AMPfret deciphers adenylate-dependent AMPK activation mechanism, Nat. Commun. 10 (2019) 1038.
[61] J. Garcia-Bermudez, J.M. Cuezva, The ATPase inhibitory factor 1 (IF1): a master regulator of energy metabolism and of cell survival, Biochim. Biophys. Acta 1857 (2016) 1167–1182.
[62] F. Vogel, C. Bornhovd, W. Neupert, A.S. Reichert, Dynamic subcompartmentaliza- tion of the mitochondrial inner membrane, J. Cell Biol. 175 (2006) 237–247.
[63] A. Dlaskova, T. Spacek, H. Engstova, J. Spackova, A. Schrofel, B. Holendova, K. Smolkova, L. Plecita-Hlavata, P. Jezek, Mitochondrial cristae narrowing upon higher 2-oxoglutarate load, Biochim. Biophys. Acta Bioenerg. 1860 (2019) 659–678.
[64] J. Habersetzer, I. Larrieu, M. Priault, B. Salin, R. Rossignol, D. Brethes, P. Paumard, Human F1F0 ATP synthase, mitochondrial ultrastructure and OXPHOS impairment: a (super-)complex matter? PLoS One 8 (2013) e75429.
[65] P. Paumard, J. Vaillier, B. Coulary, J. Schaeffer, V. Soubannier, D.M. Mueller, D. Brethes, J.P. di Rago, J. Velours, The ATP synthase is involved in generating mitochondrial cristae morphology, EMBO J. 21 (2002) 221–230.
[66] N.V. Dudkina, G.T. Oostergetel, D. Lewejohann, H.P. Braun, E.J. Boekema, Row-like organization of ATP synthase in intact mitochondria determined by cryo-electron tomography, Biochim. Biophys. Acta 1797 (2010) 272–277.
[67] P.D. Gavin, M. Prescott, S.E. Luff, R.J. Devenish, Cross-linking ATP synthase com- plexes in vivo eliminates mitochondrial cristae, J. Cell Sci. 117 (2004) 2333–2343.
[68] N.V. Dudkina, J. Heinemeyer, W. Keegstra, E.J. Boekema, H.P. Braun, Structure of dimeric ATP synthase from mitochondria: an angular association of monomers in- duces the strong curvature of the inner membrane, FEBS Lett. 579 (2005) 5769–5772.
[69] T. Brandt, A. Mourier, L.S. Tain, L. Partridge, N.G. Larsson, W. Kuhlbrandt, Changes of mitochondrial ultrastructure and function during ageing in mice and Drosophila, Elife 6 (2017).
[70] B. Daum, A. Walter, A. Horst, H.D. Osiewacz, W. Kuhlbrandt, Age-dependent dissociation of ATP synthase dimers and loss of inner-membrane cristae in mi- tochondria, Proc. Natl. Acad. Sci. U. S. A. 110 (2013) 15301–15306.
[71] E. Koltai, N. Hart, A.W. Taylor, S. Goto, J.K. Ngo, K.J. Davies, Z. Radak, Age-as- sociated declines in mitochondrial biogenesis and protein quality control factors are minimized by exercise training, Am. J. Phys. Regul. Integr. Comp. Phys. 303 (2012) R127–R134.
[72] R. Acin-Perez, J.A. Enriquez, The function of the respiratory supercomplexes: the plasticity model, Biochim. Biophys. Acta 1837 (2014) 444–450.
[73] S. Cogliati, C. Frezza, M.E. Soriano, T. Varanita, R. Quintana-Cabrera, M. Corrado, S. Cipolat, V. Costa, A. Casarin, L.C. Gomes, E. Perales-Clemente, L. Salviati, P. Fernandez-Silva, J.A. Enriquez, L. Scorrano, Mitochondrial cristae shape de- termines respiratory chain supercomplexes assembly and respiratory efficiency, Cell 155 (2013) 160–171.

14 References

Abrahamsson S, Chen J, Hajj B, Stallinga S, Katsov AY, Wisniewski J, Mizuguchi G, Soule P, Mueller F, Darzacq CD, Darzacq X, Wu C, Bargmann CI, Agard DA, Dahan M & Gustafsson MGL (2013) Fast multicolor 3D imaging using aberration-corrected multifocus microscopy. *Nature Methods* **10:** 60–63

Acin-Perez R & Enriquez JA (2014) The function of the respiratory supercomplexes: The plasticity model. *Biochimica et Biophysica Acta (BBA) - Bioenergetics* **1837:** 444–450

Acín-Pérez R, Fernández-Silva P, Peleato ML, Pérez-Martos A & Enriquez JA (2008) Respiratory Active Mitochondrial Supercomplexes. *Molecular Cell* **32:** 529–539

Akabane S, Uno M, Tani N, Shimazaki S, Ebara N, Kato H, Kosako H & Oka T (2016) PKA Regulates PINK1 Stability and Parkin Recruitment to Damaged Mitochondria through Phosphorylation of MIC60. *Molecular Cell* **62:** 371–384

Alkhaja AK, Jans DC, Nikolov M, Vukotic M, Lytovchenko O, Ludewig F, Schliebs W, Riedel D, Urlaub H, Jakobs S & Deckers M (2011) MINOS1 is a conserved component of mitofilin complexes and required for mitochondrial function and cristae organization. *MBoC* **23:** 247–257

Allen RD, Schroeder CC & Fok AK (1989) An investigation of mitochondrial inner membranes by rapid-freeze deep-etch techniques. *The Journal of Cell Biology* **108:** 2233–2240

Appelhans T, Beinlich FRM, Richter CP, Kurre R & Busch KB (2018) Multi-color Localization Microscopy of Single Membrane Proteins in Organelles of Live Mammalian Cells. *JoVE (Journal of Visualized Experiments)***:** e57690

Appelhans T & Busch K (2017a) Single Molecule Tracking and Localization of Mitochondrial Protein Complexes in Live Cells. In *Mitochondria: Practical Protocols*, Mokranjac D & Perocchi F (eds) pp 273–291. New York, NY: Springer New York Available at: https://doi.org/10.1007/978-1-4939-6824-4_17 [Accessed January 30, 2019]

Appelhans T & Busch KB (2017b) Dynamic imaging of mitochondrial membrane proteins in specific sub-organelle membrane locations. *Biophys Rev* **9:** 345–352

Appelhans T (2014) 3D Reconstruction Microscopy of Mitochondria via Single Membrane Proteins Localization, Master Thesis, University of Osnabrück

Appelhans T, Richter CP, Wilkens V, Hess ST, Piehler J & Busch KB (2012) Nanoscale Organization of Mitochondrial Microcompartments Revealed by Combining Tracking and Localization Microscopy. *Nano Lett.* **12:** 610–616

Arnold I, Pfeiffer K, Neupert W, Stuart RA & Schägger H (1998) Yeast mitochondrial F1F0-ATP synthase exists as a dimer: identification of three dimer-specific subunits. *The EMBO Journal* **17:** 7170–7178

Arselin G, Giraud M-F, Dautant A, Vaillier J, Brèthes D, Coulary-Salin B, Schaeffer J & Velours J (2003) The GxxxG motif of the transmembrane domain of subunit e is involved in the dimerization/oligomerization of the yeast ATP synthase complex in the mitochondrial membrane. *European Journal of Biochemistry* **270:** 1875–1884

Baker LA, Watt IN, Runswick MJ, Walker JE & Rubinstein JL (2012) Arrangement of subunits in intact mammalian mitochondrial ATP synthase determined by cryo-EM. *PNAS* **109:** 11675–11680

Balsa E, Soustek MS, Thomas A, Cogliati S, García-Poyatos C, Martín-García E, Jedrychowski M, Gygi SP, Enriquez JA & Puigserver P (2019) ER and Nutrient Stress Promote Assembly of Respiratory Chain Supercomplexes through the PERK-eIF2α Axis. *Molecular Cell* **74:** 877-890.e6

Barbot M, Jans DC, Schulz C, Denkert N, Kroppen B, Hoppert M, Jakobs S & Meinecke M (2015) Mic10 Oligomerizes to Bend Mitochondrial Inner Membranes at Cristae Junctions. *Cell Metabolism* **21:** 756–763

Barrientos A (2002) In vivo and in organello assessment of OXPHOS activities. *Methods* **26:** 307–316

Bazán S, Mileykovskaya E, Mallampalli VKPS, Heacock P, Sparagna GC & Dowhan W (2013) Cardiolipin-dependent Reconstitution of Respiratory Supercomplexes from Purified Saccharomyces cerevisiae Complexes III and IV. *J. Biol. Chem.* **288:** 401–411

Beheiry ME & Dahan M (2013) ViSP: representing single-particle localizations in three dimensions. *Nature Methods* **10:** 689–690

Beinlich FRM, Drees C, Piehler J & Busch KB (2015) Shuttling of PINK1 between Mitochondrial Microcompartments Resolved by Triple-Color Superresolution Microscopy. *ACS Chemical Biology* **10:** 1970–1976

Betzig E, Patterson GH, Sougrat R, Lindwasser OW, Olenych S, Bonifacino JS, Davidson MW, Lippincott-Schwartz J & Hess HF (2006) Imaging Intracellular Fluorescent Proteins at Nanometer Resolution. *Science* **313:** 1642–1645

Blachly-Dyson E & Forte M (2001) VDAC channels. *IUBMB Life* **52:** 113–118

Blum TB, Hahn A, Meier T, Davies KM & Kühlbrandt W (2019) Dimers of mitochondrial ATP synthase induce membrane curvature and self-assemble into rows. *PNAS* **116:** 4250–4255

Bohnert M, Wenz L-S, Zerbes RM, Horvath SE, Stroud DA, von der Malsburg K, Müller JM, Oeljeklaus S, Perschil I, Warscheid B, Chacinska A, Veenhuis M, van der Klei IJ, Daum G, Wiedemann N, Becker T, Pfanner N & van der Laan M (2012) Role of mitochondrial inner membrane organizing system in protein biogenesis of the mitochondrial outer membrane. *MBoC* **23:** 3948–3956

Bohnert M, Zerbes RM, Davies KM, Mühleip AW, Rampelt H, Horvath SE, Boenke T, Kram A, Perschil I, Veenhuis M, Kühlbrandt W, van der Klei IJ, Pfanner N & van der Laan M (2015) Central Role of Mic10 in the Mitochondrial Contact Site and Cristae Organizing System. *Cell Metabolism* **21:** 747–755

Bulthuis EP, Adjobo-Hermans MJW, Willems PHGM & Koopman WJH (2019) Mitochondrial Morphofunction in Mammalian Cells. *Antioxid Redox Signal* **30:** 2066–2109

Busch KB, Deckers-Hebestreit G, Hanke GT & Mulkidjanian AY (2013) Dynamics of bioenergetic microcompartments. *Biological Chemistry* **394:** 163–188

Chen B-C, Legant WR, Wang K, Shao L, Milkie DE, Davidson MW, Janetopoulos C, Wu XS, Hammer JA, Liu Z, English BP, Mimori-Kiyosue Y, Romero DP, Ritter AT, Lippincott-Schwartz J, Fritz-Laylin L, Mullins RD, Mitchell DM, Bembenek JN, Reymann A-C, et al (2014) Lattice Light Sheet Microscopy: Imaging Molecules to Embryos at High Spatiotemporal Resolution. *Science* **346:** 1257998

Chen H, Detmer SA, Ewald AJ, Griffin EE, Fraser SE & Chan DC (2003) Mitofusins Mfn1 and Mfn2 coordinately regulate mitochondrial fusion and are essential for embryonic development. *J. Cell Biol.* **160:** 189–200

Cogliati S, Enriquez JA & Scorrano L (2016) Mitochondrial Cristae: Where Beauty Meets Functionality. *Trends in Biochemical Sciences* **41:** 261–273

Coleman B, Hantgan RR & Cunningham C Tightly Associated Cardiolipin in the Bovine Heart Mitochondrial ATP Synthase as Analyzed by 31P Nuclear Magnetic Resonance Spectroscopy. **:** 8

Colombini M, Blachly-Dyson E & Forte M (1996) VDAC, a channel in the outer mitochondrial membrane. *Ion Channels* **4:** 169–202

Darshi M, Mendiola VL, Mackey MR, Murphy AN, Koller A, Perkins GA, Ellisman MH & Taylor SS (2011) ChChd3, an Inner Mitochondrial Membrane Protein, Is Essential for Maintaining Crista Integrity and Mitochondrial Function. *J. Biol. Chem.* **286:** 2918–2932

Davies KM, Anselmi C, Wittig I, Faraldo-Gómez JD & Kühlbrandt W (2012) Structure of the yeast F1Fo-ATP synthase dimer and its role in shaping the mitochondrial cristae. *PNAS* **109:** 13602–13607

Davies KM, Strauss M, Daum B, Kief JH, Osiewacz HD, Rycovska A, Zickermann V & Kühlbrandt W (2011a) Macromolecular organization of ATP synthase and complex I in whole mitochondria. *PNAS* **108:** 14121–14126

Davies KM, Strauss M, Daum B, Kief JH, Osiewacz HD, Rycovska A, Zickermann V & Kühlbrandt W (2011b) Macromolecular organization of ATP synthase and complex I in whole mitochondria. *PNAS* **108:** 14121–14126

Deng G, Li S, Sun Z, Li W, Zhou L, Zhang J, Gong P & Cai L (2018) Near-infrared fluorescence imaging in the largely unexplored window of 900-1,000 nm. *Theranostics* **8:** 4116–4128

Deng Y & Shaevitz JW (2009) Effect of aberration on height calibration in three-dimensional localization-based microscopy and particle tracking. *Appl. Opt., AO* **48:** 1886–1890

Ding C, Wu Z, Huang L, Wang Y, Xue J, Chen S, Deng Z, Wang L, Song Z & Chen S (2015) Mitofilin and CHCHD6 physically interact with Sam50 to sustain cristae structure. *Scientific Reports* **5:** 16064

Dolezal P, Likic V, Tachezy J & Lithgow T (2006) Evolution of the Molecular Machines for Protein Import into Mitochondria. *Science* **313:** 314–318

Dual Role of Mitofilin in Mitochondrial Membrane Organization and Protein Biogenesis (2011) *Developmental Cell* **21:** 694–707

Dudkina NV, Kouřil R, Peters K, Braun H-P & Boekema EJ (2010) Structure and function of mitochondrial supercomplexes. *Biochimica et Biophysica Acta (BBA) - Bioenergetics* **1797:** 664–670

Eble KS, Coleman WB, Hantgan RR & Cunningham CC (1990) Tightly associated cardiolipin in the bovine heart mitochondrial ATP synthase as analyzed by 31P nuclear magnetic resonance spectroscopy. *J. Biol. Chem.* **265:** 19434–19440

Esparza-Perusquía M, Olvera-Sánchez S, Pardo JP, Mendoza-Hernández G, Martínez F & Flores-Herrera O (2017) Structural and kinetics characterization of the F1F0-ATP synthase dimer. New repercussion of monomer-monomer contact. *Biochimica et Biophysica Acta (BBA) - Bioenergetics* **1858:** 975–981

Eydt K, Davies KM, Behrendt C, Wittig I & Reichert AS Cristae architecture is determined by an interplay of the MICOS complex and the F1FO ATP synthase via Mic27 and Mic10. *Microb Cell* **4:** 259–272

Friedman JR, Lackner LL, West M, DiBenedetto JR, Nunnari J & Voeltz GK (2011) ER Tubules Mark Sites of Mitochondrial Division. *Science* **334:** 358–362

Friedman JR, Mourier A, Yamada J, McCaffery JM & Nunnari J (2015) MICOS coordinates with respiratory complexes and lipids to establish mitochondrial inner membrane architecture. *eLife* Available at: https://elifesciences.org/articles/07739 [Accessed October 16, 2019]

Fronzes R, Weimann T, Vaillier J, Velours J & Brèthes D (2006) The Peripheral Stalk Participates in the Yeast ATP Synthase Dimerization Independently of e and g Subunits. *Biochemistry* **45:** 6715–6723

Gao YQ, Yang W & Karplus M (2005) A Structure-Based Model for the Synthesis and Hydrolysis of ATP by F1-ATPase. *Cell* **123:** 195–205

Gavin PD, Prescott M & Devenish RJ (2005) F1F0-ATP Synthase Complex Interactions In Vivo Can Occur in the Absence of the Dimer Specific Subunit e. *J Bioenerg Biomembr* **37:** 55–66

Gohil VM, Sheth SA, Nilsson R, Wojtovich AP, Lee JH, Perocchi F, Chen W, Clish CB, Ayata C, Brookes PS & Mootha VK (2010) Nutrient-sensitized screening for drugs that shift energy metabolism from mitochondrial respiration to glycolysis. *Nature Biotechnology* **28:** 249–255

Greenfield D, McEvoy AL, Shroff H, Crooks GE, Wingreen NS, Betzig E & Liphardt J (2009) Self-Organization of the Escherichia coli Chemotaxis Network Imaged with Super-Resolution Light Microscopy. *PLOS Biology* **7:** e1000137

Guarani V, McNeill EM, Paulo JA, Huttlin EL, Fröhlich F, Gygi SP, Vactor DV & Harper JW (2015) QIL1 is a novel mitochondrial protein required for MICOS complex stability and cristae morphology. *eLife* Available at: https://elifesciences.org/articles/06265 [Accessed November 7, 2019]

Gugel H, Bewersdorf J, Jakobs S, Engelhardt J, Storz R & Hell SW (2004) Cooperative 4Pi Excitation and Detection Yields Sevenfold Sharper Optical Sections in Live-Cell Microscopy. *Biophysical Journal* **87:** 4146–4152

Guo H, Bueler SA & Rubinstein JL (2017) Atomic model for the dimeric FO region of mitochondrial ATP synthase. *Science* **358:** 936–940

Gustavsson A-K, Petrov PN, Lee MY, Shechtman Y & Moerner WE (2018) 3D single-molecule super-resolution microscopy with a tilted light sheet. *Nature Communications* **9:** 123

Habersetzer J, Ziani W, Larrieu I, Stines-Chaumeil C, Giraud M-F, Brèthes D, Dautant A & Paumard P (2013) ATP synthase oligomerization: From the enzyme models to the mitochondrial morphology. *The International Journal of Biochemistry & Cell Biology* **45:** 99–105

Hahn A, Parey K, Bublitz M, Mills DJ, Zickermann V, Vonck J, Kühlbrandt W & Meier T (2016) Structure of a Complete ATP Synthase Dimer Reveals the Molecular Basis of Inner Mitochondrial Membrane Morphology. *Molecular Cell* **63:** 445–456

Hajj B, Wisniewski J, Beheiry ME, Chen J, Revyakin A, Wu C & Dahan M (2014) Whole-cell, multicolor superresolution imaging using volumetric multifocus microscopy. *PNAS* **111:** 17480–17485

Hao X, Antonello J, Allgeyer ES, Bewersdorf J & Booth MJ (2017) Aberrations in 4Pi Microscopy. *Optics Express* **25:** 14049

Harner M, Körner C, Walther D, Mokranjac D, Kaesmacher J, Welsch U, Griffith J, Mann M, Reggiori F & Neupert W (2011) The mitochondrial contact site complex, a determinant of mitochondrial architecture. *The EMBO Journal* **30:** 4356–4370

Hekman C, Tomich JM & Hatefi Y (1991) Mitochondrial ATP synthase complex. Membrane topography and stoichiometry of the F0 subunits. *J. Biol. Chem.* **266:** 13564–13571

Hell S & Stelzer EHK (1992) Properties of a 4Pi confocal fluorescence microscope. *J. Opt. Soc. Am. A, JOSAA* **9:** 2159–2166

Hell SW & Nagorni M (1998) 4Pi confocal microscopy with alternate interference. *Opt. Lett., OL* **23:** 1567–1569

Hell SW & Wichmann J (1994) Breaking the diffraction resolution limit by stimulated emission: stimulated-emission-depletion fluorescence microscopy. *Optics Letters* **19:** 780

Hess ST, Girirajan TPK & Mason MD (2006) Ultra-High Resolution Imaging by Fluorescence Photoactivation Localization Microscopy. *Biophysical Journal* **91:** 4258–4272

Hessenberger M, Zerbes RM, Rampelt H, Kunz S, Xavier AH, Purfürst B, Lilie H, Pfanner N, van der Laan M & Daumke O (2017) Regulated membrane remodeling by Mic60 controls formation of mitochondrial crista junctions. *Nature Communications* **8:** 15258

Hoppins S, Collins SR, Cassidy-Stone A, Hummel E, DeVay RM, Lackner LL, Westermann B, Schuldiner M, Weissman JS & Nunnari J (2011) A mitochondrial-focused genetic interaction map reveals a scaffold-like complex required for inner membrane organization in mitochondria. *J Cell Biol* **195:** 323–340

Hu YS, Zimmerley M, Li Y, Watters R & Cang H (2014) Single-Molecule Super-Resolution Light-Sheet Microscopy. *ChemPhysChem* **15:** 577–586

Huang B, Jones SA, Brandenburg B & Zhuang X (2008a) Whole-cell 3D STORM reveals interactions between cellular structures with nanometer-scale resolution. *Nature Methods* **5:** 1047–1052

Huang B, Wang W, Bates M & Zhuang X (2008b) Three-Dimensional Super-Resolution Imaging by Stochastic Optical Reconstruction Microscopy. *Science* **319:** 810–813

Huang F, Sirinakis G, Allgeyer ES, Schroeder LK, Duim WC, Kromann EB, Phan T, Rivera-Molina FE, Myers JR, Irnov I, Lessard M, Zhang Y, Handel MA, Jacobs-Wagner C, Lusk CP, Rothman JE, Toomre D, Booth MJ & Bewersdorf J (2016) Ultra-High Resolution 3D Imaging of Whole Cells. *Cell* **166:** 1028–1040

Huang X, Fan J, Li L, Liu H, Wu R, Wu Y, Wei L, Mao H, Lal A, Xi P, Tang L, Zhang Y, Liu Y, Tan S & Chen L (2018) Fast, long-term, super-resolution imaging with Hessian structured illumination microscopy. *Nature Biotechnology* **36:** 451–459

Huisken J, Swoger J, Bene FD, Wittbrodt J & Stelzer EHK (2004) Optical Sectioning Deep Inside Live Embryos by Selective Plane Illumination Microscopy. *Science* **305:** 1007–1009

Huynen MA, Mühlmeister M, Gotthardt K, Guerrero-Castillo S & Brandt U (2016) Evolution and structural organization of the mitochondrial contact site (MICOS) complex and the mitochondrial intermembrane space bridging (MIB) complex. *Biochimica et Biophysica Acta (BBA) - Molecular Cell Research* **1863:** 91–101

Ikon N & Ryan RO (2017) Cardiolipin and mitochondrial cristae organization. *Biochimica et Biophysica Acta (BBA) - Biomembranes* **1859:** 1156–1163

Ishihara N, Eura Y & Mihara K (2004) Mitofusin 1 and 2 play distinct roles in mitochondrial fusion reactions via GTPase activity. *Journal of Cell Science* **117:** 6535–6546

Jakobs S & Wurm CA (2014) Super-resolution microscopy of mitochondria. *Current Opinion in Chemical Biology* **20:** 9–15

Jans DC, Wurm CA, Riedel D, Wenzel D, Stagge F, Deckers M, Rehling P & Jakobs S (2013a) STED super-resolution microscopy reveals an array of MINOS clusters along human mitochondria. *PNAS* **110:** 8936–8941

Jans DC, Wurm CA, Riedel D, Wenzel D, Stagge F, Deckers M, Rehling P & Jakobs S (2013b) STED super-resolution microscopy reveals an array of MINOS clusters along human mitochondria. *PNAS* **110:** 8936–8941

Jaqaman K, Loerke D, Mettlen M, Kuwata H, Grinstein S, Schmid SL & Danuser G (2008) Robust single-particle tracking in live-cell time-lapse sequences. *Nat Methods* **5:** 695–702

Jiko C, Davies KM, Shinzawa-Itoh K, Tani K, Maeda S, Mills DJ, Tsukihara T, Fujiyoshi Y, Kühlbrandt W & Gerle C (2015) Bovine F1Fo ATP synthase monomers bend the lipid bilayer in 2D membrane crystals. *eLife* Available at: https://elifesciences.org/articles/06119 [Accessed March 12, 2020]

Juette MF, Gould TJ, Lessard MD, Mlodzianoski MJ, Nagpure BS, Bennett BT, Hess ST & Bewersdorf J (2008) Three-dimensional sub–100 nm resolution fluorescence microscopy of thick samples. *Nature Methods* **5:** 527–529

Kim SY, Gitai Z, Kinkhabwala A, Shapiro L & Moerner WE (2006) Single molecules of the bacterial actin MreB undergo directed treadmilling motion in Caulobactercrescentus. *PNAS* **103:** 10929–10934

Kondadi AK, Anand R, Hänsch S, Urbach J, Zobel T, Wolf DM, Segawa M, Liesa M, Shirihai OS, Weidtkamp-Peters S & Reichert AS (2020) Cristae undergo continuous cycles of membrane remodelling in a MICOS-dependent manner. *EMBO reports* **n/a:** e49776

Kutik S, Guiard B, Meyer HE, Wiedemann N & Pfanner N (2007) Cooperation of translocase complexes in mitochondrial protein import. *The Journal of Cell Biology* **179:** 585–591

Laan MVD, Rissler M & Rehling P (2006) Mitochondrial preprotein translocases as dynamic molecular machines. *FEMS Yeast Research* **6:** 849–861

Lapuente-Brun E, Moreno-Loshuertos R, Acín-Pérez R, Latorre-Pellicer A, Colás C, Balsa E, Perales-Clemente E, Quirós PM, Calvo E, Rodríguez-Hernández MA, Navas P, Cruz R, Carracedo Á, López-Otín C, Pérez-Martos A, Fernández-Silva P, Fernández-Vizarra E & Enríquez JA (2013) Supercomplex Assembly Determines Electron Flux in the Mitochondrial Electron Transport Chain. *Science* **340:** 1567–1570

Letts JA, Fiedorczuk K & Sazanov LA (2016) The architecture of respiratory supercomplexes. *Nature* **537:** 644–648

Manley S, Gillette JM & Lippincott-Schwartz J (2010) Single-Particle Tracking Photoactivated Localization Microscopy for Mapping Single-Molecule Dynamics. *Methods Enzymol* **475:** 109–120

Manley S, Gillette JM, Patterson GH, Shroff H, Hess HF, Betzig E & Lippincott-Schwartz J (2008) High-density mapping of single-molecule trajectories with photoactivated localization microscopy. *Nature Methods* **5:** 155–157

Meyer B, Wittig I, Trifilieff E, Karas M & Schägger H (2007) Identification of Two Proteins Associated with Mammalian ATP Synthase. *Molecular & Cellular Proteomics* **6:** 1690–1699

Michaud M, Gros V, Tardif M, Brugière S, Ferro M, Prinz WA, Toulmay A, Mathur J, Wozny M, Falconet D, Maréchal E, Block MA & Jouhet J (2016) AtMic60 Is Involved in Plant Mitochondria Lipid Trafficking and Is Part of a Large Complex. *Current Biology* **26:** 627–639

Minauro-Sanmiguel F, Wilkens S & García JJ (2005) Structure of dimeric mitochondrial ATP synthase: Novel F0 bridging features and the structural basis of mitochondrial cristae biogenesis. *PNAS* **102:** 12356–12358

Mitchell P (1961) Coupling of Phosphorylation to Electron and Hydrogen Transfer by a Chemi-Osmotic type of Mechanism. *Nature* **191:** 144

Mitchell P & Moyle J (1967) Chemiosmotic Hypothesis of Oxidative Phosphorylation. *Nature* **213:** 137–139

Mühleip AW, Joos F, Wigge C, Frangakis AS, Kühlbrandt W & Davies KM (2016) Helical arrays of U-shaped ATP synthase dimers form tubular cristae in ciliate mitochondria. *PNAS* **113:** 8442–8447

Neupert W & Herrmann JM (2007) Translocation of proteins into mitochondria. *Annu. Rev. Biochem.* **76:** 723–749

Okuno D, Iino R & Noji H (2011) Rotation and structure of FoF1-ATP synthase. *J Biochem* **149:** 655–664

Otera H, Wang C, Cleland MM, Setoguchi K, Yokota S, Youle RJ & Mihara K (2010) Mff is an essential factor for mitochondrial recruitment of Drp1 during mitochondrial fission in mammalian cells. *J Cell Biol* **191:** 1141–1158

Ott C, Ross K, Straub S, Thiede B, Götz M, Goosmann C, Krischke M, Mueller MJ, Krohne G, Rudel T & Kozjak-Pavlovic V (2012) Sam50 Functions in Mitochondrial Intermembrane Space Bridging and Biogenesis of Respiratory Complexes. *Molecular and Cellular Biology* **32:** 1173–1188

Paumard P, Vaillier J, Coulary B, Schaeffer J, Soubannier V, Mueller DM, Brèthes D, di Rago J-P & Velours J (2002) The ATP synthase is involved in generating mitochondrial cristae morphology. *The EMBO Journal* **21:** 221–230

Pelicano H, Martin DS, Xu R-H & Huang P (2006) Glycolysis inhibition for anticancer treatment. *Oncogene* **25:** 4633–4646

Pfanner N, Laan M van der, Amati P, Capaldi RA, Caudy AA, Chacinska A, Darshi M, Deckers M, Hoppins S, Icho T, Jakobs S, Ji J, Kozjak-Pavlovic V, Meisinger C, Odgren PR, Park SK, Rehling P, Reichert AS, Sheikh MS, Taylor SS, et al (2014) Uniform nomenclature for the mitochondrial contact site and cristae organizing system. *J Cell Biol* **204:** 1083–1086

Pfanner N, Wiedemann N, Meisinger C & Lithgow T (2004) Assembling the mitochondrial outer membrane. *Nature Structural & Molecular Biology* **11:** 1044–1048

Pham TD, Pham PQ, Li J, Letai AG, Wallace DC & Burke PJ (2016) Cristae remodeling causes acidification detected by integrated graphene sensor during mitochondrial outer membrane permeabilization. *Sci Rep* **6:** 1–12

Pickrell AM & Youle RJ (2015) The Roles of PINK1, Parkin, and Mitochondrial Fidelity in Parkinson's Disease. *Neuron* **85:** 257–273

Rabl R, Soubannier V, Scholz R, Vogel F, Mendl N, Vasiljev-Neumeyer A, Körner C, Jagasia R, Keil T, Baumeister W, Cyrklaff M, Neupert W & Reichert AS (2009) Formation of cristae and crista junctions in mitochondria depends on antagonism between Fcj1 and Su e/g. *The Journal of Cell Biology* **185:** 1047–1063

Ram S, Prabhat P, Ward ES & Ober RJ (2009) Improved single particle localization accuracy with dual objective multifocal plane microscopy. *Opt. Express, OE* **17:** 6881–6898

Rampelt H, Bohnert M, Zerbes RM, Horvath SE, Warscheid B, Pfanner N & van der Laan M (2017) Mic10, a Core Subunit of the Mitochondrial Contact Site and Cristae Organizing System, Interacts with the Dimeric F1Fo-ATP Synthase. *Journal of Molecular Biology* **429:** 1162–1170

Rampelt H, Wollweber F, Gerke C, de Boer R, van der Klei IJ, Bohnert M, Pfanner N & van der Laan M (2018) Assembly of the Mitochondrial Cristae Organizer Mic10 Is Regulated by Mic26-Mic27 Antagonism and Cardiolipin. *J. Mol. Biol.* **430:** 1883–1890

Rieger B, Junge W & Busch KB (2014b) Lateral pH gradient between OXPHOS complex IV and F_0F_1 ATP-synthase in folded mitochondrial membranes. *Nature Communications* **5:** 3103

Rust MJ, Bates M & Zhuang X (2006) Sub-diffraction-limit imaging by stochastic optical reconstruction microscopy (STORM). *Nature Methods* **3:** 793–796

Sahl SJ, Hell SW & Jakobs S (2017) Fluorescence nanoscopy in cell biology. *Nature Reviews Molecular Cell Biology* **18:** 685–701

Salewskij K, Rieger B, Hager F, Arroum T, Duwe P, Villalta J, Colgiati S, Richter CP, Psathaki OE, Enriquez JA, Dellmann T & Busch KB (2020) The spatio-temporal organization of mitochondrial F1FO ATP synthase in cristae depends on its activity mode. *Biochimica et Biophysica Acta (BBA) - Bioenergetics* **1861:** 148091

Scherer WF, Syverton JT & Gey GO (1953) Studies on the Propagation in Vitro of Poliomyelitis Viruses: Iv. Viral Multiplication in a Stable Strain of Human Malignant Epithelial Cells (strain Hela) Derived from an Epidermoid Carcinoma of the Cervix. *Journal of Experimental Medicine* **97:** 695–710

Schlame M & Ren M (2009) The role of cardiolipin in the structural organization of mitochondrial membranes. *Biochimica et Biophysica Acta (BBA) - Biomembranes* **1788:** 2080–2083

Schütz GJ, Trabesinger W & Schmidt T (1998) Direct observation of ligand colocalization on individual receptor molecules. *Biophys J* **74:** 2223–2226

Seelert H, Dani DN, Dante S, Hauß T, Krause F, Schäfer E, Frenzel M, Poetsch A, Rexroth S, Schwaßmann HJ, Suhai T, Vonck J & Dencher NA (2009) From protons to OXPHOS supercomplexes and Alzheimer's disease: Structure–dynamics–function relationships of energy-transducing membranes. *Biochimica et Biophysica Acta (BBA) - Bioenergetics* **1787:** 657–671

Shao L, Kner P, Rego EH & Gustafsson MGL (2011) Super-resolution 3D microscopy of live whole cells using structured illumination. *Nature Methods* **8:** 1044–1046

Shen H, Tauzin LJ, Baiyasi R, Wang W, Moringo N, Shuang B & Landes CF (2017) Single Particle Tracking: From Theory to Biophysical Applications. *Chem. Rev.* **117:** 7331–7376

Shtengel G, Galbraith JA, Galbraith CG, Lippincott-Schwartz J, Gillette JM, Manley S, Sougrat R, Waterman CM, Kanchanawong P, Davidson MW, Fetter RD & Hess HF (2009) Interferometric fluorescent super-resolution microscopy resolves 3D cellular ultrastructure. *PNAS* **106:** 3125–3130

Soubannier V, Rusconi F, Vaillier J, Arselin G, Chaignepain S, Graves P-V, Schmitter J-M, Zhang JL, Mueller D & Velours J (1999) The Second Stalk of the Yeast ATP Synthase Complex: Identification of Subunits Showing Cross-Links with Known Positions of Subunit 4 (Subunit b). *Biochemistry* **38:** 15017–15024

Soubannier V, Vaillier J, Paumard P, Coulary B, Schaeffer J & Velours J (2002) In the Absence of the First Membrane-spanning Segment of Subunit4(b), the Yeast ATP Synthase Is Functional but Does Not Dimerize or Oligomerize. *J. Biol. Chem.* **277:** 10739–10745

Stephan T, Roesch A, Riedel D & Jakobs S (2019) Live-cell STED nanoscopy of mitochondrial cristae. *Scientific Reports* **9:** Available at: http://www.nature.com/articles/s41598-019-48838-2 [Accessed October 16, 2019]

Stock D, Gibbons C, Arechaga I, Leslie AGW & Walker JE (2000) The rotary mechanism of ATP synthase. *Current opinion in structural biology*

Sukhorukov VM & Bereiter-Hahn J (2009) Anomalous Diffusion Induced by Cristae Geometry in the Inner Mitochondrial Membrane. *PLOS ONE* **4:** e4604

Sukhorukov VM, Dikov D, Busch K, Strecker V, Wittig I & Bereiter-Hahn J (2010) Determination of protein mobility in mitochondrial membranes of living cells. *Biochimica et Biophysica Acta (BBA) - Biomembranes* **1798:** 2022–2032

Szeto HH (2014) First-in-class cardiolipin-protective compound as a therapeutic agent to restore mitochondrial bioenergetics. *British Journal of Pharmacology* **171:** 2029–2050

Thompson MA, Casolari JM, Badieirostami M, Brown PO & Moerner WE (2010) Three-dimensional tracking of single mRNA particles in Saccharomyces cerevisiae using a double-helix point spread function. *Proceedings of the National Academy of Sciences* **107:** 17864–17871

Tokunaga M, Imamoto N & Sakata-Sogawa K (2008) Highly inclined thin illumination enables clear single-molecule imaging in cells. *Nature Methods* **5:** 159–161

Tomasetig L, Di Pancrazio F, Harris DA, Mavelli I & Lippe G (2002) Dimerization of F0F1ATP synthase from bovine heart is independent from the binding of the inhibitor protein IF1. *Biochimica et Biophysica Acta (BBA) - Bioenergetics* **1556:** 133–141

Ueno H, Suzuki T, Kinosita K & Yoshida M (2005) ATP-driven stepwise rotation of FoF1-ATP synthase. *PNAS* **102:** 1333–1338

Vogel F, Bornhövd C, Neupert W & Reichert AS (2006) Dynamic subcompartmentalization of the mitochondrial inner membrane. *J Cell Biol* **175:** 237–247

van der Laan M, Horvath SE & Pfanner N (2016) Mitochondrial contact site and cristae organizing system. *Curr. Opin. Cell Biol.* **41:** 33–42

von Diezmann A, Shechtman Y & Moerner WE (2017) Three-Dimensional Localization of Single Molecules for Super-Resolution Imaging and Single-Particle Tracking. *Chem. Rev.* **117:** 7244–7275

von der Malsburg K, Müller JM, Bohnert M, Oeljeklaus S, Kwiatkowska P, Becker T, Loniewska-Lwowska A, Wiese S, Rao S, Milenkovic D, Hutu DP, Zerbes RM, Schulze-Specking A, Meyer HE, Martinou J-C, Rospert S, Rehling P, Meisinger C, Veenhuis M, Warscheid B, et al (2011) Dual Role of Mitofilin in Mitochondrial Membrane Organization and Protein Biogenesis. *Developmental Cell* **21:** 694–707

Wagner K, Rehling P, Sanjuán Szklarz LK, Taylor RD, Pfanner N & van der Laan M (2009) Mitochondrial F1Fo-ATP Synthase: The Small Subunits e and g Associate with Monomeric Complexes to Trigger Dimerization. *Journal of Molecular Biology* **392:** 855–861

Walker JE (1998) ATP Synthesis by Rotary Catalysis (Nobel lecture). *Angewandte Chemie International Edition* **37:** 2308–2319

Walker JE, Runswick MJ & Saraste M (1982) Subunit equivalence in Escherichia coli and bovine heart mitochondrial F1F0 ATPases. *FEBS Letters* **146:** 393–396

Watt IN, Montgomery MG, Runswick MJ, Leslie AGW & Walker JE (2010) Bioenergetic cost of making an adenosine triphosphate molecule in animal mitochondria. *PNAS* **107:** 16823–16827

Wildanger D, Patton BR, Schill H, Marseglia L, Hadden JP, Knauer S, Schönle A, Rarity JG, O'Brien JL, Hell SW, Smith JM (2012) Solid Immersion Facilitates Fluorescence Microscopy with Nanometer Resolution and Sub-Ångström Emitter Localization. *Adv.Mater.* **24**, OP309–OP313

Wilkens V (2012) Spatio-temporal organization of single membrane proteins in distinct microcompartments of dynamic mitochondria in mammalian cells, Dissertation, University of Osnabrück

Wilkens V, Kohl W & Busch K (2013) Restricted diffusion of OXPHOS complexes in dynamic mitochondria delays their exchange between cristae and engenders a transitory mosaic distribution. *J Cell Sci* **126:** 103–116

Wilmes S, Beutel O, Li Z, Francois-Newton V, Richter CP, Janning D, Kroll C, Hanhart P, Hötte K, You C, Uzé G, Pellegrini S & Piehler J (2015) Receptor dimerization dynamics as a regulatory valve for plasticity of type I interferon signaling. *The Journal of Cell Biology* **209:** 579–593

Wittig I, Velours J, Stuart R & Schägger H (2008) Characterization of Domain Interfaces in Monomeric and Dimeric ATP Synthase. *Molecular & Cellular Proteomics* **7:** 995–1004

Wolf DM, Segawa M, Kondadi AK, Anand R, Bailey ST, Reichert AS, van der Bliek AM, Shackelford DB, Liesa M & Shirihai OS (2019) Individual cristae within the same mitochondrion display different membrane potentials and are functionally independent. *The EMBO Journal* **n/a:** e101056

Xie J, Marusich MF, Souda P, Whitelegge J & Capaldi RA (2007) The mitochondrial inner membrane protein Mitofilin exists as a complex with SAM50, metaxins 1 and 2, coiled-coil-helix coiled-coil-helix domain-containing protein 3 and 6 and DnaJC11. *FEBS Letters* **581:** 3545–3549

Yamaguchi R, Janssen E, Perkins G, Ellisman M, Kitada S & Reed JC (2011) Efficient Elimination of Cancer Cells by Deoxyglucose-ABT-263/737 Combination Therapy. *PLOS ONE* **6:** e24102

You C, Marquez-Lago TT, Richter CP, Wilmes S, Moraga I, Garcia KC, Leier A & Piehler J (2016) Receptor dimer stabilization by hierarchical plasma membrane microcompartments regulates cytokine signaling. *Sci Adv* **2:** Available at: https://www.ncbi.nlm.nih.gov/pmc/articles/PMC5135388/ [Accessed December 20, 2019]

Zorova LD, Popkov VA, Plotnikov EY, Silachev DN, Pevzner IB, Jankauskas SS, Babenko VA, Zorov SD, Balakireva AV, Juhaszova M, Sollott SJ & Zorov DB (2018) Mitochondrial membrane potential. *Anal Biochem* **552:** 50–59

15 Statutory Declaration

This thesis was compiled in the School of Biology / Chemistry at the University of Osnabrück, in the research group of Prof. Dr. Jacob Piehler

I declare that I have developed and written the enclosed dissertation completely by myself, and have not used sources or means without declaration in the text. Any thoughts from others or literal quotations are clearly marked. The dissertation was not used in the same or in a similar version to achieve an academic grading at the University of Osnabrück or another comparable college or university and is not being published elsewhere.

Osnabrück,

Timo Dellmann

16 Acknowledgement

First of all, I would like to thank Prof. Dr. Jacob Piehler for giving me the opportunity to work on SPT of mitochondrial proteins and to establish 3D TALM, in his research group.

Next, I would like to thank Prof. Dr. Karin B. Busch for her valuable advices and making it possible to finish my doctorate in Osnabrück. I am really grateful for the constant support and the nice working atmosphere. Thanks for giving me the responsibility of the TIRF microscopes.

I feel grand gratitude for the exchange of knowledge with Dr. Rainer Kurre. Thank you for helping me with the 3D tracking software, the constant and excellence support on the microscopes and helping me setting up the TIRF microscope in Prof. Dr. Karin B. Buschs laboratory. Thank you for being a member of my thesis committee.

My very special thanks go to Dr. Christian P. Richter, as the majority of the used softwares was implemented or even written by him. Thank you, Christian, for the helpful software to align the cylindrical lens and writing the software MitoOrientedDynamics.

I like to thank Dr. Christop Drees, Maximillian Hafer and Tim Wedeking for the inspiring discussions.

Furthermore, I like to thank all the lab members in Karins laboratory. Espacially, Patrick, Kirill and Frances. Thank you for making the lab life easy and efficient.

Finally, I would like to thank my wife and my son for their constant support. Thank you Svenja you were solid as a rock when the tide was strong. Thank you Jannes for making me laugh and showing me what is really important in life.